UNDERSTANDING AND MODELING THE BEHAVIOR OF A HARMONIC DRIVE GEAR TRANSMISSION

BY

TIMOTHY DOUGLAS TUTTLE

B. S., MASSACHUSETTS INSTITUTE OF TECHNOLOGY
(MAY 1990)

SUBMITTED TO THE DEPARTMENT OF MECHANICAL ENGINEERING
IN PARTIAL FULFILLMENT OF THE REQUIREMENTS FOR THE DEGREE OF

MASTER OF SCIENCE
IN MECHANICAL ENGINEERING

AT THE

MASSACHUSETTS INSTITUTE OF TECHNOLOGY

MAY 1992

SIGNATURE OF AUTHOR _____
DEPARTMENT OF MECHANICAL ENGINEERING
MAY 1, 1992

CERTIFIED BY _____
PROFESSOR WARREN P. SEERING
THESIS SUPERVISOR

ACCEPTED BY _____
AIN. A. SONIN
CHAIRMAN, DEPARTMENTAL GRADUATE COMMITTEE

UNDERSTANDING AND MODELING THE BEHAVIOR OF A HARMONIC DRIVE GEAR TRANSMISSION

BY
TIMOTHY DOUGLAS TUTTLE

SUBMITTED TO THE DEPARTMENT OF MECHANICAL ENGINEERING ON MAY 8, 1992
IN PARTIAL FULFILLMENT OF THE REQUIREMENTS FOR THE DEGREE OF
MASTER OF SCIENCE IN MECHANICAL ENGINEERING

ABSTRACT

As harmonic-drive transmissions find increased use and acceptance among engineers and designers, the demand for an accurate and reliable understanding of harmonic-drive operating behavior becomes great. Additionally, for applications such as robot control that require precise mathematical models, representations that can describe the dynamic performance of harmonic drives are also required. My research explores the operation of harmonic-drive transmissions through experimental investigation and analyzes modeling strategies that can be used predict this observed behavior.

In my experimental examination, I characterized the magnitude and typical behavior of several important transmission properties. In particular, kinematic error was confirmed to appear primarily at frequencies that were multiples of the wave-generator rotational velocity, and static stiffness measurements were found to yield non-linear profiles that were corrupted by transmission friction. Additional measurements of static and dynamic friction demonstrated that energy dissipation in harmonic drives varies non-linearly with velocity and periodically with rotation and can escalate during system resonance. Following this investigation of individual properties, step-response data were collected which revealed surprisingly agitated transmission behavior. Specifically, due to the problematic influence of system resonance in typical harmonic-drive operating ranges, dynamic-response results demonstrated violent torque and velocity fluctuations as well as sudden unexpected increases in rotational velocity. Using the understanding of transmission properties gained from experimental analysis, this unusual dynamic behavior was rationalized.

In my theoretical analysis, five different models were developed to describe harmonic-drive operation. First, an ideal transmission representation was implemented that showed very poor performance under dynamic conditions. When non-linear frictional losses were appended to this ideal representation, model integrity improved. In order capture the important influence of resonant vibration on system performance, non-linear compliance and kinematic error were introduced into the harmonic-drive representation. The resulting model demonstrated resonant frequencies and resulting vibrations close to experimental observations but remained ignorant of the enhanced frictional losses at resonance. By developing a simplified geometric representation of gear-tooth meshing that included Coulomb friction at the gear-tooth interface, the elusive resonance losses were replicated and model performance improved. Although this meshing model failed to capture the subtleties of harmonic-drive operation at resonance, its close conceptual relationship to actual gear tooth behavior will make it a valuable tool for rapid estimation and theoretical contemplation.

Research Supervisor: Dr. Warren P. Seering
Professor of Mechanical Engineering

Since I came to MIT, I have worked with many people who have influenced my outlook and attitude. I have been fortunate. With rare exceptions, the people I have met have displayed consistently both compassion and conviction. They have shared their strengths and have made me stronger. It is through their example that I have learned my obligation to contribute no less to the future than I have received and will receive.

For their positive influence on my work in this document I want to acknowledge

Warren Seering
Whit Rappole
Mimi
Trevor
Brian Avery
Andrew Christian
Tina
Andrew
Mike Caine
Ben
Rocky
Lukas Rueker
Ken Chang
Eric Vaaler
George
Cindy
Sarath Krishnaswami
Jim Hyde
Mom and Dad

It was fun.

This report describes work done at the Artificial Intelligence Laboratory at the Massachusetts Institute of Technology. Funding for this research was provided by NASA Goddard Space Flight Center through the University of Iowa, contract number V80380.

Table of Contents

List of Figures

List of Tables

Chapter 1: Introduction

A good mechanical designer holds a clear awareness of the capabilities and limitations of his design. For most designers, this awareness rests heavily on a firm understanding of the individual components that comprise the entire assembly. For mechanical systems employing harmonic drives, a designer can gain confidence in the performance of the overall mechanism if the operation of the harmonic drive is clearly understood. Additionally, for applications, such as robot control, which require mathematical models to describe system performance, a thorough understanding of the behavior of harmonic-drive transmissions is essential. The purpose of my investigation is to identify important attributes that influence the operation of harmonic-drive transmissions and to relate these attributes to overall dynamic behavior. On the basis of insight gained from this empirical analysis, I hope to develop mathematical models that can be used to predict reliably the dynamic performance of harmonic-drive transmissions.

I began my investigation of harmonic-drives with an experimental analysis of kinematic, static, and dynamic behavior. In particular, I recorded and analyzed kinematic position error, compliance, and frictional losses in the transmission. From these results I discovered that friction and flexibility in the harmonic drives can be highly non-linear and very sensitive to changes in environmental and operating conditions. Because of these poorly behaved transmission properties, the dynamic response of the transmission was often equally erratic and unpredictable. Specifically, operation in regions that excited system resonance bred significant energy losses and surprisingly turbulent behavior. Despite the complexity of these experimental observations, I undertook to develop simple harmonic-drive representations to describe the discovered behavior. In total, five different models were derived and evaluated to illustrate the range of accuracy that could be delivered by harmonic-drive representations of varied complexity. From these models, the importance of friction, compliance, and kinematic-error on model performance was emphasized as was the importance of gear-tooth meshing geometry in the transmission.

Results from these models were encouraging and informative, but more detailed representations are required to capture fully the subtleties of harmonic-drive behavior.

In this document, I will describe completely the results of my experimental and theoretical analysis of harmonic drives. I will begin this presentation with a summary of existing research that is related to my investigation. Second, I will display and discuss the results of my experimental inquiry into important transmission properties and dynamic response. Third, I will develop several theoretical models to describe the observed behavior, and last, I will offer conclusions and recommendations to guide future work.

1.1 The Harmonic Drive

Since its conception by Walt Musser in 1955, the harmonic drive has found widespread use and acceptance among mechanical designers. This nascent mechanical transmission, occasionally labeled "strain-wave gearing", employs a continuous deflection wave along a non-rigid gear to allow gradual engagement of gear teeth. Because of this unconventional gear-tooth meshing action, harmonic drives can deliver very high reduction ratios in a very small package. As a peripheral consequence, the radical mechanical operation of this gear train defies conventional understanding of gear behavior and creates a new arena for exploration and understanding. Following this impetus for investigation, several independent researchers have made valuable contributions to the state of harmonic-drive technology in the past thirty years. In addition to surveying the operational principles and utility of harmonic transmissions, this section will attempt to present a brief yet broad summary of existing research insights related to my investigation.

1.1.1 The Principles of Operation

Every harmonic drive is composed of the three distinct parts illustrated in figure 1.1: the wave-generator, the flexspline, and the circular spline. The wave-generator is a ball-bearing assembly with a rigid, elliptical inner-race and a flexible, thin-walled outer race. The flexspline is a thin-walled, flexible cup adorned with small, external gear teeth around its rim. When assembled, the wave-generator is nested inside the flexspline, causing the flexible gear-tooth circumference on the flexspline to adopt the elliptical profile

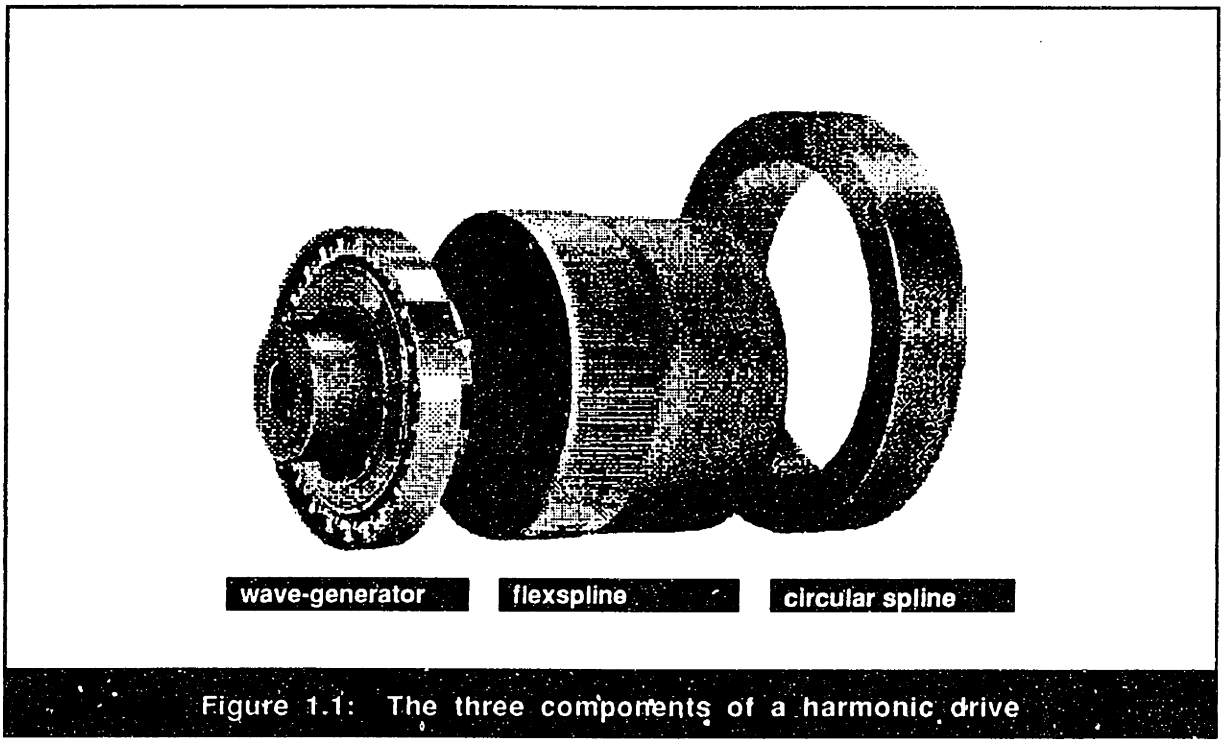

Figure 1.1: The three components of a harmonic drive

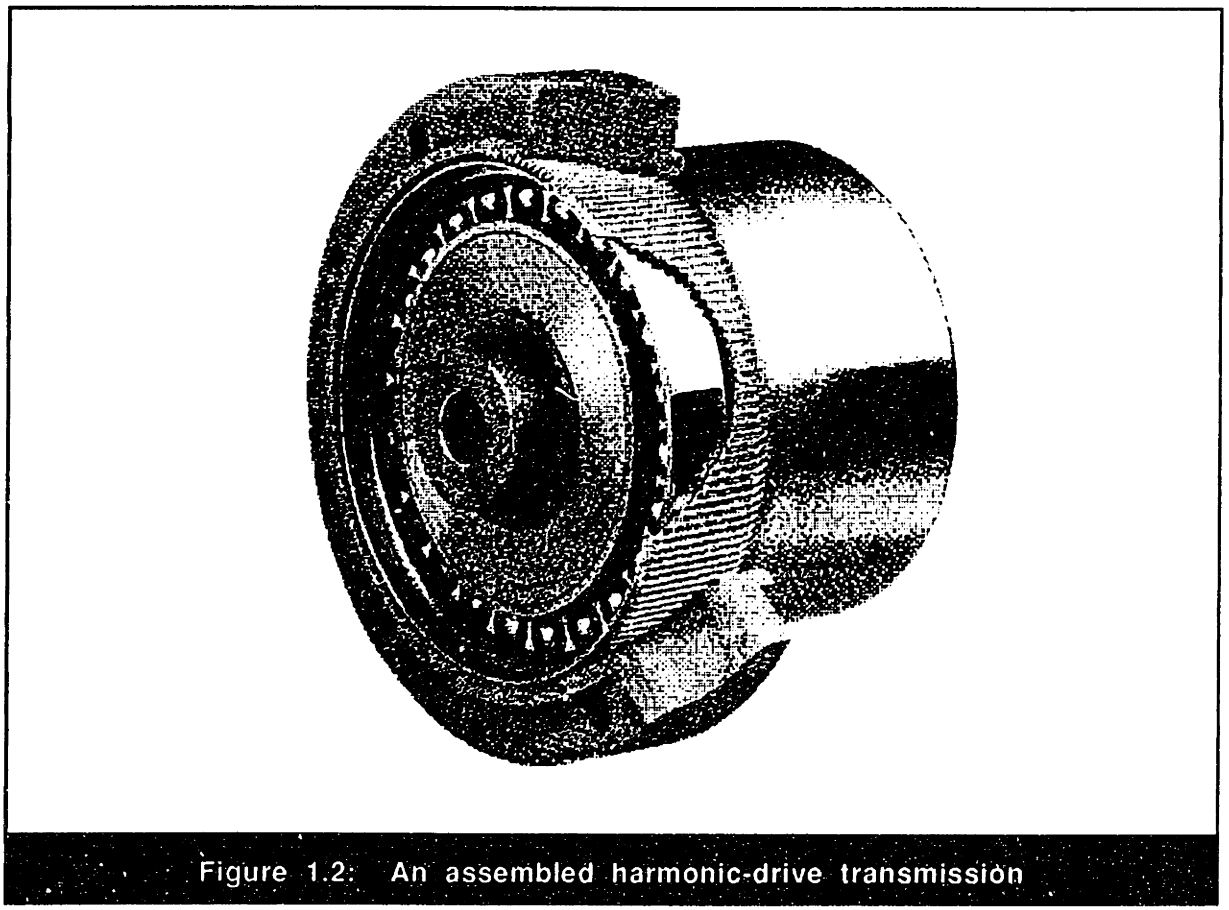

Figure 1.2: An assembled harmonic-drive transmission

of the wave-generator. The circular spline is a rigid ring with internal teeth machined along a slightly larger pitch diameter than those of the flexspline. When the flexspline-and-wave-generator assembly is inserted into the circular spline, the external teeth on the flexspline mesh with the internal teeth on the circular spline along the major axis of the wave-generator ellipse. A correctly assembled harmonic drive with a cut-away section is shown in figure 1.2.

If properly assembled, all three components of the transmission can rotate at different but coupled velocities on the same axis. The rotational mechanism, as illustrated in figure 1.3, begins when rotation of the wave-generator carries the zone of gear-tooth engagement with its major axis. When this zone is propagated 180° around the circumference of the circular spline, the flexspline, which contains two fewer teeth than the circular spline, will lag by one tooth relative to the circular spline. Through this gradual and continuous engagement of slightly offset gear teeth, every rotation of the wave-generator moves the flexspline two teeth back on the circular spline. Through this unconventional mechanism, gear ratios up to 320:1 can be achieved in a single transmission.

Since the harmonic drive has three rotational ports, it boasts a versatility unavailable to standard gear transmissions. Specifically, in its most popular configuration, the circular spline is fixed to ground and a low-torque, high-speed motor driving the wave-generator can produce high-torque, low-speed rotation on the flexspline. Similarly, with the flexspline mounted to ground, the torque on the wave-generator can be magnified and transmitted through the circular spline. If either the circular spline or flexspline is used as an input, the wave-generator can be driven at high velocities and low torques. In general, by using different combinations of rotations on the three harmonic-drive components, numerous differential-gearing functions and reduction ratios can be achieved.

1.1.2 Performance Features and Applicability

Currently, commercial harmonic drives are manufactured by two companies: The Harmonic Drive Machinery Group in Wakefield, MA, USA, and Harmonic Drive Systems, Incorporated, in Tokyo, Japan. Available harmonic drive products include the standard cup-type gearing, pancake transmissions, housed units, and motor-driven motion-control systems. Typical gear ratios of commercial drives range from 50:1 to 320:1, and

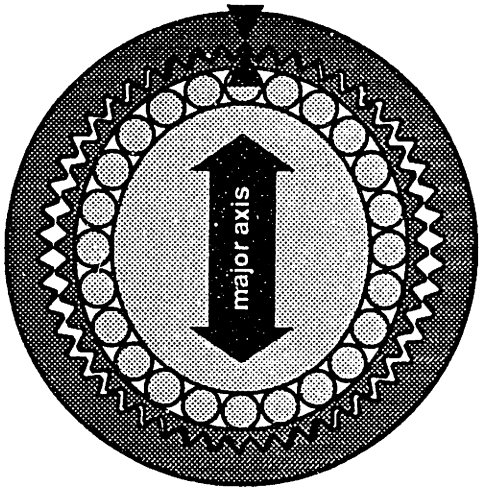

Initially, the flexpline and circular-spline gear-teeth are aligned.

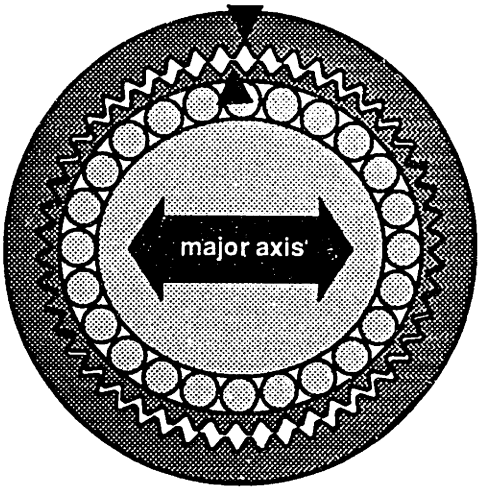

After a 90° rotation of the wave-generator, the flexspline tooth has moved a half-tooth back on the circular spline.

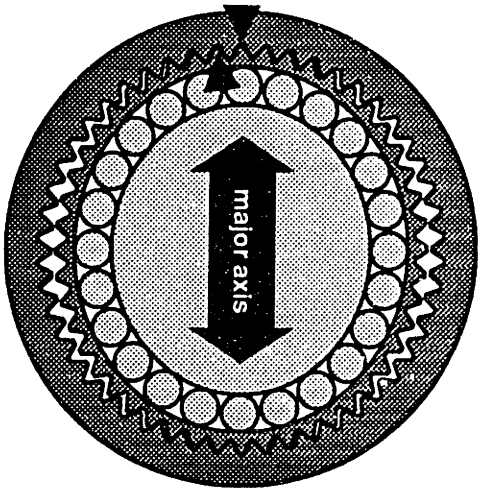

After a 180° rotation of the wave-generator, the flexspline tooth has moved one tooth back on the circular spline.

Figure 1.3: The harmonic-drive operating mechanism

efficiencies can approach 90 percent. The smallest transmissions can provide a respectable maximum torque output of about 3.5 N-m (30.0 in-lbs), while the heavy-duty units boast up to 10,000 N-m (89,000 in-lbs) of torque capacity.

Because of its unique operating principles, the harmonic drive displays performance features both superior and inferior to conventional gear transmissions. These advantages and disadvantages are itemized in Table 1.1 and Table 1.2.

The unique performance features of the harmonic drive have captured the attention of designers in many fields. Specifically, due to their accuracy and simple construction,

Table 1.1: Performance advantages of harmonic-drive transmissions

High torque capacity	Since torque is transmitted through multiple-tooth contact, harmonic drives can withstand high loads at small pitch-diameters.
Concentric geometry	Since all three harmonic-drive components are concentric and coaxial, designers can drastically reduce power-train size and complexity.
Lightweight and compact design	Requiring only three basic elements, the harmonic drive can deliver extremely high gear ratios in a small package.
Zero backlash	Natural gear preloading and predominantly radial tooth-engagement eliminate virtually all transmission backlash.
High Efficiency	If properly lubricated, typical efficiencies of harmonic-drive transmissions can reach 80 to 90 percent.
Backdrivability	Due to their high efficiency, wave-generator rotation can be driven through the flexspline or circular spline.

Table 1.2: Performance disadvantages of harmonic-drive transmissions

High flexibility	Due to the high loads seen by the wave-generator and gear teeth, moderate operating torques can produce substantial transmission torsion.
Kinematic error	Due to manufacturing inaccuracies, harmonic drives exhibit a small but ubiquitous position error across the transmission.
Resonance vibration	Since torque fluctuations produced by kinematic error can interact with the low stiffness of the transmission to excite resonances, high vibration amplitudes may be generated in some operating ranges.
Non linearity	Both the flexibility and frictional losses in the drive exhibit highly nonlinear behavior.
Poorly understood	Compared to conventional gear transmissions, relatively little exploration has been done of the unusual operating mechanisms in the harmonic drive.

harmonic drives have been used successfully in industrial robots, assembly equipment, and measuring instruments. Heavy-duty applications such as machine tools and printing presses have also utilized harmonic drives for their high-torque capabilities. Additionally, space and aircraft systems often employ harmonic drives for their lightweight and compact geometry.

1.1.3 The State of Harmonic-Drive Technology

Throughout its short existence, the harmonic drive has enjoyed continuously increasing international attention from designers as well as researchers. In the Soviet Union, substantial research, predominantly performed on a harmonic drive featuring a wave-generator with two rollers instead of an elliptical bearing, has provided valuable insight into the structural and dynamic properties of the drive as well as its suitability for heavy-duty applications. More recently, Japanese researchers have explored such areas as transmission stiffness, positioning accuracy, and tooth-meshing mechanisms in an effort to develop new gear-tooth geometries and improve harmonic-drive performance. Investigating harmonic drive performance in robotics and aerospace applications, researchers in the United States have also contributed constructive insights about the limits of harmonic-drive applicability.

The reference list at the end of this document contains citations for numerous papers encompassing the scope harmonic-drive research worldwide. Primarily, this research has been focused in six major areas: (1) vibration and dynamic behavior, (2) kinematic error, (3) torsional stiffness, (4) structural analysis, (5) robotics applications, and (6) gear-tooth geometry. Since my investigation is particularly focused on the dynamic and static performance of harmonic drives, past research on dynamic behavior, positional error, and torsional stiffness received most of my attention. In an effort to overview the current state of harmonic drive technology, a description of the fundamental mechanisms of harmonic-drive operation as well as relevant insights presented in existing literature will be summarized in this section.

1.1.3.1 Fundamental Operating Principles

In commercial catalogs, every harmonic drive is assigned a transmission ratio, N, which describes its position, velocity, and torque behavior. Specifically, given a known

rotation on two of the three harmonic-drive ports as well as a value for N, the ideal rotation of the third harmonic-drive port can be predicted by the equation

$$\theta_{wg} = (N + 1)\,\theta_{cs} - N\,\theta_{fs}\,, \tag{1.1}$$

where θ_{wg} is the rotation of the wave-generator, θ_{cs} is the rotation of the circular spline, and θ_{fs} is the rotation of the flexspline. All three rotations in this equation are defined in the same frame of reference. Similarly, given that N is constant under ideal assumptions, the derivative of this relationship yields a similar velocity constraint:

$$\omega_{wg} = (N + 1)\,\omega_{cs} - N\,\omega_{fs}\,, \tag{1.2}$$

where ω_{wg}, ω_{cs}, and ω_{fs} represent the angular velocities of the three harmonic-drive components relative to the same velocity reference. From these equations, it can be seen that, if the circular-spline velocity is zero, the wave-generator will rotate N-times faster than the flexspline in the opposite direction. In a different configuration, a grounded flexspline dictates that the wave-generator will spin (N+1) times faster than the circular spline in the same direction. By applying the law of power conservation to the three ports of the harmonic drive, the ideal torque behavior of the transmission can also be defined:

$$T_{wg} = \frac{1}{(N + 1)}\,T_{cs} = -\frac{1}{N}\,T_{fs}\,, \tag{1.3}$$

where T_{wg}, T_{cs}, and T_{fs} are the torques, defined with identical sign conventions, seen by the three harmonic-drive components. From this identity, it can be seen that the torque on one port of the harmonic drive dictates the ideal torque seen by the other two ports. Notice that the torque on the flexspline is nearly equivalent to the torque on the circular spline, which is approximately N-times greater than the torque on the wave-generator. By applying the torque, velocity, and position equations presented above, the dynamic behavior of a harmonic drive transmission under ideal assumptions can be completely defined.

1.1.3.2 Kinematic Error

In applications requiring high positional accuracy, the inherent kinematic errors manifested by harmonic drives expose the shortcomings of an ideal transmission model. This position error, θ_{err}, is typically measured by subtracting the rotation at the output of

the harmonic drive from the input rotation scaled by the ideal gear ratio for the given transmission configuration:

$$\theta_{err} = \frac{\theta_{in}}{\text{gear ratio}} - \theta_{out} \,. \tag{1.4}$$

Based on experimental observation, manufacturers' catalogs report that the magnitude of this position error typically varies periodically at a frequency of twice the wave-generator rotational velocity. Additionally, the amplitude of this periodic error often modulates twice per flexspline or circular-spline revolution as illustrated in figure 1.4. One manufacturer, [3], reports that the peak-to-peak amplitude of the kinematic error on all harmonic drive models rarely exceeds 0.033 degrees of output rotation (2 arc minutes), while the other, [4], claims that peak-to-peak error is inversely proportional to pitch-diameter and ranges from 0.095 degrees (5.7 arc minutes) to 0.013 degrees (0.8 arc minutes). Both manufacturers claim that position-error can be reduced further on a custom basis. [3, 4]

The root of harmonic-drive kinematic inaccuracy has been attributed to several different sources. As reported by Nye and Kraml in [24], harmonic-drive manufacturers claim that the position error is caused predominantly by manufacturing and assembly imperfections. Specifically, tooth-placement errors on both the circular spline and

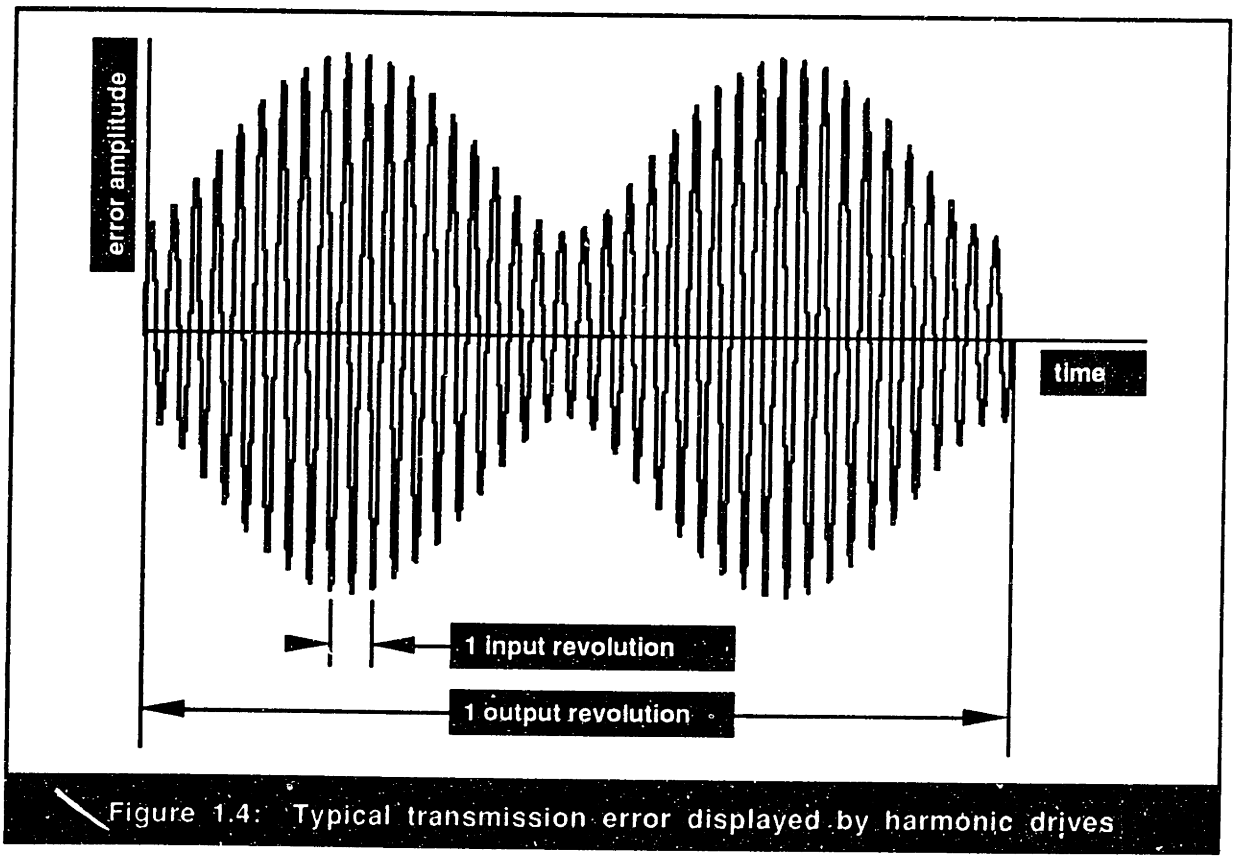

Figure 1.4: Typical transmission error displayed by harmonic drives

flexspline, out-of-roundness in the three transmission components, as well as misalignment during assembly can account for the majority of kinematic imperfection. By developing a detailed model which translated expected manufacturing and assembly errors into overall transmission error, Emel'yanov, et al., [20], made accurate predictions of experimentally observed position error. Klypin, et al., [23], used Emal'yanov's model to develop a computer simulation and further confirm the presence of numerous manufacturing and assembly errors in the measured transmission error. More recently, Yanabe, et al., [28], used precise experimental equipment to measure tooth-placement errors and concluded that the origins of position error lie mostly in the angular pitch errors of the flexspline and circular spline. In contrast to these conclusions, investigations by Hsia, [21, 22], and Ahmadian, [19], have focused blame for kinematic inaccuracies on inherent errors in the operating principles of harmonic drives irrespective of manufacturing and assembly errors. Both researchers developed kinematic models to predict position error based on transmission geometry and operating behavior.

In addition to postulating probable sources for kinematic error, the experimental investigations of Yanabe, et al., [28], and Nye and Kraml, [24], have lent further insight into the repeatability and variation of typical gear-error waveforms. By measuring the position error of multiple harmonic drives over one complete output rotation, both researchers observed that the resulting error signature can display frequency components at two cycles per wave-generator revolution and several subsequent harmonics. Typically, error components occurring once per wave-generator revolution are not found since they are canceled by the symmetry of the wave-generator, which ensures two-point contact between of the flexspline and circular spline. As Nye and Kraml summarized, the primary error component was seen at two cycles per wave-generator revolution with the next nine harmonics contributing up to fifty-five percent of the total kinematic error. The authors regret that there is no method for predicting the frequency components of the position error signal for an arbitrary harmonic drive other than careful measurement. By exposing a range of harmonic drive models to a variety of environmental and operational conditions, Nye and Kraml catalogued variations in position-error due to (1) temperature, (2) wear, (3) pitch diameter, (4) misalignment, (5) improper assembly, and (6) overloading. Based on this new knowledge of gear-error behavior, Nye and Kraml then successfully developed an electronic motion-control scheme designed to compensate for known kinematic inaccuracies.

Additional observations in [28] and [24] record the presence of the significant amplitude modulation or beating in position error waveforms of most harmonic drives

while a few transmissions showed little or no amplitude modulation. Both authors concur that the presence of amplitude modulation over several wave-generator cycles is caused by the summation of the circular spline and flexspline gear-error components; since these two error waveforms appear at slightly different frequencies, constructive and deconstructive interference of the two error signals is manifested by low-frequency beating.

1.1.3.3 Torsional Stiffness

Under ideal assumptions, a harmonic-drive transmission is treated as a perfectly rigid gear reduction. However, due to the relatively low torsional stiffness of harmonic drives, a more detailed understanding of transmission flexibility is often required for accurate modeling. Available research results have focused on understanding the characteristic shape and variation of the non-linear stiffness profile and pinpointing sources of transmission flexibility.

Harmonic drive stiffness is commonly measured by locking the wave-generator and measuring the rotation of the output (circular spline or flexspline) as the result of an applied load. As described in a manufacturer's catalog, [3], the typical shape of the stiffness curve for a harmonic drive loaded in both direction is shown in figure 1.5. This curve illustrates two characteristic properties of harmonic-drive flexibility: increasing stiffness with

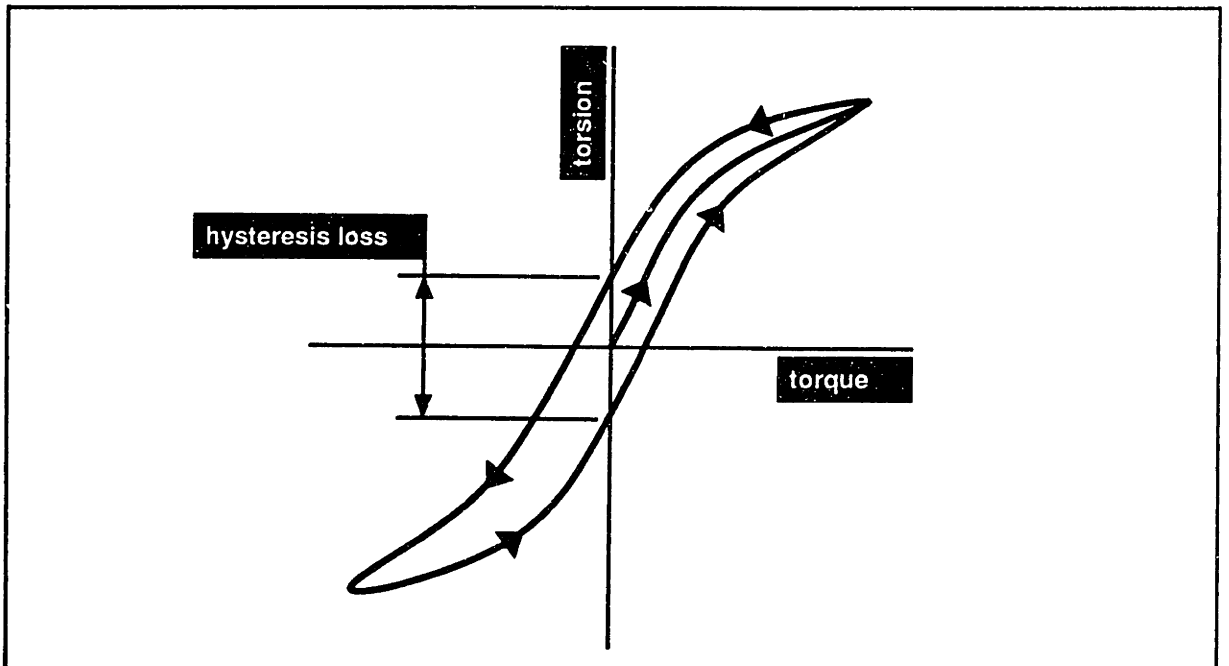

Figure 1.5: Typical stiffness profile displayed by harmonic drives

displacement and hysteresis loss. To capture the non-linear stiffness behavior. manufacturers, [3, 4], suggest using piecewise linear approximations whereas several independent researchers, [11, 18], prefer a cubic polynomial approximation. For certain modeling applications, other researchers, [42, 52] have had success using a linear stiffness approximation. At low applied torques, soft wind-up in the transmission due to this non-linear stiffness behavior can sometimes act like backlash. Fortunately, manufacturers claim that this deceptive non-linearity is kept below 0.05 degrees of output rotation (3 arc minutes). The hysteresis loss in a harmonic drive is a phenomenon more difficult to model than the stiffness, and consequently, it is ignored often. In support of this neglect, the manufacturer's catalog, [3], reassures modelers that the total loss is typically less than 0.033 degrees of output rotation (2 arc minutes).

The primary sources of flexibility in harmonic-drive transmissions has been a topic of much investigation and speculation. By performing tests on high-torque harmonic drives with two-cam wave-generators, Margulis, et al., [29], concluded that the largest component in the total torsional compliance was the deformation of the wave-generator. Specifically, it was observed that high radial forces on the wave-generator can cause substantial radial deflection allowing relative rotation across the transmission. By performing similar stiffness tests on conventional harmonic drives with elliptical-bearing wave-generators, Yanabe, et al., [32], also noticed that, due to the high radial forces seen by the wave-generator, resulting deflection in the wave-generator bearing can greatly influence transmission torsion. The zones of maximum loading on the wave-generator were predicted using a finite-element model of the flexspline. Research by Nye, [65], attributed the characteristic non-linear profile of harmonic-drive stiffness curves to increasing gear-tooth contact area under applied loads. Qualitative observations indicated that the axial length of the contact interface between meshing gear teeth can vary from ten percent, under no-load conditions, up to 100 percent, when fully loaded. The importance of gear-tooth contact on transmission stiffness was confirmed by Kiyosawa, et al., [57], when flexibility was dramatically reduced in harmonic drives with a modified gear-tooth profile designed to increase the tooth-engagement zone. In summary, existing research indicates that most transmission compliance can be traced to wave-generator deformation, but gear-tooth contact-area and meshing-zone, which can effect the load-distribution inside the harmonic drive, are influential in determining the shape of the stiffness profile.

As a consequence of the relatively complex compliance mechanisms of the harmonic drive, significant variations can occur in transmission stiffness for a given drive. In particular, a manufacturer's catalog, [3], cautions that stiffness profiles measured from

a single drive can vary as much as ±30 percent. Nye, [65], confirms the magnitude of this variability and observes its dependence on the integrity of internal fit-up. Specifically, he notes that stiffness typically increases with tighter meshing of gear teeth and increased internal loading. Experimental results from Nye and Hikada, et al., [11], indicate that, since wave-generator orientation often influences gear-tooth loading, transmission stiffness can vary significantly with wave-generator rotation. Further investigation by Nye produced theoretical loading models which successfully described the influence of gear-tooth preloading on stiffness and predicted preload- and stiffness-relaxation due to gear-tooth wear.

1.1.3.4 Frictional Losses

Another performance metric in which harmonic-drive behavior falls short of ideal is frictional dissipation. Manufacturer's catalogs, [3, 5], report typical transmission power losses greater than ten percent. This transmission inefficiency is manifested by lower output torques than ideal assumptions would predict. Further research by Mariler and Richard, [52], among others, reports that the velocity-dependent damping in harmonic-drive transmissions increases less sharply at higher velocities than lower velocities and might even decrease at very high velocities. Based on these observations, the authors recommend using a cubic approximation to capture this non-linear damping behavior. Research has also been performed to understand the behavior of velocity-independent losses, such as static and Coulomb friction, in harmonic drives. Specifically, Nye, [65], reports that starting torque values for harmonic-drive transmission can fluctuate greatly as a function of the orientation of the wave-generator. The author attributes this variation to different levels of gear-tooth preloading causing fluctuating static friction torques over one revolution of the wave-generator. Static and kinematic models developed by Nye and others, [39], rely on geometric models of gear-tooth rubbing to estimate Coulomb friction forces on the gear teeth and wave-generator.

1.1.3.5 Dynamic Behavior

Due to the non-ideal behavior of harmonic-drive kinematic accuracy, stiffness, and frictional losses, ideal-transmission models are often insufficient to describe accurately the dynamic behavior of harmonic drives. In the past, many researchers, such as [42], have

opted to capture harmonic-drive dynamics using linear stiffness and damping relationships while others, [44, 51, 52], required non-linear representations to ensure model accuracy. In order to capture the torque fluctuations induced by kinematic error, a few researchers, such as [11, 18], supplement their models with a sinusoidal torque function derived from position-error fluctuations or measured directly. For many applications in which non-ideal transmission behavior becomes dominant, harmonic-drive manufacturer's frequently recommend adjustment of the operating envelope to a region less plagued by transmission dynamics. Some research, such as [13], has been focused on developing simple models to predict operating regions in which harmonic drives are well-behaved.

Depending on the design and operating conditions, several researchers note that strikingly non-ideal behavior can be exhibited in harmonic-drive systems. Specifically, experimental measurements by Hikada, et al., [11], and Volkov, et al, [18], reveal that harmonic drives typically exhibit vibrations at twice the frequency of wave-generator rotation and several subsequent harmonics. It was also noticed that the amplitude of vibration increased when one of these frequencies coincided with the natural frequency of the harmonic-drive system. Furthermore, plots of resonance vibration presented by Hikada, et al., illustrated the same twice-per-output-revolution amplitude modulation seen in position-error signatures. By developing a simple non-linear vibration model which captured the behavior of tooth-meshing errors, Hikada, et al., illustrated the direct influence of position error on dynamic vibration. Further comparison between model predictions and experimental results revealed the importance of representing the variation in stiffness with wave-generator angle to ensure model accuracy. Another non-linear vibration model developed by Volkov, et al., was able to predict observed system non-linearities such as vibrations at subharmonics of the wave-generator excitation frequency due to the non-linear harmonic-drive stiffness.

1.2 The Scope of My Investigation

The results of my research yielded several insights which may be useful to harmonic-drive users and designers. From my experimental analysis, I characterized the magnitude and typical behavior of several important transmission properties. In particular, kinematic error was confirmed to appear primarily at frequency-multiples of the wave-generator angular velocity, and static stiffness measurements were found to yield non-linear profiles that were corrupted by transmission friction. Additional measurements of static

and dynamic friction demonstrated that energy dissipation in harmonic drives varies non-linearly with velocity and periodically with rotation and can escalate during system resonance. By comparing these empirical observations to manufacturer's estimates, I discovered that, due to the fickle nature of most harmonic-drive attributes, catalog predictions often fail to describe the observed behavior. Following this investigation of individual properties, overall dynamic response measurement showed surprisingly agitated transmission behavior. Specifically, due to the problematic influence of system resonance in typical harmonic-drive operating ranges, dynamic response data demonstrated violent torque and velocity fluctuations as well as sudden unexpected increases in operating velocity. Using the understanding of transmission properties gained from experimental analysis, this unusual dynamic behavior was rationalized.

Using the experimental findings as a reference, five different theoretical models were developed to describe harmonic-drive operation. First, an ideal transmission representation was constructed that showed very poor performance under dynamic conditions. When non-linear frictional losses were appended to this ideal representation, model integrity improved. In order capture the important influence of resonant vibration on system performance, non-linear compliance and kinematic error were introduced into the harmonic-drive representation. The resulting model demonstrated resonant frequencies and resulting vibrations close to experimental observations but remained ignorant to the enhanced frictional losses at resonance. By developing a simplified geometric representation of gear-tooth meshing that included Coulomb friction at the gear-tooth interface, the elusive resonance losses were replicated and model performance improved. Unfortunately, due inaccuracies that remained in this model and the difficulty of estimating reliable values for transmission properties, a more detailed representation of gear-tooth meshing behavior is required to improve model integrity. Nevertheless, the relatively simple mathematics of this representation and its close conceptual relationship to the actual transmission makes it a valuable tool for fostering an intuitive understanding of harmonic-drive operation.

1.3 The Organization of this Document

The presentation of research findings in this document begins with a complete discussion of my experimental investigation. First, I will describe the testing apparatus and instrumentation followed by a discussion of four important harmonic-drive properties: (1)

kinematic-error, (2) stiffness, (3) starting torque, and (4) dynamic friction. For each of these topics, the testing procedure will be described, experimental results will be presented, and conclusions will be made about the observed behavior. Using this empirical insight, dynamic-response measurements will then be characterized and rationalized in terms of important transmission properties. With experimental dynamic measurements to serve as a metric for model performance, my theoretical exploration of harmonic-drive operation will then be outlined. This presentation begins with a discussion of the dynamic models developed to simulate the testing apparatus followed by a description of five different harmonic-drive representations. For each of these transmission models, equations of motion will be derived, accuracy and reliability will be evaluated, and conclusions will be drawn about the potential usefulness and applicability of each representation. Based on results from these theoretical models as well as the findings of the experimental inquiry, conclusions and recommendations will be made about rewarding areas for future research.

Chapter 2: Experimental Analysis

A sound understanding of harmonic-drive behavior is vital for making well-informed design decisions about applications employing harmonic-drives. Additionally, the development of a reliable transmission model rests heavily upon accurate characterization of harmonic-drive performance parameters. Given this impetus for improved understanding, several tests have been performed to investigate the kinematic, static, and dynamic properties of this unique transmission.

From my experimental investigation, I have collected data to characterize the kinematic error, stiffness, and friction behavior of three harmonic-drive test specimens and have identified relationships between these transmission properties and overall harmonic-drive dynamic response. In general, I observed that, due to the inseparable interaction between friction, compliance, and transmission error, accurate characterization of these properties was difficult in many cases. Not surprisingly, because of this complication, catalog estimates of these values were often unreliable. Nevertheless, given the collected data, simple mathematical representations were constructed to extract useful information for dynamic modeling. Perhaps more importantly, from the qualitative understanding gained from the experimental analysis of harmonic-drive position error, stiffness, and friction, typical harmonic-drive dynamic response patterns were identified and rationalized in terms of the observed transmission properties.

This section is dedicated to presenting the findings of my experimental investigation into these areas. To accomplish this task, the experimental apparatus used for all harmonic-drive testing will be discussed first followed by a presentation of results from each of the experimental tests. During this presentation of the individual experiments, specific testing procedures will be outlined, results will be discussed and conclusions will be formed. The discussion of results in each of these sub-sections not only focuses on observed experimental behavior but also addresses experimental accuracy, catalog predictions, and potential modeling strategies. Finally, with the insight gained from all of the experimental tests, typical dynamic-response behavior observed on harmonic drives will be presented and characterized.

2.1 Description of Testing Apparatus

All experimental testing for this project was performed on a three-joint, planar robot with harmonic-drive transmissions. This testing facility is shown in figure 2.1. To allow for straightforward data collection on the three harmonic drives, the apparatus was designed so that each joint could be removed from the robot and operated independently. For the purpose of this document, these three joints, each sporting a different harmonic drive, will be referenced by numbers 1, 2 and 3. This section is devoted to describing the design and instrumentation of these three joints followed by an overview of the data-acquisition methods used for each testing assembly.

2.1.1 Hardware Design and Sensor Locations

Due to the functional requirements of the robot, each of the three joint assemblies requires a different design. Serving as the robot base, joint 1 is the largest and most powerful of the three testing facilities. Joint 2 places second in bulk and brawn, relying on a slightly smaller motor and transmission than joint 1. With a much lower torque capacity than its two companions, joint 3 is significantly smaller in size than joint 1 or 2. Tables 2.1 and 2.2 summarize important motor and transmission properties for each of the three joints, and in light of these differences, the specific design of these three testing stations can now be discussed.

Table 2.1: Specifications for the three harmonic drives tested

	Joint 1	Joint 2	Joint 3
Model Number *	1M	5C	1C
Catalog Transmission Ratio	160:1	160:1	80:1
Pitch Diameter	8.14 cm (3.20 in)	6.35 cm (2.50 in)	3.56 cm (1.40 in)
Maximum Output Torque	280 N-m (2470 in-lb)	140 N-m (1240 in-lb)	15.8 N-m (140 in-lb)

* The harmonic-drive models tested were purchased from the Harmonic Drive Machinery Group and are listed in catalog reference [4].

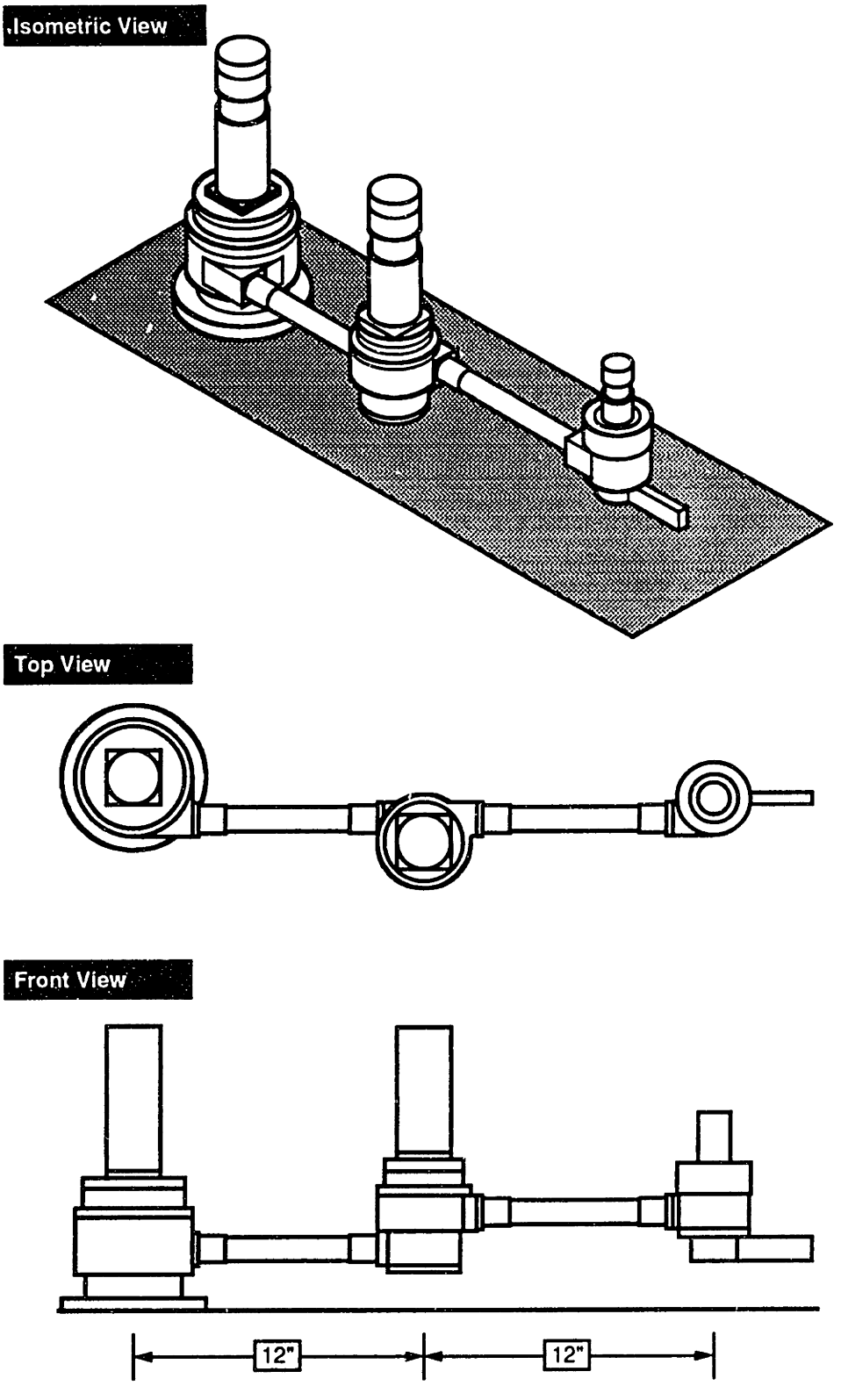

Figure 2.1: Harmonic-drive testing apparatus

Table 2.2: Motor specifications for the three testing stations			
	Joint 1	Joint 2	Joint 3
Model Number	Aerotech 1035DC	Aerotech 1017DC	Clifton SmCo AS-780
Peak Torque	1.84 N-m (16.25 in-lb)	0.92 N-m (8.13 in-lb)	0.35 N-m (3.13 in-lb)
Maximum Speed	6000 rpm	6500 rpm	8000 rpm
Torque Constant	0.06 N-m/amp (0.53 in-lb/amp)	0.03 N-m/amp (0.26 in-lb/amp)	0 04 N-m/amp (0.36 in-lb/amp)
Back EMF Constant	6.30 volts/krpm	3.04 volts/krpm	4.25 volts/krpm

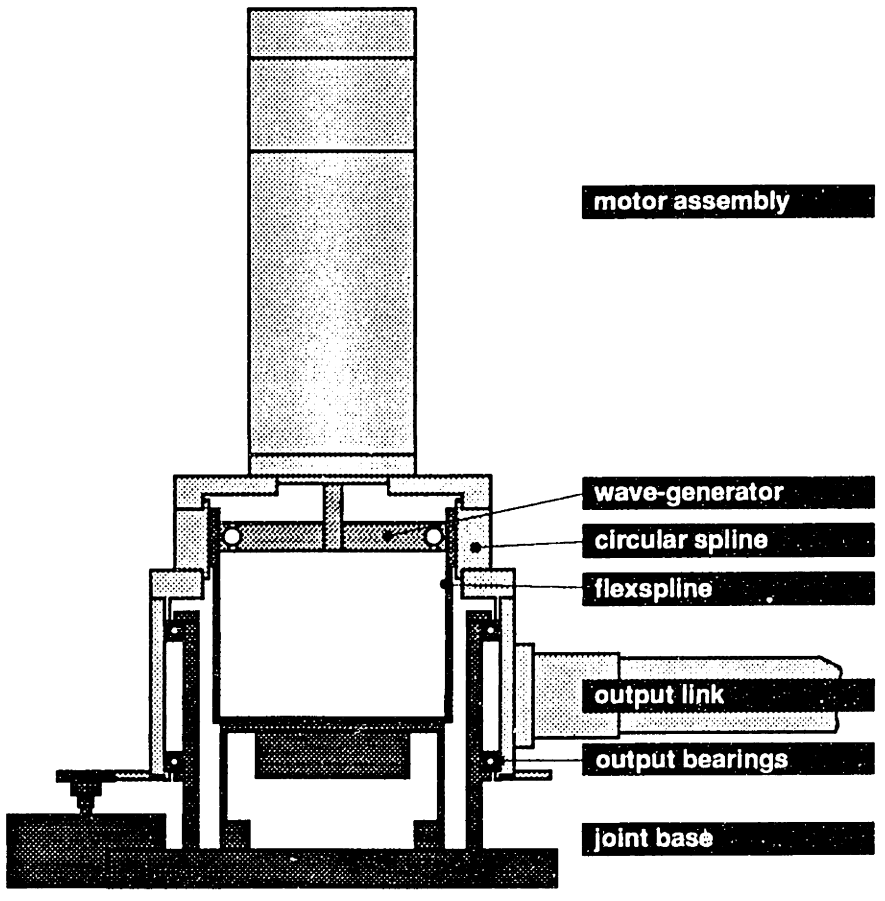

Figure 2.2: Cross-section of joint 1

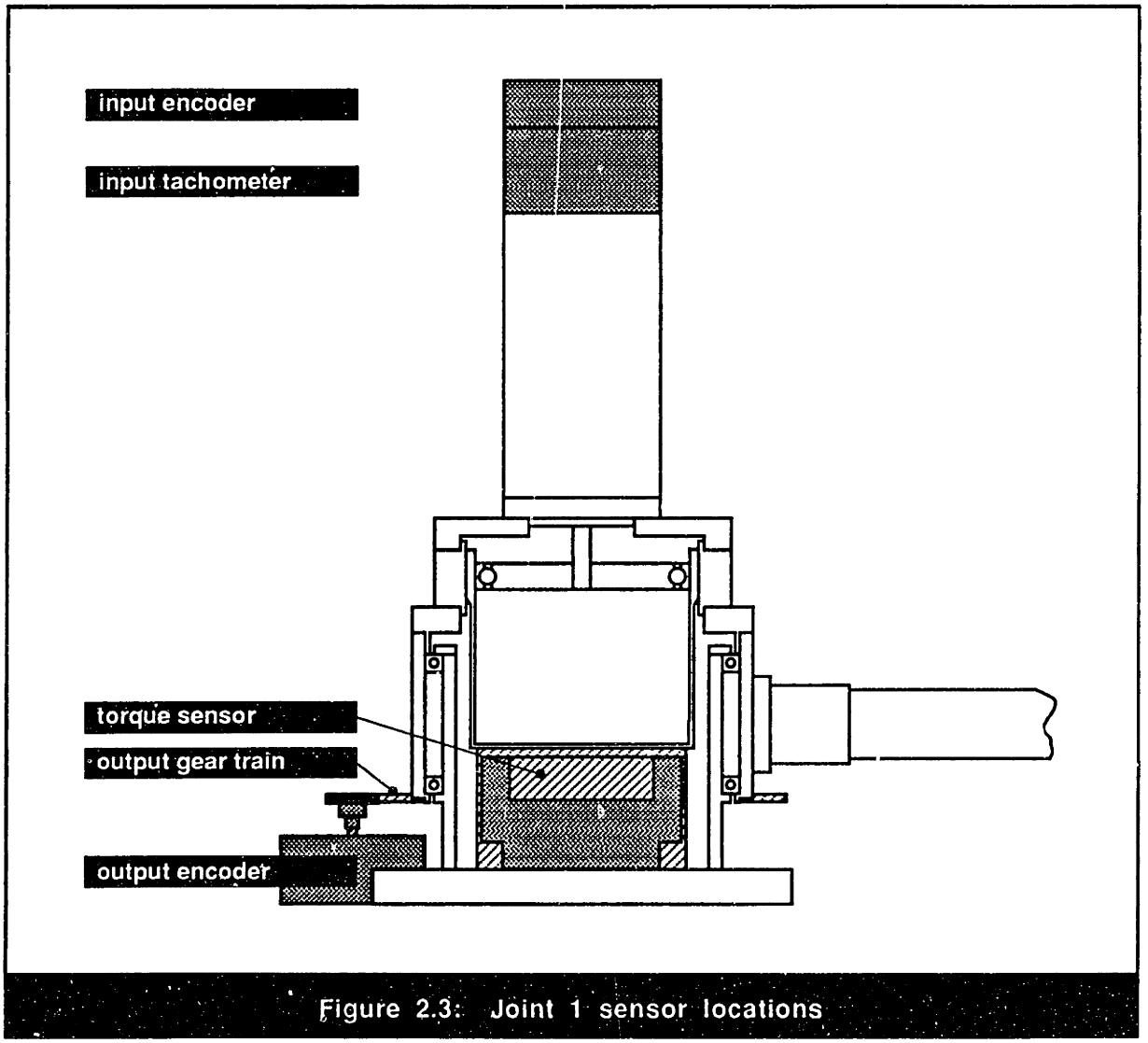

Figure 2.3: Joint 1 sensor locations

The design of the first harmonic-drive testing station, joint 1, is shown in figure 2.2. From this cross-section, it can be seen that the flexspline of the harmonic drive is mounted to ground while the wave-generator is driven by a DC motor mounted to the circular spline. The output link of this joint is supported by a pair of angular-contact bearings and is driven by the circular spline of the harmonic drive. This joint also contains two encoders, one torque sensor, and a tachometer whose locations are illustrated in figure 2.3. From this diagram, it can be seen that the input encoder and tachometer measure the rotation of the motor shaft with respect to the motor housing which is mounted to the circular spline. The output encoder is mounted to ground and measures the absolute rotation of the circular spline through a gear pair with an 8:1 reduction ratio. Lastly, since the only rigid connection between the drive train and ground is the torque sensor at the flexspline output, this sensor can be used to measure directly the torque across the transmission as seen by the flexspline.

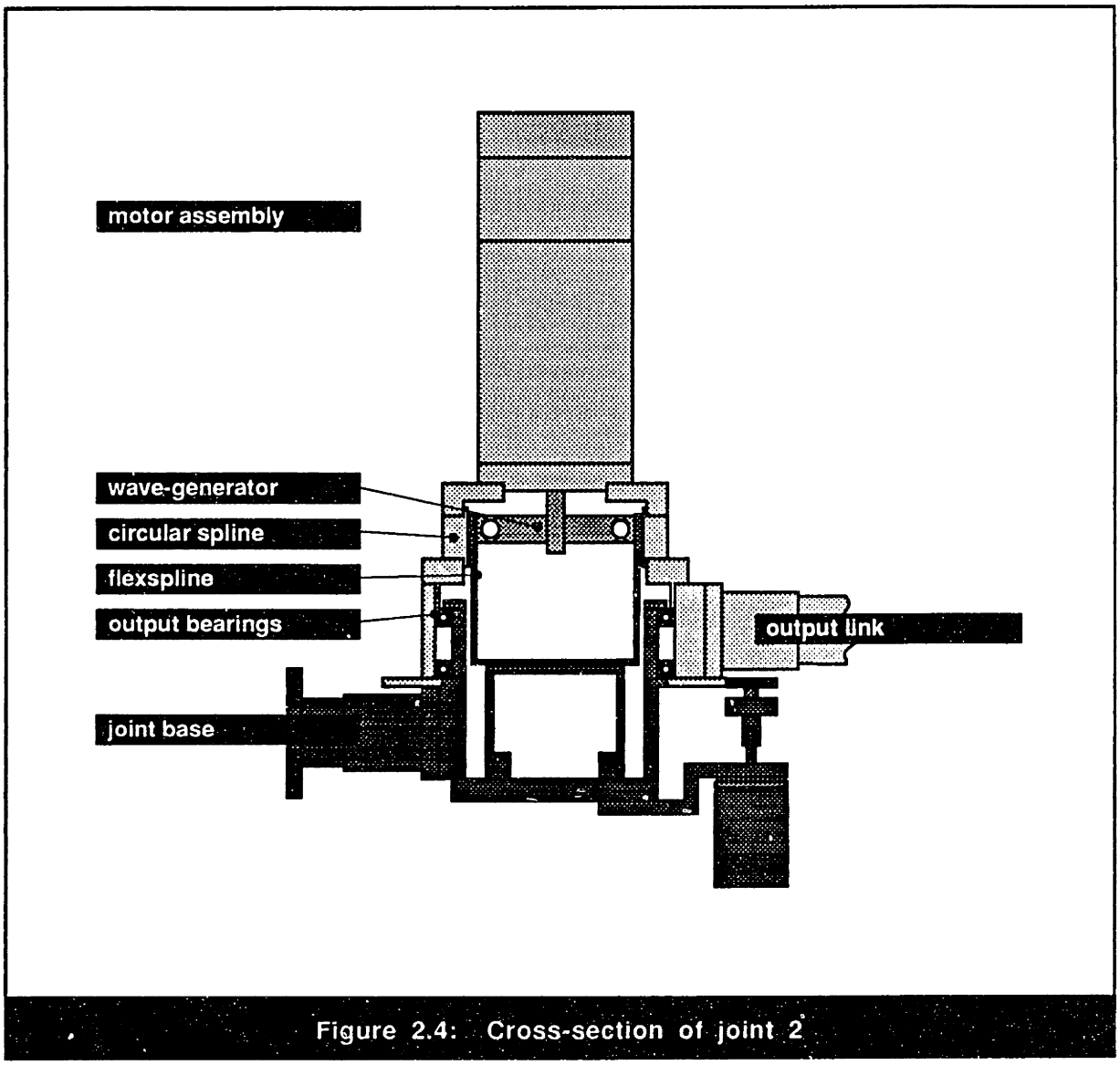

Figure 2.4: Cross-section of joint 2

As illustrated in Figure 2.4, the design of joint 2 is almost identical to joint 1. Specifically, on the input side of the joint, the wave-generator is driven by a motor mounted to the circular spline, while the rotation of the output link is driven by the circular spline. As seen on joint 1, the flexspline is attached to ground and angular-contact bearings are used to support the rotation of the output link. The instrumentation similarities between joint 1 and 2 are also apparent from the schematic in figure 2.5. As explained for joint 1, the input encoder and tachometer monitor the rotation of the motor shaft with respect to the circular spline while the output torque sensor measures all torque seen at the flexspline. Due to design restrictions, the output rotation on joint 2 is measured by a resolver rather than a rotary encoder as used on joint 1. This resolver directly measures the angular position and velocity of the circular spline with respect to ground through a gear pair with a 6.67:1 reduction ratio.

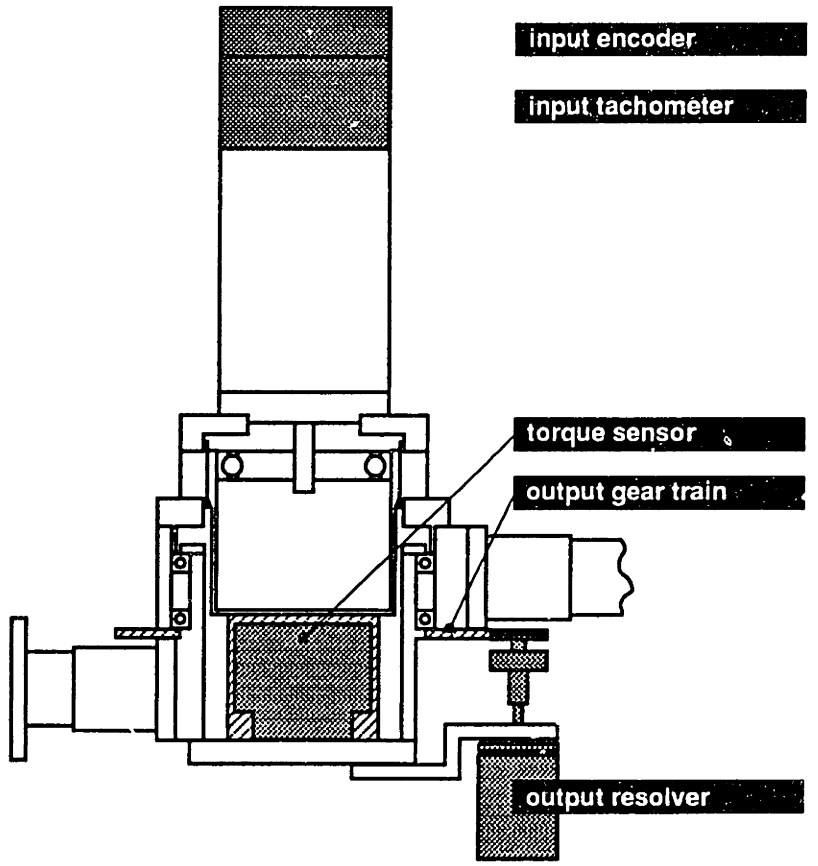

Figure 2.5: Joint 2 sensor locations

The third and final testing station, as illustrated in figure 2.6, relies on a design configuration substantially different from the two other joints. In particular, while the wave-generator is still driven by a motor mounted to the circular spline, the output rotation of the joint is transmitted through the flexspline and the circular spline is attached to ground. This unique design not only allows for unrestrained rotation of the output link but also provides a facility for examining harmonic-drive behavior under a different operating configuration. From the sensor locations outlined in figure 2.7, it can be seen that, unlike the other two joints, the input encoder directly measures absolute motor rotation and there is no input tachometer. On the output side, a resolver measures the flexspline rotation with respect to ground through a gear-pair with a 7.2:1 reduction ratio. Since the torque sensor connects both the motor and circular spline to ground, it can measure directly the combined torque of the wave-generator and circular spline, or equivalently, the torque seen at the flexspline.

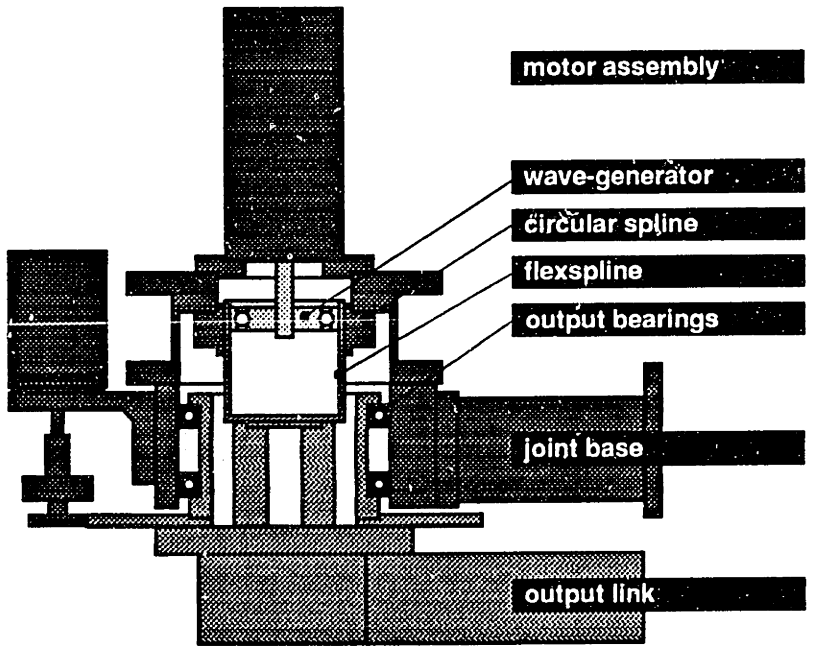

Figure 2.6: Cross-section of joint 3

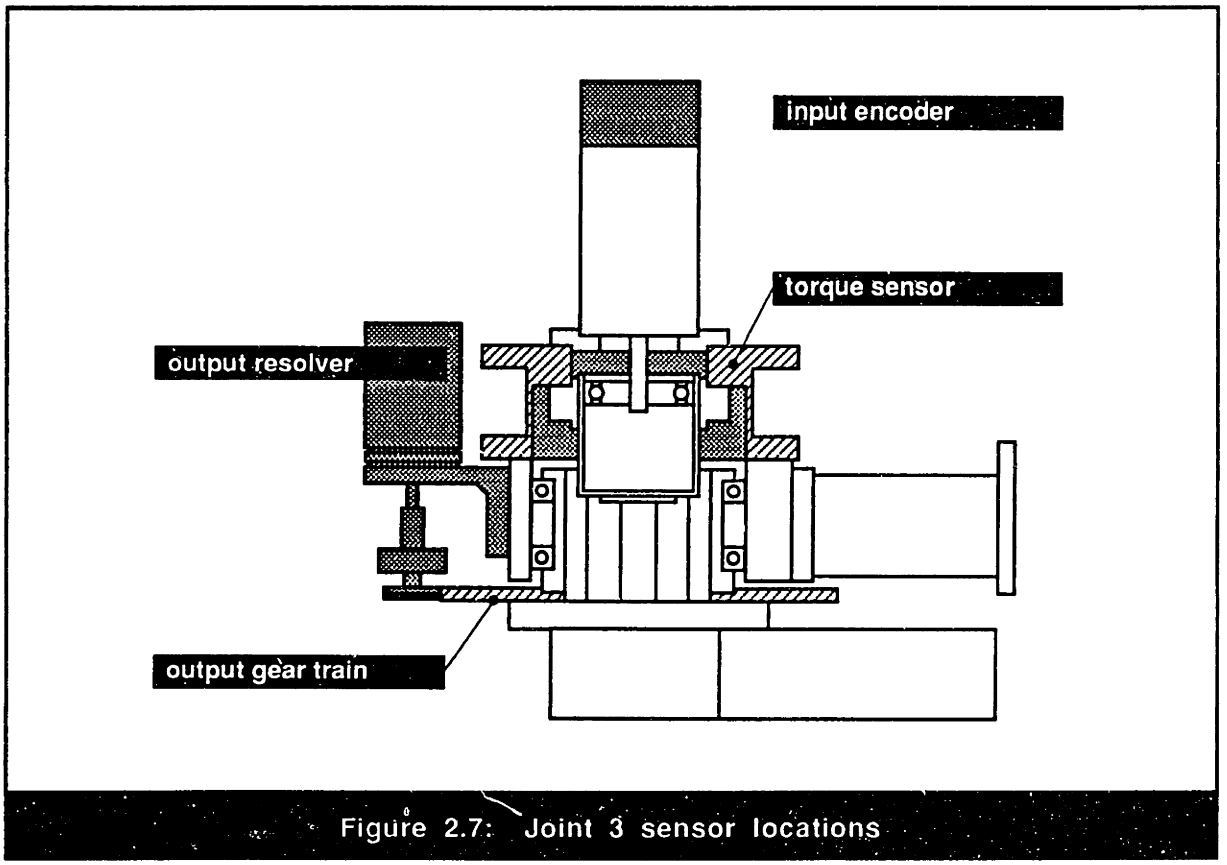

Figure 2.7: Joint 3 sensor locations

2.1.2 Sensor Processing and Interpretation

In order to monitor sensors and control motors on each joint, the data-acquisition system and motor-controller illustrated in figure 2.8 was used. Using a software environment called CONDOR, developed at the MIT Artificial Intelligence Laboratory, computer code was compiled on a Sun 3/180 workstation and loaded onto a series of Ironics processor boards. When executed, this code could then collect sensor information from the data-acquisition boards and sensor-processing circuits shown in figure 2.8. To control the motors, desired motor currents were specified on the D to A board and then amplified through an Aerotech 4020-LS DC Servo Amplifier. By monitoring the amplifier current with the A to D board, measurements of motor current and torque could be gathered.

In order to extract useful information about harmonic-drive behavior, a thorough understanding of sensor measurement is required. First, relationships must be made between the measurements seen by the sensors on each joint and the rotations and torques on the individual harmonic-drive components. Given the variable names defined in table

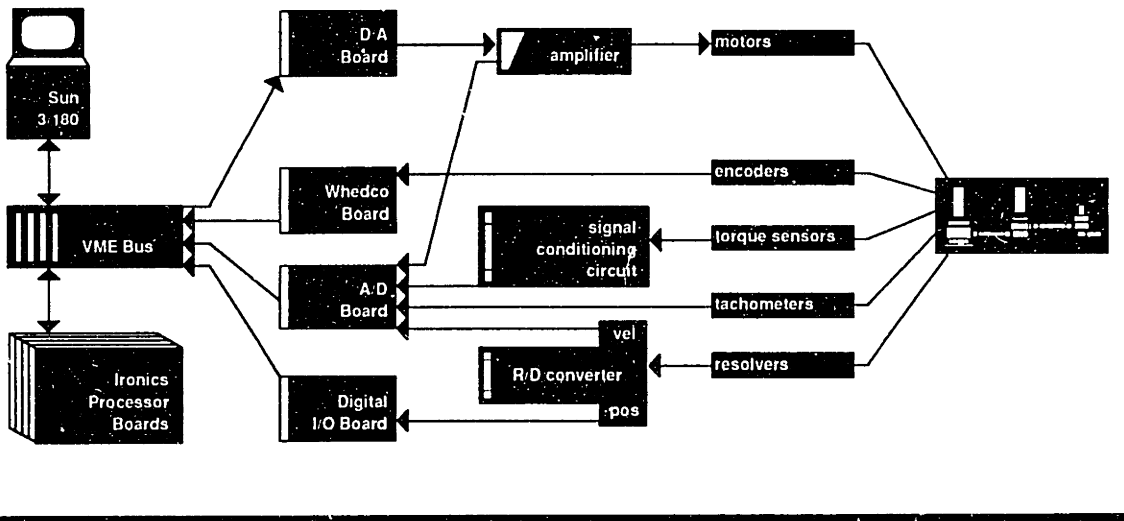

Figure 2.8: Experimental data acquisition system and controller

2.3, the input and output rotations with respect to ground are defined in table 2.4, and the sensor-measurement relationships are defined in table 2.5. Second, as presented in table 2.6, sensor resolution and accuracy must be characterized, and, lastly, sensors must be calibrated. Experimental calibration procedures and results are reported in Appendix A. From this catalog of sensor information, experimental data can now be used to accurately measure the dynamic, static, and kinematic performance of the three harmonic-drive test specimens.

Table 2.3: Description of important harmonic-drive variables

θ_{wg}, θ_{fs}, and θ_{cs}	Angular position of the wave-generator, flexspline, and circular spline, respectively, as referenced from ground.
ω_{wg}, ω_{fs}, and ω_{cs}	Angular velocity of the wave-generator, flexspline, and circular spline, respectively, as referenced from ground.
T_{wg}, T_{fs}, and T_{cs}	Torque experienced by the wave-generator, flexspline, and circular spline, respectively.

Table 2.4: Absolute joint rotation in terms of harmonic-drive variables

	Joint 1	Joint 2	Joint 3
Input Rotation	ω_{wg}	ω_{wg}	ω_{wg}
Output Rotation	ω_{cs}	ω_{cs}	ω_{fs}

Table 2.5: Sensor measurements in terms of harmonic-drive variables			
	Joint 1	**Joint 2**	**Joint 3**
Input Position Sensor	$\theta_{wg} - \theta_{cs}$	$\theta_{wg} - \theta_{cs}$	θ_{wg}
Input Velocity Sensor	$\omega_{wg} - \omega_{cs}$	$\omega_{wg} - \omega_{cs}$	no sensor
Input Current Sensor	motor amps	motor amps	motor amps
Output Position Sensor	θ_{cs}	θ_{cs}	θ_{fs}
Output Velocity Sensor	no sensor	ω_{cs}	ω_{fs}
Output Torque Sensor	T_{fs}	T_{fs}	T_{fs}

Table 2.6: Sensor resolution for the three testing stations			
	Joint 1	**Joint 2**	**Joint 3**
Input Position Sensor	± 0.045 input ° (± 2.7 arc min)	± 0.045 input ° (± 2.7 arc min)	± 0.09 input ° (± 5.4 arc min)
Input Velocity Sensor	± 30 input °/sec (± 5.0 rpm)	± 30 input °/sec (± 5.0 rpm)	none
Input Current Sensor	± 0.057 amps	± 0.061 amps	± 0.057 amps
Output Position Sensor	± 0.0023 output ° (± 0.14 arc min)	± 0.0008 output ° (± 0.05 arc min)	± 0.0008 output ° (± 0.05 arc min)
Output Velocity Sensor	none	± 0.8 output °/sec (0.13 rpm)	± 2.8 output °/sec (0.47 rpm)
Output Torque Sensor	± 0.45 N-m (± 4.0 in-lb)	± 0.57 N-m (± 5.0 in-lb)	± 0.034 N-m (± 0.3 in-lb)

2.2 Kinematic Error Measurement

The goal of my experimental investigation of harmonic-drive kinematic properties was to accurately characterize the position-error signatures of the three harmonic-drive specimens. As a result of this investigation, I not only confirmed the expected position-error magnitude and frequency distribution over typical frequency ranges but also characterized transmission accuracy at other rotational frequencies. Based on high-resolution experimental findings, evidence was found to trace the origins of kinematic inaccuracy to flexspline and circular-spline gear error. This section outlines the method used to collect kinematic-error data as well as the results and conclusions gained from this experimental analysis.

2.2.1 Experimental Procedures

Due to complications in separating harmonic-drive position-error components from kinematic inaccuracies inherent in the test apparatus, two different experimental procedures were required to measure position-error data. The general procedure was used for the majority of experimental trials while the phase-shift procedure was required to resolve transmission error that varied over one output rotation of the harmonic-drive. These two procedures are outlined below.

2.2.1.1 General Procedure

In order to collect position-error data, the three harmonic-drive testing stations were used to measure input and output rotation over a range of motion. By assuming quasi-static conditions, kinematic-error data was collected while the joint was rotated at a small but non-zero velocity. The typical procedure for data-acquisition and processing is listed below.

1. By sending a constant current to the joint motor that exceeds the transmission starting torque, rotate the harmonic drive at the slowest velocity at which resonance vibration is minimal.

2. Collect input and output position information from the joint sensors at equally spaced time intervals over a given motion range.

3 Calculate the position error, θ_{err}, using the equation:

$$\theta_{err} = \frac{\theta_{in}}{\text{gear ratio}} - \theta_{out} . \qquad (2.1)$$

4 Plot the resulting position-error signal versus the number of input, or wave-generator, revolutions to analyze the shape of the error signature.

5 Linearly interpolate the time-based position-error signal to produce data points that are equally spaced by input rotation.

6 Take an FFT of the interpolated data vector to identify the frequency components of the error signature in terms of input revolutions.

By adjusting the range of transmission rotation and the number of data points accumulated, FFT spectra spanning a wide range of frequencies were collected. Assuming that at least two data points per cycle are required to measure position-error frequency components, position-sensor resolution limits the cycles per angular position, or spatial frequency, that can be measured on each harmonic drive. These spatial frequency upper-bounds are listed in table 2.7.

Table 2.7: Highest measurable spatial frequencies

	limited by	$\frac{\text{cycles}}{\text{input revolution}}$
Joint 1	output encoder	250.0
Joint 2	output resolver	1365.0
Joint 3	input encoder	1000.0

2.2.1.2 Phase-Shift Procedure

Since a typical harmonic-drive position-error signature is composed of waveforms located at distinct spatial frequencies, most error components arising from harmonic-drive inaccuracies could be easily distinguished from inherent kinematic errors in the testing apparatus. Unfortunately, since position inaccuracy in the output sensor gear appeared at the same frequency as a potential harmonic-drive error component, a separate data-collection procedure was required to separate these two error components. More precisely, using the data-collection procedure above, harmonic-drive position-error components

occurring once every output revolution, and harmonics, were contaminated by inaccuracies in the output sensor gear which appeared at the same frequency. To distill the contribution of the harmonic drive from this aggregate error waveform, a second set of position-error data in which the harmonic drive was physically rotated by a fraction of a revolution relative to the output sensor gear was required. In other words, after the first set of kinematic-error data was obtained, the angular position of the harmonic-drive relative to the output gear was shifted by a known amount before the second data set was collected. By taking an FFT of these two signals, subtracting them, and scaling the result appropriately, the harmonic-drive error-component could be accurately identified.

The theoretical basis for this experimental procedure can be clarified by assuming that the position-error waveform collected from the harmonic drive testing apparatus has three components: (1) $h_1(\theta)$, a first error signal at a spatial frequency of once-per-output revolution , (2) $h_2(\theta)$, a second signal at a spatial frequency of once-per-output revolution, and (3) $g(\theta)$, a third signal composed of various other components at different frequencies, where θ is a measurement of angular position. Therefore, the aggregate position-error signal, $h_{sum1}(\theta)$, can be defined as

$$h_{sum1}(\theta) = h_1(\theta) + h_2(\theta) + g(\theta) \tag{2.2}$$

Now assume that a second signal is collected in which the first component was rotated by a known phase shift, $\Delta\theta$, in the positive θ-direction. This signal, $h_{sum2}(\theta)$, is described by

$$h_{sum2}(\theta) = h_1(\theta - \Delta\theta) + h_2(\theta) + g(\theta) \tag{2.3}$$

Taking the Fourier transform of both equations yields

$$H_{sum1}(\omega) = H_1(\omega) + H_2(\omega) + G(\omega) \text{ , and} \tag{2.4}$$

$$H_{sum2}(\omega) = H_1(\omega)\, e^{-i\omega\Delta\theta} + H_2(\omega) + G(\omega) \tag{2.5}$$

where ω is the spatial frequency in radians per rotational unit. By subtracting these two equations, it can be seem that the $H_2(\omega)$ and $G(\omega)$ terms disappear leaving an equation in terms of $H_1(\omega)$ and the two aggregate error signals:

$$H_1(\omega) = \frac{H_{sum1}(\omega) - H_{sum2}(\omega)}{1 - e^{-i\omega\Delta\theta}}, \tag{2.6}$$

for $\omega \Delta\theta \neq 2\pi n$, n = 0, 1,2, ... Therefore, if a phase shift, can be accurately introduced into the harmonic-drive error component, it can be easily extracted from two sets of position-error data using this equation.

The procedure used to collect and process two sets of position-error data according to this theory is itemized below.

1. Set the zero setpoint for input and output position sensors on the given testing station.
2. Move the joint at a slow, non-resonating velocity by sending a current to the joint motor.
3. Read input and output position data at equally spaced time intervals.
4. Calculate the kinematic error from equation (2.1).
5. Filter this position error data at every time step using a linear FIR digital low-pass filter to prevent aliasing of high-frequency position error components into sampled data.
6. Return the joint to its original position after this data run is complete.
7. Interpolate the first set of position error data to generate data points that are equally spaced by input rotation rather than time.
8. Introduce a phase shift into either the harmonic drive, the output gear, or both by rotating that component a measured number of degrees.
9. Collect the second set of data using the same procedure used to gather the first set.
10. Interpolate this data set over the identical range of rotation used in the first set of data.
11. Take an FFT of both data sets to yield frequency-domain data.
12. Subtract the two resulting vectors of frequency domain data at all frequencies and scale the difference according to equation (2.6) to yield the magnitude spectrum of the phase-shifted position-error component.
13. Take an inverse FFT of this spectrum to produce the waveform of the phase-shifted position-error component if desired.

2.2.2 Discussion of Results

The results of several experimental tests on harmonic-drive kinematic error are presented in this section. After the importance of these results has been analyzed, comparisons will be made to catalog predictions of harmonic-drive position-error, and modeling representations of observed behavior will be discussed. Based on these findings, conclusions will be made about kinematic error in harmonic drives.

2.2.2.1 Characteristic Harmonic-Drive Error

For organizational clarity, I have divided my position-error experimental findings into four sub-sections. The first section describes the most significant harmonic-drive error, which appears at frequencies corresponding to multiples of input, or wave-generator, rotations. The second section presents results from high-resolution tests on these same error components. The third section focuses on error components that vary with output rotation while the fourth section focuses on high-frequency error signals which oscillate many times every wave-generator revolution. In each of these sections, experimental data will be interpreted and factors which can influence measured results will be discussed.

2.2.2.1.1 Error at the Input Rotation Frequency

Figures 2.9 through 2.14 illustrate the typical position-error waveforms observed on the three harmonic drives as well as the spatial FFT results which indicate the frequency content of these error signatures. For all of these plots, position-error magnitude is measured in degrees of output (flexspline or circular spline) rotation and plotted in terms of input (wave-generator) revolutions. In both the FFT and waveform plots, significant energy content can be seen at frequencies lower than one cycle-per-input-revolution. These low-frequency error components are due primarily to position inaccuracies in the output sensor gear train and should not be mistaken for harmonic-drive error. Unfortunately, the tooth-passing frequency of the output sensor gear-train appears on the joint 2 FFT spectrum at 3.0 cycles-per-input-revolution. When viewing this plot, the error component observed at this frequency should not be attributed to the harmonic-drive transmission. Table 2.8 summarizes the peak-to-peak error magnitudes observed on the three harmonic drives.

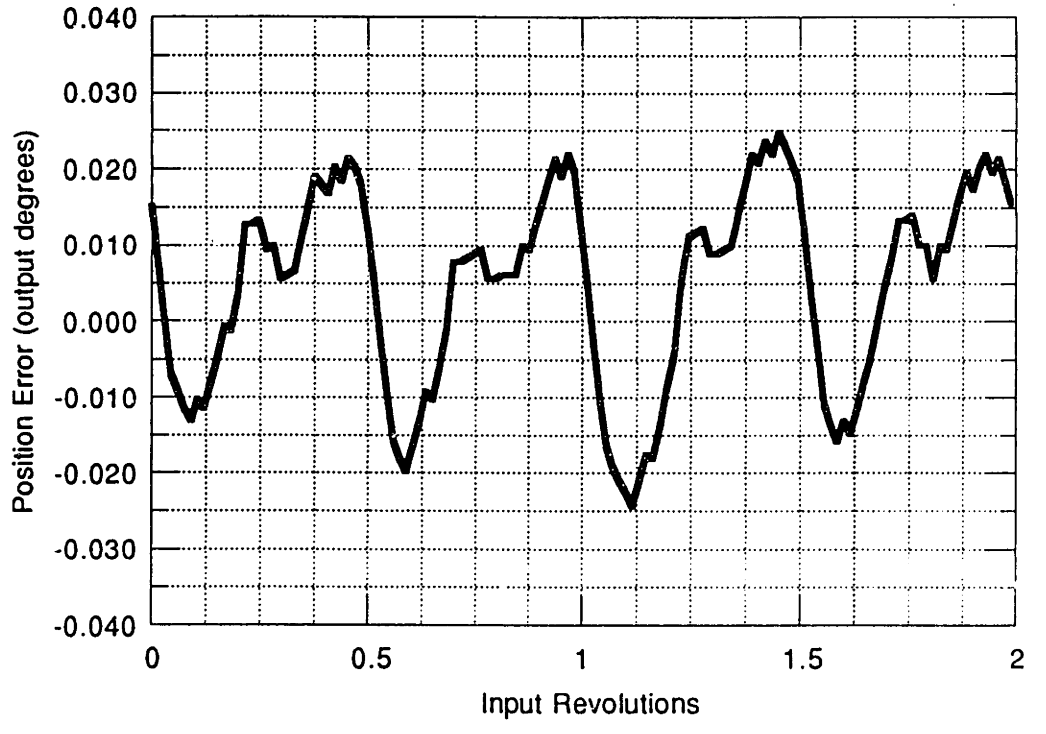

Figure 2.9: Joint 1 position-error waveform at the input rotation frequency

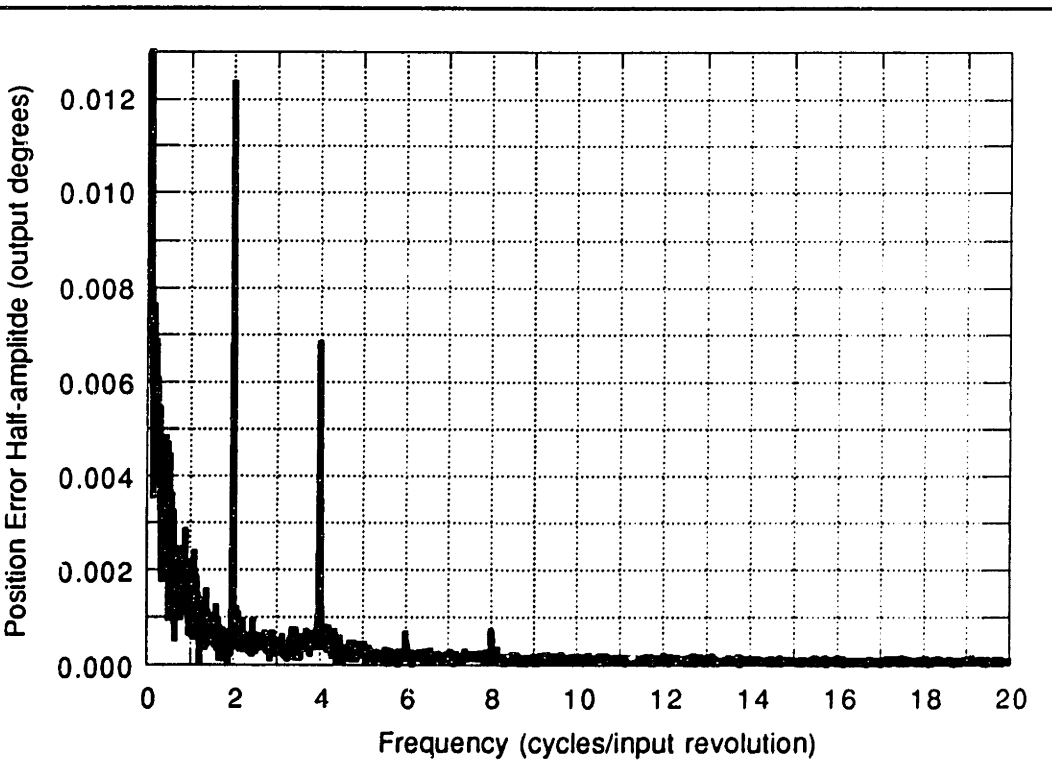

Figure 2.10: FFT of joint 1 position error in cycles per input revolution

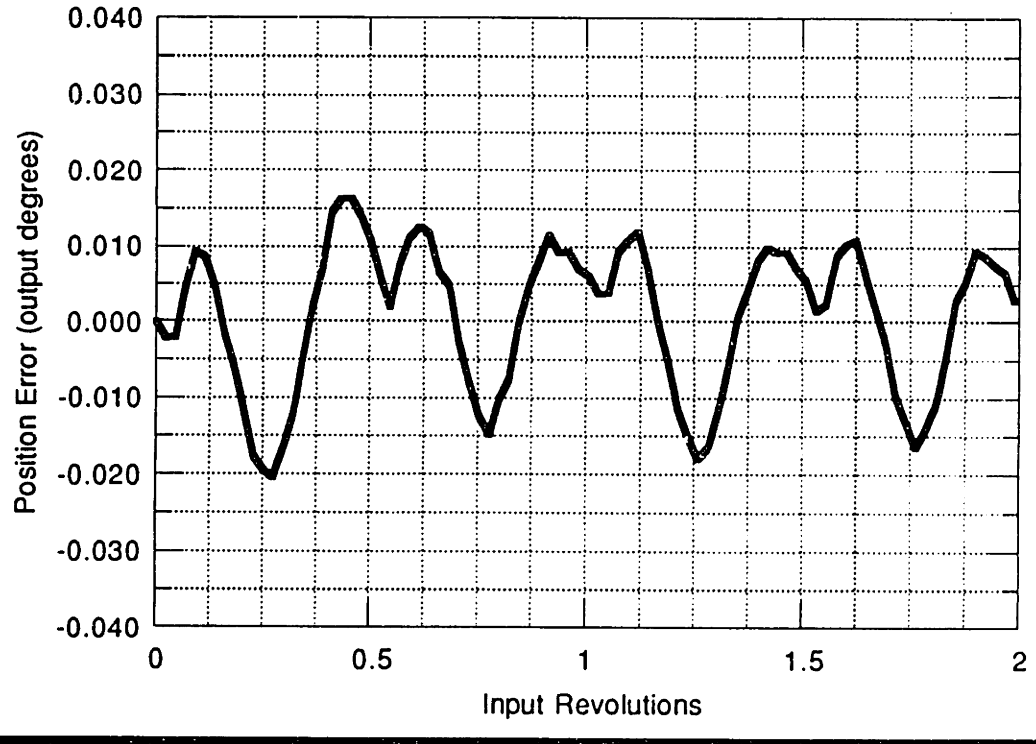

Figure 2.11: Joint 2 position-error waveform at input rotation frequency

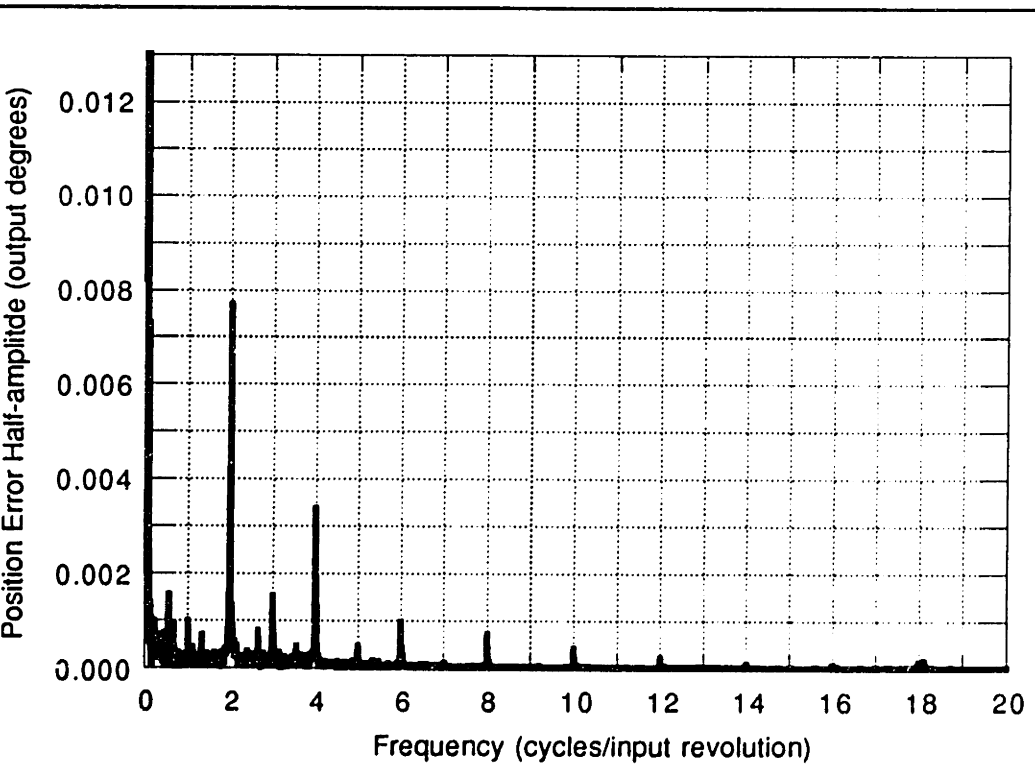

Figure 2.12: FFT of joint 2 position error in cycles per input revolution

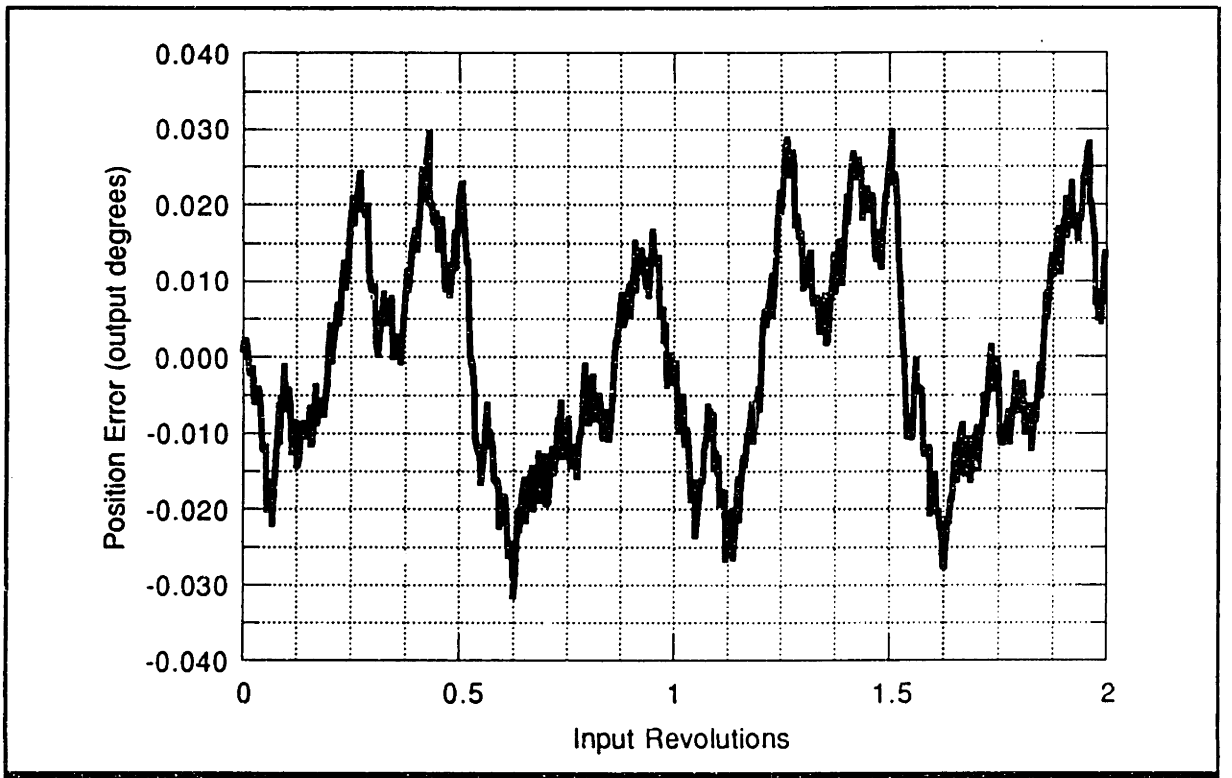

Figure 2.13: Joint 3 position-error waveform at input rotation frequency

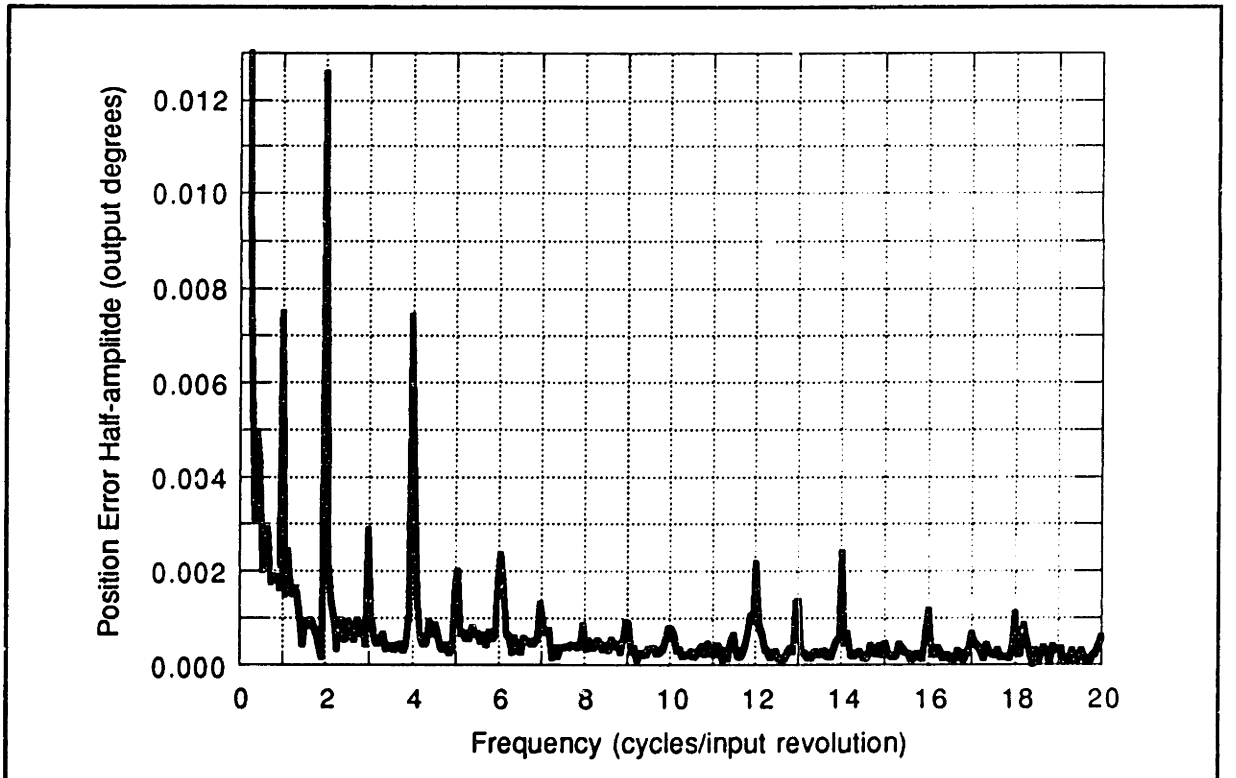

Figure 2.14: FFT of joint 3 position error in cycles per input revolution

Table 2.8: Total peak-to-peak position error for the three harmonic drives			
	Joint 1	Joint 2	Joint 3
Measured value (output °)	0.045	0.030	0.060
Quoted value (output °)	0.042	0.053	0.095

As past research suggests, the kinematic-error results display a primary error component at 2.0 cycles-per-input-revolution with smaller contributing components appearing in the next eight harmonics. As noted by Nye and Kraml, [24], in many FFT spectra, such as the ones for joints 2 and 3, the error component of the last observable harmonic, eighteen cycles-per-input-revolution, was surprisingly large in amplitude. Harmonic content contributed typically less than sixty percent of the total error signal. Additionally, in many FFT spectra, such as the ones for joint 2 and 3, error components were seen at 1.0 cycles-per-input-revolution and subsequent harmonics. This observation is not surprising since any misalignment or improper mounting of harmonic-drive components could likely produce kinematic error at this frequency.

Through qualitative observations made during experimentation, I noticed a strong sensitivity of error magnitude and composition on joint velocity. More specifically, slight changes in the joint velocity during data collection caused noticeable variation in the position error signatures. For example, some tests, especially on joint 2 and 3, revealed discrepancies in error amplitude of up to 100 percent. Through investigations into the dynamic behavior which will be discussed later, it was discovered that, due to the high fluctuating torques excited by transmission error during rotation, significant torsional deflection can occur in the harmonic drive which increases or decreases position error. Since the harmonic drives on joint 2 and 3 have lower stiffness than the one on joint 1, it is likely that they are more susceptible to kinematic-error contamination by torsional deflection. The results presented above were collected carefully at slow velocities which exhibited minimal resonance vibration. Despite this experimental prudence, the true accuracy of the above results can only be determined by understanding the dynamic behavior of the transmission. Consequently, due to this breakdown of the quasi-static assumption, future position-error testing should be conducted on a stationary transmission in order to ensure measurement accuracy.

By disassembling and reassembling the harmonic drive testing equipment between experiments, I observed some interesting behavior in the position-error profiles. In

particular, for a few tests, the largest position-error component appeared at four cycles-per-wave-generator revolution rather than two, and harmonic content of the aggregate error waveform increased substantially. Fortunately, no significant changes in the overall position-error magnitude were observed in the testing apparatus due to joint reassembly. However, as Nye and Kraml note in [24], since alignment can influence the magnitude of kinematic error in harmonic drives, I would not have been surprised if less careful reassembly resulted in different kinematic-error measurements.

2.2.2.1.2 High-Resolution FFT Analysis of Primary Error Component

To satisfy my curiosity, I performed a few tests in which I increased the FFT resolution around the two-cycles-per-input-revolution frequency by increasing the number of sampled data points. Not surprisingly, I discovered that separate and distinct error components appeared at the primary transmission-error frequency. Figure 2.15 shows an FFT magnitude spectrum for joint 1 magnified around the frequency of 2.0 cycles-per-input-revolution. As illustrated in this plot, an error component not only appears at the frequency of 2.0, but also at 2.0125 cycles-per-input-revolution. These two components can be explained by assuming that most harmonic-drive inaccuracy occurs due to gear-tooth

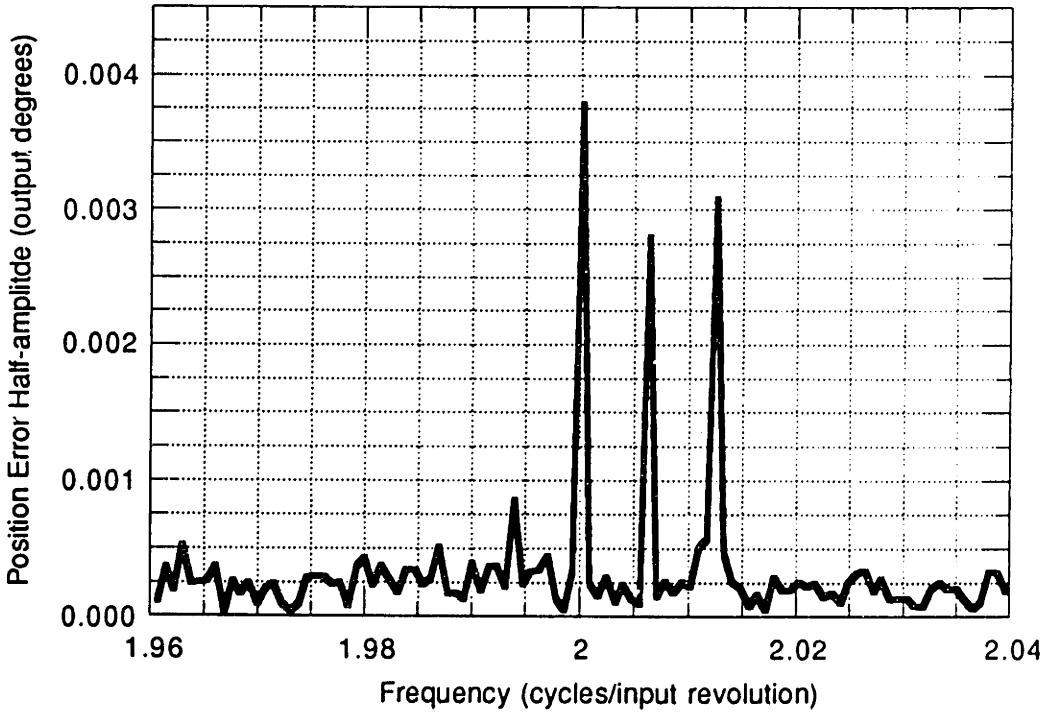

Figure 2.15: High resolution FFT of joint 1 primary position-error

placement error and realizing that, during joint rotation, the flexspline moves relative to the circular spline. Specifically, since the input position sensor on joint 1 measures wave-generator rotation with respect to the circular spline, one-half revolution of the wave-generator will rotate the tooth-meshing zone exactly 180 degrees around the circular spline and complete one-cycle of the circular spline gear-error waveform. At the same time, since the circular spline will rotate one tooth ahead of the flexspline after this 180 degree wave-generator rotation, the flexspline gear-tooth error waveform will have completed one complete cycle plus one gear tooth or (1 + (1/N)) cycles. Therefore, since the gear ratio, N, on joint 1 is 160, for every complete rotation of the wave-generator the circular spline gear-tooth error will have completed two complete cycles and the flexspline gear error will have completed 2 (1 + (1/160)) or 2.0125 cycles. From this explanation, it can be seen that the error component in figure 2.15 that appears at two cycles-per-input-revolution is due to the circular spline gear-tooth-placement error and the error component that appears at 2.0125 cycles-per-input-revolution is due to the flexspline gear-tooth-placement error. Figure 2.15 also illustrates an error occurring at 2.00625 cycles-per-input-revolution which is probably due to the non-sinusoidal nature of the other two neighboring components.

This high-resolution FFT analysis of the characteristic harmonic-drive kinematic-error frequencies may prove useful for many purposes. First, the presence of two distinct error components is strong evidence to reinforce the belief that the primary source of kinematic error in harmonic drives is due to gear-tooth inaccuracy in the flexspline and circular spline. Additionally, since this method can be used to extract quickly the individual position-error components due to the flexspline and circular spline, it may prove useful for characterizing the manufacturing accuracy of these two components as well as their individual performance accuracy under varied operating conditions. Lastly, since the amplitude modulation, or beating, that can appear in kinematic-error signatures is a product of these two distinct error components, the amount of beating in a given drive can be identified easily from the magnitude of these two individual errors.

2.2.2.1.3 Error at the Output Rotation Frequency

Using the phase-shift procedure described previously to separate the harmonic-drive error components at low spatial frequencies from the position inaccuracies of the output sensor gear-train, the FFT spectra shown in figures 2.16 and 2.17 were found. For both of these plots, position error was measured in degrees of output position with respect

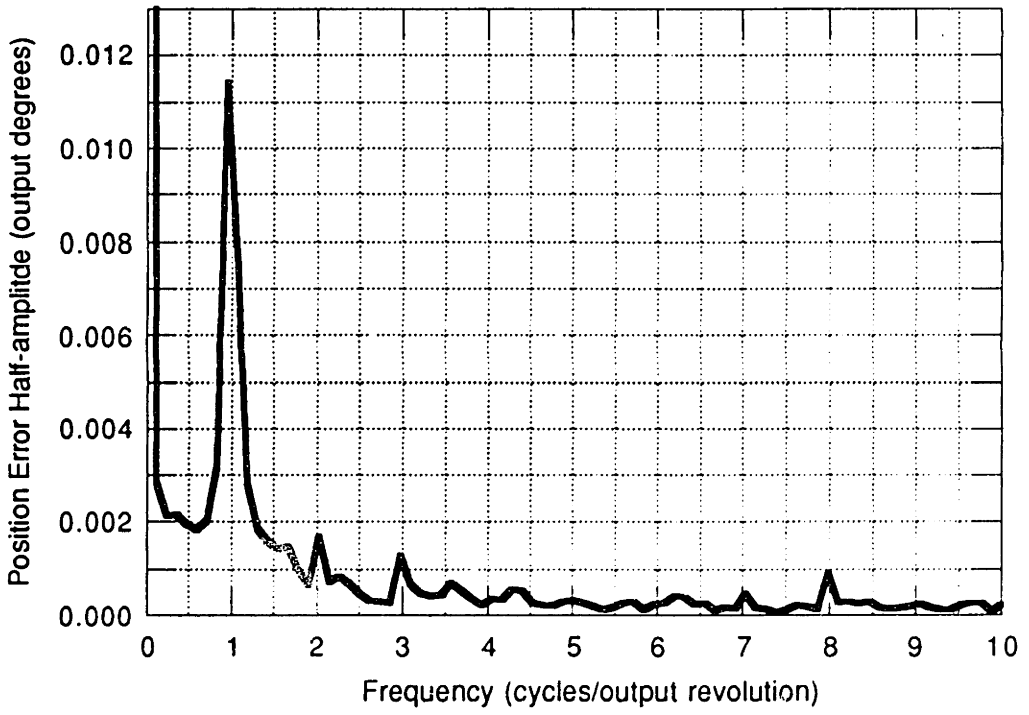

Figure 2.16: FFT of joint 1 position error in cycles per output revolution

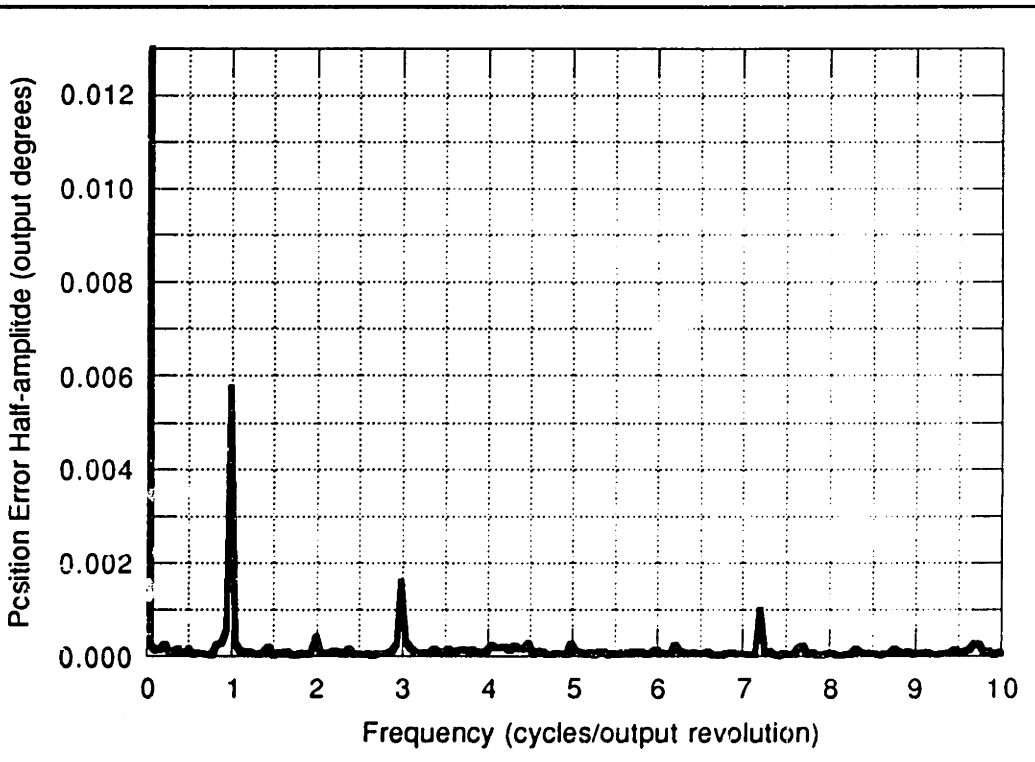

Figure 2.17: FFT of joint 3 position error in cycles per output revolution

to the frequency of output (circular-spline or flexspline), rather than input, rotation. From figure 2.16, it can be seen that the joint 1 harmonic drive exhibits a low-frequency error component occurring once per output revolution. The FFT peak that appears at 8.0 cycles-per-output-revolution is caused by inaccuracy in the output sensor pinion and should be ignored. In Figure 2.17, the error components for the joint 3 harmonic drive appear primarily at 1.0 and 3.0 cycles-per-output-revolution. Again, the FFT spike occurring at 7.2 cycles-per-output-revolution is due to the output sensor pinion and should not be mistaken for harmonic-drive error. In both of these plots, the aggregate low-frequency error component due to harmonic-drive transmission-error remains significantly less than the harmonic-drive error observed at multiples of the input rotation frequency. Unfortunately, due to the limitations of the testing apparatus, the low-frequency position error of the joint 2 harmonic drive could not be measured.

By performing a theoretical sensitivity analysis of the data-collection procedure, I determined that deviations in the final FFT error results due to known measurement uncertainly in the apparatus should be less than five percent. However, the results from several different trials showed variations in harmonic-drive error magnitude approaching sixty percent. This variance illustrated the high sensitivity of the low-frequency harmonic-drive error on operating conditions such as rotational velocity.

The source of this low-frequency harmonic-drive error is probably a combination of harmonic-drive gear error and assembly errors. For example, it is conceivable that tooth-placement errors on the rotating output harmonic-drive component (circular spline or flexspline) could causes position deviations over one output rotation. Additionally, any misalignment of the flexspline or circular spline could cause similar position errors at multiples of the output rotation frequency.

2.2.2.1.4 Error at High Frequencies

Another set of experiments that I performed focused on higher rotational frequencies in order to detect the passing of harmonic-drive teeth in the position-error data. As figures 2.18 and 2.19 illustrate, essentially no position error components are visible at high spatial frequencies. Since the joint 2 harmonic drive has 320 gear teeth which engage for every input revolution, any contribution of the tooth-profile error to the aggregate position error should appear in figure 2.18 at a frequency of 320 cycles-per-input-

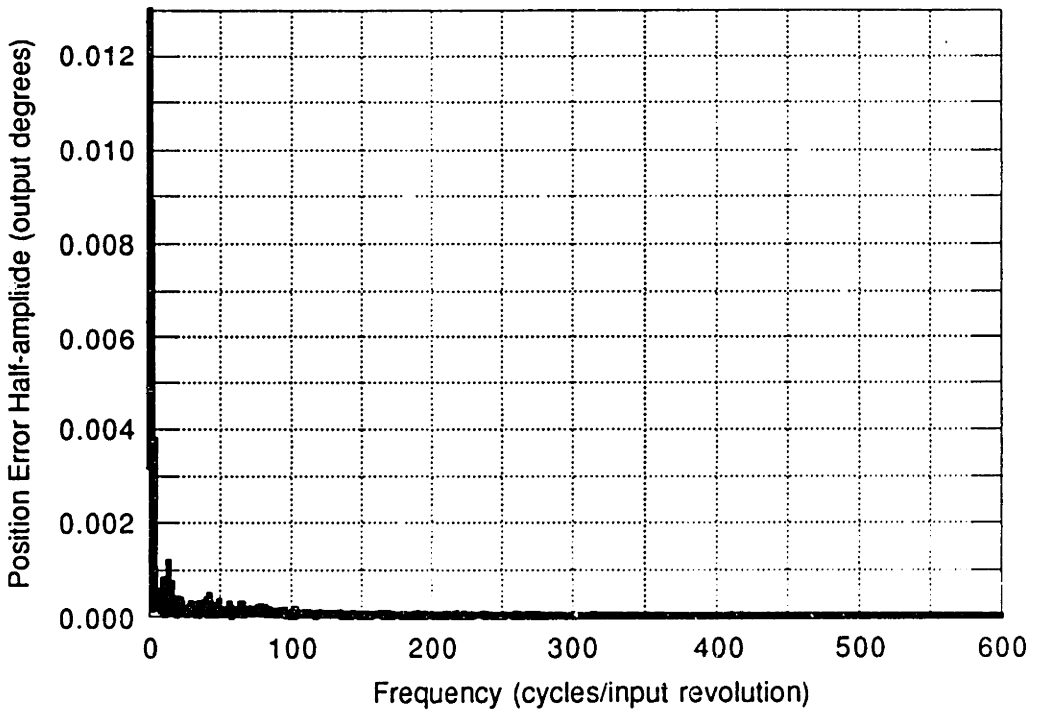

Figure 2.18: FFT of joint 2 high-frequency position error

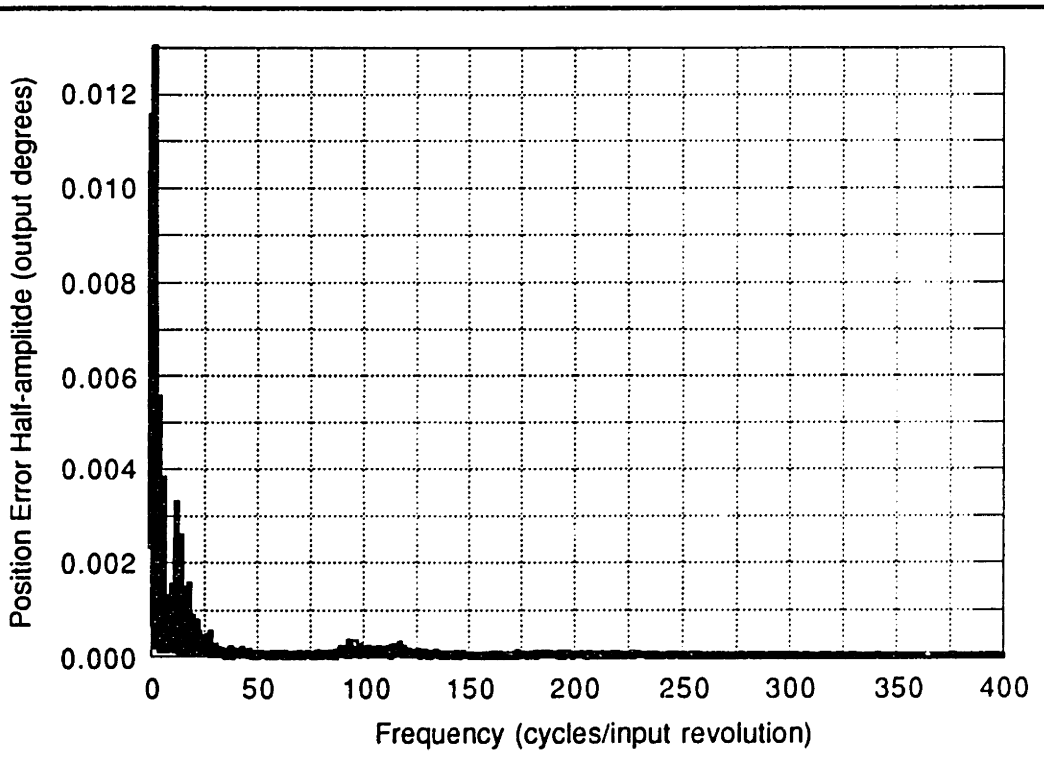

Figure 2.19: FFT of joint 3 high-frequency position error

revolution. Similarly, since the joint 3 harmonic drive contains 160 gear teeth, the tooth-passing frequency should be seen at 160 cycles-per-input-revolution in figure 2.19. However, for both joints, no detectable error component was found at these frequencies. This unexpected result can be justified by recognizing that, at any point in time, the harmonic drive has several teeth in contact due to the concentric nature of its design and the shape of the wave-generator. Close observation revealed that the harmonic drives tested typically had up to twenty teeth in contact on both sides of the wave-generator. Given this result, it is unlikely that the individual error of a single gear tooth could manifest itself in the aggregate position-error spectrum. Unfortunately, the high-frequency error components on the joint 1 harmonic drive could not be measured due to resolution limitations of the output position sensor.

2.2.2.2 Comparison to Catalog Values

As listed in Table 2.8 in section 2.2.2.1.1, catalog predictions of harmonic-drive inaccuracy are compared to the combined amplitude of the error components measured at multiples of the input rotation frequency. From these values, it can be seen that the peak-to-peak error magnitude of the observed waveforms was less than or near the manufacturer's quoted accuracy ratings. Also, as noted in the catalogs, the primary error component in all cases occurred twice every wave-generator rotation, but the catalogs failed to offer any predictions about the harmonic content of these signals or error components at other frequencies.

2.2.2.3 Modeling Considerations

Having measured the magnitude of the harmonic-drive kinematic-error components at a range of different frequencies, a mathematical representation of this behavior can be easily constructed. Specifically, by using a harmonic series, the aggregate effect of the important individual error components can be compiled:

$$\theta_{erfn} = A_1 \sin(\omega_1\theta_1 + \phi_1) + A_2 \sin(\omega_2\theta_2 + \phi_2) + \ldots, \qquad (2.7)$$

where A is the half-amplitude, ω is the spatial frequency, θ is a measure of rotation, and ϕ is the phase of the given error component. Depending of the required accuracy of this representation, the number of terms in the harmonic series can be varied. Typically, in the

modeling efforts to be discussed later, I relied mainly on the two largest error components, which appeared at twice- and four-times every input revolution. The resulting harmonic-series representation of this error is

$$\theta_{erfn} = A_1 \sin(2\theta_{in} + \phi_1) + A_2 \sin(4\theta_{in} + \phi_2), \tag{2.8}$$

where θ_{in} is the rotation of the harmonic-drive input. To be truly accurate, as indicated in the high-resolution tests presented above, two distinct error components should be included for each of the two terms in this series to account for the individual error contributions of the flexspline and circular spline which occur at slightly different frequencies. However, since it is unlikely that this small change will significantly influence performance of a dynamic model, this effect will be ignored.

2.2.3 Kinematic Error Conclusions

As discussed above, the experimental investigation of harmonic-drive kinematic error has confirmed previously observed behavior of position-error profiles as well as lent new insight about the sources and stability of harmonic-drive transmission inaccuracy. In particular, the magnitude of all observed position error-signals agreed with manufacturer's specifications and the primary frequencies of aggregate error appeared at 2.0 cycles-per-input-revolution and subsequent harmonics. Additionally, these primary error components were confirmed to be produced by two separate error signals most likely due to the gear-tooth error on the circular spline and flexspline. Furthermore, a small but measurable amount of kinematic error was found at the frequency of output revolution while no significant position-error components were detected at the significantly higher tooth-passing frequencies. Based on these results, a simple harmonic series of the individual error components was generated in order to predict harmonic-drive kinematic error. Since transmission compliance can influence position-error measurements even at small rotational velocities, it is recommended that future kinematic tests on harmonic drives be performed under truly static circumstances.

2.3 Stiffness Testing

The purpose of my investigation into harmonic-drive flexibility was two-fold: (1) I wanted to collect accurate stiffness data for the three harmonic-drive specimens to include in my dynamic models, and (2) I hoped gain a better understanding of possible ranges and sources of variation in typical stiffness profiles. As a result of my investigation, I not only characterized the harmonic-drive non-linear stiffness behavior and hysteresis loss, but also discovered that harmonic-drive stiffness measurements are surprisingly fickle and very dependent on assembly and operating conditions. This section is devoted to describing the testing procedure used to collect stiffness data as well as presenting the results of my investigation.

2.3.1 Experimental Procedure

The three harmonic-drive test stations were used to collect stiffness data by locking the wave-generator to the circular spline and applying a range of loads to a long output link. Figure 2.20 illustrates the testing equipment for joint 1 used to apply loads to the harmonic

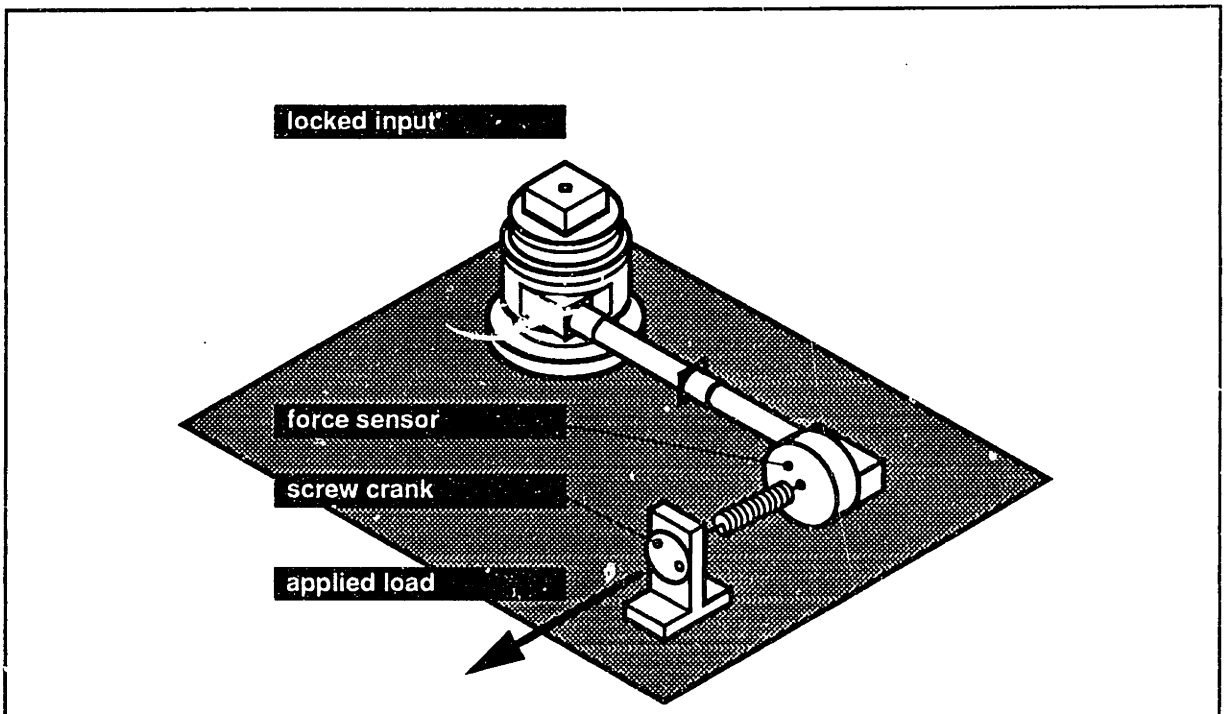

Figure 2.20: Apparatus for harmonic-drive stiffness tests

drive which is typical of the apparatus for the other two joints. The testing procedure used on each joint is as follows.

1. Lock the wave-generator of the harmonic drive to be tested to its circular spline with a rigid fixture.
2. Apply a load to the end of the output link of the joint using the screw-crank apparatus.
3. Read and store output rotation data from the output position sensor and output torque data from the torque sensor.
4. Continue collecting data for a range of positive and negative applied loads until the stiffness curve is complete.

This straightforward procedure was used to collect multiple sets of stiffness data on each transmission and generate the results presented below.

2.3.2 Discussion of Results

The stiffness results collected on the three harmonic drives can be divided into three separate categories. First, a typical stiffness profile for each of the tested transmissions is discussed and variations in these measurements with environmental and operating conditions are outlined. Second, these stiffness results are compared to manufacturer's quoted values in order to identify and explain discrepancies, and, lastly, theoretical methods for capturing the observed stiffness behavior are considered.

2.3.2.1 Characteristic Stiffness Profiles

Figures 2.21, 2.22. and 2.23 illustrate the measured stiffness curves on the three harmonic drives. Due to torque-sensor loading limitations, the joint 1 harmonic drive was loaded to 35 percent of its rated maximum torque, the joint 2 harmonic drive was loaded to 45 percent of its rated maximum torque, and the joint 3 harmonic drive was loaded to 90 percent of its rated maximum torque These torque limitations, however, encompass the entire range of dynamic behavior seen by the harmonic drive in experiments to be discussed later. All three stiffness profiles exhibit noise due to limitations on position sensor resolution.

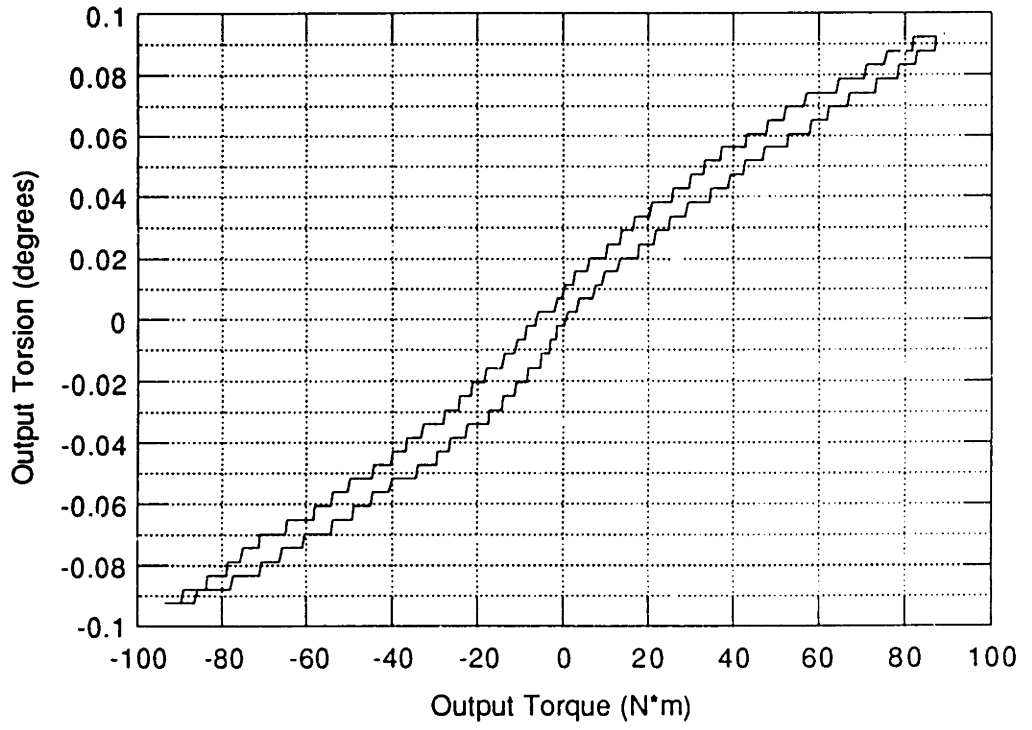

Figure 2.21: Joint 1 harmonic-drive stiffness curve

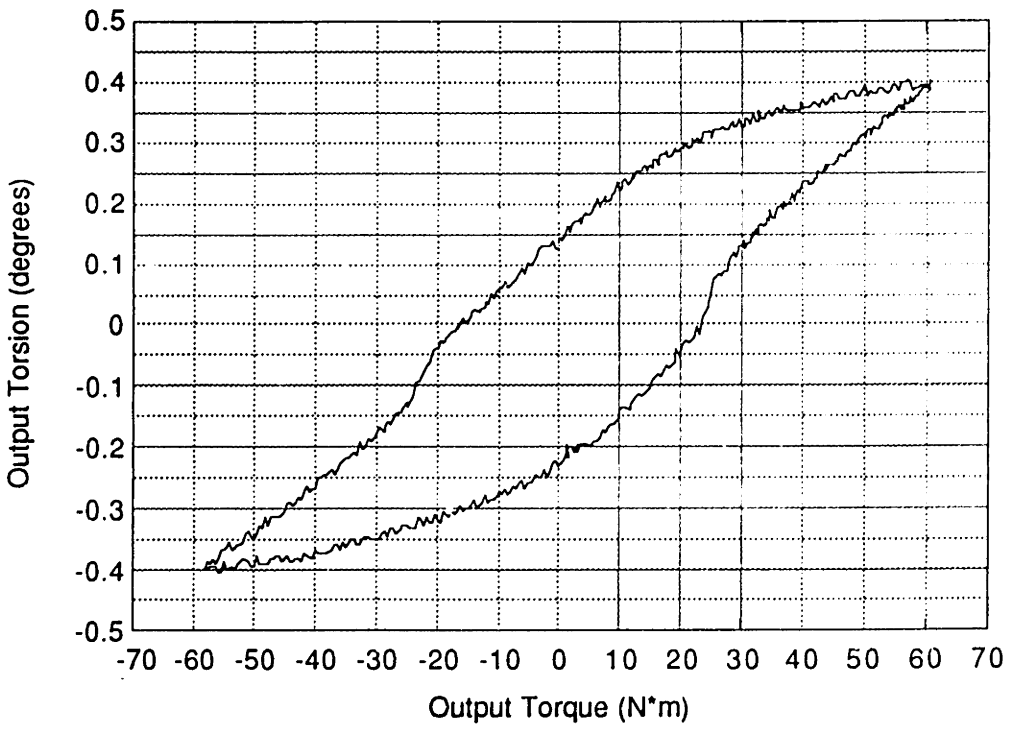

Figure 2.22: Joint 2 harmonic-drive stiffness curve

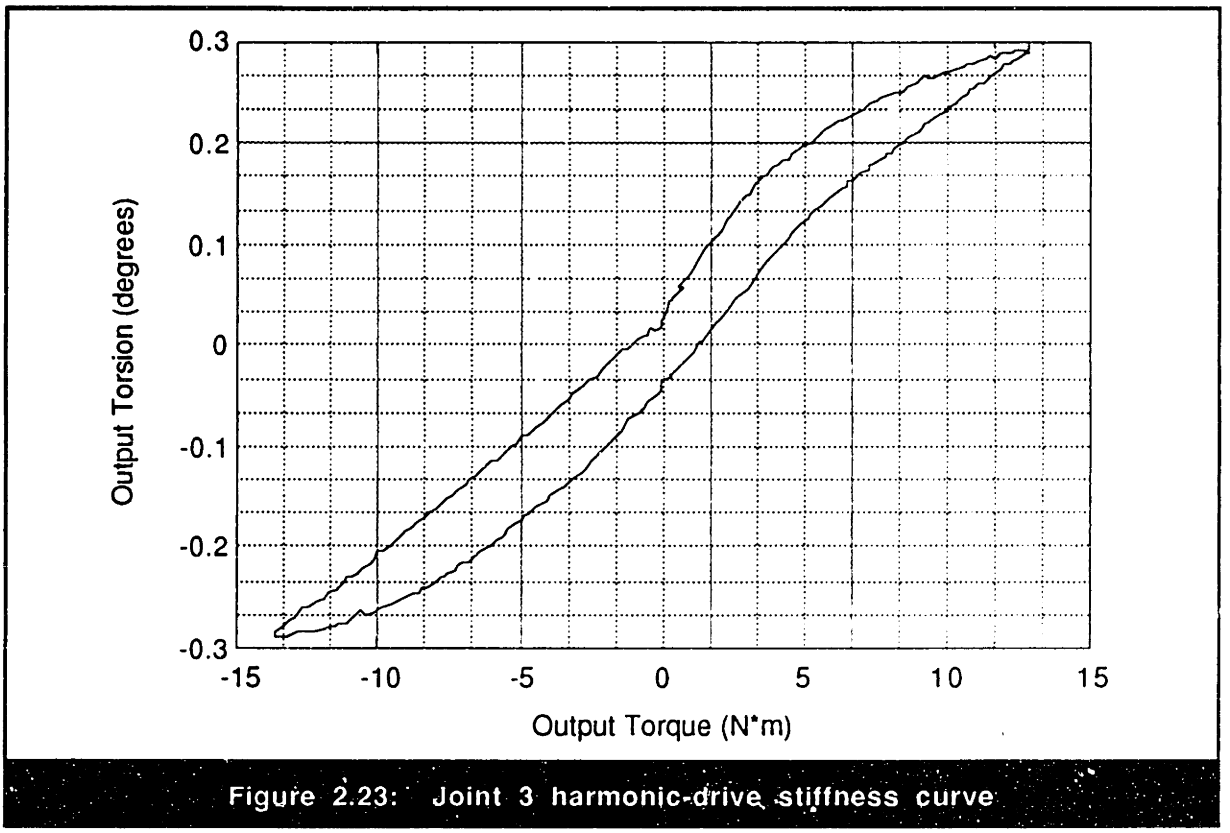

Figure 2.23: Joint 3 harmonic-drive stiffness curve

As mentioned in manufacturer's catalogs, all three harmonic drives exhibit a non-linear stiffness with appreciable hysteresis loss. As illustrated in figure 2.21, the harmonic drive on joint 1 displays a fairly well-behaved stiffness profile with a nearly linear stiffness and little hysteresis over the test range. As explained in the catalog, increased loading on this harmonic drive should increase the non-linearity of the stiffness curve. The stiffness profile of the joint 2 harmonic drive, as illustrated in figure 2.22, shows significant non-linearity despite being loaded over only 45 percent of its rated torque range. Additionally, a hysteresis loss is visible which is substantially larger than the loss observed on the other two harmonic drives. Since no backlash was present in the joint 2 testing apparatus, this hysteresis can be blamed on a combination of static friction and very low stiffness levels at low applied torques, also called soft wind-up, which can sometimes act like backlash. The stiffness curve for the joint 3 harmonic drive, as presented in figure 2.23, shows very typical behavior with a non-constant slope and a modest amount of hysteresis.

Another set of stiffness tests that I performed were aimed at gaining a qualitative understanding of how stiffness varied with environmental and operating conditions. In particular, I used the joint 1 testing station to collect data for a range of different preloads and wave-generator angles. Figure 2.24 shows three stiffness curves generated from data

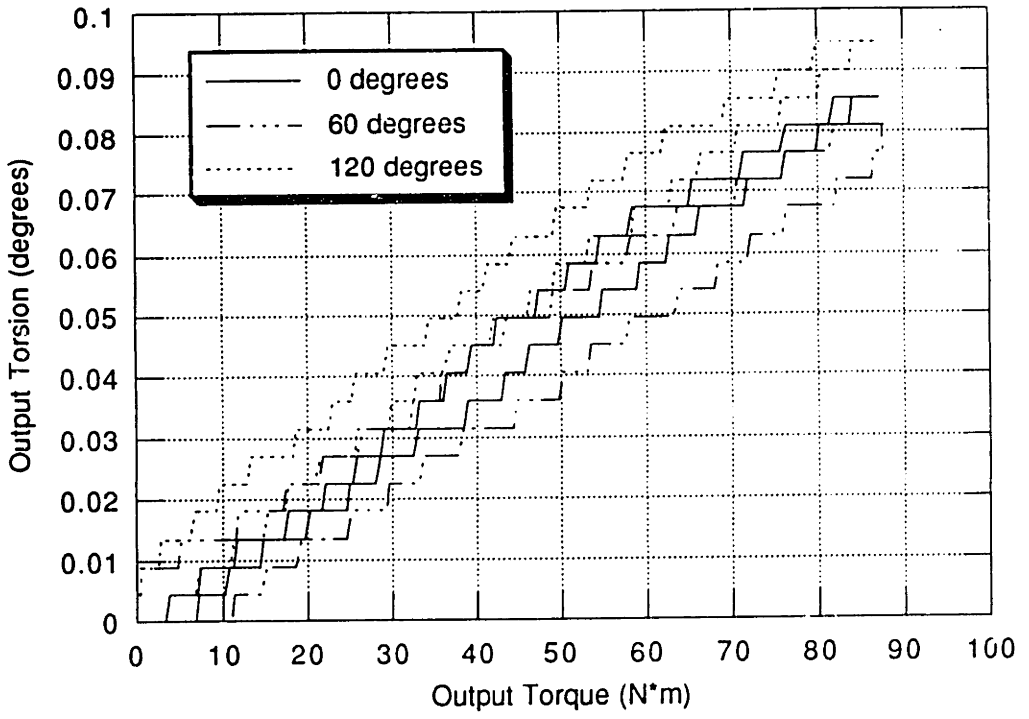

Figure 2.24: Joint 1 stiffness curves for different wave-generator angles

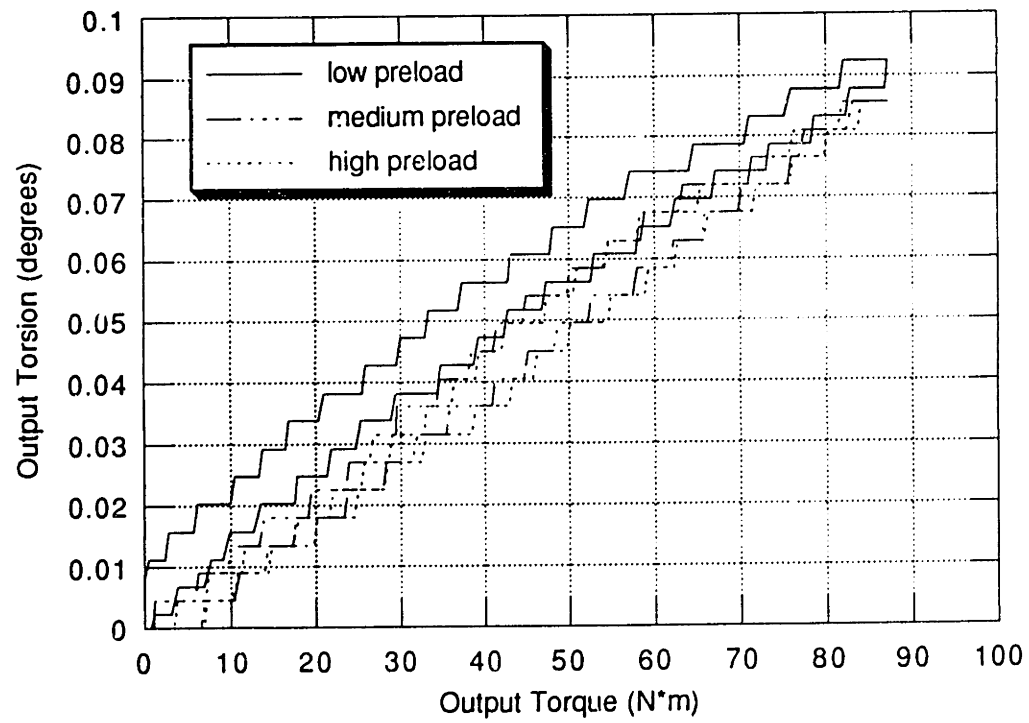

Figure 2.25: Joint 1 stiffness curves for different wave-generator preloads

collected with the wave-generator major-axis locked in different positions relative to the circular spline. As the difference between these curves indicates, variations in stiffness of up to 25 percent may be measured due to different orientations of the wave-generator. Figure 2.25 illustrates three different stiffness curves collected when the preload between the harmonic drive gear teeth was varied by changing the depth of the wave-generator in the flexspline. While wave-generator depth is not a direct indicator of gear-tooth preload, it was observed to influence the radial loading of the harmonic drive in many cases. The test labeled "high preload" corresponds to the case where the wave-generator was pushed into the flexspline to its maximum depth while the low-preload case saw the wave-generator at minimum depth. From the stiffness curves in this plot, it can be seen that slight variations in preload can also influence the value of harmonic-drive stiffness.

In general, from the range of behavior illustrated in the stiffness results, it can be concluded that the variation in stiffness profiles between different harmonic drives can be substantial. As seen on joints 1 and 2, one drive can behave relatively linearly in the low-to-medium torque range while another can exhibit a strikingly non-linear profile over the same loading range. Additionally, the presence of hysteresis due to phenomenon such as friction and soft wind-up may be dominant in one harmonic drive while unnoticeable in another. Furthermore, the substantial variations in harmonic drive flexibility due to such factors as preloading and input orientation indicate the sensitivity of stiffness measurements. This gloomy forecast for the predictability of harmonic-drive flexibility grows more overcast when these results are compared to manufacturer's quoted values.

2.3.2.2 Comparison to Catalog Values

In manufacturer's catalog [4], a piecewise-linear-approximation method is proposed for predicting harmonic-drive stiffness. In particular, two-piece linear fits are quoted for the case of a standard stiffness profile and an optimal, or maximum-stiffness, profile. Figures 2.26, 2.27, and 2.28 show these two piecewise linear approximations compared to the measured stiffness for each harmonic-drive model. As these results illustrate, the joint 1 harmonic-drive stiffness is considerably different from the quoted values while the transmission stiffness on joints 2 and 3 more closely resembles the catalog stiffness profiles. More specifically, on joint 1, the measured harmonic-drive stiffness is about 30 percent greater than the optimal stiffness curve and about 60 percent greater than the

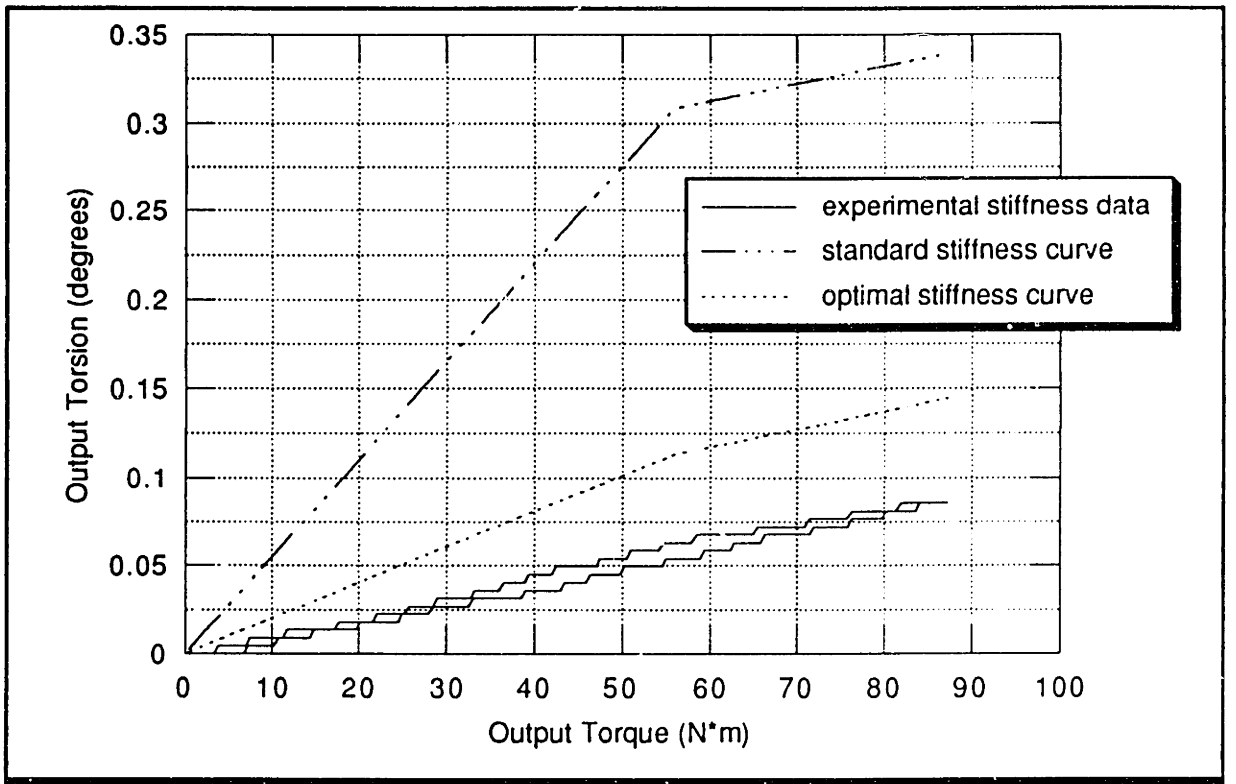

Figure 2.26: Joint 1 linear approximations to stiffness data

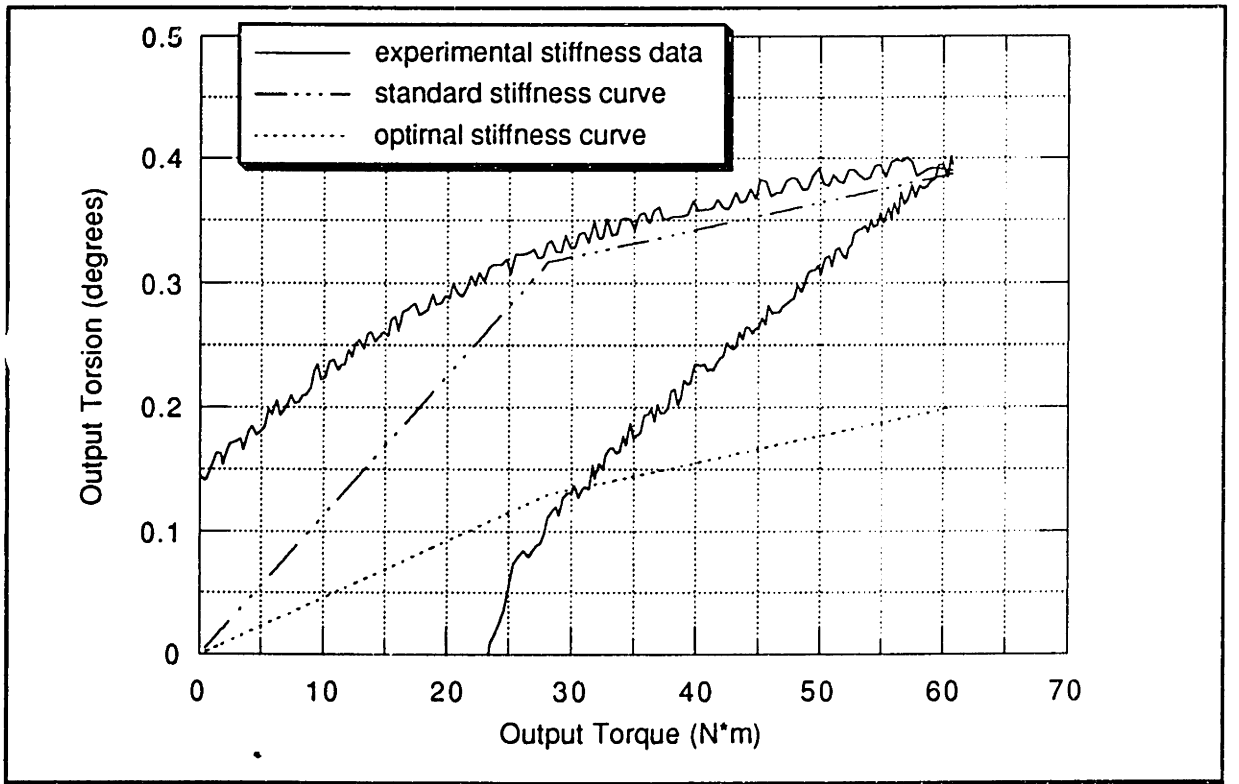

Figure 2.27: Joint 2 linear approximations to stiffness data

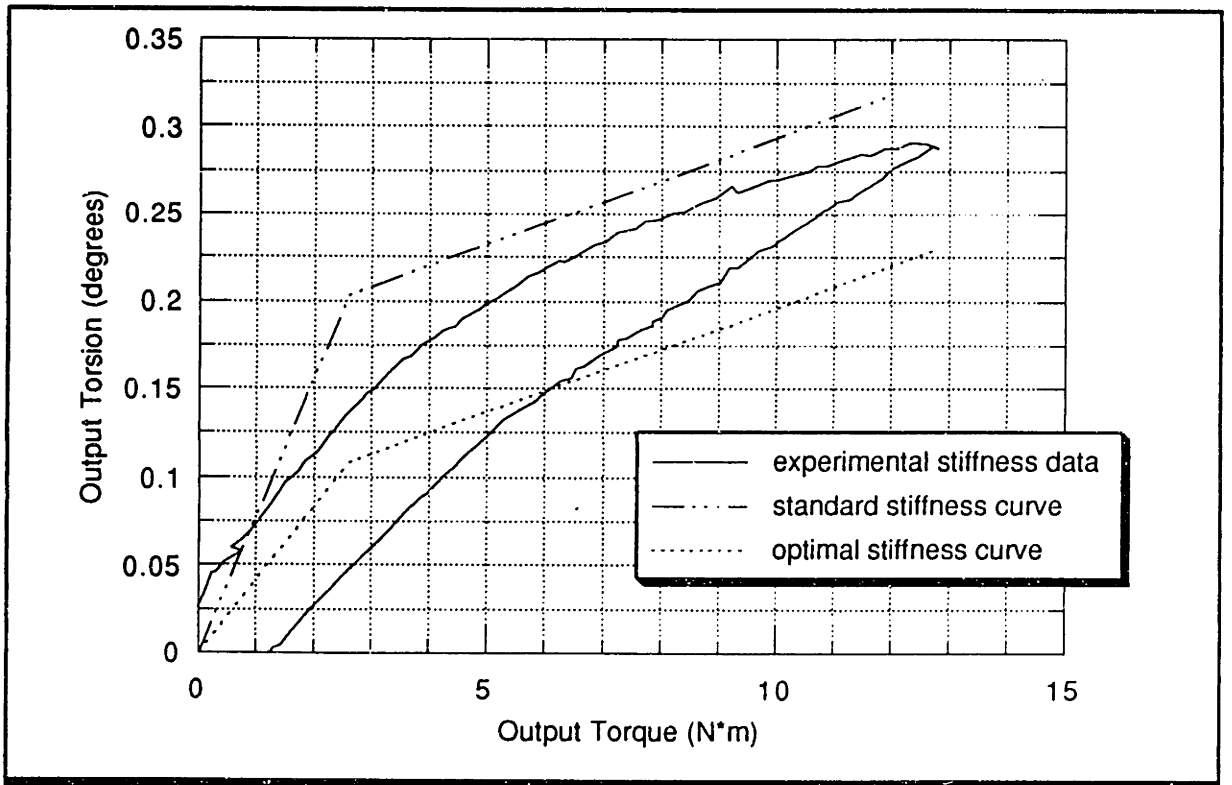

Figure 2.28: Joint 3 linear approximations to stiffness data

standard stiffness curve. As noted in past research, this unexpectedly high stiffness can probably be explained by a high gear-tooth preload in the harmonic drive. The lack of hysteresis loss observed on joint 1 also supports this postulation since a higher preload would eliminate any soft wind-up in the transmission. On joint 2, the measured stiffness while loading the harmonic drive is slightly lower than the standard stiffness approximation while the optimal quoted stiffness agrees closely with the unloading portion of the measured stiffness curve. On joint 3, both the loading and unloading portions of the measured stiffness curve have a slope that agrees with the standard stiffness approximation within about 10 percent. In partial confirmation of the discrepancies between predicted and measured stiffness values, manufacturer's catalog [3] warns that a 30 percent variation between quoted and actual stiffness values is not uncommon. In terms of hysteresis, catalog [3] states that hysteresis loss rarely exceeds 0.033 degrees of output torsion and that soft wind-up is kept below 0.05 output degrees of rotation. This prediction holds true for joints 1 and 3 but is greatly underestimated for the joint 2 harmonic drive.

This comparison between experimental data and catalog predictions exposes the shortcomings of manufacturer's estimates. Multiple stiffness curves collected on each harmonic-drive assembly illustrated that experimental results were fairly repeatable to

within about ten or fifteen percent. However, measured values of stiffness and hysteresis loss differed unpredictably and significantly from quoted values. In a few instances such as the joint 1 stiffness profile and the joint 2 hysteresis loss, measured values even fell outside of the manufacturer's predictability tolerances.

2.3.2.3 Modeling Considerations

Figures 2.29, 2.30, and 2.31 show cubic approximations to the stiffness curves for the three harmonic drives. In all cases, the cubic polynomial was fit to the portion of the stiffness data collected during joint loading rather than unloading. From these results, it can be seen that cubic approximations can accurately capture the shape of experimental stiffness data. Based on this result, cubic representations of non-linear harmonic-drive stiffness will be used in dynamic modeling efforts to be discussed later.

One measure of the accuracy of harmonic-drive stiffness representation is whether or not it can replicate the observed hysteresis losses. Capturing these effects is dependent on type of dynamic model used for the harmonic-drive and the placement of the flexibility within this model. Conversely, given a harmonic-drive model which can describe

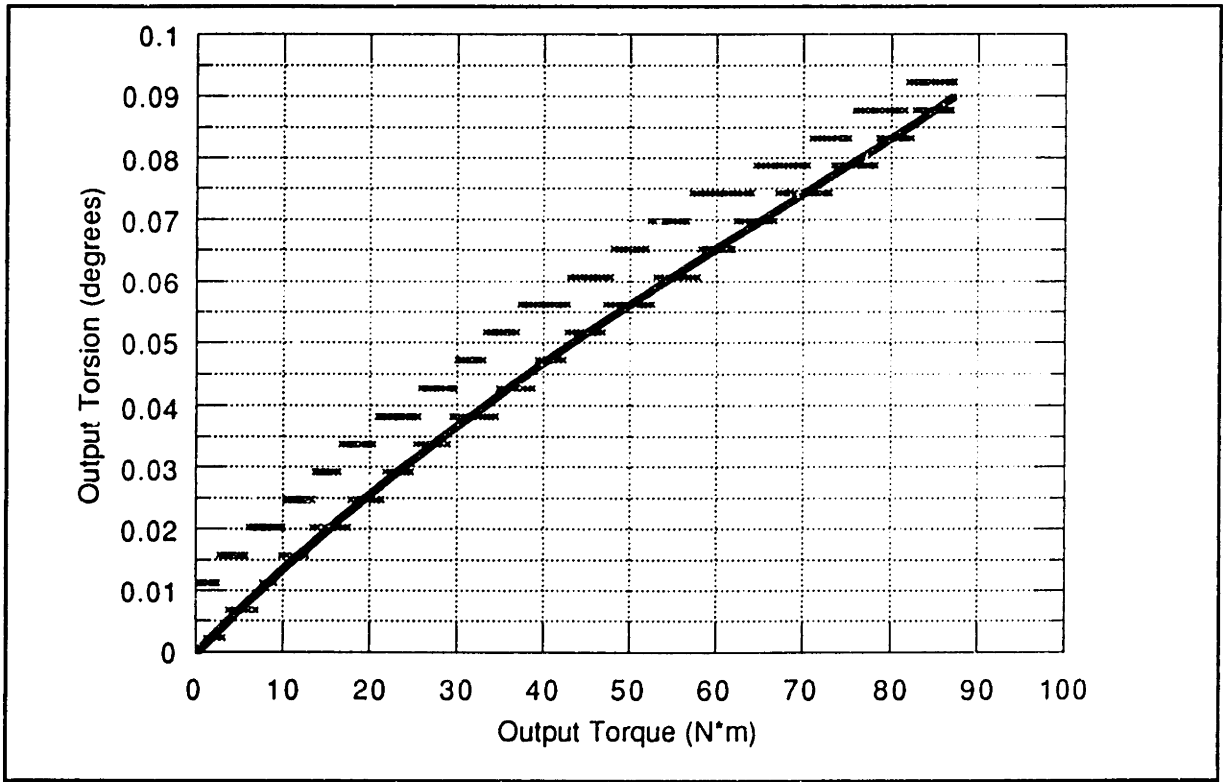

Figure 2.29: Cubic-fit of joint 1 harmonic-drive stiffness data

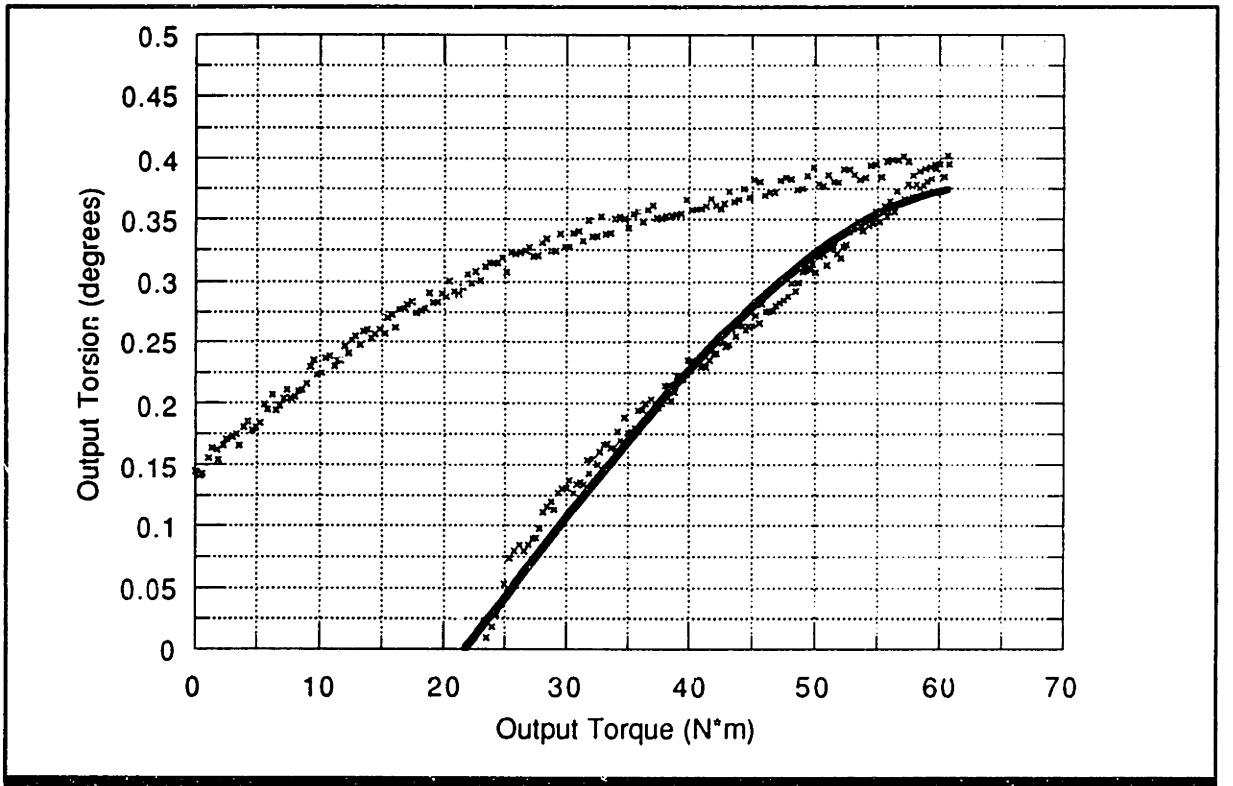

Figure 2.30: Cubic-fit of joint 2 harmonic-drive stiffness data

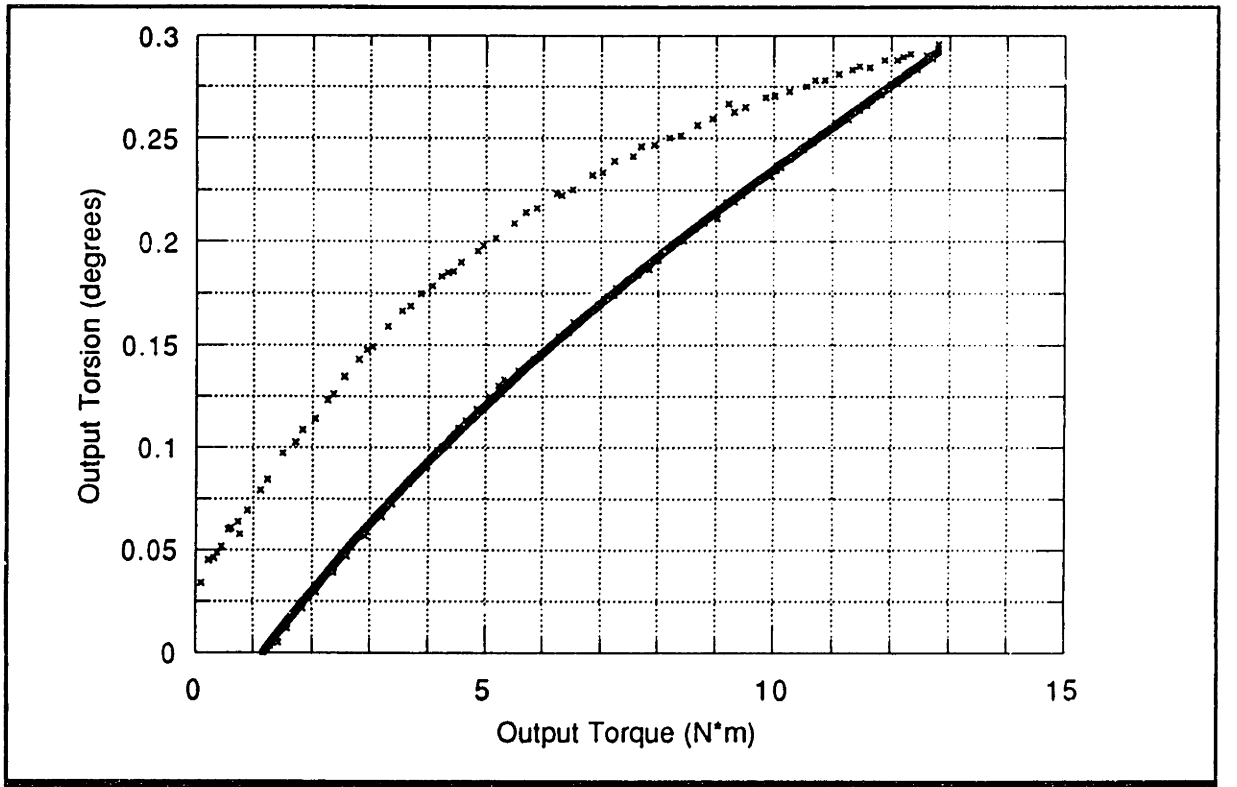

Figure 2.31: Cubic-fit of joint 3 harmonic-drive stiffness data

hysteresis loss, the measured stiffness profiles can be used to make estimates of the friction present in harmonic drives. As discussed later in this document, dynamic models of harmonic drives were developed which capitalized on the friction information stored in the hysteresis loss of the stiffness measurements.

As the observed variation in measured stiffness values indicates, a truly accurate model of harmonic-drive stiffness should describe the dependence of the stiffness profile on parameters such as input angle and gear-tooth preloading. Although I did not perform enough tests to develop a quantitative characterization of these effects, additional measurement of harmonic-drive stiffness over different operating conditions could be performed easily to characterize empirically an accurate stiffness function. Alternatively, a much more difficult but meaningful approach to this problem would be to develop an analytical model which can predict stiffness variations based on harmonic-drive geometry and the physics of operation. I will save this formidable task for later research.

2.3.2.4 A Note on Input Diametral Stiffness

If the wave-generator of an assembled harmonic drive is rotated manually, the torque required to rotate the transmission varies noticeably over one wave-generator revolution. If the circular spline is then removed and the same test is performed on the wave-generator and flexspline alone, the same torque variation is still observed. Although difficult to notice on some drives due to excessive friction, this cyclic torque has a tendency to rotate the wave-generator to preferred orientation when the load is released from the input. These qualitative observations indicate the influence of a diametral flexibility which acts on the harmonic-drive input due to manufacturing and assembly errors in the wave-generator and flexspline. Quick estimates of this input torque amplitude placed its magnitude at about 0.01 N-m for joint 1 and about 0.001 N-m for joints 2 and 3. For most applications, this cyclic torque is significantly less than the operating torque of the harmonic drive and can be ignored. However, in some applications, especially at low velocities, the presence of this cyclic torque can produce variations in rotational velocity at a frequency of twice-per-input-revolution. Consequently, to improve performance of a dynamic model, a simple sinusoidal torque function which varies at the this frequency can be included to replicate the effect of this input diametral flexibility.

2.3.3 Stiffness Conclusions

The most significant conclusion that can be derived from the results in this section in that accurate measurement and prediction of harmonic-drive stiffness profiles can be very difficult. Not only are catalog estimates likely to be significantly different from actual values, but experimental measurement can also vary substantially as a function of operational conditions such as wave-generator angle and preload. To foreshadow issues which appear later in this document during dynamic modeling discussions, the static and coulomb friction which are manifested as hysteresis loss in stiffness measurements compound the problem of extracting accurate stiffness information. Since these friction phenomena are unpredictable and difficult to separate from pure transmission stiffness, the accuracy and usefulness of harmonic drive-stiffness measurements becomes even more nebulous.

2.4 Starting-Torque Measurement

Due to static friction in the harmonic-drive transmission, a finite input torque is required to effect output rotation. The purpose of my investigation into this harmonic drive property was to obtain accurate values for the amount of static friction present in harmonic-drive transmissions and, more importantly, gain insight about the mechanism and behavior of velocity-independent friction in harmonic drives. As a result of this experimental investigation, predicted starting-torque magnitudes were confirmed but their substantial variation with several operating and environmental conditions exposed the complexity of physical mechanism behind the values. This section outlines the procedure used for these tests as well as the experimental observations and resulting conclusions.

2.4.1 Experimental Procedure

The procedure used for these experiments was designed to collect accurate measurements of starting torque in order to understand the amount of static friction present in a stationary harmonic drive. This procedure is listed below.

1. Warm-up the given testing station to a typical operating temperature by running the harmonic drive for several minutes.

2. Gradually apply a current to the input motor while collecting input torque data from the current sensor, and position data from the input encoder.

3. Calculate the harmonic-drive starting torque by subtracting the catalog value for the motor starting torque from the maximum motor torque reached just before the joint began to rotate.

The total starting torque in each harmonic-drive testing station is composed of the individual starting torques due to (1) the input motor, (2) the harmonic drive, and (3) the output bearings. Since the starting torque exerted by the output bearings, as measured from the input, will be very small, accurate values for the harmonic-drive starting torque can be found simply by subtracting the motor starting-torque from the measured value.

2.4.2 Discussion of Results

The results of several qualitative and quantitative investigations into starting-torque behavior are presented below. First, typical starting-torque values will be discussed in light of environmental and operational conditions which can influence their magnitude. Additionally, these values will be compared to catalog predictions and analyzed to gain insight about potential modeling methods. Based on these results, conclusions about harmonic-drive starting-torque behavior will be drawn.

2.4.2.1 Characteristic Starting-Torque Behavior

Table 2.9 lists the measured starting torques for all three harmonic drives. These starting-torque measurements, however, were observed to vary considerably with the rotational position of the harmonic-drive output (flexspline or circular spline). These variations, as listed in table 2.9, can be explained by noting that any misalignment of the flexspline or circular spline, for example, is likely to influence gear-tooth meshing and, consequently, gear-tooth friction over one output revolution. Since these starting-torque values provide a direct measurement of static friction, the substantial variation in starting torque with output position illustrates the sensitivity of static friction in harmonic drives. To further support this unfortunate consequence, additional observations revealed a strong dependency between harmonic-drive starting torque and operating temperature. In a few cases, if testing equipment was not warmed-up before data collection, starting torques could increased by up to 80 percent. This troublesome effect can be explained partially by the increase in lubricant viscosity which increases interface friction at lower temperatures. Additional variables which can constrain the accurate measurement and prediction of harmonic-drive static friction are wave-generator orientation and gear-tooth preload. As noted in previous research, since the orientation of the wave-generator as well as the applied preload can influence the tightness-of-fit between the flexspline and circular spline, static friction has been observed to waver considerably under the influence of these two factors. For example, experimental tests presented in [65] showed that starting torque could vary as much as 50 percent over one rotation of the wave-generator. Due to the limitations of the testing equipment, I was not able to confirm this result, however qualitative observations clearly demonstrated the importance of input angle and preload on starting-torque measurement.

Table 2.9: Input starting-torque values for the three harmonic drives			
	Joint 1	Joint 2	Joint 3
Measured value (N-m)	0.084	0.031	0.005
Quoted value (N-m)	0.078	0.035	0.007
Variation with output angle	10 %	25 %	15 %

2.4.2.2 Comparison to Catalog Values

In addition to listing the measured harmonic-drive starting-torques, table 2.9 presents predicted values as quoted in manufacturer's catalog [4]. By comparing these results, it can be seen that the predicted no-load starting torques agree fairly well with the experimental results. However, as discussed above, the accuracy of both the experimental and catalog values is questionable due to the large number of factors which can greatly influence the magnitude of harmonic-drive starting torque.

2.4.2.3 Modeling Considerations

Since, by definition, static friction occurs only when velocity is zero, developing an accurate model of this phenomenon is not critical for predicting harmonic-drive behavior at non-zero velocities. However, by assuming that velocity-independent friction, such as Coulomb friction, behaves similarly to static friction, conclusions can be drawn about friction components at non-zero velocities. For example, due to the preload between the harmonic-drive gear teeth, a non-zero contact and rubbing force will always exist. From the definition of Coulomb friction, this non-zero normal force should always generate proportional frictional losses at all speeds of harmonic-drive operation. A truly accurate model of this coulomb friction behavior should use the harmonic-drive geometry to derive a value for the gear-tooth preload which can then be used to calculate the resulting Coulomb friction. Alternatively, for the sake of simplicity, these frictional losses due to preloading can be approximated by either a constant frictional torque or a function which replicates the typical behavior of the Coulomb friction. By assuming that the static friction results have a magnitude and behavior similar to this velocity-independent friction function, estimates of harmonic-drive frictional losses at non-zero operating velocities due to Coulomb friction

can be made. These insights about velocity-independent friction gained from starting-torque measurements will also be supplemented by the dynamic damping measurements presented below.

2.4.3 Starting-Torque Conclusions

As illustrated by experimental results, harmonic-drive no-load starting torques can be relatively large in magnitude and very dependent on operating and environmental conditions. While experimental measurements agreed fairly well with catalog values, the dependence of these values on factors such as gear-tooth preload, input and output orientation, and operating temperature undercuts the validity and usefulness of these numbers. However, by assuming similarities between this observed static-friction behavior and inherent Coulomb friction in the transmission, a useful understanding of velocity-independent friction behavior at non-zero velocities can be gained.

2.5 Dynamic Friction Measurement

All harmonic drives exhibit a finite power loss during operation due to gear-tooth-rubbing friction and damping in the wave-generator bearing. The purpose of my investigation into these harmonic-drive frictional effects was to obtain accurate measurements of the losses in the three harmonic-drive specimens as well as gain a better understanding of the origins and magnitudes of harmonic-drive friction. As a result of my experimental investigation, I not only estimated values for the velocity-independent offset-torque experienced by harmonic drives at non-zero velocities, but I also characterized the non-linear damping profile for each harmonic-drive specimen. Additionally, due to torque fluctuations excited by system resonance, I discovered that frictional losses in certain operating regimes can increase dramatically. This section is devoted to outlining the procedure used for these tests as well as presenting interesting experimental results. Based on these results, conclusions are drawn about the nature of frictional losses in harmonic-drive transmissions.

2.5.1 Experimental Procedure

The procedure used for these experiments was designed to collect dynamic friction data for a range of rotational velocities. This procedure is listed below.

1. Warm-up the given testing station to a typical operating temperature by running the harmonic drive for several minutes.
2. Send a constant current to the DC motor and wait until an equilibrium rotational velocity is reached.
3. Measure the input motor torque at this velocity.
4. Collect data at several different operating velocities by repeating the two previous steps.

Assuming that the rotational velocity during data collection was truly constant, the input motor torque should exactly balance the damping torque at the given velocity. Therefore, by collecting input torque data over a range of different velocities, the damping profile for each harmonic drive was constructed.

2.5.2 Discussion of Results

The results of my experimental investigation of harmonic drive dynamic losses are presented in this section. First, characteristic loss profiles will be presented and analyzed followed by a comparison of these values to catalog predictions. Based on this information, representations will be proposed to model friction behavior and conclusions will be made.

2.5.2.1 Characteristic Friction Behavior

By using the procedure described above, the input motor torque required to operate the harmonic drive at a constant velocity was used to determine the damping torque of the transmission at different velocities. Due to the harmonic-drive kinematic error, the equilibrium velocity reached by the harmonic drive in many trials experienced noticeable fluctuation. In these cases, the average equilibrium velocity was used to determine the damping torque. The resulting torque and velocity data that was collected on each testing station directly characterized the total friction torque in the system. This total damping torque included not only the friction present in the harmonic drive but also the damping present in the input motor and output bearings as well. By assuming that, since the harmonic drive output rotates at relatively small velocities, the damping contribution from the output bearings was negligible, the frictional torque due solely to the harmonic-drive transmission was calculated by subtracting the motor damping from the measured aggregate friction-torque. Figures 2.32, 2.34, and 2.36 illustrate the total measured friction-torque plotted with the motor damping, while figures 2.33, 2.35, and 2.37 show the extracted harmonic drive friction-torque component.

From the six plots shown below, several observations about dynamic friction losses in harmonic drives can be made. First, as figures 2.32, 2.34, and 2.36 illustrate, the friction torque generated in the harmonic drive is much larger than any other damping losses in the testing equipment. This anticipated result pronounces the importance of accounting for transmission losses in harmonic-drive models and calculations. Second, as labeled in figures 2.33, 2.35, and 2.37, each drive passes through operating regions in which frictional losses are amplified due to dynamic resonance vibration. More specifically, at operating velocities where the position error of the harmonic drive excites joint resonances, the resulting torque fluctuations can increase friction in the transmission

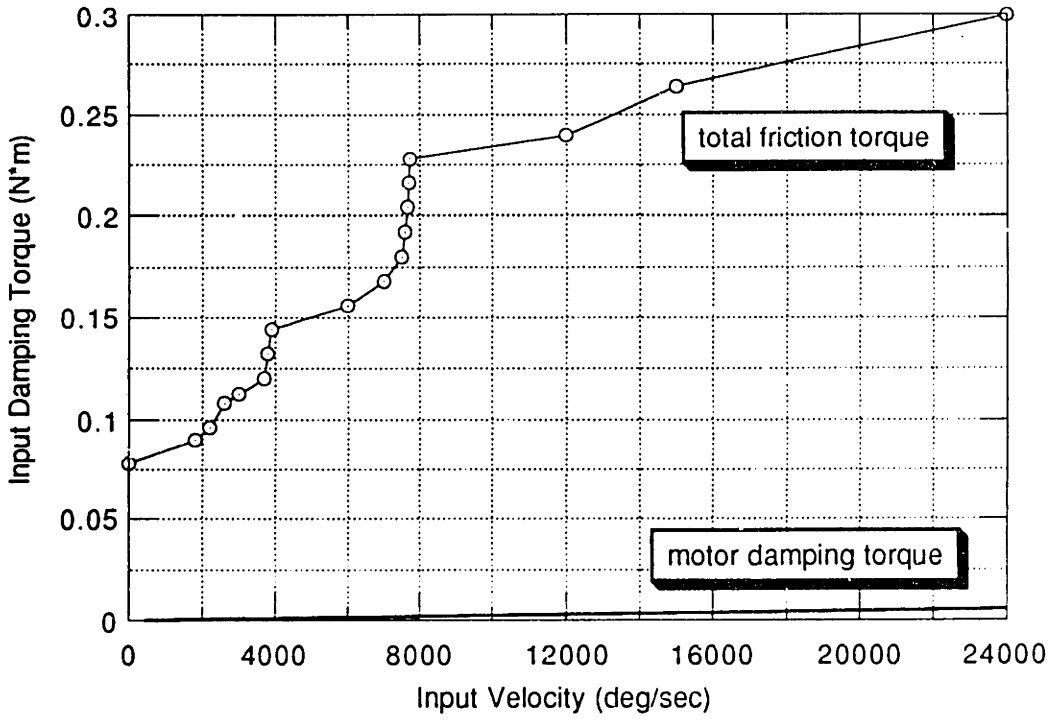

Figure 2.32: Joint 1 aggregate-friction and motor-damping curves

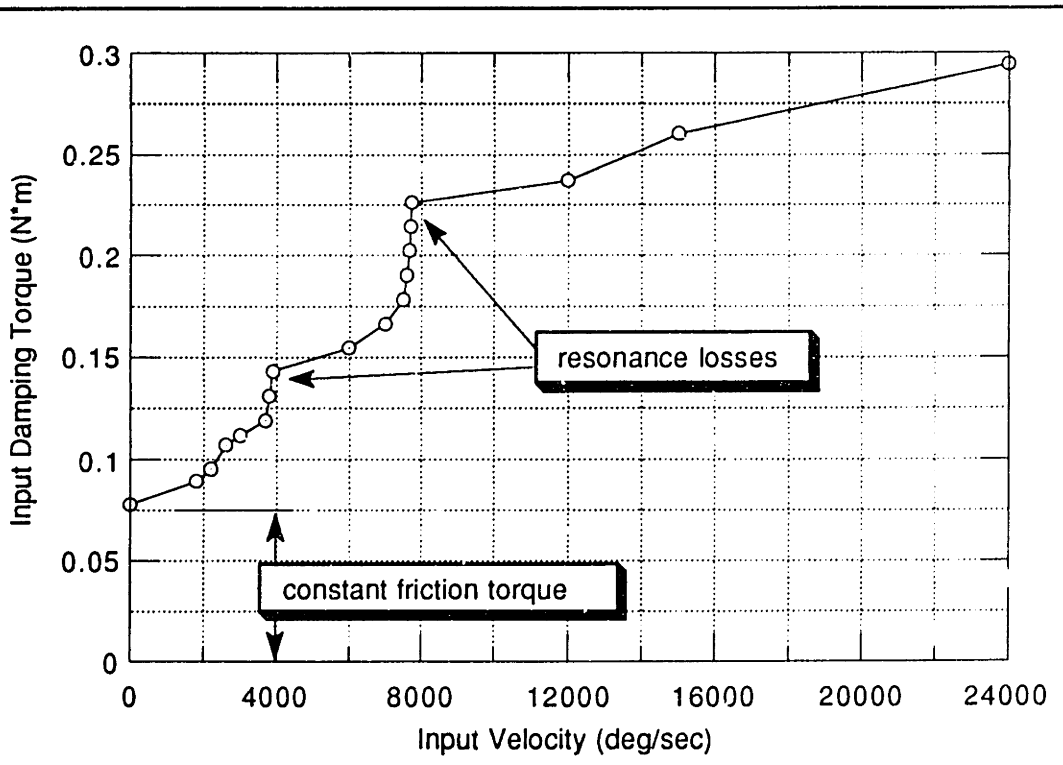

Figure 2.33: Damping curve for the joint 1 harmonic drive

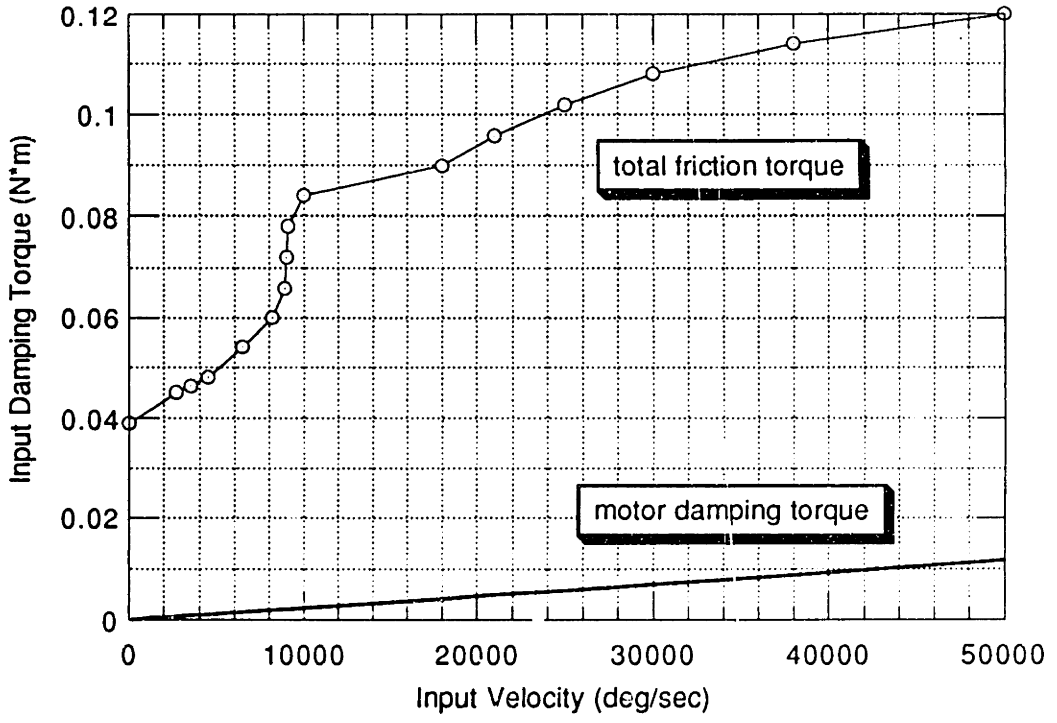

Figure 2.34: Joint 2 aggregate-friction and motor-damping curves

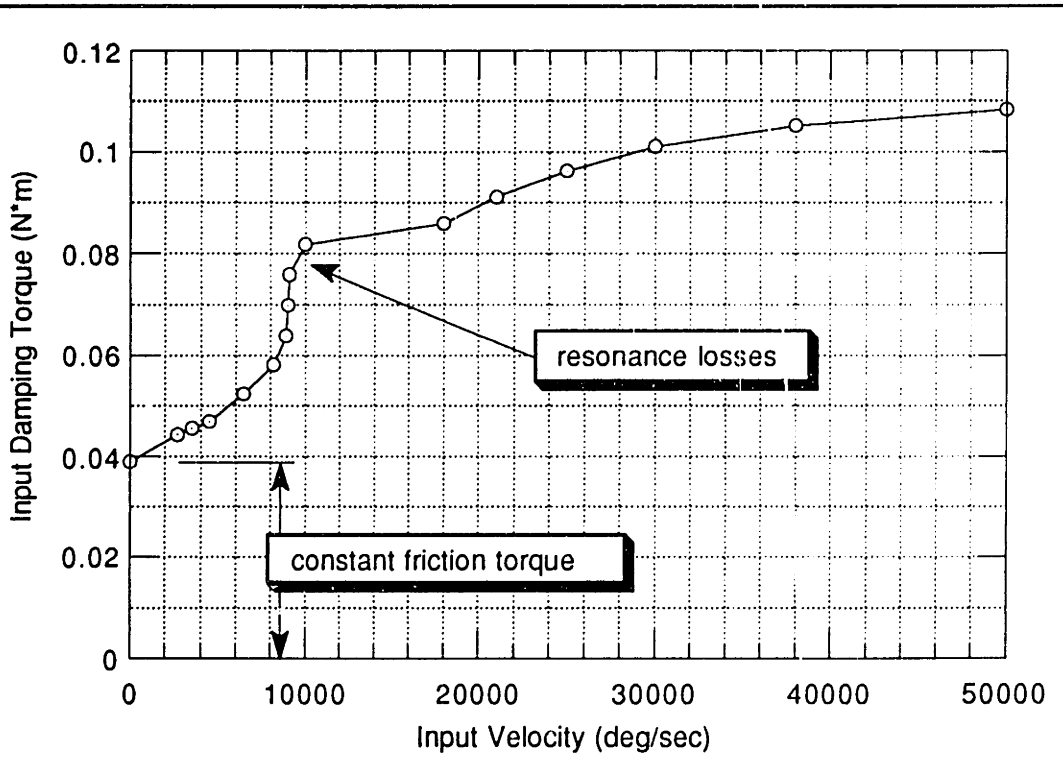

Figure 2.35: Damping curve for the joint 2 harmonic drive

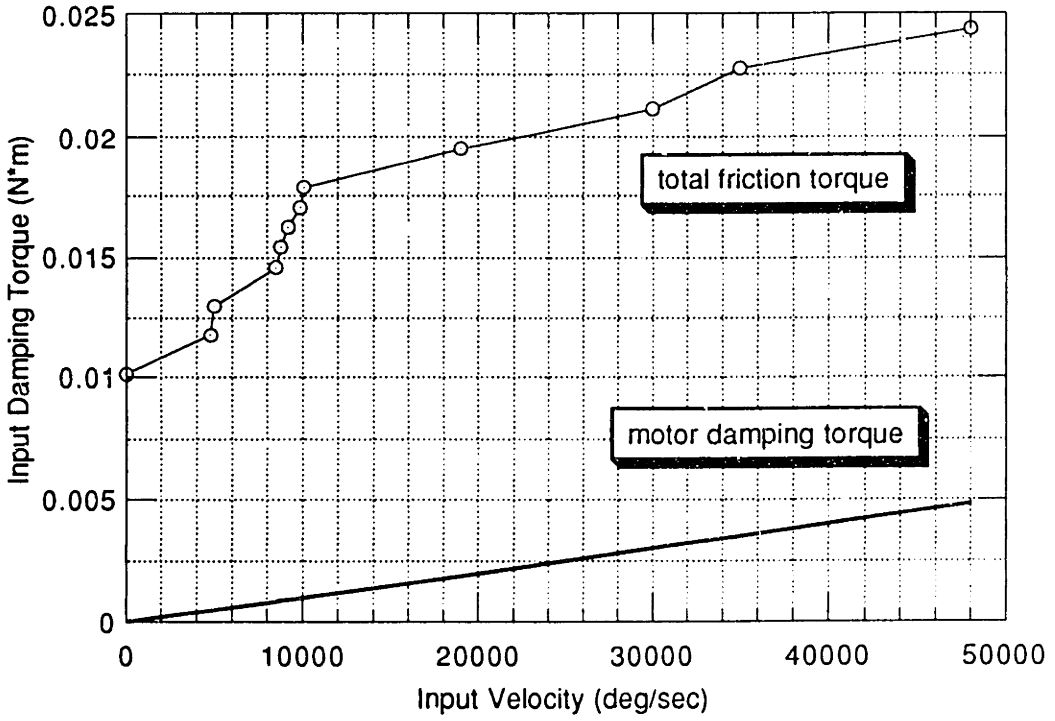

Figure 2.36: Joint 3 aggregate-friction and motor-damping curves

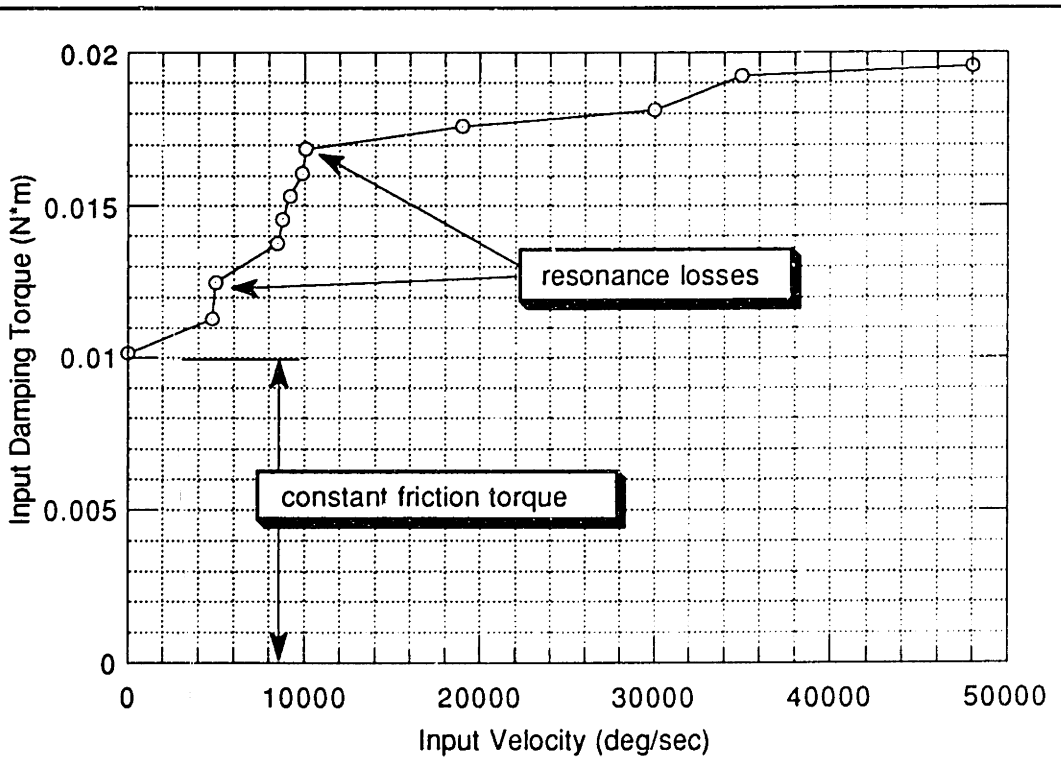

Figure 2.37: Damping curve for the joint 3 harmonic drive

and dissipate extra energy. Depending on the location of these resonances as dictated by the design of the harmonic-drive system, the frictional losses excited in these regimes are likely to dominate harmonic-drive behavior for a significant range of operating velocities. Third, the shape of the damping curve and the torque-offset experienced at low rotational velocities can lend insight into the nature of the non-zero, velocity-independent friction-torque resulting from the harmonic-drive gear-tooth preload. As discussed in the previous section, Coulomb friction at the gear-tooth interface due to non-zero gear-tooth loading influences the starting-torque of the harmonic drive as well as friction-torque offset experienced at non-zero velocities. Rough estimates of this velocity-independent offset-torque are derived from the damping-curve profiles in figures 2.33, 2.35, and 2.37 and are labeled "constant friction torque". As explained previously, these frictional offsets may be constant with respect to velocity but are likely to be influenced by other parameters such as, input and output rotational angle, operating temperature, and preload.

As observed in most other harmonic-drive properties, dynamic damping is not immune to outside influence. Specifically, qualitative observations showed that damping could dramatically rise with an increase in gear-tooth preload. This unsurprising effect can undoubtedly be explained by higher gear-tooth rubbing losses induced by increased loading. As indicated in manufacturer's catalogs, frictional losses typically increase with higher gear-ratios and lower operating torques and temperatures. Also, the type and amount of lubricant used in the transmission can strongly influence dynamic friction measurements. Lastly, although difficult to distinguish from velocity-independent frictional losses, it would not surprise me if dynamic losses experienced noticeable variation with output and input position.

2.5.2.2 Comparison to Catalog Values

Harmonic drive catalogs, [3, 4], characterize the dynamic losses experienced in the transmission by providing efficiency ratings at different operating velocities. These efficiency ratings are derived by comparing the friction torque in the transmission to the rated torque of the harmonic drive at different operating velocities. Harmonic-drive catalogs specify the rated torque for each drive by using bearing-life equations to calculate the operating torques required to ensure a constant wave-generator bearing life at all operating velocities. Using this definition of the rated torque and the experimental frictional

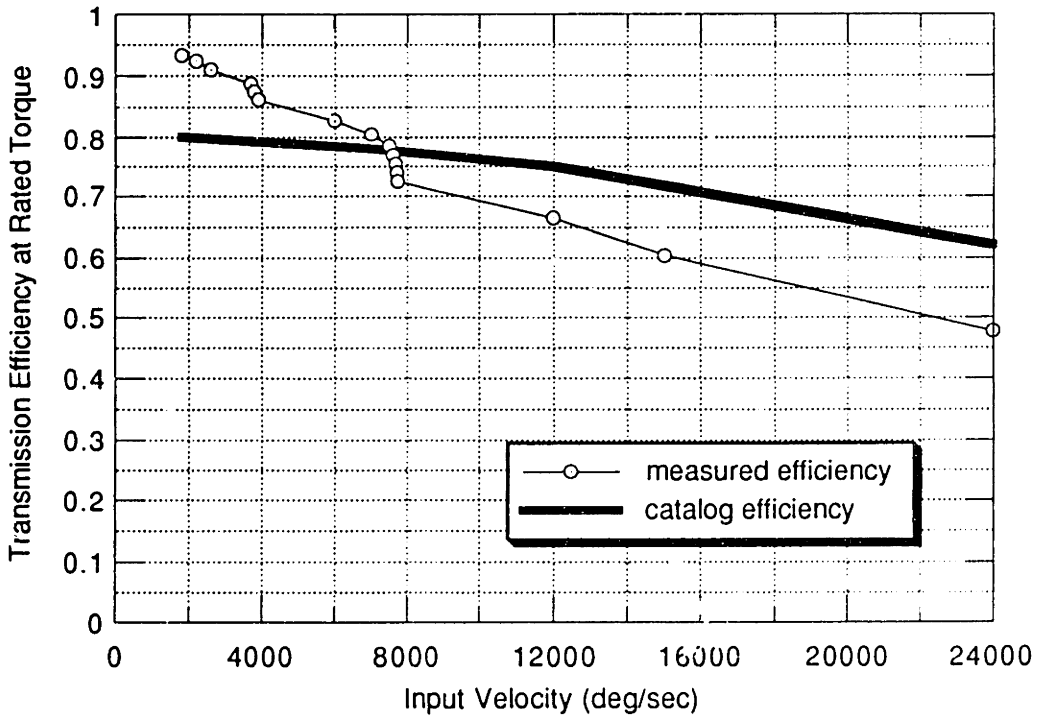

Figure 2.38: Joint 1 harmonic drive efficiency

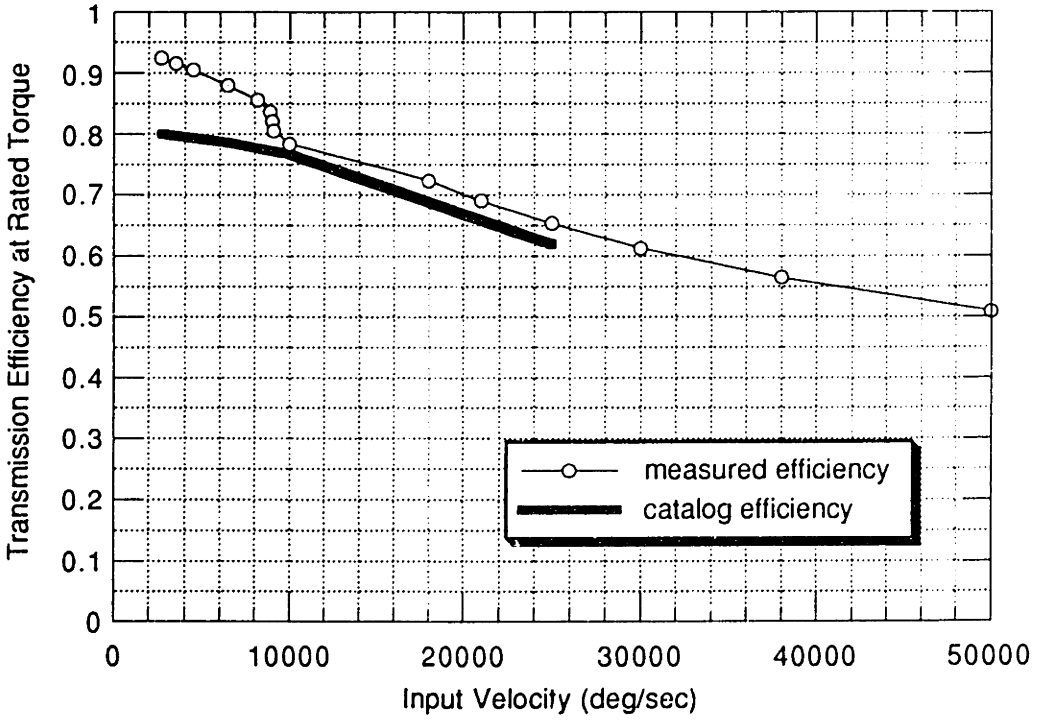

Figure 2.39: Joint 2 harmonic drive efficiency

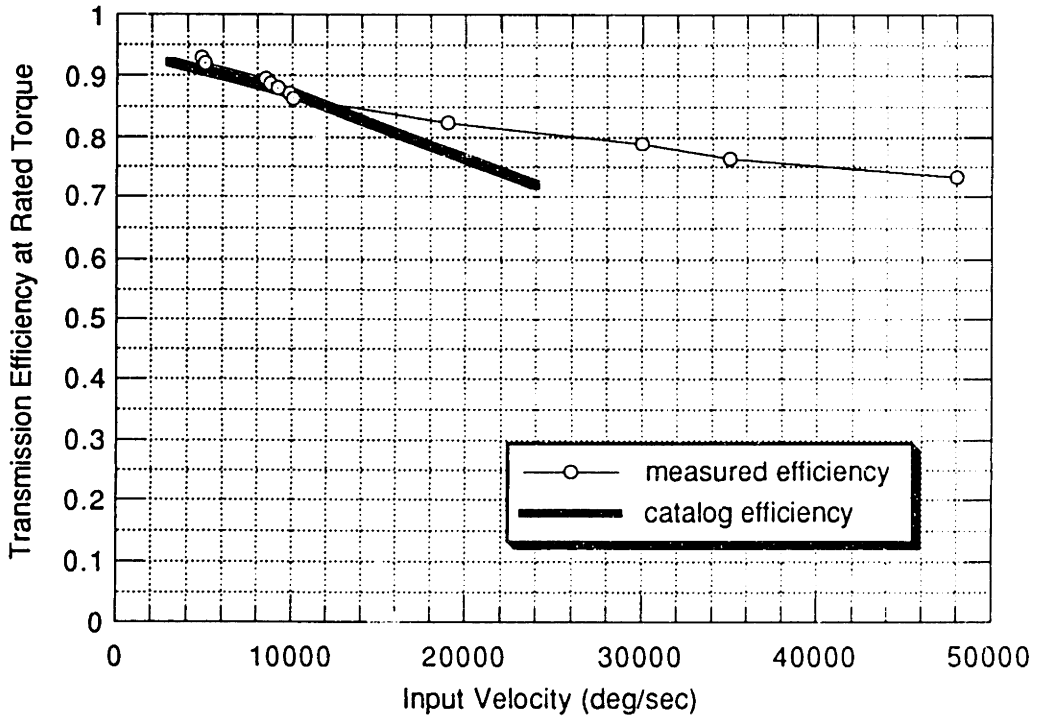

Figure 2.40: Joint 3 harmonic drive efficiency

losses, the resulting transmission efficiency was calculated for each harmonic drive. Figures 2.38, 2.39, and 2.40 illustrate these experimental efficiencies as well as the catalog efficiency curves from [4]. Given that the catalog values are provided as rough estimates, these three plots demonstrate that the catalog efficiencies are relatively similar to the experimental results. For all three experimental curves, the dramatic efficiency loss that occurs during resonance is apparent, and, since the location of these system resonances is dependent on harmonic-drive compliance as well as the inertias of the specific harmonic-drive system, it is not expected that catalog efficiency curves should capture this behavior. Additional discrepancies between experimental and predicted results can be accounted for by a number of environmental factors such lubrication or operating temperature.

2.5.2.3 Modeling Considerations

In order to accurately model harmonic-drive friction at non-zero velocities, three separate friction components must be represented: (1) velocity-independent friction, (2) velocity-dependent friction, and (3) friction at resonance. The first of these three components is the non-zero Coulomb-like friction that occurs in harmonic drives due to

gear-tooth preload. In its simplest form, this component can be represented by a constant torque at all velocities, but, as discussed above, a truly accurate model should incorporate influences from such factors as input and output orientation and gear-tooth preload. The second friction component, namely non-linear velocity-dependent damping, can be better understood by ignoring the resonance losses in the damping profiles of figures 2.33, 2.35, and 2.37. The resulting damping curves, as shown in figures 2.41, 2.42, and 2.43, can be approximated accurately by cubic functions. Given these two models of harmonic-drive friction components, the representation will be complete if the behavior of resonance losses can be captured. Unfortunately, this last friction component is somewhat more difficult to model since it depends on the dynamic torques experienced by the harmonic drive. Consequently, a representation which produces these effects must be developed in conjunction with a complete dynamic model of the transmission as will be discussed later.

2.5.3 Friction and Damping Conclusions

From the results presented in this section, I can conclude that frictional losses in harmonic drives at non-zero velocities are characterized by (1) a velocity-independent offset

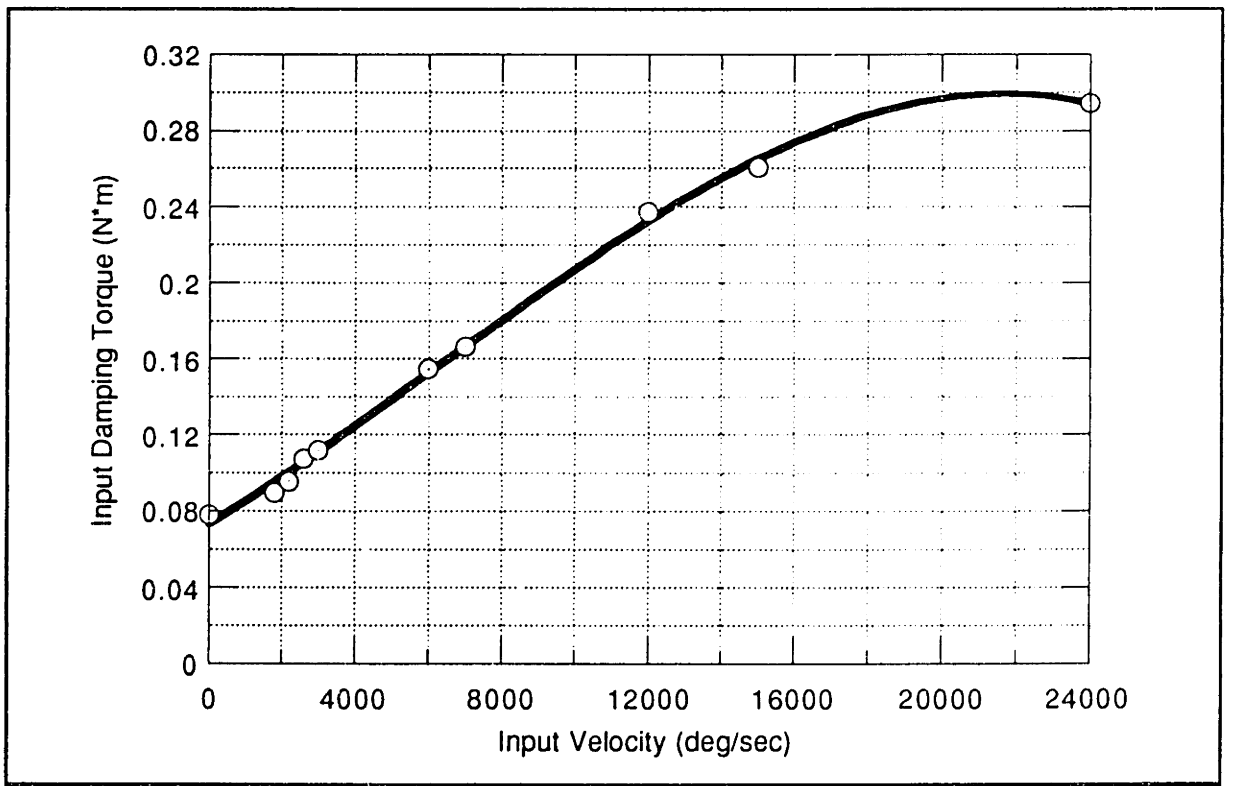

Figure 2.41: Cubic fit of joint 1 non-resonance harmonic-drive damping

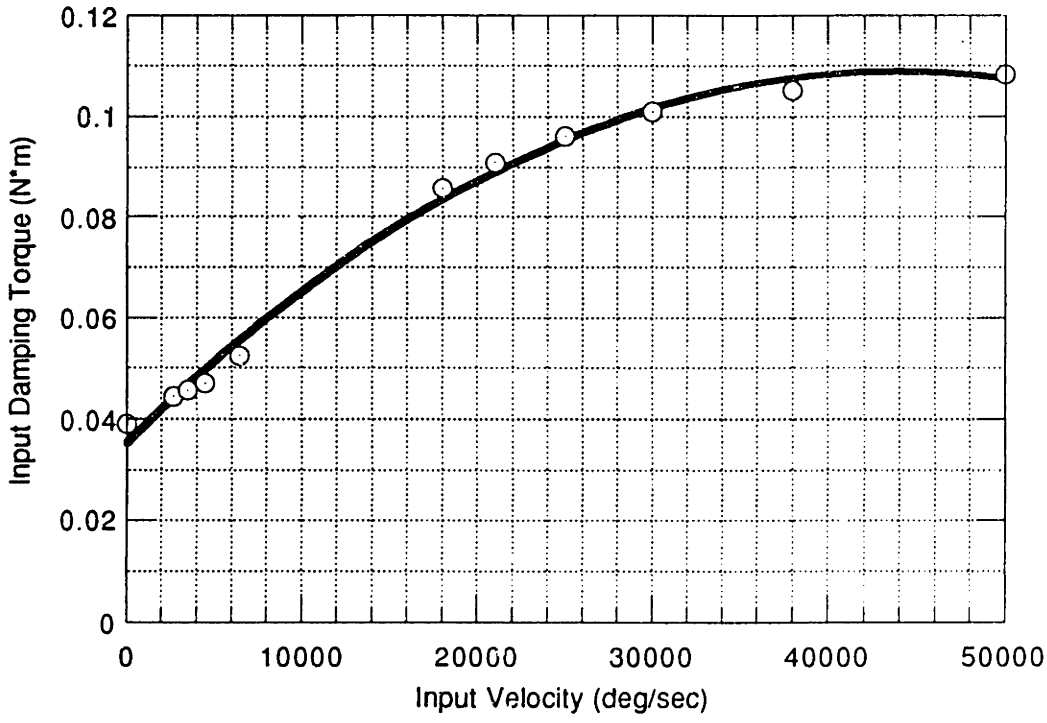

Figure 2.42: Gubic fit of joint 2 non-resonance harmonic-drive damping

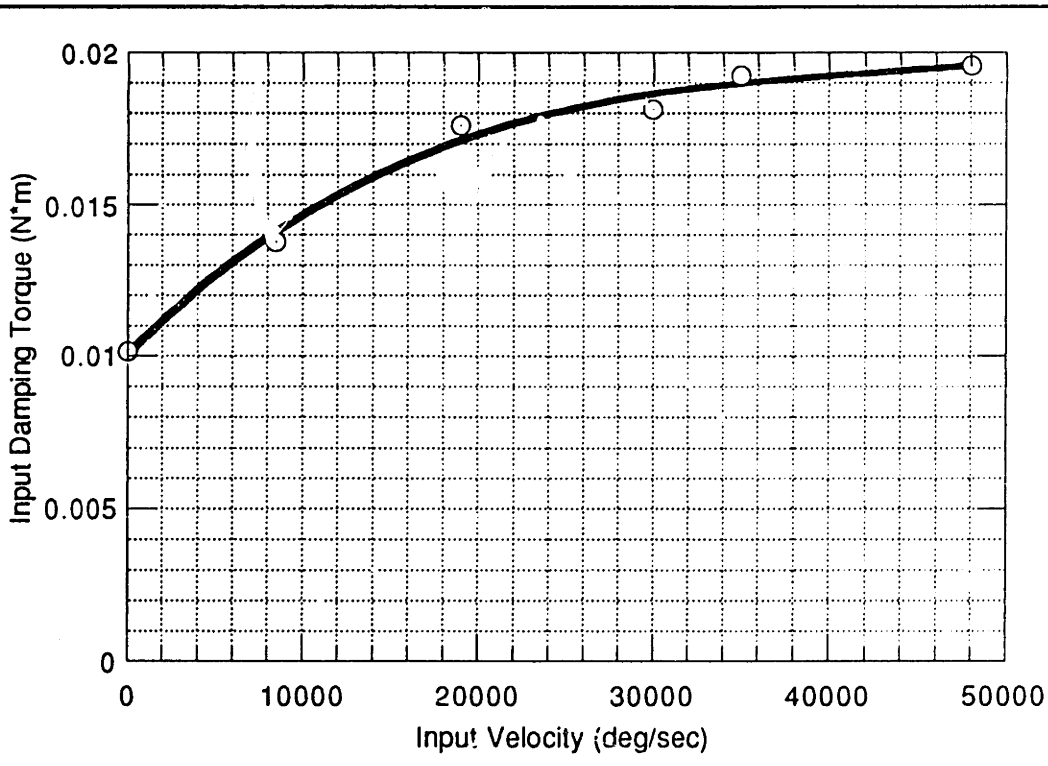

Figure 2.43: Cubic fit of joint 3 non-resonance harmonic-drive damping

torque, (2) a non-linear damping torque, and (3) an additional torque loss during system resonance. Useful measurements for the first two of these frictional components can be made by analyzing the shape of the damping profile of a given harmonic drive while accurate representation of the third friction mechanism is more elusive . Due to the dependence of transmission friction on environmental and operating conditions, catalog efficiency curves can only be used to get a rough approximation of harmonic-drive losses at different velocities.

2.6 Dynamic Response Measurement

With the insight gained from the kinematic and static experimental results presented above, the dynamic behavior of harmonic-drives can now be analyzed and interpreted. The purpose of this final investigation is threefold: (1) to fortify an empirical understanding of harmonic-drive dynamic behavior by identifying relationships between the observed dynamic response and known transmission properties such as stiffness, kinematic error, and friction, (2) to generalize about typical harmonic-drive dynamics based on experimental information collected from the three harmonic-drive specimens, and (3) to fully characterize the dynamic step-response behavior of the three harmonic drives in order to establish a reference point for the generation of theoretical models. The results of this investigation illustrated that there are several dynamic properties common to all of the harmonic drives tested. In particular, all transmissions displayed dramatic non-linear resonance behavior when the spatial frequency of the kinematic error harmonics coincided with the first resonant mode of the harmonic-drive system. In all cases, these resonances appeared over a substantial portion of the harmonic-drive operating range and behavior in these areas was uncommonly turbulent and unpredictable. This section is devoted to describing the experimental procedure used on the three testing stations as well as analyzing the collected dynamic-response data. Based on the information interpreted from the dynamic-response plots, modeling issues will be addressed and conclusions will be drawn.

2.6.1 Experimental Procedure

In order to investigate the dynamic behavior of harmonic drives, step-response data was featured exclusively as an indicator of overall harmonic-drive performance. Specifically, data was collected on all joints for harmonic-drive rotation resulting from a series of step-commands in current sent to the input motors. As illustrated in figure 2.44, each testing station was configured with a different output inertia representing a typical load for the given harmonic-drive. Additionally, the input inertias varied as dictated by the motor armature and wave-generator on each joint. A listing of all these inertia values is given in table 2.10. Using these three testing facilities, the experimental procedure listed below was performed.

1. Warm-up the given testing station to a typical operating temperature by running the harmonic drive for several minutes.

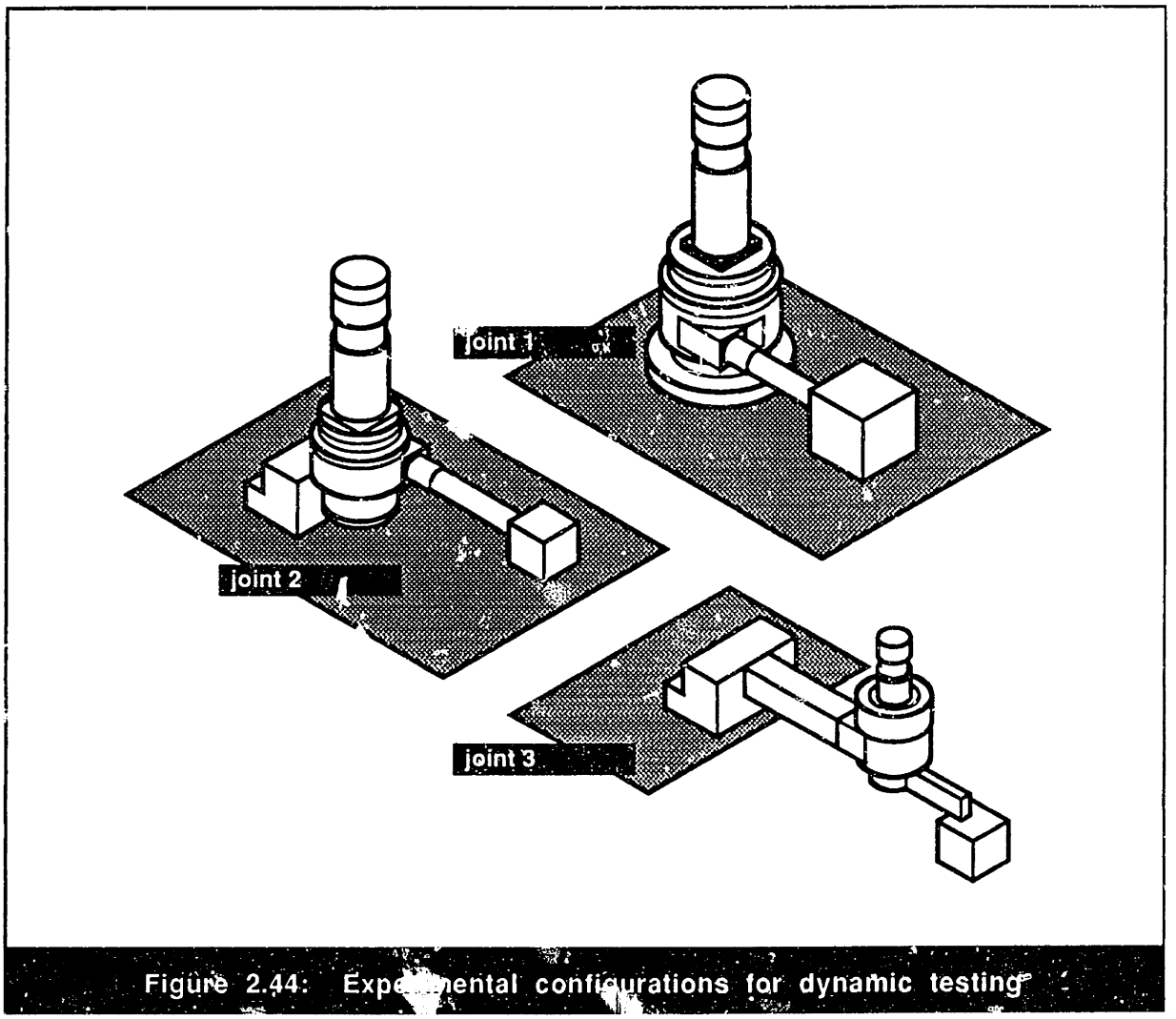

Figure 2.44: Experimental configurations for dynamic testing

2. Position the joint output at a known starting position.

3. Send a step-command of current to the DC motor amplifiers.

4. Collect data from the position sensors, current sensor, and torque sensor for several seconds of joint operation.

5. Derive velocity and kinematic error response from the position-sensor data.

6. Collect data at several different input-current step-commands by repeating this procedure.

The motor-current commands used in each trial ranged from the lowest current that could overcome transmission starting-torque to the current-saturation limit of the motor amplifiers. The resulting velocity effected by these current commands spanned the typical recommended operating range for the three harmonic drives. In all cases, current step-

Table 2.10: Inertia parameters for the dynamic-response tests			
	Joint 1	Joint 2	Joint 3
wave-generator inertia	1.8e-4 kg-m^2	4.8e-5 kg-m^2	3.2e-6 kg-m^2
motor-armature inertia	3.8e-5 kg-m^2	2.8e-5 kg-m^2	2.0e-6 kg-m^2
total input inertia	2.2e-4 kg-m^2	7.6e-5 kg-m^2	5.2e-6 kg-m^2
output mass	2.828 kg	0.7027 kg	0.7027 kg
mounting arm length	0.308 m	0.282 m	0.112 m
total output inertia	0.268 kg-m^2	0.056 kg-m^2	0.0088 kg-m^2

commands were incremented at regular intervals small enough to capture the variations in dynamic behavior with increased current. From the resulting myriad of data sets, a handful were extracted which effectively characterized the dynamic response over the entire experimental range of operation.

2.6.2 Discussion of Results

In this section, several time-response plots will nucleate discussion of harmonic-drive dynamic behavior. From these plots, several characteristic behavioral patterns will be highlighted and used to gain insight into possible harmonic-drive modeling representations. Lastly, based on this improved understanding of harmonic-drive dynamic behavior, conclusions will be made about typical and predictable harmonic-drive dynamic response.

2.6.2.1 Characteristic Dynamic Behavior

All of the results from my experimental investigation of harmonic-drive dynamic behavior are illustrated in a series of time-response plots featured in Appendix D. These plots illustrate the position, velocity, and torque information gathered for the three harmonic drives for several different step-responses which fully capture the range of observed transmission behavior. For convenience, table 2.11 lists the figure numbers for all of the experimental plots in Appendix D. Throughout this section, references will be made to several of these plots in order to outline key features of the observed dynamic response. The discussion of characteristic harmonic-drive dynamic response will be

Table 2.11: Summary of experimental data-plot numbers in Appendix D			
	Joint 1	Joint 2	Joint 3
Input Position	D.1.1	D.2.1	D.3.1
Input Velocity	D.1.2	D.2.2	D.3.2
Input Current	D.1.3	D.2.3	D.3.3
Output Position	D.1.4	D.2.4	D.3.4
Output Velocity - view 1	D.1.5	D.2.5	D.3.5
Output Velocity - view 2	D.1.6	D.2.6	D.3.6
Output Torque	D.1.7	D.2.7	D.3.7
Dynamic Position Error	D.1.8	D.2.8	D.3.8

structured by first outlining typical behavioral patterns as observed in the velocity response, and then discussing the influence of these patterns on torque, current, position and position error measurements.

2.6.2.1.1 Typical Dynamic Behavior Patterns

In all of the step-response plots collected, underlying commonalities in dynamic behavior can be seen. However, the most illustrative information about the nuances of harmonic-drive dynamic behavior can be found in the velocity time-response plots in Appendix D. Specifically, from the input velocity curves illustrated in figures D.1.2, D.2.2, and D.3.2, four unexpected dynamic characteristics observed in all three transmissions become apparent:

1. A substantial portion of the operating range of each harmonic drive is contaminated by resonance vibration.

2. These regions of resonance act as energy sinks which constrain the increase of average rotational velocity for increasingly larger current commands.

3. An unpredictable jump in velocity can frequently occur when the transmission harnesses just enough energy to push through a system resonance.

4. Due to variations in frictional resistance over one output revolution of the transmission, significant variation in rotational velocity can result.

These surprising features which are common to the measured response of all three harmonic-drives will be discussed in order.

From the listed time-response illustrations, it can be seen that the input velocity of the three harmonic drives passes through regions where significant resonance vibration can occur. These resonant regions occur when the frequency of kinematic-error fluctuations, which occurs at multiples of input, or wave-generator, rotational speeds, coincides with the primary temporal resonance of the harmonic-drive system. Since the harmonic-drive transmission flexibility behaves non-linearly, there is no distinct frequency of system resonance. Instead, as the torque-fluctuation amplitude increases, the effective stiffness of the transmission increases which results in an increase of the frequency of system resonance. This variation in temporal resonant behavior is manifested in a range of operating velocities which can excite system resonance. On joint 1, two separate resonances can be observed at input speeds of around 4000 and 8000 degrees/second. The vibration in the first of these two regions can be attributed to the kinematic-error excitation which occurs four times every input revolution and the second region can be blamed on the twice-per-input-revolution position-error component. As implied, the resulting frequency of velocity fluctuation that occurs at each of these resonances is identical to the rotational speed of the harmonic-drive input times the spatial frequency of the responsible kinematic-error excitation. On joint 2, the amplitude fluctuations at resonance are smaller than observed on joint 1, but regions of resonant behavior can still be found at about 10000 degrees/second and , to a lesser extent, 20000 degrees/second. These two regimes can be attributed to the kinematic-error fluctuations occurring at 2.0 and 1.0 cycles-per-input-revolution, respectively. On joint 3, three resonant areas can be observed at the approximate input velocities of 5000, 10000, and 20000 degrees/second, and can be directly associated with the kinematic error occurring at 4.0, 2.0, and 1.0 cycles-per-input-revolution, respectively. The lack of any significant system resonance on joint 1 corresponding to a frequency of once-per-input-revolution is not surprising since, as illustrated previously in figure 2.10, no appreciable kinematic error component was measured at that frequency. Additionally, kinematic-error harmonics appearing at frequencies higher than 4.0 cycles-per-input-revolution have no effect on any of the observed dynamic responses since the resulting excitation frequencies exceeded the system resonant regions at the slowest experimental operating velocities.

An unfortunate consequence of the resonance experienced by the harmonic drives is the dramatic dissipation of energy which occurs in these regions. Specifically, from figure D.1.2, it can be observed that input current commands from 2.0 to about 2.4 amps achieve

roughly the same final rotational velocity at the first region of resonance, and current commands ranging from 2.8 to 4.0 amps all produce the same final velocity in the second resonance regime. Similarly, as illustrated in figures D.2.2 and D.3.2, identical behavior can be observed around the resonance regimes on joints 2 and 3. The velocity limitation at resonance can be attributed to the dramatic increase in Coulomb-like friction at system resonance due to the large torque fluctuations experienced in the transmission. In other words, as a step command in current brings the system closer to resonant velocity, the torque fluctuations due to resonance begin to increase. With this increase in torque amplitude, energy is increasingly dissipated by a Coulomb-like friction mechanism presumably at the gear-teeth interface. Due to this increasing energy loss as the velocity nears the resonant areas, fluctuations in velocity increase but the average velocity remains roughly the same. Because of this self-reinforcing frictional mechanism, the harmonic-drive velocity is prolonged at the frequency at which kinematic error fluctuations excite system resonance. This problem is heightened by the non-linear nature of the stiffness since increases in torque fluctuation as the system approaches resonance also increase the natural frequency of vibration. This effect further prevents the input current from pushing through the harmonic-drive resonances since the temporal resonant frequency increases alongside the increase in the rotational velocity and resulting spatial excitation frequency, of the harmonic drive. In summary, because of the escalating frictional losses and the increase in natural frequency which occur as rotational velocities approach system resonance, a wide range of input current steps can fall victim to these resonance traps. As an explanatory note, the velocity truncation present in the response of the highest current step on each velocity plot is due to the saturation limits of the current amplifiers and should not be attributed to resonance losses.

In partnership with the frictional losses which occur at system resonance, unpredictable jumps in rotational velocity frequently appear when velocities exit resonant areas. As illustrated for joint 1 in figure D.1.2, the step response for a 4.0-amp current command holds a relatively constant velocity of about 8000 degrees/second at resonance for two seconds then unexpectedly jumps to a final velocity of about 15000 degrees/second. Additionally, for joint 3, figure D.3.2 illustrates similar behavior for the current steps of 0.28, 0.48, and 0.52 amps. This unfortunate dynamic behavior can be blamed on three familiar physical mechanisms: (1) the non-linear characteristic of the harmonic-drive stiffness profile, (2) the increase in energy dissipation which occurs at system resonance, and (3) the large variation in friction which occurs over one output revolution of the harmonic drive. First, due to the stiffening-spring characteristic of the

harmonic drive, a resonance singularity often appears when the frequency of resonance excitation slightly exceeds the natural frequency of vibration. More specifically, as the amplitude of torque vibration increases, the equivalent stiffness of the harmonic drive also increases as does the natural frequency of system vibration resulting in a frequency spectrum similar to the one show in figure 2.45. However, when the harmonic-drive velocity breaks through this resonant region, resonance vibration drops immediately due to the unstable decline in both torque-vibration amplitude and natural frequency of resonance. This non-linear dynamic behavior is commonly referred to as a jump resonance. The second accomplice in this jump-resonance behavior is the frictional loss at resonance. Due to these losses, as discussed in the previous paragraph, velocity is restricted in resonant regions. However, when the harmonic-drive jumps to non-resonating behavior, the resonance losses disappear and the leftover energy increases rotational velocity dramatically. If the non-linear stiffness and resonance losses were the only factors influencing jump-resonance behavior, it is likely that this unpredictable response would only appear a very small range of input current commands. However, as observed in the experimental results, these jump-resonant responses occur for a surprisingly large range of input currents and appear far too often during normal harmonic-drive operation. The origin of this unfortunate consequence can be found in the large variation in frictional resistance that can exist in harmonic drives over one output rotation. Due to this variation in energy dissipation, all operating velocities somewhat near jump-resonance behavior can harness enough energy to break through the resonance when frictional variations with output

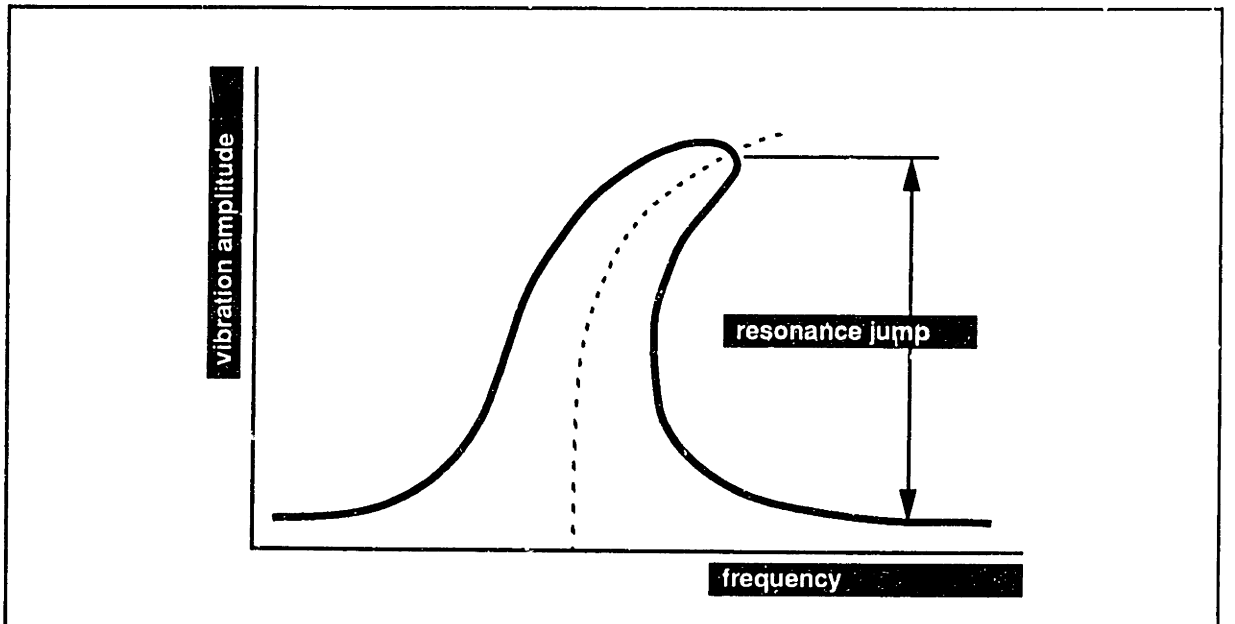

Figure 2.45: Non-linear resonance frequency spectrum

rotation decrease. Depending on the magnitude of these frictional variations, a wide range of operating velocities can be kicked out of resonance due to this decrease in friction. In conclusion, due to the interaction of non-linear compliance, resonance losses, and friction variation, the stability of harmonic drive operation can be seriously undercut by drastic and sudden jumps in operating velocity.

As noted above to be a contributing agent in jump-resonance behavior, the substantial variation in harmonic-drive friction with output rotation can also be observed in the velocity time-response plots. As illustrated in all of the response curves of figure D.2.2, the variation observed on joint 2 can cause tremendous low-frequency velocity variation over one output revolution. To a lesser but noticeable extent, similar variations also appear in the response curves for joints 1 and 3 in figures D.1.2 and D.3.2. These velocity fluctuations were used to characterize the value of the friction-torque variation on each harmonic-drive specimen as summarized in table 2.12. As the low-frequency oscillations in velocity indicate, this frictional variation can be expectedly non-sinusoidal. The most likely source of this unfortunate behavior is variations in the tightness of fit between the flexspline and circular-spline gear teeth, which can be caused by several factors such as improper mounting, component misalignment, and manufacturing errors.

Table 2.12: Variation in output friction torque with output angle

	Joint 1	Joint 2	Joint 3
Torque half-amplitude (N-m)	0.6	1.3	0.03

2.6.2.1.2 Influence of Observed Behavior on System Properties

Based on the understanding of typical step-response characteristics gained from the input-velocity response, the behavior of the measured harmonic-drive position, current, torque, position error, and output velocity can now be better understood. In particular, as illustrated in figures D.1.5, D.2.5, D.3.5, D.1.6, D.2.6, and D.3.6, the harmonic-drive output velocity response behaves very similarly to the input velocity except that vibrations due to kinematic-error fluctuations and system resonance are much larger. Note that the joint 3 output velocity is negative since the flexspline, rather than the circular spline, is used for output rotation on that joint. Additionally, on the joint 3 output-velocity response, distinct periodic velocity fluctuations appear at higher velocities. These fluctuations are caused by the output sensor pinion and should not be attributed to harmonic-drive

behavior. Also note that the beating in output velocity oscillation amplitude at high velocities seen on joints 1 and 2 is due to aliasing in the sampled data rather than an actual physical mechanism.

The current response measured from the motor amplifiers is illustrated in figures D.1.3, D.2.3, and D.3.3. Since the motor current is linearly proportional to the motor torque, as dictated by the motor torque constant, the behavior of the harmonic drive input torque can be understood. From the response curves for each joint, it can be seen that at low current commands, the amplifiers can sustain a fairly constant input torque in the face of harmonic-drive torque fluctuations. However, at higher current commands, the current amps have difficulty keeping pace with the higher frequency torque fluctuations and noticeable variations in current amplitude occur. The highest current-command response in each figures illustrate the vulnerability of the current signal when the amplifier saturates from the high motor velocity. Due to imperfections in the A to D board, significant electrical noise appears in the current signals on joints 2 and 3. Fortunately, this noise had no effect on the dynamic response of the harmonic-drive systems.

The output torque response measured from the torque sensor on each joint is illustrated in figures D.1.7, D.2.7, and D.3.7. As a reminder, because of the location of the torque sensor on each joint, this measured response is a direct reading of the torque experienced at the flexspline of the harmonic drives. This output torque has two contributions: (1) the dynamic torques generated by the acceleration of the output inertia, and (2) the damping torque produced by the output bearings. Since the damping torque in the output bearings is very small compared to the inertial torques generated by the position-error fluctuations, the measured torque response in all cases oscillated around zero at all velocities. As shown on all three joints, torque fluctuations can become extremely large at velocities which excite system resonance. For example, on the largest harmonic-drive system, joint 1, torque readings reached a powerful 80 N-m during system resonance. As expected, the frequency of torque fluctuation is identical to the frequency of velocity fluctuation which is equal to the rotational speed of the input times the position-error excitation frequency at the appropriate resonance.

The input and output position response measured on the three harmonic-drive specimens is illustrated in figures D.1.1, D.2.1, and D.3.1, and figures D.1.4, D.2.4, and D.3.4. From these plots, it can be seen that substantial fluctuation noticed on the velocity plots is virtually unnoticeable on position measurements. However, due to increased frictional losses at resonances, the increases in final position for constant increases in the

current-step input is by no means constant. For all tests, the input and output position responses display identical behavior except that they differ in magnitude by the given harmonic-drive reduction ratio.

As shown in figures D.1.8, D.2.8, and D.3.8, the position-error response of a single trial is shown for the three harmonic drives. The given plots were selected to illustrate typical position-error behavior near a system resonance and were derived by subtracting the output position from the input position divided by the gear ratio for the given step-response trial. The important feature to note in these plots is the amplification of position error at system resonance due to torsion across the harmonic-drive transmission. As the plots illustrate, this effect can increase the dynamic position inaccuracy measured across the drives by an order of magnitude over static tests. This large effect of dynamic torque fluctuations on the measured position-error illustrates the importance of static tests to ensure accurate measurements of harmonic-drive kinematic error. As an explanatory note, the low-frequency oscillations seen in the position-error response are due to manufacturing errors in the output sensor gear and pinion and should not be attributed to the harmonic drive.

In general, changes in the dynamic response for identical step-response trials was minimal as long as harmonic-drive parameters remained unchanged. For example, since, as discussed earlier, factors such as harmonic-drive preload, assembly, lubrication, input and output orientation, and operating temperature, can greatly influence system parameters such as stiffness and frictional losses, changes in any of these conditions between trials can greatly influence dynamic response. Care was taken to make sure that these parameters remained consistent across all step-response trials on each joint.

2.6.2.2 Modeling Considerations

Based on the observations made about typical harmonic-drive step-response behavior, theories can be developed about how to model the observed dynamic effects. First, in order to accurately predict resonance behavior, the input and output inertias, kinematic error-signature, and the harmonic-drive stiffness profile must be carefully measured and introduced into a dynamic model. Second, as described above, to capture the observed jump-resonance behavior, three physical mechanisms must be modeled: (1) the non-linear stiffness profile, (2) the Coulomb-like frictional losses at resonance, and (3) the variation in friction with output rotation. The first and last of these three items can be

measured relatively easily and modeled by mathematical functions which approximate the observed behavior. The second item, however, relies on the interaction between torque fluctuations in the harmonic-drive and rubbing at the gear-tooth interface. Therefore, any model that is supposed to accurately describe frictional losses at resonance must include a representation which predicts the dynamic forces acting on the gear-tooth geometry. Additionally, as illustrated in the motor-current response curves, a dynamic model of the current amplifiers might be necessary in some domains to capture the saturation behavior and dynamic fluctuations.

2.6.3 Dynamic Response Conclusions

The unusual and surprising dynamic behavior observed in harmonic drives is the result of the interaction of several transmission mechanisms. First, due to the kinematic error in the harmonic drive, resulting dynamic torque fluctuations amplified by the transmission ratio can be substantial during operation. When these large torque fluctuations are combined with the low stiffness of the transmission, significant resonance vibration can occur in typical operating ranges. Since coulomb friction at the gear-teeth interface is amplified by dynamic torque fluctuations, extra energy is dissipated at resonance and operating velocities are suppressed for increasingly larger motor currents. However, when the input motors supply enough energy to break through these resonant regions, a sudden reduction in resonance losses results in a sharp increase in velocity and a significant decrease in torque fluctuations. Since the stiffness profile in harmonic-drives is non-linear, the natural frequency of the system increases with increased torque levels. This non-linear effect has an adverse affect on dynamic behavior around system resonance since the increase in natural frequency prolongs operation at resonance and accentuates the reduction in vibration when these resonant regions are surpassed. Lastly, since harmonic drives can have a large variation in friction torque over one output revolution, the resulting substantial variation in operating velocity can greatly influence the location of the jump resonance. In order to accurately model the dynamic behavior of the harmonic drive, appropriate representations and interactions of these individual effects must be understood.

Chapter 3: Theoretical Modeling

The goal of modeling any physical mechanism is to discover the simplest representation which can replicate system performance to the desired level of accuracy. When modeling a mechanical assembly with a harmonic-drive transmission, several levels of detail can be incorporated into the harmonic-drive model to improve the integrity of the system representation. In particular, as seen in the experimental results, harmonic-drive properties which can significantly influence system performance include

[1] static, dynamic, and periodic frictional losses,

[2] non-linear transmission compliance, and

[3] kinematic transmission error .

The goal of this section is to characterize the modeling accuracy that can be achieved by incorporating different combinations of these transmission properties into a harmonic-drive representation. From the complex behavior observed in the measured dynamic-response data, finding a model which accurately characterizes harmonic-drive behavior proves to be a formidable task. However, if such a representation can be created, design and control of systems containing harmonic drives can be substantially improved. Additionally, the knowledge embedded in such a dynamic model can become a powerful medium for understanding and improving the design and operation of harmonic-drive transmissions. I hope that the results presented in this section can equip and enlighten the expanding community of harmonic-drive users and designers.

My modeling efforts have focused on developing a series of harmonic-drive models at different levels of complexity and evaluating their performance. First, I analyzed a transmission model that ignored all non-ideal transmission properties and discovered that it provided an extremely poor description of actual dynamic performance. Second, model accuracy improved when frictional losses were included into the representation, but the torque and velocity fluctuations observed in the experimental response did not appear in the

theoretical predictions. To address this issue, compliance and then kinematic error were included into the transmission model. This improved representation produced simulated results which more closely matched the experimental observations but failed to capture the significant energy losses which occur at system resonance. To eliminate this discrepancy, a final model which incorporated gear-tooth geometry and coulomb friction was developed which improved predicted performance around resonance. Unfortunately, due to the sensitivity of this model to harmonic-drive properties and the inherent difficulty in accurately measuring these properties experimentally, further research must be done to refine this representation into a viable prediction tool. Nevertheless, the novel framework developed in this model provides a simple and powerful representation for hatching and nurturing an intuitive understanding of harmonic-drive operation.

A complete description of my theoretical analysis of the harmonic-drive transmissions is presented in this section. To establish the foundation of my conceptual investigation, I will first explain the notation conventions used throughout this section and describe the numerical simulation used the dynamic equations. Next, the modeling representations used for the three harmonic-drive testing stations will be discussed apart from the individual transmission models. In light of this framework, I will then develop a series of dynamic models of increasing complexity to illustrate the range of performance delivered by different harmonic-drive representations. For each of these models, equations of motion will be derived, operating parameters will be calculated from experimental measurements, and the accuracy of simulation results will be characterized through comparison with actual harmonic-drive behavior. On the basis of these theoretical observations, conclusions and recommendations will be made for each harmonic-drive model about its usefulness and range of applicability.

3.1 Modeling Techniques and Notation Conventions

Modeling techniques and conventions will remain consistent for all of the dynamic models presented in this section. Specifically, Newton's method will be employed exclusively to determine dynamic force interactions and derive equations of motion. The position, velocity and torque variables used in these equations will be illustrated in a figure for each model and governed by the following conventions:

1. θ-variables represent rotational position.
2. ω-variables indicate angular velocity.
3. T-variables denote torque.
4. All variables are referenced from ground.
5. All positions and velocities are defined to be positive in the clockwise direction when viewed from the input-side of the harmonic drive.
6. All torques are defined to be positive in the direction in which they will act when a positive load is applied to the input inertia and the output inertia remains stationary.
7. The positions, velocities, and torques seen by the three ports of the harmonic drive will have the subscripts wg for the wave-generator, fs for the flexspline, and cs for the circular spline.

Additional variables such as model parameters and constants that are used for the testing-station models are defined in table 3.1. Similarly, table 3.2 lists descriptions of the variables which will appear in the five different harmonic-drive models to be developed later. Sporting this notation lifejacket, I will now plunge into the depths of equation derivation and analysis for five different harmonic-drive models.

In order to accommodate different harmonic-drive models, the equations of motion for the testing-stations will treat the transmission as a black box with three interacting ports: the wave-generator, the flexspline, and the circular-spline. Velocities and torques will be transmitted through these three ports but the testing station models will be blind to the actual dynamics inside the transmission. Following the complete derivation of the testing-

Table 3.1: Explanation of variable names for testing-station models

i_m	current sent to the DC motors by the amplifiers
J_{in}	input inertia (motor armature and wave-generator)
J_{out}	output inertia (load mounted at harmonic-drive output)
b_{in}	linear damping coefficient for input friction
b_{out}	linear damping coefficient for output friction
K_t	motor torque constant
K_b	motor back-EMF constant

Table 3.2: Explanation of variable names for harmonic-drive models

N	harmonic-drive catalog gear-ratio
$T_{b\_constant}$	velocity-independent friction torque in the harmonic-drive
$T_{b\_dynamic}$	velocity-dependent friction torque in the harmonic-drive
T_{b_cyclic}	friction torque in the harmonic-drive which varies with output position
$b_{constant}$	value of the velocity-independent friction torque
b_1	linear damping coefficient
b_2	cubic damping coefficient
A_b	half-amplitude of the cyclic-friction torque function
ϕ_b	phase of the cyclic-friction torque function
k_1	linear stiffness coefficient
k_2	cubic stiffness coefficient
A_1	half-amplitude of the first kinematic-error component at output
A_2	half-amplitude of the second kinematic-error component at output
A_3	half-amplitude of the third kinematic-error component at output
ϕ_1	phase of the first kinematic-error sinusoid
ϕ_2	phase of the second kinematic-error sinusoid
ϕ_3	phase of the third kinematic-error sinusoid
μ	Coulomb friction coefficient at the harmonic-drive gear-tooth interface

station models, five different harmonic-drive models will be developed that can be inserted easily into the overall system models. Since the inertias of the wave-generators are included with the motor armature inertias, no inertia elements are needed in any of these harmonic-drive representations. Consequently, the equations of motion for each will consist solely of algebraic rather than differential equations. These algebraic equations will

outline the relationships between the torques and rotations on the three harmonic-drive ports. In particular, since the inertias in the testing stations dictate the position and velocity seen at the input and output of the harmonic-drive, equations will be developed to relate these rotations to the torques experienced by the transmission. Additionally, because these equations completely characterize the three-port behavior of the harmonic-drive, any two-port configuration of the transmission can be represented easily by setting the rotation of the non-rotating harmonic-drive port to zero.

Due to the complexity of the differential equations generated when the harmonic-drive models are inserted into the overall system models, analytical solutions describing dynamic behavior were rarely available. However, using a Runga-Kutta numerical integration scheme with adaptive step-size control, the dynamic behavior specified by a set of differential equations could be simulated over a given time period for a specific set of input conditions. The code which was developed to generate dynamic time-response data for different harmonic-drive models is listed in Appendix B. In addition to calculating the forces, positions, and velocities predicted by the differential equations, this simulation code determines the energy distribution in the system and can be used generate static stiffness data as well.

To facilitate the development of new harmonic-drive representations in the computer simulation, the modularity of the different harmonic-drive models was preserved by collecting the equations for each in a single function. These harmonic-drive functions can be used to calculate the torque on the three harmonic-drive ports when the corresponding positions and velocities are specified. If the proper input parameters and variable definitions are provided, these harmonic-drive functions can be extracted easily from the code in Appendix B and used in other dynamic simulations.

When executed on a Sun SPARCstation ELC, typical simulation times for a four-second time-response using the more complex harmonic-drive models were much less than one minute. Although the exact time for simulation is influenced not only by the complexity of the dynamic equations but by the desired accuracy and nature of the system parameters as well, in general, the small computational requirements of the harmonic-drive models presented below suit them well for rapid numerical simulation. Additionally, it is likely that simulation performance can be further improved through refinement of the code which calculates values using the dynamic equations.

3.2 Modeling the Experimental Apparatus

To distinguish the dynamic effects of the harmonic-drive transmission from dynamic behavior observed in the experimental apparatus, dynamic models of the testing stations are required. Since, of the three testing assemblies, two different design configurations exist, two separate dynamic models must be constructed. Once this is done, different harmonic-drive representations can be inserted into these models, and dynamic behavior of the aggregate system can be simulated for a range of transmission models. This section is devoted to describing the two models developed to capture the behavior of the experimental equipment and deriving the corresponding equations of motion.

3.2.1 Description of Models

As described in section 2.1, two different designs were incorporated into the harmonic-drive testing facilities in order to observe harmonic-drive behavior in different operating configurations. On joints 1 and 2, the wave-generator is driven by the input motor, the circular spline carries the output rotations, and the flexspline is mounted to ground. On joint 3, the wave-generator is still driven by the input motor, but the output is conveyed through the harmonic-drive flexspline while the circular spline is attached to ground. These two different joint designs are illustrated in figures 3.1 and 3.2.

The relative location of important model parameters can be understood from these figures. First, for both joint configurations, the DC motor applies a torque to the input inertia which is composed of the motor armature and the harmonic-drive wave-generator. Additionally, each joint sports an output inertia consisting of a large mass mounted to the end of the output link on the output port of the transmission. Due to motor damping, a friction torque can be seen between the motor shaft and the motor housing, and similarly, the output bearings introduce a finite friction torque between output rotation and ground. Since, the motor housing on joints 1 and 2 rotates with the circular spline, the absolute rotation seen by the input inertia is equal to the sum of the input and output rotation. The input inertia on joint 3, on the other hand, sees the direct rotation of the motor shaft relative to ground.

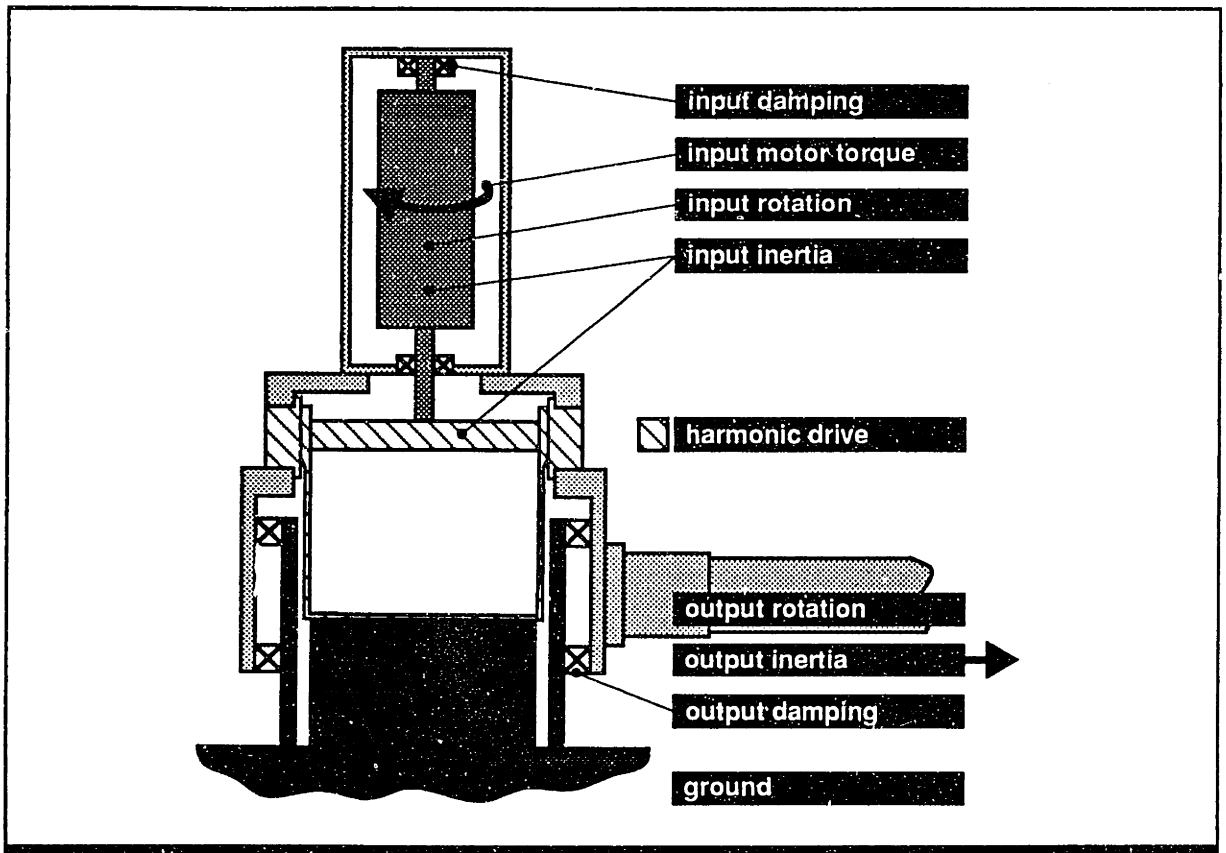

Figure 3.1: Schematic of apparatus design for joints 1 and 2

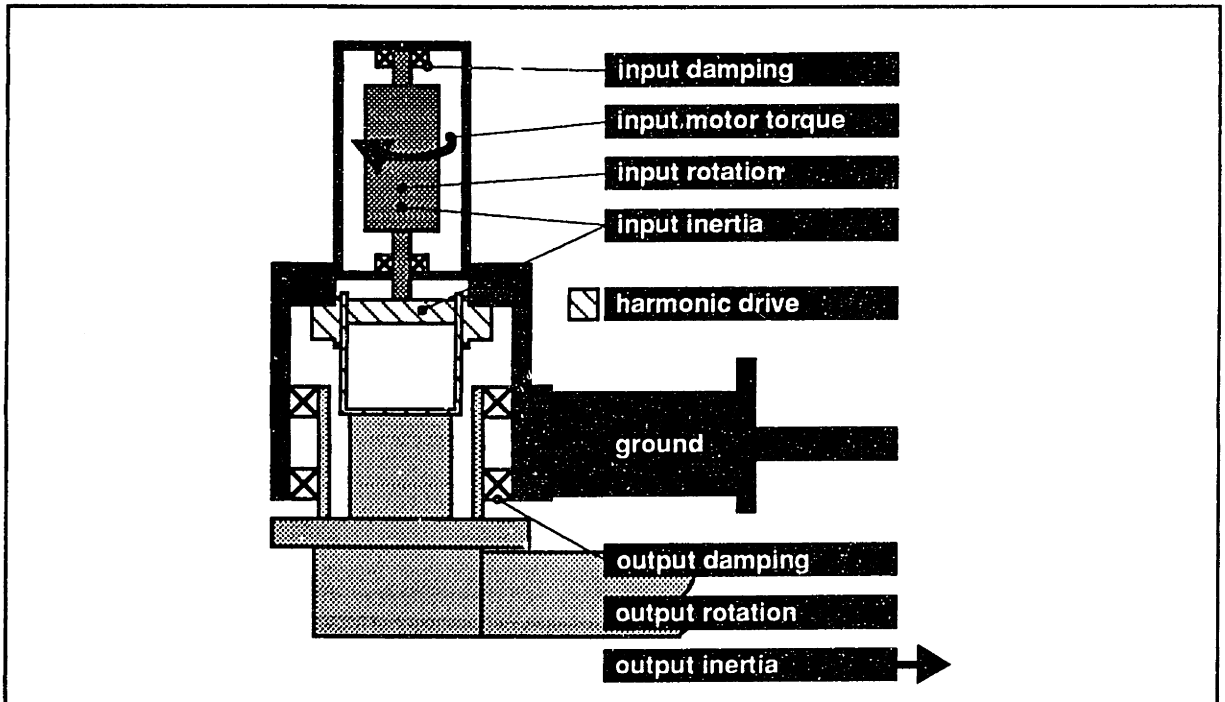

Figure 3.2: Schematic of apparatus design for joint 3

Based on this understanding of the motion constraints and operating parameters, two simple lumped parameter models distilled from the two joint designs are shown in figures 3.3 and 3.4. As illustrated in these figures, the harmonic-drive model is represented as a black box with three ports that transmit the torque and rotation seen by the wave-generator, flexspline, and circular spline. Different models that capture harmonic-drive behavior in varied levels of detail will be developed later and substituted into this black box.

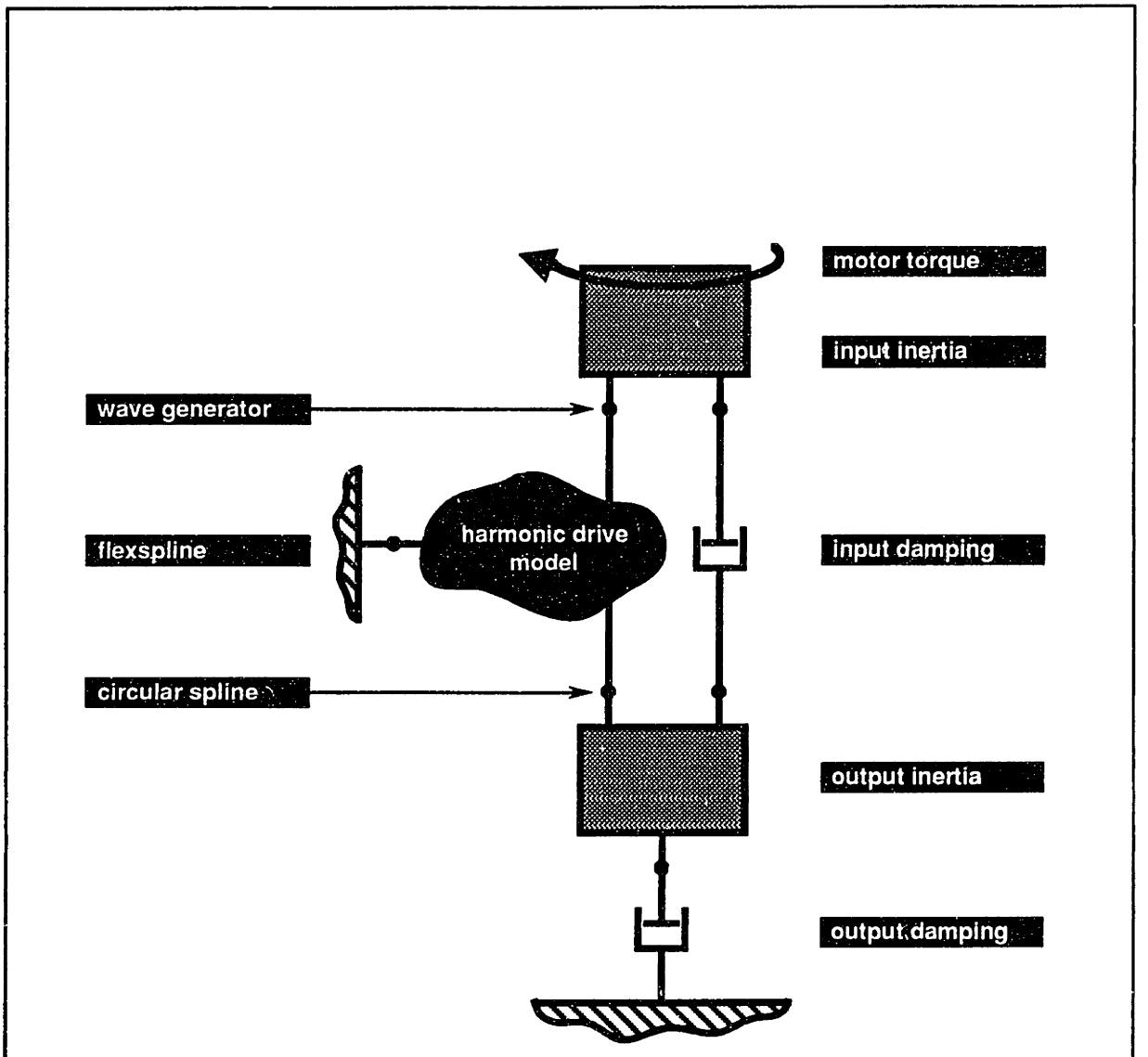

Figure 3.3: Lumped-parameter model for joints 1 and 2

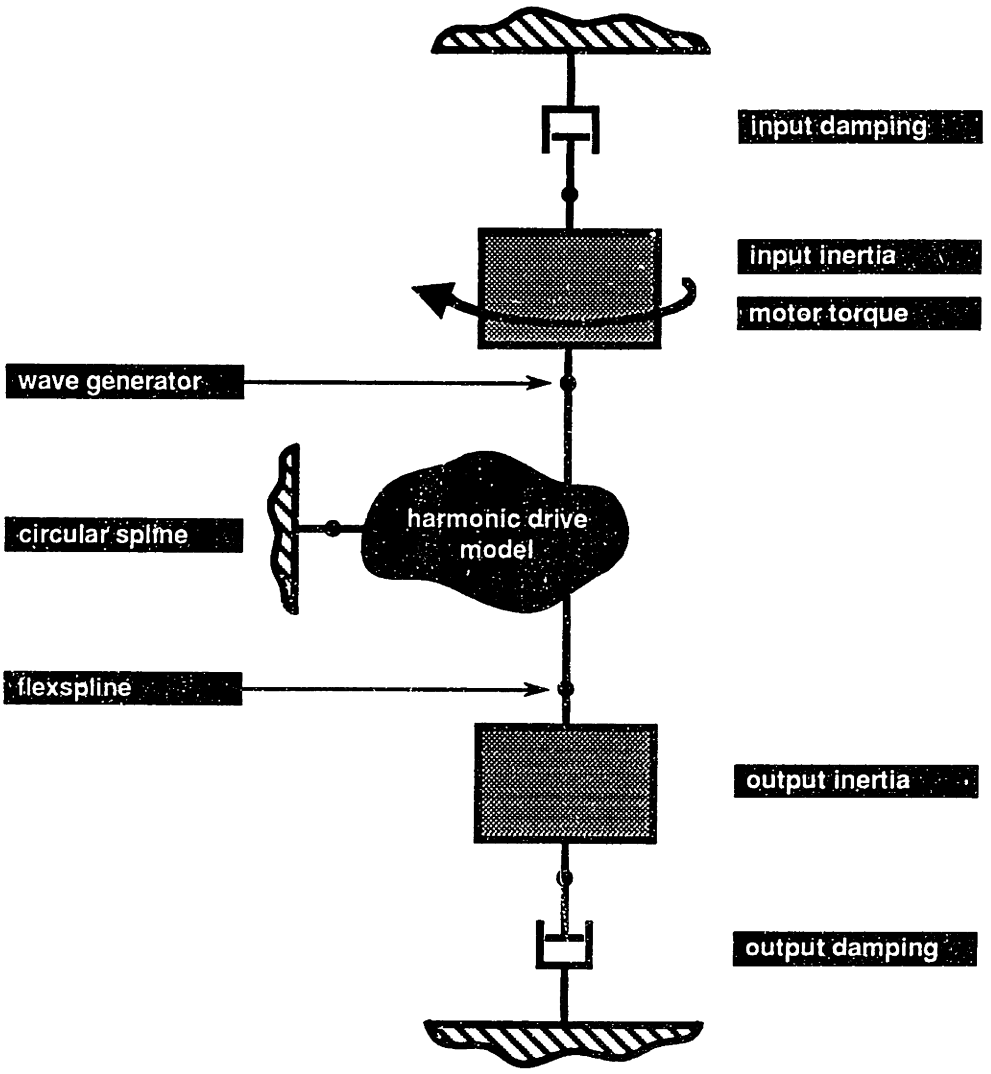

Figure 3.4: Lumped-parameter model for joint 3

3.2.2 Derivation of Equations of Motion

Using the lumped-parameter models illustrated and described above, the generation of dynamic equations is straightforward. The variable names shown for both models in figures 3.5 and 3.6 will be used throughout this derivation and governed by the notation conventions itemized in section 3.1. For further clarity, important model parameters were summarized previously in table 3.1. Using the given notation, naming conventions, and parameter definitions, the equations of motion for joints 1 and 2 will now be derived followed by a similar derivation for joint 3.

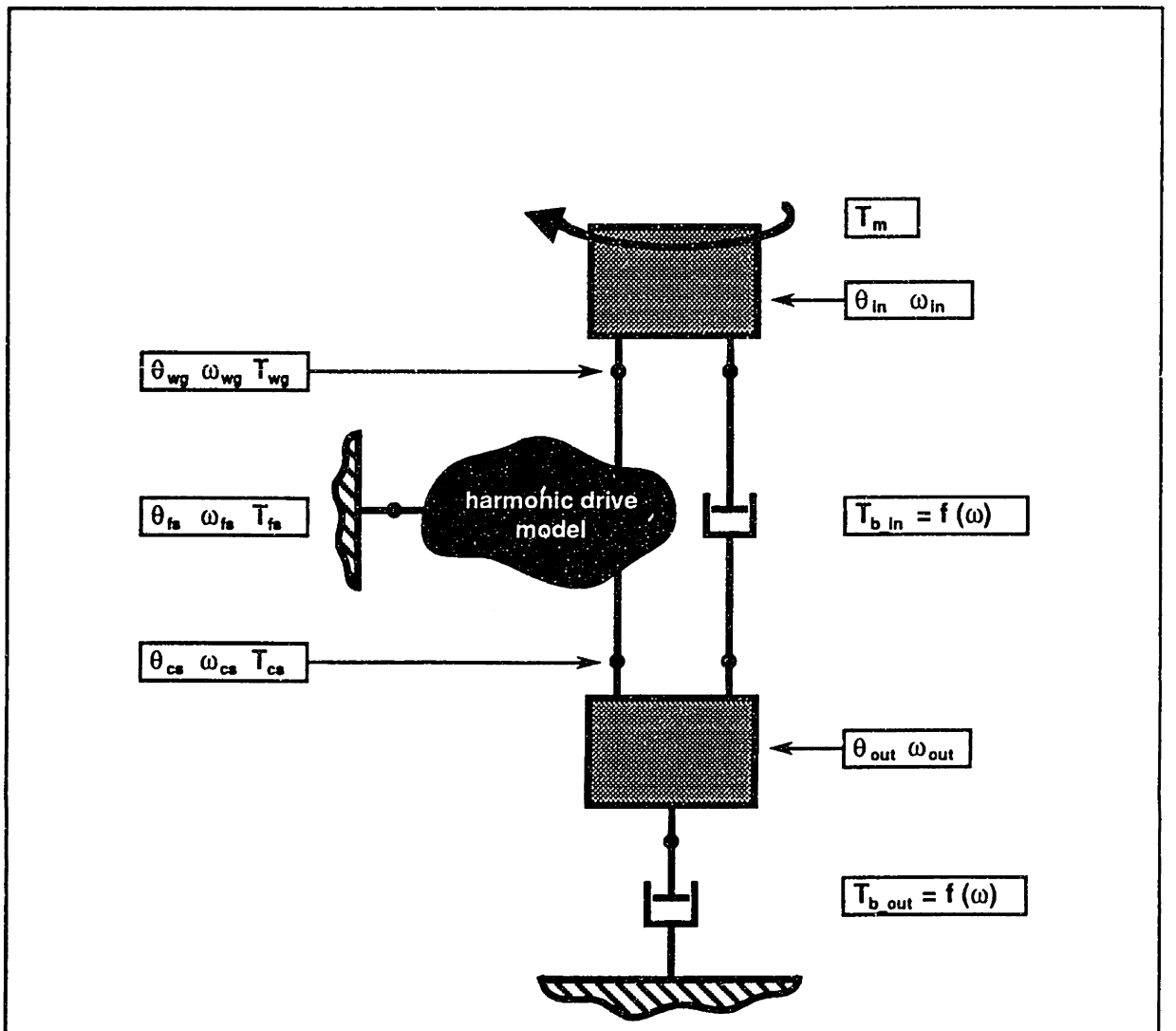

Figure 3.5: Variable notation for the model of joints 1 and 2

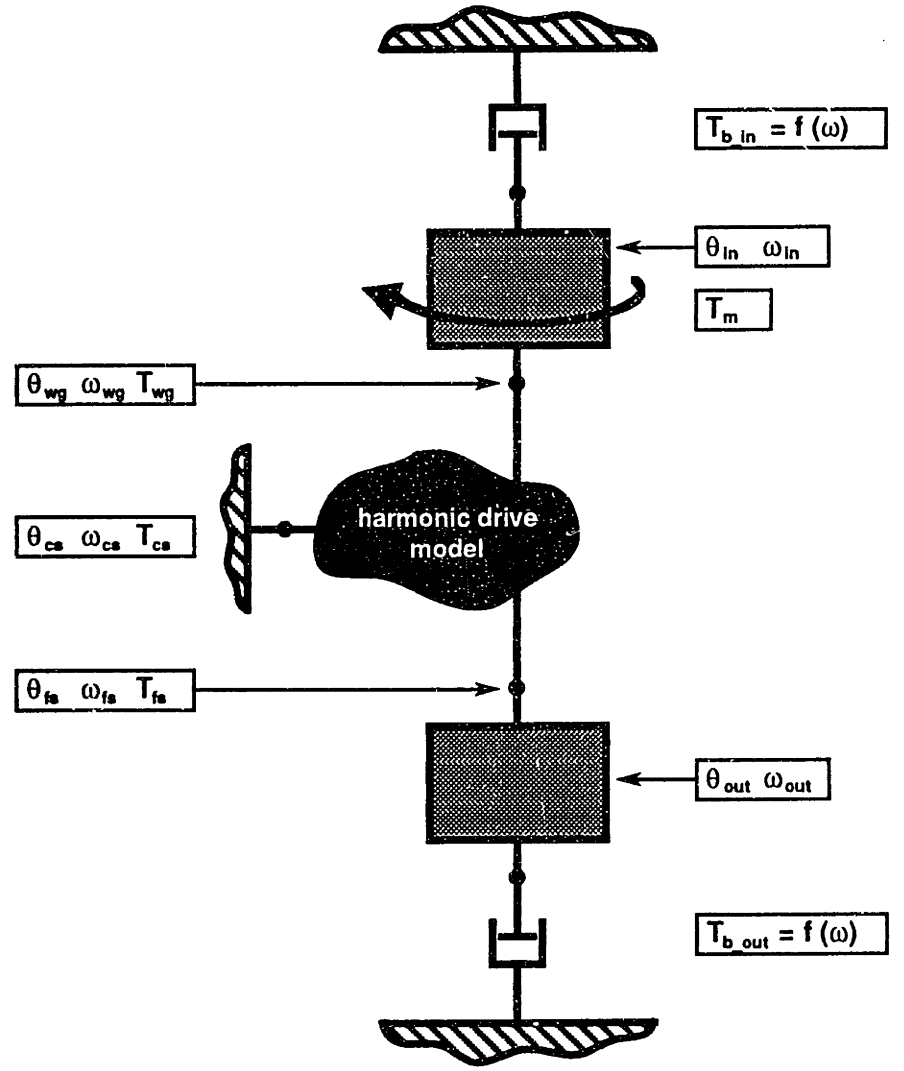

Figure 3.6: Variable notation for the model of joint 3

By applying Newton's Law to the input and output inertias in the model shown in figure 3.3, the resulting equations of motion for joints 1 and 2 are

$$J_{in}\ddot{\theta}_{in} = T_m - T_{b\_in} - T_{wg}\,, \tag{3.1}$$

and

$$J_{out}\ddot{\theta}_{out} = T_{cs} - T_{b\_out} + T_{b\ in}\,. \tag{3.2}$$

In order to solve these equations, the torques on the right-hand side of each equation must be expressed in terms of the state variables, θ_{in} and θ_{out}. This can be done readily for the damping torques by assuming that they are linear functions of velocity:

$$T_{b\_in} = b_{in}\left(\dot{\theta}_{in} - \dot{\theta}_{out}\right), \text{ and} \tag{3.3}$$

$$T_{b\_out} = b_{out}\,\dot{\theta}_{out}\,. \tag{3.4}$$

Since the motor torque is linearly proportional to the current produced by the motor amplifiers, T_m can also be determined:

$$T_m = K_t\, i_m\,, \tag{3.5}$$

where the amplifier current, i_m, can be found from the equations presented in Appendix C which describe the saturation limits of the amplifiers. The remaining unknown torque components, T_{wg} and T_{cs}, can be found by specifying the kinematic constraints imposed by the system on the three harmonic-drive ports and calculating the resulting torques using one of the harmonic-drive models presented later in this section. Since each port of the harmonic drive is directly coupled to either ground or one of the inertias, these kinematic constraints are simply

$$\theta_{wg} = \theta_{in}\,, \tag{3.6}$$

$$\theta_{fs} = 0\,, \text{ and} \tag{3.7}$$

$$\theta_{cs} = \theta_{out}\,. \tag{3.8}$$

Therefore, given these equations, and any dynamically complete harmonic-drive representation, the equations of motion are fully defined.

The equations of motion for the joint 3 testing station are very similar to those listed above for joints 1 and 2. Using figure 3.4, they can be determined readily to be

$$J_{in}\ddot{\theta}_{in} = T_m - T_{b\_in} - T_{wg}\,, \text{ and} \tag{3.9}$$

$$J_{out}\ddot{\theta}_{out} = -\,T_{fs} - T_{b\_out}\,. \tag{3.10}$$

The output damping torque for this model can still be calculated using equation (3.4) above, but the input damping torque must be determined from

$$T_{b\_in} = b_{in}\,\dot{\theta}_{in}\,. \tag{3.11}$$

Additionally, the motor torque expression remains the same as equation (3.5) above, but the kinematic constraints on the harmonic-drive ports are now

$$\theta_{wg} = \theta_{in} , \tag{3.12}$$

$$\theta_{fs} = \theta_{out} , \text{ and} \tag{3.13}$$

$$\theta_{cs} = 0 . \tag{3.14}$$

Therefore, by substituting these constraints into a harmonic-drive model, calculating the resulting torques on the harmonic-drive ports, and substituting them into the equations of motion listed above, the dynamic behavior of the joint 3 testing station is fully defined.

3.2.3 Model Parameter Calculation

Having derived the governing equations for the two different harmonic-drive testing stations, dynamic response can be simulated once values have been determined for the given model parameters. First, the input inertia can be found by summing the catalog inertia values for the wave-generator and the motor armature, and the output inertia can be calculated from the weight and location of the output mass on each joint. Since all other output inertia components on each joint were negligible compared to the inertia of the output mass, they were ignored in the output inertia calculations. All important inertia values are summarized in table 2.10 and reproduced in table 3.3 below. Second, a value for the input damping coefficient can be obtained from the DC motor catalog, and the damping in the output bearings can be found from roller-bearing catalog specifications.

Table 3.3: Parameter values for the testing-station models

	Joint 1	Joint 2	Joint 3
J_{in} (kg-m^2)	2.2e-4	7.6e-5	5.2e-6
J_{out} (kg-m^2)	0.268	0.056	0.0088
b_{in} (N-m/(input deg/sec))	2.3e-7	2.3e-7	1.0e-7
b_{out} (N-m/(output deg/sec))	<7.0e-4	< 7.0e-4	< 4.0e-4
K_t (N-m/amp)	0.06	0.03	0.04
K_b (volts/(input deg/sec))	1.05e-3	5.07e-4	7.08e-4

These values are also listed in table 3.3. Lastly, as mentioned above, the torque produced by the DC motor is linearly proportional to the current it receives from the amplifiers. This current is specified by the desired input command and remains true to this value unless high motor velocities cause the current amplifiers to saturate. Using the catalog motor specifications listed in table 3.3 and the measured motor velocity, appendix C presents a simple algorithm which can be used to capture saturation behavior. Having developed representations which describe testing-station operation and determined values for corresponding model parameters, attention can now be focused directly on the harmonic-drive transmission.

3.3 Harmonic-Drive Model 1: Ideal Transmission

At a bare minimum, a harmonic-drive model should be able to describe the overall gear-reduction properties of the transmission. Since the harmonic-drive has three independent rotational components, equations which describe three-port transmission behavior must be used. Based on the information provided in manufacturer's catalogs, a simple three-port harmonic-drive transmission model, as illustrated in figure 3.7, can be characterized by the following equations:

$$\theta_{wg} = (N + 1)\,\theta_{cs} - N\,\theta_{fs}\,, \tag{3.15}$$

$$\omega_{wg} = (N + 1)\,\omega_{cs} - N\,\omega_{fs}\,, \text{ and} \tag{3.16}$$

$$T_{wg} = \frac{1}{(N + 1)}\,T_{cs} = \frac{1}{N}\,T_{fs}\,. \tag{3.17}$$

Note that a positive value of T_{fs} will cause a negative rotation of the flexspline since it is defined to be positive in the direction opposite to T_{wg} and T_{cs}. As previously discussed, N is the catalog gear ratio and the remaining variables are illustrated in figure 3.8. Using these equations, the positions, velocities, and torques for any harmonic-drive configuration are completely defined.

When this representation is substituted into the different joint-configuration models presented above, the input inertia becomes directly coupled to the output inertia creating a first-order system. Consequently, any step input in motor current should produce an exponential increase in velocity up to the point where the motor torque matches the dynamic

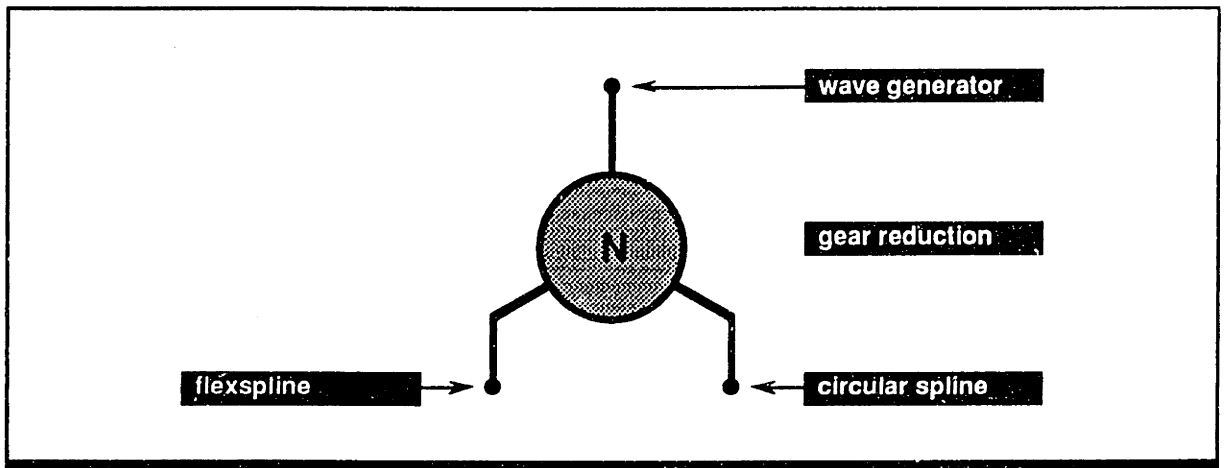

Figure 3.7: An ideal harmonic-drive representation

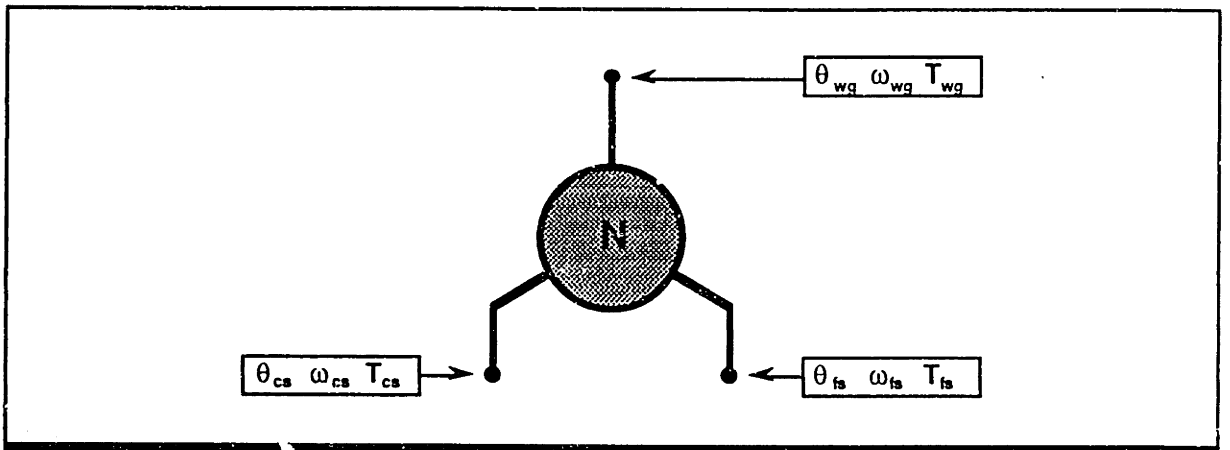

Figure 3.8: Notation for the ideal harmonic-drive model

damping torque of the motor and output bearings. This behavior is illustrated in the simulated input velocity responses for the three harmonic-drive testing stations shown in figures 3.9, 3.10 and 3.11.

By comparing these predicted input-velocity responses to the experimental input-velocity responses shown in Appendix-D-figures D.1.2, D.2.2, and D.3.2, it can be seen that the steady-state velocities achieved using the ideal transmission model are several orders-of-magnitude higher than the actual system. Additionally, the velocity fluctuations observed in the experimental results do not appear in the model predictions. These two unsurprising discrepancies can be accounted for by the lack of any frictional losses or

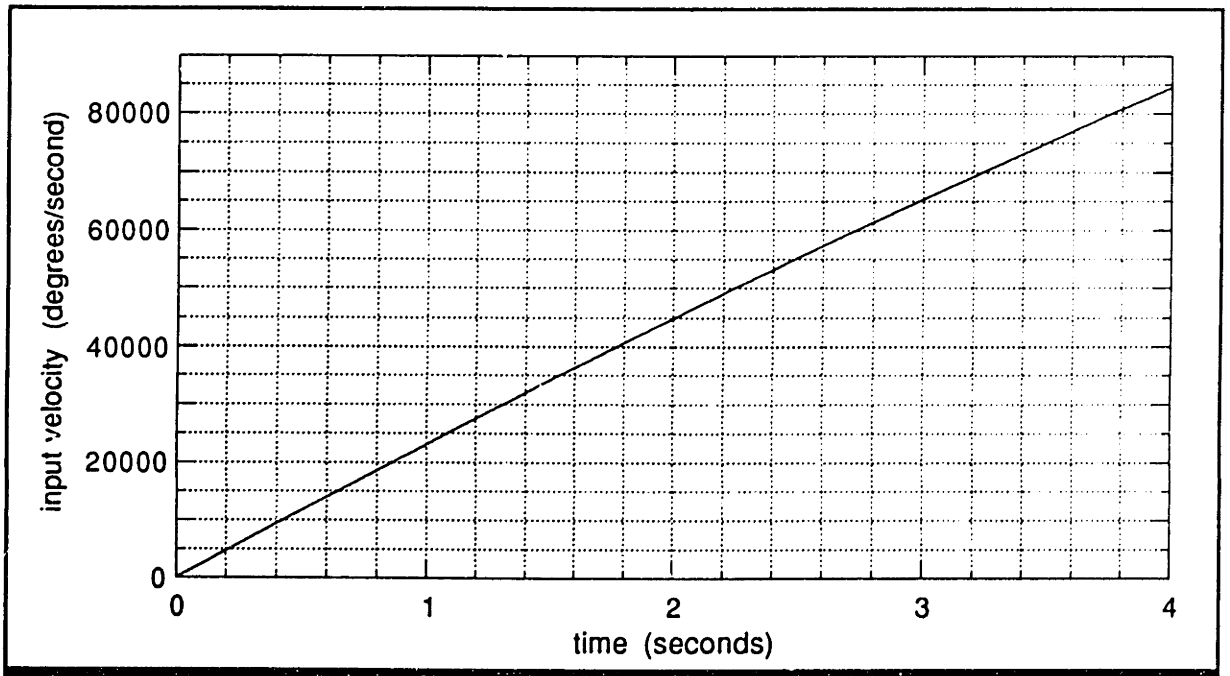

Figure 3.9: Joint 1 ideal-model input-velocity for a 1.6 amp step

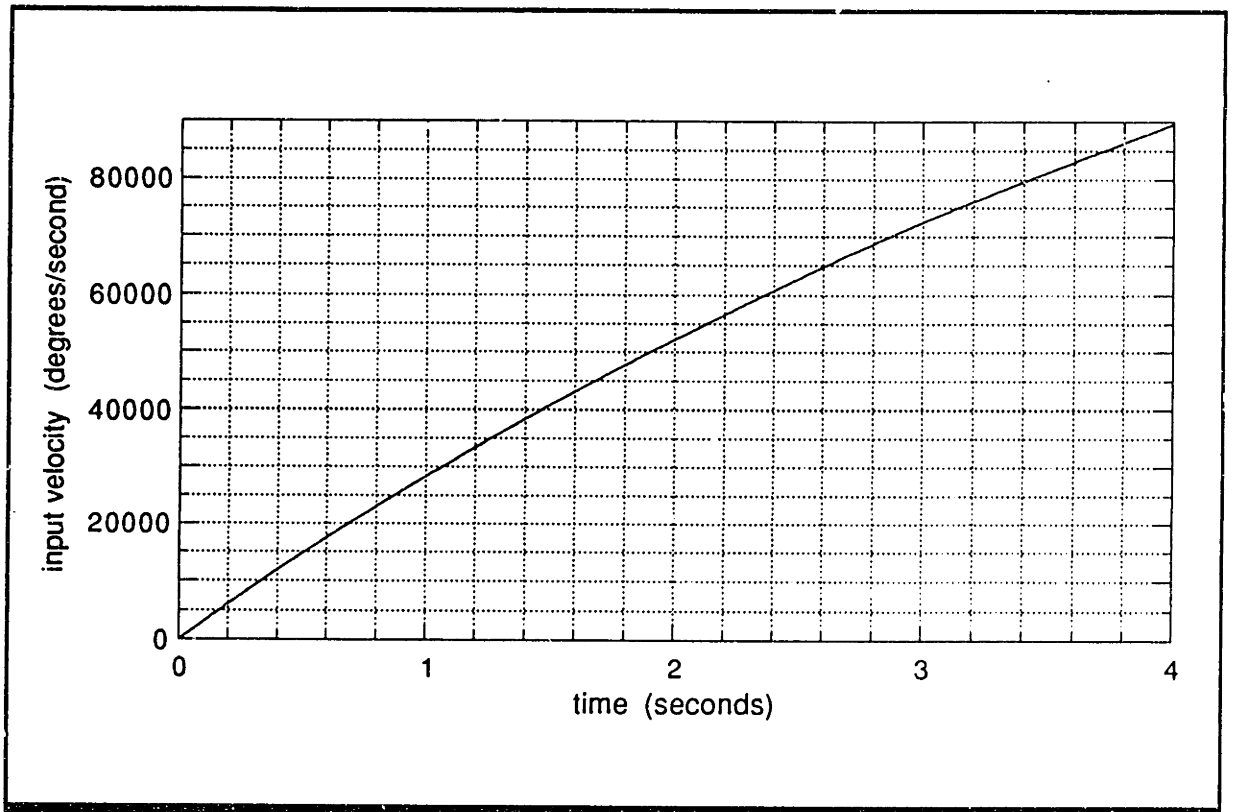

Figure 3.10: Joint 2 ideal-model input-velocity for a 1.4 amp step

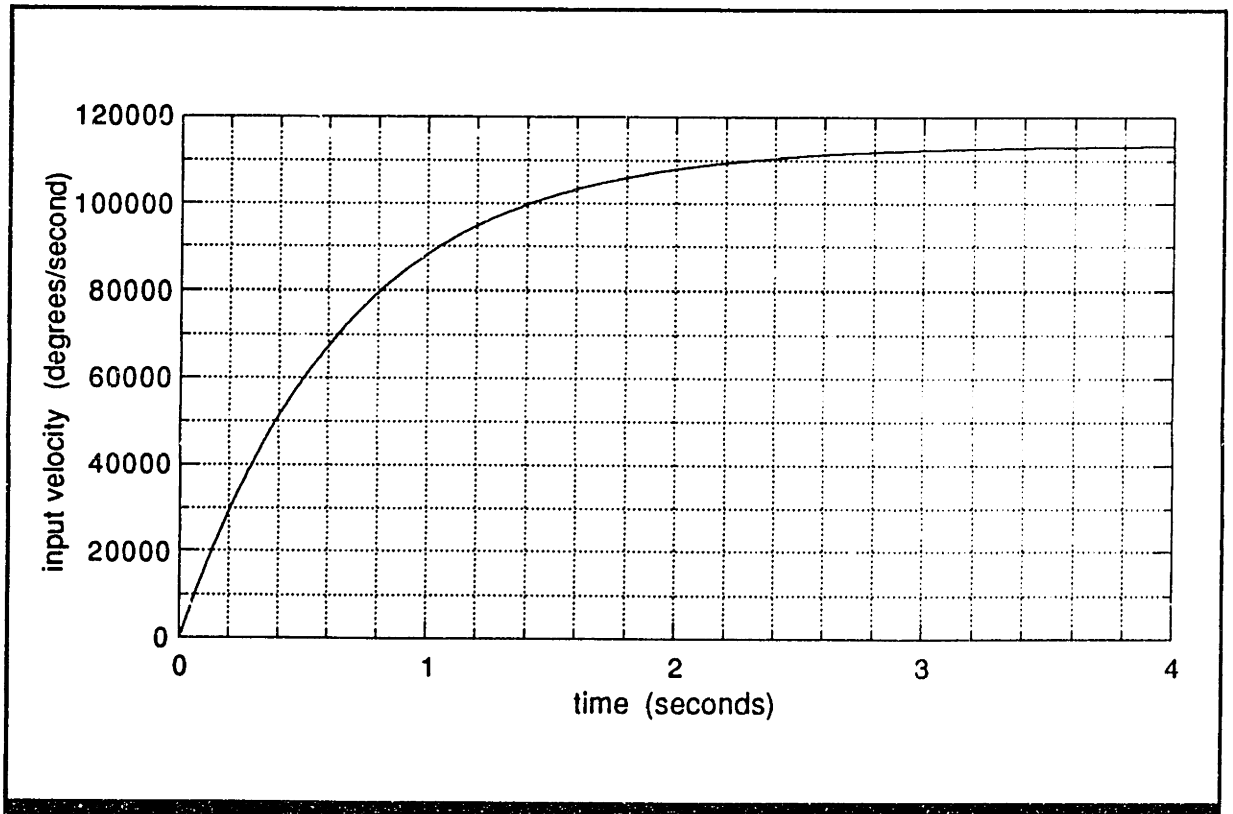

Figure 3.11: Joint 3 ideal-model input-velocity for a 0.28 amp step

kinematic error in the transmission model. Given this justification for poor model performance, it can be concluded that the only circumstances where this representation may prove useful is when harmonic-drive frictional losses are small compared to other losses in the mechanical system and when velocity and torque fluctuations are unimportant. For example, under static loading, when dynamic friction is zero, this model can be used to accurately predict torques when applied loads are significantly greater than the static friction in the transmission. Additionally, in static positioning applications where the desired accuracy is lower than the kinematic error in the transmission, this model may be useful to calculate the rotational displacement of the harmonic-drive ports.

3.4 Harmonic-Drive Model 2: Transmission with Frictional Losses

As concluded from the poor results of the ideal model, energy losses in the transmission must be acknowledged in order resurrect the simulated velocity response. By matching the frictional torque in the model to the motor torque resulting from the input current, accurate recreations of experimental steady-state velocity values can be achieved. Furthermore, by including a periodic friction function which varies with the position of the transmission output, the undulations in steady-state velocity observed in the experimental results can also be replicated. As discussed below, by incorporating these simple modifications, the response of the ideal transmission model can be improved substantially.

3.4.1 Description of Model 2

The bulk of energy dissipation in harmonic-drives can be blamed on two sources: (1) losses in the wave-generator bearing and (2) friction due to gear-tooth meshing. Of these two candidates, it is probable that the majority of the frictional dissipation results from gear-tooth-rubbing action between the flexspline and circular spline. Based on this assumption, a new harmonic-drive model is shown in figure 3.12 in which a dissipation element is included between the flexspline and circular spline. Since the location of these frictional losses in the model can greatly influence simulated behavior, careful investigation was performed to justify this representation.

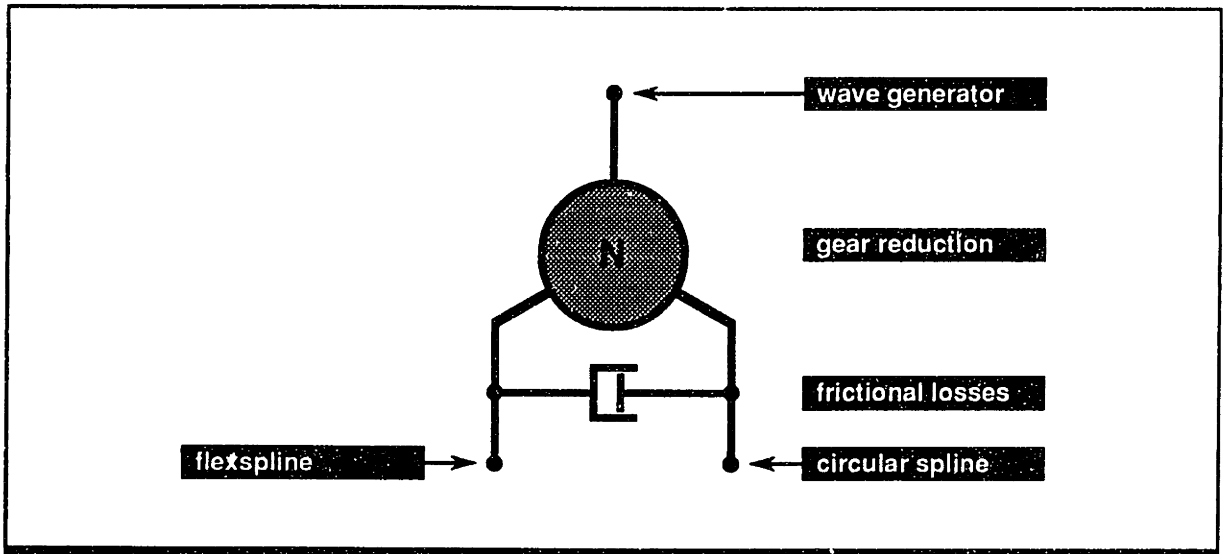

Figure 3.12: A harmonic-drive model with friction

In addition to conceptually capturing the rubbing losses between the flexspline and circular spine gear teeth, the location for the frictional losses shown in figure 3.12 was selected for several additional reasons. First, as shown in figures D.1.7, D.2.7, and D.3.7, since torque-sensor readings in experimental dynamic response measurements display very large fluctuations but virtually no frictional bias torque, it can be concluded that the torque sensors are blind to any frictional torque present in the harmonic drive. On joint 1, for example, if the friction losses in the model were placed between the circular spline and ground, the torque sensor mounted to the flexspline would not only see any torque fluctuations on the output inertia but would also directly measure the frictional torque from the transmission losses. By moving these frictional losses to act between the flexspline and circular-spline, the torque sensors for both joint configurations ignore these losses and return results that more closely resemble the experimental observations. As another justification for the selected location of transmission losses, any static friction included in this dissipation element will be manifested as hysteresis loss in a stiffness profile collected from either output port of the transmission. On the other hand, if the friction mechanism occurred between the wave-generator and either output port, hysteresis loss would appear only in the stiffness profile collected from the output port connected to that friction element. From this distinction, it seems highly probable that frictional torques in the harmonic-drive occur primarily between the flexspline and circular spline gear-teeth and can account for the hysteresis loss observed in experimental stiffness profiles. To substantiate this claim empirically, results were gathered from models employing different friction mechanisms and the integrity of the representation derived in this section was verified.

3.4.2 Derivation of Dynamic Equations

The addition of frictional losses to the ideal transmission model complicates the dynamic equations only slightly. Since, using this new representation, the torque seen by the flexspline and circular spline is the combined torque of the ideal transmission element and the frictional torque, the following equations result:

$$T_{fs} = T_{n\_fs} - T_b \text{ , and} \tag{3.18}$$

$$T_{cs} = T_{n\_cs} - T_b \text{ .} \tag{3.19}$$

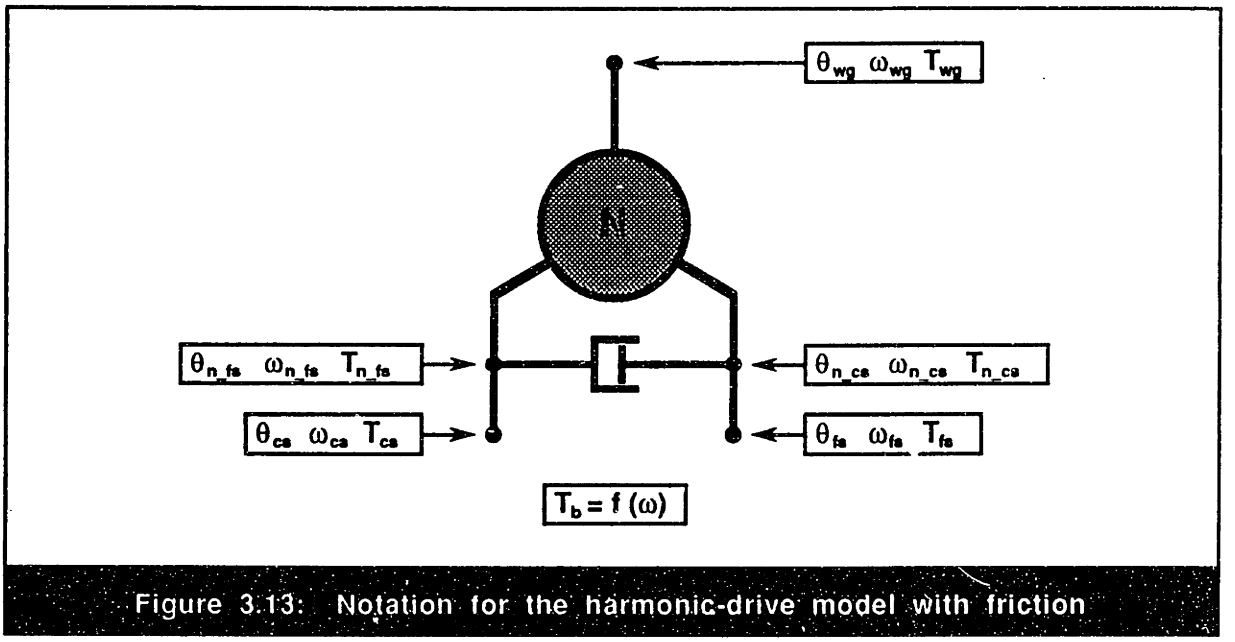

Figure 3.13: Notation for the harmonic-drive model with friction

In these equations, T_b is the aggregate friction-torque function and, as implied by the sign conventions stated previously, T_{n_fs} is defined to be positive in the opposite direction of T_{n_cs}. The variables used in these equations and the rest of this derivation are illustrated in figure 3.13. Using the ideal-transmission torque relationship in equation (3.17), the torque on the wave-generator can be directly related to T_{n_fs} and T_{n_cs}:

$$T_{wg} = \frac{1}{(N+1)} T_{n\_cs} = \frac{1}{N} T_{n\_fs} \,. \tag{3.20}$$

Given these three equations, the torque constraints on the model are complete, however, the friction-torque function, T_b, must be defined in order to finish the representation. As observed in experimental results, harmonic-drive friction typically has three components: (1) a velocity-independent friction term, (2) a non-linear velocity-dependent damping function, and (3) a periodic friction torque which varies with output rotation. Experimental observations also suggest that frictional losses can be greatly influenced by other parameters such as preload, wave-generator orientation, and operating temperature. For the sake of model simplicity, these frictional influences will be ignored. Additionally, experimental results show that harmonic-drives exhibit a substantial static-friction torque which must be overcome before rotation can occur. Since this stiction torque is also influenced by several parameters such as preload and input angle, an accurate model of this property relies heavily on careful experimental characterization. Once this experimental understanding is complete, a stiction model can be implemented by placing appropriate constraints on the minimum motor torque required to effect rotation. Although

this model was developed in the computer simulation, it will be ignored here since it only influences dynamic behavior when velocities are close to zero and consequently has little effect on the experimental and theoretical dynamic response. Given these assumptions, the friction function which provided optimal results with minimal complexity is defined as

$$T_b = T_{b\_constant} + T_{b\_dynamic} + T_{b\_cyclic} , \tag{3.21}$$

where

$$T_{b\_constant} = b_{constant} , \tag{3.22}$$

$$T_{b\_dynamic} = b_1 (\omega_{n\_cs} - \omega_{n\_fs}) + b_2 (\omega_{n\_cs} - \omega_{n\_fs})^3 , \text{ and} \tag{3.23}$$

$$T_{b\_cyclic} = A_b \sin ((\theta_{n\_cs} - \theta_{n\_fs}) + \phi_b) . \tag{3.24}$$

As equation (3.21) states, this model captures the three facets of friction behavior noticed in the experimental results. First, the velocity-independent friction component, as described in equation (3.22), is represented by a single value, $b_{constant}$. Second, since experimental data indicated that velocity-dependent friction could be accurately captured by a cubic relationship, the dynamic-friction torque defined in equation (3.23) is a cubic function of the relative velocity between the flexspline and circular spline. In this equation b_1 and b_2 represent the linear and cubic damping coefficients, respectively. Since all observed experimental behavior indicates that dynamic damping is highly non-linear, a linear damping representation is likely to cause inaccurate model performance. Third, periodic variations in the frictional torque are captured in the sinusoidal function in equation (3.24). As this relationship indicates, frictional torque fluctuations of half-amplitude A_b complete one cycle every time the circular-spline makes one complete rotation relative to the flexspline. To match this model to experimental observations, a phase-shift of ϕ_b is also included in this equation. Using the experimental results from sections 2.4, 2.5, and 2.6 of this document, values for the friction parameters $b_{constant}$, b_1, b_2, A_b, and ϕ_b can be determined readily.

With the given definition of the harmonic-drive friction, the transmission model is virtually complete. The only remaining task is to realize that the variables θ_{n_fs}, θ_{n_cs}, ω_{n_fs} and ω_{n_cs} are identical to the variables θ_{fs}, θ_{cs}, ω_{fs} and ω_{cs} respectively, due to the kinematic constraints in the model. Given this identity, the friction-torque function can be calculated based on the rotations specified on the harmonic-drive ports and the remaining torques in the transmission can be found.

3.4.3 Evaluation of Simulated Results

Using values for the harmonic-drive friction parameters taken directly from the experimental observations, several numerical simulations were performed for each harmonic-drive over a range of current commands. As a sole indicator of model performance, the resulting input-velocity response for the three different harmonic drives is illustrated in figures 3.14, 3.15, and 3.16. These three plots can be compared to the experimental input-velocity response shown in figures D.1.2, D.2.2, and D.3.2 in Appendix D to evaluate model integrity.

By comparing the theoretical and experimental time-response, it is clear that the harmonic-drive model which includes frictional losses boasts performance greatly improved over the ideal transmission representation. In particular, for high velocities, input velocity predictions are almost identical to experimental observations on each joint. For all these curves, response is very similar to first order-system response where the time-constant is dictated by the total system inertia and the steady-state velocity is reached when the motor torque matches the total friction torque. The only discrepancies between these high-velocity response curves is in the shape of the velocity fluctuations due to friction variations with output rotation. By replacing the simple sinusoidal friction in the model with a more complex function which closely resembles the actual torque variations in the transmission, it is likely that theoretical predictions could replicate the actual response almost exactly. Low-velocity response predictions also show promise since theoretical steady-state velocities and curve shapes show good agreement with experimental results.

Despite these modeling successes, simulation performance plummets around velocities which excite system resonance. Specifically, the substantial velocity fluctuations which pervade the experimental velocity response are absent in the theoretical predictions. These velocity fluctuations can become extreme around resonance and utterly dominate system behavior. Since the model fails to capture these disturbances, steady-state velocities and curve-shapes are markedly different from actual results. Additionally, as illustrated in figures D.1.5, D.2.5, and D.3.5, the more prominent fluctuations in output velocity are substantial even at high velocities. Since the output-velocity response predicted by the model, although not shown here, will capture none of this agitated behavior, simulation accuracy struggles through all ranges of operation. As a final criticism of the virtue of this harmonic-drive model, the periodic velocity fluctuations due to cyclic friction, as shown in figure 3.15 in particular, are smaller in amplitude at high velocities than the experimental

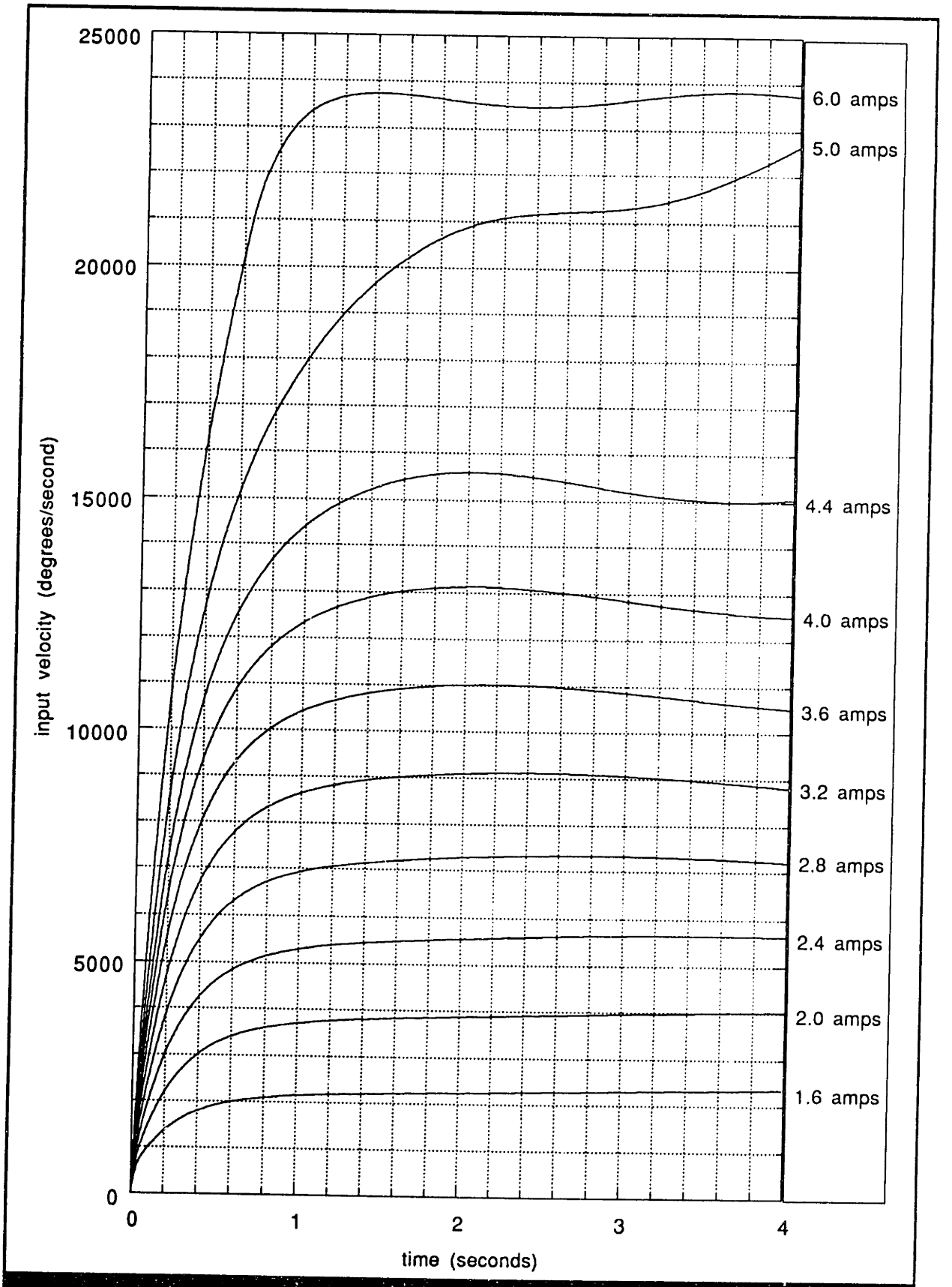

Figure 3.14: Joint 1 input-velocity response for a model with friction

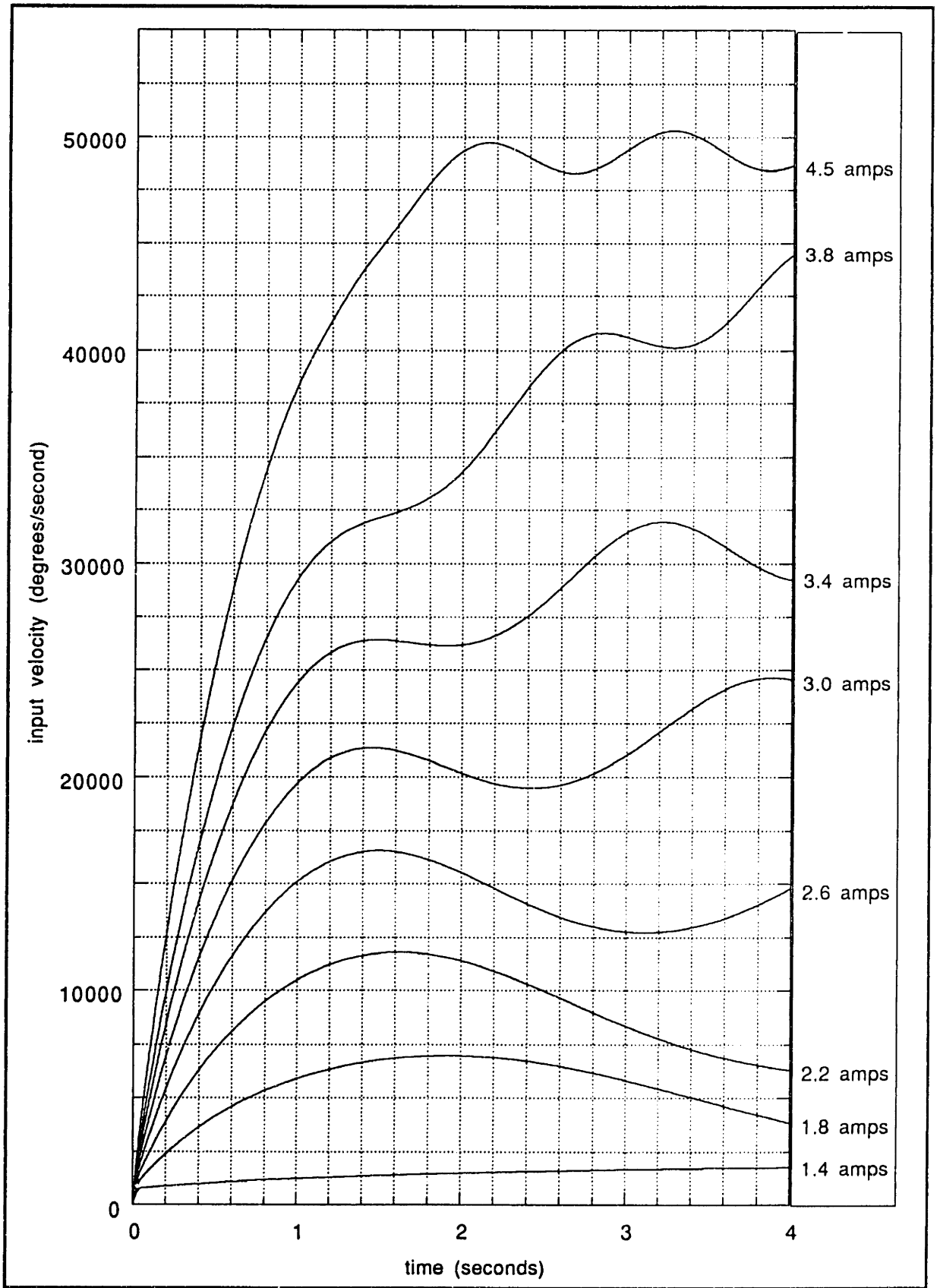

Figure 3.15: Joint 2 input-velocity response for a model with friction

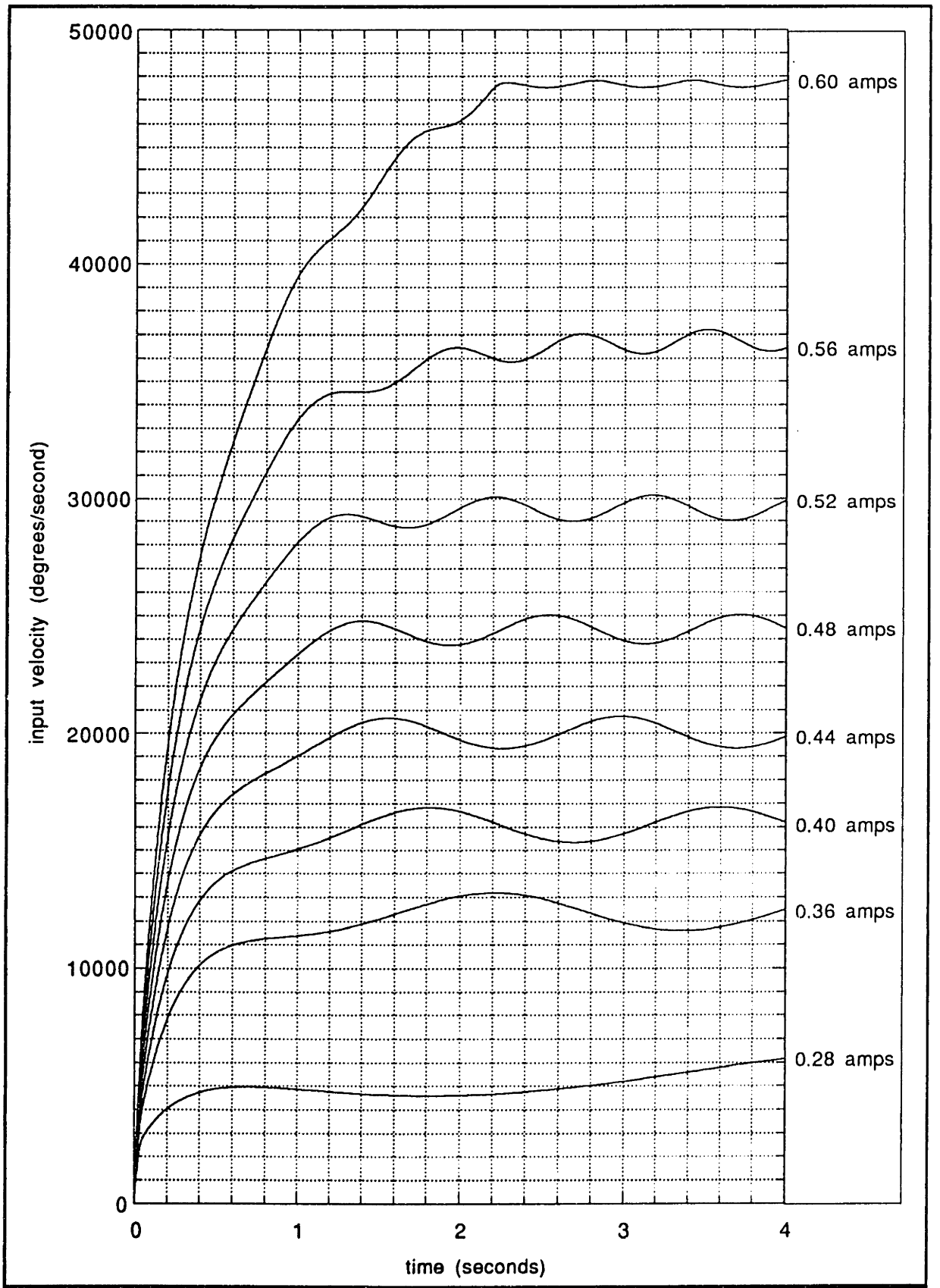

Figure 3.16: Joint 3 input-velocity response for a model with friction

results. However, at low velocities, these periodic variations are in closer agreement with experimental response. This unfortunate behavior indicates that the amplitude of the cyclic friction function is not constant as anticipated, but may indeed vary with such variables as rotational velocity.

3.4.4 Model 2 Conclusions

Based on the performance of the harmonic-drive model with frictional losses, if small velocity fluctuations can be tolerated, it is probable that this model may prove useful for predicting the dynamic behavior of harmonic-drive systems designed to operate predominantly at velocities far removed from regions of resonant behavior. However, in order to ensure the accuracy of this model, a comprehensive experimental friction characterization is first required. In particular, transmission friction must be measured for a range of velocities and output orientations under the identical environmental and operating conditions to be experienced during normal operation. Since the velocity-independent friction torque looms relatively large at small rotational velocities, accurate characterization of this value ensures good model performance at low velocities. Conversely, dynamic friction forces, which become significant at high velocities, govern model performance for large current inputs. Lastly, careful measurement of experimental cyclic friction is rewarded by accurate reproduction of the resulting velocity fluctuations. By following these guidelines, this simple transmission model can be used to make accurate predictions for a limited range of harmonic-drive systems.

In conclusion, the results of this section illustrate that the harmonic-drive model with friction performs significantly better than the ideal transmission model. Due to the incorporation of observed energy dissipation into the model, average steady-state velocities show fairly close agreement for operating regions where resonant vibration is minimal. Unfortunately, since the model ignores kinematic position-error variations, theoretical predictions are devoid of the velocity fluctuations which appear throughout the experimental response. Additionally, because these velocity fluctuations become intense during system resonance, theoretical results become very inaccurate over a large portion of the observed operating range. Based on these shortcomings, it is clear that an accurate model must capture velocity turbulence and resonance behavior. Since, as discussed previously, this behavior is spawned from the interaction between kinematic error and

transmission compliance, an improved model should acknowledge these two harmonic-drive properties.

3.5 Harmonic-Drive Model 3: Transmission with Friction and Compliance

As published research suggests, once frictional behavior is captured, the first strategy adopted by designers to improve performance of harmonic-drive models is to include a linear or non-linear compliance in the transmission. Since this compliance transforms the first-order model into a second-order system, a vibration mode appears and resonance phenomenon can be anticipated. This section outlines this new model and demonstrates that, unless large torque loads are present in the representation as well, the compliant transmission model does little to improve simulation performance over the model with friction alone.

3.5.1 Description of Model 3

A lumped-parameter schematic illustrating the harmonic-drive model with compliance and friction is illustrated in figure 3.17. Since, as noted in previous research, harmonic-drive compliance occurs in the wave-generator as well as the gear-teeth, I chose to locate the ideal spring on the input side of the gear-reduction in this model. However, by adjusting the coefficients of the stiffness function appropriately, this compliance can be

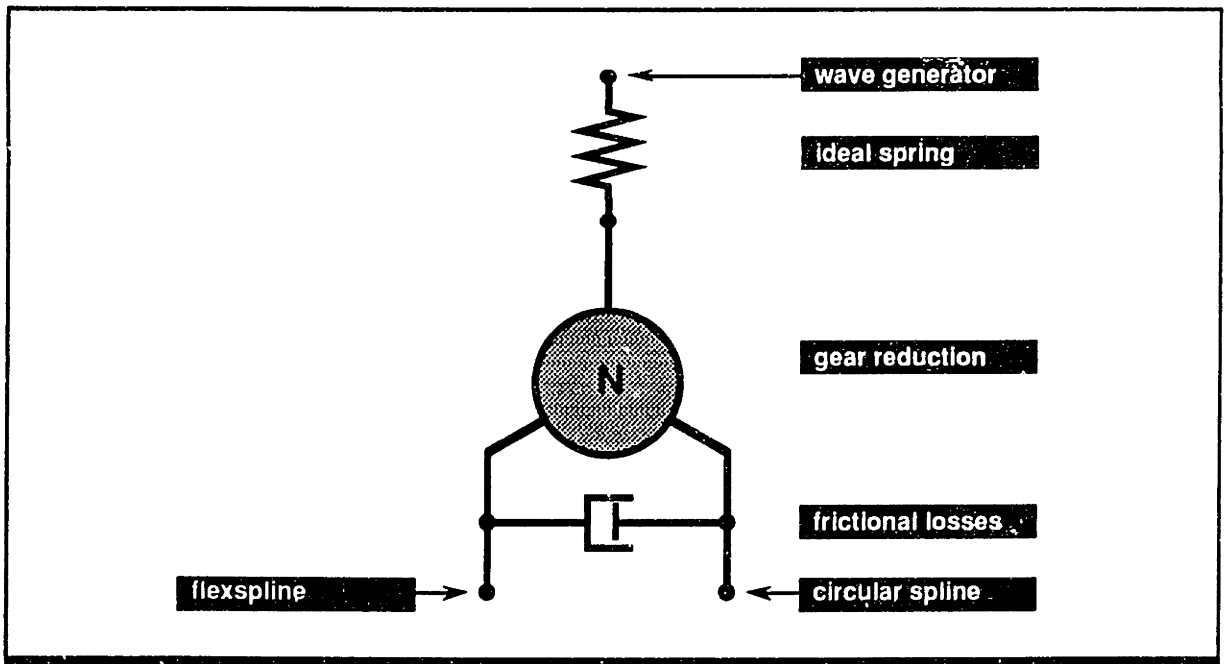

Figure 3.17: A harmonic-drive model with friction and compliance

reflected to either of the other two ports of the transmission with no effect on the dynamic behavior of the system. Due to the location of the friction element with respect to the compliance in this model, the stiffness profile measured from either output port of the transmission will display the characteristic hysteresis loss due to the velocity-independent friction component in the friction-torque function.

3.5.2 Derivation of Dynamic Equations

Given this simple lumped-parameter model and the notation definitions illustrated in figure 3.18, the derivation of the equations of motion is straightforward. First, using force-balance equations in (3.18) and (3.19) as well as the friction function in (3.21), the torque on the output ports of the harmonic-drive, T_{fs} and T_{cs}, can be related to the variables

T_{n_fs} and T_{n_cs}. Second, using the ideal gear-reduction relationship provided in equation (3.17), these torques can then be equated to the torque across the spring and the torque at the wave-generator:

$$T_k = T_{wg} = T_{n\_wg} = \frac{1}{(N+1)} T_{n\_cs} = \frac{1}{N} T_{n\_fs} . \qquad (3.25)$$

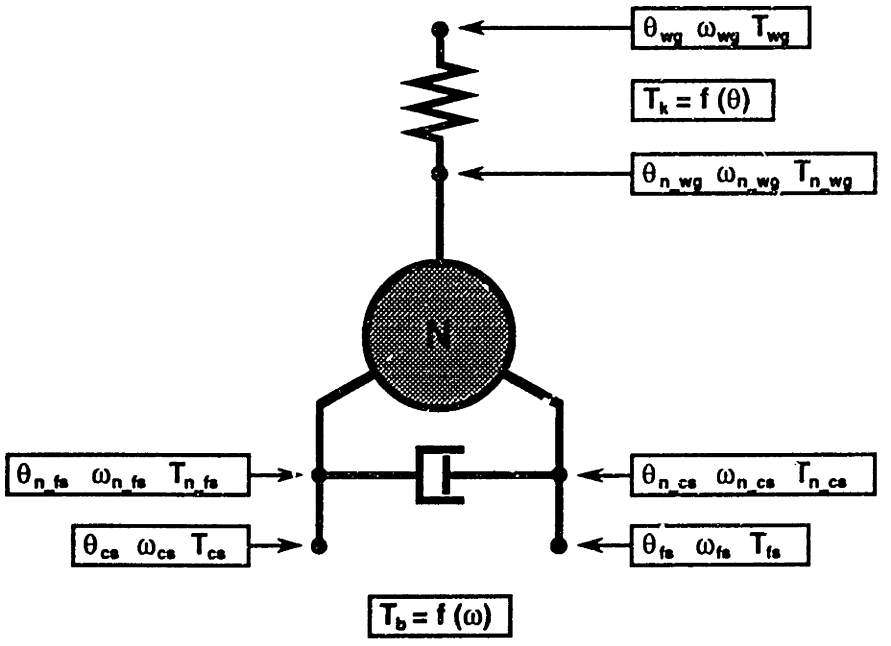

Figure 3.18: Notation for the model with friction and compliance

Given this identity, the torques on all three harmonic-drive ports can be calculated once the torque across the spring is known.

To calculate the transmission stiffness, several different functions can be used. Specifically, depending on the exact shape of the stiffness profile for a particular harmonic-drive, a linear stiffness relationship may suffice. However, as observed in the experimental stiffness observations, most harmonic-drives, especially under heavy loading, display distinctly non-linear compliance. Also as seen in the experimental results, this non-linear behavior can be captured typically by a cubic relationship:

$$T_k = k_1 (\theta_{wg} - \theta_{n\_wg}) + k_2 (\theta_{wg} - \theta_{n\_wg})^3 , \tag{3.26}$$

where k_1 and k_2 are the linear and cubic stiffness constants, respectively. To further refine this stiffness characterization, a more complex equation could be used which includes the influence of wave-generator orientation and gear-tooth preload on the stiffness profile. Since, as experimental observations indicate, this influence can cause fluctuations in stiffness profiles of over thirty percent, a truly accurate stiffness function cannot ignore these effects. However, since the necessity for this level of detail is unclear, these influences will be neglected and the simple cubic relationship in (3.26) will be featured exclusively in the dynamic model.

The derivation of equations for this model can be completed by recognizing that kinematic constraints dictate θ_{n_fs} is equal to θ_{fs} and θ_{n_cs} is equal to θ_{cs}. From these identities, θ_{n_wg} can now be found from the kinematic requirement of the ideal transmission model in equation (3.15):

$$\theta_{n\_wg} = (N + 1)\, \theta_{cs} - N\, \theta_{fs} . \tag{3.27}$$

Given values for θ_{wg}, θ_{fs}, and θ_{cs}, these equations can be used to calculate the resulting torques on the three ports of the harmonic-drive transmission.

3.5.3 Model 3 Results and Conclusions

To evaluate the validity of the stiffness representation used in this model, two hallmarks can be employed. First, the stiffness function should replicate the experimental dynamic behavior observed at system resonance. In particular, resonant frequencies and vibration amplitudes in the model should coincide with observed experimental behavior.

Second, when static stiffness data is generated from the transmission model, it should closely resemble the experimental stiffness profiles. Specifically, if the interaction between the model friction and compliance is accurate, the hysteresis loss and curve shape in the actual stiffness data should be captured. In order to observe the influence of resonant behavior, both of these criteria will be discussed in light of the harmonic-drive model which includes kinematic transmission error to be discussed later.

Using experimental stiffness results to determine the stiffness coefficients k_1 and k_2, simulated time-response results were collected for this representation. As anticipated, due to low dynamic loads and relatively high transmission stiffness, dynamic response behaved almost identically to the response of the ideal transmission model with friction shown in figures 3.14, 3.15, and 3.16. Consequently, unless high inertial or applied loads are experienced by the harmonic-drive system, the inclusion of a compliant element in the transmission model provides no significant advantages over the harmonic-drive representation with friction alone. However, in harmonic-drive applications designed to apply forces or experience high acceleration, the compliant behavior of the transmission cannot be ignored and this model may be useful for predicting system behavior in limited ranges of operation. Unfortunately, due to kinematic position error, substantial torque fluctuations are far too common during normal harmonic drive operation. Because of this menacing transmission property, compliant behavior becomes a major factor in determining dynamic response and must be addressed for a wide range of harmonic-drive operating conditions.

3.6 Harmonic-Drive Model 4: Transmission with Friction, Compliance and Kinematic-Error

As concluded from the performance of the harmonic-drive model with friction losses, prediction of the velocity fluctuations and resonant behavior in the experimental response is essential to secure model accuracy in all operating regions. Since velocity fluctuations result from kinematic position error, this transmission property must be recognized in an improved representation. Also, since resonance occurs when the natural frequency of the system, as governed by the inertias and transmission compliance, coincides with the frequency of kinematic-error disturbances, the interaction between flexibility and position error must also be captured in the model. Lastly, since the frequency of kinematic-error fluctuations is directly related to the rotational velocity of the transmission, accurate frictional losses in the transmission are required to regulate operating speeds. As presented in this section, a new model which incorporates these three transmission properties demonstrates improved accuracy over a wider range of system operation.

3.6.1 Description of Model 4

As illustrated in figure 3.19, the improved harmonic-drive model contains a cyclic kinematic-error element as well as the transmission compliance and frictional losses discussed in the previous models. Since the kinematic error in the harmonic-drives is intimately related to the gear-meshing mechanism itself, it is situated in the model adjacent to the gear-reduction element. Although I chose to place this cyclic position-error component on the input side of the transmission, it can be reflected to any port of the transmission without disturbing simulation performance. This additional component introduces a cyclic position function into the model which varies as a function of the transmission rotational position. Since kinematic error results primarily from gear-tooth placement inaccuracies on the flexspline and circular spline, a strictly accurate representation of this error would include two separate error functions, one at the gear-meshing frequency of the flexspline and the other at the gear-meshing frequency of the circular spline. Since these two disturbance frequencies are almost identical, complexity

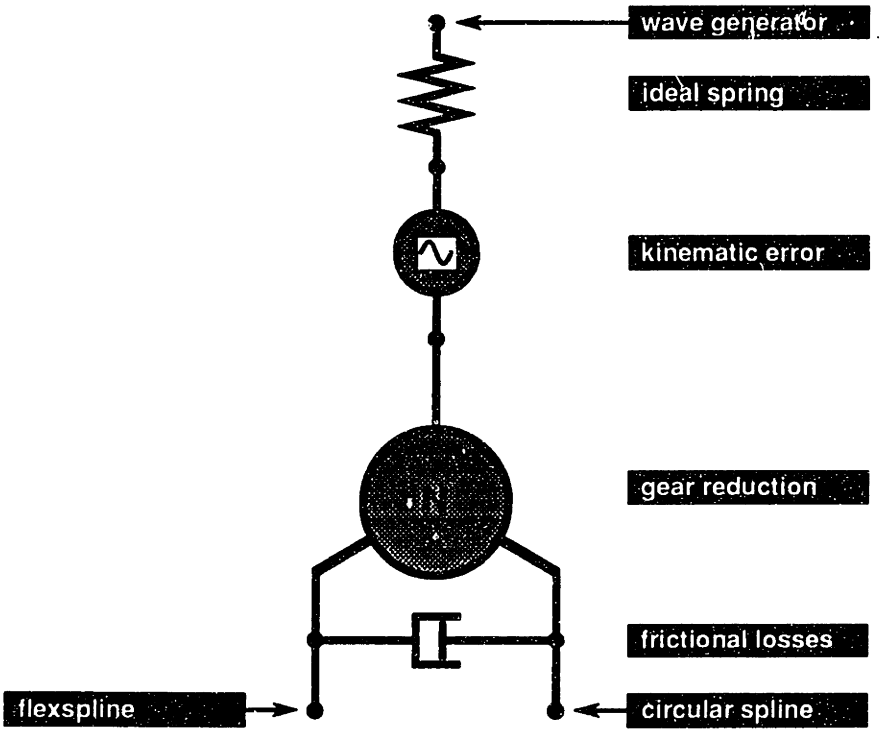

Figure 3.19: Harmonic-drive model 4

can be reduced with little penalty on model accuracy by combining these two components into a single function.

As discussed in section 2.3.2.4 of this document, a separate cyclic-torque disturbance mechanism exists in harmonic-drives which is independent of torque fluctuations caused by kinematic error. This phenomenon is caused by radial loads exerted by the flexspline on the wave-generator which tend to orient the wave-generator along a preferred axis of alignment. Since this input diametral torque-variation can be observed when the flexspline is not assembled into the circular spline, it has no relationship to the kinematic inaccuracies in gear-tooth meshing. In order to represent this phenomenon, a cyclic input torque acting at the wave-generator was included in the model to capture this spring-like behavior. However, as simulation results indicated, since the magnitude of this torque function was small compared to the kinematic-error disturbance, its affect on dynamic performance could only be observed at slow operating speeds if at all. Based on this conclusion, this cyclic input torque will be ignored in the model derived in this section, but should not be forgotten in future models which require enhanced accuracy.

3.6.2 Derivation of Dynamic Equations

Using the notation outlined in figure 3.20, the constitutive relationships for the transmission components that have been described previously can be summarized as follows. First, as dictated by the position, velocity and torque constraints specified in equations (3.15), (3.16), and (3.17) the ideal three-port gear-reduction element can be characterized by three relationships:

$$\theta_{n\_wg} = (N + 1)\,\theta_{n\_cs} - N\,\theta_{n\_fs}\,, \tag{3.28}$$

$$\omega_{n\_wg} = (N + 1)\,\omega_{n\_cs} - N\,\omega_{n\_fs}\,, \text{ and} \tag{3.29}$$

$$T_{n\_wg} = \frac{1}{(N + 1)}\,T_{n\_cs} = \frac{1}{N}\,T_{n\_fs}\,. \tag{3.30}$$

Second, using the non-linear damping function developed in model 2, the constitutive relationship for the friction element in the model is

$$T_b = T_{b\_constant} + T_{b\_dynamic} + T_{b\_cyclic}\,, \tag{3.31}$$

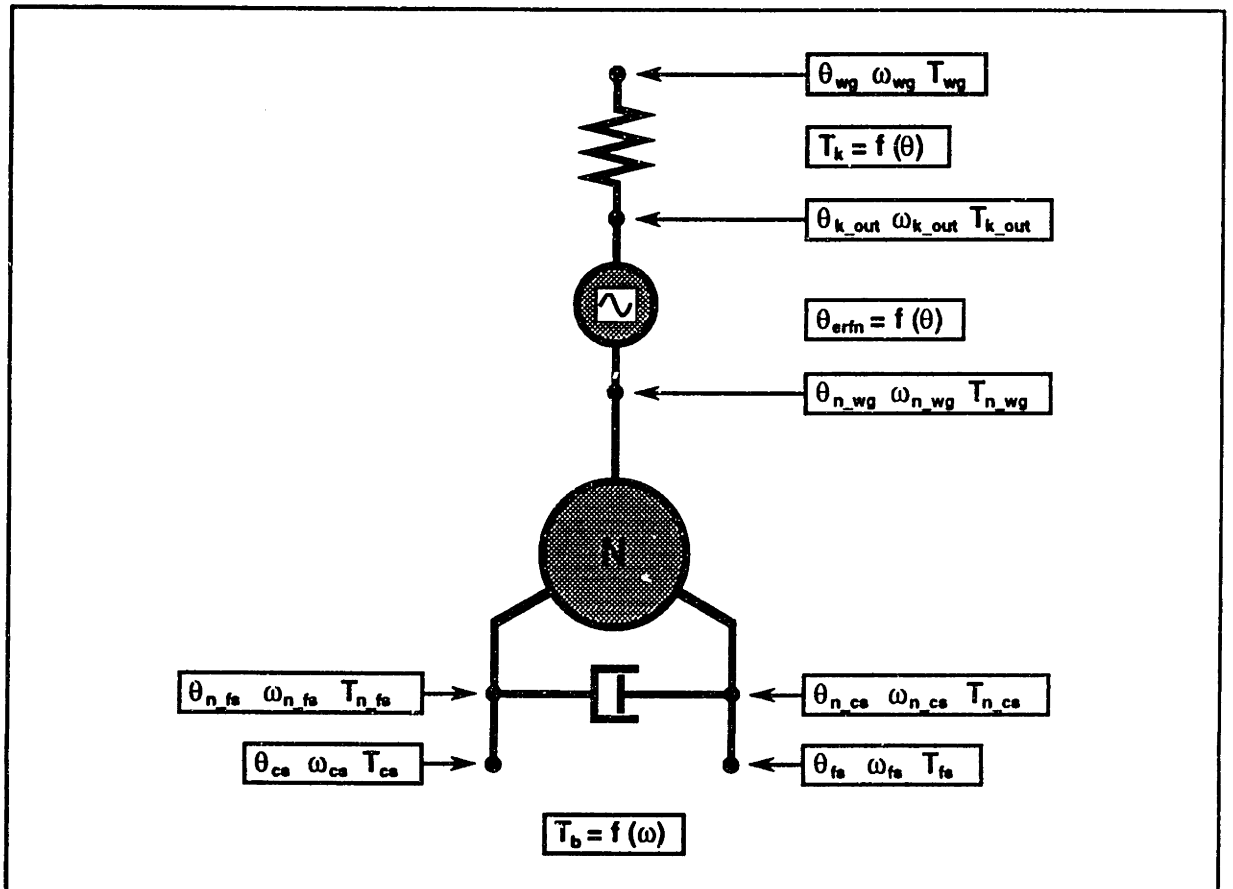

Figure 3.20: Notation for harmonic-drive model 4

where the three independent friction-torque functions are defined in equations (3.22), (3.23) and (3.24). Third, as discussed in the third model and defined in equation (3.26), the torque function provided by the stiffness element can be described by

$$T_k = k_1 (\theta_{wg} - \theta_{k\_out}) + k_2 (\theta_{wg} - \theta_{k\_out})^3 . \tag{3.32}$$

Given these definitions for the gear-reduction, frictional, and stiffness properties of the transmission, the constitutive constraints in the model will be complete once the torque and rotation behavior of the kinematic-error element is characterized.

As observed in experimental measurements, kinematic position-error signatures in harmonic drives can occur at many different frequencies. However, as observed in dynamic response data and verified by model performance, the only frequencies which influenced the dynamic behavior of the three different harmonic-drive systems occurred at one, two, and four cycles every wave-generator revolution. The reason for this is twofold: (1) the magnitude of kinematic error at other frequencies was smaller than these primary error components, and (2) other frequencies were either too high or too low to excite system resonance for the observed range of harmonic-drive operating velocities. For other systems which operate at slower velocities and have lower natural frequencies, for example, kinematic error at higher harmonics may need to be included. Based on this understanding, the representation chosen to describe the position error in the harmonic-drive transmission is a harmonic series of the three error components:

$$\theta_{erfn} = A_1 \sin (\theta_{wg} + \phi_1) + A_2 \sin (2\theta_{wg} + \phi_2) + A_3 \sin (4\theta_{wg} + \phi_3) . \tag{3.33}$$

Notice that, in this equation, each term is a sinusoidal function of the wave-generator rotation, θ_{wg}, with a specific amplitude, A_i, and phase, ϕ_i, describing the magnitude and relative orientation of each error component. Since these error components result from gear error on the flexspline and circular spline, a strictly accurate representation would have these functions vary with harmonics of the gear-tooth meshing frequencies. For example, in joint configuration 1 where the flexspline is attached to ground, every rotation of the wave-generator propagates the tooth-engagement zone completely around the flexspline circumference but fails to reach two teeth on the circular spline. Consequently, the frequency of the flexspline gear-tooth error components correspond exactly with the rotational frequency of the wave-generator while the frequency of the circular-spline gear-error components vary with the difference between the wave-generator and circular spline

rotation. However, since the input rotation is much larger that the output rotation in the transmission, this distinction can be neglected and the aggregate kinematic error can be varied as a function of the wave-generator rotation alone. In models which desire to capture the kinematic behavior of the harmonic drive to a higher level of detail, this clarification may be important.

Given this representation for the position error in harmonic-drives, the constitutive relationships for the kinematic-error element in figure 3.20 can be defined. First, using the error-function, θ_{erfn}, given in equation (3.33) the position constraint on this element can be specified as

$$\theta_{n\_wg} = \theta_{k\_out} + N\,\theta_{erfn} . \tag{3.34}$$

Since the magnitude of the error function is measured in terms of degrees of output rotation, it must be scaled by the transmission gear-ratio. The velocity constraint on this element can be defined by taking the derivative of the position constraint:

$$\omega_{n\_wg} = \omega_{k\_out} + N \frac{d}{dt}\theta_{erfn} , \tag{3.35}$$

where, given the relationship in (3.33) the derivative of the error function can be defined as

$$\frac{d}{dt}\theta_{erfn} = \omega_{wg} A_1 \cos(\theta_{wg} + \phi_1) + 2\,\omega_{wg} A_2 \cos(2\theta_{wg} + \phi_2) + 4\,\omega_{wg} A_3 \cos(4\theta_{wg} + \phi_3) , \text{ or} \tag{3.36}$$

$$\frac{d}{dt}\theta_{erfn} = \omega_{wg}\,\omega_{erfn} , \text{ where} \tag{3.37}$$

$$\omega_{erfn} = A_1 \cos(\theta_{wg} + \phi_1) + 2 A_2 \cos(2\theta_{wg} + \phi_2) + 4 A_3 \cos(4\theta_{wg} + \phi_3) . \tag{3.38}$$

Using this definition, the velocity constraint in equation (3.35) can now be rewritten as

$$\omega_{n\_wg} = \omega_{k\_out} + N\,\omega_{wg}\,\omega_{erfn} . \tag{3.39}$$

By applying the law of power conservation, this velocity constraint can be used to derive the torque constraint across the position-error element. First, the power at the input port of the element must always equal the power at the output:

$$P_{in} = P_{out} , \text{ or} \tag{3.40}$$

$$T_{k\_out}\,\omega_{k\_out} = T_{n\_wg}\,\omega_{n\_wg} . \tag{3.41}$$

By substituting the velocity constraint in (3.39) into this equation, the torque constraint becomes

$$T_{k\_out}\,\omega_{k\_out} = T_{n\_wg}\,(\omega_{k\_out} + N\,\omega_{wg}\,\omega_{erfn})\,. \tag{3.42}$$

Since the velocity variations across the spring will be small compared to average velocity values, ω_{k_out} can be assumed to be identical to ω_{wg} and the torque relationship reduces to:

$$T_{k\_out} = T_{n\_wg}\,(1 + N\,\omega_{erfn})\,. \tag{3.43}$$

Therefore, using this relationship and the equation for ω_{erfn} in (3.38) the torque constraint required to ensure power conservation across the kinematic-error element is complete.

Having developed the position, velocity, and torque constraints for the position error in the model, the constitutive relationships governing model performance are complete, and the equations of motion can be finished by specifying the remaining kinematic and torque-balance relationships. Specifically, as seen in equations (3.18) and (3.19), a torque-balance across the output ports of the harmonic-drive yields the relationships

$$T_{fs} = T_{n\_fs} - T_b\,, \text{ and} \tag{3.44}$$

$$T_{cs} = T_{n\_cs} - T_b\,. \tag{3.45}$$

Also, by performing a similar force balance across the spring on the input of the transmission the following relationship results:

$$T_{wg} = T_k = T_{k\_out}\,. \tag{3.46}$$

Lastly, by specifying the kinematic constraints at the output ports of the harmonic-drive, namely

$$\theta_{n\_cs} = \theta_{cs}\,, \text{ and} \tag{3.47}$$

$$\theta_{n\_fs} = \theta_{fs}\,, \tag{3.48}$$

the equations of motion are complete. Therefore, using the equations presented in this section, the positions and velocities at the three harmonic-drive ports can be directly related to the torques across the harmonic-drive.

3.6.3 Calculation of Input Parameters

In order to simulate dynamic performance using the equations for model 4, estimates need to be made for the values of the friction, stiffness and kinematic error in the harmonic-drives. Using the experimental friction data provided in section 2.5 of this document, the constant, dynamic, and cyclic friction values required by equation (3.31) were easily determined. Since these values were extracted directly from dynamic response observations, they provided accurate and reliable results in the dynamic model.

Estimating the values for the non-linear stiffness element in model 4 proved to be more complex than capturing friction behavior. In particular, due to the precarious influence of friction on the static stiffness measurements outlined in section 2.3 of this document, the resulting stiffness values delivered poor dynamic performance when inserted into the model. As a more direct method of determining the dynamic stiffness properties of each transmission, the experimental dynamic-response measurements outlined in section 2.6 were used to identify the resonant frequencies of the three harmonic-drive systems. From this known frequency and the given inertia values, the linear component of the ideal stiffness element could be adjusted to match the observed resonance. Given this linear component, the cubic stiffness coefficient required by equation (3.32) was selected so that the static stiffness profile generated by the model most closely resembled the experimental static stiffness behavior. Figures 3.21, 3.22, and 3.23 illustrate the resulting stiffness profiles used in the three joint-models as compared to experimental data and catalog predictions. In each of these plots, it can be seen that the theoretical stiffness profiles show significant deviation for the static stiffness measurements. In particular, the hysteresis loss in each curve, as dictated by the constant friction component used in the model, $T_{b\_constant}$, while producing good dynamic response, is unreliable as a predictor for static hysteresis loss. Additionally, the shape of the theoretical stiffness profiles required to ensure good dynamic response in the three harmonic-drive models provides a poor estimate of the measured static-stiffness profiles. As this comparison illustrates, for all three joints, the experimental measurements typically yield static stiffness values that are higher than the actual dynamic stiffness in the drive. This discrepancy is not surprising since Coulomb-like friction in the transmission can increase the measured torque values during static stiffness measurement. To address this problem, a new model will be developed later which predicts these Coulomb-friction effects.

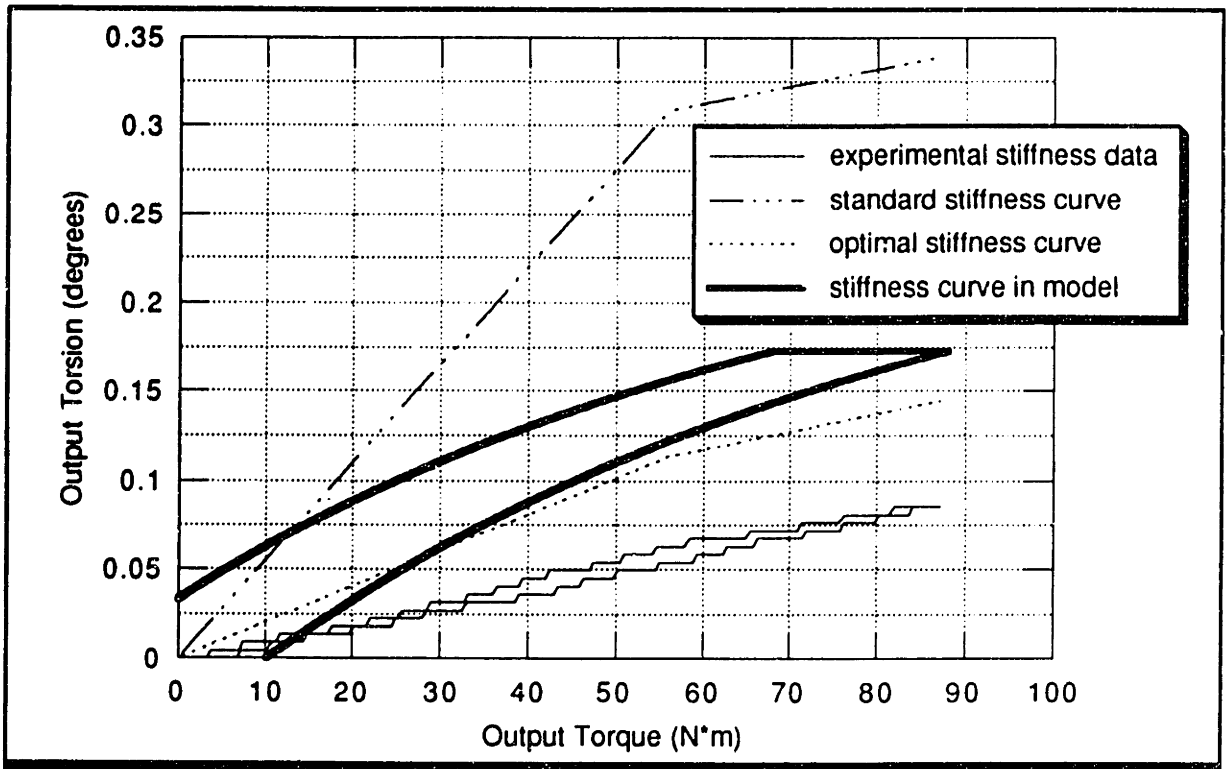

Figure 3.21: Joint 1 stiffness profile for harmonic-drive model 4

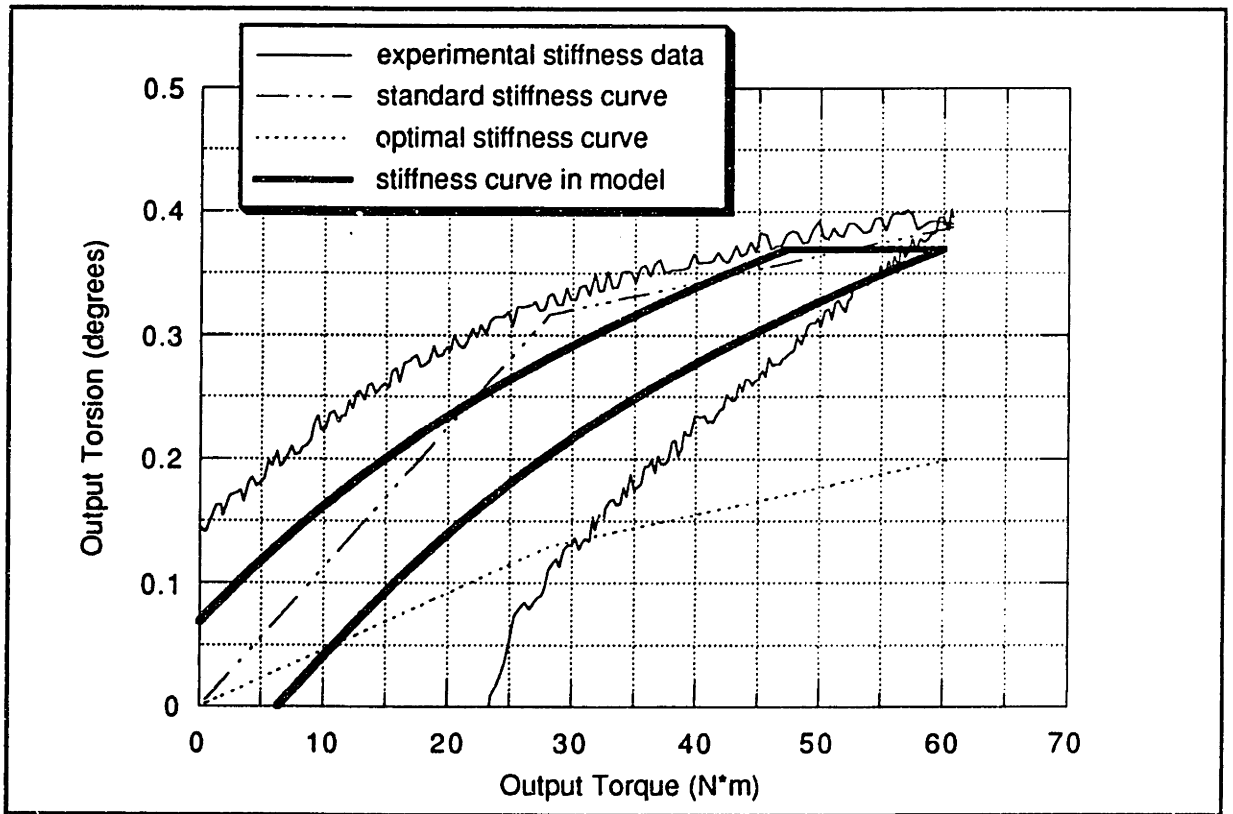

Figure 3.22: Joint 2 stiffness profile for harmonic-drive model 4

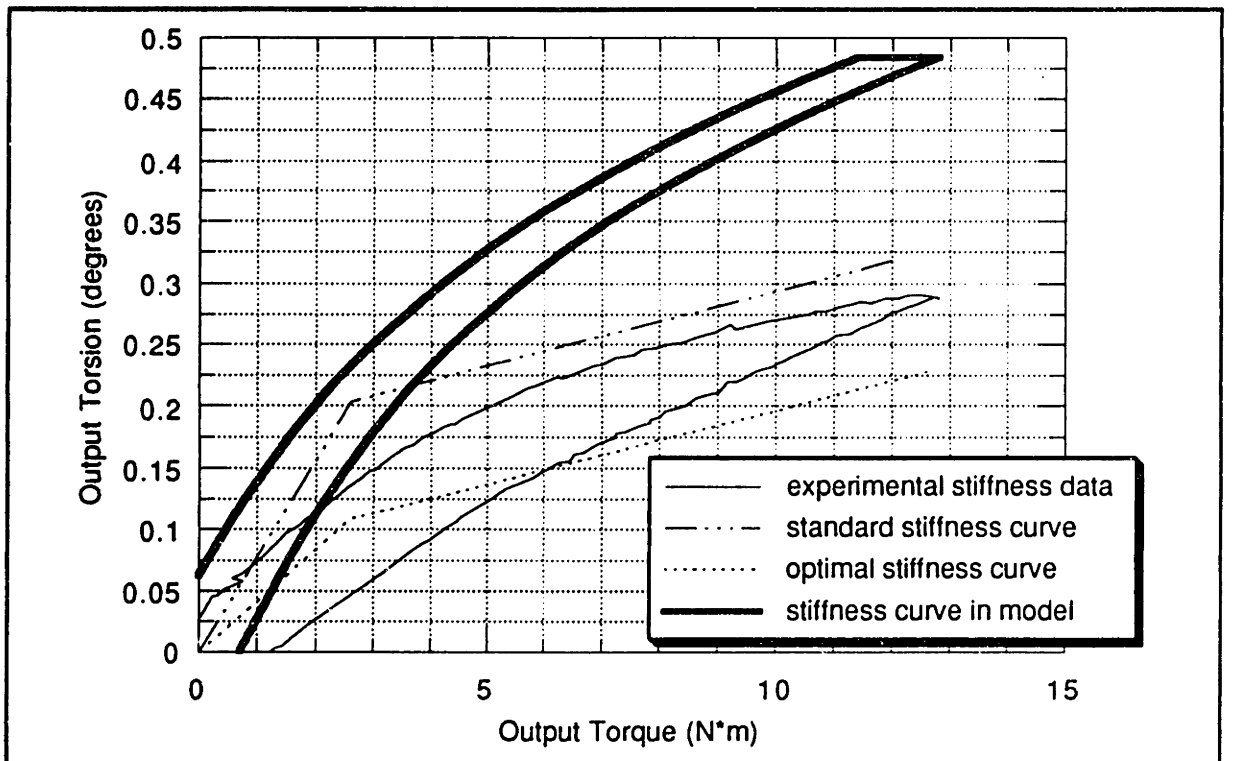

Figure 3.23: Joint 3 stiffness profile for harmonic-drive model 4

Given the friction and stiffness properties, the only remaining parameters that need to be determined are the magnitudes of the kinematic-error components in equation (3.33). The amplitudes of the three error components were determined by matching the amplitude of the dynamic position error predicted by the model to experimental values. In theory, if kinematic error on the testing apparatus could be measured under truly static conditions, direct estimates of these error components could be made. However, since data on the apparatus can only be collected for non-zero operating velocities, dynamic vibrations which induce transmission compliance contaminate the kinematic-error data. As presented in section 2.2 of this document, by operating the harmonic-drives at slow velocities where resonance vibration was minimal, measurements were made of the kinematic error in the three harmonic drives. In table 3.4, these experimental estimates are compared to the error values which provided optimal dynamic performance in the theoretical model. By comparing these results, it can be seen that, in most cases, values near the experimental measurements provided accurate dynamic response simulations, but, in a few instances, differences between experimental and theoretical values could deviate by up to a factor of two. From this discrepancy, two possible conclusions can be drawn: (1) slow operating velocities can significantly influence the magnitude of the position-error measured in the experimental apparatus, and (2) the model developed in this section does not fully capture

Table 3.4: Kinematic-error components in model 4 vs. measured values

	A_1 (output °)	A_2 (output °)	A_3 (output °)
Joint 1: theoretical	0.000	0.023	0.008
Joint 1: experimental	0.001	0.013	0.007
Joint 2: theoretical	0.001	0.015	0.006
Joint 2: experimental	0.001	0.008	0.004
Joint 3: theoretical	0.005	0.010	0.005
Joint 3: experimental	0.007	0.013	0.007

the influence of kinematic error on dynamic vibrations in the transmission. Since additional dynamic simulations with the theoretical model illustrated that dynamic vibrations could cause significant amplification of transmission position error at small operating velocities, it is likely that the first of these two conclusions is most responsible for the difference between experimental and theoretical parameters.

3.6.4 Evaluation of Simulated Results

The harmonic-drive model developed in this section was inserted into the overall system models for the two joint configurations and dynamic step-response simulations were then performed to replicate the experimental results. Using the experimental parameters for friction, stiffness, and kinematic error discussed previously, time-response data was collected over a range of motor-current steps for the three harmonic-drive testing-station models. These simulated results are presented in appendix E in the identical format used for the experimental time-response results of appendix D. In particular, graphs are shown which illustrate the position, velocity, and torque response for the observed range of harmonic-drive operating behavior. Table 3.5 is reproduced from a similar index in appendix E and summarizes the figure numbers for all of the simulated dynamic-response plots. By directly comparing these plots to the experimental results in appendix D, the capacity of the dynamic model to predict actual harmonic-drive behavior can be evaluated.

Based on how accurately the theoretical predictions in appendix E compare to the experimental results in appendix D, the benefits of this model are summarized below:

[1] Position, velocity and torque response in the model shows good agreement to actual data at operating speeds removed from regions of resonant behavior.

Table 3.5: Summary of simulated time-response plots in appendix E			
	Joint 1	Joint 2	Joint 3
Input Position	E.1.1	E.2.1	E.3.1
Input Velocity	E.1.2	E.2.2	E.3.2
Input Current	E.1.3	E.2.3	E.3.3
Output Position	E.1.4	E.2.4	E.3.4
Output Velocity - view 1	E.1.5	E.2.5	E.3.5
Output Velocity - view 2	E.1.6	E.2.6	E.3.6
Output Torque	E.1.7	E.2.7	E.3.7
Dynamic Position Error	E.1.8	E.2.8	E.3.8

[2] System resonances occur at the same operating velocities and consequently display the same vibration frequencies as experimental results.

[3] Amplitudes of input and output velocity fluctuation near resonance are relatively close to the experimentally observed amplitudes.

Conversely, by noting the differences between predicted and actual behavior, the limitations of this model can also be observed:

[1] At current-steps which result in velocities that excite system resonance, model predictions of operating velocity are typically much higher than observed in the experimental results.

[2] The model also fails to capture the sudden velocity-jump behavior that occurs when the system breaks through a resonant region.

[3] Amplitude of output torque fluctuation near resonance, especially on joints 1 and 3, is somewhat lower than the experimental torque-fluctuation amplitude.

These limitations on the accuracy of theoretical predictions lend insight into possible areas for model improvement. First, since the predicted velocities near system resonance are much higher that the observed velocities, it is clear that this model fails to capture the enhanced frictional dissipation which appears due to resonant vibration. As discussed in light of experimental results, this dissipation probably results from a Coulomb-like frictional torque which increases with the amplitude of torque fluctuations in the

transmission. Since, in the three drives tested, the resonance phenomenon dominates transmission behavior in a wide portion of the observed operating range, an accurate harmonic-drive model cannot ignore these resonance losses. As a second consequence of this resonance-dissipation absence, the velocity jump that occurs in experimental response when resonance vibrations cease does not appear in the theoretical response. Consequently, any improved representation which is able to replicate friction loss at resonance is likely to show this unusual velocity behavior as well. Furthermore, since a friction model at resonance is likely to supplement dynamic torque fluctuations with variations in frictional torque, the low torque-amplitudes observed on the joints 1 and 3 in this model may also improve. As a final note, the experimental current response on all three joints displays electrical noise which is not reproduced in the current response of the model. Since this noise had no effect on the dynamic performance of the actual system, it was completely ignored in the simulation.

3.6.5 Model 4 Conclusions

The simulated results of the harmonic-drive model presented in this section demonstrate that, by including the combined effect of friction, compliance, and kinematic error in the model, performance can be significantly improved over models that do not acknowledge all three of these transmission properties. In particular, the velocity and torque fluctuations which appear in the experimental response can now be reproduced due to the kinematic error in the model. Additionally, due to the interaction of the kinematic error and compliance, system resonances appear in the theoretical predictions that match the experimental results. Unfortunately, since the model fails to capture frictional losses which occur at resonance, simulation accuracy decays at velocities which excite resonance vibration. Based on these conclusions, it seems likely that this model may be useful for predicting performance of dynamic systems that typically operate far from regions of resonant behavior. Since the kinematic-error effects are featured in this model, static positioning applications which require high accuracy may also benefit from predictions delivered by this model. However, for any application which requires accurate predictions of transmission behavior over a wide operating range, an improved harmonic-drive representation which can predict frictional losses at resonance is required.

Another conclusion which can be made from this model is that reliable measurements of transmission stiffness are difficult to obtain. In particular, when stiffness

curves collected from static measurements were used in the model, the resulting dynamic response held few similarities to actual behavior. As explained above, this discrepancy can be blamed on the inaccuracy of static stiffness measurements due to friction in the harmonic-drive. From the substantial differences between the theoretical and actual static stiffness profiles discussed previously, it can be concluded that interaction between stiffness and friction in the actual system is far more complex than the model recognizes. Based on this result, an improved harmonic-drive model, in addition to improving predictions at dynamic resonance, should also better represent the static stiffness behavior in the transmission. In order to improve model performance, dynamic response data had to be used to isolate the natural frequency of the system and derive the corresponding transmission flexibility. Although this new stiffness data provided good dynamic results, slight changes in its value could cause significant shifts in the operating velocities which excited resonant behavior. This unfortunate result demonstrates that, unless an extremely accurate model is developed which can reliably predict transmission stiffness from static measurements, it is likely that static stiffness data will never be useful for accurate predictions of harmonic-drive dynamic behavior.

Perhaps the most important conclusion that can be drawn from the results in this section is that accurate harmonic-drive modeling is a very complex task. The scope of the model presented in this section represents the maximum useful complexity that can be included in a model that ignores more complex geometric interaction of the harmonic-drive components. Since the resulting model performance was completely unreliable for large portions of the harmonic-drive operating ranges, the forecast is gloomy for designers who wish to make accurate predictions using a simple transmission representation. In a final attempt to create a model that can make accurate predictions while still containing a manageable amount of complexity, a representation will be developed below which incorporates the three transmission properties used in model 4 into a simplified representation of harmonic-drive gear-tooth interaction.

3.7 Harmonic-Drive Model 5: Transmission Including Gear-Tooth Geometry

An accurate representation of harmonic-drive behavior cannot exist without incorporating frictional losses, transmission compliance, and kinematic error. However, as model 4 illustrated, these three properties are not the only factors which influence harmonic-drive behavior. Additionally, a mechanism which dissipates energy during system resonance and influences static friction measurements must also be captured. To accomplish this task, I have transplanted the friction, compliance, and kinematic error effects developed in the previous models into a new framework which imitates the gear-tooth meshing action inside the harmonic drive. As discussed in this section, the increase in complexity introduced by this new representation is rewarded by a substantial increase in model performance.

3.7.1 Description of Model 5

In order to develop a model that mimics gear-tooth meshing action in the harmonic drive, a more intimate understanding of harmonic drive operation is required. Figure 3.24 depicts close-ups of the gear tooth meshing geometry for a section of a harmonic-drive. For the case where the flexspline is fixed to ground, clockwise rotation of the wave-generator will cause the flexspline gear teeth to be pushed into the circular spline gear-teeth along the major axis of the wave-generator. Since the flexspline has two fewer teeth than the circular spline, the mating gear teeth will be slightly misaligned before meshing. Consequently, as the flexspline teeth are pushed radially into the circular spline teeth, the leading, or right-hand-side, face of the flexspline teeth will slide along the trailing, or left-hand-side, face of the circular-spline teeth during engagement. The forces generated as the teeth slide against each other will cause the gear teeth in the meshing zone to align and, consequently, push the circular spline in the clockwise direction. For the case where the circular spline is fixed to ground, clockwise rotation of the wave-generator still pushes the flexspline teeth into the circular-spline teeth along its major axis. However, since the circular spline cannot move, the forces generated as the flexspline teeth slide along the circular spline teeth result in counterclockwise rotation of the flexspline.

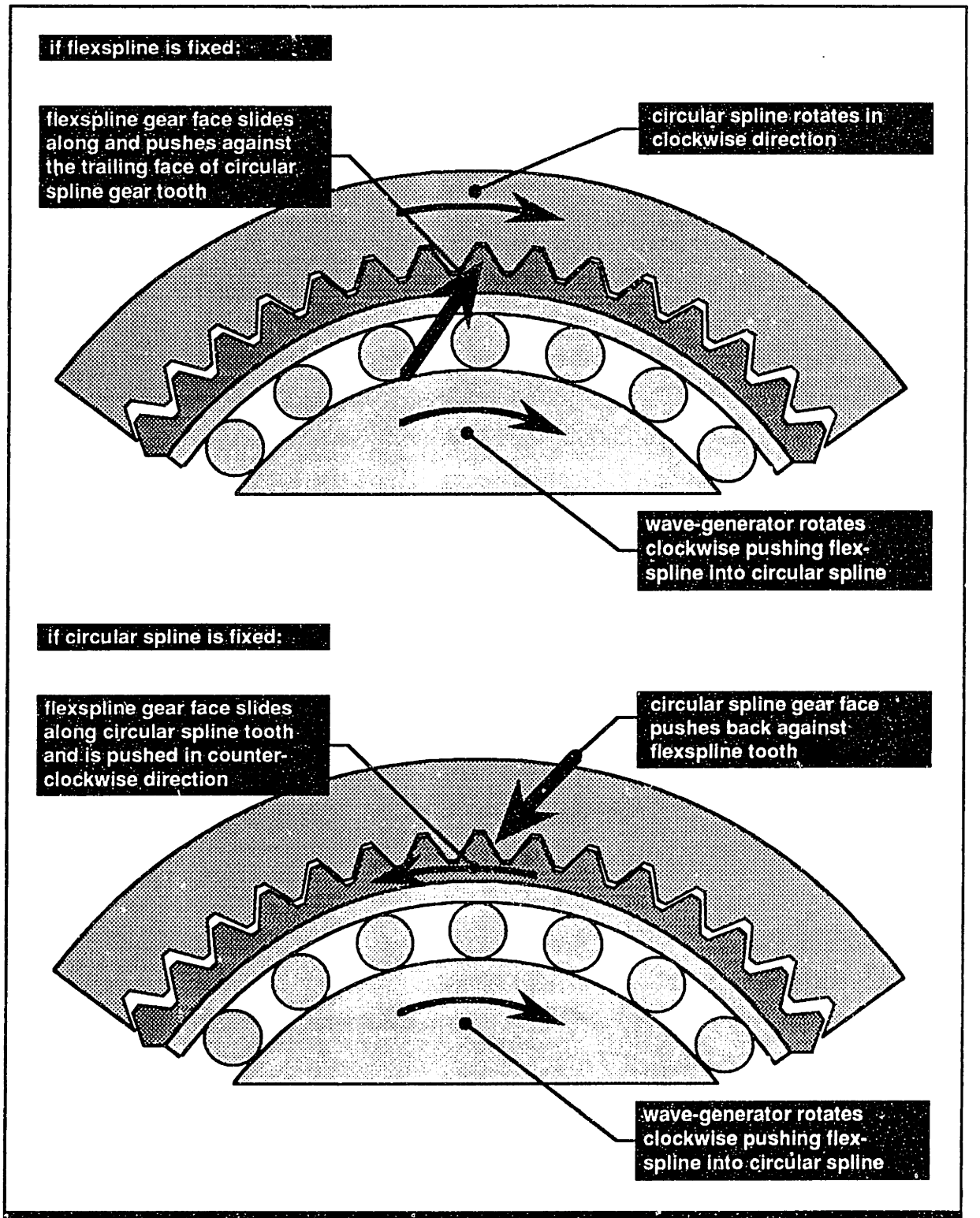

Figure 3.24: Close-up of harmonic-drive gear-tooth action

Using this understanding of gear-tooth meshing action, assumptions can be made which reduce the complexity required in a harmonic-drive model which mimics this behavior. First, by realizing that during normal harmonic-drive operation, anywhere from

ten to greater than fifty teeth can be in contact between the circular spline and flexspline, the effect of individual gear teeth can be ignored in a dynamic model. This assumption was confirmed by the kinematic error results in section 2.2.2.1.4 which discovered that the error of individual teeth was not detectable. Consequently, in order to capture the aggregate effects of gear-tooth meshing, a model which describes sliding on a single continuous gear-tooth surface should suffice. Second, since the gear-teeth are very small compared to the pitch-diameter of the transmission, the localized motion of the gear-teeth during meshing shows little trace of the overall rotational motion. Based on this assumption, a model which describes this gear-tooth action can be simplified by using translational rather than rotational motion. Using these two assumptions, a dynamic model that captures the aggregate effect of the gear-tooth meshing mechanism is illustrated in figure 3.25.

The simplified gear-tooth meshing model in figure 3.25 consists of a series of massless inclined planes which embody the wave-generator and gear-tooth geometry of the

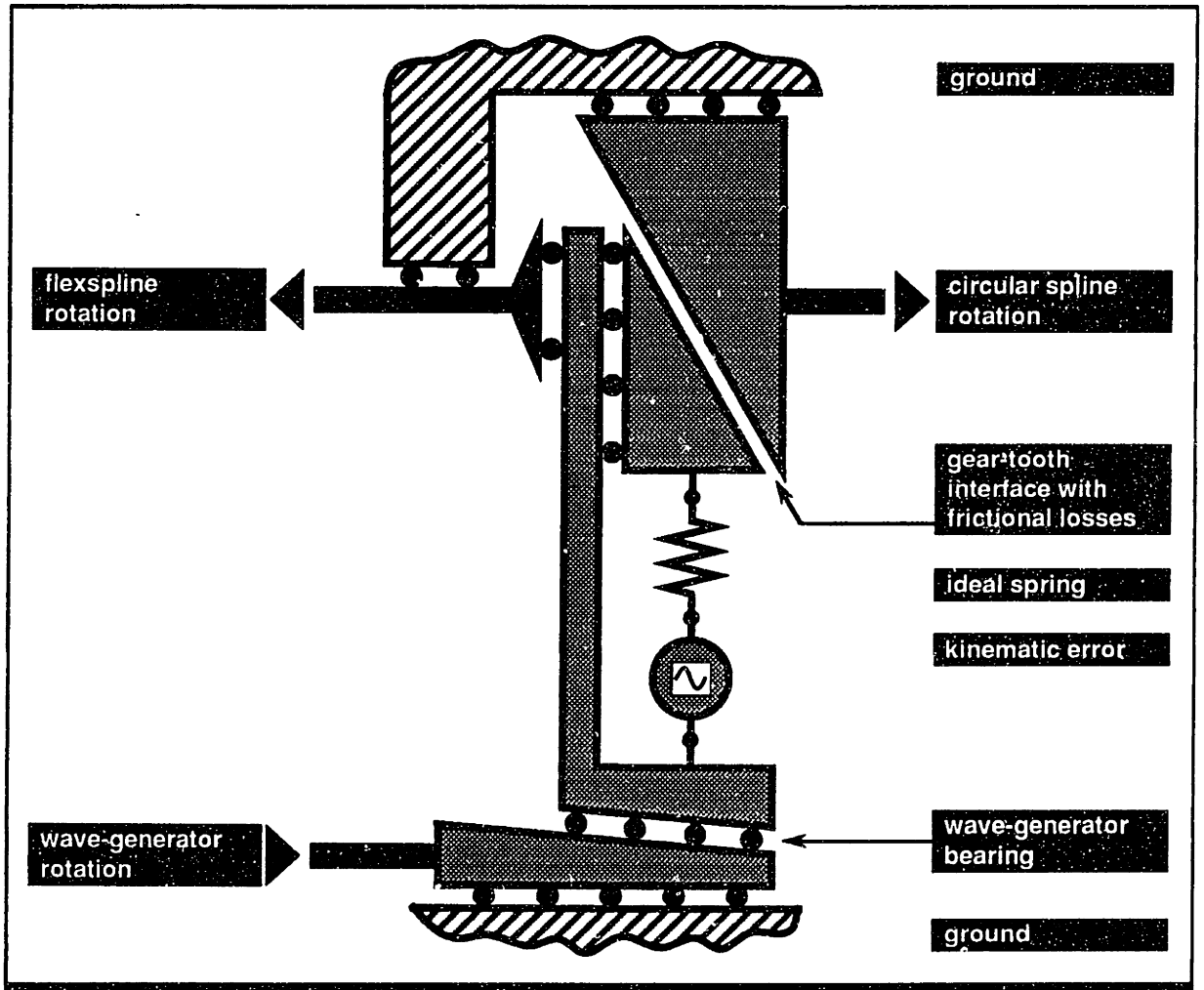

Figure 3.25: Schematic of harmonic-drive model with gear-tooth geometry

actual transmission. These planes are confined to horizontal and vertical motion by a series of ideal rollers and rigid surfaces. In particular, note that the output ports of the wave-generator, flexspline, and circular spline are all restricted solely to horizontal motion so they can be interfaced easily with an overall system model. Although this cannot be illustrated in the schematic, by assuming that all of the surfaces which constrain motion are infinitely long, this model can be used to describe all ranges of transmission operation.

By comparing the actual transmission in figure 3.24 to the model in 3.25, several parallels can be drawn between actual and modeled behavior. First, horizontal motion in the model corresponds directly to rotation of the harmonic-drive components and vertical motion in the model corresponds to radial movement in the harmonic drive. Second, the low-angle plane and inclined bearing surface on the bottom of the model schematic correspond to the wave-generator in the actual drive. The mechanical advantage and kinematic properties of the wave-generator eccentricity are captured by the low-angle of this wedge. Since the wave-generator motion pushes the flexspline gear teeth into the circular spline, a third parallel can be drawn between the two central wedges and the flexspline in the actual system. Similarly, the wedge at the top of the model schematic which mates with the flexspline wedge corresponds directly to the circular-spline in the actual system. So that this model effectively replicates the gear-tooth rubbing action in the actual transmission, the angle of both the flexspline and circular spline mating wedges is identical to the traditional harmonic-drive gear-tooth angle of thirty degrees. The angle of the wave-generator wedge at the bottom of the schematic can be calculated from the gear-ratio of the particular harmonic drive as discussed later.

A better understanding of the likeness between the model in figure 3.25 and the actual transmission can be gained by considering the case where the flexspline is fixed to ground. Under this condition, as discussed previously, clockwise rotation of the wave-generator in an actual transmission produces clockwise rotation of the circular spline. This relative motion results since the wave-generator pushes the flexspline gear teeth into the circular spline gear teeth, and the forces at the gear-tooth interface drive the circular spline in the clockwise direction. Identical behavior can be seen in the schematic in figure 3.25 if the flexspline port is fixed to ground. Specifically, the clockwise rotation of the wave-generator can be mimicked by sliding the wave-generator wedge in the model horizontally to the right. Due to this motion, the two flexspline wedges in the model, which are not allowed to move horizontally, slide vertically upward and push against the circular-spline wedge. This vertical motion directly parallels the engagement of the gear teeth that occurs in the actual transmission. Continuing the analogy, the vertical motion of the flexspline

wedges in the model causes the circular-spline wedge to move horizontally to the right. Again, this horizontal motion mimics the clockwise rotation that results in the circular spline of the actual transmission. By fixing the circular-spline port in this model to ground, a similar exercise can be performed to relate model behavior to the meshing action in an actual harmonic drive under a different operating configuration.

Given this geometric framework which describes the motion and force constraints present in harmonic drives, remaining dynamic effects can be incorporated by introducing friction, compliance, and kinematic-error properties. Specifically, since it is likely that most frictional loss in harmonic-drives is generated from rubbing at the gear-tooth interface, all friction in this model is localized at the contact surface between the flexspline and circular spline wedges. However, unlike the previous model, Coulomb friction properties are also included at this contact surface to provide a mechanism for demonstrating increased losses at system resonance. Compliant behavior, on the other hand, is not as easy to pinpoint as friction. In particular, past research has indicated that, in addition to deflection in both the flexspline and circular spline gear-teeth, significant deflection may also occur radially in the wave-generator as well. Since no information was available to supervise the distribution of the overall transmission compliance into these individual locations, a single stiffness element was included at the flexspline for simplicity. In order to maximize the influence of friction at the gear-tooth interface on static stiffness measurements in the model, this spring was oriented vertically rather than horizontally. Lastly since kinematic error in harmonic drives is caused mainly by gear-tooth manufacturing errors on both the circular spline and flexspline, two separate error function should be included which vary the positions of the flexspline and circular-spline gear-tooth surfaces. However, since the combined effect of these two error elements can be closely approximated by a single error function, only one kinematic-error element is included in the model. For the sake of simplicity, this element is located at the flexspline. Also, since numerical problems can arise if the velocity at the input of this element becomes zero, the kinematic error is oriented vertically rather than horizontally . If future models require improved accuracy, this error function can be distributed into different locations in the model.

As illustrated in experimental dynamic-response results, such as figures D.1.7, D.2.7, and D.3.7 in Appendix D, torque variations in harmonic-drives typically fluctuate to large positive and negative values. From the model schematic in figure 3.25, it can be seen that, if the normal force at the gear-tooth contact surface becomes negative due to this alternating torque, the coulomb friction function at that surface becomes undefined. By

better understanding how the load is carried by the harmonic-drive gear-teeth during these torque oscillations, a new model can be developed to capture this behavior. In particular, as figure 3.26 illustrates, when the driving torque across the gear-teeth is positive, the load is carried by the gear-teeth surfaces which push the circular spline in the positive direction.

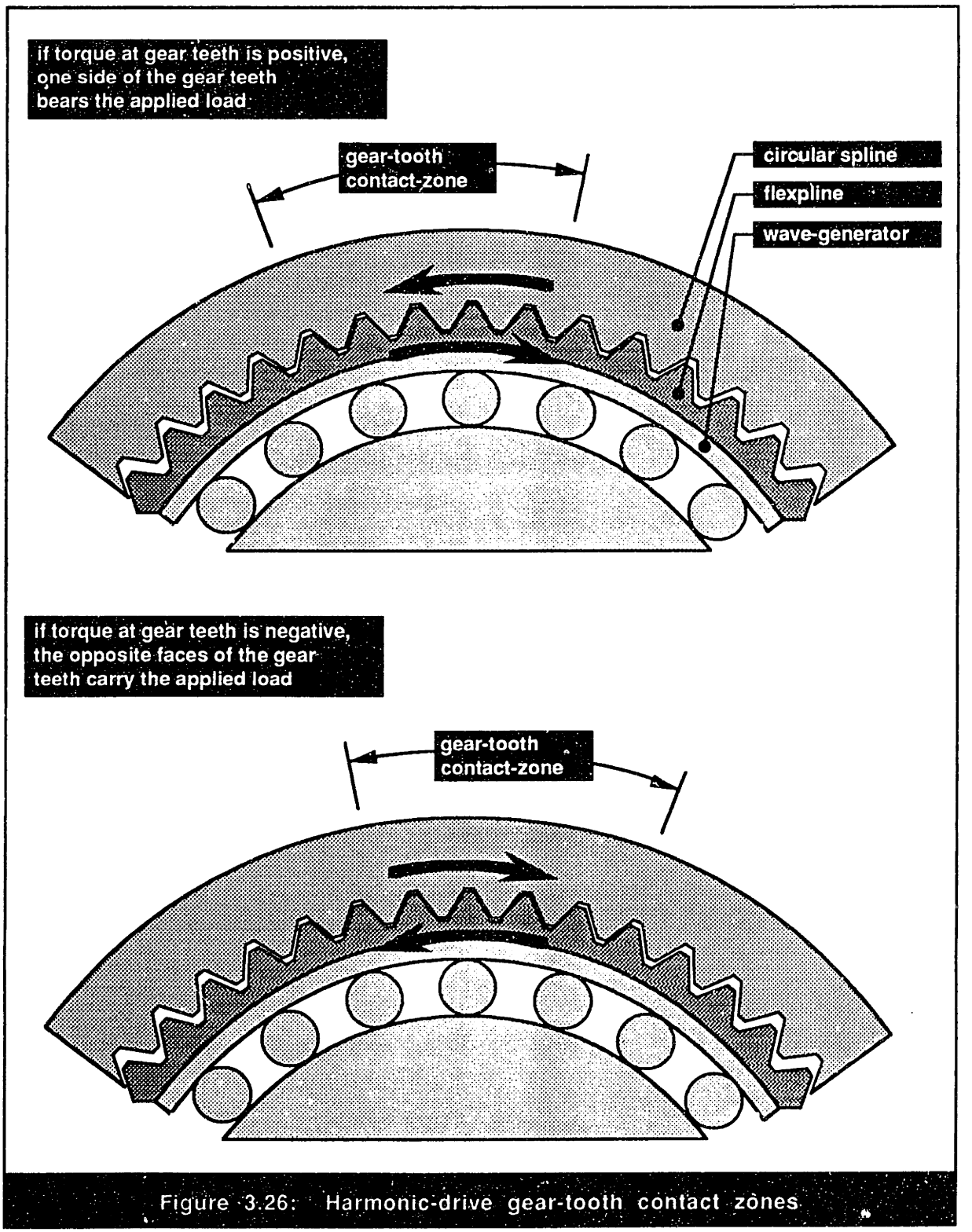

Figure 3.26: Harmonic-drive gear-tooth contact zones

However, when the driving torque becomes negative due to inertial vibrations, the transmission velocity is still in the same direction but the opposite face of the gear teeth must bear the resulting load. In order to capture this behavior in a dynamic model, the representation shown in figure 3.27 can be used whenever the normal force at the gear tooth interface becomes negative. Since this new model is essentially a mirror image of the previous one, the normal force at the gear-tooth interface becomes positive and resulting coulomb friction can be easily determined. Using this representation along with the previous one, an attempt was made to mimic both positive and negative gear-tooth loading in the harmonic-drive model by rapidly switching between models during simulation. Unfortunately, since the numerical simulation used to solve the equations of motion was not very tolerant of discontinuous changes in the dynamic equations, a solution could not be reached. Instead, the single representation in figure 3.25 was used exclusively, and whenever the normal force at the gear-tooth surface became negative, the coulomb friction

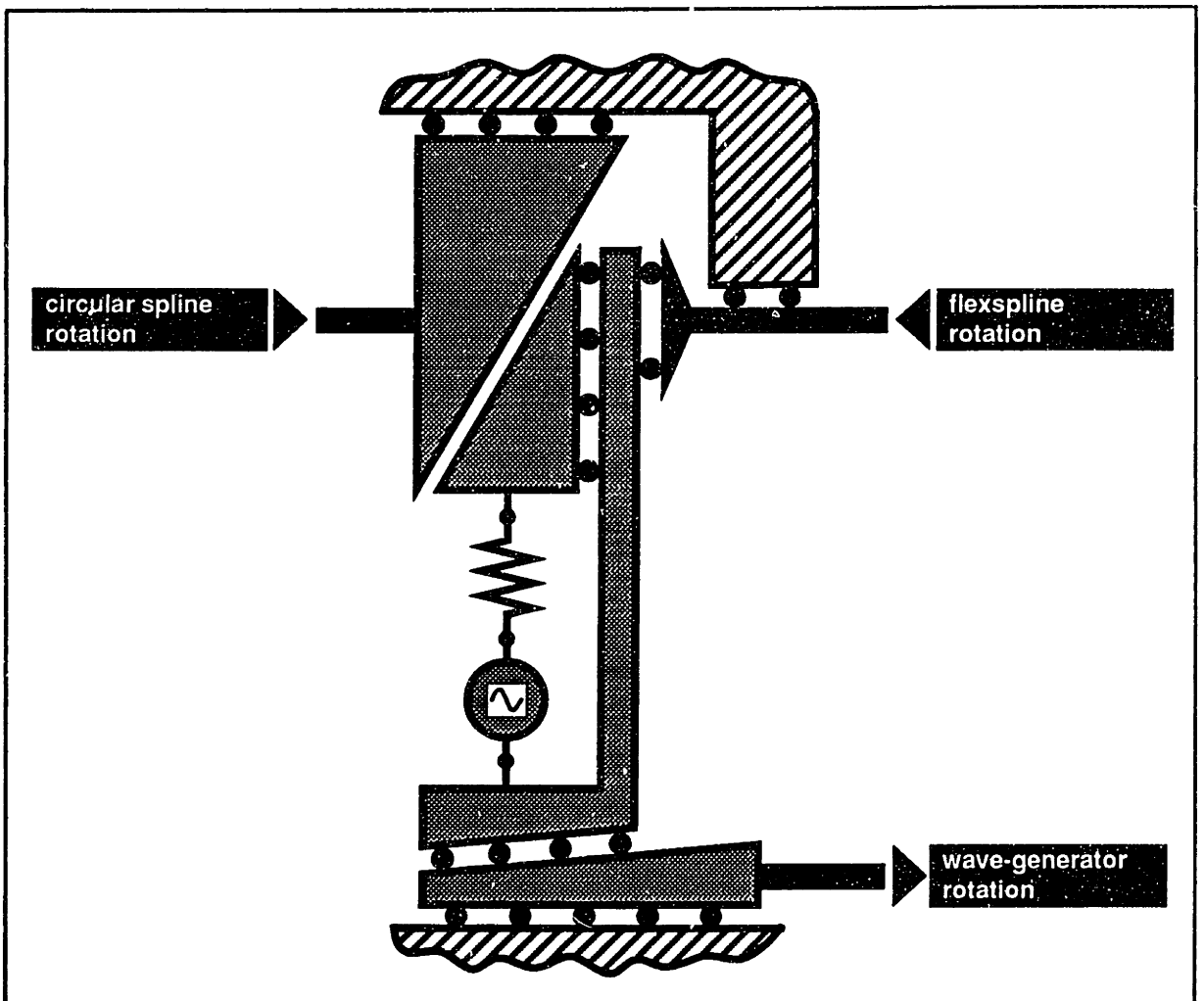

Figure 3.27: Revised transmission model for negative-torque loading

was set to zero. This inaccurate assumption most likely represents the main shortcoming of this model and identifies an important area for further improvement.

3.7.2 Derivation of Dynamic Equations

Before the derivation of the equations of motion for this system can begin, notation conventions must first be established. Specifically, the variable names for the positions and velocities and their corresponding sign conventions are illustrated in figure 3.28. As this figure illustrates, positions are defined by the symbol θ and velocities are represented by the symbol ω. Sign conventions for all of the kinematic variables in the model, except θ_{fs} and ω_{fs}, are defined to be positive in the direction they will travel when the wave-generator is moved in the positive direction. Similarly, torque conventions are illustrated in figure 3.29. For all of these variables the symbol T is used, and positive torque is defined in the direction it will act when a load is applied in the positive direction on the wave-generator while the flexspline and circular spine are kept stationary. As illustrated in both these figures, the geometric angles of both the wave-generator and the gear-teeth in the model are defined by the symbol α. These geometric angles should not be confused with the angular position coordinate, θ.

Given the variable names provided in these two figures, the geometric constraints in the model will be used to define the kinematic equations governing model motion. First, due to the inclined face of the wave-generator wedge, the horizontal motion of the wave-generator and flexspline can be directly related to the vertical motion of the flexspline base by the equations

$$\theta_{tooth\_base} = \tan \alpha_{wg} (\theta_{wg} - \theta_{fs}), \text{ and} \tag{3.49}$$

$$\omega_{tooth\_base} = \tan \alpha_{wg} (\omega_{wg} - \omega_{fs}). \tag{3.50}$$

Similarly, due to the gear-tooth angle, the circular-spline and flexspline horizontal motion can be used to determine the vertical motion of the flexspline tip:

$$\theta_{tooth\_tip} = \frac{1}{\tan \alpha_{tooth}} (\theta_{cs} - \theta_{fs}), \text{ and} \tag{3.51}$$

$$\omega_{tooth\_tip} = \frac{1}{\tan \alpha_{tooth}} (\omega_{cs} - \omega_{fs}). \tag{3.52}$$

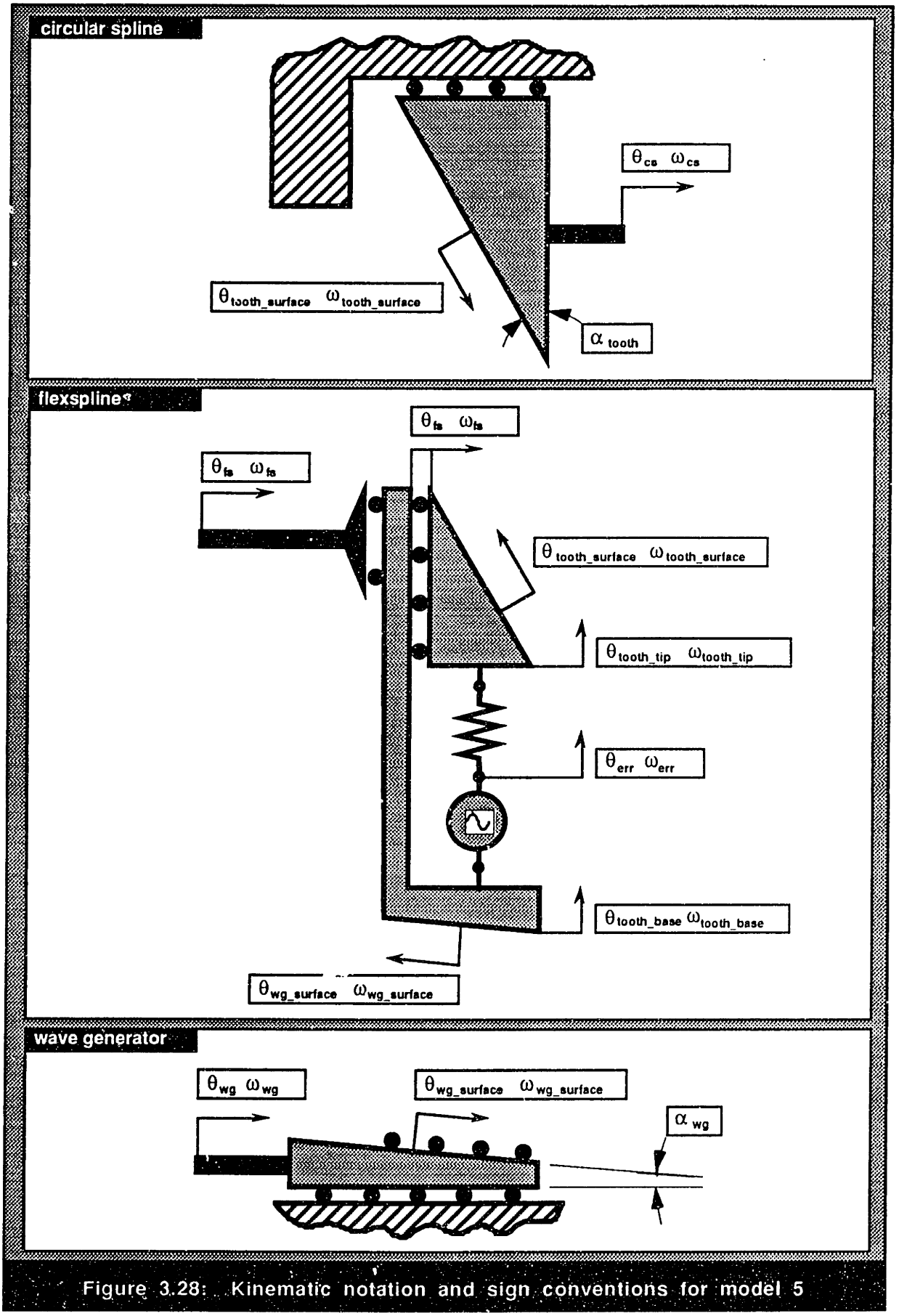

Figure 3.28: Kinematic notation and sign conventions for model 5

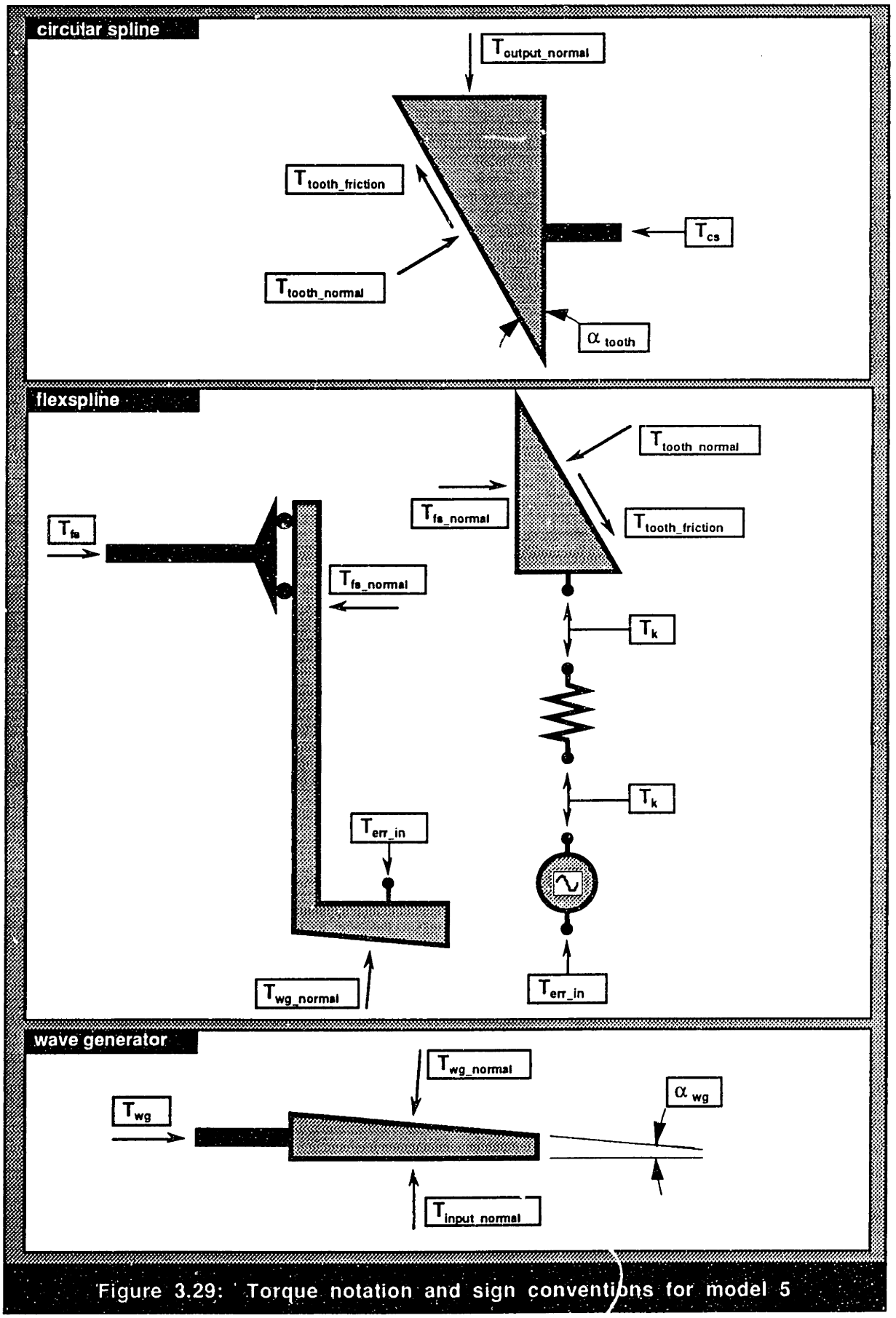

Figure 3.29: Torque notation and sign conventions for model 5

Using these equations and the geometry of the model, the equations specifying the motion at both the wave-generator surface and the gear-tooth surface can be derived:

$$\theta_{wg\_surface} = \cos \alpha_{wg}\, \theta_{wg} + \sin \alpha_{wg}\, \theta_{tooth\_base} - \cos \alpha_{wg}\, \theta_{fs}\,, \quad (3.53)$$

$$\omega_{wg\_surface} = \cos \alpha_{wg}\, \omega_{wg} + \sin \alpha_{wg}\, \omega_{tooth\_base} - \cos \alpha_{wg}\, \omega_{fs}\,, \quad (3.54)$$

$$\theta_{tooth\_surface} = \cos \alpha_{tooth}\, \theta_{tooth\_tip} + \sin \alpha_{tooth}\, \theta_{cs} - \sin \alpha_{tooth}\, \theta_{fs}\,, \text{ and} \quad (3.55)$$

$$\omega_{tooth\_surface} = \cos \alpha_{tooth}\, \omega_{tooth\_tip} + \sin \alpha_{tooth}\, \omega_{cs} - \sin \alpha_{tooth}\, \omega_{fs}\,. \quad (3.56)$$

Now that the kinematic relationships are complete, the angle of the wave-generator wedge required to reproduce the motion in the actual transmission can be found. Specifically, given the gear-tooth angle, α_{tooth}, and the catalog gear ratio, N, the wave-generator angle can be determined exactly from the equation:

$$\alpha_{wg} = \arctan\left(\frac{1}{(N+1)\tan \alpha_{tooth}}\right). \quad (3.57)$$

If these kinematic constraints are indeed accurate, they should produce the same relationship between the positions and velocities of the wave-generator, flexspline, and circular spline as observed in the actual system. As a confirmation of this fact, while ignoring kinematic error and compliance in the model, equations (3.49), (3.50), (3.51), (3.52), and (3.57) can be combined to reproduce the ideal three-port transmission equations presented in section 3.3. Based on this result, the position and velocity relationships presented above provide a complete and accurate description of the kinematic behavior of harmonic drives.

Now that the kinematics of the harmonic-drive model with gear-tooth geometry are better understood, the constitutive relationships which govern the behavior of the individual model elements will be derived. First, as seen in previous models, the friction at the gear-tooth interface is composed of (1) a velocity-independent, constant torque, (2) a velocity-dependent, damping torque, and (3) a cyclic torque function. However, as a new and important improvement to this model, a Coulomb friction function is also included at the gear tooth surface. The resulting aggregate friction function is

$$T_b = T_{b\_constant} + T_{b\_dynamic} + T_{b\_cyclic} + T_{b\_coulomb}\,, \quad (3.58)$$

where

$$T_{b\_constant} = b_{constant} , \tag{3.59}$$

$$T_{b\_dynamic} = b_1 \omega_{tooth\_surface} + b_2 (\omega_{tooth\_surface})^3 , \tag{3.60}$$

$$T_{b\_cyclic} = A_b \sin ((\theta_{cs} - \theta_{fs}) + \phi_b) , \text{ and} \tag{3.61}$$

$$T_{b\_coulomb} = \mu T_{tooth\_normal} . \tag{3.62}$$

In these equations, μ represents the Coulomb friction coefficient at the gear-tooth interface and the remaining parameters, as seen before, are defined in table 3.3.

Unlike this friction relationship which contains a new term for the Coulomb losses, the stiffness equation used in this model resembles closely the cubic relationship seen in previous models:

$$T_k = k_1 (\theta_{err} - \theta_{tooth\_tip}) + k_2 (\theta_{err} - \theta_{tooth\_tip})^3 . \tag{3.63}$$

Following the example set by model 4, the kinematic error function used in model 5 will be a harmonic series of three error components. However, slightly different than model 4, since the kinematic-error function is located on the flexspline, it should vary as a function of the flexspline gear-tooth meshing position rather than the wave-generator position. Considering that every tooth on the flexspline will mesh once when the wave-generator makes one complete revolution relative to the flexspline, the position which governs the kinematic-error function should be $\theta_{wg} - \theta_{fs}$. Adopting the syntax used for model 4 in equation (3.33), this kinematic error function becomes

$$\theta_{erfn} = A_1 \sin (\theta_{wg\_rel} + \phi_1) + A_2 \sin (2\theta_{wg\_rel} + \phi_2) + A_3 \sin (4\theta_{wg\_rel} + \phi_3) , \tag{3.64}$$

where

$$\theta_{wg\_rel} = \theta_{wg} - \theta_{fs} . \tag{3.65}$$

Similarly, the derivative of this function can also be defined as

$$\frac{d}{dt} \theta_{erfn} = \omega_{wg\_rel} \omega_{erfn} , \text{ where} \tag{3.66}$$

$$\omega_{erfn} = A_1 \cos(\theta_{wg\_rel} + \phi_1) + 2 A_2 \cos(2\theta_{wg\_rel} + \phi_2) + 4 A_3 \cos(4\theta_{wg\_rel} + \phi_3), \text{ and} \quad (3.67)$$

$$\omega_{wg\_rel} = \omega_{wg} - \omega_{fs}. \quad (3.68)$$

Note that, unlike previous models, since the magnitude of the kinematic-error function in model 5 does not translate directly to rotation of the flexspline or circular spline, the values of the position-error amplitudes, A_1, A_2, and A_3, must be adjusted as discussed later. Given the position-error function and its derivative, the position, velocity and torque constraints can be derived as done for model 4. Specifically, by definition, the position and velocity constraints across the kinematic-error element are

$$\theta_{err} = \theta_{tooth\_base} + \theta_{erfn}, \text{ and} \quad (3.69)$$

$$\omega_{err} = \omega_{tooth\_base} + \omega_{wg\_rel}\, \omega_{erfn}. \quad (3.70)$$

By requiring that power be conserved, the following equation can also be derived:

$$T_{err\_in}\, \omega_{tooth\_base} = T_k\, \omega_{err}. \quad (3.71)$$

Using the kinematic-error relationship in equation (3.70) and the geometric constraint in equation (3.50), this power relationship can be converted easily into the desired torque constraint on the kinematic error element:

$$T_{err\_in} = \left(1 + \frac{\omega_{erfn}}{\tan \alpha_{wg}}\right) T_k. \quad (3.72)$$

At last, with the torque, velocity, and position relationships for the kinematic error fully defined, the constitutive relationships required in the model are complete.

Having calculated both the kinematic and constitutive constraints on the model, the task that remains is to balance the forces across the elements in the transmission. This can be accomplished by summing the forces separately for the four different geometric shapes in the model. For the wedge representing the wave-generator, balancing the forces in the horizontal and vertical directions yields the equations

$$T_{wg} = T_{wg\_normal} \sin \alpha_{wg}, \text{ and} \quad (3.73)$$

$$T_{input\_normal} = T_{wg\_normal} \cos \alpha_{wg}. \quad (3.74)$$

Likewise, the equations for the flexspline base are

$$T_{fs} = T_{fs\_normal} - T_{wg\_normal} \sin \alpha_{wg} \text{ , and} \quad (3.75)$$

$$T_{err\_in} = T_{wg\_normal} \cos \alpha_{wg} \text{ ,} \quad (3.76)$$

and the equations for the flexspline tip are

$$T_{fs\_normal} = T_{tooth\_normal} \cos \alpha_{tooth} - T_{tooth\_friction} \sin \alpha_{tooth}, \text{ and} \quad (3.77)$$

$$T_k = T_{tooth\_normal} \sin \alpha_{tooth} + T_{tooth\_friction} \cos \alpha_{tooth}. \quad (3.78)$$

Using the same procedure, the force-balance equations for the remaining circular-spline wedge complete the dynamic constraints:

$$T_{cs} = T_{tooth\_normal} \cos \alpha_{tooth} - T_{tooth\_friction} \sin \alpha_{tooth} \text{ , and} \quad (3.79)$$

$$T_{output\_normal} = T_{tooth\_normal} \sin \alpha_{tooth} + T_{tooth\_friction} \cos \alpha_{tooth}. \quad (3.80)$$

To solve these equations, (3.74), (3.76), (3.78), and (3.80) can be combined with the constitutive torque-relationship for the kinematic error element in order to determine T_{input_normal}, T_{wg_normal}, T_{output_normal}, and T_{tooth_normal} in terms of known quantities. Then, by substituting these values along with equation (3.77) into equations (3.73), (3.75), and (3.79), the expressions for the torques on the wave-generator, flexspline, and circular spline can be found. When the positions and velocities of the three harmonic-drive ports are known, these equations, combined with the kinematic and constitutive relationships presented above, can be used to calculate all torques experienced by transmission.

3.7.3 Calculation of Input Parameters

Before the equations in model 5 can be used to simulate dynamic response, values for friction, stiffness and kinematic-error properties need to be determined. In the case of friction, experimental measurements presented in section 2.5 provided good results when used in previous dynamic models. However, in order to use these same values in model 5, the experimental friction results, which were measured from the input side of the transmission, need to be reflected to the gear-tooth interface, where they will appear in the model. The appropriate scaling factor which relates the wave-generator velocity to the

gear-tooth surface velocity can be easily found from the kinematic relationships presented above. On joint configuration 1, for example, this scaling factor is

$$B = \frac{1}{(N + 1) \sin \alpha_{tooth}}, \text{ where} \tag{3.81}$$

$$\omega_{tooth\_surface} = B\ \omega_{wg}\ . \tag{3.82}$$

Given this scaling factor, the values for the tooth-surface friction coefficients required to generate the same losses observed experimentally can be calculated readily. By assuming that any power dissipated by a friction source located at the wave-generator should be identical to the power dissipated when the friction is located at the gear-tooth interface, the experimental friction results can be directly related to friction parameters at the gear-tooth interface. In the case of velocity independent friction, this analysis yields the result

$$b_{constant} = \frac{b_{constant\_wg}}{B}\ , \tag{3.82}$$

where $b_{constant}$ is the constant friction at the gear-tooth interface from equation (3.59), $b_{constant\_wg}$ is the constant friction measured at the gear-tooth interface, and B is the scaling factor presented in equation (3.81). Since the amplitude of the cyclic friction in equation (3.61) is also independent of velocity, it can be calculated in an identical manner. However, the dynamic friction coefficients in equation (3.60), since they are linear and cubic functions of velocity, must be scaled by factors of B^2 and B^4, respectively.

Since no experimental data were collected to measure the Coulomb friction in the transmission, the remaining friction equation, (3.62), cannot be calculated using the same method used to derive the other friction terms. Instead, tabulated handbook values for typical Coulomb friction coefficients were used. Specifically, for lubricated steel-to-steel contact, listed values ranged from 0.03 to 0.16, and using this range as a guide, friction coefficients were then adjusted to optimize model performance. The resulting coefficients that delivered good model performance were 0.15 for joint 1, 0.05 for joint 2 and 0.10 for joint 3. However, simulated results illustrated that small changes in these friction values within the quoted range could greatly influence the dynamic response. This unfortunate result identifies a serious barrier to accurate harmonic-drive modeling since reliable Coulomb friction values are notoriously difficult to identify.

Having determined useful values for the friction in the harmonic-drive model, the second property that needs to be evaluated is transmission flexibility. As was the case in

the previous model, static stiffness measurement were of little help in determining the ideal compliance for the model. Instead, the resonances that appeared in the experimental time-response data were used to identify the natural frequencies of each harmonic-drive system. Given these frequencies, the inertias seen by the spring, as reflected through the geometry of the model, were used to calculate the linear component of the ideal compliance required to produce the same resonant behavior. With the linear coefficient fixed, the cubic stiffness coefficient was adjusted to reproduce the curvature in the measured static-stiffness profiles and provide good dynamic-response behavior around resonance. In particular, cubic-stiffness values were adjusted to increase or decrease the velocity range over which vibrations were sustained in each system resonance. Using these stiffness parameters, static stiffness simulations were performed using the harmonic-drive model, and results are shown in figures 3.30, 3.31, and 3.32.

By comparing the theoretical stiffness predictions to experimental results and catalog values, as shown in the three figures, useful insights about model integrity can be gained. First, since the Coulomb friction introduced in this model influences static stiffness predictions, the simulated theoretical compliance curves show a stiffer profile than the ideal stiffness alone would predict. More specifically, under static loading conditions, in order to effect torsion at the transmission output, both the model stiffness and Coulomb

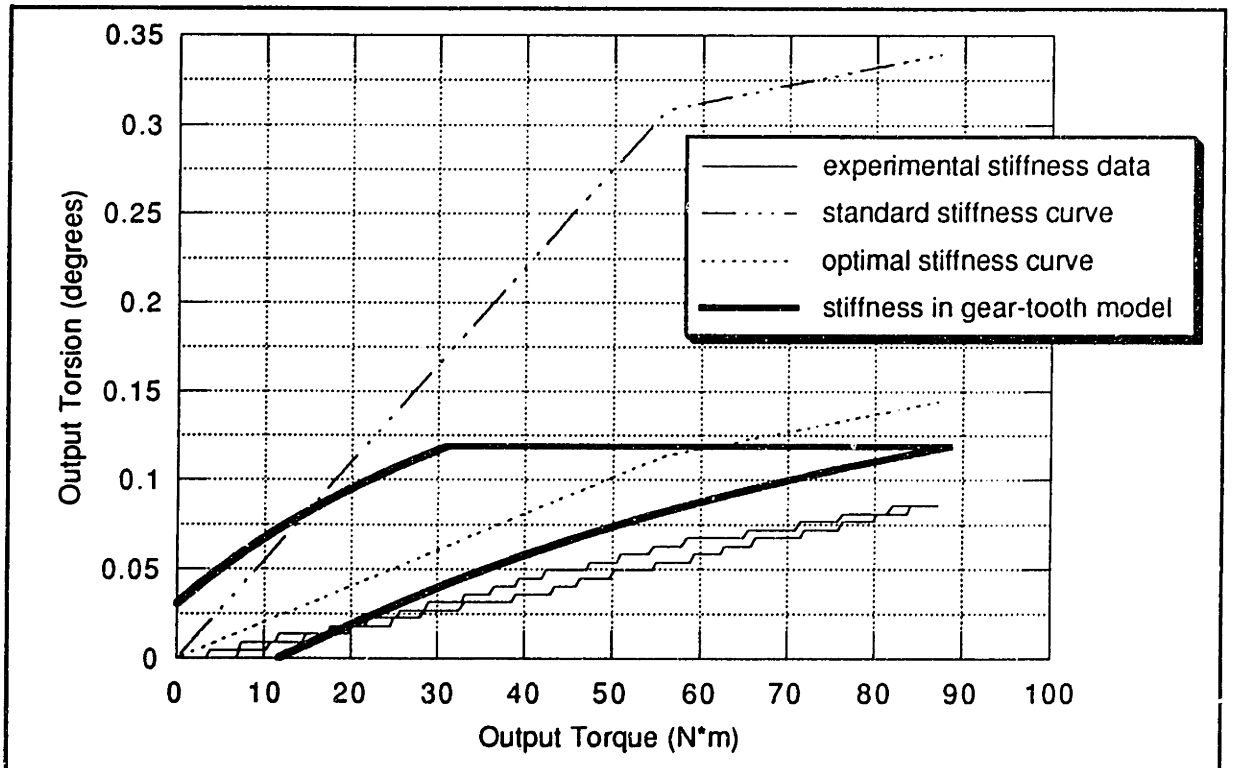

Figure 3.30: Joint 1 stiffness profile for harmonic-drive model 5

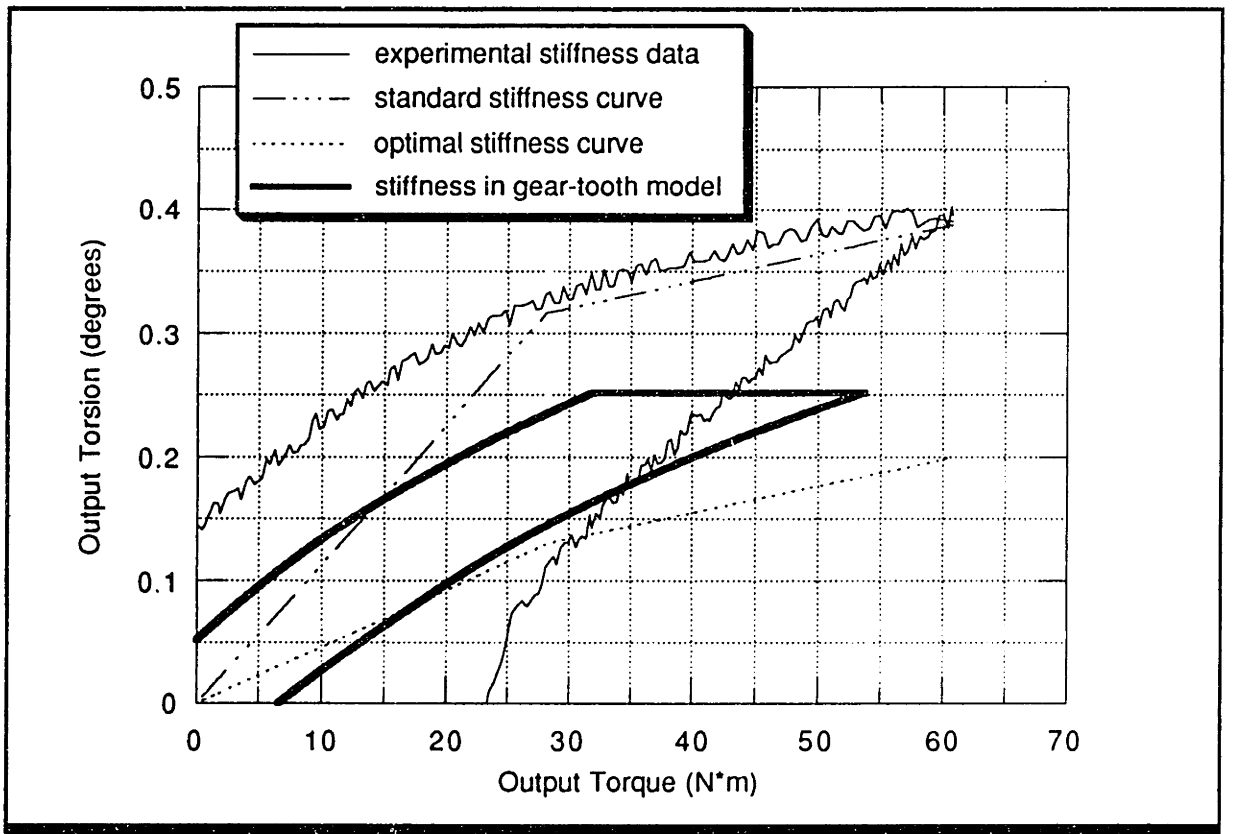

Figure 3.31: Joint 2 stiffness profile for harmonic-drive model 5

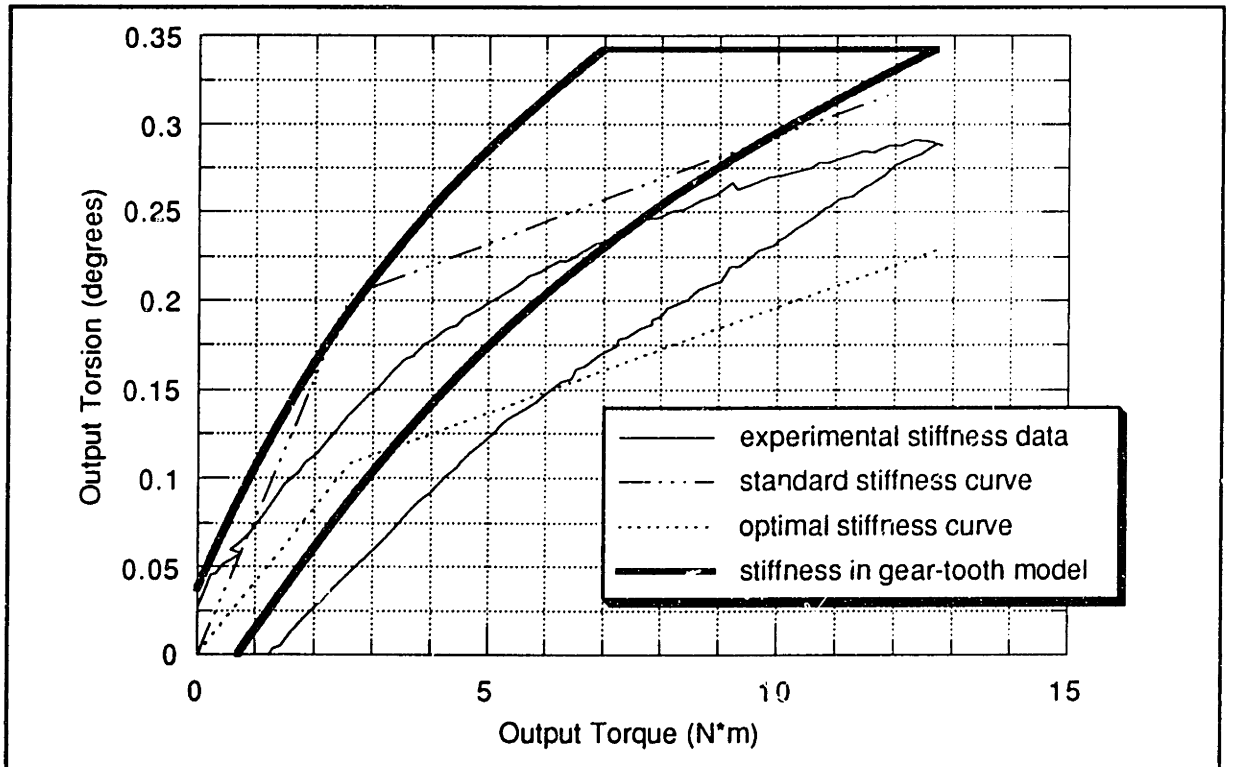

Figure 3.32: Joint 3 stiffness profile for harmonic-drive model 5

friction must be overcome. Since the magnitude of the Coulomb friction force at the gear-tooth surface increases as the load on the surface increases, the applied load required to overcome this friction force increases linearly as the load increases. During static stiffness measurements, this variation in Coulomb-friction force will appear as an increase in the measured stiffness during joint loading and a decrease in stiffness when the joint is unloaded. This behavior can be observed in all of the theoretical stiffness profiles in figures 3.30, 3.31, and 3.32. As illustrated most clearly on joints 1 and 3, this apparent increase in stiffness during loading produces theoretical stiffness measurements that more closely resemble the experimental stiffness profiles. This result is positive evidence that the gear-tooth mechanism captured in the model more closely mimics the physical behavior in the actual system. However, since in all cases, the overall shapes of the predicted stiffness profiles show poor agreement to measured values, the actual friction mechanism in harmonic drives is probably much more complicated than this model recognizes.

The second hallmark which can be used to evaluate the accuracy of the theoretical stiffness predictions in hysteresis loss. In the model, hysteresis in the calculated stiffness profiles is governed by the velocity-independent friction component as well as the Coulomb friction at the gear-tooth interface. In particular, the constant friction term provides a fixed-width difference between the loading and unloading stiffness curves while the Coulomb friction adds a hysteresis-width component that increases linearly with the applied load. The combined effect of these two friction factors can be seen in the theoretical stiffness curves in figures 3.30, 3.31, and 3.32. From the poor agreement between the predicted and experimental hysteresis loss it can be concluded that, although the specified friction values provided good dynamic response, the interaction between friction and compliance in the actual system is more complex that the model acknowledges.

Now that values for the friction and compliance effects in the transmission model have been isolated, the only parameters that remain unknown are the kinematic-error amplitudes of equation (3.64). As discussed previously, since low-velocity measurements of these position-error components proved somewhat unreliable due to dynamic vibrations, the values were selected in the previous model by matching predicted and experimental dynamic position-error. In theory, since the resulting values used in model 4 should describe the absolute kinematic error in the transmission, the same numbers should also apply to the new harmonic-drive model with gear-tooth geometry. When these kinematic-error amplitudes were reflected appropriately through the geometry of model 5 and incorporated into the simulation, however, the resulting dynamic-response predictions fell short of performance expectations. Specifically, the torque-fluctuation amplitudes that

resulted from the given kinematic-error values were much smaller than the experimental values. Because of these diminished torques, the amount of dissipation at resonance due to Coulomb friction was lower than observed in the actual system. To remedy this problem, it was discovered that, with slight adjustments to the calculated kinematic-error values, model predictions improved greatly. The final values which delivered optimal model performance are listed in Table 3.6 and compared to the experimental predictions from section 2.2. Based on this evolution of reliable kinematic-error values, a few useful conclusions can be derived. First, since the amplitudes which provided good results in model 4 performed less admirably in model 5, it is clear that the mechanisms used to introduce kinematic-error effects in both these models are incomplete. For example, as discussed previously, if the model including gear-tooth geometry could also incorporate the transmission behavior when the normal force at the gear-tooth interface reverses direction, it is likely that the influence of kinematic error on dynamic behavior could change dramatically. Additionally, from the difference between low-velocity measurements and theoretical values shown in table 3.6, the reliability of kinematic-error measurements which are not taken under truly static conditions is further questioned. In conclusion, the unfortunate result which can be derived from these observations is that the accurate kinematic error estimates are elusive. However, through careful parameter adjustment based on a good understanding of system dynamic operation, values can be chosen that deliver relatively good model performance.

Table 3.6: Kinematic-error components in model 5 vs. measured values

	A_1 (output °)	A_2 (output °)	A_3 (output °)
Joint 1: theoretical	0.000	0.020	0.008
Joint 1: experimental	0.001	0.013	0.007
Joint 2: theoretical	0.003	0.022	0.006
Joint 2: experimental	0.001	0.008	0.004
Joint 3: theoretical	0.003	0.015	0.005
Joint 3: experimental	0.007	0.013	0.007

3.7.4 Evaluation of Simulated Results

By inserting the harmonic-drive model developed in this section into the overall system models for the two joint configurations, dynamic step-response simulations were

performed to replicate the experimental results. Using the experimental parameters for friction, stiffness, and kinematic error discussed previously, time-response data was collected over a range of motor-current steps for the three harmonic-drive testing-station models. These simulated results are presented in appendix F in the identical format used for the experimental time-response results of appendix D and the model 4 simulation results in appendix E. In particular, graphs are shown which illustrate the position, velocity, and torque response for the observed range of harmonic-drive operating behavior. Table 3.7 is extracted from a similar index in appendix F and summarizes the figure numbers for all of the simulated dynamic-response plots. By directly comparing these plots to the experimental results in appendix D, the capacity of the dynamic model to predict actual harmonic-drive behavior can be evaluated. As an explanatory note, the electrical noise present in current-sensor readings was not reproduced in the model simulation since it had no influence on the dynamic behavior of the system.

Table 3.7: Summary of simulated time-response plots in appendix F

	Joint 1	Joint 2	Joint 3
Input Position	F.1.1	F.2.1	F.3.1
Input Velocity	F.1.2	F.2.2	F.3.2
Input Current	F.1.3	F.2.3	F.3.3
Output Position	F.1.4	F.2.4	F.3.4
Output Velocity - view 1	F.1.5	F.2.5	F.3.5
Output Velocity - view 2	F.1.6	F.2.6	F.3.6
Output Torque	F.1.7	F.2.7	F.3.7
Dynamic Position Error	F.1.8	F.2.8	F.3.8

From these results, several performance advantages of the harmonic-drive model with gear-tooth geometry can be noted:

[1] Due to Coulomb friction losses at the gear-tooth interface, the steady-state velocities reached by current-steps which excite system resonance are much closer to the experimental values than in previous models.

[2] The surprising jumps in velocity that appear in the experimental response when the velocity exceeds the resonance range are also observed in the simulated response.

[3] Velocities which excite resonance behavior are almost identical between predicted and actual response.

[4] As seen in previous models, overall predicted response shows good agreement to experimental data at operating speeds removed from regions of resonant behavior.

By noting the difference between the experimental and theoretical results, the shortcomings of this model can be recognized as well:

[1] On joints 2 and 3, in particular, input currents that could generate velocities high enough to break through resonant regions were lower than observed in experimental response.

[2] Compared to experimental response, amplitudes of torque fluctuation were too low on joint 1 and too high on joints 2 and 3.

[2] The predicted dynamic position error at system resonance was greater than experimental observations for all three joints.

From the improvements in simulated response shown by this model over its predecessors, it is clear that gear-tooth geometry and Coulomb friction are essential components for predicting harmonic-drive behavior during resonance. However, from the discrepancies between the theoretical and actual response, it also clear that a more detailed representation is required before reliable predictions of harmonic-drive performance can be made. In particular, as discussed previously, a model that can accommodate the shift in system dynamics that occurs when the torque at the gear-teeth changes direction should be able to improve predicted results. Currently, the model in this section avoids this complication by setting the Coulomb friction at the gear-tooth interface to zero whenever the normal force on the gear-tooth surface becomes negative. It is likely that a new model, which captures more accurately the actual friction behavior at the gear-teeth, will improve predicted performance by (1) increasing loss at system resonance and (2) limiting dynamic position error and velocity fluctuations while preserving torque amplitudes. If the new model can indeed deliver these effects, the model predictions should resemble more closely the actual dynamic response and, consequently, improve the accuracy and reliability of the representation.

By analyzing the influence of model parameters on overall dynamic response behavior, the sensitivity of a few important variables was characterized. First, variations in transmission compliance, which can influence greatly the natural frequency of vibration,

caused substantial deviations in the resulting dynamic response. Since experimental results illustrate that resonant behavior governs system performance for a wide range of operating velocities, it is not surprising that small variations in model stiffness can have a profound effect on dynamic response. Second, variations in the coefficient of Coulomb friction, μ, were also shown to influence dynamic response especially at system resonance. Surprisingly, decreasing the value of this coefficient often resulted in increased resonance losses due to heightened system vibration and torque fluctuations. Lastly, the output friction included in the system model had a surprisingly important relationship on dynamic behavior. Because increases in this variable resulted in higher normal-forces at the gear-tooth interface, resonance losses from Coulomb friction were very dependent on its value. A model in which Coulomb friction acts for both positive and negative normal torques may not show this same dependence. These observations emphasize the necessity of accurate characterization of harmonic-drive stiffness and friction properties for reliable model performance.

3.7.5 Other Models

In order to evaluate alternative strategies which might improve the performance of the harmonic-drive model with gear-tooth geometry, additional representations were developed. First, in order to capture the compliance of the torque sensors on each joint, an additional spring was included in the model at the grounded port of the transmission. However, because of the kinematic constraints of this new compliance and the cubic relationship of the harmonic-drive flexibility, the algebraic equations of motion could not be solved analytically. To remedy this problem, an additional state variable was introduced into the model by attaching an inertia to the spring on the grounded port of the transmission. This additional variable allowed for easy algebraic solution of the resulting equations, but , since the system was very stiff, numerical solutions were time-consuming. Results collected from a few simulations, however, indicated that the new inertia and flexibility on the grounded port of the harmonic-drive had a negligible effect on the dynamic response of the system. Finally, as mentioned previously, a numerical strategy was developed to solve simultaneously the two different sets of dynamic equations that describe harmonic-drive operation for positive and negative torques at the gear-tooth interface. Unfortunately, since no numerical algorithm was found that could solve the discontinuous set of equations reliably, I will resign this problem for later research.

3.7.6 Model 5 Conclusions

The model presented in this section represents a first attempt to incorporate gear-tooth-rubbing action into a dynamic model of a harmonic drive. As the simulated results illustrated, since this model included Coulomb friction losses at the gear-tooth interface, energy dissipation increased during system resonance and dynamic response integrity improved greatly in these areas. However, even with this new level of detail in the model, discrepancies between predicted and actual response indicate that the dynamics of harmonic-drive operation are still even more complex. However, since this is the only model which can boast even partially describing harmonic-drive response in all ranges of operation, it may be useful in any application in which understanding harmonic-drive operation through resonant regions is required. Since the mathematical complexity of this model is relatively minimal, it is an ideal candidate for making quick estimates of operating behavior, but, if more accurate information is required, I hope that this model can provide a template for more complex representations which better capture the subtleties of harmonic-drive behavior. In the very least, the model presented in this section can prescribe a definite lower bound on the level of detail required in harmonic-drive models to deliver reliable results.

One of the most discouraging conclusions that can be drawn from the results in this section is that accurate characterization of transmission properties can be very difficult but, unfortunately, also essential for good model performance. In fact, the only way in which accurate values could be determined for the stiffness and coulomb friction in this model was through careful measurement of dynamic response over a wide range of operation. By comparing these dynamic response measurements to the simulated results, the stiffness and friction values could be painstakingly adjusted to optimize model performance. Static stiffness tests and catalog predictions provided little guidance in this task. Based on this result, it seems unlikely that the model in this section, or any similar representation for that matter, will ever be able to make accurate predictions of dynamic performance using solely catalog values or simple experimental observations. Consequently, for applications in which an accurate harmonic-drive model is required,there are no shorcuts around a detailed experimental analysis of the actual harmonic-drive system.

Perhaps the most useful feature of the model in this section is its intimate conceptual relationship to the actual behavior in harmonic drives. Since this model depicts the interaction of the three different transmission components, harmonic-drive properties such as friction, compliance, and kinematic error can be placed at locations which have a definite

physical meaning in relationship to the real system. Furthermore, because of this conceptual analogy, the model can be improved easily and expanded to incorporate new properties resulting from future investigation into transmission behavior. Because of these features, harmonic-drive designers might find this model valuable for collecting quick and useful information about how adjustments in operating parameters, such as gear-tooth angle and frictional losses, can influence overall dynamic response. Engineers and designers, on the other hand, might find this model valuable for fostering an intuitive understanding of harmonic-drive operating behavior.

Chapter 4: Conclusions

As presented in this document, my research was targeted at understanding the operating behavior of harmonic-drive transmissions and developing mathematical representations to describe the observed performance. From my experimental investigation, several properties of harmonic drives where characterized and related to the overall dynamic behavior of the transmission. By developing models to simulate the experimental observations, the importance of many harmonic-drive properties was categorized and the complexity of the harmonic-drive operating mechanism was exposed. This section summarizes the important insights gained from both the experimental and theoretical investigations and presents recommendations for future harmonic-drive research and implementation.

4.1 Experimental Conclusions

The first set of experimental tests I performed were directed at understanding the magnitude and origins of kinematic position-error in harmonic drives. From the collected results, I confirmed past findings which identified primary error components to vary cyclically at twice the speed of the wave-generator and subsequent harmonics. Further exploration of kinematic error at higher frequencies demonstrated that the kinematic signature of individual gear-teeth was too small to be measured. Lastly, by isolating individual error components at both the circular spline and flexspline gear-meshing frequency, I confirmed that the dominant source of kinematic inaccuracy in harmonic drives can be traced to the gear-tooth errors. From evidence discovered through dynamic modeling analysis, I realized that, due to fluctuating inertial forces which induce transmission compliance, kinematic-error measurements can be corrupted greatly even at small operating velocities.

The second experimental voyage I undertook was the accurate characterization of harmonic-drive stiffness properties. In addition to cataloging the non-linear stiffness profiles for three harmonic-drives, perhaps the most important insight I gained on this journey was that stiffness measurements taken under static conditions are highly influenced by static friction in the transmission. Because of this unfortunate result, static stiffness measurements were of little use in determining stiffness properties for harmonic-drive dynamic models. To make matters worse, these stiffness measurements were observed to deviate from catalog predictions and vary widely with wave-generator angle and gear-tooth preload. Since the accuracy of harmonic-drive representations developed later was highly sensitive to stiffness values, the volatile nature of harmonic-drive stiffness identifies a primary barrier to harmonic-drive modeling efforts.

Static and dynamic friction in harmonic drives were the third suspects to be experimentally audited. In particular, starting-torque measurements were made on three harmonic drives which confirmed past results demonstrating that factors such as wave-generator angle and gear-tooth preload can greatly affect static friction. Next, experimental tests performed at non-zero velocities illustrated that the dynamic friction in harmonic drives has three components: (1) a velocity-independent torque probably due to coulomb-like friction resulting from gear-tooth preload, (2) a non-linear dynamic torque caused by the lubrication effects in the transmission, and (3) an increased energy loss during system resonance resulting from high torque fluctuations which increase coulomb-like friction at the gear-teeth. The increased losses at resonance, in particular, were sighted for causing unusual and unpredictable behavior during harmonic-drive operation. Lastly, to add an extra element of complexity, the velocity-independent friction torque was observed to vary considerably with the output rotation of the transmission.

Using the results collected for harmonic-drive kinematic error, compliance, and friction properties, the overall dynamic response of the transmission was scrutinized. From this investigation, several behavior patterns common to the three harmonic drives tested were identified and related to known transmission properties. First, all dynamic response showed significant velocity and torque fluctuations due to the kinematic inaccuracies of the transmission. Second, due to the relatively low stiffness of harmonic drives, these fluctuations excited dynamic resonances over a substantial range of the harmonic-drive operating envelope. Torque and velocity oscillations were observed to increase dramatically in these resonant regions. Third, since coulomb-like friction increased energy dissipation at resonance, large increases in motor current produced little or no increase in operating velocity around resonance. Additionally, due to this energy loss at

resonance, dramatic jumps in velocity were observed when the system finally exceeded these resonant regimes. Fourth, since the harmonic-drive stiffness is non-linear, the natural frequency of vibration increased with increased torque levels at resonance. This rise in resonant frequency increased the velocity range which excited system resonance and accentuated the velocity jump that occurred when these resonance ranges were exceeded. Lastly, due to friction variation with output rotation, the location of the velocity jump at resonance exit was observed to vary unpredictably.

If a single conclusion must be derived from the experimental results of my research, it should be that harmonic-drive properties are very dependent on operating and environmental conditions. In particular, stiffness and friction investigations demonstrated that factors such as input orientation, output orientation, gear-tooth preload, and operating temperature can greatly influence measured values. In an attempt to unify these results, I propose a final description to explain the observed behavior. Specifically, due to the slightly different gear-tooth spacing on the circular spline and flexspline, a small amount of gear-tooth deflection is required to ensure tight meshing. This deflection, in turn, dictates the necessity for a non-zero preloading force at the gear-tooth interface. As a fortunate side-effect of this gear-tooth loading, backlash in harmonic-drives is minimal. However, since this force increases the amount of Coulomb friction during gear-tooth rubbing, the friction in the transmission is greatly influenced by the tightness-of-fit at the gear teeth. Similarly, since harmonic-drive stiffness is probably directly proportional to the metal-to-metal contact area at the gear-tooth interface and a tight gear-tooth fit results in a large contact area, it is reasonable to assume that harmonic-drive stiffness should vary with gear-tooth preloading as well. Using this description of the gear tooth mechanism, an explanation can be made to describe the increases in both stiffness and friction that were observed in the experimental results when the preload was increased. Developing this theory further, the influence of kinematic error on gear-tooth preloading can also be related to variations in harmonic-drive properties. Specifically, as kinematic-error results demonstrate, geometric inaccuracies exist in the gear-teeth of harmonic drive transmissions. These inaccuracies are likely to cause variations in the tightness of fit between the circular spline and flexspline gear teeth when these two components are rotated relative to each other. Based on this assumption, it is likely that both friction and stiffness in the transmission should also vary due to this fluctuation in gear-tooth preload that occurs when either the input or output port of the transmission is rotated. Using this explanation, the experimental variations in stiffness and friction with input and output orientation can be justified. Lastly, since other conditions such as gear-tooth wear and operating temperature

can influence the tightness of gear-tooth meshing, stiffness and friction are vulnerable to these influences as well. In general, using this argument, any variation in an environmental or operating conditions which can affect loading at the gear-tooth interface will be manifested in the stiffness and friction of the transmission. I am optimistic that future work in this area can not only quantify this interdependence of transmission properties but can also develop mathematical representations to predict experimental measurements under static and dynamic conditions.

4.2 Theoretical Modeling Conclusions

In my theoretical investigation, five different harmonic-drive models are presented to illustrate the level of detail required to reproduce actual harmonic-drive behavior to different degrees of accuracy. Since each of these models boasts three-port behavior, all possible harmonic-drive operating configurations can be easily reproduced. Additionally, since none of these models contain inertia terms, simple algebraic equations are adequate to fully define model performance. Based on the results from my investigation of these five models, the applicability of different harmonic-drive modeling strategies will now be summarized.

I began my investigation with an analysis of an ideal transmission model. Not surprisingly, since this representation failed to capture any of the frictional losses of the actual system, predicted operating velocities were orders-of-magnitude higher than in reality. To improve performance, I then included frictional losses into the dynamic representation. Specifically, dynamic friction, velocity-independent friction, and position-dependent friction were all appended to the ideal transmission model. As expected, this model predicted velocities which matched experimental observations in most ranges but failed to capture the resonant vibration observed in the actual system. Based on these results, it was concluded that, for systems where resonant behavior does not appear within the operating envelope of the harmonic drive, this simple representation may suffice.

Unfortunately, in the three transmissions studied, system resonance appeared frequently and dominated behavior over a substantial range of harmonic-drive operating velocities. In order to capture these effects, both non-linear compliance and kinematic error were incorporated into the system model. By using stiffness values estimated from dynamic observations, the resulting predictions of resonant behavior from the model agreed closely with the experimental results. Unfortunately, since this improved harmonic-drive

model was incapable of describing the losses which occur at system resonance, model predictions at velocities which excited resonance vibration were still inaccurate. Based on these results, it was concluded that this model provides a slightly more accurate representation than it predecessor for describing the dynamic behavior of systems which experience little resonance vibration.

In a final attempt to improve model performance, a representation was developed which incorporated a simplified gear-tooth meshing mechanism with Coulomb friction at the gear-tooth interface. Because of enhanced dissipation from the Coulomb friction at system resonance, this model better reproduced the actual velocities and torques that occurred in resonant regimes. In particular, the sudden velocity jumps that were observed in the experimental response when velocities exceeded resonant regions also appeared in the simulated response. From these optimistic results, it was concluded that the gear-tooth meshing mechanism plays a significant role in harmonic-drive operation and cannot be ignored in an accurate harmonic-drive model. Unfortunately, since some torque levels and velocity fluctuations predicted by this model differed from experimental observations, the need for more detailed representations was demonstrated. Nevertheless, it was concluded that, with careful estimation of input parameters, this model may prove useful in applications in which understanding harmonic-drive operation through resonant regions is required.

From the results of the five transmission models, the complexity of the task of harmonic-drive modeling has been exposed. Not only are friction, compliance, and kinematic error essential factors for describing harmonic-drive behavior, but the gear-tooth meshing dynamics also play an essential role in determining the overall performance of the transmission. Additionally, experimental results indicate that the actual values of these transmission properties can vary significantly with environmental and operating conditions, which makes accurate characterization of these effects difficult if not impractical. To make matters worse, not only are reliable measurements of transmission properties difficult to obtain, but, for stiffness and coulomb friction in particular, precise estimates are critical for good model performance. In fact, the only way in which accurate values could be determined for the parameters in this model was by measuring carefully the dynamic response over a wide range of operation and adjusting of model parameters to match this observed response. This unfortunate result reveals that reliable harmonic drive models cannot be developed unless experimental data from the actual harmonic-drive system are available. In the face of these modeling obstacles, it seems unlikely that any model which does not capture the physics of harmonic-drive operation to a much greater level of detail

will ever be able to deliver accurate and reliable performance over all operating regions. Given this conclusion, I hope the models developed in this investigation will act as a springboard from which to launch more detailed future explorations.

4.3 Recommendations

Given the conclusions of my experimental and theoretical investigation, I can offer a few recommendations to designers wishing to model systems employing harmonic drives. The first step in understanding the extent to which harmonic-drive dynamics may influence system performance is it to determine the prominence of resonance vibration within the operating range of the transmission. Due to the unreliability of static measurements and catalog predictions of stiffness values, resonance vibration can be accurately located only during actual system operation. However, an order-of-magnitude estimate for the natural frequency of the system can be made by using linearized catalog stiffness values and system inertia measurements. If a harmonic of the rotational velocity of the wave-generator relative to the flexspline coincides with the estimated natural frequency of the system at any point in the operating envelope of the transmission, it is likely that resonant vibration will occur. Since resonant vibration greatly influences operating behavior and is difficult to model, the best solution to this dilemma is to revise the machine specifications to avoid these ranges of operation.

For researchers embarking upon experimental investigations of harmonic-drive behavior, I can make a few suggestions about worthy areas for exploration. Specifically, in order to provide accurate stiffness data for harmonic-drive models, a reliable method for removing the friction component from static stiffness measurements would be enormously valuable. Alternatively, modeling efforts would also benefit from an experimental procedure that could reliably measure harmonic-drive compliance dynamically. Since harmonic-drive stiffness and friction can vary considerably with such factors as gear-tooth preload and wave-generator angle, empirical data describing these variations could be very beneficial for anticipating ranges of parameter variation in different harmonic drives. Additionally, since many harmonic-drive properties are influenced by rotational direction, an experimental investigation in this area could also prove worthwhile. Lastly, since dynamic representations have been shown to depend strongly on accurate friction measurements, a method for experimentally separating different friction components

present in harmonic drives would be useful for improving performance of harmonic-drive models.

Lastly, for future harmonic-drive modelers, I propose a few areas for investigation that seem most fruitful. In particular, as described in detail previously, a harmonic-drive representation that can describe the transition that occurs when the torque at the gear teeth changes direction should show improved results over the models in this document. After this improvement has been implemented, a model which predicts the influence of gear-tooth preload on transmission friction and compliance is also likely to improve dynamic response. Finally, since the kinematic error in harmonic-drives probably influences the gear-tooth preload itself, a representation which incorporates this behavior will more accurately represent the actual physical mechanism inside the harmonic-drive transmission.

Chapter 5: Reference List

This section contains citations for literature referenced in this thesis as well as citations for related harmonic-drive research. For convenience, the list of references on harmonic-drive research has been subdivided into categories describing the nature of the literature and popular areas of study. Papers which could fit reasonably into more than one category are listed only once.

The references presented below were compiled from International CD-ROM database searches for harmonic-drive-related literature published in the past ten years. Additional references were obtained from library literature searches and reference lists from individual papers. The majority, but not all of these papers were located in the MIT Libraries.

5.1 Harmonic-Drive-Related References

5.1.1 Manufacturer's Literature

[1] *Harmonic Drive Gearing: Precision Gearheads Close Couple Model*
HD Systems, Inc., Hauppauge, NY.

[2] *Harmonic Drive Gearing: Precision DC Servo Actuators,*
HD Systems, Inc., Hauppauge, NY.

[3] *Harmonic Drive Gearing: Cup Type HDUC and HIUC Component Sets,*
HD Systems, Inc., Hauppauge, NY.

[4] *Harmonic Drive Precision Reduction Gearing Designers' Manual,*
Harmonic Drive Machinery Group, Peabody, MA.

[5] *The World of Harmonic Drive Gearing,*
HD Systems, Inc., Hauppauge, NY.

5.1.2 Reference Textbooks

[6] Ivanov, M. N.,
Harmonic Gear Transmissions,
Vysshaya shkola, M., 1981, 184 pages. (Russian)

[7] Volkov, D. P., et al.,
Harmonic Drives,
Tekhnika, Kiev, 1976, 222 pages. (Russian)

5.1.3 Vibration and Dynamic Behavior

[8] Aliev, N. A.,
Investigations of Vibrations of Flexible Gears of Harmonic Drives, Based on the 2TEM Pipe-Stacker Winch Drive,
Thesis, MVTU, Moscow, 1981, 14 pages.

[9] Aliev, N. A.,
"Determination of the Natural Vibration Frequency of a Flexible Gear in a Harmonic Drive",
Mosstankin,
1983, 5 pages. (Russian)

[10] Aliev, N. A.,
"A Study of the Dynamic Behavior of Flexible Gears in Harmonic Drives",
Soviet Engineering Research,
Vol. 6, No. 6, June 1986, pp 2-5.

[11] Hidaka, T., Ishida, T., Zhang, Y., Sasahara, M., and Y. Tanioka,
"Vibration of a Strain-Wave Gearing in an Industrial Robot"

Proceedings of the 1990 International Power Transmission and Gearing Conference - New Technology Power Transmission,
published by ASME, New York, NY, pp 789-794.

[12] Hidaka, Teruaki, Ishida, Takeshi, Zhang, You-lin, Sentoku, Hirofumi, Sasahara, Masakatsu, and Yoshihiro Tanioka,
"Theoretical Analysis of the Vibration in a Robot due to a Strain Wave Gearing",
Nihon Kikai Gakkai Ronbunshu,
Part C, Vol. 55, No. 516, August 1989, pp. 1864-1871. (Japanese)

[13] Popov, P. K., et al.,
"Calculation of the Critical Speeds of a Drive With Harmonic Gear Transmission",
Soviet Engineering Research,
Vol. 7, No. 3, March 1987, pp 17-18.

[14] Ostapski, Wieslaw,
"Analysis of Some Aspects of the Harmonic Drive Dynamic",
Modeling, Simulation & Control A: General Physics (Matter & Waves), Electrical & Electronics Engineering,
Vol. 9, No. 1, 1987, pp 21-33.

[15] Ostapski, Wieslaw,
"Influence of Manufacturing and Assembly Errors on Dynamics of Harmonic Drive",
Modeling, Simulation & Control B: Mechanical & Thermal Engineering, Materials & Resources, Chemistry,
Vol. 10, No. 4, 1987, pp 1-12.

[16] Revin, A. I.,
Dynamic Model of a Harmonic Gear Power Transmission,
Proc. of Bauman MHTS (Moscow Higher Technical School), No. 408, 1984, pp 27-32. (Russian)

[17] Sabot, J., Bouchareb, A., and Ph. Briere,
"Dynamic Perturbations Induced By Speed Reducing Gears in Robotics",
Proceedings of the 7th World Congress - Theory of Machines and Mechanisms,
Vol. 2, pp 1083-1087. (French)

[18] Volkov, D. P., and Yu N. Zubkov,
"Vibrations in a Drive With a Harmonic Gear Transmission",

Russian Engineering Journal,
Vol. 58, No. 5, 1978, pp 11-15.

5.1.4 Kinematic Error

[19] Ahmadian, M.,
Kinematic Modeling and Positional Error Analysis of Flexible Gears,
Clemson University Research Report Under Grant No. RI-A-86-8, 1987.

[20] Emel'yanov, A. F., et al.,
"Calculation of the Kinematic Error of a Harmonic Gear Transmission Taking into Account the Compliance of Elements",
Soviet Engineering Research,
Vol. 3, No. 7, 1983, pp 7-10.

[21] Hsia, Lih-Min,
Harmonic Gear Drive Position Error Analysis,
Technical Report, Jet Propulsion Laboratory, August, 1986.

[22] Hsia, Lih-Min,
"The Analysis and Design of Harmonic Gear Drives",
Proceedings of the 1988 IEEE International Conference on Systems, Man, and Cybernetics,
Vol. 1, 1988, pp 616-619.

[23] Klypin, A. V., et al.,
"Calculation of the Kinematic Error of a Harmonic Drive On a Computer",
Soviet Engineering Research,
Vol. 5, No. 11, November 1986, pp 8-13.

[24] Nye, Ted W., and Robert P. Kraml,
"Harmonic Drive Gear Error: Characterization and Compensation for Precision Pointing and Tracking",
Proceedings of the 25th Aerospace Mechanisms Symposium,
1991, pp 237-252.

[25] Popov, P. K.,
Investigation of Angular Positioning Errors of the Output Shaft of a Harmonic Drive,
Thesis, MVTU, Moscow, 1972, 15 pages. (Russian)

[26] Popov, P. K., et al.,
A Mathematical Model of the Process of Origination of a Kinematic Error in a Harmonic Gear Transmission,
Trudy, MVTU, Moscow, No. 287, 1978, pp 50-55. (Russian)

[27] Popov, P. K., and L. O. Shtripling,
"Dynamic Model of Incidence of Kinematic Error of a Harmonic Gear Transmission",
Izvestiya vuzov. Mashinostroenie,
No. 1, 1986, pp 46-50. (Russian)

[28] Yanabe, Shigeo, Ito, Akihiko, Okamoto, Atsushi, Yamaguchi, Toshiaki, Ikeda, Masaki, and Hiroshi Fujita,
"Rotational Transmission Error of Harmonic Drive Device",
Nihon Kikai Gakkai Ronbunshu,
Part C, Vol. 56, No. 521, January 1990, pp. 148-153. (Japanese)

5.1.5 Torsional Stiffness

[29] Margulis, M. V., and D. P. Volkov,
"Calculation of the Torsional Rigidity of a Harmonic Power Drive with a Disc Generator",
Soviet Engineering Research,
Vol. 7, No. 6, June 1987, pp 17-19.

[30] Margulis, M. V., and D. P. Volkov,
"Method of Calculating the Radial Stiffness of the Casing of a Large High-Torque Harmonic Transmission",
Soviet Engineering Research,
Vol. 4, No. 10, 1984, pp. 8-12.

[31] Popov, P. K.,
"Torsional Stiffness of a Harmonic Drive",
Russia, M.V.S.S.O., Izvestia V. U. Z. Mashinostroenie,
No. 4, 1972, pp. 43-47. (Russian)

[32] Yanabe, Shigeo, Ishizuka, Shinichi, Yamaguchi, Toshiaki, and Masaki Ikeda,
"Torsional Stiffness of Harmonic Drive Reducers",
Nihon Kikai Gakkai Ronbunshu,
Part C, Vol. 55, No. 509, January 1989, pp. 216-221. (Japanese)

5.1.6 Structural Analysis

[33] Alfutov, N. A., and S. S. Klenikov,
"Calculation of Forces of Interaction of Harmonic Drive Elastic Elements By a Step-by-Step Method",
Russian Engineering Journal,
Vol. 58, No. 7, 1978, pp 16-19.

[34] Ivanov, M. N., and V. V. Sheiko,
"The Deformation Shape of the Elastic Gear in a Harmonic Transmission with a Generator Featuring Two Large Rollers",
Izvestiya Vysshikh Uchebnykh Zavedenii, Matematika,
No. 11, 1970, pp 32-36.

[35] Kosova, N. V., et al.,
"Stress Concentration in Gear Rim of Flexspline of Harmonic Drive",
Soviet Engineering Research,
Vol. 2, No. 3, 1982, pp 15-18.

[36] Priimakov, A. G., and V. I. Rudnitskii,
"Stress-Strain State and Fatigue Strength of Triple Harmonic Power Drives with Metal-Polymer Flexsplines",
Soviet Engineering Research,
Vol. 4, No. 4, June 1984, pp 20-22.

[37] Shamsutdinov, F. A.,
"The Transverse Stiffness of the Flexible Wheel of a Harmonic Gear Transmission",
Russia, M.V.S.S.O., Izvestiya V. U. Z. Mashinostroenie,
No. 2, 1984, pp 36-40. (Russian)

[38] Shuvalov, S. A.,
"Calculation of Harmonic Drives with Allowance for Pliancy of the Links",
Russian Engineering Journal,
Vol. 54, No. 6, 1974, pp 47-52.

[39] Shuvalov, S. A.,
"Calculation of Forces Acting on Members of a Harmonic Gear Drive",
Russian Engineering Journal,
Vol. 59, No. 10, 1979, pp 5-9.

[40] Sinkevich, Yu. B.,
"Effect of Teeth on the Rim Rigidity of the Flexible Gear Wheel of a Harmonic Drive",
Russian Engineering Journal,
Vol. 58, No. 7, 1978, pp 19-22.

5.1.7 Robotics Applications Employing Harmonic Drives

[41] Carlson, J. H.,
"Harmonic Drives for Servomechanisms",
Machine Design,
Vol. 57, No. 1, January 10, 1985, pp 102-106.

[42] Chapel, J. D., and R. Su,
"Application of H-infinity Control Design Techniques to Improve Dynamics of Dexterous Manipulation",
Proceedings of the SPIE - The International Society for Optical Engineering,
Vol. 1387, 1991, pp. 284-295.

[43] Chiba, Jiro,
"Adaptive Control Cuts Position Servo Vibration",
PCIM,
June 1990.

[44] Good, M. C., Sweet, L. M., and K. L. Strobel,
"Dynamic Models for Control System Design of Integrated Robots and Drive Systems",
Sensors and Controls for Automated Manufacturing and Robotics
Published by ASME, New York, NY, 1984, pp. 253-269, or
Transactions of the ASME - Journal of Dynamic Systems, Measurement, and Control,
Vol. 107, March 1985, pp 53-59.

[45] Hashimoto, Minoru,
"Robot Motion Control Based on Joint Torque Sensing",
IEEE International Conference on Robotics and Automation,
Vol. 1, 1989, pp. 256-261.

[46] Hewit, J. R.,
"The Control of Robots and Manipulators with Flexible Transmission Elements",
IEE Colloquium on Recent Advances in Robot Control,
Published by IEE, London, Digest No. 22, 1987, pp 1/1-1/11.

[47] Hudoba, M.,
"Harmonic Gear Boxes for Servo Drives",
Automatizace,
Vol. 32, No. 2, February 1989, pp 44-47. (Slovak)

[48] Kalas, D., Kardos, J., and I. Zemanovic,
"Application of a Modified LSSM Structure to the Synthesis of Robust Servosystems of Robots with a Flexible Reducer",
Electrotechnicky Casopis,
Vol. 41, No. 5, 1990, pp 393-399. (Slovak)

[49] Karlen, J. P., Thompson, J. M., Vold, H. I., Farrell, J. D., and P. H. Eismann,
"A Dual-Arm Dexterous Manipulator System With Anthropomorphic Kinematics",
Proceedings of the 1990 IEEE International Conference on Robotics and Automation,
Vol. 1, Published by IEEE Computer Society Press, Los Alamitos, CA, 1990, pp 368-373.

[50] Kojima, Hiroyuki, Uesugi, Sasagu, Nezu, Kikuo, and Kenji Sakamoto,
"Path Control of a Horizontal Two-Link Robot Driven by Step Motors",
Nihon Kikai Gakkai Ronbunshu,
Part C, Vol. 56, No. 525, May 1990, pp 1217-1222.

[51] Lee, K. Y., de la Torre, A. J., and R. W. Beekman,
"Decoupled Non-linear Robotic Control with Series Compliance and Bounded Inputs",
Proceedings of the IEEE Conference on Decision and Control Including The Symposium on Adaptive Processes,
Vol. 1, 1989, pp 712-715.

[52] Marilier, T., and J. A. Richard,
"Non-Linear Mechanic and Electric Behavior of a Robot Axis With a 'Harmonic-Drive' Gear",
Robotics and Computer-Integrated Manufacturing,
Vol. 5, No. 2-3, 1989, pp 129-136.

[53] Ostapski, W.,
"Optimization of Harmonic Drive Applied in Industrial Robot",
Modeling Simulation & Control B: Mechanical & Thermal Engineering, Materials & Resources, Chemistry,
Vol. 17, No. 1, 1988, pp 25-35.

[54] Sakuta, Hiroshi, Yoshitani, Yutaka, and Takihiro Yonezawa,
"Vibration Absorption Control of Robot Arm By Software Servomechanism",
Nihon Kikai Gakkai Ronbunshu,
Vol. 54, No. 497, January 1988, pp 217-220.

[55] Thompson, Bruce R.,
The PHD: A Planar, Harmonic Drive Robot for Joint Torque Control,
MIT Masters Thesis, Department of Mechanical Engineering, and
MIT Artificial Intelligence Laboratory Technical Report No. 1247,
May 1990.

5.1.8 Gear-Tooth Profile

[56] Ishikawa, S.,
"The Gear Geometry of Tooth Engagement in Harmonic Drive",
Proceedings of the JSME Semi-International Symposium,
1967, pp 97-104.

[57] Kiyosawa, Y., Sasahara, M., and S. Ishikawa,
"Performance of a Strain Wave Gearing Using a New Tooth Profile",
Proceedings of the 1989 International Power Transmission and Gearing Conference: New Technologies for Power Transmissions of the 90's",
Published by ASME, New York, NY, 1989, pp 607-612.

[58] Kondo, K., and J. Takada,
"Study on Tooth Profiles of the Harmonic Drive",
Proceedings of the 1989 International Power Transmission and Gearing Conference: New Technologies for Power Transmissions of the 90's",
Published by ASME, New York, NY, 1989, pp 627-634.

[59] Peter, J.,
"Investigation of the Engagement of Harmonic Drives - Part II",
Acta Technica Academiae Scientiarum Hungaricae,
Vol. 94, No. 3-4, 1982, pp 223-233.

[60] Shen Yun-Wen,
"On the Profile of the Harmonic Drive Gearing",
Chilun (Gearing),
Vol. 10, No. 4, 1986, pp 51-56. (Chinese)

[61] Terplan, Z., and J. Peter,
"Differences Between Harmonic Drives and Epicyclic Gear Drives Based on Gear Tooth Action",
Proceedings of the Sixth World Conference on the Theory of Machines and Mechanisms,
Vol. 2, Published by Halsted Press, New York, NY, 1984, pp 846-849.

[62] Xie, Jin-rui, and Lin-zhi Sun,
"Meshing Analysis Method of Harmonic Gear Drive Using Symmetric Disc Wavegenerator",
Proceedings of the 1984 International Symposium on Design and Synthesis",
Published by the Japan Society of Precision Engineers, Tokyo, 1984, pp 270-274.

5.1.9 Operating Life and Tooth-Wear

[63] Abakumov, A. N., and N. I. Tseitlin,
"Effect of the Geometrical Parameters of Flexsplines and of the Load Transmitted by Them on Their Life",
Soviet Engineering Research,
Vol. 2, No. 8, 1982, pp. 43-46.

[64] Ivashov, E. N. and M. I. Nekrasov,
"Calculation of the Wear of Harmonic Gears",
Soviet Engineering Research,
Vol. 4, No. 1, 1984, pp. 18-20.

[65] Nye, T. W.,
"Harmonic Drives: Determining Wear Life Based on Stiffness Considerations",
Proceedings of the 1989 International Power Transmission and Gearing Conference: New Technologies for Power Transmission in the 90's,
Published by ASME, New York, NY, 1989, pp 867-877.

[66] Volkov, D. P., and M. P. Golovin,
"Endurance of Flexsplines of Harmonic Gear Drives",
Soviet Engineering Research,
Vol. 2, No. 8, 1982, pp. 46-48.

5.1.10 Hermetically-Sealed Transmissions

[67] Abramov, V. A., and I. S. Kuz'min,
"Sealed Harmonic Drive With Cylindrical Flexspline",
Russian Engineering Journal,
Vol. 60, No. 1, 1980, pp 20-21.

[68] Hayashi, Yuzo, and Toshimi Yamada,
"Development of the Harmonic Drive Rotary Feedthrough",
Vacuum,
Vol. 41, No. 7-9, 1990, pp 1948-1950.

[69] Istomin, S. N.,
"Choosing the Geometrical Parameters of the Flexible Wheel of a Hermetically Sealed Harmonic Gear Transmission",
Soviet Engineering Research,
Vol. 5, No. 7, 1985, pp 15-17.

5.1.11 Other Research on Harmonic Drives

[70] Abramov, V. A., and I. S. Kuz'min,
"Machining Harmonic Drive Generator Cams in an NC Milling Machine",
Russian Engineering Journal,
Vol. 60, No. 2, 1980, pp 33-34.

[71] Abramov, V. A., and I. S. Kuz'min,
"Adjustable Forced Deformation Generators of a Harmonic Drive",
Russian Engineering Journal,
Vol. 60, No. 7, 1980, pp 21-22.

[72] Chesnykh, P. P.,
Investigation of Service Features of a Flexible Gear in a High-Power

Harmonic Drive,
Thesis, MATI, Moscow, 1974, 168 pages. (Russian)

[73] Diamond, Albert,
"Sizing Harmonic Drives",
Machine Design,
March 22, 1990

[74] Emel'yanov, et al.,
"Rig Tests on the Feed Drive of an NC Machine Tool With Harmonic Gear",
Soviet Engineering Research,
Vol. 2, No. 11, 1982, pp 71-73.

[75] Fichtner, K.,
"Harmonic Drive Units in Precision Engineering",
Feinwerktechnik & Messtechnik,
Vol. 94, No. 2, March 1986, pp 83-84. (German)

[76] Finogenov, V. A., and A. E. Vidmaer,
"Internal Heat Exchange in General-Purpose Harmonic Reduction Gear Drives",
Soviet Engineering Research,
Vol. 2, No. 8, 1982, pp 49-51.

[77] Gulyas, M.,
"Harmonic Drive in Special Purpose Machines and Materials Handling Systems",
Proceedings of the Second Seminar on Single Purpose Machines,
Published by OMIKK-Technoinform, Budapest, 1983, pp 43-55. (German)

[78] Lasocki, Lech, and Andrzej Dudek,
"Transmission Gears of High Transmission Ratio: Part II",
Przeglad Mechaniczny,
Vol. 48, Pt. 1, No. 7, April 1989, pp 14-16. (Polish)

[79] Margulis, et al.,
"Dimensional-Functional Analysis of Heavily Loaded High-Torque Harmonic Gearing",
Soviet Engineering Research,
Vol. 5, No. 8, 1985, pp 7-12.

[80] Peter, J.,
"Harmonic Drive and Its Industrial Application in Special Machine Tools and Robots",
Proceedings of the Second Seminar on Single Purpose Machines,
Published by OMIKK-Technoinform, Budapest, 1983, pp 234-247. (German)

[81] Priimakov, A. G., and A. V. Leusenko,
"Introducing Harmonic Gear Units for Power Transmission",
Soviet Engineering Research,
Vol. 9, No. 3, 1989, pp 55-57.

[82] Priimakov, A. G., and V. I. Rudnitskii,
"Experimental Determination of Temperature Deformations of Metal-Polymer Flexible Wheels in Harmonic Transmissions",
Soviet Engineering Research,
Vol. 7, No. 10, 1987, pp 9-11.

[83] Rubtsov, I. V., Chirov, A. A., and V. M. Zav'yalov,
"Technological Problems of Improving the Durability of Flexible Gears",
Izvestiya Vysshikh Uchebnykh Zavedenii, Mashinostroenie,
No. 8, 1987, pp 62-66. (Russian)

5.2 General References

[84] *Motion Control Product Guide,*
Aerotech, 1990, Pittsburg, PA.

[85] Press, William H., Flannery, Brian P., Teukolsky, Saul A., and William T. Vetterling,
Numerical Recipies in C: The Art of Scientific Computing,
Published by Cambridge University Press, New York, 1988.

Appendix A: Sensor Calibration

This appendix describes the calibration procedures and results for all of the experimental sensors.

A.1 Encoders

Using processing boards to count encoder pulses, encoder measurements were directly translated into degrees of rotation. In order to make this simple conversion, the Whedco boards were initialized with the number of lines on each encoder wheel and the number of counts to extract for each line. These parameters are listed in table A.1 for each encoder. The three input encoders directly measured motor rotation, while the output encoder on joint 1 monitored output rotation through an 8:1 gear reduction.

Table A.1: Encoder calibration parameters

	lines / rev	counts / line
Joint 1 input encoder	1000	1, 2, or 4
Joint 1 output encoder	2500	1, 2, or 4
Joint 2 input encoder	1000	1, 2, or 4
Joint 3 input encoder	500	1, 2, or 4

A.2 Resolvers

The resolver position information was returned as a 16-bit number representing a fraction of a complete rotation of the resolver shaft. Consequently, to convert this signal into degrees of resolver rotation, the number of resolver counts was multiplied by (360.0

degrees / 2^{16} counts). The resulting value was then converted to degrees of output rotation by factoring in the sensor gear-ratio of 6.66, on joint 2, or 7.2, on joint 3.

The resolver converter electronics could also return an analog voltage proportional to the resolver velocity. Since this information was never used, the resolver velocity was not calibrated.

A.3 Tachometers

The tachometers on joint 1 and 2 were calibrated by simultaneously collecting raw velocity data, measured in A to D counts, and encoder position data, measured in degrees. The tachometer data was then integrated to yield raw position data which was compared to the actual encoder position data to derive a calibration factor. Figures A.1 and A.2 show the linear fits of integrated tachometer position data versus encoder data for the two tachometers. The resulting calibration factors and their associated uncertainty are summarized in table A.2.

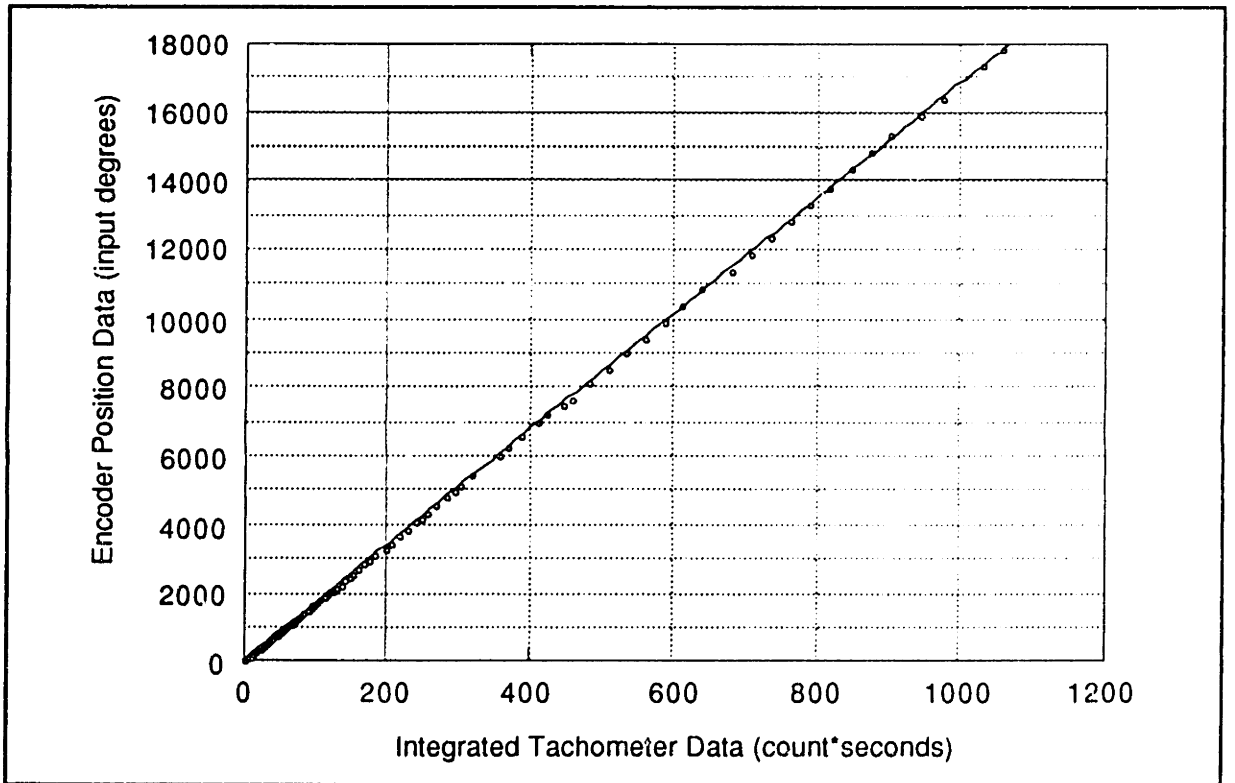

Figure A.1: Linear fit of joint 1 tachometer calibration data

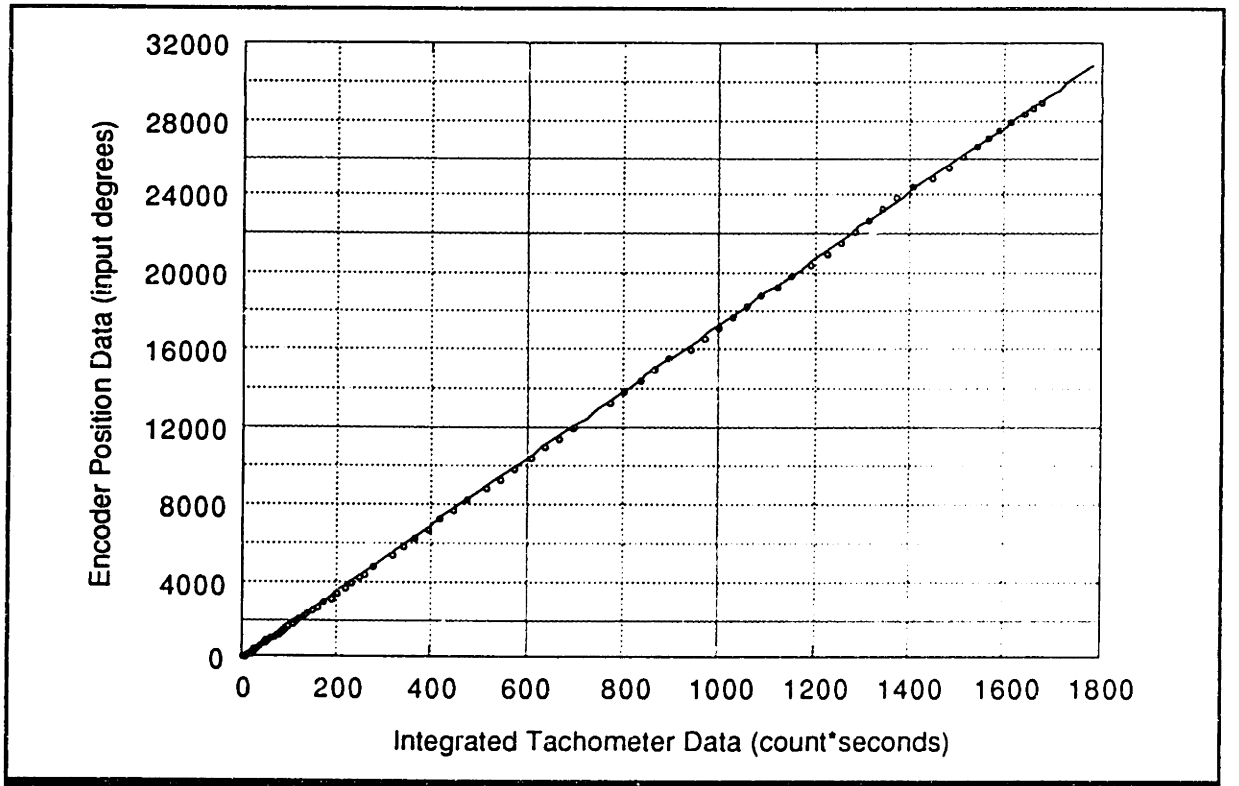

Figure A.2: Linear fit of joint 2 tachometer calibration data

Table A.2: Tachometer calibration factors

	Input °/sec count	uncertainty
Joint 1 input tachometer	16.85	0.4 %
Joint 2 input tachometer	17.33	0.4 %

A.4 Current Sensors

The current produced by the amplifiers used to drive the DC motors was monitored by the A to D board. A to D counts were calibrated against amperes by recording the number of counts for a range of known currents measured with an ammeter. The resulting calibration values are summarized in table A.3 for the three joints.

Table A.3: Current sensor calibration factors	
	amps / count
Joint 1 Current Sensor	0.0115
Joint 2 Current Sensor	0.0122
Joint 3 Current Sensor	0.0115

A.5 Torque Sensors

Torque sensor signals were processed by a conditioning circuit which returned a voltage proportional to the torque experienced by the sensor. This voltage was monitored by a 12-bit A to D channel which read the signal in A to D counts. This A to D reading was calibrated against actual torque measurements produced by a pre-calibrated, JR-3 six-axis force gauge. The calibration procedure for all three joints began by rigidly locking the wave-generator to the circular spline using a specially designed fixture. As illustrated in figure A.3, the force sensor was mounted on the end of the output link for each joint and a force was applied in the direction of joint rotation. By multiplying the force reading by the radius of the applied load, an accurate measurement of the resulting torque was found. Using this method, torque data was collected from both the JR-3 force sensor and the uncalibrated torque sensor over a range of applied loads in both directions. This data is shown in figures A.4 through A.9 for the three sensors in both loading directions. The calibration factors derived from averaging the linear-fits to this data in both direction are summarized in table A.4 for each testing station.

Table A.4: Torque sensor calibration factors			
	N-m / count	in-lb / count	uncertainty
Joint 1 torque sensor	0.0437	0.3864	0.8 %
Joint 2 torque sensor	0.0290	0.2567	0.8 %
Joint 3 torque sensor	0.0065	0.0572	1.8 %

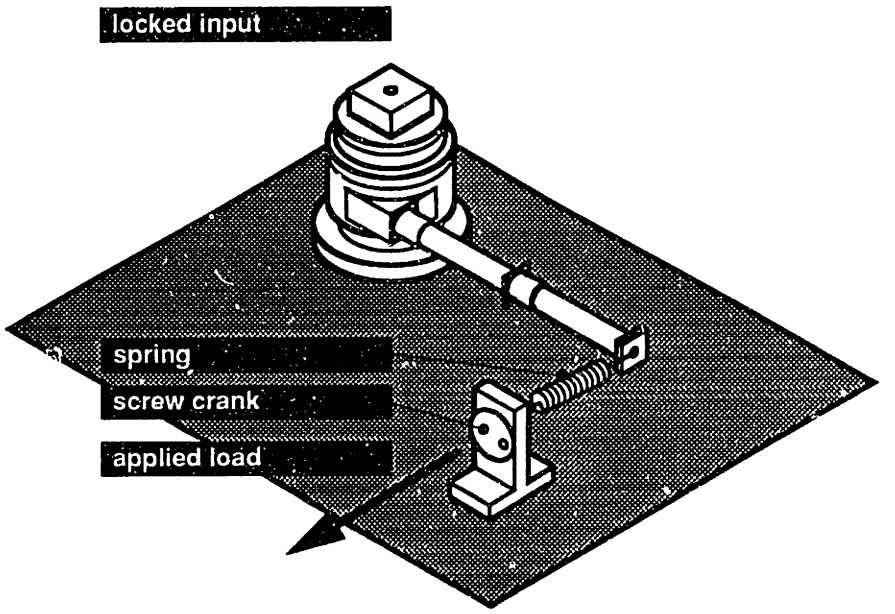

Figure A.3: Experimental apparatus used to calibrate torque sensors

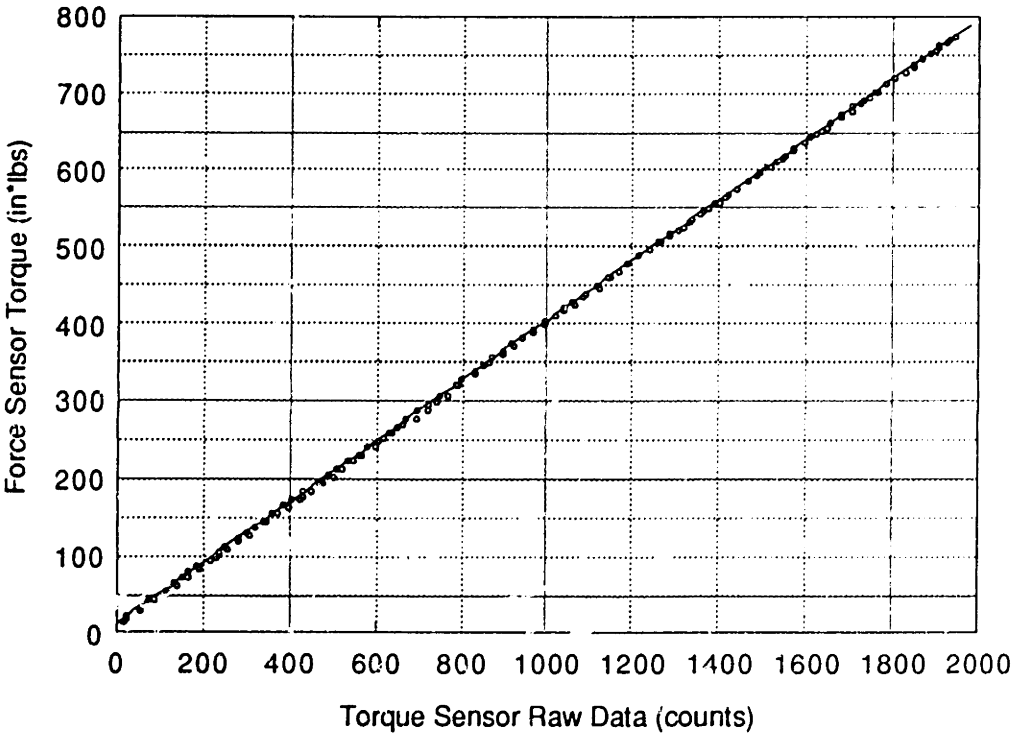

Figure A.4: Joint 4 torque sensor calibration data for positive loading

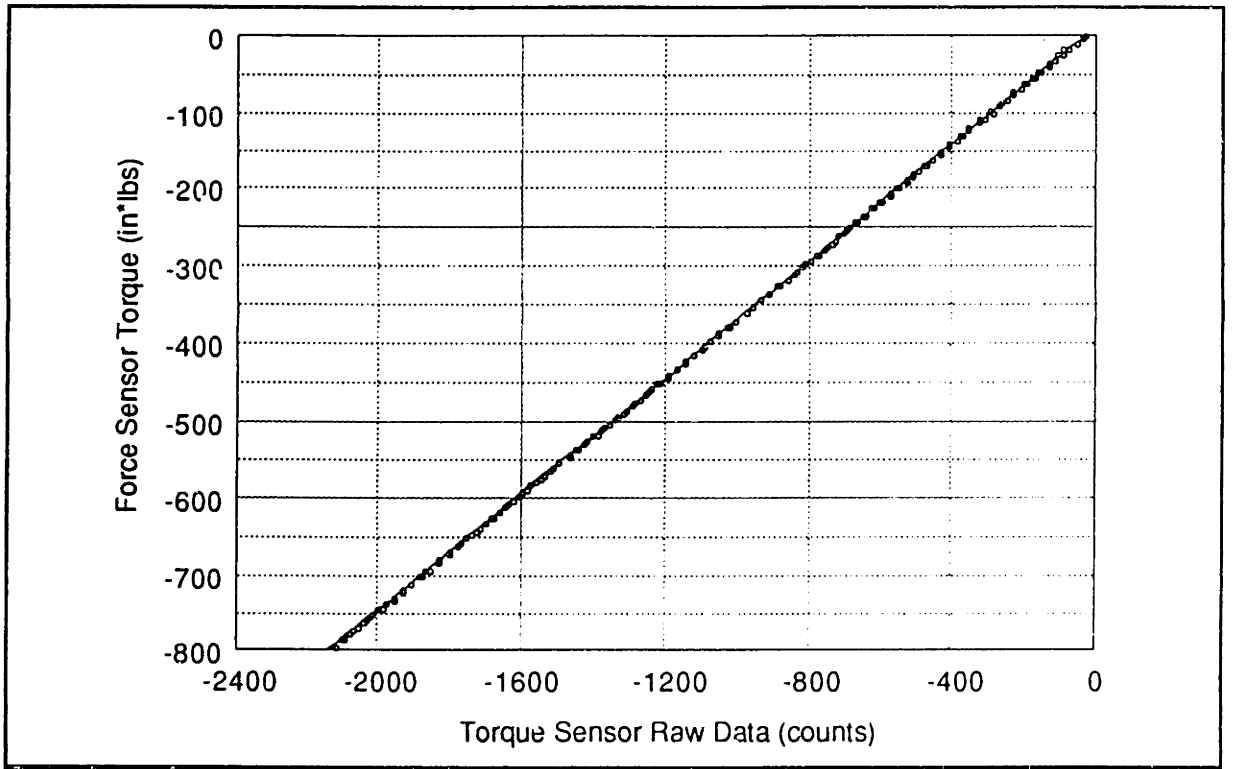

Figure A.5: Joint 1 torque sensor calibration data for negative loading

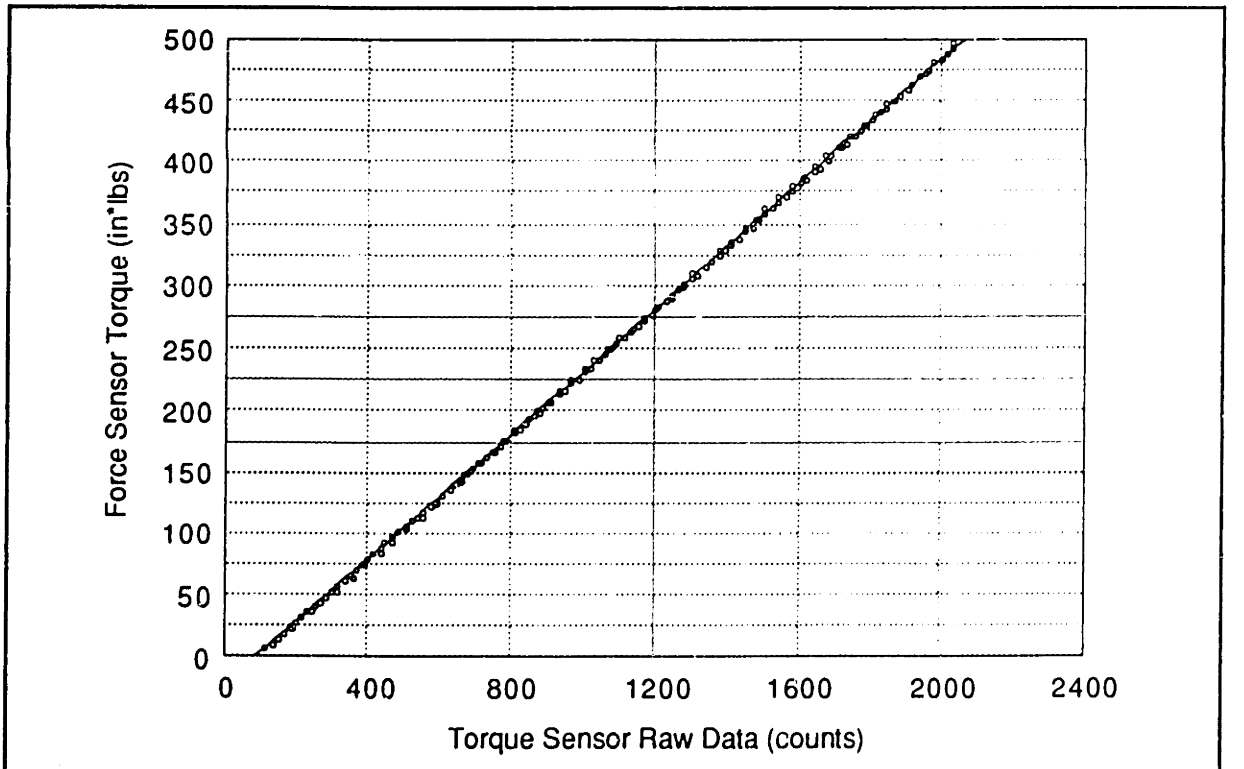

Figure A.6: Joint 2 torque sensor calibration data for positive loading

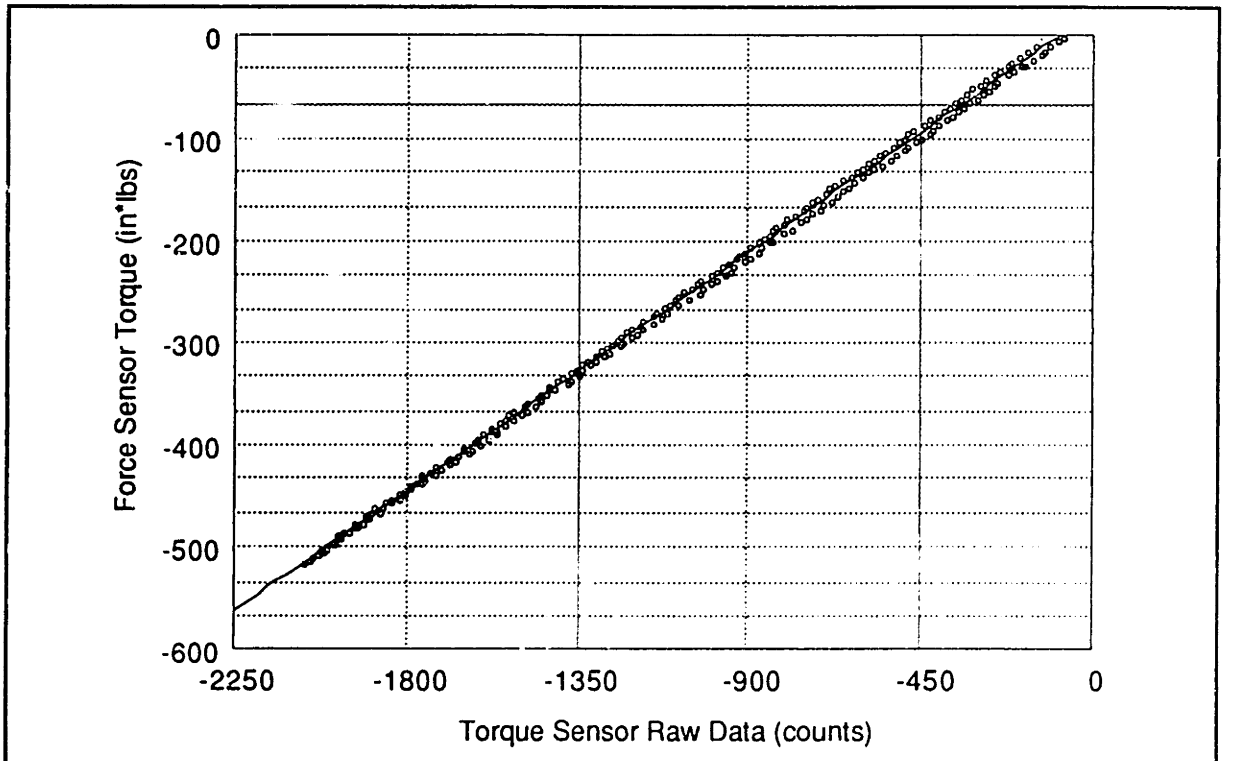

Figure A.7: Joint 2 torque sensor calibration data for negative loading

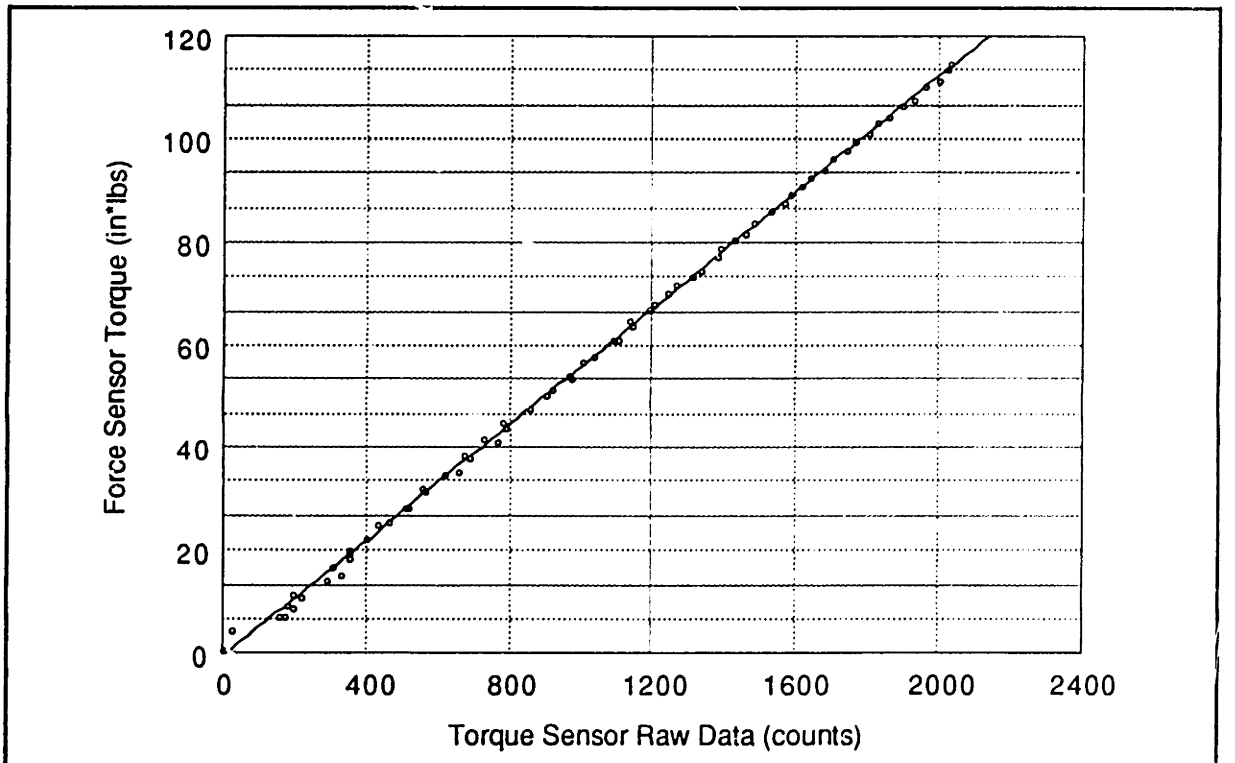

Figure A.8: Joint 3 torque sensor calibration data for positive loading

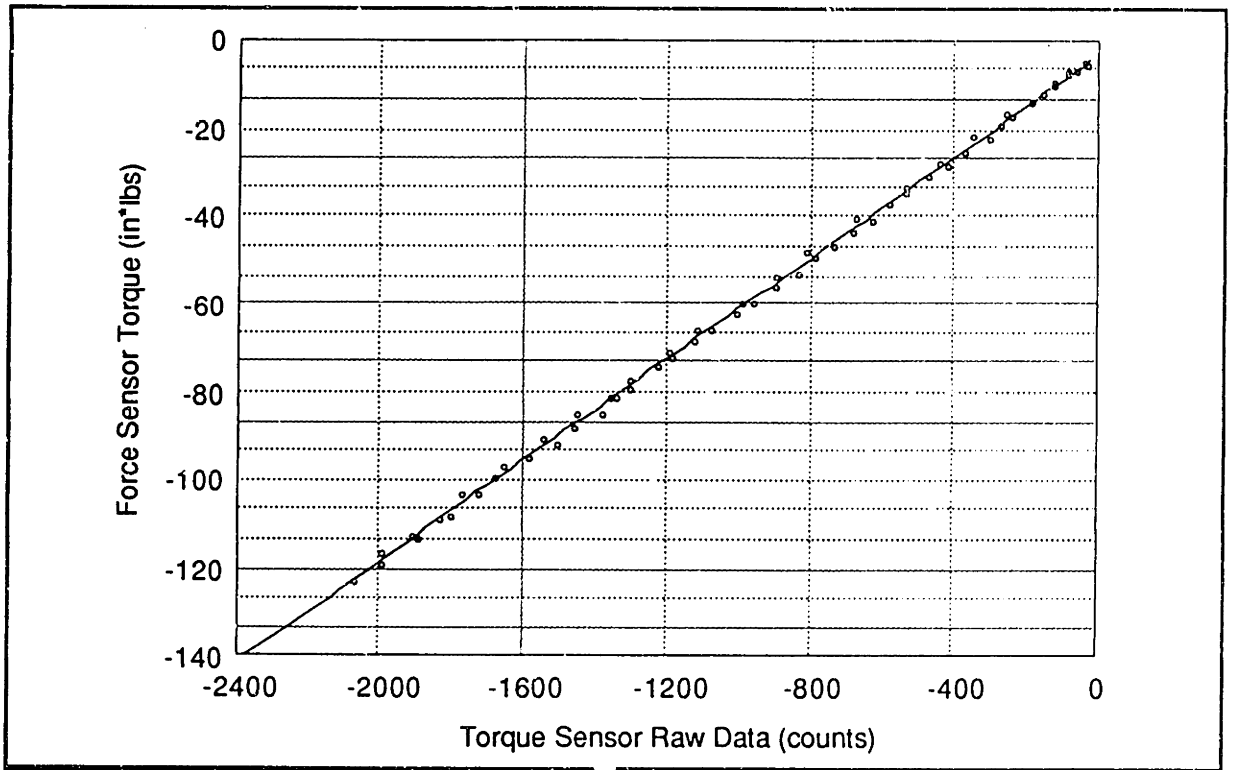

Figure A.9: Joint 3 torque sensor calibration data for negative loading

Appendix B: Simulation Code

The computer code that was used to numerically solve the differential equations describing the dynamic behavior of the different harmonic-drive models is listed in this appendix. The header-file of variable definitions used by this program is also presented after the main program listing. In addition, this program relies on a function, not listed here, which can integrate ordinary differential equations. The function I used was a Runga-Kutta solver with adaptive stepsize control taken largely from reference (85), *Numerical Recipes in C*. During execution, this program reads the input parameters from a file, calculates and integrates the specified equations of motion, and outputs time-response data for the variable names specified in another file. I hope that this code can serve as template for rapid development of future harmonic-drive simulations.

```
/* This is file hd_model.c.  It contains the simulation code used to solve a
 * system of differential equations which characterize the behavior of a
 * harmonic drive.  Included in this file are two function which calculate
 * equations of motion for the two different joint configurations used for
 * the three harmonic-drive testing stations.  The first two joints (shoudler
 * and elbow) use configuration1 and the third joint (wrist) uses the second
 * configuration.  Additionally, code to calculate the equations for two
 * different harmonic-drive models is also included in this file.  This code
 * is located in three separate functions which can be called arbitrarily
 * by any function which calculated the equations of motion of a dynamic
 * system.  If desired, this program can also return the energy distribution
 * in the simulation and the stiffness of the given model. */

#include <stdio.h>
#include <stdlib.h>
#include <math.h>
#include <string.h>
#include "hd_model.h"

/* Declare and initialize the global variables.  */
int debug = FALSE;
int calc_energy = FALSE;
int print_energy = FALSE;
int stiffness_flag = FALSE;
int stiffness_flag2 = FALSE;
int ideal_flag = FALSE;
int fast_plot;
int plot = FALSE;
int model;
int joint = JOINT_TO_TEST;
```

```
int num_selected_output_var = 0;
int system_order = ORDER;
int index[NUM_OF_OUTPUT_VAR];
float current_time;
char graph_title[NUM_OF_OUTPUT_VAR][50];
char graph_units[NUM_OF_OUTPUT_VAR][50];
char output_datafile[NUM_OF_OUTPUT_VAR][100];
char plot_datafile[NUM_OF_OUTPUT_VAR][100];

/* Initialize some useful character strings.      */
char gnuplot_filename[] = "plot_commands.gnu";
char *joint_name[NUM_OF_AXIS] = {"shld", "elb", "wrist"};
char outdatapath[] = "/home/me/tut/robot/hd/model/final_model/simulation_data/";
char indatapath[] = "/home/me/tut/robot/hd/model/final_model/simulation_code/";
char plotdatapath[] = "/home/me/tut/robot/hd/model/final_model/plot_data/";

/* Initialize the array of maximum velocity contraints on the non-linear
 * damping functions for each model. */
float max_friction_vel[HD_MODELS][NUM_OF_AXIS] = {{135.0, 300.0, 500.0},
                                                  {250.0, 550.0, 1000.0}};

/* Declare the functions which contain the equations of motion and the
 * Runge-Kutta solver function which is defined in the file rkqc.c. */
void derivs_config1(double, double *, double *);
void derivs_config2(double, double *, double *);
extern void rkqc(double *,double *,int,double *,double,
                 double,double *,double *,double *,void (*)());

/* Declare the functions which calculate the energy for both of the two
 * joint configurations and the total system energy. */
void calculate_config_energy(double);
void calculate_total_energy(double *, double *);

/* Declare functions which calculate the total equations of motion for the
 * harmonic-drive system when the transmission is ideal.  in this case, the
 * system reduced to a first-order system. */
void derivs_ideal_config1(double, double *, double *);
void derivs_ideal_config2(double, double *, double *);

/* Declare a pointer to a function that will hold the appropriate pointer to
 * the function which will calculate the equations of motion. */
void (*ptr_derivs)(double, double *, double *);

/* Declare the individual functions which calculate the input parameters, dynamic
 * equations and energy values for the different harmonic-drive models. */
void calculate_rotary_params(void);
void rotary_hd_model(double, double, double, double, double, double,
                     double *, double *, double *);
void rotary_hd_energy(double);
void calculate_gear_tooth_params(void);
void gear_tooth_hd_model(double, double, double, double, double, double,
                         double *, double *, double *);
void gear_tooth_hd_energy(double);

/* Now initialize these functions into arrays of function pointers for
 * easy access. */
void (*calculate_params[HD_MODELS])(void)
     = {calculate_rotary_params, calculate_gear_tooth_params};
void (*hd_model[HD_MODELS])(double, double, double, double, double, double,
                            double *, double *, double *)
     = {rotary_hd_model, gear_tooth_hd_model};
void (*hd_energy[HD_MODELS])(double)
     = {rotary_hd_energy, gear_tooth_hd_energy};
```

```
/* Declare the functions which (1) calculate stiffness data, (2) model the
 * saturation limits of the current amplifiers, and (3) determine the static
 * and dynamic friction values, respectively. */
void collect_stiffness_data(void);
double iregulate(double, double, double);
double calculate_friction(double, double, double, double, double,
                          double, double, double, double, double);

/* Declare the rest of the functions. */
void get_arguments(int argc, char **argv);
void usage(void);
void read_input_data(FILE *);
void read_input_filenames(FILE *);
void print_input_parameters(void);
void print_variables(void);
void export_vectors(FILE *, double *, double *, int, char *);
void generate_gnuplot_file(char *);



/*****************************************************************************/
/*                                                                           */
/*    Main Program                                                           */
/*                                                                           */
/*****************************************************************************/


/* This main program opens and reads the input data files, initializes appropriate
 * variables and prints/plots the results. */
main(int argc, char **argv)
{
  int h, i, j;
  int num_of_trials[NUM_OF_AXIS] = {SHLD_NUM_OF_DATA_RUNS,
                                    ELB_NUM_OF_DATA_RUNS,
                                    WRIST_NUM_OF_DATA_RUNS};
  int good_steps[1], bad_steps[1];
  float input_amps[NUM_OF_AXIS][SHLD_NUM_OF_DATA_RUNS] =
    {{1.6, 2.0, 2.4, 2.8, 3.2, 3.6, 4.0, 4.4, 5.0, 6.0},
     {1.4, 1.8, 2.2, 2.6, 3.0, 3.4, 3.8, 4.5, 0.0, 0.0},
     {0.28, 0.36, 0.40, 0.44, 0.48, 0.52, 0.56, 0.60, 0.0, 0.0}};
  char unix_command[200];
  char vector_name[100];
  char *input_datafile[NUM_OF_AXIS] = {"hd_shld_input_data.dat",
                                       "hd_elb_input_data.dat",
                                       "hd_wrist_input_data.dat"};
  FILE *infile;
  FILE *outfile[NUM_OF_OUTPUT_VAR];
  extern int kount;

  /* Read and process the command-line arguments. */
  get_arguments(argc, argv);

  /* Open the input data file for the given joint, read the simulation
   * parameters from the file, and then close the input file. */
  open_file(&infile, indatapath, input_datafile[joint]);
  read_input_data(infile);
  close_file(infile);

  /* Calculate necessary parameters for the given model from the values read
   * from the input file. */
  (*(calculate_params[model]))();

  /* Print out the input data if in debugging mode. */
  if (debug)
```

```
   print_input_parameters();

/* Set the pointer to the appropriate function containing the equations of
 * motion. */
if(joint == WRIST)
  {
    if(ideal_flag)
     ptr_derivs = derivs_ideal_config2;
    else
     ptr_derivs = derivs_config2;
  }
else
  {
    if(ideal_flag)
     ptr_derivs = derivs_ideal_config1;
    else
     ptr_derivs = derivs_config1;
  }

/* If stiffness data is to be collected, jump to the appropriate function. */
if(stiffness_flag)
  collect_stiffness_data();

/* Now read in the data from the other input file that provides information
 * about what data to output. */
open_file(&infile, indatapath, "hd_input_filenames.dat");
read_input_filenames(infile);
close_file(infile);

/* Now if the largest line number in the index[] vector is greater than
 * or equal to the first line of the energy variables in the second
 * input data file, then energy is required as an output, so that the
 * energy flag should be set so that energy is calculated. */
if(index[num_selected_output_var-1] >= TOTAL_ENERGY)
  calc_energy = TRUE;

/* If the energy is to be calculated, increase the order of the system
 * to ORDER+1 in order to accomodate the additional total energy variable
 * which is to be integrated as a member of the state variable. */
if(calc_energy)
  system_order = ORDER + 1;

/* If the -plot option is not selected, set the number of trials to 1. */
if(!plot)
  num_of_trials[joint] = 1;

/* Now run the simulation num_of_trials-times by calling odeint(). Function
 * odeint() contains the Runga-Kutta numerical solver which calls the functions,
 * listed below which calculate the equations of motion for the selected dynamic
 * system. */
for(j = 0; j < num_of_trials[joint]; j++)
  {
    /* Change the value of the requested motor current if necessary. */
    if(plot)
     irequested = input_amps[joint][j];

    /* Restore or initialize the xstart[] values. */
    for(i = 0; i < (ORDER+1); i++)
     xstart[i] = xstart_sav[i];

    printf("\n Starting simulation at %f amps.... \n", irequested);
    odeint(xstart, system_order, initial_time, final_time, EPS, INITIAL_STEP,
          MINIMUM_STEP, good_steps, bad_steps, ptr_derivs, rkqc);
    printf("\n Simulation complete. \n");
```

```
      if(debug)
       {
         printf("\n Number of good steps taken: %d", good_steps[0]);
         printf("\n Number of bad  steps taken: %d\n", bad_steps[0]);
       }

      /* Initialize all output files, export the desired output data to them,
       * and close the files.  If the -plot option is selected, then save
       * the specified data in the plot_data directory with the appropriate
       * filename. */
      for(i = 0; i < num_selected_output_var; i++)
       {
         if(plot)
           {
             sprintf(plot_datafile[i], "%s.%4.2famps",
                    output_datafile[i], input_amps[joint][j]);
             create_file(&(outfile[i]), plotdatapath, plot_datafile[i]);
             export_vectors(outfile[i], time, output_data[i+1], kount,
                          output_datafile[i]);
           }
         else
           {
             create_file(&(outfile[i]), outdatapath, output_datafile[i]);
             export_vectors(outfile[i], time, output_data[i+1], kount,
                          output_datafile[i]);
           }
         close_file(outfile[i]);
       }

      /* Now plot the results using xgraph, if slow printable plotting is desired,
       * or gnuplot, if the fast_plot option is selected. */
      if(!plot)
       {
         if(fast_plot)
           {
             generate_gnuplot_file(gnuplot_filename);
             sprintf(unix_command, "gnuplot %s%s", outdatapath, gnuplot_filename);
             printf("\n Executing the unix command: %s\n", unix_command);
             system(unix_command);
           }
         else
           {
             for(i = 0; i < num_selected_output_var; i++)
              {

                sprintf(unix_command, "xgraph %s%s -t Harmonic_Drive_Simulation\
                  -y %s_%s -x Time_sec &", outdatapath, output_datafile[i],
                        graph_title[i], graph_units[i]);
                printf("\n Executing the unix command: %s\n", unix_command);
                system(unix_command);
              }
           }
       }
    }
}



/*****************************************************************************/
/*                                                                           */
/*    Functions which describe the dynamics of the two joint configurations. */
/*                                                                           */
/*****************************************************************************/
```

```
/* Function derivs_config1() can be used to solve the equations of motion for the
 * harmonic drive joint configuration in which: (1) the motor drives the wave-
 * generator and is mounted to the circular spline, (2) the flexspline is attached
 * tc ground, and (3) the circular spline is the output port. */
void derivs_config1(t, x, dxdt)
double t;
double x[], dxdt[];
{
  /* Set the global time variable to the current time. */
  current_time = t;

  /* Set the local variable definitions to the value of the state variable
   * determined on the previous step. */
  v[POS_IN]  = x[POS_IN_INDEX];
  v[POS_OUT] = x[POS_OUT_INDEX];
  v[VEL_IN]  = x[VEL_IN_INDEX];
  v[VEL_OUT] = x[VEL_OUT_INDEX];

  /* From these positions and velocities, call the appropriate harmonic drive
   * model to calculate the resulting torques. */
  (*(hd_model[model]))(v[POS_IN], 0.0, v[POS_OUT],
                       v[VEL_IN], 0.0, v[VEL_OUT],
                       &(v[TORQUE_WG]), &(v[TORQUE_FS]), &(v[TORQUE_CS]));

  /* Set the value of torque sensor to the torque read on the flexspline. */
  v[TORQUE_SENSOR] = -v[TORQUE_FS];

  /* Calculate the motor torque as a function of current:
   * Note that the current, iactual, is calculated by the function
   * iregulate() which takes into account the non-linear behavior of the
   * current amps. Note that v[CURRENT_SENSOR] must be initialized to zero.
   * Recall that the relative velocity of the motor is the absolute motor
   * velocity minus the absolute output velocity. */
  v[CURRENT_SENSOR] = iregulate(v[CURRENT_SENSOR], irequested,
                                (v[VEL_IN] - v[VEL_OUT]));
  v[TORQUE_MOTOR] = motor_kt * v[CURRENT_SENSOR];

  /* Calculate the input and output damping. */
  v[TORQUE_B_IN] = b_in * (v[VEL_IN] - v[VEL_OUT]);
  v[TORQUE_B_OUT] = b_out * v[VEL_OUT];

  /* Finally, calculate the equations of motion. */
  dxdt[POS_IN_INDEX] = v[VEL_IN];
  dxdt[VEL_IN_INDEX] = (1.0 / (CONV * inertia_in)) * (v[TORQUE_MOTOR] -
                                                      v[TORQUE_B_IN] -
                                                      v[TORQUE_WG]);
  dxdt[POS_OUT_INDEX] = v[VEL_OUT];
  dxdt[VEL_OUT_INDEX] = (1.0 / (CONV * inertia_out)) * (v[TORQUE_CS] -
                                                        v[TORQUE_B_OUT] +
                                                        v[TORQUE_B_IN]);

  /* Now calculate the values that the sensors actually read. */
  v[INPUT_POSITION_SENSOR] = v[POS_IN] - v[POS_OUT];
  v[INPUT_VELOCITY_SENSOR] = v[VEL_IN] - v[VEL_OUT];
  v[OUTPUT_POSITION_SENSOR] = v[POS_OUT];
  v[OUTPUT_VELOCITY_SENSOR] = v[VEL_OUT];
  v[POSITION_ERROR] = (v[INPUT_POSITION_SENSOR] / N) - v[OUTPUT_POSITION_SENSOR];

  /* If the total energy is selected as an output variable, call
   * the function that calculates the total power and integrates
   * it using the runga-kutta solver.  */
  if(calc_energy)
    calculate_total_energy(x, dxdt);
```

```
  /* If the debugging option is selected, call the function to print
   * out some variables. */
  if(debug)
    print_variables();
}



/* Function derivs_config2() can be used to solve the equations of motion for
 * the harmonic drive joint configuration in which: (1) the motor drives the
 * wave-generator and is mounted to the circular spline, (2) the flexspline is
 * attached to the output link, and (3) the circular spline attached to ground. */
void derivs_config2(t, x, dxdt)
double t;
double x[], dxdt[];
{
  /* Set the global time variable to the current time. */
  current_time = t;

  /* Set the local variable definitions to the value of the state variable
   * determined on the previous step. */
  v[POS_IN]  = x[POS_IN_INDEX];
  v[POS_OUT] = x[POS_OUT_INDEX];
  v[VEL_IN]  = x[VEL_IN_INDEX];
  v[VEL_OUT] = x[VEL_OUT_INDEX];

  /* From these positions and velocities, call the appropriate harmonic drive
   * model to calculate the resulting torques. */
  (*(hd_model[model]))(v[POS_IN], v[POS_OUT], 0.0,
                       v[VEL_IN], v[VEL_OUT], 0.0,
                       &(v[TORQUE_WG]), &(v[TORQUE_FS]), &(v[TORQUE_CS]));

  /* Calculate the motor torque as a function of current:
   * Note that the current, iactual, is calculated by the function
   * iregulate() which takes into account the non-linear behavior of the
   * current amps.  Note that v[CURRENT_SENSOR] must be initialized to zero. */
  v[CURRENT_SENSOR] = iregulate(v[CURRENT_SENSOR], irequested, v[VEL_IN]);
  v[TORQUE_MOTOR] = motor_kt * v[CURRENT_SENSOR];

  /* Calculate the input and output damping. */
  v[TORQUE_B_IN] = b_in * v[VEL_IN];
  v[TORQUE_B_OUT] = b_out * v[VEL_OUT];

  /* The torque sensor is mounted between the motor and circular spline and
   * ground, and therefore sees the reaction torque from the motor, the motor
   * damping torque, and the circular spline torque. */
  v[TORQUE_SENSOR] = v[TORQUE_CS] - v[TORQUE_MOTOR] + v[TORQUE_B_IN];

  /* Finally, calculate the equations of motion. */
  dxdt[POS_IN_INDEX] = v[VEL_IN];
  dxdt[VEL_IN_INDEX] = (1.0 / (CONV * inertia_in)) * (v[TORQUE_MOTOR] -
                                                      v[TORQUE_B_IN] -
                                                      v[TORQUE_WG]);
  dxdt[POS_OUT_INDEX] = v[VEL_OUT];
  dxdt[VEL_OUT_INDEX] = (1.0 / (CONV * inertia_out)) * (-v[TORQUE_FS] -
                                                        v[TORQUE_B_OUT]);

  /* Now calculate the values that the sensors actually read. */
  v[INPUT_POSITION_SENSOR] = v[POS_IN];
  v[INPUT_VELOCITY_SENSOR] = v[VEL_IN];
  v[OUTPUT_POSITION_SENSOR] = v[POS_OUT];
  v[OUTPUT_VELOCITY_SENSOR] = v[VEL_OUT];
  v[POSITION_ERROR] = (v[INPUT_POSITION_SENSOR] / N) + v[OUTPUT_POSITION_SENSOR];
```

```
  /* If the total energy is selected as an output variable, call
   * the function that calculates the total power and integrates
   * it using the runga-kutta solver. */
  if(calc_energy)
    calculate_total_energy(x, dxdt);

  /* If the debugging option is selected, call the function to print
   * out some variables. */
  if(debug)
    print_variables();
}



/*****************************************************************************/
/*                                                                           */
/*    Functions which describe the energy of the two joint configurations.   */
/*                                                                           */
/*****************************************************************************/


/* Function calculate_total_energy() calculates the total power in the system
 * of equations presented in derivs_config1() or derivs_config2().  This power
 * is determined on every time step and stored in the state vector which is
 * is solved by the Runge-Kutta solver.  This can be used to verify that energy
 * is being conserved in both dynamic models. */
void calculate_total_energy(x, dxdt)
double x[], dxdt[];
{
  double power_b_in, power_hd_out;

  /* First store the integrated power in the total energy variable. */
  v[TOTAL_ENERGY]= x[ENERGY];

  /* Now calculate the input damping power loss depending on the joint
   * configuration.  Also calculate the appropriate torque on the output
   * port of the harmonic drive. */
  if(joint == WRIST)
    {
      power_b_in = v[TORQUE_B_IN] * (v[VEL_IN]*CONV);
      power_hd_out = -v[TORQUE_FS] *  (v[VEL_OUT]*CONV);
    }
  else
    {
      power_b_in = v[TORQUE_B_IN] * ((v[VEL_IN] - v[VEL_OUT])*CONV);
      power_hd_out = v[TORQUE_CS] *  (v[VEL_OUT]*CONV);
    }

  /* Calculate the total instantaneous power in the system. */
  dxdt[ENERGY] = ((v[TORQUE_MOTOR] * (v[VEL_IN]*CONV)) -
                 (inertia_in * (v[VEL_IN]*CONV) * (dxdt[VEL_IN_INDEX]*CONV)) -
                 (inertia_out * (v[VEL_OUT]*CONV) * (dxdt[VEL_OUT_INDEX]*CONV)) -
                 (v[TORQUE_WG] * (v[VEL_IN]*CONV)) +
                 (power_hd_out) -
                 (power_b_in) -
                 (v[TORQUE_B_OUT] * (v[VEL_OUT]*CONV)));
}



/* Function calculate_config_energy() is called by the function odeint() after
 * each complete time step.  This function takes the current simulation time
 * step and uses a simple Euler integration scheme to determine the energy in
```

```
 * the system, excluding the harmonic drive.  Since this function relies on
 * values calculated in the harmonic drive energy function, it should be called
 * after the specific harmonic-drive energy function is called.  Due to the
 * similarities between the equations in derivs_config1() and derivs_config2(),
 * this energy function is valid for both models. */
void calculate_config_energy(delta_t)
double delta_t;
{
  double vel_in_rad, vel_out_rad;

  /* Be sure that all velocities and positions are in radians to ensure
   * proper unit-matching. */
  vel_in_rad = v[VEL_IN] * CONV;
  vel_out_rad = v[VEL_OUT] * CONV;

  /* Calculate the energy input by the motor to the system by integrating
   * its power input over time. */
  v[MOTOR_ENERGY] = v[MOTOR_ENERGY] +  (delta_t * v[TORQUE_MOTOR] * vel_in_rad);

  /* Calculate the kinetic energy of the inertias from (I*(w^2)/2). */
  v[KINETIC_ENERGY_IN] = (inertia_in * vel_in_rad * vel_in_rad) / 2.0;
  v[KINETIC_ENERGY_OUT] = (inertia_out * vel_out_rad * vel_out_rad) / 2.0;

  /* Calculate the damping energy by integrating the power dissipation over
   * time. */
  if(joint == WRIST)
    v[INPUT_DAMPING_ENERGY] = (v[INPUT_DAMPING_ENERGY] +
                               (delta_t * (v[TORQUE_B_IN] * vel_in_rad)));
  else
    v[INPUT_DAMPING_ENERGY] = (v[INPUT_DAMPING_ENERGY] +
                               (delta_t * (v[TORQUE_B_IN] *
                                           (vel_in_rad - vel_out_rad))));
  v[OUTPUT_DAMPING_ENERGY] = (v[OUTPUT_DAMPING_ENERGY] +
                              (delta_t * (v[TORQUE_B_OUT] * vel_out_rad)));

  /* Now calculate some aggregate quantities.  */
  v[TOTAL_KINETIC_ENERGY] = v[KINETIC_ENERGY_IN] + v[KINETIC_ENERGY_OUT];
  v[TOTAL_INPUT_ENERGY] = v[MOTOR_ENERGY];
  v[TOTAL_LOST_ENERGY] = (v[INPUT_DAMPING_ENERGY] +
                          v[WG_FRICTION_ENERGY] +
                          v[TOOTH_TIP_FRICTION_ENERGY] +
                          v[TOOTH_SURFACE_TOTAL_LOSS_ENERGY] +
                          v[OUTPUT_DAMPING_ENERGY]);

  /* Now print out the energy values if the print_energy option is selected. */
  if (print_energy)
    {
      printf("\n total energy:              %25.20lf", v[TOTAL_ENERGY]);
      printf("\n total kinetic energy:      %20.15lf", v[TOTAL_KINETIC_ENERGY]);
      printf("\n total potential energy:    %20.15lf", v[TOTAL_POTENTIAL_ENERGY]);
      printf("\n total input energy:        %20.15lf", v[TOTAL_INPUT_ENERGY]);
      printf("\n total lost energy:         %20.15lf", v[TOTAL_LOST_ENERGY]);
      printf("\n motor energy:              %20.15lf", v[MOTOR_ENERGY]);
      printf("\n kinetic energy in:         %20.15lf", v[KINETIC_ENERGY_IN]);
      printf("\n kinetic energy out:        %20.15lf", v[KINETIC_ENERGY_OUT]);
      printf("\n spring energy:             %20.15lf", v[SPRING_ENERGY]);
      printf("\n cyclic torque energy:      %20.15lf", v[CYCLIC_ENERGY]);
      printf("\n delta_t:                   %20.15lf", delta_t);
      printf("\n");
    }
}
```

```
/*****************************************************************************/
/*                                                                           */
/*    Functions which describe behavior of system with ideal transmission.   */
/*                                                                           */
/*****************************************************************************/

/* Function derivs_ideal_config1() calculates the equations of motion for a
 * configuration-1 sytstem that has an ideal harmonic-drive transmission. */
void derivs_ideal_config1(t, x, dxdt)
double t;
double x[], dxdt[];
{
  /* Set the global time variable to the current time. */
  current_time = t;

  /* Set the local variable definitions to the value of the state variable
   * determined on the previous step. */
  v[POS_IN]  = x[POS_IN_INDEX];
  v[POS_OUT] = x[POS_OUT_INDEX];
  v[VEL_IN]  = x[VEL_IN_INDEX];
  v[VEL_OUT] = x[VEL_OUT_INDEX];

  /* Calculate the motor torque as a function of current.  For the ideal
   * model, assume that the current amps function ideally as well. */
  v[CURRENT_SENSOR] = irequested;
  v[TORQUE_MOTOR] = motor_kt * v[CURRENT_SENSOR];

  /* Calculate the input and output damping. */
  v[TORQUE_B_IN] = b_in * (v[VEL_IN] - v[VEL_OUT]);
  v[TORQUE_B_OUT] = b_out * v[VEL_OUT];

  /* Finally, calculate the equations of motion. */
  dxdt[POS_IN_INDEX] = v[VEL_IN];
  dxdt[VEL_IN_INDEX] = ((1.0 / (CONV * (inertia_in +
                                  (inertia_out/((N+1.0)*(N+1.0)))))) *
                      (v[TORQUE_MOTOR] - v[TORQUE_B_IN] -
                       ((v[TORQUE_B_OUT] - v[TORQUE_B_IN])/(N+1.0))));
  dxdt[POS_OUT_INDEX] = dxdt[POS_IN_INDEX]/(N+1.0);
  dxdt[VEL_OUT_INDEX] = dxdt[VEL_IN_INDEX]/(N+1.0);

  /* Now calculate the values that the sensors actually read. */
  v[INPUT_POSITION_SENSOR] = v[POS_IN] - v[POS_OUT];
  v[INPUT_VELOCITY_SENSOR] = v[VEL_IN] - v[VEL_OUT];
  v[OUTPUT_POSITION_SENSOR] = v[POS_OUT];
  v[OUTPUT_VELOCITY_SENSOR] = v[VEL_OUT];
  v[POSITION_ERROR] = (v[INPUT_POSITION_SENSOR] / N) - v[OUTPUT_POSITION_SENSOR];
  v[TORQUE_FS] = (-N/(N+1.0)) * (((CONV * inertia_in) *
                                  (dxdt[VEL_IN_INDEX]/(N+1.0))) +
                                 v[TORQUE_B_OUT] - v[TORQUE_B_IN]);
  v[TORQUE_SENSOR] = -v[TORQUE_FS];

  /* Calculate the torques on the remaining harmonic-drive ports. */
  v[TORQUE_WG] = (-1.0/N) * v[TORQUE_FS];
  v[TORQUE_CS] = (-(N+1.0)/N) * v[TORQUE_FS];

  /* If the total energy is selected as an output variable, call
   * the function that calculates the total power and integrates
   * it using the runga-kutta solver.  */
  if(calc_energy)
    calculate_total_energy(x, dxdt);

  /* If the debugging option is selected, call the function to print
   * out some variables. */
  if(debug)
```

```
    print_variables();
}



/* Function derivs_ideal_config2() calculates the equations of motion for a
 * configuration-2 sytstem that has an ideal harmonic-drive transmission. */
void derivs_ideal_config2(t, x, dxdt)
double t;
double x[], dxdt[];
{
  /* Set the global time variable to the current time. */
  current_time = t;

  /* Set the local variable definitions to the value of the state variable
   * determined on the previous step. */
  v[POS_IN]  = x[POS_IN_INDEX];
  v[POS_OUT] = x[POS_OUT_INDEX];
  v[VEL_IN]  = x[VEL_IN_INDEX];
  v[VEL_OUT] = x[VEL_OUT_INDEX];

  /* Calculate the motor torque as a function of current.  For the ideal
   * model, assume that the current amps function ideally as well. */
  v[CURRENT_SENSOR] = irequested;
  v[TORQUE_MOTOR] = motor_kt * v[CURRENT_SENSOR];

  /* Calculate the input and output damping. */
  v[TORQUE_B_IN] = b_in * v[VEL_IN];
  v[TORQUE_B_OUT] = b_out * v[VEL_OUT];

  /* Finally, calculate the equations of motion. */
  dxdt[POS_IN_INDEX] = v[VEL_IN];
  dxdt[VEL_IN_INDEX] = ((1.0 / (CONV * (inertia_in - (inertia_out/(N*N))))) *
                        (v[TORQUE_MOTOR] - v[TORQUE_B_IN] -
                         (v[TORQUE_B_OUT]/N)));
  dxdt[POS_OUT_INDEX] = dxdt[POS_IN_INDEX] / (-N);
  dxdt[VEL_OUT_INDEX] = dxdt[VEL_IN_INDEX] / (-N);

  /* Now calculate the values that the sensors actually read. */
  v[INPUT_POSITION_SENSOR] = v[POS_IN] - v[POS_OUT];
  v[INPUT_VELOCITY_SENSOR] = v[VEL_IN] - v[VEL_OUT];
  v[OUTPUT_POSITION_SENSOR] = v[POS_OUT];
  v[OUTPUT_VELOCITY_SENSOR] = v[VEL_OUT];
  v[POSITION_ERROR] = (v[INPUT_POSITION_SENSOR] / N) + v[OUTPUT_POSITION_SENSOR];
  v[TORQUE_FS] = -(((CONV * inertia_out) * (dxdt[VEL_IN_INDEX]/(-N))) +
                   v[TORQUE_B_OUT]);

  /* Calculate the torques on the remaining harmonic-drive ports. */
  v[TORQUE_WG] = (-1.0/N) * v[TORQUE_FS];
  v[TORQUE_CS] = (-(N+1.0)/N) * v[TORQUE_FS];

  /* The torque sensor is mounted between the motor and circular spline and
   * ground, and therefore sees the reaction torque from the motor, the motor
   * damping torque, and the circular spline torque. */
  v[TORQUE_SENSOR] = v[TORQUE_CS] - v[TORQUE_MOTOR] + v[TORQUE_B_IN];

  /* If the total energy is selected as an output variable, call
   * the function that calculates the total power and integrates
   * it using the runga-kutta solver.  */
  if(calc_energy)
    calculate_total_energy(x, dxdt);

  /* If the debugging option is selected, call the function to print
   * out some variables. */
```

```
  if(debug)
    print_variables();
}



/*****************************************************************************/
/*                                                                           */
/*   Functions determining equations for two different harmonic-drive models.*/
/*                                                                           */
/*****************************************************************************/


/* Function rotary_hd_model() calculates the three-port harmonic-drive
 * equations for a non-ideal rotational model. */
void rotary_hd_model(pos_wg, pos_fs, pos_cs,
                     vel_wg, vel_fs, vel_cs,
                     torque_wg, torque_fs, torque_cs)
double pos_wg, pos_fs, pos_cs;
double vel_wg, vel_fs, vel_cs;
double *torque_wg, *torque_fs, *torque_cs;
{
  /* Store the velocities and positions and the fs, cs, and wg ports
   * in the global data vector to begin calculations. */
  v[POS_WG] = pos_wg;
  v[POS_FS] = pos_fs;
  v[POS_CS] = pos_cs;
  v[VEL_WG] = vel_wg;
  v[VEL_FS] = vel_fs;
  v[VEL_CS] = vel_cs;

  /* Calculate the continuity constraint of the cyclic torque. */
  v[POS_K] = v[POS_WG];
  v[VEL_K] = v[VEL_WG];

  /* Calculate some other continuity constraints. */
  v[POS_N_FS] = v[POS_FS];
  v[VEL_N_FS] = v[VEL_FS];
  v[POS_N_CS] = v[POS_CS];
  v[VEL_N_CS] = v[VEL_CS];

  /*  Determine the kinematic error function and its derivative such that
   *  (d/dt)v[ERFN] = v[VEL_WG] v[DERF]. */
  v[ERFN] = ((error_amplitude0 * Sin(((1.0 * v[POS_WG]) + error_phase0) * CONV)) +
             (error_amplitude1 * Sin(((2.0 * v[POS_WG]) + error_phase1) * CONV)) +
             (error_amplitude2 * Sin(((4.0 * v[POS_WG]) + error_phase2) * CONV)));
  v[DERF] = ((1.0 * CONV * error_amplitude0 *
              Cos(((1.0 * v[POS_WG]) + error_phase0) * CONV)) +
             (2.0 * CONV * error_amplitude1 *
              Cos(((2.0 * v[POS_WG]) + error_phase1) * CONV)) +
             (4.0 * CONV * error_amplitude2 *
              Cos(((4.0 * v[POS_WG]) + error_phase2) * CONV)));

  /* Now calculate the position and velocity equations imposed by the
   * three-port hamonic-drive gear-reduction with position error included. */
  v[POS_N_WG] = (((N + 1.0) * v[POS_N_CS]) -
                 (N * v[POS_N_FS]) +
                 (N * v[ERFN]));
  v[VEL_N_WG] = (((N + 1.0) * v[VEL_N_CS]) -
                 (N * v[VEL_N_FS]) +
                 (N * v[VEL_WG] * v[DERF]));

  /* Calculate the static, dynamic, and cyclic friction which acts between the
   * circular spline and flexspline. */
```

```
  v[VEL_HD_FRICTION] = v[VEL_N_CS] - v[VEL_N_FS];
  v[TORQUE_HD_FRICTION] =
    calculate_friction(v[VEL_HD_FRICTION],
                       b_hd_constant, b_hd1, b_hd2,
                       stiction_torque_hd, stiction_vel_hd,
                       v[POS_OUT],
                       cyclic_friction_amp_hd, cyclic_friction_phase_hd,
                       (max_friction_vel[model][joint]));

  /* For the sake of continuity in the simulation, ramp the constant friction
   * in the harmonic drive from zero to the desired value if at the
   * beginning of the step-response trial.  */
  if(!(stiffness_flag || stiffness_flag2))
    if(current_time < 0.05)
      v[TORQUE_HD_FRICTION] = ((((current_time - 0.05)/0.05) + 1.0) *
                               v[TORQUE_HD_FRICTION]);

  /* Find the harmonic drive stiffness coefficients:  */
  v[K1] = (k1_constant +
           k1_amplitude * Sin(((2.0 * v[POS_WG]) + k1_phase) * CONV));
  v[K2] = (k2_constant +
           k2_amplitude * Sin(((2.0 * v[POS_WG]) + k2_phase) * CONV));

  /* Calculate the torque on the spring. */
  v[TORQUE_K] = ((v[K1] * (v[POS_K] - v[POS_N_WG])) +
                 (v[K2] * Power((v[POS_K] - v[POS_N_WG]), 3)));

  /* Calculate the compatibility, or torque-balance, requirement. */
  v[TORQUE_N_WG] = v[TORQUE_K];

  /* Calculate the cyclic torque. */
  v[TORQUE_CYCLIC] = (cyclic_amplitude *
                      Sin(((2.0 * v[POS_WG]) + cyclic_phase) * CONV));

  /* Now apply the torque constraint imposed by the three-port gear-reduction
   * with position error included.  Note that the torque on the flexspline
   * is defined to be positive in the negative rotation direction. */
  v[TORQUE_N_FS] = -((-N / (1.0 - (N * v[DERF]))) * v[TORQUE_N_WG]);
  v[TORQUE_N_CS] = ((N + 1.0) / (1.0 - (N * v[DERF]))) * v[TORQUE_N_WG];

  /* Finally, calculate the torque on all of the harmonic-drive ports. */
  v[TORQUE_WG] = v[TORQUE_K] - v[TORQUE_CYCLIC];
  v[TORQUE_FS] = v[TORQUE_N_FS] - v[TORQUE_HD_FRICTION];
  v[TORQUE_CS] = v[TORQUE_N_CS] - v[TORQUE_HD_FRICTION];

  /* Finally, return the torques on the three hd ports. */
  *torque_wg = v[TORQUE_WG];
  *torque_fs = v[TORQUE_FS];
  *torque_cs = v[TORQUE_CS];
}



/* Function gear_tooth_hd_model() calculates the three-port harmonic-drive
 * equations for the harmonic drive representation which uses inclined planes to
 * simulate the tooth-rubbing behavior inside the drive. */
void gear_tooth_hd_model(pos_wg, pos_fs, pos_cs,
                         vel_wg, vel_fs, vel_cs,
                         torque_wg, torque_fs, torque_cs)
double pos_wg, pos_fs, pos_cs;
double vel_wg, vel_fs, vel_cs;
double *torque_wg, *torque_fs, *torque_cs;
{
  /* Store the velocities and positions and the fs, cs, and wg ports
```

```
 * in the global data vector to begin calculations. */
v[POS_WG] = pos_wg;
v[POS_FS] = pos_fs;
v[POS_CS] = pos_cs;
v[VEL_WG] = vel_wg;
v[VEL_FS] = vel_fs;
v[VEL_CS] = vel_cs;

/* First, calculate the continuity (or kinematic) constraints.
 *
 * Find the velocity of the wave-generator with respect to the flexspline. */
v[POS_WG_RELATIVE] = v[POS_WG] - v[POS_FS];
v[VEL_WG_RELATIVE] = v[VEL_WG] - v[VEL_FS];

/*  Determine the kinematic error function and its derivative such that
 *  (d/dt)v[ERFN] = v[VEL_WG_RELATIVE] v[DERF]. */
v[ERFN] = (N*tanl * ((error_amplitude0 *
                     Sin(((1.0 * v[POS_WG_RELATIVE]) + error_phase0) * CONV)) +
                     (error_amplitude1 *
                     Sin(((2.0 * v[POS_WG_RELATIVE]) + error_phase1) * CONV)) +
                     (error_amplitude2 *
                     Sin(((4.0 * v[POS_WG_RELATIVE]) + error_phase2) * CONV))));
v[DERF] = (N*tanl * ((1.0 * CONV * error_amplitude0 *
                     Cos(((1.0 * v[POS_WG_RELATIVE]) + error_phase0) * CONV)) +
                     (2.0 * CONV * error_amplitude1 *
                     Cos(((2.0 * v[POS_WG_RELATIVE]) + error_phase1) * CONV)) +
                     (4.0 * CONV * error_amplitude2 *
                     Cos(((4.0 * v[POS_WG_RELATIVE]) + error_phase2) * CONV))));

/* Find the radial (vertical) movement of the tooth base. */
v[POS_TOOTH_BASE] = tanl * v[POS_WG_RELATIVE];
v[VEL_TOOTH_BASE] = tanl * v[VEL_WG_RELATIVE];

/* Find the radial movement at the output of the position error element.  */
v[POS_ERR] = v[POS_TOOTH_BASE] + v[ERFN];
v[VEL_ERR] = v[VEL_TOOTH_BASE] + (v[VEL_WG_RELATIVE] * v[DERF]);

/* Find the radial movement of the tooth tip. */
v[POS_TOOTH_TIP] = (v[POS_CS] - v[POS_FS]) / tan2;
v[VEL_TOOTH_TIP] = (v[VEL_CS] - v[VEL_FS]) / tan2;

/* Find the velocity at the wave-generator surface. */
v[POS_WG_SURFACE] = ((cosl * v[POS_WG]) +
                    (sinl * v[POS_TOOTH_BASE]) -
                    (cosl * v[POS_FS]));
v[VEL_WG_SURFACE] = ((cosl * v[VEL_WG]) +
                    (sinl * v[VEL_TOOTH_BASE]) -
                    (cosl * v[VEL_FS]));

/* Find the velocity at the gear-tooth surface. */
v[POS_TOOTH_SURFACE] = ((cos2 * v[POS_TOOTH_TIP]) +
                       (sin2 * v[POS_CS]) -
                       (sin2 * v[POS_FS]));
v[VEL_TOOTH_SURFACE] = ((cos2 * v[VEL_TOOTH_TIP]) +
                       (sin2 * v[VEL_CS]) -
                       (sin2 * v[VEL_FS]));


/* Now, calculate the Constitutive Relationships:
 *
 * Find the wave-generator friction. */
v[TORQUE_WG_FRICTION] =
  calculate_friction(v[VEL_WG_SURFACE],
                     b_wg_constant, b_wg1, b_wg2,
```

```
                    0.0, 0.0, 0.0, 0.0, 0.0, 1000000.0);

/* Find the friction at the tooth tip. */
v[TORQUE_TOOTH_TIP_FRICTION] =
  calculate_friction((v[VEL_TOOTH_BASE]- v[VEL_TOOTH_TIP]),
                    b_tooth_tip_constant, b_tooth_tip1, b_tooth_tip2,
                    0.0, 0.0, 0.0, 0.0, 0.0, 1000000.0);

/* The total friction at the gear-tooth surface is due to the coulomb friction
 * (mu * N), the constant friction (b_tooth_surface_constant), the velocity-
 * dependent friction, and the cyclic friction.  Calculate the component due
 * to everything except the coulomb friction. */

v[TORQUE_TOOTH_SURFACE_FRICTION] =
  calculate_friction(v[VEL_TOOTH_SURFACE],
                    b_tooth_surface_constant, b_tooth_surface1, b_tooth_surface2,
                    stiction_torque_tooth, stiction_vel_tooth,
                    v[POS_OUT],
                    cyclic_friction_amp_tooth, cyclic_friction_phase_tooth,
                    (max_friction_vel[model][joint]));


/* Find the harmonic drive stiffness coefficients:  */
v[K1] = (k1_constant +
        k1_amplitude * Sin(((2.0 * v[POS_WG_RELATIVE]) + k1_phase) * CONV));
v[K2] = (k2_constant +
        k2_amplitude * Sin(((2.0 * v[POS_WG_RELATIVE]) + k2_phase) * CONV));

/* Calculate the torque on the spring. */
v[TORQUE_K] = ((v[K1] * (v[POS_ERR] - v[POS_TOOTH_TIP])) +
             (v[K2] * Power((v[POS_ERR] - v[POS_TOOTH_TIP]), 3)));

/* Calculate the cyclic torque. */
v[TORQUE_CYCLIC] = (cyclic_amplitude *
                   Sin(((2.0 * v[POS_WG_RELATIVE]) + cyclic_phase) * CONV));

/* From the power conservation constraint on the position error element
 * calculate the torque seen on the input side. */
v[TORQUE_ERR_IN] = (1.0 + (v[DERF] / tan1)) * v[TORQUE_K];

/* Set the sign of mu to control the direction of the coulomb friction force
 * along the gear-tooth surface.  The sign of mu should be identical to the
 * sign of the surface rubbing-velocity.  */
mu = copysign(mu_save, v[VEL_TOOTH_SURFACE]);

/* If stiffness data is being collected, the friction acts in the opposite
 * direction as the joint is being loaded. */
if(stiffness_flag)
  mu = -mu_save;

/* Now calculate the force/torque compatibility equations:
 *
 * Determine the output normal force. */
v[TORQUE_OUTPUT_NORMAL] = v[TORQUE_K] + v[TORQUE_TOOTH_TIP_FRICTION];

/* For the sake of continuity in the simulation, ramp the constant friction
 * on the gear-tooth surface from zero to the desired value if at the
 * beginning of the step-response trial.  This is a quick fix that should
 * be implemented in more general terms for all of the constant friction
 * components. */
if(!(stiffness_flag || stiffness_flag2))
  if(current_time < 0.05)
    v[TORQUE_TOOTH_SURFACE_FRICTION] = ((((current_time - 0.05)/0.05) + 1.0) *
                                       v[TORQUE_TOOTH_SURFACE_FRICTION]);
```

```
  /* Find the gear-tooth normal force. Note that this equation might need to
   * be calculated iteratively if the velocity is zero since the coulomb
   * friction becomes a different function of the normal force.  For now, I
   * will start my simulations at a non-zero initial velocity so that the
   * velocity will never be zero. */
  v[TORQUE_TOOTH_SURFACE_NORMAL] = ((v[TORQUE_OUTPUT_NORMAL] -
                                    (cos2 * v[TORQUE_TOOTH_SURFACE_FRICTION])) /
                                   (sin2 + (mu * cos2)));

  /* If the gear-tooth surface-normal is negative then the mechanism through
   * which the friction acts at the gear-tooth surface changes.  In order to
   * describe this new mechanism, a different, but similar, model is needed.
   * Unfortunately, changing to the new model at this point in the simulation
   * poses significant numerical problems.  To avoid this mess, when the normal
   * force becomes negative, I will set the coulomb friction to zero and
   * recalculate the tooth-surface normal force. */
  if(v[TORQUE_TOOTH_SURFACE_NORMAL] < 0.0)
    {
      mu = 0.0;
      v[TORQUE_TOOTH_SURFACE_NORMAL] = ((v[TORQUE_OUTPUT_NORMAL] -
                                        (cos2 * v[TORQUE_TOOTH_SURFACE_FRICTION])) /
                                       (sin2 + (mu * cos2)));
    }
  /* Given this correct tooth-surface normal force, the coulomb friction and
   * total friction at the tooth interface can be calculated. */
  v[TORQUE_TOOTH_SURFACE_COULOMB] = mu * v[TORQUE_TOOTH_SURFACE_NORMAL];
  v[TORQUE_TOOTH_SURFACE_TOTAL_LOSS] = (v[TORQUE_TOOTH_SURFACE_COULOMB] +
                                        v[TORQUE_TOOTH_SURFACE_FRICTION]);

  /* Calculate the input normal force. */
  v[TORQUE_INPUT_NORMAL] = v[TORQUE_ERR_IN] + v[TORQUE_TOOTH_TIP_FRICTION];

  /* Now determine the normal force on the wave-generator. */
  v[TORQUE_WG_NORMAL] = (1.0 / cos1) * (v[TORQUE_INPUT_NORMAL] +
                                        (v[TORQUE_WG_FRICTION] * sin1));

  /* Find the normal force on the tooth tip. */
  v[TORQUE_TOOTH_TIP_NORMAL] = ((cos2 * v[TORQUE_TOOTH_SURFACE_NORMAL]) -
                                (sin2 * v[TORQUE_TOOTH_SURFACE_TOTAL_LOSS]));

  /* Now the torques on the wave_generator, flexspline, and circular spline can
   * be determined. */
  v[TORQUE_WG] = ((v[TORQUE_CYCLIC]) +
                  (v[TORQUE_WG_FRICTION] * cos1) +
                  (v[TORQUE_WG_NORMAL] * sin1));
  v[TORQUE_FS] = ((v[TORQUE_TOOTH_TIP_NORMAL]) -
                  (v[TORQUE_WG_FRICTION] * cos1) -
                  (v[TORQUE_WG_NORMAL] * sin1));
  v[TORQUE_CS] = ((v[TORQUE_TOOTH_SURFACE_NORMAL] * cos2) -
                  (v[TORQUE_TOOTH_SURFACE_TOTAL_LOSS] * sin2));

  /* Finally, return the torques on the three hd ports. */
  *torque_wg = v[TORQUE_WG];
  *torque_fs = v[TORQUE_FS];
  *torque_cs = v[TORQUE_CS];
}


/*****************************************************************************/
/*                                                                           */
/*    Functions which describe the energy of each harmonic-drive model.      */
/*                                                                           */
```

```
/*****************************************************************************/


/* Function rotary_hd_energy() calculates the energy for the non-ideal, rotary
 * harmonic-drive model.  It is called by the function odeint() after the completion
 * of each time step in order to integrate the individual energy components of the
 * harmonic drive model with tooth rubbing.  This function takes the current time
 * step of the solver and integrates the energy over that time step using a simple
 * Euler integration scheme.  As you might expect, these energy calculations can
 * sometimes have appreciable error, but they are useful, for the most part. */
void rotary_hd_energy(delta_t)
double delta_t;
{
  double vel_wg_rad, vel_fs_rad, vel_cs_rad;
  double vel_hd_friction_rad;
  static double old_pos_k = 0.0;

  /* Be sure that all velocities and positions are in radians to ensure
   * proper unit-matching. */
  vel_wg_rad = v[VEL_WG] * CONV;
  vel_fs_rad = v[VEL_FS] * CONV;
  vel_cs_rad = v[VEL_CS] * CONV;
  vel_hd_friction_rad = v[VEL_HD_FRICTION] * CONV;

  /* Calculate the potential energy stored in the spring by integrating
   * the spring force over the spring displacement. */
  v[SPRING_ENERGY] = (v[SPRING_ENERGY] +
                      ((((v[POS_K] - v[POS_N_WG]) - old_pos_k) * CONV) *
                       v[TORQUE_K]));

  /* Calculate the cyclic torque energy by integrating the power over time. */
  v[CYCLIC_ENERGY] = (v[CYCLIC_ENERGY] +
                      (delta_t * vel_wg_rad * (-v[TORQUE_CYCLIC])));

  /* Calculate the energy lost to friction by integrating the power dissipation
   * over time. */
  v[HD_FRICTION_ENERGY] = (v[HD_FRICTION_ENERGY] +
                           (delta_t * (v[TORQUE_HD_FRICTION] * vel_hd_friction_rad)));

  /* Calculate total potential energy in the system assuming the cyclic torque
   * can be treated like a spring. */
  v[TOTAL_POTENTIAL_ENERGY] = v[SPRING_ENERGY] + v[CYCLIC_ENERGY];

  old_pos_k = (v[POS_K] - v[POS_N_WG]);
}



/* Function gear_tooth_hd_energy() calculates the energy for the harmonic-drive
 * model which includes gear-tooth-rubbing effects.  It is called by the function
 * odeint() after the completion of each time step in order to integrate the
 * individual energy components of the harmonic drive model with tooth rubbing.
 * This function takes the current time step of the solver and integrates the
 * energy over that time step using a simple Euler integration scheme.  As you
 * might expect, these energy calculations can sometimes have appreciable error,
 * but they are useful, for the most part. */
void gear_tooth_hd_energy(delta_t)
double delta_t;
{
  double vel_wg_rad, vel_fs_rad, vel_cs_rad;
  double vel_wg_surface_rad, vel_tooth_surface_rad;
  double vel_tooth_tip_rad, vel_tooth_base_rad;
  static double old_pos_k = 0.0;
```

```
  /* Be sure that all velocities and positions are in radians to ensure
   * proper unit-matching. */
  vel_wg_rad = v[VEL_WG] * CONV;
  vel_fs_rad = v[VEL_FS] * CONV;
  vel_cs_rad = v[VEL_CS] * CONV;
  vel_wg_surface_rad = v[VEL_WG_SURFACE] * CONV;
  vel_tooth_surface_rad = v[VEL_TOOTH_SURFACE] * CONV;
  vel_tooth_tip_rad = v[VEL_TOOTH_TIP] * CONV;
  vel_tooth_base_rad = v[VEL_TOOTH_BASE] * CONV;

  /* Calculate the potential energy stored in the spring by integrating
   * the spring force over the spring displacement. */
  v[SPRING_ENERGY] = (v[SPRING_ENERGY] +
                      ((((v[POS_ERR] - v[POS_TOOTH_TIP]) - old_pos_k) * CONV) *
                       v[TORQUE_K]));

  /* Calculate the cyclic torque energy by integrating the power over time. */
  v[CYCLIC_ENERGY] = (v[CYCLIC_ENERGY] +
                      (delta_t * vel_wg_rad * (-v[TORQUE_CYCLIC])));

  /* Calculate the energy lost to friction by integrating the power dissipation
   * over time. */
  v[WG_FRICTION_ENERGY] = (v[WG_FRICTION_ENERGY] +
                           (delta_t * (v[TORQUE_WG_FRICTION] * vel_wg_surface_rad)));
  v[TOOTH_TIP_FRICTION_ENERGY] = (v[TOOTH_TIP_FRICTION_ENERGY] +
                                  (delta_t *
                                   (v[TORQUE_TOOTH_TIP_FRICTION] *
                                    (vel_tooth_base_rad - vel_tooth_tip_rad))));
  v[TOOTH_SURFACE_FRICTION_ENERGY] = (v[TOOTH_SURFACE_FRICTION_ENERGY] +
                                      (delta_t *
                                       (v[TORQUE_TOOTH_SURFACE_FRICTION] *
                                       vel_tooth_surface_rad)));
  v[TOOTH_SURFACE_COULOMB_ENERGY] = (v[TOOTH_SURFACE_COULOMB_ENERGY] +
                                     (delta_t *
                                      (v[TORQUE_TOOTH_SURFACE_COULOMB] *
                                      vel_tooth_surface_rad)));
  v[TOOTH_SURFACE_TOTAL_LOSS_ENERGY] = (v[TOOTH_SURFACE_COULOMB_ENERGY] +
                                        v[TOOTH_SURFACE_FRICTION_ENERGY]);

  /* Calculate total potential energy in the system assuming the cyclic torque
   * can be treated like a spring. */
  v[TOTAL_POTENTIAL_ENERGY] = v[SPRING_ENERGY] + v[CYCLIC_ENERGY];

  old_pos_k = (v[POS_ERR] - v[POS_TOOTH_TIP]);
}



/*****************************************************************************/
/*                                                                           */
/*    Functions which calculate model parameters based on input values.      */
/*                                                                           */
/*****************************************************************************/


/* Function calculate_rotary_params() is used to take the input parameter
 * values and determine relevant parameters for the simple non-ideal rotary
 * harmonic-drive model. */
void calculate_rotary_params()
{
  double reduction_factor;
  double frequency;
  double temp1, temp2;
```

```
  /* Reflect the non-linear stiffness coefficients as measured from the output
   * side of the transmission to the input side. */
  k1_constant = (k1_output_constant / Power(N, 2));
  k1_amplitude = (k1_output_amplitude / Power(N, 2));
  k1_phase = k1_output_phase;
  k2_constant = (k2_output_constant / Power(N, 4));
  k2_amplitude = (k2_output_amplitude / Power(N, 4));
  k2_phase = k2_output_phase;

  /* Calculate the coulomb friction in the harmonic drive based on the width
   * of the hysteresis loop in the harmonic-drive stiffness profile. */
  b_hd_constant = (hysteresis_width / 2.0);

  /* Calculate the reduction ratio between the input rotation and the velocity
   * seen by the friction element mounted between the flexspline and circular
   * spline ports. */
  if(joint == WRIST)
    reduction_factor = N;
  else
    reduction_factor = (N + 1.0);

  /* Calculate the dynamic friction coefficients by subtracting the input
   * and output damping components from the total dynamic friction using
   * conservation of power.  These coefficients should be positive. */
  b_hd1 = ((Power(reduction_factor, 2)) * (b_total1 - b_in)) - b_out;
  b_hd2 = ((Power(reduction_factor, 4))) * b_total2;

  /* Convert the stiction and cyclic friction from input rotation units to
   * output rotation.  Don't upset the signs of these values. */
  stiction_torque_hd = reduction_factor * stiction_torque;
  stiction_vel_hd = (stiction_vel / reduction_factor);
  cyclic_friction_amp_hd = reduction_factor * cyclic_friction_amplitude;
  cyclic_friction_phase_hd = cyclic_friction_phase;

  /* Calculate the natural frequency of the non-rigid vibrational mode of the
   * two-mass system assuming linear stiffness. */
  temp1 = ((k1_constant / CONV) *
          ((1.0 /inertia_in) +
           (1.0 / (inertia_out / (Power(reduction_factor, 2.0))))));
  temp2 = (1.0 / (Power(2.0, 1.5) * PI));
  frequency = (temp2 * Power((2.0 * temp1), 0.5));
  printf("\n\n The natural frequency of the non-rigid vibrational mode\n");
  printf(" for a two-mass linear system is: %f Hz.\n", frequency);
  printf(" Therefore, resonance vibration should appear at input rotational\n");
  printf(" velocities of: %f input_deg/sec.\n", ((frequency * 360.0) / 4.0));
  printf("                %f input_deg/sec.\n", ((frequency * 360.0) / 2.0));
  printf("                %f input_deg/sec.\n", ((frequency * 360.0) / 1.0));

  /* Print out these new parameters if in debugging mode. */
  if(debug)
    {
      printf("\n b_hd_constant:          %4.20lf", b_hd_constant);
      printf("\n b_hd1:                  %4.20lf", b_hd1);
      printf("\n b_hd2:                  %4.20lf", b_hd2);
      printf("\n k1_constant:            %4.20lf", k1_constant);
      printf("\n k2_constant:            %4.20lf\n", k2_constant);
      printf("\n");
    }
}



/* Function calculate_gear_tooth_params() is used to take the input parameter
 * values and determine: (1) trigonometric and geometric relationships, (2) the
```

```
 * tooth surface friction coefficients, and (3) the ideal spring stiffness
 * coefficients.  */
void calculate_gear_tooth_params()
{
  double stiffness_factor_A;
  double stiffness_factor_B;
  double wg_to_tooth_factor;
  double damping_factor_A;
  double damping_factor_B;
  double damping_factor_C;
  double damping_factor_D;
  double inertia_in_eff, inertia_out_eff;
  double temp1, temp2, frequency;

  /* Initialize the coulomb friction coefficient. */
  mu = mu_save;

  /* Calculate the gear-tooth trig values. */
  tan2 = tan(CONV * tooth_angle);
  sin2 = sin(CONV * tooth_angle);
  cos2 = cos(CONV * tooth_angle);

  /* The wg_angle can be found from the gear ratio and the tooth angle
   * using the relationship: (1/(N+1)) = tan1 tan2. */
  wg_angle = atan(1.0 / (tan2 * (N + 1.0)));
  tan1 = tan(wg_angle);
  sin1 = sin(wg_angle);
  cos1 = cos(wg_angle);

  /* Now calculate the stiffness of the spring that deforms vertically
   * from the rotational stiffness provided. */
  stiffness_factor_A = (cos2 + (mu * sin2)) / (sin2 - (mu * cos2));
  stiffness_factor_B = -(1.0 / (tan1 - (1.0 / tan2)));
  k1_constant = (k1_output_constant *
                (stiffness_factor_B / (stiffness_factor_A - tan1)));
  k1_amplitude = (k1_output_amplitude *
                  (stiffness_factor_B / (stiffness_factor_A - tan1)));
  k1_phase = k1_output_phase;
  k2_constant = (k2_output_constant *
                (Power(stiffness_factor_B, 3) / (stiffness_factor_A - tan1)));
  k2_amplitude = (k2_output_amplitude *
                  (Power(stiffness_factor_B, 3) / (stiffness_factor_A - tan1)));
  k2_phase = k2_output_phase;

  /* From the hysteresis width on the stiffness curve and the values of the
   * other constant friction components in the harmonic drive, determine
   * the appropriate constant friction component on the gear tooth surface. */
  b_tooth_surface_constant = ((1.0 / ((stiffness_factor_A * cos2) + sin2)) *
                              ((hysteresis_width / 2.0) -
                               ((stiffness_factor_A - tan1) * b_tooth_tip_constant) -
                               (((sin1 * tan1) + cos1) * b_wg_constant)));

  /* Scale the stiction torque and cyclic friction torque from the input
   * side (wg) to the gear tooth surface. */
  wg_to_tooth_factor = (1.0 / ((tan1 * cos2) + (tan1 * sin2 * tan2)));
  stiction_torque_tooth = wg_to_tooth_factor * stiction_torque;
  stiction_vel_tooth = (stiction_vel / wg_to_tooth_factor);
  cyclic_friction_amp_tooth = wg_to_tooth_factor * cyclic_friction_amplitude;
  cyclic_friction_phase_tooth = cyclic_friction_phase;

  /* By applying conservation of power to the damping components in the
   * model, the linear and cubic coefficients for the gear-tooth-surface
   * damping can be found by subtracting the known damping components from
   * the total joint damping and matching coefficients.  This has to be
```

```
   * done differently for configuration 1 and configuration 2 since the
   * dampers outside the harmonic drive depend on different velocities. */
  damping_factor_A = ((cos2 / tan2) + sin2);
  damping_factor_B = (cos1 + (sin1 * tan1));
  damping_factor_C = (1.0 / (N + 1.0));
  damping_factor_D = (1.0 + (1.0 / N));
  if(joint == WRIST)
    {
      b_tooth_surface1 = ((b_total1 -
                           b_in -
                           (b_wg1 * (Power((damping_factor_B * damping_factor_D), 2))) -
                           (b_out * (Power((-1.0 / N), 2)))) /
                          (Power((damping_factor_A * (1.0 / N)), 2)));
      b_tooth_surface2 = ((b_total2 -
                           (b_wg2 * (Power((damping_factor_B * damping_factor_D), 4))))
/
                          (Power((damping_factor_A * (1.0 / N)), 4)));
    }
  else
    {
      b_tooth_surface1 = ((b_total1 -
                           b_in -
                           (b_wg1 * (Power((damping_factor_B), 2))) -
                           (b_out * (Power((damping_factor_C), 2)))) /
                          (Power((damping_factor_A * damping_factor_C), 2)));
      b_tooth_surface2 = ((b_total2 -
                           (b_wg2 * (Power((damping_factor_B), 4)))) /
                          (Power((damping_factor_A * damping_factor_C), 4)));
    }

  /* Calculate the natural frequency of the non-rigid vibrational mode of the
   * two-mass system assuming linear stiffness.  First calculate the effective
   * input and output inertias seen by the internal spring, then use the
   * ideal linear stiffness value, with friction removed, to determine the
   * resulting natural frequency of the linear system. */
  inertia_in_eff = (inertia_in / (tan1 * tan1));
  inertia_out_eff = (inertia_out * tan2 * tan2);
  temp1 = ((k1_constant / CONV) *
           ((1.0 /inertia_in_eff) + (1.0 / inertia_out_eff)));
  temp2 = (1.0 / (Power(2.0, 1.5) * PI));
  frequency = (temp2 * Power((2.0 * temp1), 0.5));
  printf("\n\n The natural frequency of the non-rigid vibrational mode\n");
  printf(" for a two-mass linear system is: %f Hz.\n", frequency);
  printf(" Therefore, resonance vibration should appear at input rotational\n");
  printf(" velocities of: %f input_deg/sec.\n", ((frequency * 360.0) / 4.0));
  printf("                %f input_deg/sec.\n", ((frequency * 360.0) / 2.0));
  printf("                %f input_deg/sec.\n", ((frequency * 360.0) / 1.0));

  /* Print out these new parameters if in debugging mode. */
  if(debug)
    {
      printf("\n wg_angle:                 %4.20lf deg", (wg_angle / CONV));
      printf("\n b_tooth_surface_constant: %4.20lf", b_tooth_surface_constant);
      printf("\n b_tooth_surface1:         %4.20lf", b_tooth_surface1);
      printf("\n b_tooth_surface2:         %4.20lf", b_tooth_surface2);
      printf("\n k1_constant:              %4.20lf", k1_constant);
      printf("\n k2_constant:              %4.20lf\n", k2_constant);
      printf("\n");
      printf("\n tooth surface to input scaling factor: %4.20lf\n",
             (1.0 / (damping_factor_A * damping_factor_C)));
    }
}
```

```
/*****************************************************************************/
/*                                                                           */
/*  Functions which model the friction and amplifiers and collect stiffness data.  */
/*                                                                           */
/*****************************************************************************/


/* Function iregulate() takes as arguments the present amp current, the requested
 * amp current, and the current motor velocity and returns the actual current that
 * the amps can produce. */
double iregulate(ipresent, irequested, omega)
double ipresent;
double irequested;
double omega;
{
  double voltage_upper_limit;
  double voltage_lower_limit;
  double current_upper_limit;
  double current_lower_limit;
  double current1, current2;
  double ireturn;

  /* Make sure that the current requested is within the amp's operating range. */
  if (irequested > IMAX)
    {
      fprintf(stderr, "\n WARNING: requested current is above allowed amp range!\n");
      printf("\n Current Time: ");
      irequested = IMAX;
    }
  else if (irequested < -IMAX)
    {
      fprintf(stderr, "\n WARNING: requested current is below allowed amp range!\n");
      printf("\n Current Time: ");
      irequested = -IMAX;
    }

  /* At the present operating current, ipresent, calculate the maximum
   * allowable voltage that the amps can provide as calculated from
   * the voltage-current curves for the amps in the Aerotech catalog.
   * Assume that, if the current is negative, the maximum voltage that the
   * amp can reach is the saturation voltage, VMAX.  Also assume that the
   * minimum voltage for negative current is described by a curve similar
   * to the voltage-current for positive current and voltage.  Lastly, the
   * minimum voltage for positive current is equal to the negative voltage
   * threshold of the amp, -VMAX. */
  if(ipresent >= 0)
    {
      if(ipresent <= IMAX)
        voltage_upper_limit = VMAX + VI_SLOPE * ipresent;
      else
        voltage_upper_limit = VMAX + VI_SLOPE * IMAX;
      voltage_lower_limit = -VMAX;
    }
  else
    {
      if(ipresent >= -IMAX)
        voltage_lower_limit = -VMAX + VI_SLOPE * ipresent;
      else
        voltage_lower_limit = -VMAX + VI_SLOPE * (-IMAX);
      voltage_upper_limit = VMAX;
    }

  /* Now from this maximum or minimum allowed voltage at present current, calculate
```

```
   * the allowable current range that the requested current can achieve by assuming
   * that the amp voltage is equal to the voltage across the motor (= Kb * velocity
   * or back EMF) plus the voltage drop due to current flowing through the amp
   * resistance. */
  current1 = (voltage_upper_limit - (motor_kb * omega))/amp_resistance;
  current2 = (voltage_lower_limit - (motor_kb * omega))/amp_resistance;
  if(current1 < current2)
    {
      current_upper_limit = current2;
      current_lower_limit = current1;
    }
  else
    {
      current_upper_limit = current1;
      current_lower_limit = current2;
    }

  /* Now, if the requested current, irequested, is between the upper and lower
   * current bounds, return the value, otherwise return the upper or lower
   * limit. */

  if((irequested <= current_upper_limit) && (irequested >= current_lower_limit))
    ireturn = irequested;
  else
    {
      if((fabs(current_lower_limit - irequested)) <
        (fabs(current_upper_limit - irequested)))
       ireturn = current_lower_limit;
      else
       ireturn = current_upper_limit;
    }

  /* Now add a relative damping factor to the current.  Make it behave so that
   * the current can't change from the old to the new value instantaneously, but,
   * instead, a part of the new value, ireturn, is averaged with part of the old
   * value, ipresent, to create the actual new current somewhere between the two
   * values.  This step is necessary to keep the amps current from fluctuating
   * rapidly between each subsequent step and possibly going unstable.  The AMP_
   * DAMPING factor is a number between 0 and 1.0 that represents the amount
   * of damping in the amps current response.  Note that since step size can vary
   * significantly, and that this damping factor is calculated on every step, the
   * amount of damping will vary with the changing step size. */
  ireturn = (AMP_DAMPING * ipresent) + ((1.0 - AMP_DAMPING) * ireturn);

  /* Give a run-time warning if the current exceeds the amp's allowed range. */
  if ((ireturn > IMAX) || (ireturn < -IMAX))
    {
      fprintf(stderr, "\n WARNING: allowable amp current range exceeded!\n");
      printf("\n Current Time: ");
    }

  return(ireturn);
}



/* Function calculate_friction() takes 10 arguments: (1) the velocity at the
 * friction interface, (2,3, and 4) the constant, linear, and cubic velocity-
 * dependent friction coefficients, (5) the stiction torque, (6) the velocity
 * where the stiction is deactivated, (7) the reference position for the cyclic
 * friction, (8 and 9) the amplitude and phase of a sinusoidal friction function,
 * and (10) the velocity for which the damping curve begins to decrease.
 * This function returns the resulting value of the friction given these
 * parameters.  Note that the friction amplitude should not be larger than
```

```
 * b_constant or else the resulting friction can become negative.  Additionally,
 * if the velocity is very small, this friction model is undefined, and a warning
 * message is given.  Finally, if the velocity is too large, the cubic term of the
 * velocity-dependent damping may decrease and become negative.  To prevent this,
 * the velocity dependent damping is calculated for omega_max at all velocities
 * greater than omega_max. */
double calculate_friction(omega,
                          b_constant, b1, b2,
                          stiction_torque, stiction_vel,
                          theta,
                          friction_amplitude, friction_phase,
                          omega_max)
double omega;
double b_constant, b1, b2;
double stiction_torque, stiction_vel;
double theta;
double friction_amplitude, friction_phase;
double omega_max;
{
  double friction, damping;

  /* Make sure that the velocity is not near zero. */
  if (((fabs(omega)) < TINY_VEL) &&
      ((stiction_torque + friction_amplitude + b_constant) != 0.0) &&
      (!stiffness_flag) && (!stiffness_flag2))
    {
      fprintf(stderr, "\n ERROR: Function calculate_friction().");
      fprintf(stderr, "\n        Velocity is near zero and the model is
undefined!\n");
      return(0.0);
    }

  /* If the stiffness data is being collected and the joint is being loaded,
   * return the velocity-independent friction as if the velocity were positive.
   * Note: do not use the stiction torque. */
  if(stiffness_flag)
    {
      friction = (-b_constant +
                 (-friction_amplitude *
                  Sin((theta + friction_phase) * CONV)));
      return(friction);
    }

  /* If stiffness data is being collected and the joint is being unloaded,
   * return the velocity-independent friction as if the velocity were positive. */
  if(stiffness_flag2)
    {
      friction = (b_constant +
                 (friction_amplitude *
                  Sin((theta + friction_phase) * CONV)));
      return(friction);
    }

  /* Make sure that the cylic friction amplitude is less than the constant friction
   * coefficient. */
  if (friction_amplitude > b_constant)
    {
      fprintf(stderr, "\n ERROR: Function calculate_friction().");
      fprintf(stderr, "\n        Cyclic friction amplitude too large!\n");
    }

  /* Calculate the static and constant friction as follows:
   * if the velocity is below the stiction_vel, calculate the friction based
   * on the linear fit between maximum stiction at zero velocity and b_constant
```

```
   * at stiction_vel.  Otherwise the friction is equal to b_constant in the
   * direction opposing the velocity.  Add the cylic friction accordingly. */
  if (omega >= stiction_vel)
    friction = (b_constant +
               (friction_amplitude *
                Sin((theta + friction_phase) * CONV)));
  else if ((omega > 0.0) && (omega < stiction_vel))
    friction = (stiction_torque +
               ((stiction_torque - b_constant)/(-stiction_vel)) * omega);
  else if (omega <= (-stiction_vel))
    friction = ((-b_constant) +
               (-friction_amplitude *
                Sin((theta + friction_phase) * CONV)));
  else
    friction = ((-stiction_torque) +
               (((-b_constant) - (-stiction_torque))/(-stiction_vel)) * omega);

  /* Now calculate the velocity-dependent friction. */
  if(fabs(omega) > omega_max)
    damping = ((b1 * copysign(omega_max, omega)) +
               (b2 * Power((copysign(omega_max, omega)), 3)));
  else
    damping = (b1 * omega) + (b2 * Power(omega, 3));

  /* Return the aggregate friction value. */
  return(friction + damping);
}



/* Function collect_stiffness_data() can be used to collect a set of output
 * position versus output torque data.  This function uses the specified
 * harmonic drive function to calculate the resulting torques when a displacement
 * is applied to the joint output.  The joint is configured with the wave
 * generator locked to the circular spline.  While the joint is being loaded,
 * data is collected in position increments of pos_increment until the maximum
 * torque is reached.  At that point, the harmonic drive model is switched since
 * the friction changes direction and the remaining data is collected.  A positive
 * stiffness curve is returned for positive displacement.  Assuming directional
 * symmetry in the drive, this curve can be flipped about the x- and y- axes to
 * determine the shape of curve for negative displacements.  Be sure to load the
 * drive in the direction that ensures that the gear-tooth-surface normal force
 * remains positive. */
void collect_stiffness_data()
{
  int i;
  double torque[STIFFNESS_POINTS];
  double displacement[STIFFNESS_POINTS];
  double pos_increment;
  double actual_disp, torque_wg, torque_fs, torque_cs;
  char unix_command[200];
  int points = STIFFNESS_POINTS;
  static double max_disp[NUM_OF_AXIS] = {0.1, 0.4, 0.35};
  static char *stiffness_filename[NUM_OF_AXIS] = {"shld_stiffness_data.dat",
                                                  "elb_stiffness_data.dat",
                                                  "wrist_stiffness_data.dat"};
  FILE *outfile, *gnufile;

  /* Calculate the position increment. */
  pos_increment = max_disp[joint] / ((double) (points/2.0));

  /* Begin loading the output link of the joint in compression. */
  for(i = 1; i <= (points/2); i++)
```

```
    {
      actual_disp = ((double) (i-1)) * pos_increment;

      if(joint == WRIST)
       {
         (*(hd_model[model]))(0.0, actual_disp, 0.0, 0.0, 0.0, 0.0,
                              &torque_wg, &torque_fs, &torque_cs);
         torque[i] = torque_fs;
       }
      else
       {
         actual_disp = -actual_disp;
         (*(hd_model[model]))(actual_disp, 0.0, actual_disp, 0.0, 0.0, 0.0,
                              &torque_wg, &torque_fs, &torque_cs);
         torque[i] = torque_cs;
       }

      displacement[i] = fabs(actual_disp);
      if(debug)
       print_variables();
    }

  /* Adjust the flags to allow proper friction values to be computed. */
  stiffness_flag = FALSE;
  stiffness_flag2 = TRUE;

  /* Collect data while unloading.  Note the appropriate harmonic drive
   * model for the reverse-friction case is selected. */
  for(i = ((points/2) + 1); i <= points; i++)
    {
      actual_disp = ((double) (points - i)) * pos_increment;

      if(joint == WRIST)
       {
         (*(hd_model[model]))(0.0, actual_disp, 0.0, 0.0, 0.0, 0.0,
                              &torque_wg, &torque_fs, &torque_cs);
         torque[i] = torque_fs;
       }
      else
       {
         actual_disp = -actual_disp;
         (*(hd_model[model]))(actual_disp, 0.0, actual_disp, 0.0, 0.0, 0.0,
                              &torque_wg, &torque_fs, &torque_cs);
         torque[i] = torque_cs;
       }

      displacement[i] = fabs(actual_disp);

      if(debug)
       print_variables();
    }

  /* Now store and print the data. */
  create_file(&outfile, outdatapath, stiffness_filename[joint]);
  export_vectors(outfile, torque, displacement, points, stiffness_filename[joint]);
  close_file(outfile);

  if(fast_plot)
    {
      create_file(&gnufile, outdatapath, gnuplot_filename);
      fprintf(gnufile, "cd '%s'\n", outdatapath);
      fprintf(gnufile, "set xlabel 'Torque (N*m)'\n");
      fprintf(gnufile, "set ylabel 'Displacement (deg)'\n");
      fprintf(gnufile, "set title 'Stiffness Curve'\n");
```

```
      fprintf(gnufile, "plot '%s'\n", stiffness_filename[joint]);
      fprintf(gnufile, "pause -1\n");
      close_file(gnufile);
      sprintf(unix_command, "gnuplot %s%s", outdatapath, gnuplot_filename);
      printf("\n Executing the unix command: %s\n", unix_command);
      system(unix_command);
    }
  else
    {
      sprintf(unix_command, "xgraph %s%s -t Stiffness_Curve\
                -y Displacement_deg -x Torque_N*m &",
              outdatapath, stiffness_filename[joint]);
      printf("\n Executing the unix command: %s\n", unix_command);
      system(unix_command);
    }

  exit(0);
}



/*****************************************************************************/
/*                                                                           */
/*    Functions which input and output data.                                 */
/*                                                                           */
/*****************************************************************************/


/* Function get_arguments() parses the command-line arguments.  */
void get_arguments(int argnum, char **args)
{
  int arg_index;

  for (arg_index = 1; arg_index < argnum; arg_index++)
    {
      if (!strcmp("-debug", args[arg_index]))
       debug = TRUE;
      else if (!strcmp("-energy", args[arg_index]))
       {
         print_energy = TRUE;
         calc_energy = TRUE;
       }
      else if (!strcmp("-stiffness", args[arg_index]))
       stiffness_flag = TRUE;
      else if (!strcmp("-ideal", args[arg_index]))
       ideal_flag = TRUE;
      else if (!strcmp("-plot", args[arg_index]))
       plot = TRUE;
      else if (!strcmp("-h",    args[arg_index]) ||
               !strcmp("-?",    args[arg_index]) ||
               !strcmp("-help", args[arg_index]))
       {
         fprintf(stderr, "\n Program %s: ",args[0]);
         usage();
         exit(0);
       }
      else
       {
         fprintf(stderr,"\n ERROR while executing %s: arguments are wrong!\n",
args[0]);
         usage();
         exit(1);
       }
    }
```

```
}



/* Function usage() prints out the proper usage of the command-line options. */
void usage()
{
  fprintf(stderr, "\n Valid command-line options:\n");
  fprintf(stderr, "     -debug :        activates debugging mode\n");
  fprintf(stderr, "     -energy:        prints energy during runtime\n");
  fprintf(stderr, "     -stiffness:     collects and plots solely stiffness data\n");
  fprintf(stderr, "     -ideal:         imposes an ideal haromonic-drive model\n");
  fprintf(stderr, "     -plot:          save plotting data for many input
currents\n");
  fprintf(stderr, "     -h, -?, -help : prints out help message\n");
}



/* Function read_input_data() parses all of the values in the input data file. */
void read_input_data(file_pointer)
FILE *file_pointer;
{
  char temp_name[50];
  double temp_number;

  while(fscanf(file_pointer, "%s %lg %*s\n", temp_name, &temp_number) != EOF)
    {
      if (0 == strcmp("inertia_in", temp_name))
       inertia_in = temp_number;
      else if (0 == strcmp("inertia_out", temp_name))
       inertia_out = temp_number;
      else if (0 == strcmp("k1_output_constant", temp_name))
       k1_output_constant = temp_number;
      else if (0 == strcmp("k1_output_amplitude", temp_name))
       k1_output_amplitude = temp_number;
      else if (0 == strcmp("k1_output_phase", temp_name))
       k1_output_phase = temp_number;
      else if (0 == strcmp("k2_output_constant", temp_name))
       k2_output_constant = temp_number;
      else if (0 == strcmp("k2_output_amplitude", temp_name))
       k2_output_amplitude = temp_number;
      else if (0 == strcmp("k2_output_phase", temp_name))
       k2_output_phase = temp_number;
      else if (0 == strcmp("hysteresis_width", temp_name))
       hysteresis_width = temp_number;
      else if (0 == strcmp("b_total1", temp_name))
       b_total1 = temp_number;
      else if (0 == strcmp("b_total2", temp_name))
       b_total2 = temp_number;
      else if (0 == strcmp("b_in", temp_name))
       b_in = temp_number;
      else if (0 == strcmp("b_wg_constant", temp_name))
       b_wg_constant = temp_number;
      else if (0 == strcmp("b_wg1", temp_name))
       b_wg1 = temp_number;
      else if (0 == strcmp("b_wg2", temp_name))
       b_wg2 = temp_number;
      else if (0 == strcmp("b_tooth_tip_constant", temp_name))
       b_tooth_tip_constant = temp_number;
      else if (0 == strcmp("b_tooth_tip1", temp_name))
       b_tooth_tip1 = temp_number;
      else if (0 == strcmp("b_tooth_tip2", temp_name))
       b_tooth_tip2 = temp_number;
```

```
 else if (0 == strcmp("cyclic_friction_amplitude", temp_name))
  cyclic_friction_amplitude = temp_number;
 else if (0 == strcmp("cyclic_friction_phase", temp_name))
  cyclic_friction_phase = temp_number;
 else if (0 == strcmp("stiction_torque", temp_name))
  stiction_torque = temp_number;
 else if (0 == strcmp("stiction_vel", temp_name))
  stiction_vel = temp_number;
 else if (0 == strcmp("b_out", temp_name))
  b_out = temp_number;
 else if (0 == strcmp("mu", temp_name))
  mu_save = temp_number;
 else if (0 == strcmp("tooth_angle", temp_name))
  tooth_angle = temp_number;
 else if (0 == strcmp("N", temp_name))
  N = temp_number;
 else if (0 == strcmp("cyclic_amplitude", temp_name))
  cyclic_amplitude = temp_number;
 else if (0 == strcmp("cyclic_phase", temp_name))
  cyclic_phase = temp_number;
 else if (0 == strcmp("error_amplitude0", temp_name))
  error_amplitude0 = temp_number;
 else if (0 == strcmp("error_phase0", temp_name))
  error_phase0 = temp_number;
 else if (0 == strcmp("error_amplitude1", temp_name))
  error_amplitude1 = temp_number;
 else if (0 == strcmp("error_phase1", temp_name))
  error_phase1 = temp_number;
 else if (0 == strcmp("error_amplitude2", temp_name))
  error_amplitude2 = temp_number;
 else if (0 == strcmp("error_phase2", temp_name))
  error_phase2 = temp_number;
 else if (0 == strcmp("motor_kt", temp_name))
  motor_kt = temp_number;
 else if (0 == strcmp("motor_kb", temp_name))
  motor_kb = temp_number;
 else if (0 == strcmp("amp_resistance", temp_name))
  amp_resistance = temp_number;
 else if (0 == strcmp("irequested", temp_name))
  irequested = temp_number;

 /* Initial conditions, */
 else if (0 == strcmp("initial_pos_in", temp_name))
  xstart_sav[POS_IN_INDEX] = temp_number;
 else if (0 == strcmp("initial_pos_out", temp_name))
  xstart_sav[POS_OUT_INDEX] = temp_number;
 else if (0 == strcmp("initial_vel_in", temp_name))
  xstart_sav[VEL_IN_INDEX] = temp_number;
 else if (0 == strcmp("initial_vel_out", temp_name))
  xstart_sav[VEL_OUT_INDEX] = temp_number;

 /* Time conditions */
 else if (0 == strcmp("initial_time", temp_name))
  initial_time = temp_number;
 else if (0 == strcmp("final_time", temp_name))
  final_time = temp_number;
 else if (0 == strcmp("step", temp_name))
  step = temp_number;

 /* Fast plotting flag. */
 else if (0 == strcmp("fast_plot", temp_name))
  fast_plot = ((int) temp_number);

 /* Desired harmonic-drive model. */
```

```
      else if (0 == strcmp("model", temp_name))
       model = ((int) temp_number);

      else
       {
         fprintf(stderr,"\n Couldn't parse parameter %s\n", temp_name);
       }
    }
}



/* Function read_input_filenames() reads the data from the second input file
 * as follows.  First it checks to see if the first value on each line is 1.
 * If the value is 1, then it stores the line number in the vector index[]
 * so that it can be used later to remember which output variables to store.
 * Additionally, this function also stores the other informaiton from each line
 * that has a 1 value to be used later for graph titles and output filenames.
 * As this function steps through each line of the input file, it counts the
 * number of output variables selected and stores the result in the variable
 * num_selected_output_var.  */
void read_input_filenames(file_pointer)
FILE *file_pointer;
{
  int line_number = 0;
  int temp_flag;
  char temp_title[50];
  char temp_units[50];

  while(fscanf(file_pointer, "%d %s %s\n", &temp_flag, temp_title, temp_units) != EOF)
    {
      if(temp_flag)
       {
         index[num_selected_output_var] = line_number;
         strcpy(graph_title[num_selected_output_var], temp_title);
         strcpy(graph_units[num_selected_output_var], temp_units);
         sprintf(output_datafile[num_selected_output_var], "%s_hd_%s.dat",
                joint_name[joint], temp_title);
         num_selected_output_var++;
       }

      line_number++;
    }
}



/* Function print_input_parameters() prints out the names and values of
 * the input parameters. */
void print_input_parameters()
{
  printf("\n");
  printf(" Model Parameters:\n");
  printf(" Input Inertia          = %4.10lf\n", inertia_in);
  printf(" Output Inertia         = %4.10lf\n", inertia_out);
  printf(" k1 constant            = %4.10lf\n", k1_output_constant);
  printf(" k1 amplitude           = %4.10lf\n", k1_output_amplitude);
  printf(" k1 phase               = %4.10lf\n", k1_output_phase);
  printf(" k2 constant            = %4.10lf\n", k2_output_constant);
  printf(" k2 amplitude           = %4.10lf\n", k2_output_amplitude);
  printf(" k2 phase               = %4.10lf\n", k2_output_phase);
  printf(" Hysteresis Width       = %4.10lf\n", hysteresis_width);
  printf(" b_total1               = %4.10lf\n", b_total1);
  printf(" b_total2               = %4.10lf\n", b_total2);
```

```
  printf(" b_in                    = %4.10lf\n", b_in);
  printf(" b_wg_constant           = %4.10lf\n", b_wg_constant);
  printf(" b_wg1                   = %4.10lf\n", b_wg1);
  printf(" b_wg2                   = %4.10lf\n", b_wg2);
  printf(" b_tooth_tip_constant    = %4.10lf\n", b_tooth_tip_constant);
  printf(" b_tooth_tip1            = %4.10lf\n", b_tooth_tip1);
  printf(" b_tooth_tip2            = %4.10lf\n", b_tooth_tip2);
  printf(" Cyclic Friction Amp     = %4.10lf\n", cyclic_friction_amplitude);
  printf(" Cyclic Friction Phase   = %4.10lf\n", cyclic_friction_phase);
  printf(" Stiction Torque         = %4.10lf\n", stiction_torque);
  printf(" Stiction Vel            = %4.10lf\n", stiction_vel);
  printf(" b_out                   = %4.10lf\n", b_out);
  printf(" mu                      = %4.10lf\n", mu_save);
  printf(" tooth_angle             = %4.10lf\n", tooth_angle);
  printf(" Gear Ratio, N           = %4.10lf\n", N);
  printf(" Cyclic Amplitdue        = %4.10lf\n", cyclic_amplitude);
  printf(" Cyclic Phase            = %4.10lf\n", cyclic_phase);
  printf(" Error Amplitude 0       = %4.10lf\n", error_amplitude0);
  printf(" Error Amplitude 1       = %4.10lf\n", error_amplitude1);
  printf(" Error Amplitude 2       = %4.10lf\n", error_amplitude2);
  printf(" Error Phase Shift0      = %4.10lf\n", error_phase0);
  printf(" Error Phase Shift1      = %4.10lf\n", error_phase1);
  printf(" Error Phase Shift2      = %4.10lf\n", error_phase2);
  printf(" Motor Torque Kt         = %4.10lf\n", motor_kt);
  printf(" Motor Back EMF Kb       = %4.10lf\n", motor_kb);
  printf(" Motor Resistance        = %4.10lf\n", amp_resistance);
  printf(" Motor Current           = %4.10lf\n", irequested);
  printf("\n");
  printf("Initial Conditions:\n");
  printf(" Input Position          = %4.10lf\n", xstart_sav[POS_IN_INDEX]);
  printf(" Output Position         = %4.10lf\n", xstart_sav[POS_OUT_INDEX]);
  printf(" Input Velocity          = %4.10lf\n", xstart_sav[VEL_IN_INDEX]);
  printf(" Output Velocity         = %4.10lf\n", xstart_sav[VEL_OUT_INDEX]);
  printf("\n");
  printf(" Initial Time            = %4.10lf\n", initial_time);
  printf(" Final Time              = %4.10lf\n", final_time);
  printf(" Step Size               = %4.10lf\n", step);
}



/* Function print_variables() prints the names and values of some
 * important torques, velocities, and positions. */
void print_variables()
{
  printf("\n");
  printf("\n pos_in:                %20.15lf", v[POS_IN]);
  printf("\n pos_out:               %20.15lf", v[POS_OUT]);
  printf("\n pos_wg:                %20.15lf", v[POS_WG]);
  printf("\n pos_fs:                %20.15lf", v[POS_FS]);
  printf("\n pos_cs:                %20.15lf", v[POS_CS]);
  printf("\n pos_n_wg               %20.15lf", v[POS_N_WG]);
  printf("\n");
  printf("\n vel_in:                %20.15lf", v[VEL_IN]);
  printf("\n vel_out:               %20.15lf", v[VEL_OUT]);
  printf("\n vel_wg:                %20.15lf", v[VEL_WG]);
  printf("\n vel_fs:                %20.15lf", v[VEL_FS]);
  printf("\n vel_cs:                %20.15lf", v[VEL_CS]);
  printf("\n");
  printf("\n torque_motor:          %20.15lf", v[TORQUE_MOTOR]);
  printf("\n torque_b_in:           %20.15lf", v[TORQUE_B_IN]);
  printf("\n torque_b_out:          %20.15lf", v[TORQUE_B_OUT]);
  printf("\n torque_wg:             %20.15lf", v[TORQUE_WG]);
  printf("\n torque_fs:             %20.15lf", v[TORQUE_FS]);
```

```
  printf("\n torque_cs:                %20.15lf", v[TORQUE_CS]);
  printf("\n torque_k:                 %20.15lf", v[TORQUE_K]);
  printf("\n torque_cyclic:            %20.15lf", v[TORQUE_CYCLIC]);
  printf("\n tooth_surface_friction:   %20.15lf", v[TORQUE_TOOTH_SURFACE_FRICTION]);
  printf("\n tooth_surf_total_loss:    %20.15lf", v[TORQUE_TOOTH_SURFACE_TOTAL_LOSS]);
  printf("\n tooth_surface_normal:     %20.15lf", v[TORQUE_TOOTH_SURFACE_NORMAL]);
  printf("\n torque_hd_friction:       %20.15lf", v[TORQUE_HD_FRICTION]);
  printf("\n");
  printf("\n current time:              %20.15lf", current_time);
  printf("\n");
  fflush(stdout);
}



/* Function export_vectors() takes a file pointer, two pointers
 * to vectors of 'kount' doubles and writes them to a
 * file, each line containing an x and y coordinate.  If the slow-
 * plotting option is selected, the filename will not be printed
 * to the first line of the file. */
void export_vectors(outfile, xvector, yvector, points, filename)
FILE *outfile;
double *xvector;
double *yvector;
int points;
char filename[];
{
  int i;

  printf("\n Exporting vector to file....");

  if(!fast_plot)
    fprintf(outfile, "\" %s\n", filename);
  for(i = 1; i <= points; i++)
    fprintf(outfile, "%12.10lf %12.10lf\n", xvector[i], yvector[i]);
  printf("done.\n");
}



/* Function generate_gnuplot_file() is called when the fast_plot option
 * is selected and creates a command file in the data directory which
 * is executed in gnuplot by a system command.  */
void generate_gnuplot_file(filename)
char filename[];
{
  int i;
  FILE *gnufile;

  create_file(&gnufile, outdatapath, filename);

  fprintf(gnufile, "cd '%s'\n", outdatapath);
  fprintf(gnufile, "set xlabel 'time (sec)'\n");

  for(i = 0; i < num_selected_output_var; i++)
    {
      fprintf(gnufile, "set title '%s'\n", graph_title[i]);
      fprintf(gnufile, "set ylabel '%s'\n", graph_units[i]);
      fprintf(gnufile, "plot '%s'\n", output_datafile[i]);
      fprintf(gnufile, "pause -1\n");
    }
  close_file(gnufile);
}
```

```
/* This is file hd_model.h.
 * It is the header file for program hd_model.c. */

/* Define a bunch of constants. */
#define SHOULDER              0
#define ELBOW                 1
#define WRIST                 2
#define JOINT_TO_TEST         WRIST
#define NUM_OF_AXIS           3
#define STIFFNESS_POINTS      1000
#define TRUE                  (1)
#define FALSE                 (0)
#define TINY_VEL              (1.0e-20)

/* Constants specifying the position of the local variables
 * in the state vector. */
#define POS_IN_INDEX          1
#define POS_OUT_INDEX         2
#define VEL_IN_INDEX          3
#define VEL_OUT_INDEX         4
#define ENERGY                5

/* The order of the system (number of state variables). */
#define ORDER                 4

/* Define index numbers for two different harmonic-drive models. */
#define ROTARY                0
#define GEAR_TOOTH            1
#define HD_MODELS             2

/* Define the degrees-to-radians conversion factor used in the equations. */
#define PI                    3.14159265359
#define CONV                  (PI/180.0)

/* Define mathematical functions to translate Mathematica's C-formatted
 * equations into a form understandable to the compiler.    */
#define Power(x,y)            pow((double) x, (double) y)
#define Sin(x)                sin((double) x)
#define Cos(x)                cos((double) x)

/* Define the simulation accuracy variable. */
#define EPS                   0.00001

/* Define a arbitrary intial step size and a minimum step size. */
#define INITIAL_STEP          0.0001
#define MINIMUM_STEP          0.0000000000000000001

/* Define constants describing the amplifier voltage-current curve. */
#define IMAX                  20.0
#define VMAX                  40.0
#define VI_SLOPE              -1.0
#define AMP_DAMPING           0.5

/* Define the number of data runs to be made if the -plot option is selected. */
#define SHLD_NUM_OF_DATA_RUNS       10
#define ELB_NUM_OF_DATA_RUNS        8
#define WRIST_NUM_OF_DATA_RUNS      8


/* Define the indicies for the vector to hold all variables that can be
 * selected for output data plots. */

/* The harmonic drive positions, velocities, and torques. */
```

```
#define POS_WG                                  0
#define POS_FS                                  1
#define POS_CS                                  2
#define POS_TOOTH_BASE                          3
#define POS_ERR                                 4
#define POS_TOOTH_TIP                           5
#define POS_WG_SURFACE                          6
#define POS_TOOTH_SURFACE                       7
#define POS_WG_RELATIVE                         8
#define POS_K                                   9
#define POS_N_WG                                10
#define POS_N_FS                                11
#define POS_N_CS                                12
#define VEL_WG                                  13
#define VEL_FS                                  14
#define VEL_CS                                  15
#define VEL_TOOTH_BASE                          16
#define VEL_ERR                                 17
#define VEL_TOOTH_TIP                           18
#define VEL_WG_SURFACE                          19
#define VEL_TOOTH_SURFACE                       20
#define VEL_WG_RELATIVE                         21
#define VEL_K                                   22
#define VEL_N_WG                                23
#define VEL_N_FS                                24
#define VEL_N_CS                                25
#define VEL_HD_FRICTION                         26
#define TORQUE_WG                               27
#define TORQUE_FS                               28
#define TORQUE_CS                               29
#define TORQUE_INPUT_NORMAL                     30
#define TORQUE_CYCLIC                           31
#define TORQUE_WG_NORMAL                        32
#define TORQUE_WG_FRICTION                      33
#define TORQUE_ERR_IN                           34
#define TORQUE_K                                35
#define TORQUE_TOOTH_TIP_NORMAL                 36
#define TORQUE_TOOTH_TIP_FRICTION               37
#define TORQUE_TOOTH_SURFACE_NORMAL             38
#define TORQUE_TOOTH_SURFACE_TOTAL_LOSS         39
#define TORQUE_TOOTH_SURFACE_COULOMB            40
#define TORQUE_TOOTH_SURFACE_FRICTION           41
#define TORQUE_CYCLIC_FRICTION                  42
#define TORQUE_OUTPUT_NORMAL                    43
#define TORQUE_N_WG                             44
#define TORQUE_N_FS                             45
#define TORQUE_N_CS                             46
#define TORQUE_HD_FRICTION                      47

/* The positions, velocities, and torques outside the harmonic drive. */
#define POS_IN                                  48
#define POS_OUT                                 49
#define VEL_IN                                  50
#define VEL_OUT                                 51
#define TORQUE_MOTOR                            52
#define TORQUE_B_IN                             53
#define TORQUE_B_OUT                            54

/* Sensor variables. */
#define INPUT_POSITION_SENSOR                   55
#define OUTPUT_POSITION_SENSOR                  56
#define INPUT_VELOCITY_SENSOR                   57
#define OUTPUT_VELOCITY_SENSOR                  58
#define CURRENT_SENSOR                          59
```

```
#define TORQUE_SENSOR                                60
#define POSITION_ERROR                               61

/* Parameter functions which can be plotted. */
#define K1                                           62
#define K2                                           63
#define ERFN                                         64
#define DERF                                         65

/* Energy Variables. */
#define TOTAL_ENERGY                                 66
#define TOTAL_KINETIC_ENERGY                         67
#define TOTAL_POTENTIAL_ENERGY                       68
#define TOTAL_INPUT_ENERGY                           69
#define TOTAL_LOST_ENERGY                            70
#define MOTOR_ENERGY                                 71
#define KINETIC_ENERGY_IN                            72
#define KINETIC_ENERGY_OUT                           73
#define SPRING_ENERGY                                74
#define CYCLIC_ENERGY                                75
#define INPUT_DAMPING_ENERGY                         76
#define WG_FRICTION_ENERGY                           77
#define TOOTH_TIP_FRICTION_ENERGY                    78
#define TOOTH_SURFACE_TOTAL_LOSS_ENERGY              79
#define TOOTH_SURFACE_COULOMB_ENERGY                 80
#define TOOTH_SURFACE_FRICTION_ENERGY                81
#define HD_FRICTION_ENERGY                           82
#define OUTPUT_DAMPING_ENERGY                        83

/* Define the number of variables in the output data vector. */
#define NUM_OF_OUTPUT_VAR                            84

/* Declare the variables for the input parameters used in the harmonic drive
 * equations. */
double k1_output_constant, k1_output_amplitude, k1_output_phase;
double k2_output_constant, k2_output_amplitude, k2_output_phase;
double hysteresis_width;
double error_amplitude0, error_phase0;
double error_amplitude1, error_phase1;
double error_amplitude2, error_phase2;
double cyclic_amplitude, cyclic_phase;
double b_wg_constant, b_wg1, b_wg2;
double b_tooth_tip_constant, b_tooth_tip1, b_tooth_tip2;
double cyclic_friction_amplitude, cyclic_friction_phase;
double mu, mu_save;
double b_total1, b_total2;
double tooth_angle, N;
double stiction_torque, stiction_vel;

/* Declare the variables for the joint parameters. */
double inertia_in, inertia_out;
double b_in, b_out;
double motor_kt, motor_kb, amp_resistance;

/* Requested step in motor current. */
double irequested;

/* Initial and final time, the stepsize interval to save results */
double initial_time, final_time, step;

/* Define the initial-condition vectors.*/
double xstart[ORDER+1], xstart_sav[ORDER+1];

/* Define a vector to hold all of the possible output data values for
```

```
 * each simulation time step. */
double v[NUM_OF_OUTPUT_VAR];

/* Define output vectors to be allocated dynamically. */
double **output_data, *time;

/* Define the parameters that are calculated from the input parameters
 * for the rotary harmonic drive model. */
double k1_constant, k1_amplitude, k1_phase;
double k2_constant, k2_amplitude, k2_phase;
double stiction_torque_hd, stiction_vel_hd;
double cyclic_friction_amp_hd, cyclic_friction_phase_hd;
double b_hd_constant, b_hd1, b_hd2;

/* Define the parameters that are calculated from the input parameters
 * for the tooth-rubbing harmonic drive model. */
double tan1, cos1, sin1, tan2, cos2, sin2;
double wg_angle;
double stiction_torque_tooth, stiction_vel_tooth;
double cyclic_friction_amp_tooth, cyclic_friction_phase_tooth;
double b_tooth_surface_constant, b_tooth_surface1, b_tooth_surface2;
```

Appendix C: Motor Amplifier Model

For most of the operating range of the harmonic-drive testing equipment, the amplifiers which supply current to the DC motors can sustain current values up to the their maximum rated current. However, at high motor velocities, back EMF generated by the motor can saturate the amplifier voltage which results in a reduction of the maximum current the amplifier can deliver. This saturation behavior can be captured by developing a few simple equations which incorporate the velocity and current limits of the amplifiers with some simplified dynamics of the motor-amplifier circuit.

Identical Aerotech model 4020-LS linear current-amplifiers were used for the three harmonic-drive testing stations. The voltage and current operating range of these amplifiers is shown in figure C.1. Using this plot, the upper and lower voltage limits of the amplifier

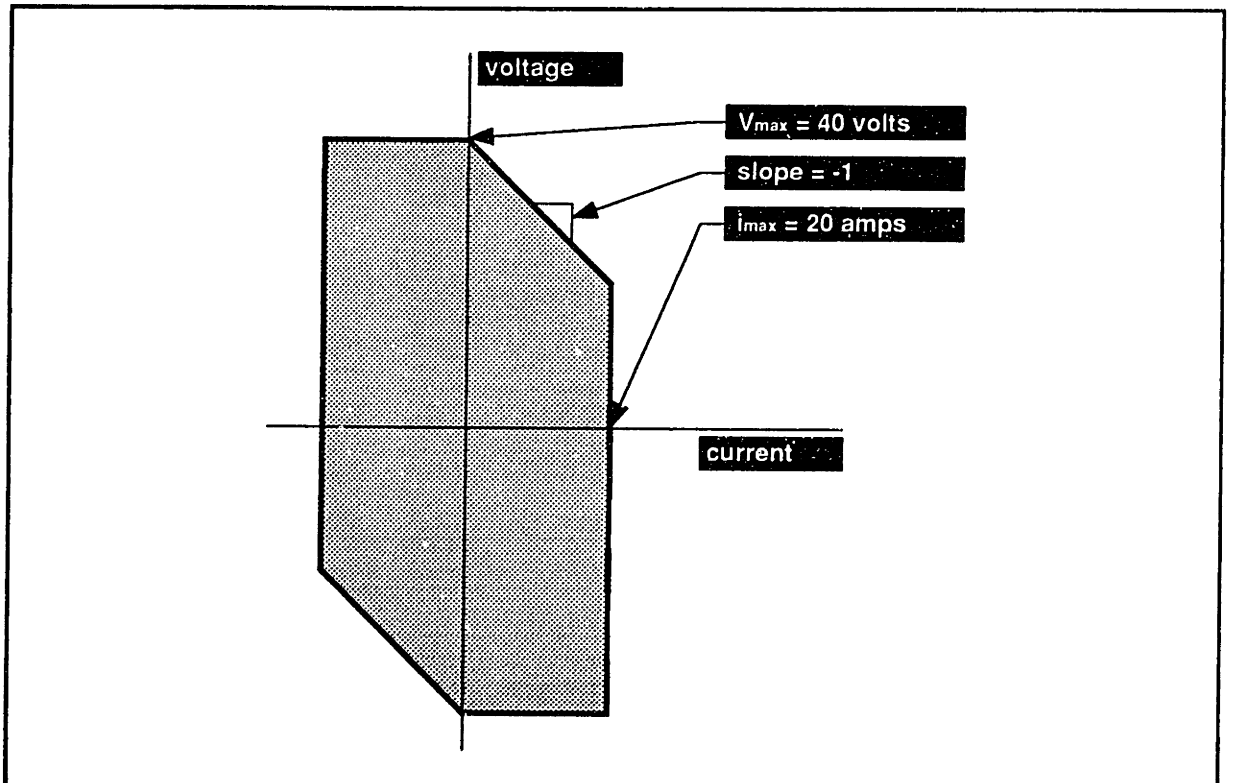

Figure C.1: Amplifier voltage and current operating domain

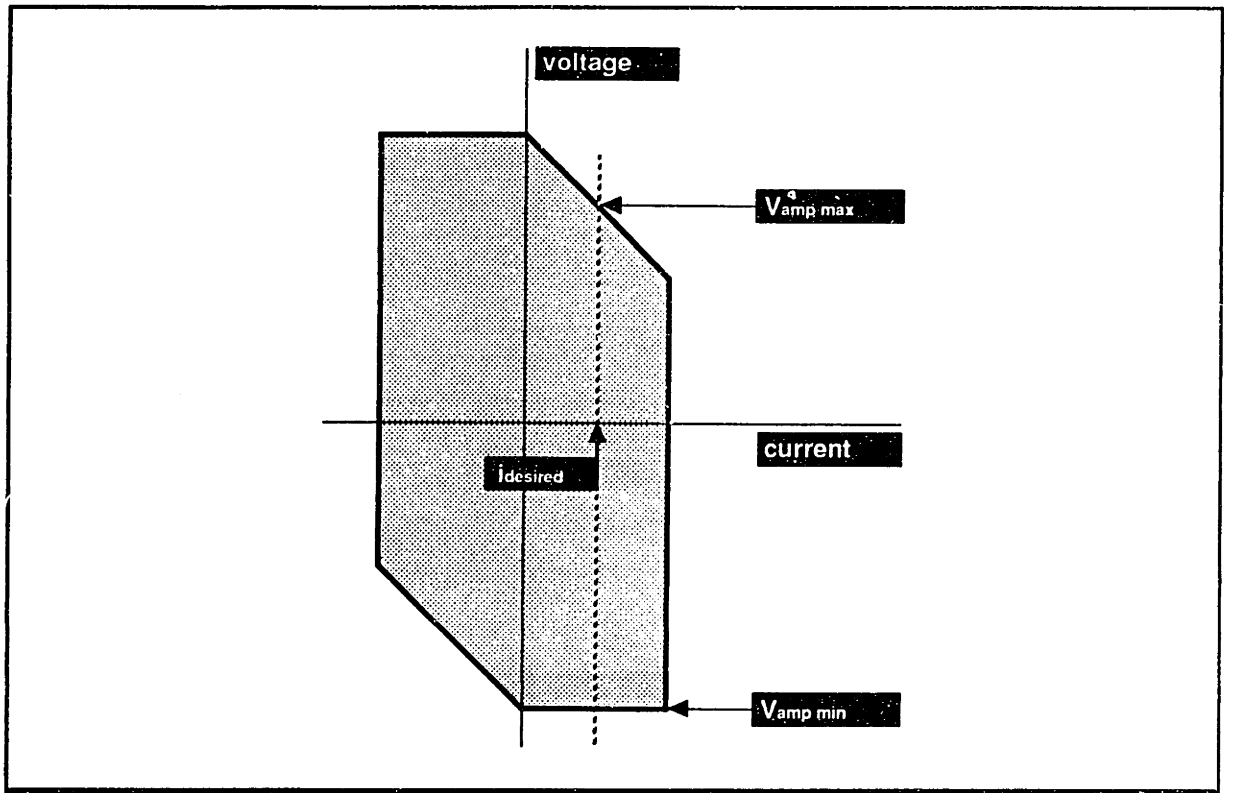

Figure C.2: Calculation of voltage bounds for a desired current

can be calculated for any desired current within the given current range, as illustrated in figure C.2. Given this upper and lower voltage-bound, an upper and lower current-bound can also be found by considering the simplified amplifier circuit shown in figure C.3. Summing the voltage around the circuit yields the equation

$$V_{amp} = V_{motor} + V_R \text{ , or} \tag{C.1}$$

$$V_{amp} = K_b \omega_{motor} + i_{amp} R \text{ ,} \tag{C.2}$$

where K_b is the back EMF constant of the motor, ω_{motor} is the motor velocity, and R is the resistance across the motor terminals. Resistance values which provided good results are listed in Table C.1 for the three harmonic-drive testing stations. By solving equation C.2 for the amplifier current, i_{amp}, and substituting the voltage upper and lower-bounds as determined in figure C.2, an upper and lower bound for the amplifier current can be

Table C.1: Resistance values for the motor amplifier model

	Joint 1	Joint 2	Joint 3
Motor Resistance (ohms)	2.1	3.1	9.5

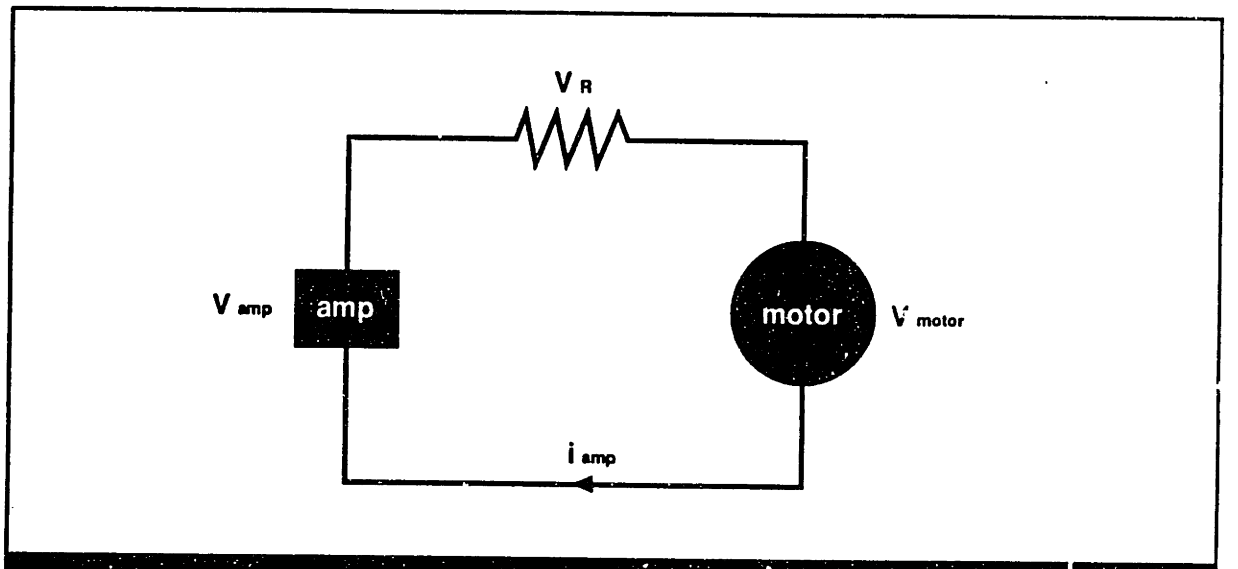

Figure C.3: Motor-amplifier simplified circuit schematic

derived:

$$i_{amp\ max} = \frac{V_{amp\ max} - K_b\omega_{motor}}{R}, \text{ and} \tag{C.3}$$

$$i_{amp\ min} = \frac{V_{amp\ min} - K_b\omega_{motor}}{R}. \tag{C.4}$$

Therefore, for a given motor operating speed and a desired current value, the instantaneous current limit on the amplifiers can be determined simply by (1) using the amplifier operating specifications to calculate the voltage limits for the requested current, and (2) substituting these voltage limits into equations (C.3) and (C.4). This model was incorporated successfully into a numerical simulation which calculated the amplifier current on every time-step.

Appendix D: Experimental Time-Response Data Plots

This appendix contains a complete set of all of the dynamic-response plots collected from the three harmonic-drive testing stations. For each harmonic-drive, input and output position were measured and used to derive input and output velocity data. The output torque on each transmission was monitored by the torque sensors while the input torque was determined from the motor-current sensor. Additionally, from the input and output position measurements, the dynamic position-error across the transmission was calculated. A summary of all of the plots shown in this appendix and their corresponding plot numbers is given in table D.1. For each of the plots listed in this table, except the dynamic position-error figure, time-response curves are plotted for several different motor-current step-commands. Depending on the visual appearance of the data, the different response curves on each of these plots are either plotted on a single axis or plotted on separate axes. For the sake of clarity, the output-velocity response data for each harmonic drive is plotted in both of these ways. In the case of the dynamic position-error plots, a single time-response curve is shown, rather than several, in order to generalize about behavior for different step inputs. A complete discussion of all of these plots can be found in section 2.6 of this document.

Table D.1: Summary of experimental time-response data-plot numbers			
	Joint 1	**Joint 2**	**Joint 3**
Input Position	D.1.1	D.2.1	D.3.1
Input Velocity	D.1.2	D.2.2	D.3.2
Input Current	D.1.3	D.2.3	D.3.3
Output Position	D.1.4	D.2.4	D.3.4
Output Velocity - view 1	D.1.5	D.2.5	D.3.5
Output Velocity - view 2	D.1.6	D.2.6	D.3.6
Output Torque	D.1.7	D.2.7	D.3.7
Dynamic Position Error	D.1.8	D.2.8	D.3.8

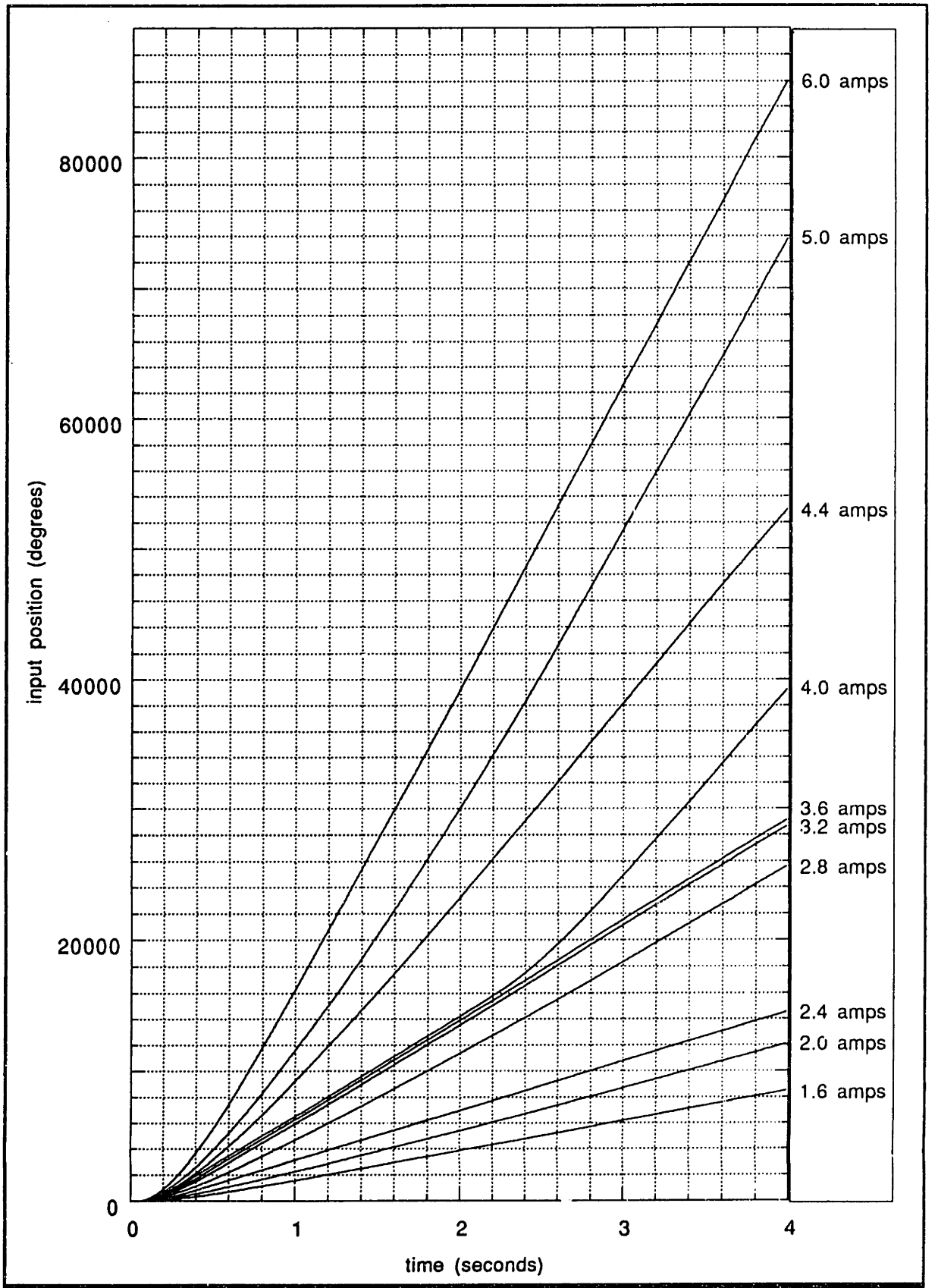

Figure D.1.1: Joint 1 input-position step-responses

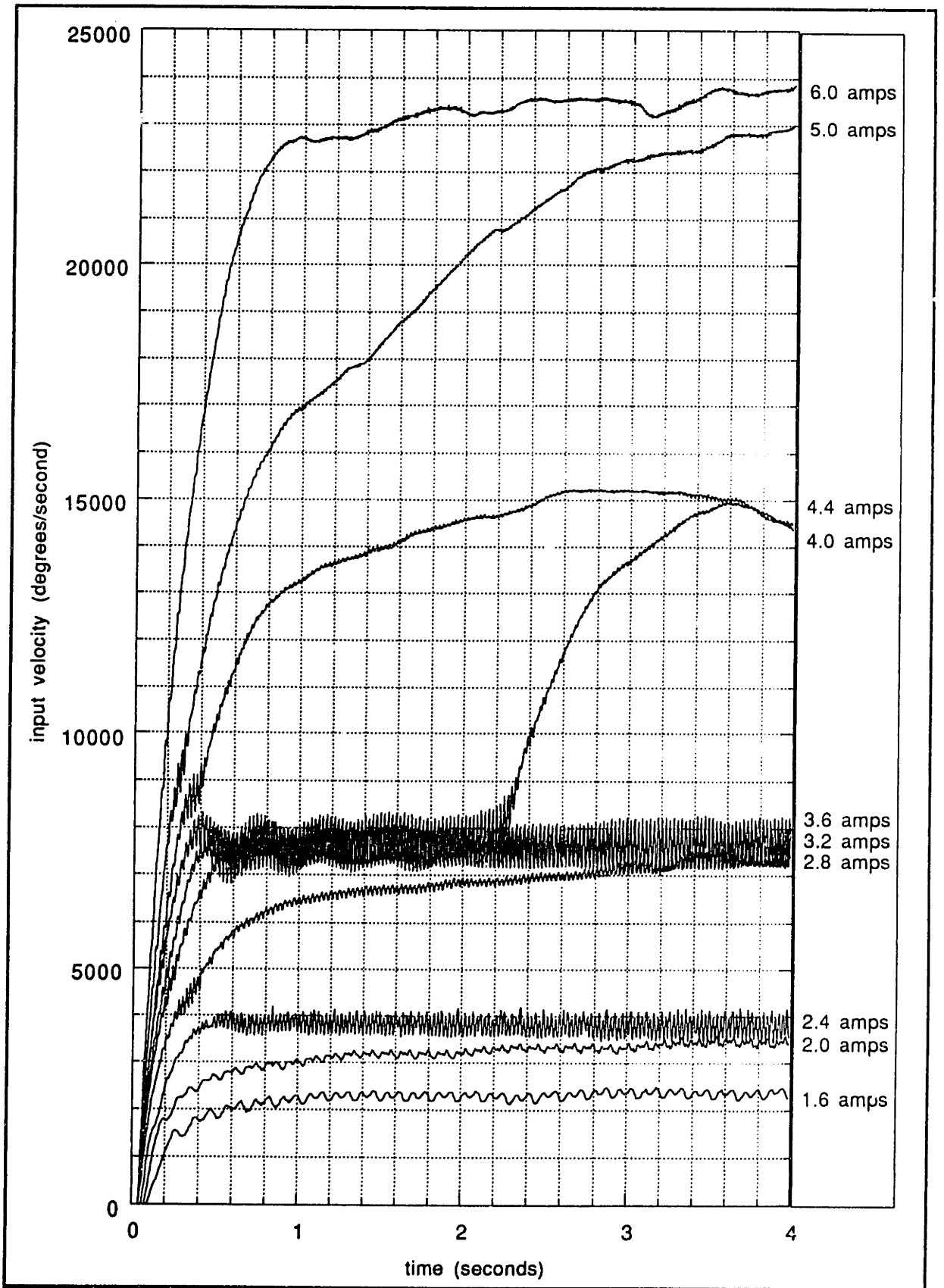

Figure D.1.2: Joint 1 input-velocity step-responses

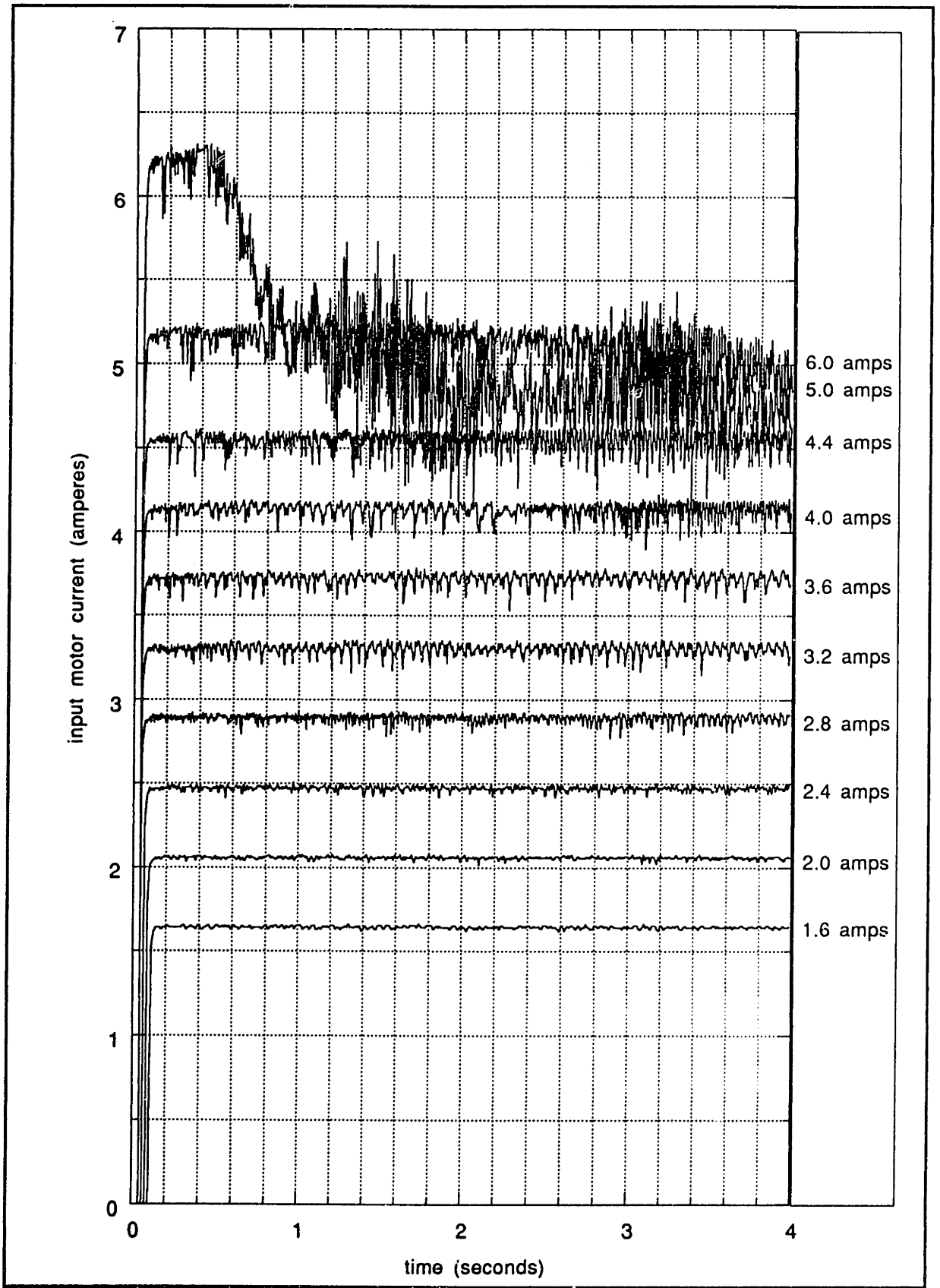

Figure D.1.3: Joint 1 input-current step-responses

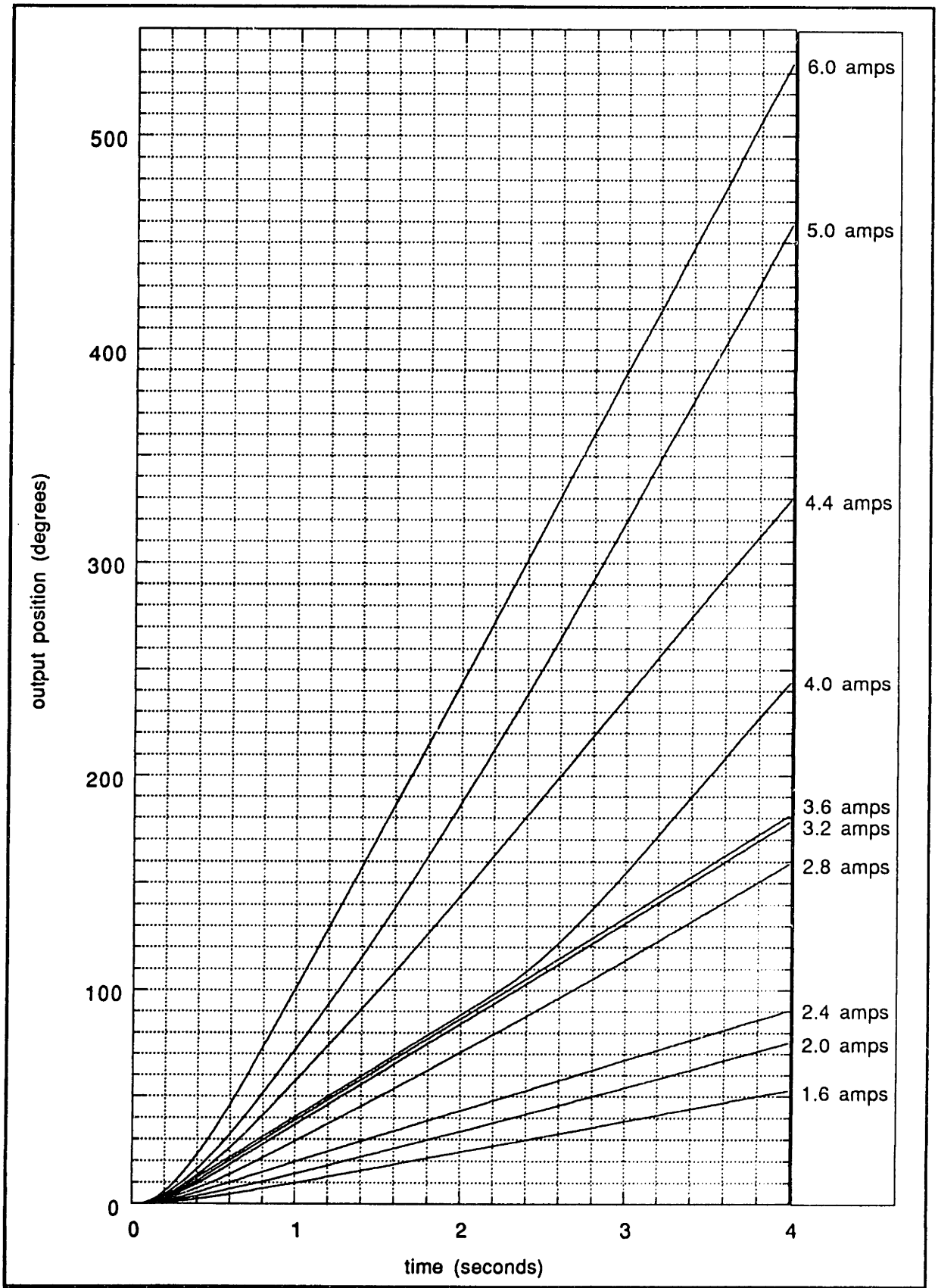

Figure D.1.4: Joint 1 output-position step-responses

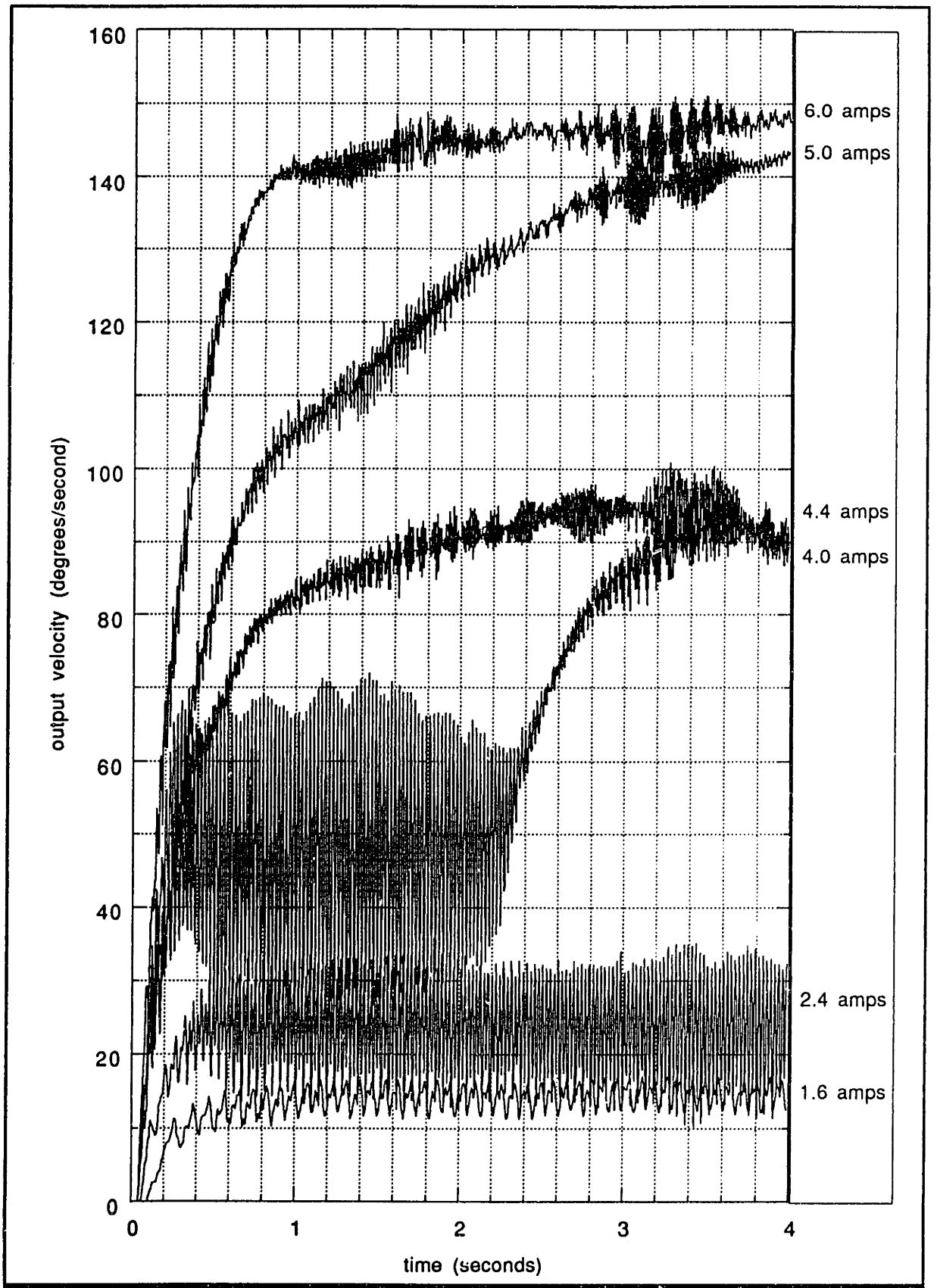

Figure D.1.5: Joint 1 output-velocity step-responses

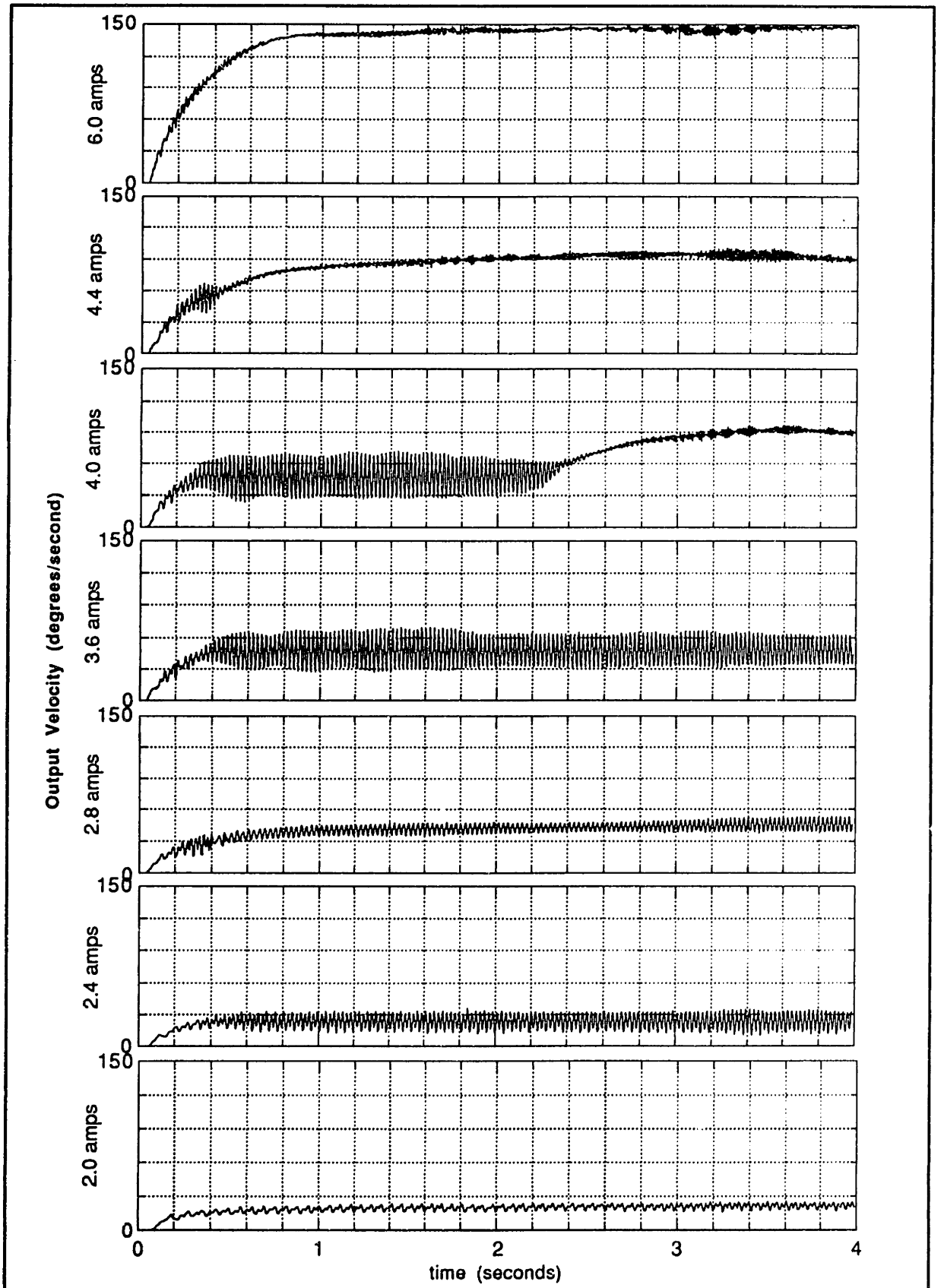

Figure D.1.6: Joint 1 output-velocity step-responses

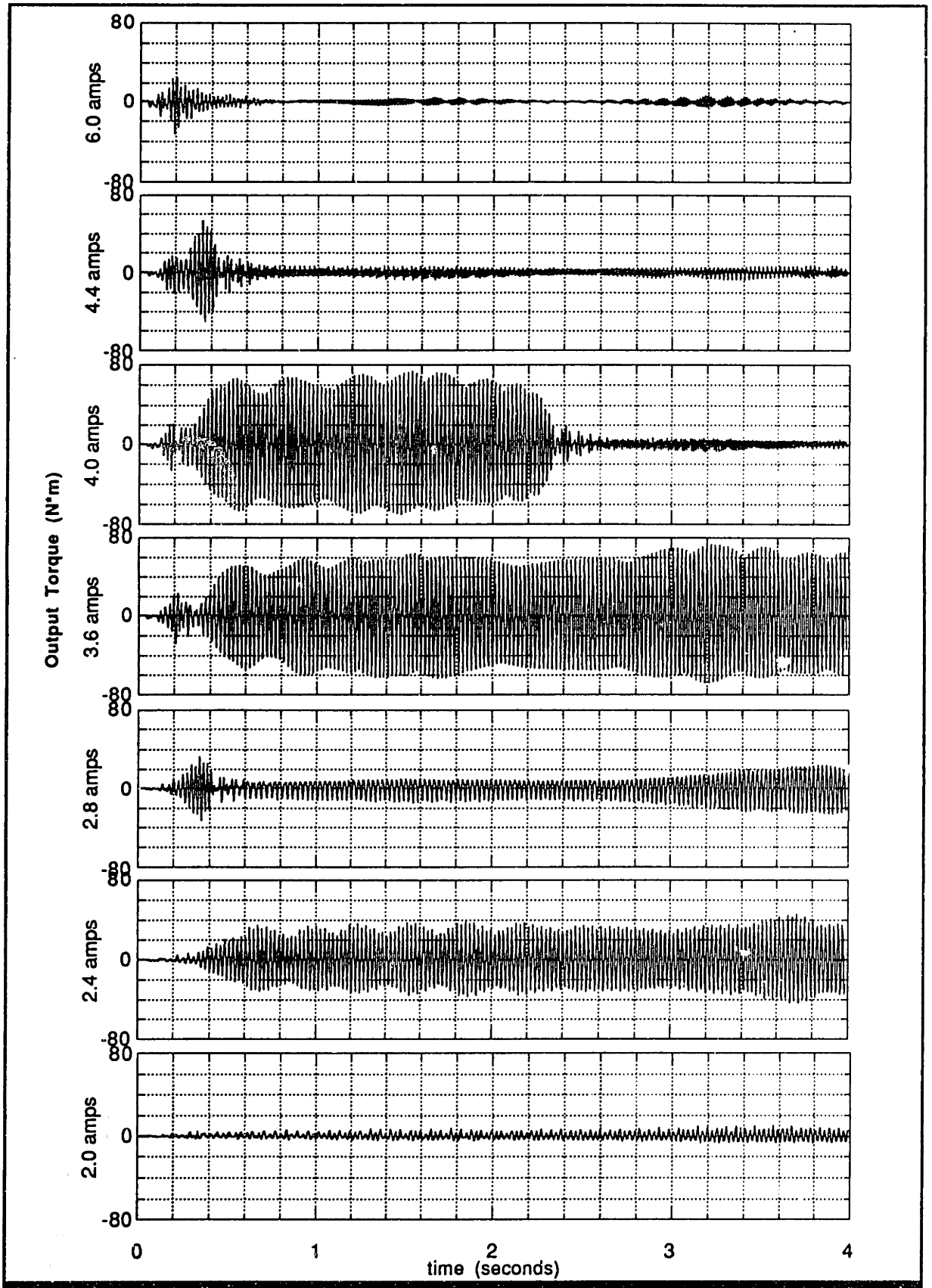

Figure D.1.7: Joint 1 output-torque step-responses

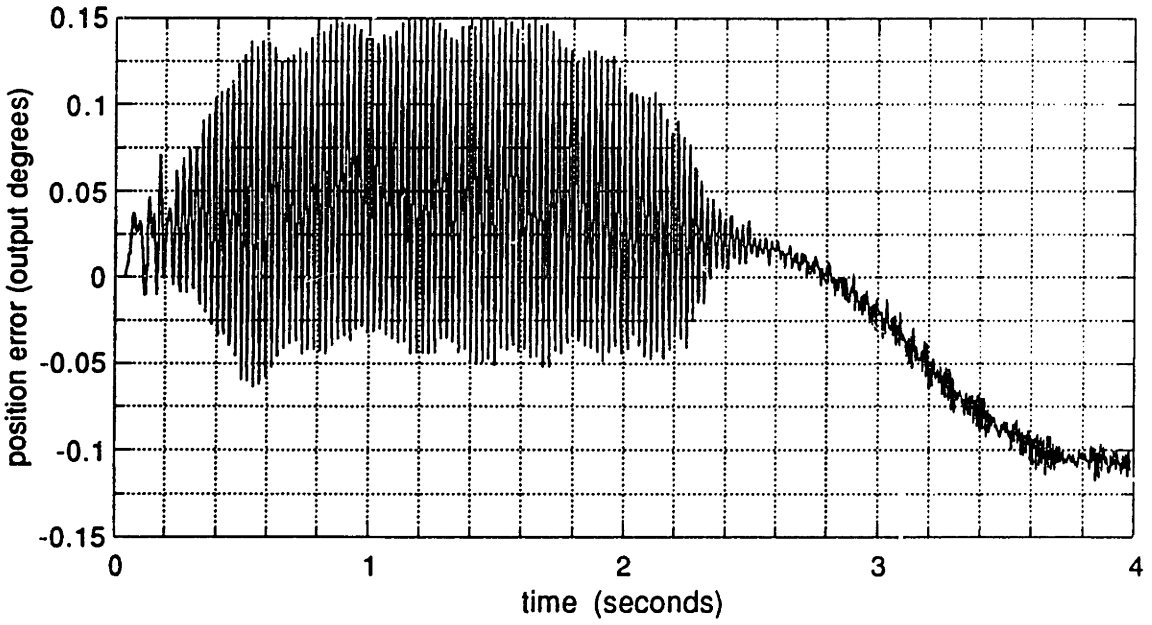

Figure D.1.8: Joint 1 dynamic position error at 4.0 amps resonance

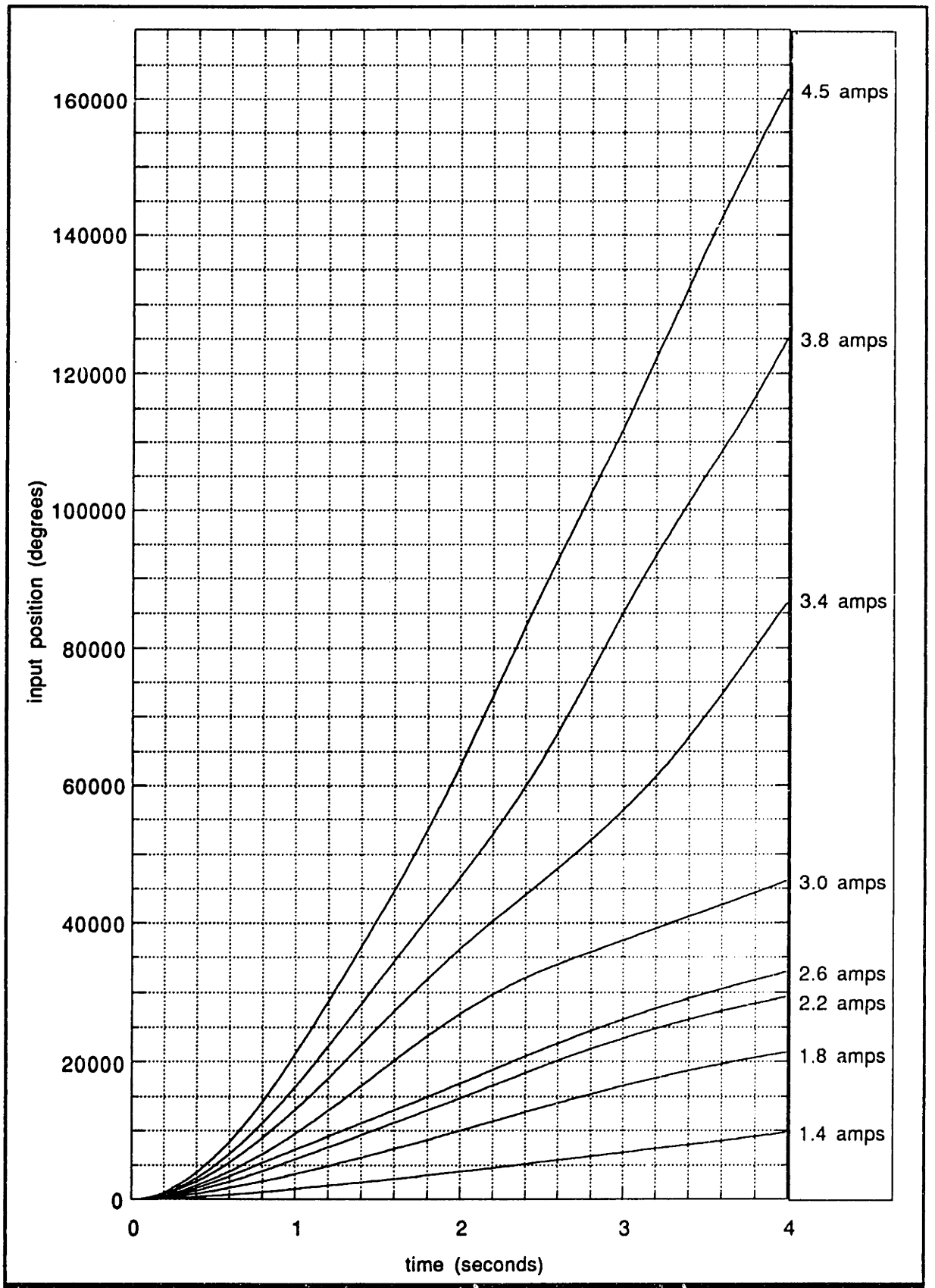

Figure D.2.1: Joint 2 input-position step-responses

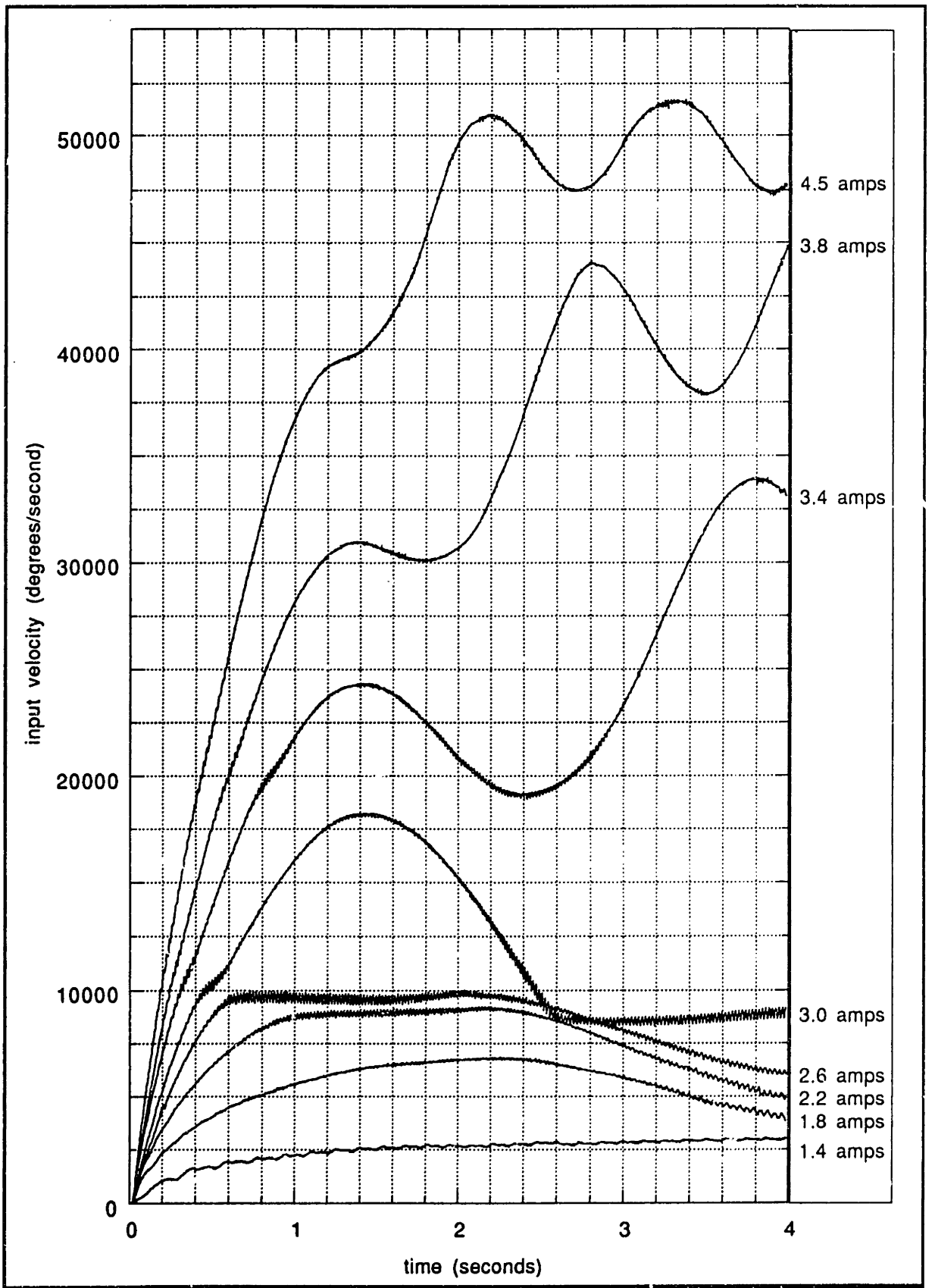

Figure D.2.2: Joint 2 input-velocity step-responses

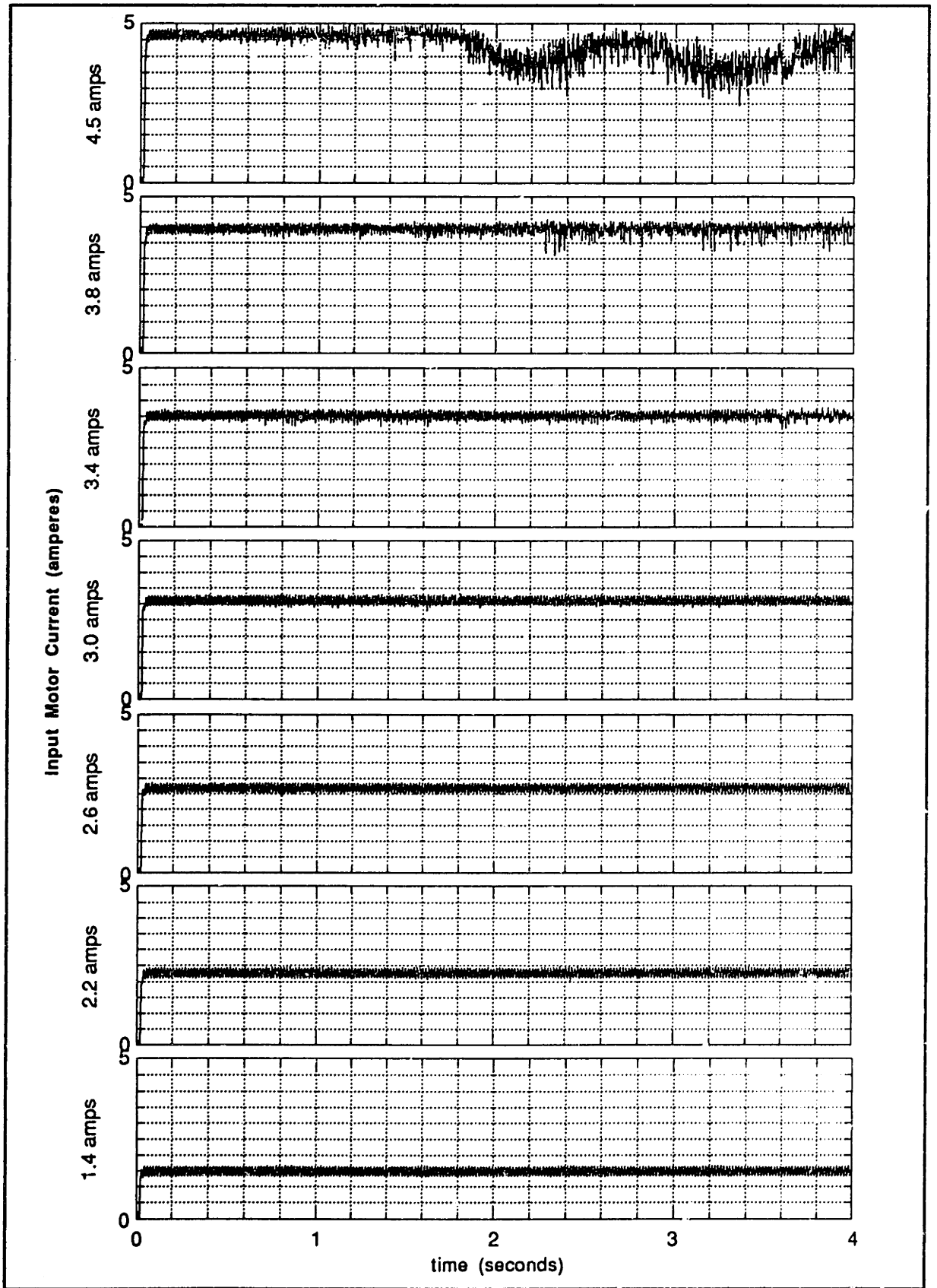

Figure D.2.3: Joint 2 input-current step-responses

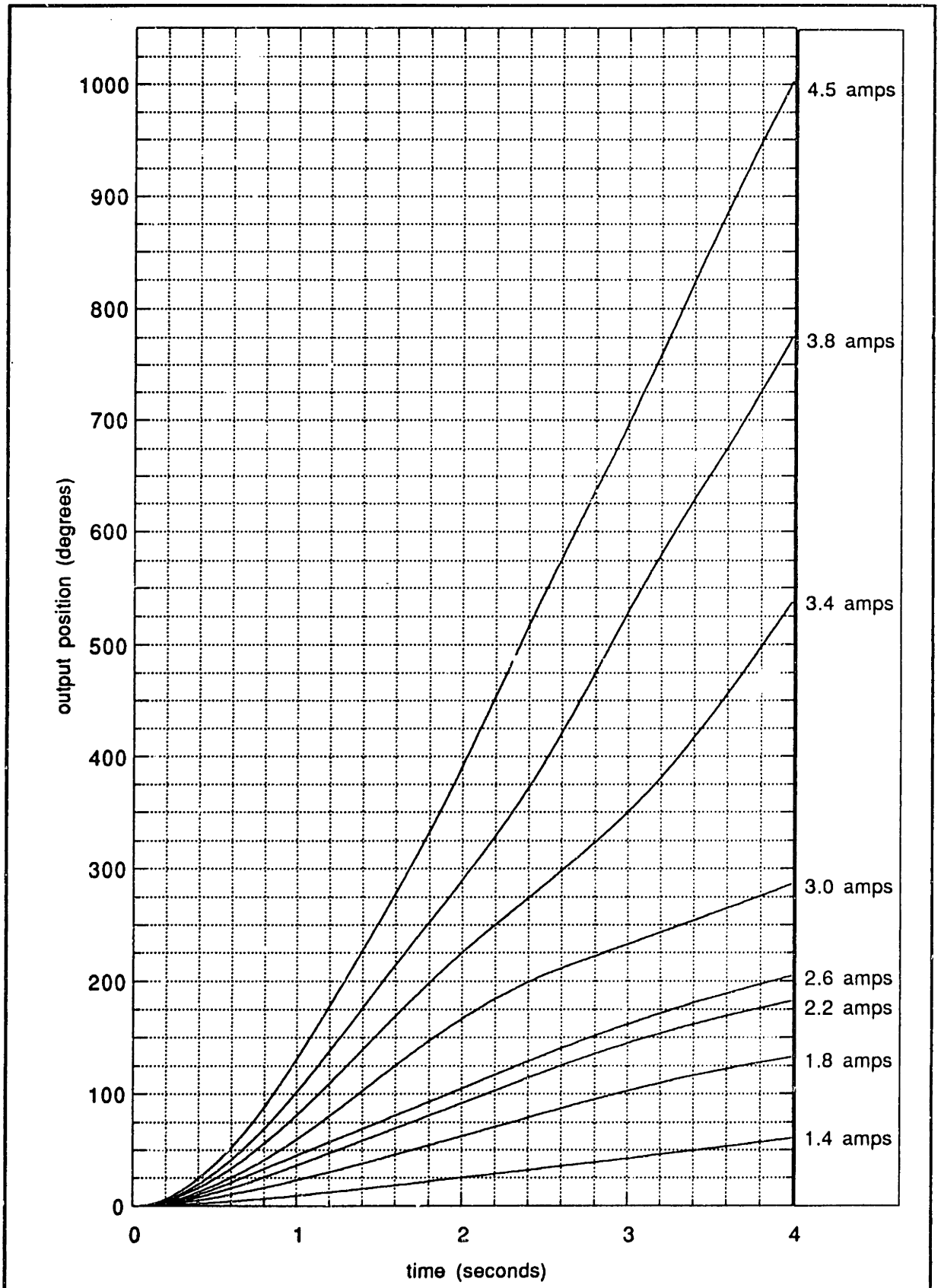

Figure D.2.4: Joint 2 output-position step-responses

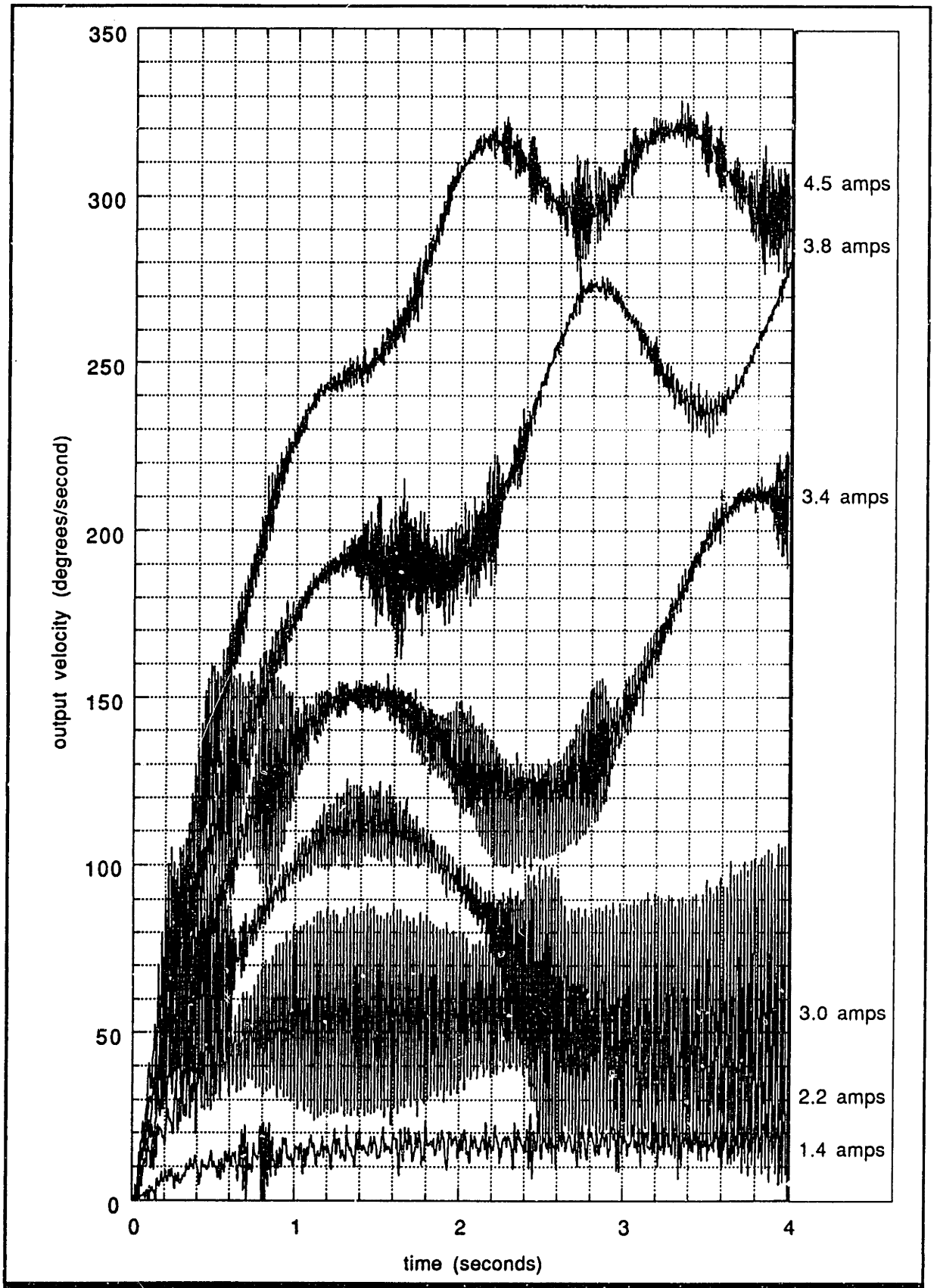

Figure D.2.5: Joint 2 output-velocity step-responses

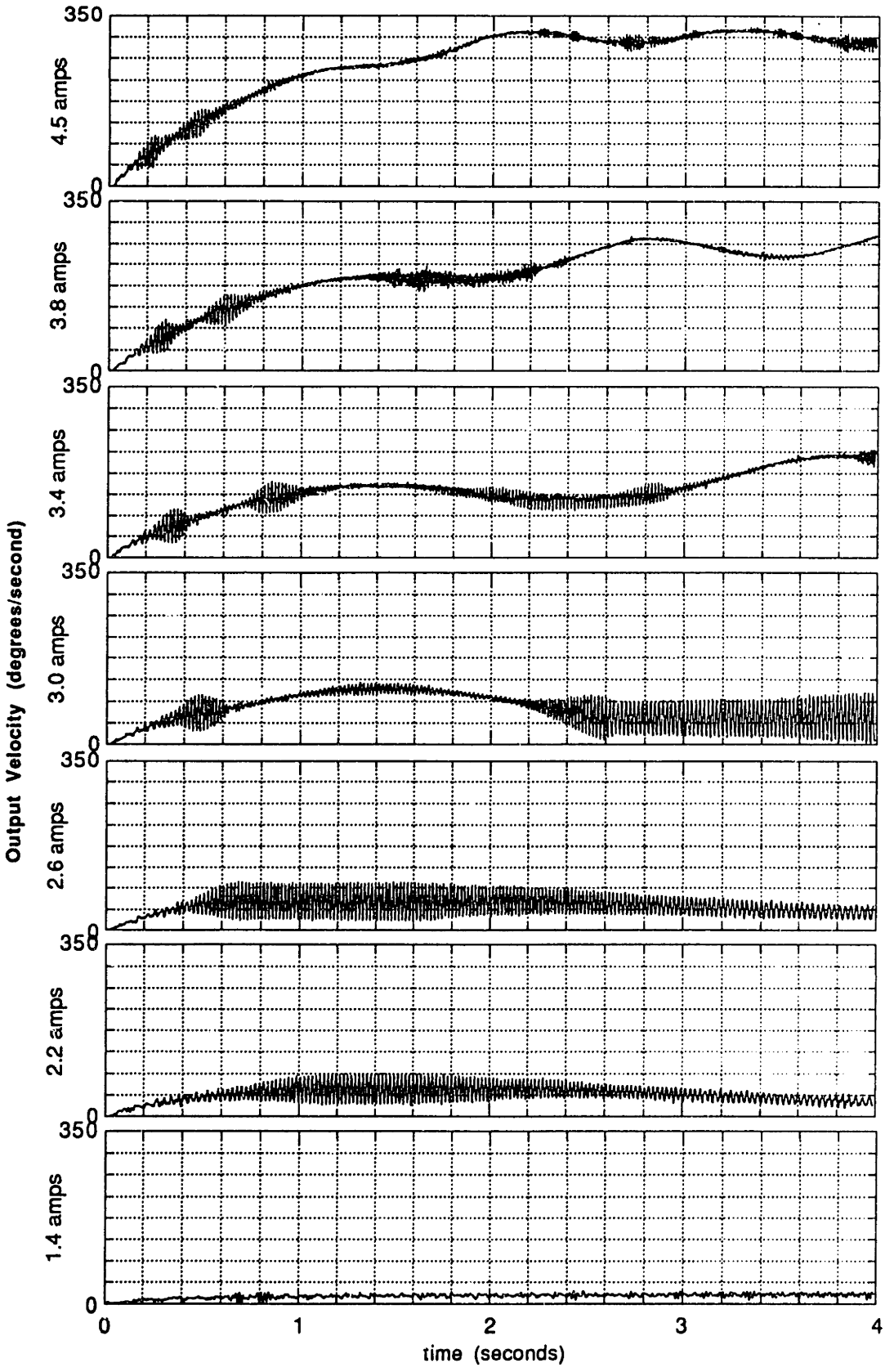

Figure D.2.6: Joint 2 output-velocity step-responses

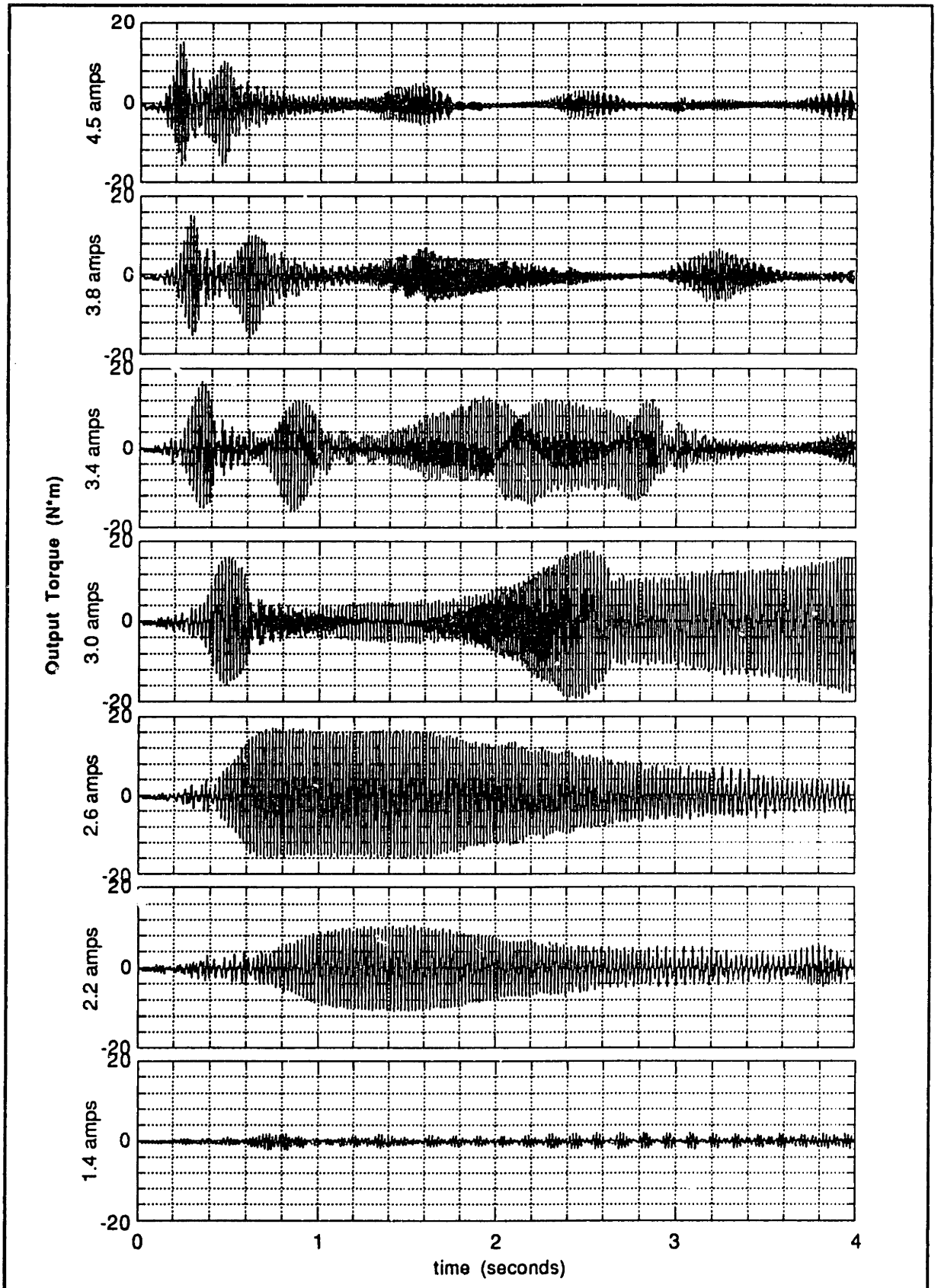

Figure D.2.7: Joint 2 output-torque step-responses

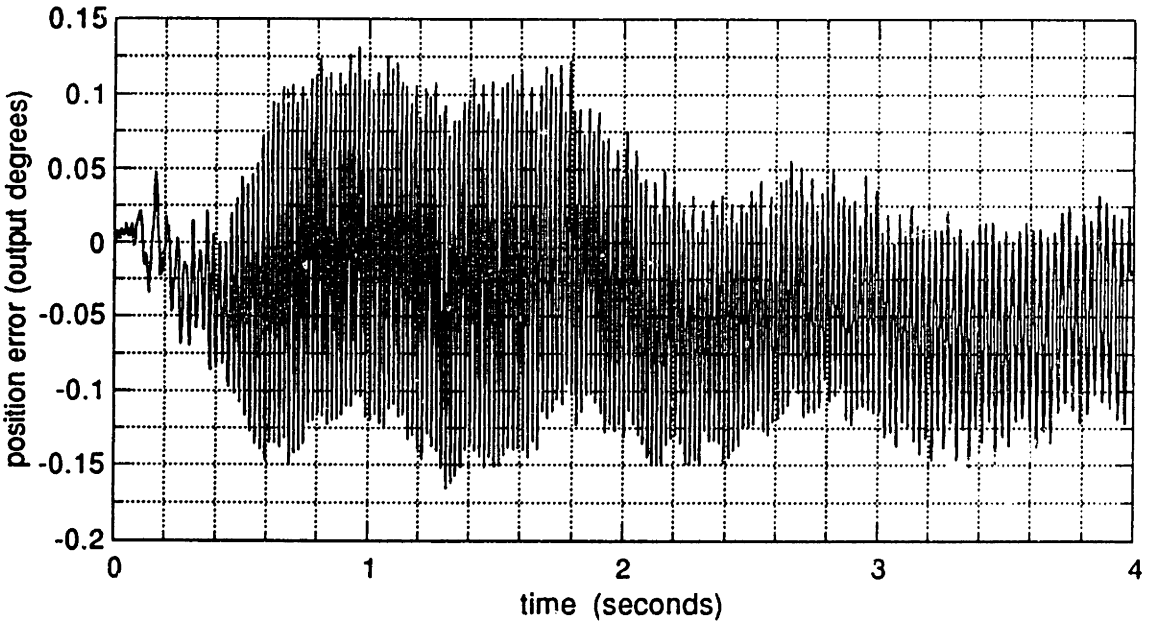

Figure D.2.8: Joint 2 dynamic position error at 2.6 amps resonance

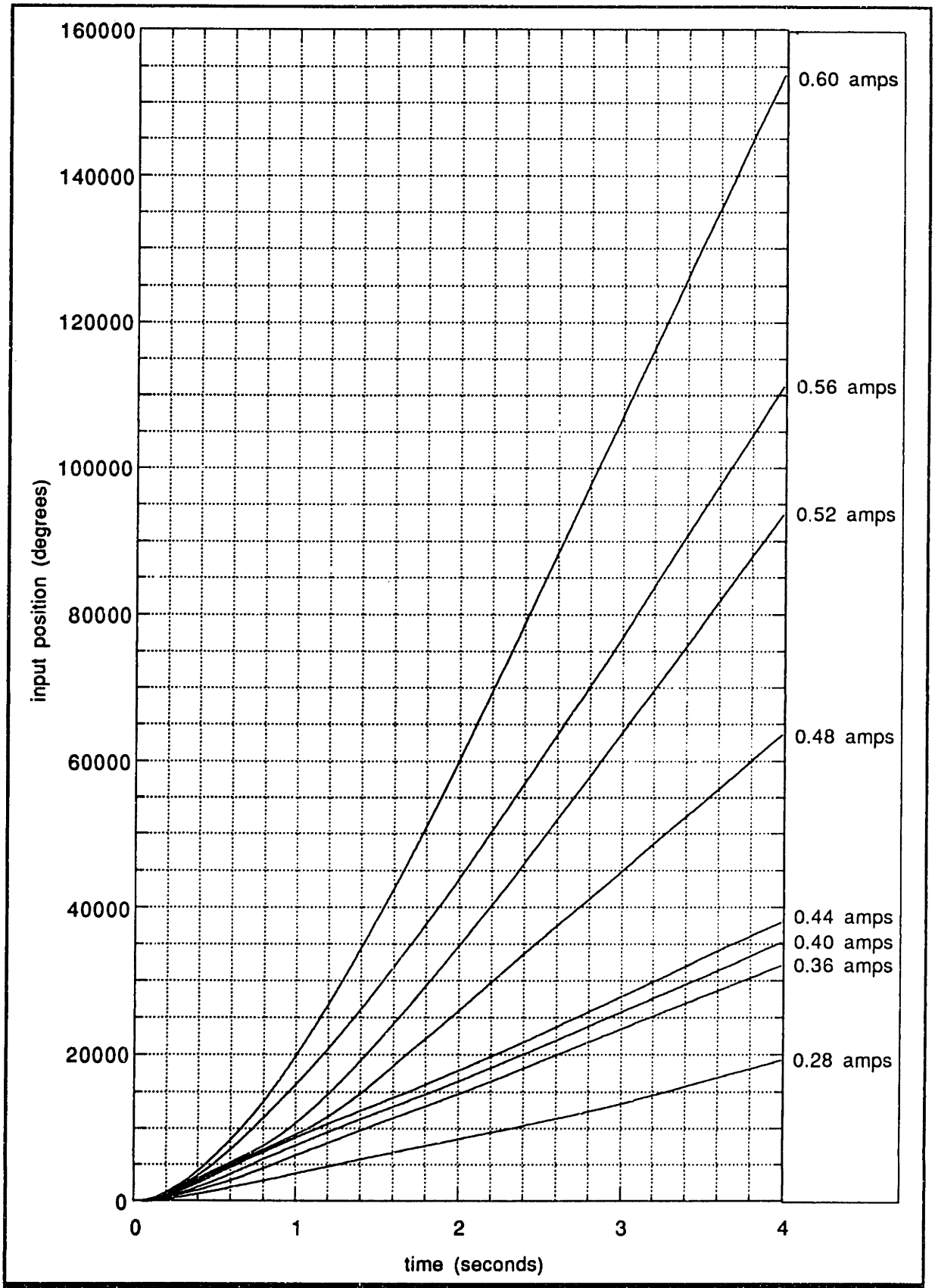

Figure D.3.1: Joint 3 input-position step-responses

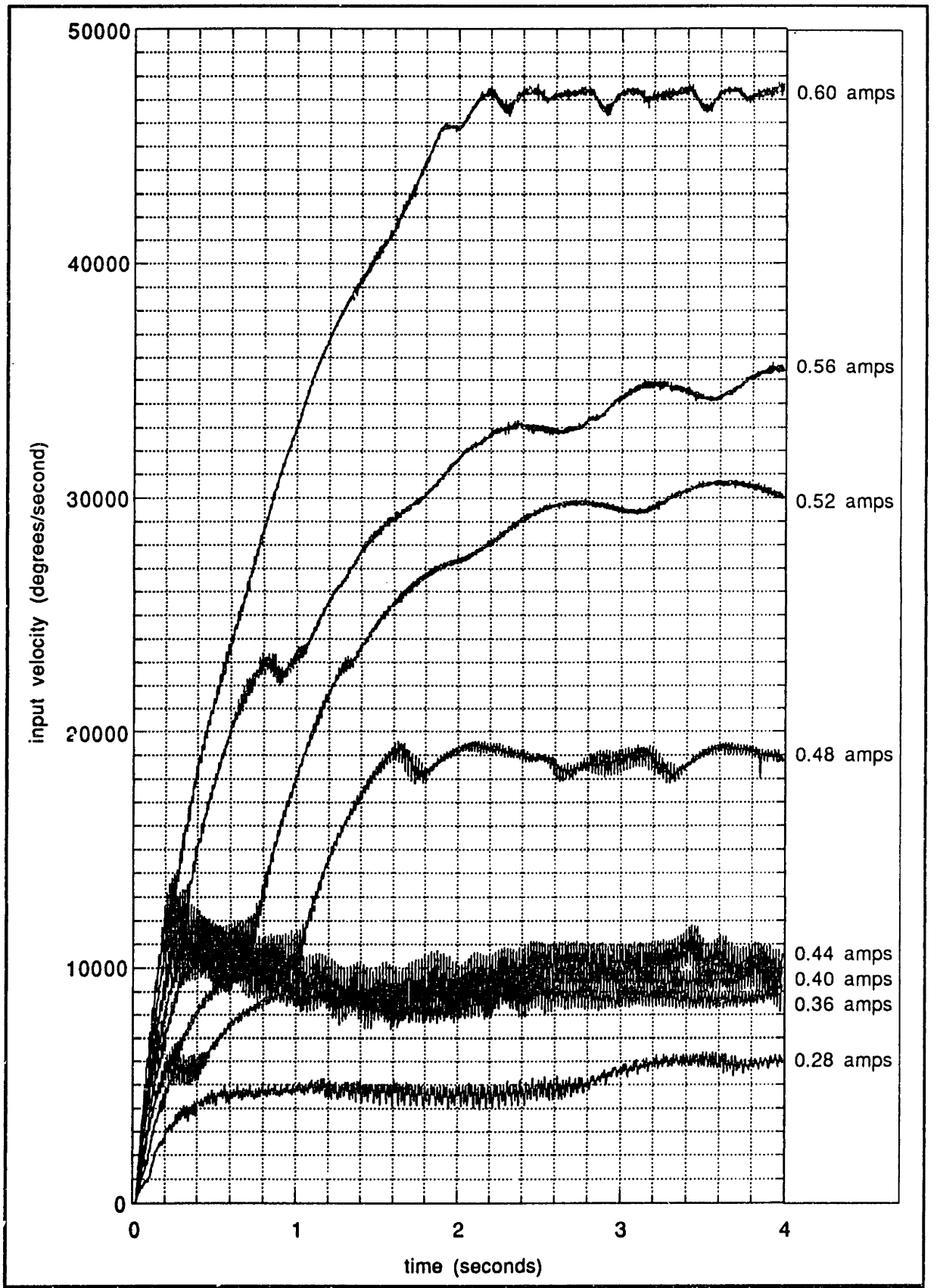

Figure D.3.2: Joint 3 input-velocity step-responses

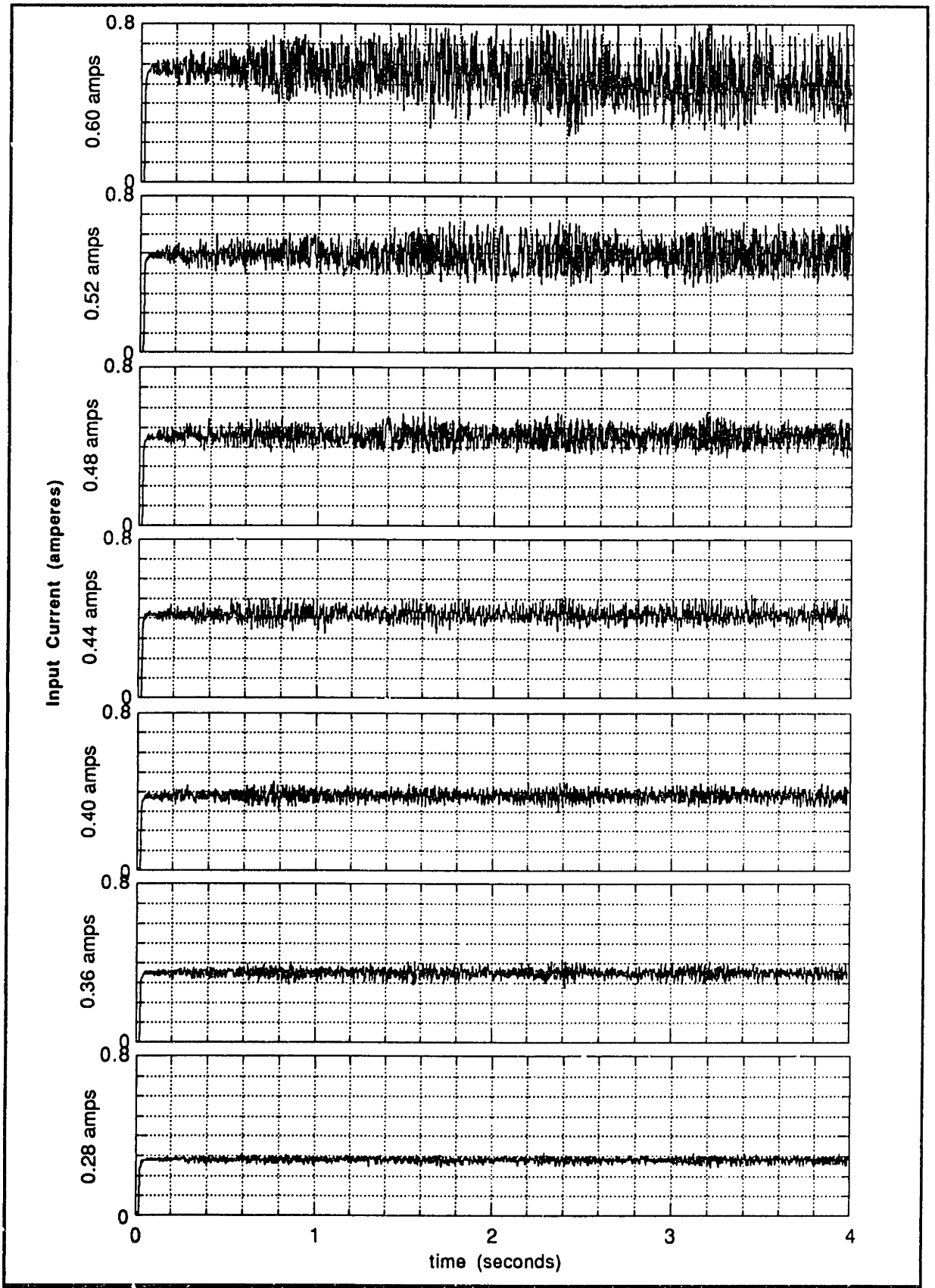

Figure D.3.3: Joint 3 input-current step-responses

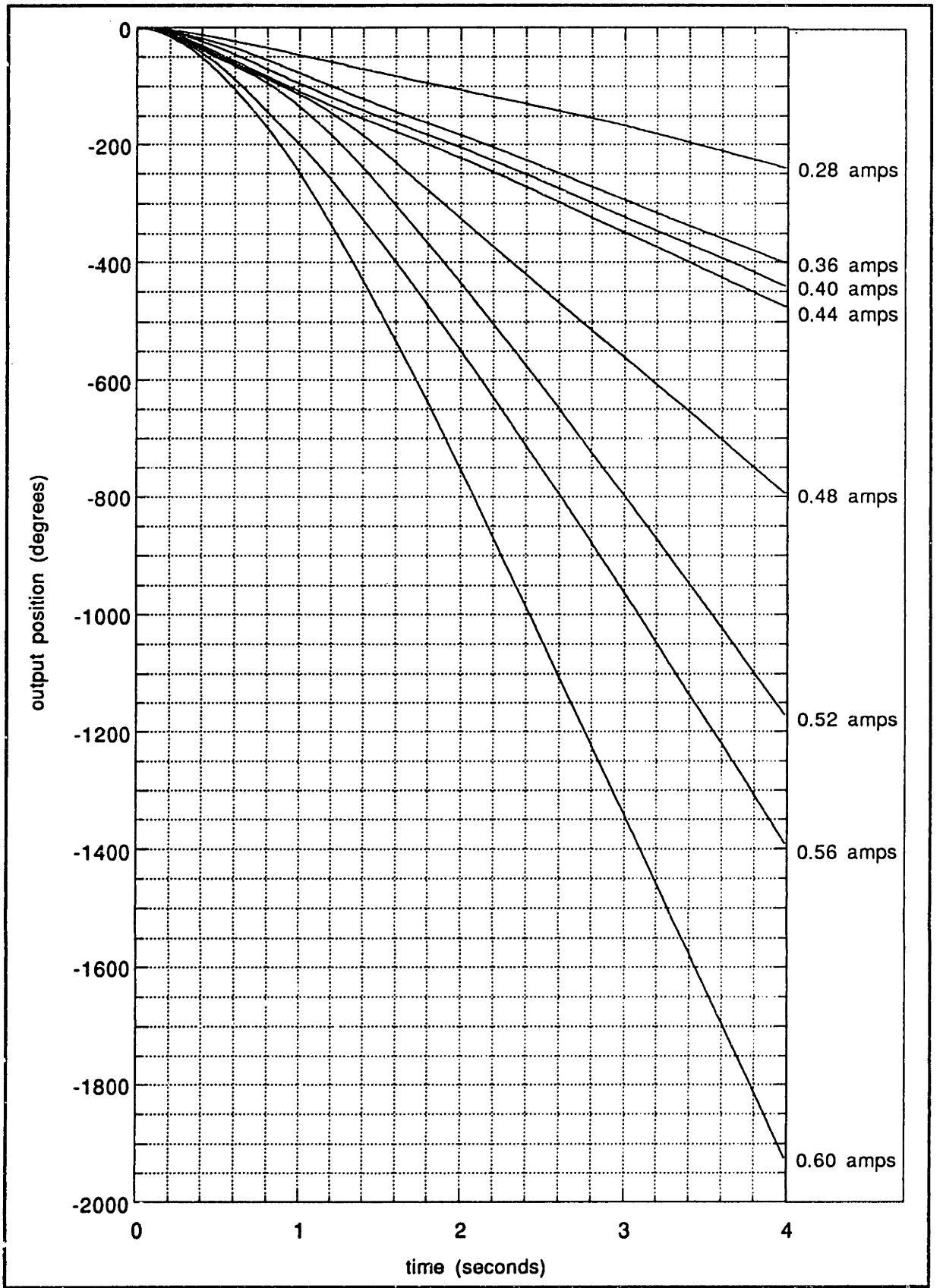

Figure D.3.4: Joint 3 output-position step-responses

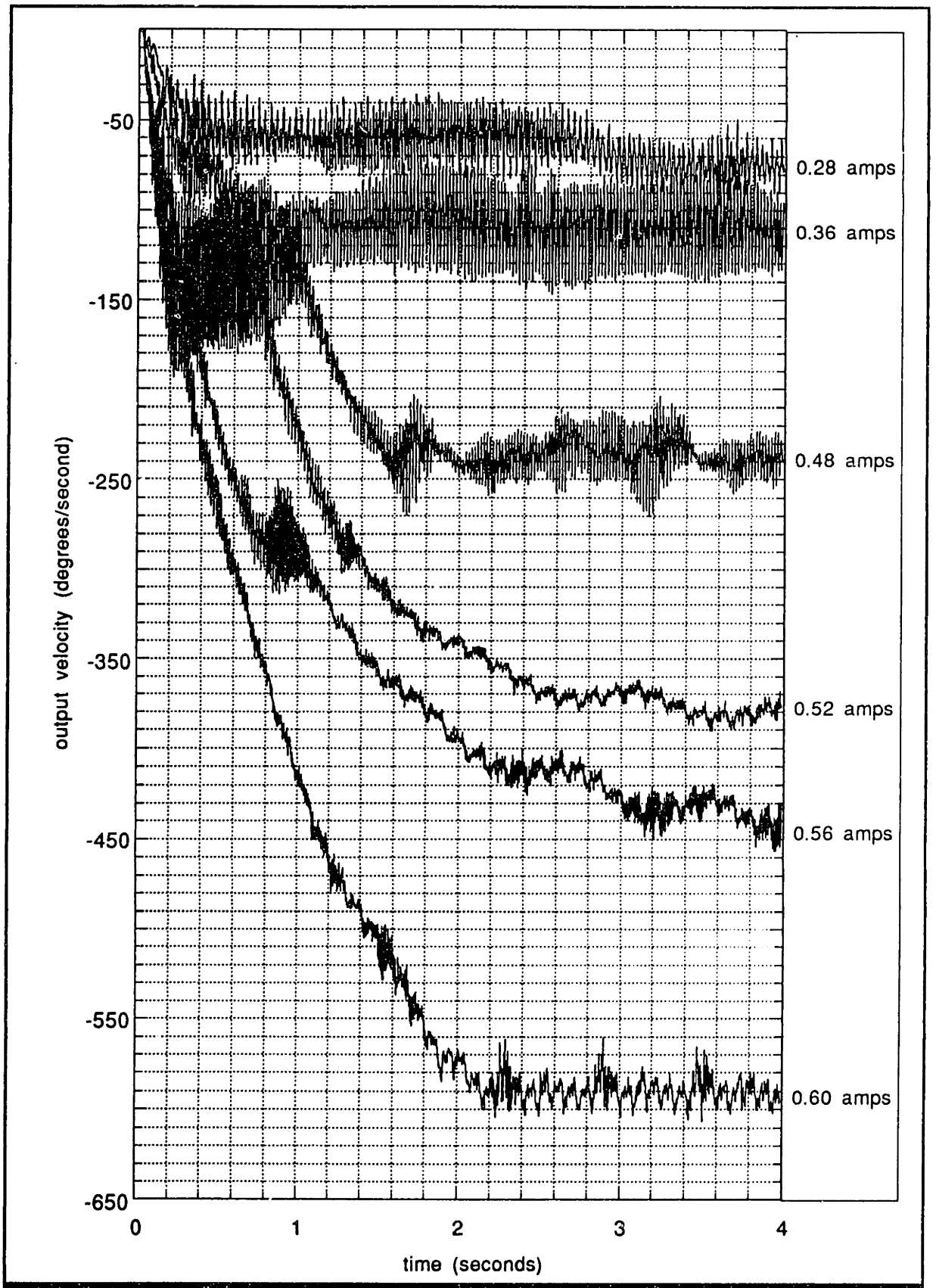

Figure D.3.5: Joint 3 output-velocity step-responses

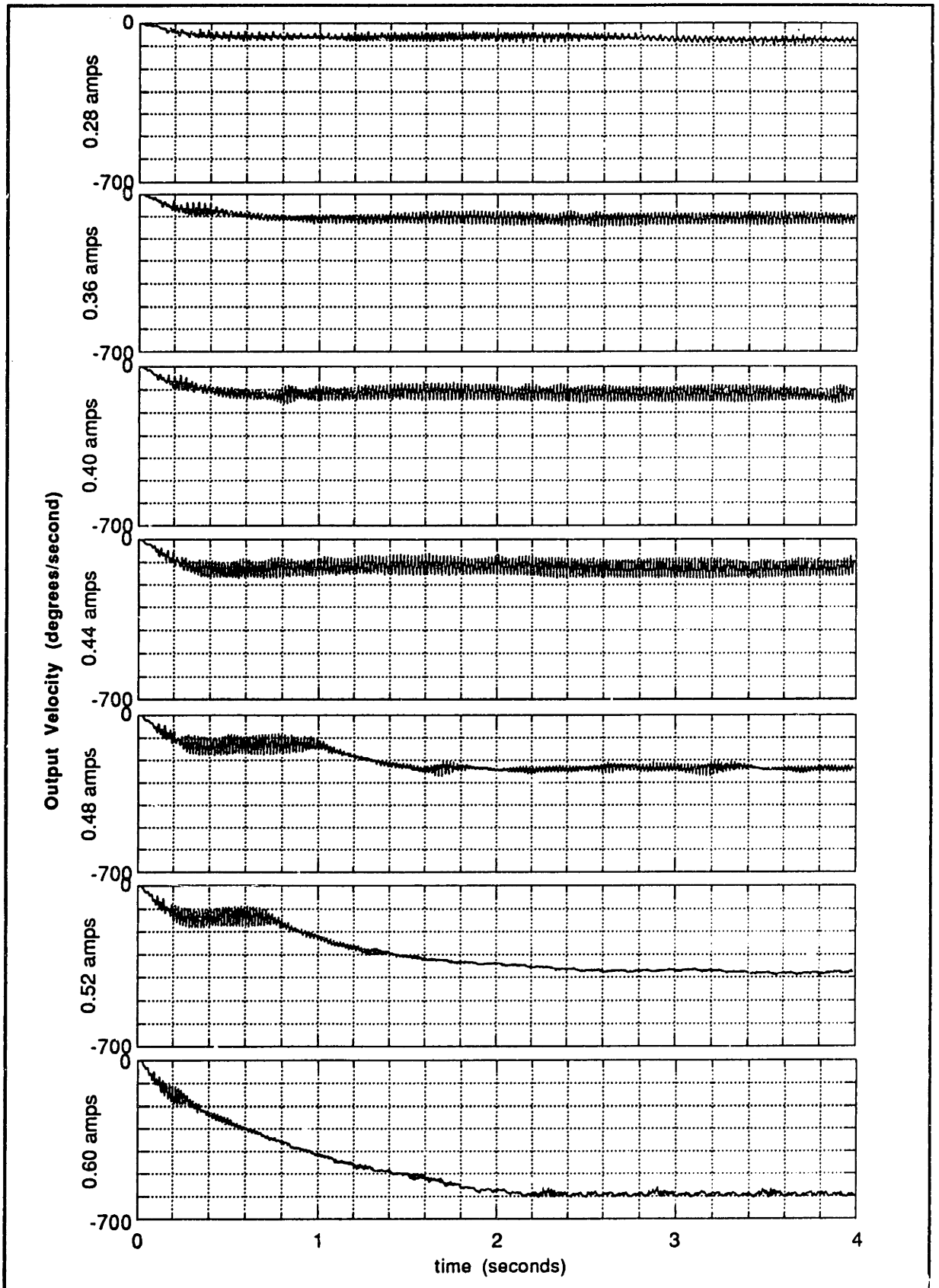

Figure D.3.6: Joint 3 output-velocity step-responses

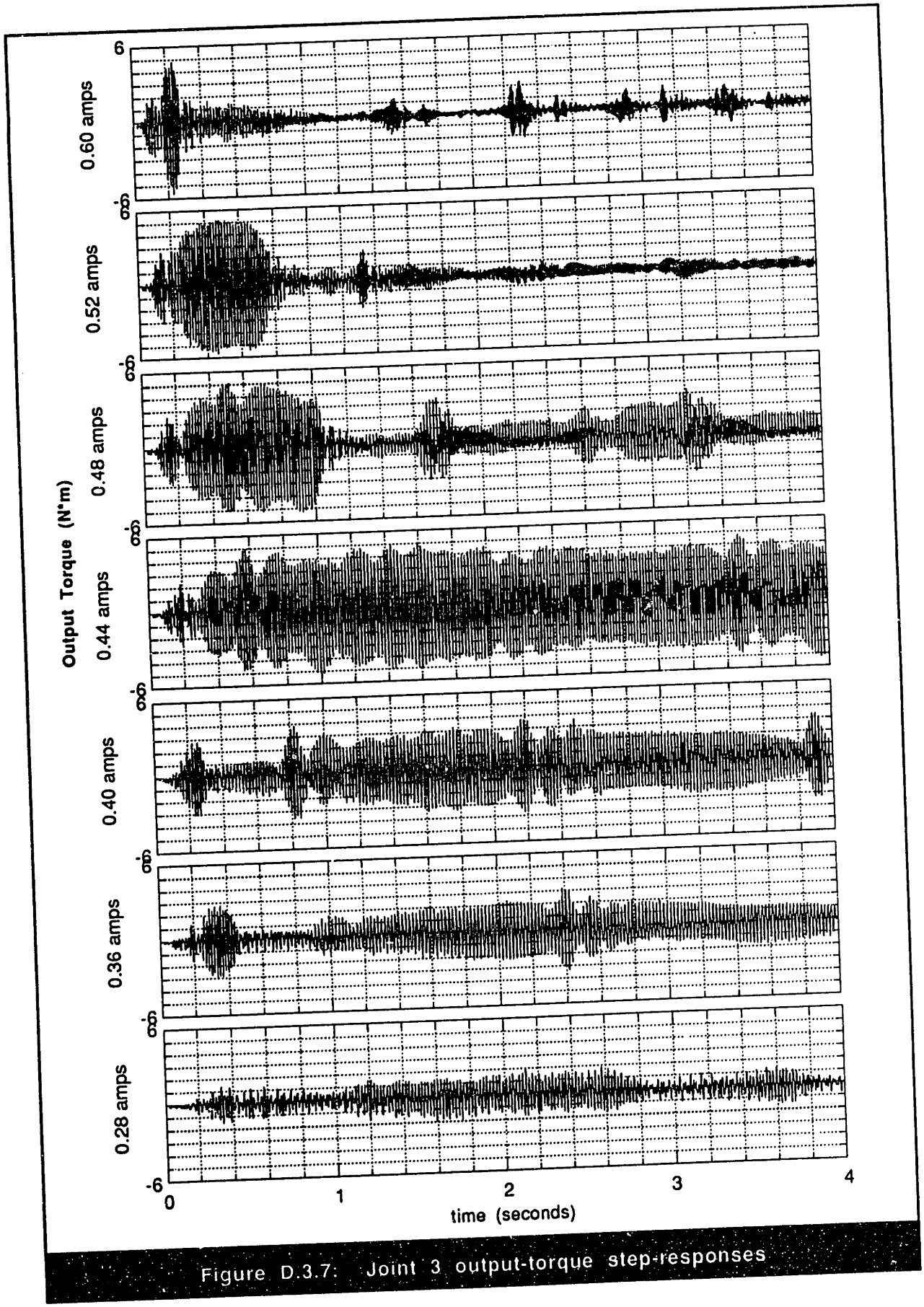

Figure D.3.7: Joint 3 output-torque step-responses

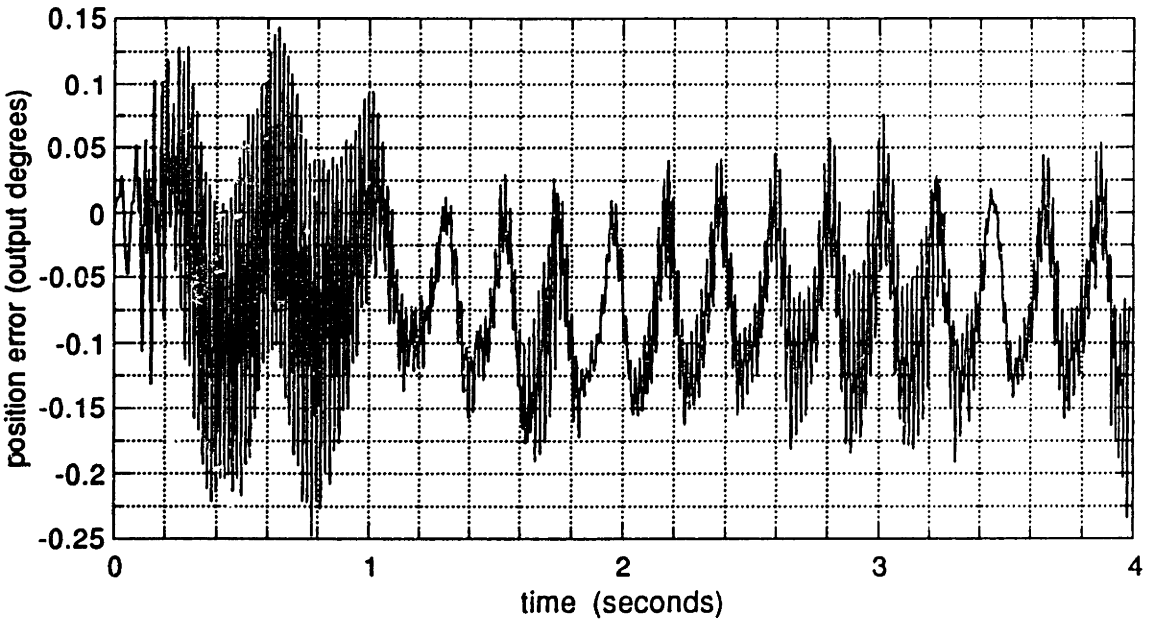

Figure D.3.8: Joint 3 dynamic position error at 0.48 amps resonance

Appendix E: Simulated Time-Response Plots for the Harmonic-Drive Model with Friction, Compliance and Kinematic Error

This appendix contains a complete collection of all of the dynamic-response plots generated for each testing station using the harmonic-drive model with friction, compliance, and kinematic error. This model is derived and these results are discussed in section 3.6 of this document. The format of these illustrations is identical to the experimental time-response results presented in appendix D so that direct comparisons can be made easily. Using the numerical simulation described in section 3.1, values for the position, velocity, and torque in the model were calculated, and from the input and output position data, the dynamic position-error across the transmission was derived. A summary of all of the plots shown in this appendix and their corresponding plot numbers is given in table E.1. For each of the plots listed in this table except the dynamic position-error figure, time-response curves are plotted for several different motor-current step-commands. Depending on the visual appearance of the data, the different response curves on each of these plots are either plotted on a single axis or plotted on separate axes. For the sake of clarity, the output-velocity response data for each harmonic drive is plotted in both of these ways. In the case of the dynamic position-error plots, a single time-response curve is shown, rather than several, from which generalizations about the behavior of dynamic position-error in all operating ranges are made.

Table E.1: Summary of simulated time-response plot numbers			
	Joint 1	**Joint 2**	**Joint 3**
Input Position	E.1.1	E.2.1	E.3.1
Input Velocity	E.1.2	E.2.2	E.3.2
Input Current	E.1.3	E.2.3	E.3.3
Output Position	E.1.4	E.2.4	E.3.4
Output Velocity - view 1	E.1.5	E.2.5	E.3.5
Output Velocity - view 2	E.1.6	E.2.6	E.3.6
Output Torque	E.1.7	E.2.7	E.3.7
Dynamic Position Error	E.1.8	E.2.8	E.3.8

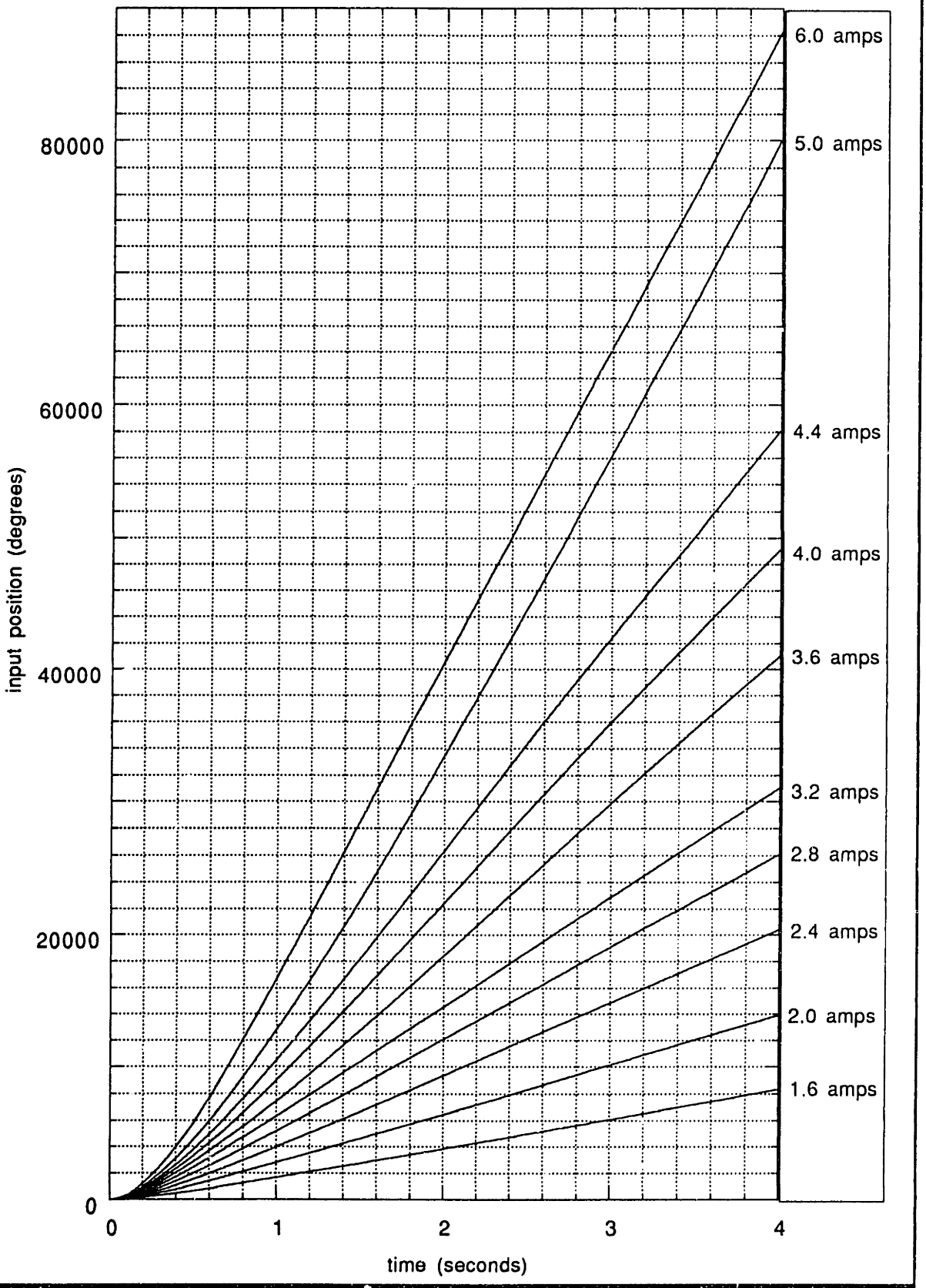

Figure E.1.1: Joint 1 input-position simulated step-responses

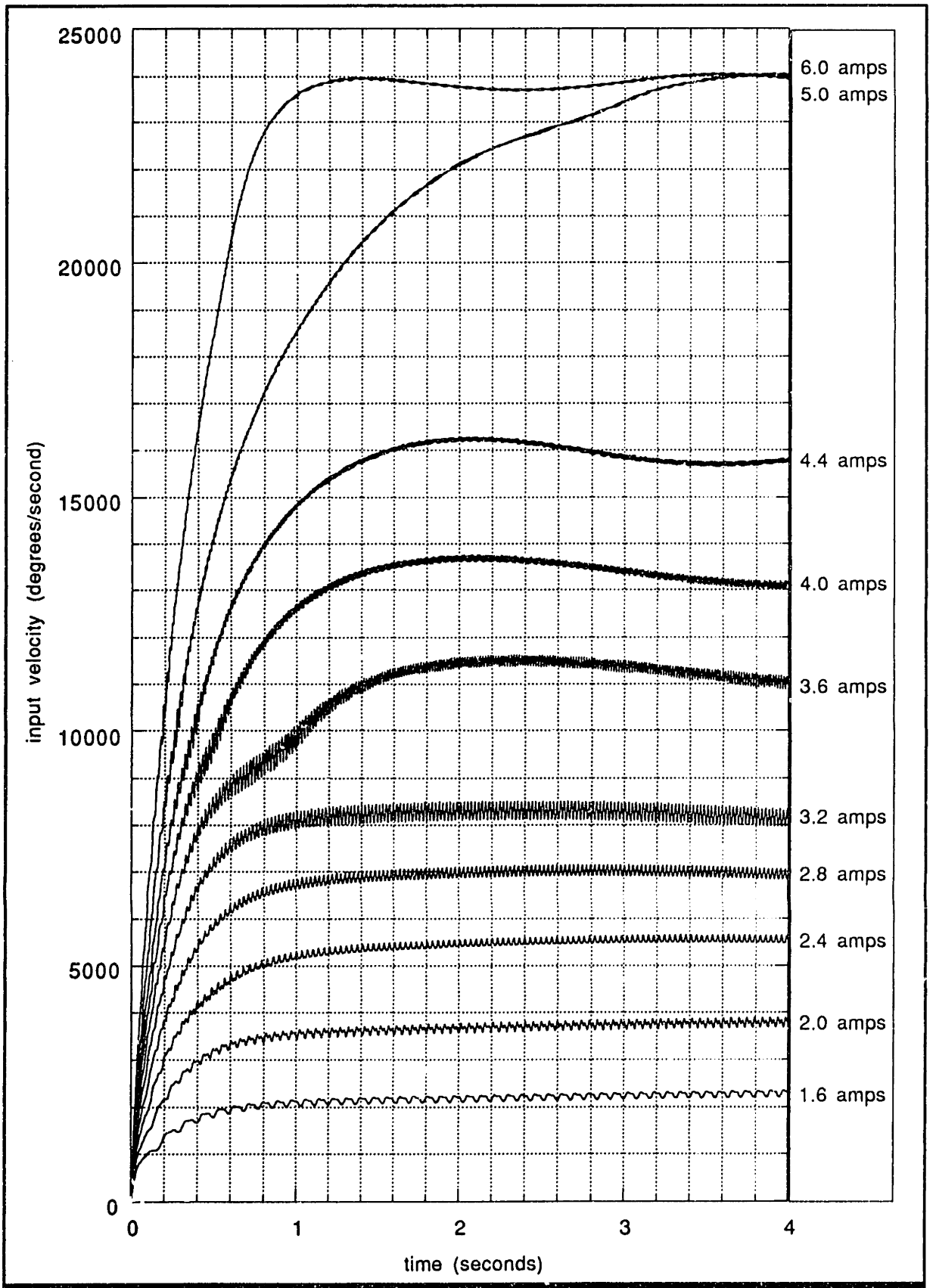

Figure E.1.2: Joint 1 input-velocity simulated step-responses

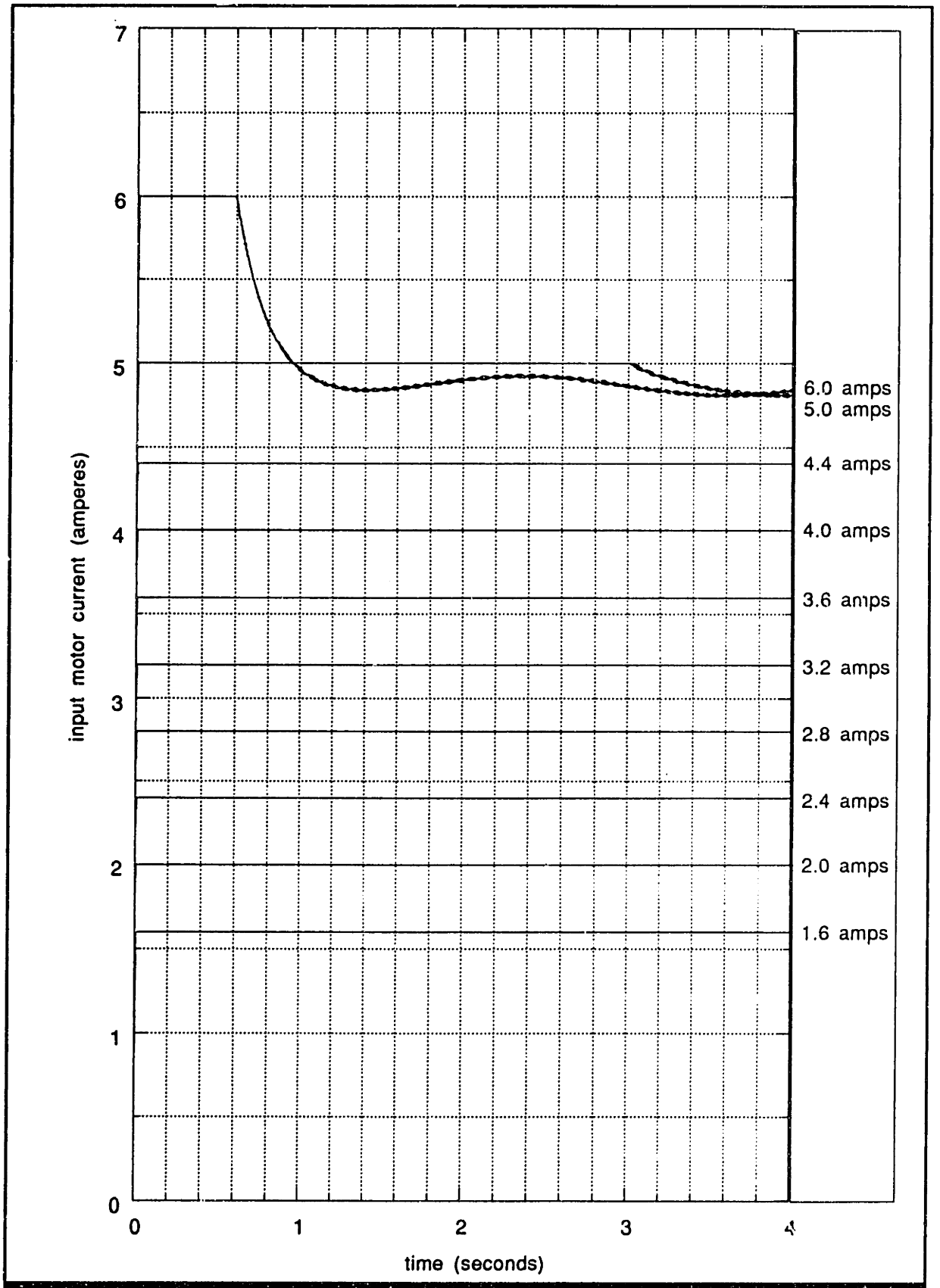

Figure E.1.3: Joint 1 input-current simulated step-responses

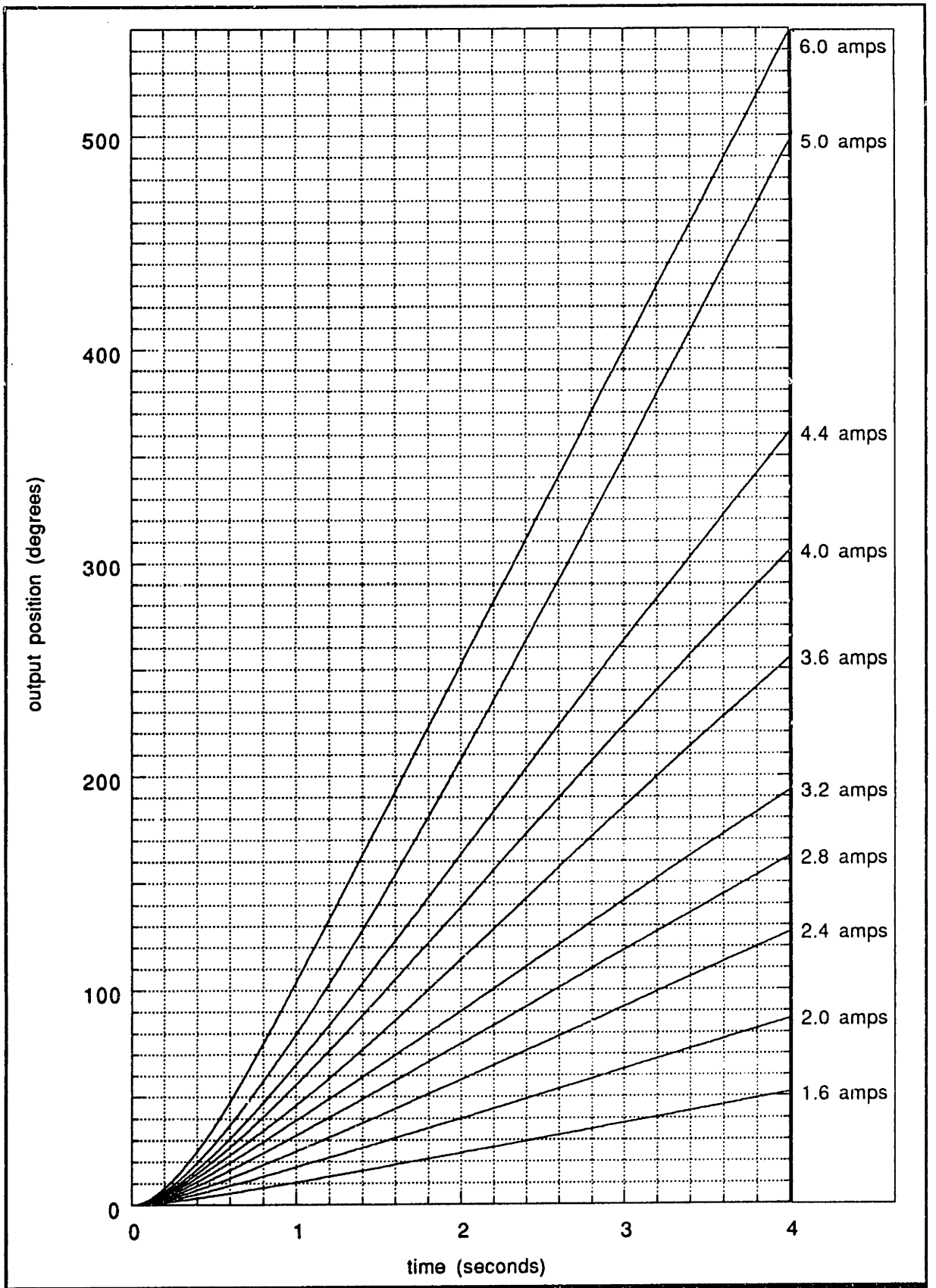

Figure E.1.4: Joint 1 output-position simulated step-responses

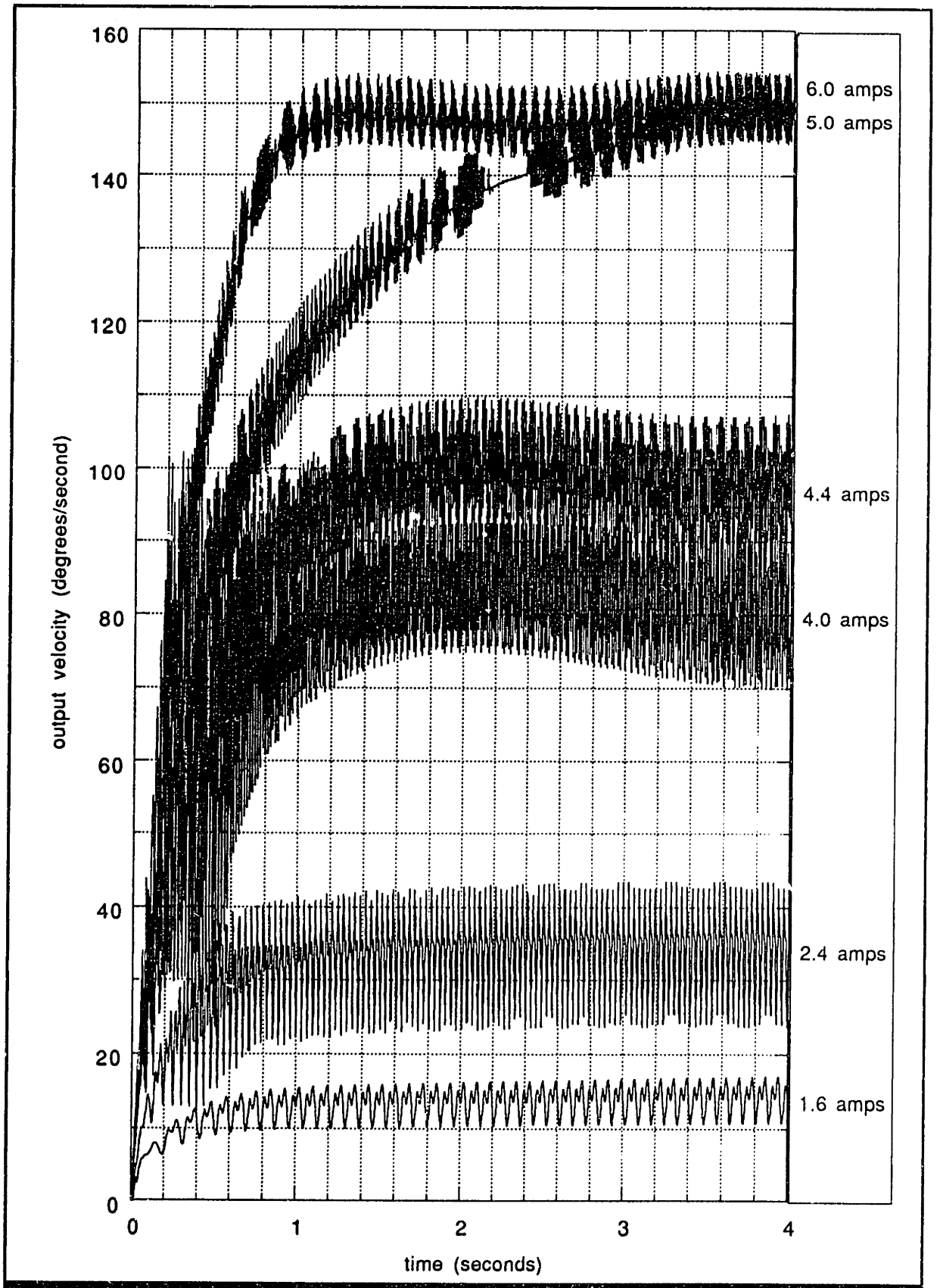

Figure E.1.5: Joint 1 output-velocity simulated step-responses

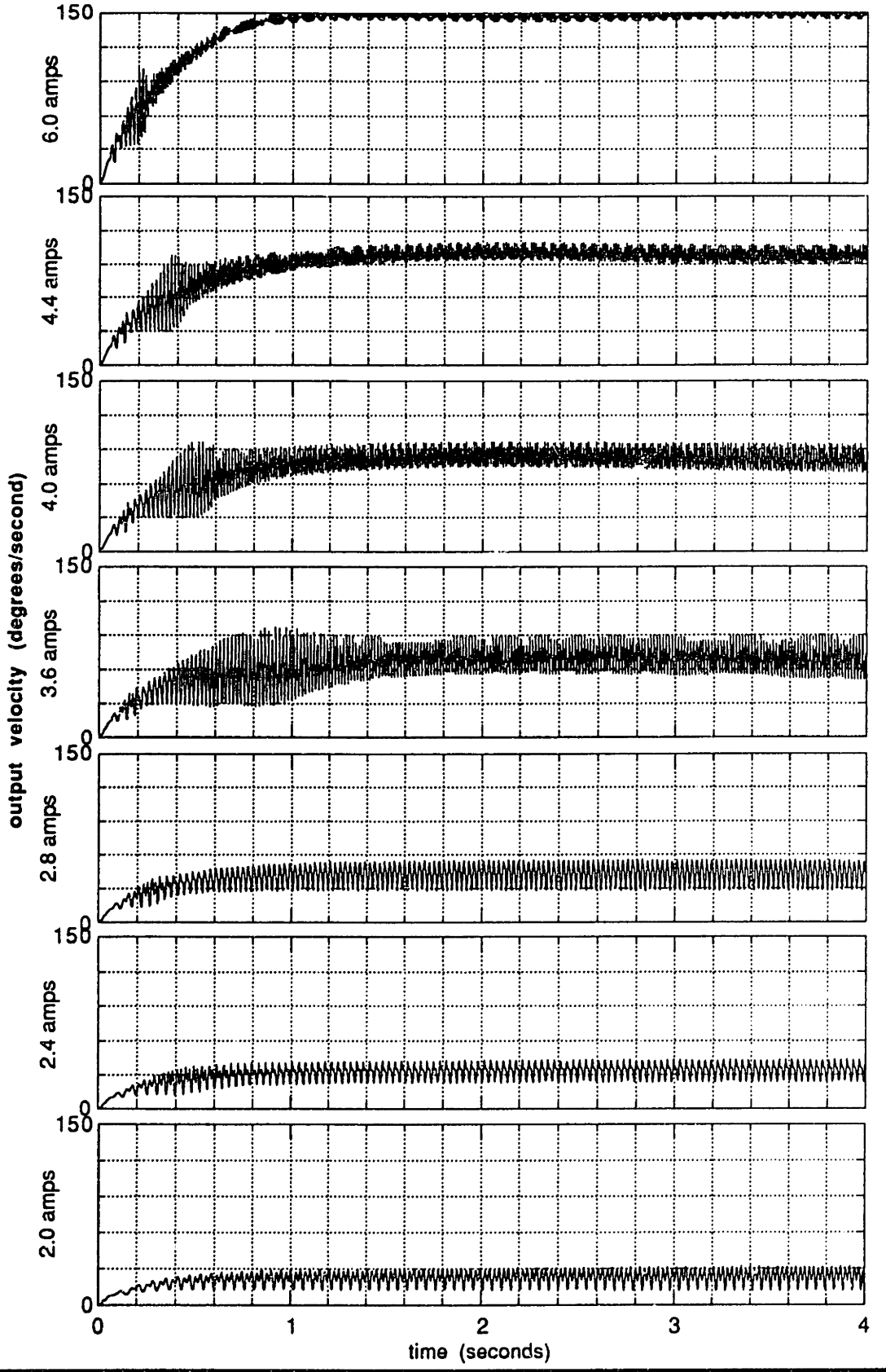

Figure E.1.6: Joint 1 output-velocity simulated step-responses

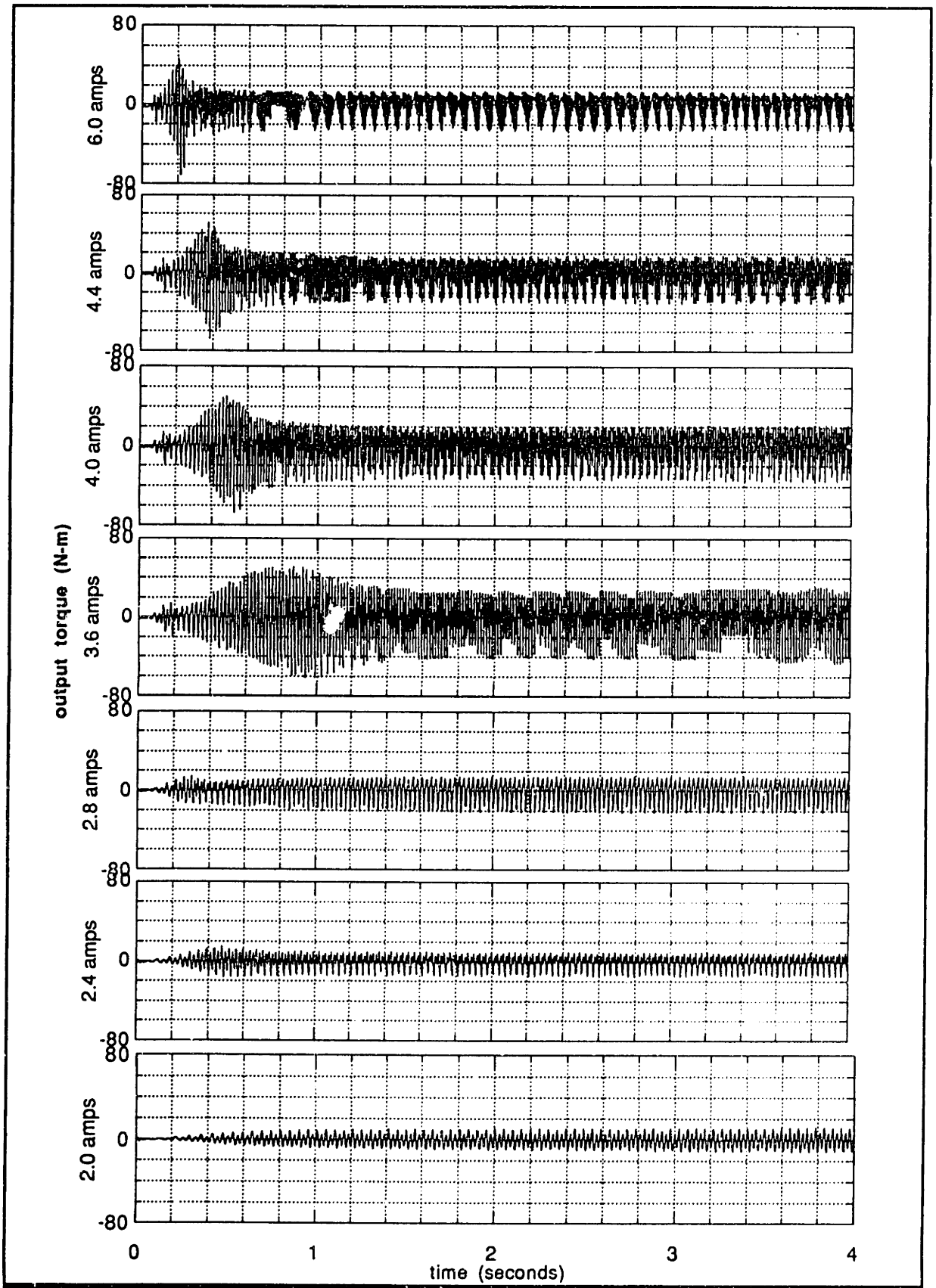

Figure E.1.7: Joint 1 output-torque simulated step-responses

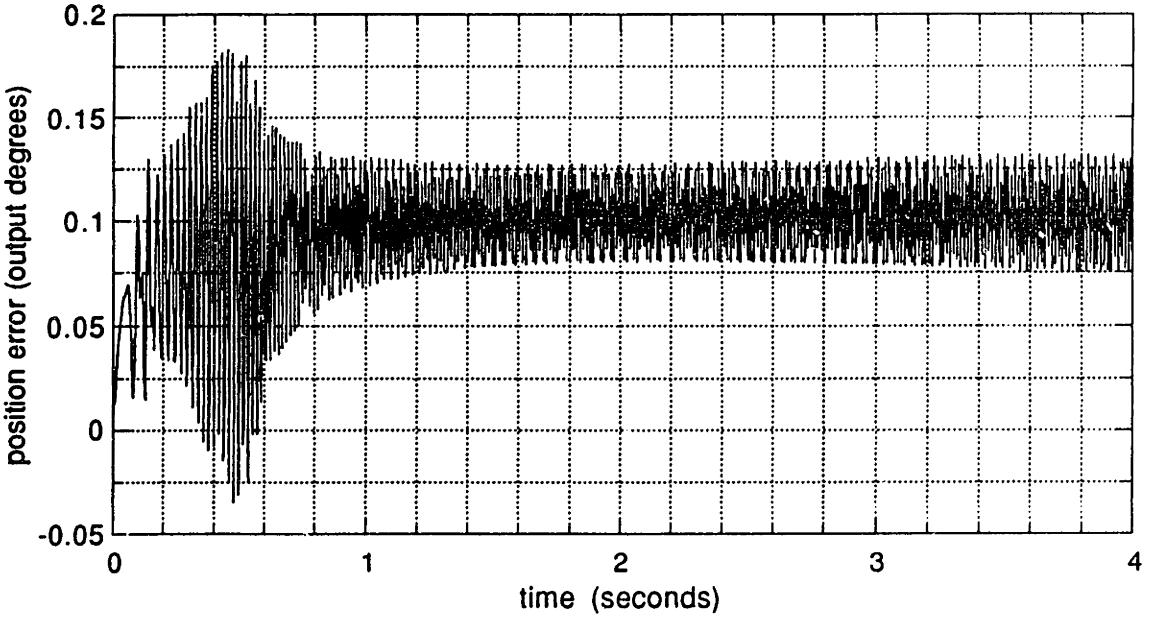

Figure E.1.8: Joint 1 simulated dynamic position error at 4.0 amps

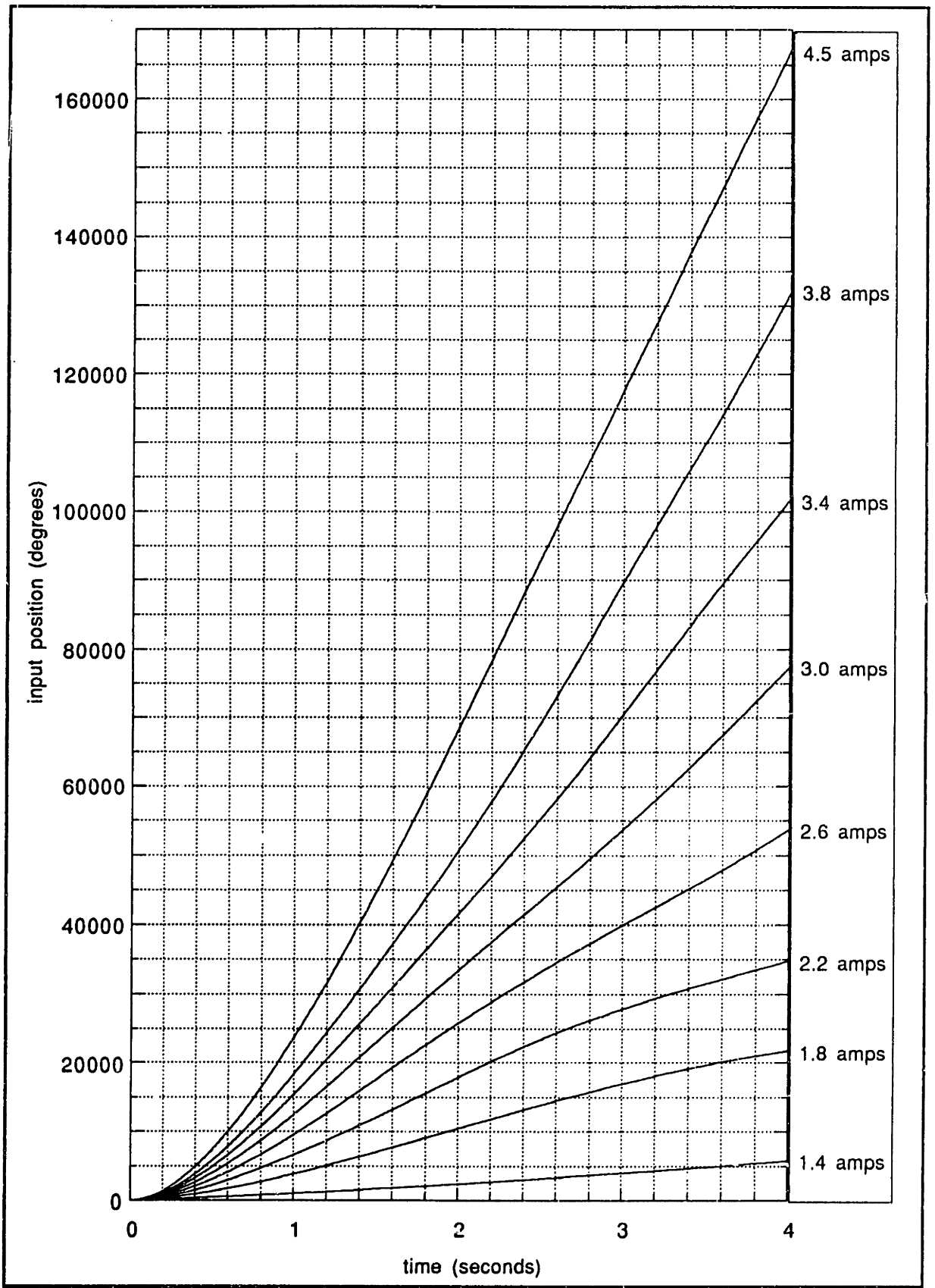

Figure E.2.1: Joint 2 input-position simulated step-responses

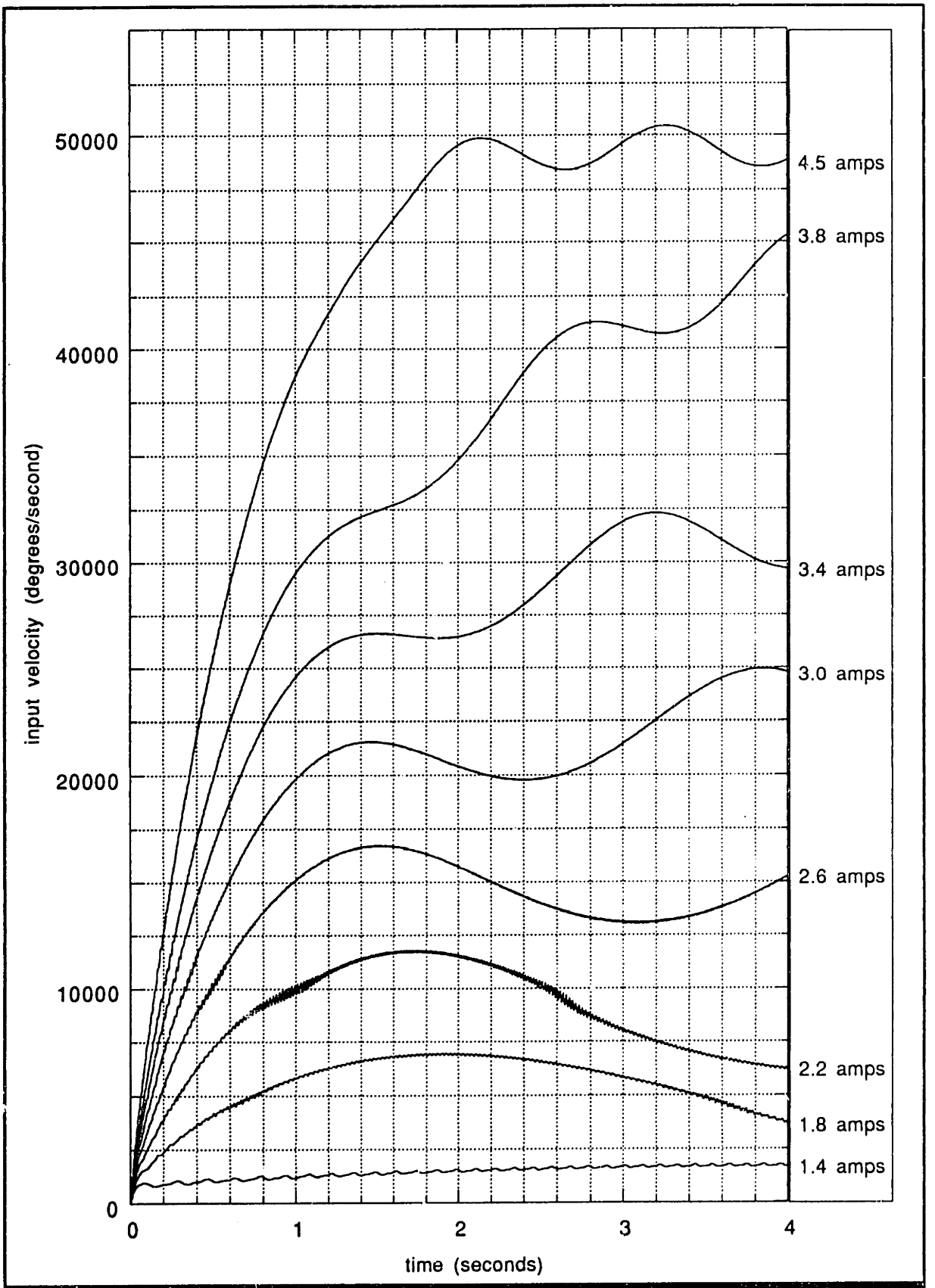

Figure E.2.2: Joint 2 input-velocity simulated step-responses

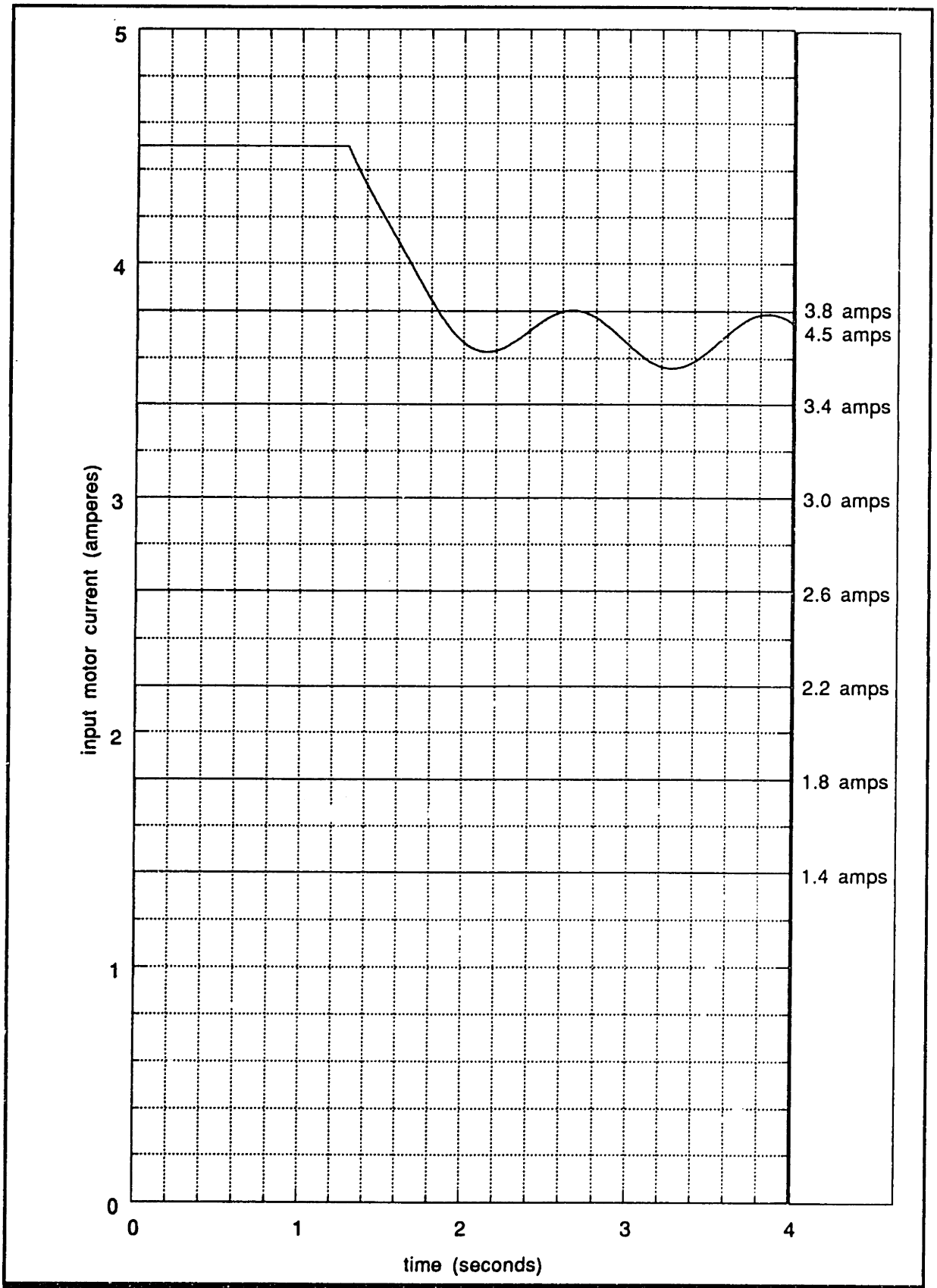

Figure E.2.3: Joint 2 input-current simulated step-responses.

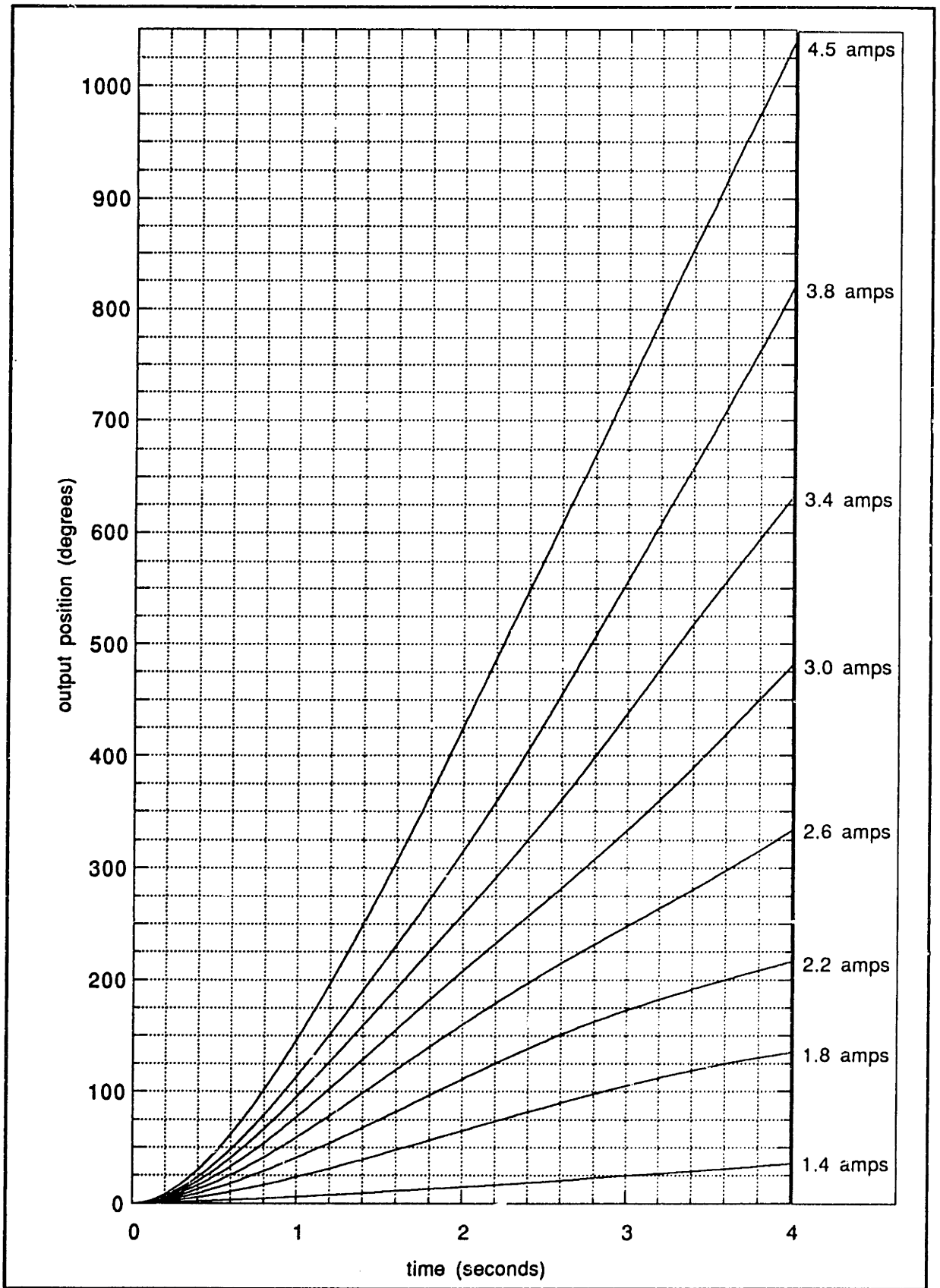

Figure E.2.4: Joint 2 output-position simulated step-responses

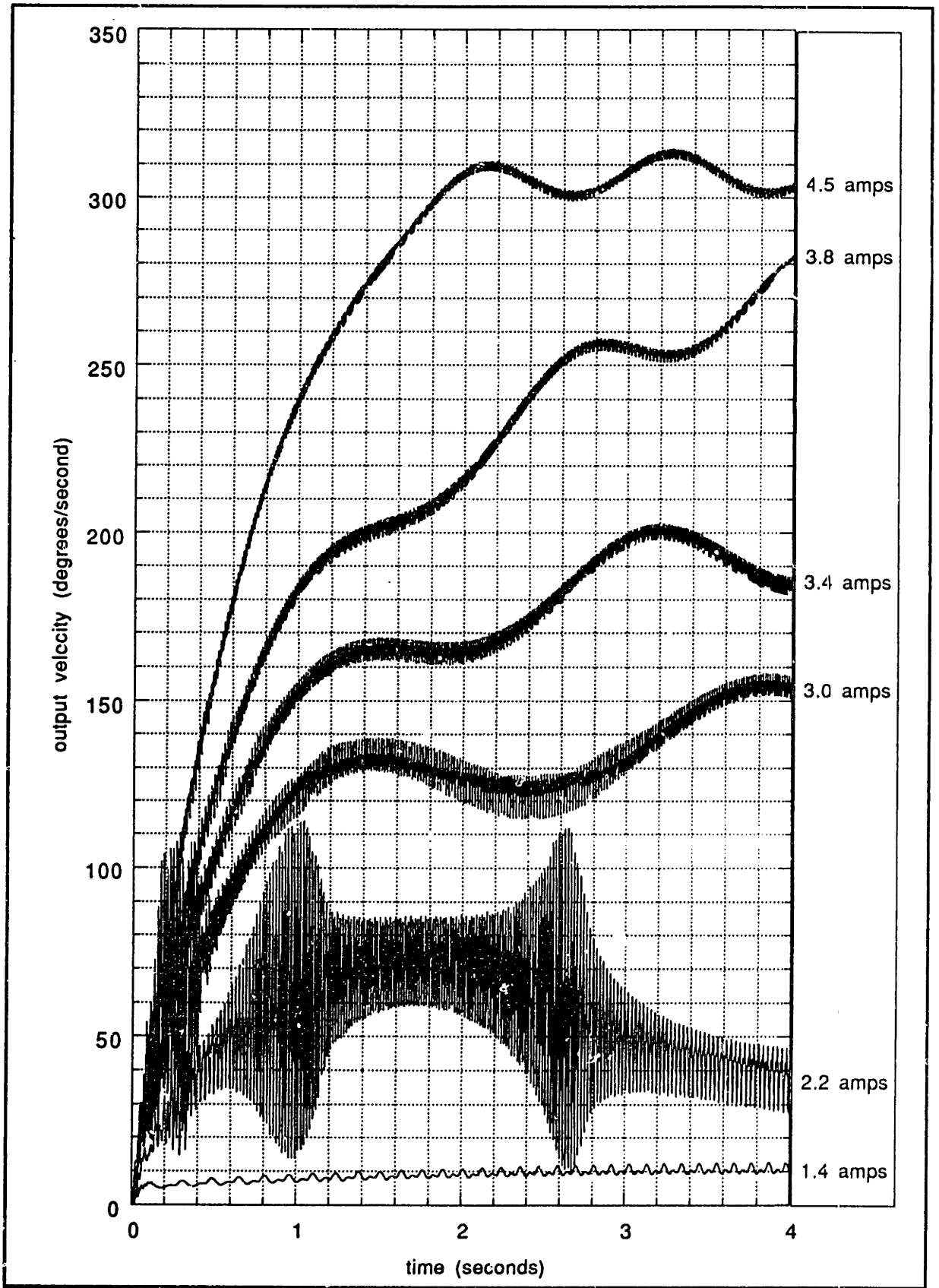

Figure E.2.5: Joint 2 output-velocity simulated step-responses

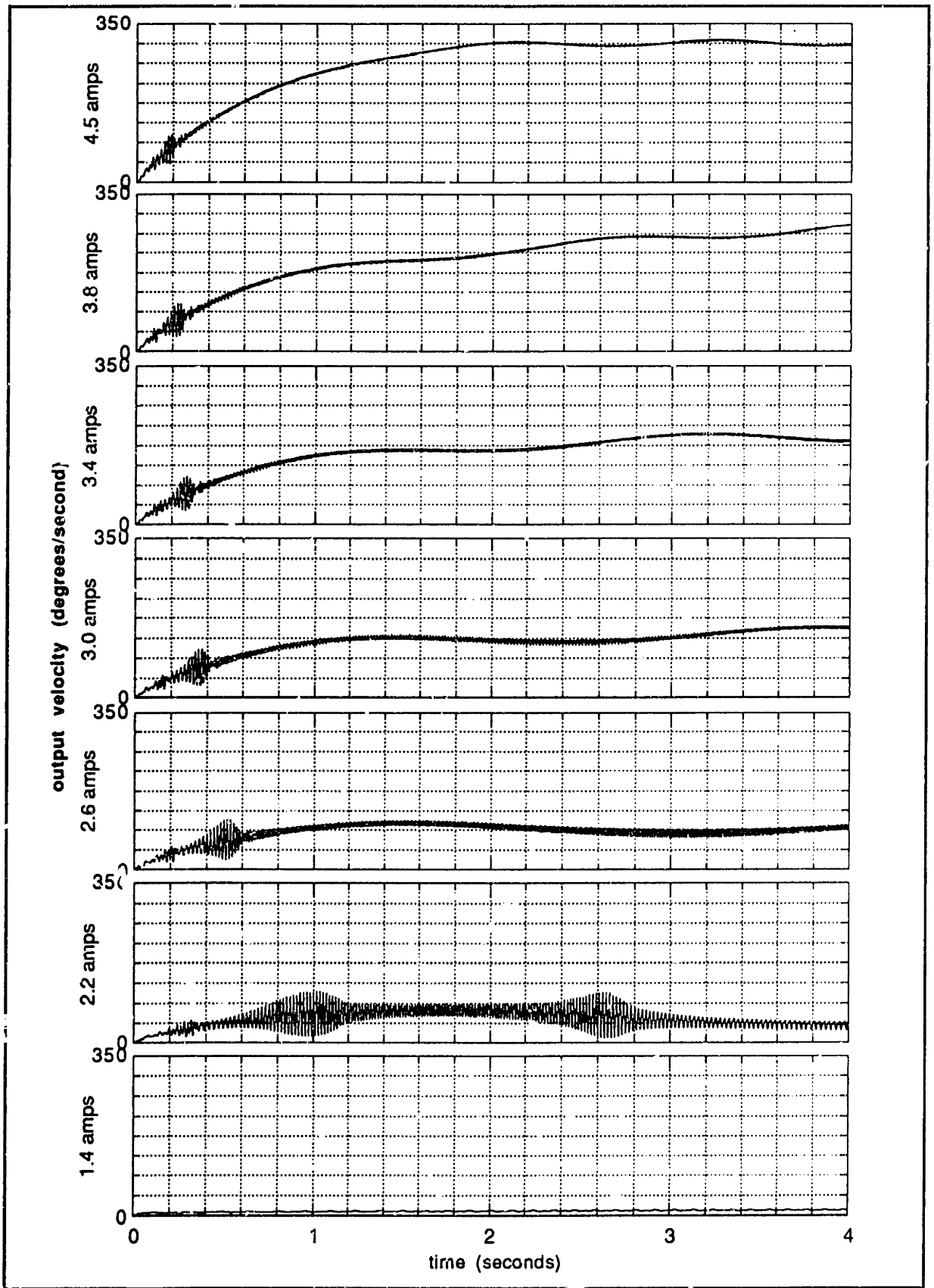

Figure E.2.6: Joint 2 output-velocity simulated step-responses.

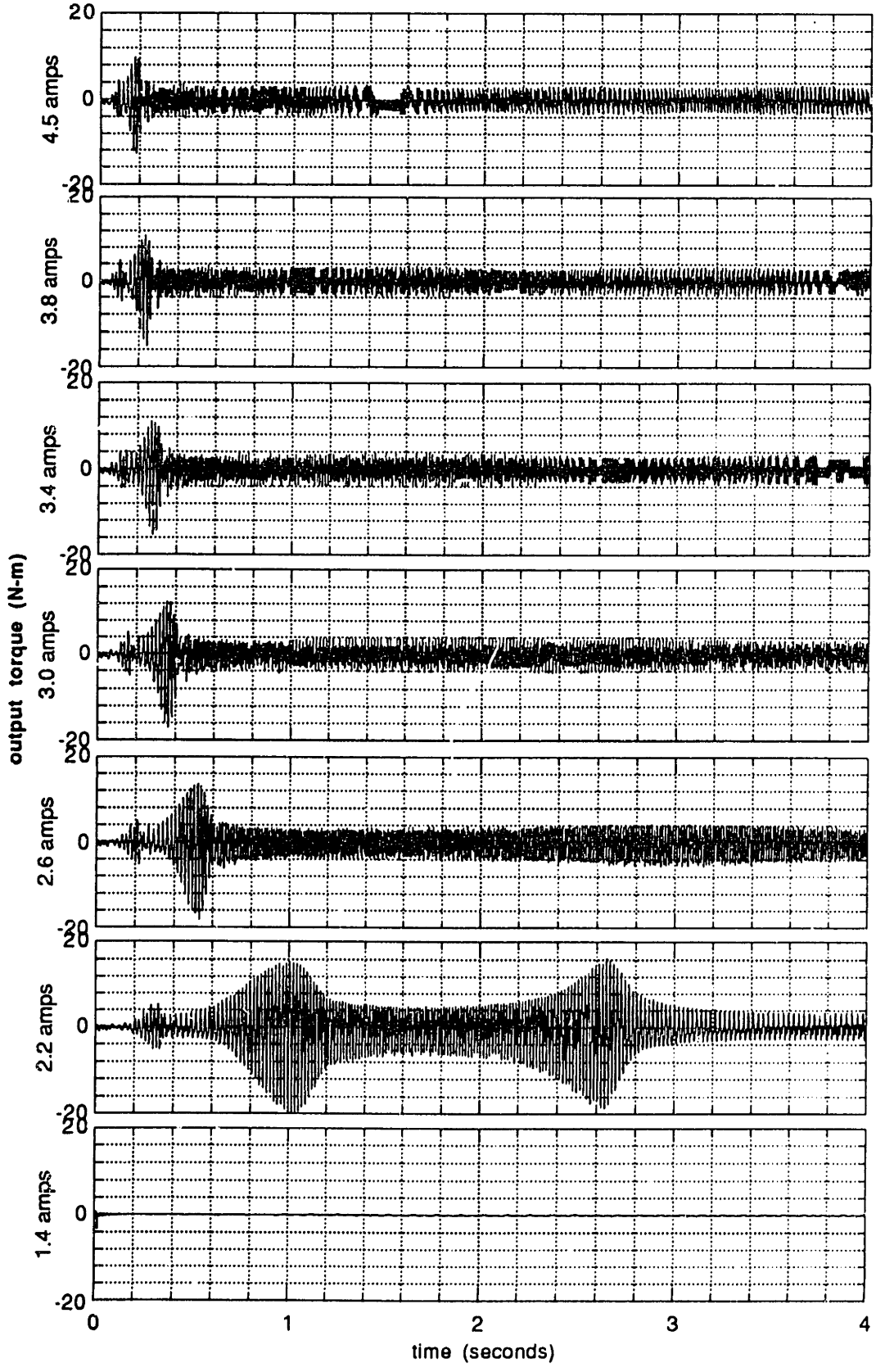

Figure E.2.7: Joint 2 output-torque simulated step-responses

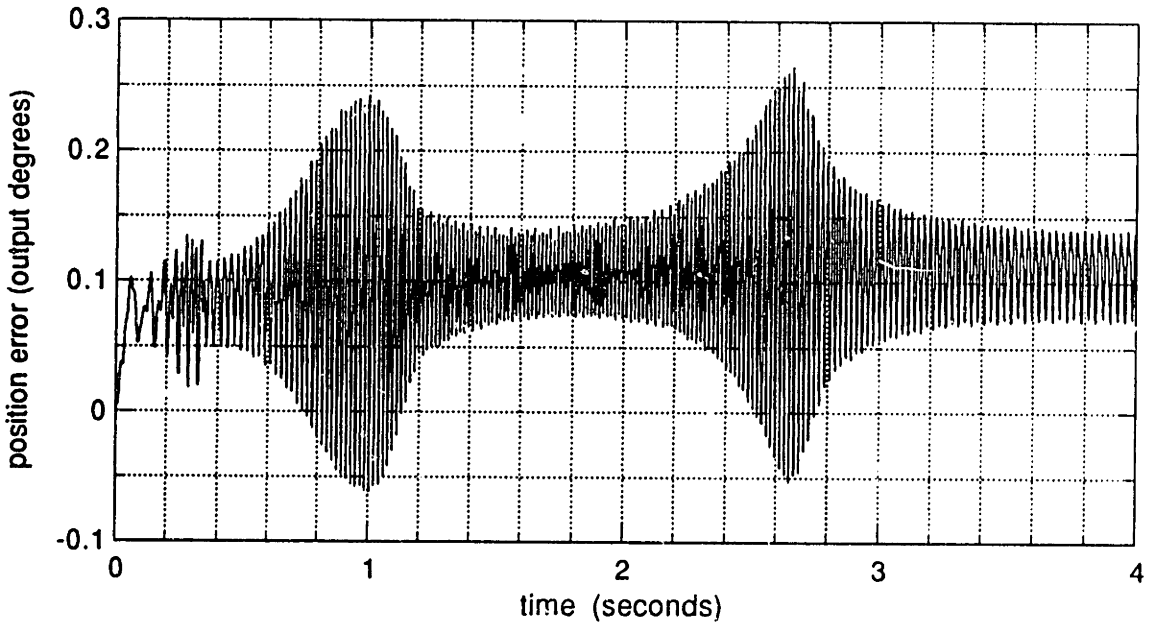

Figure E.2.8: Joint 2 simulated dynamic position error at 2.2 amps

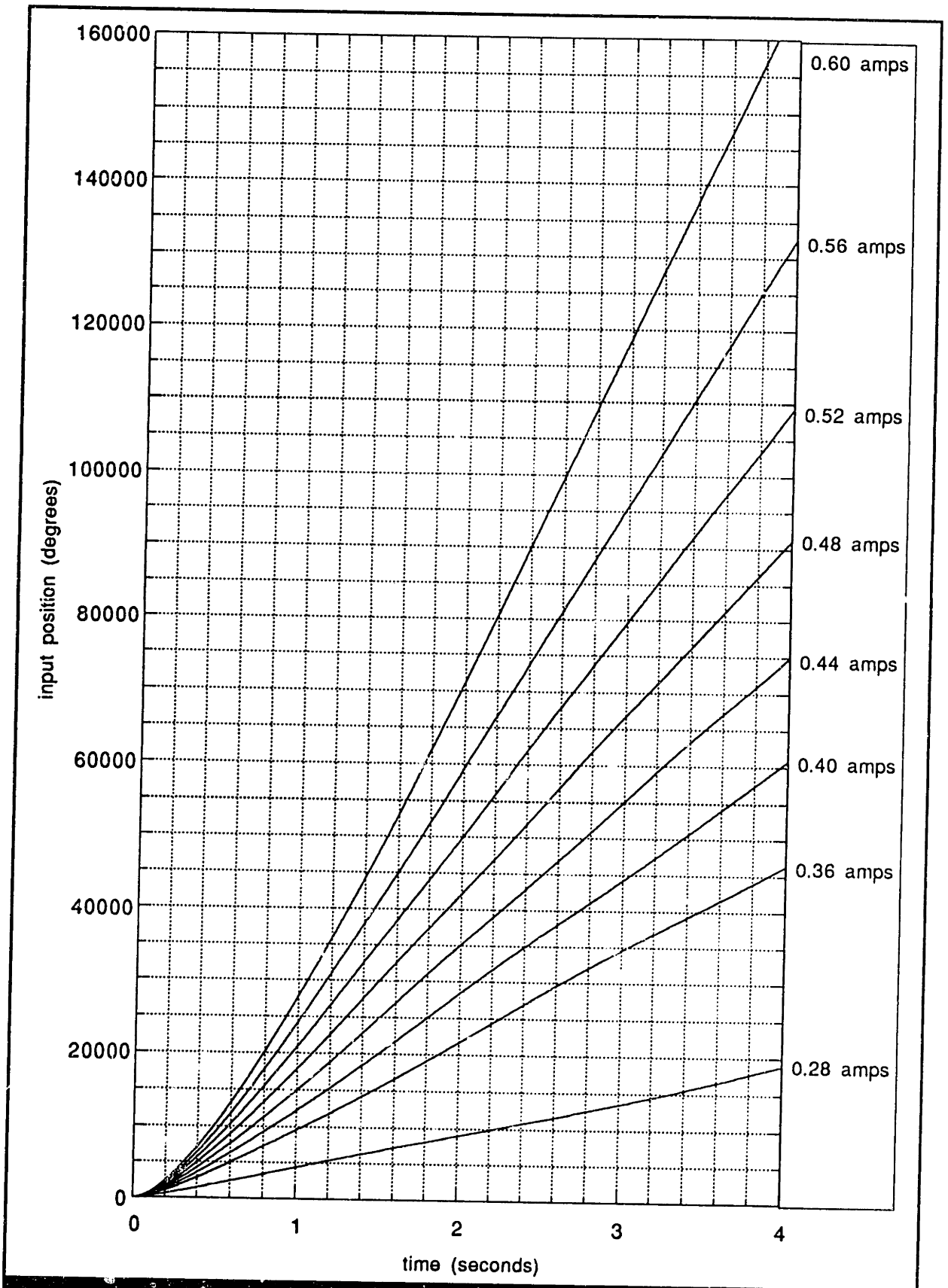

Figure E.3.1: Joint 3 input-position simulated step-responses

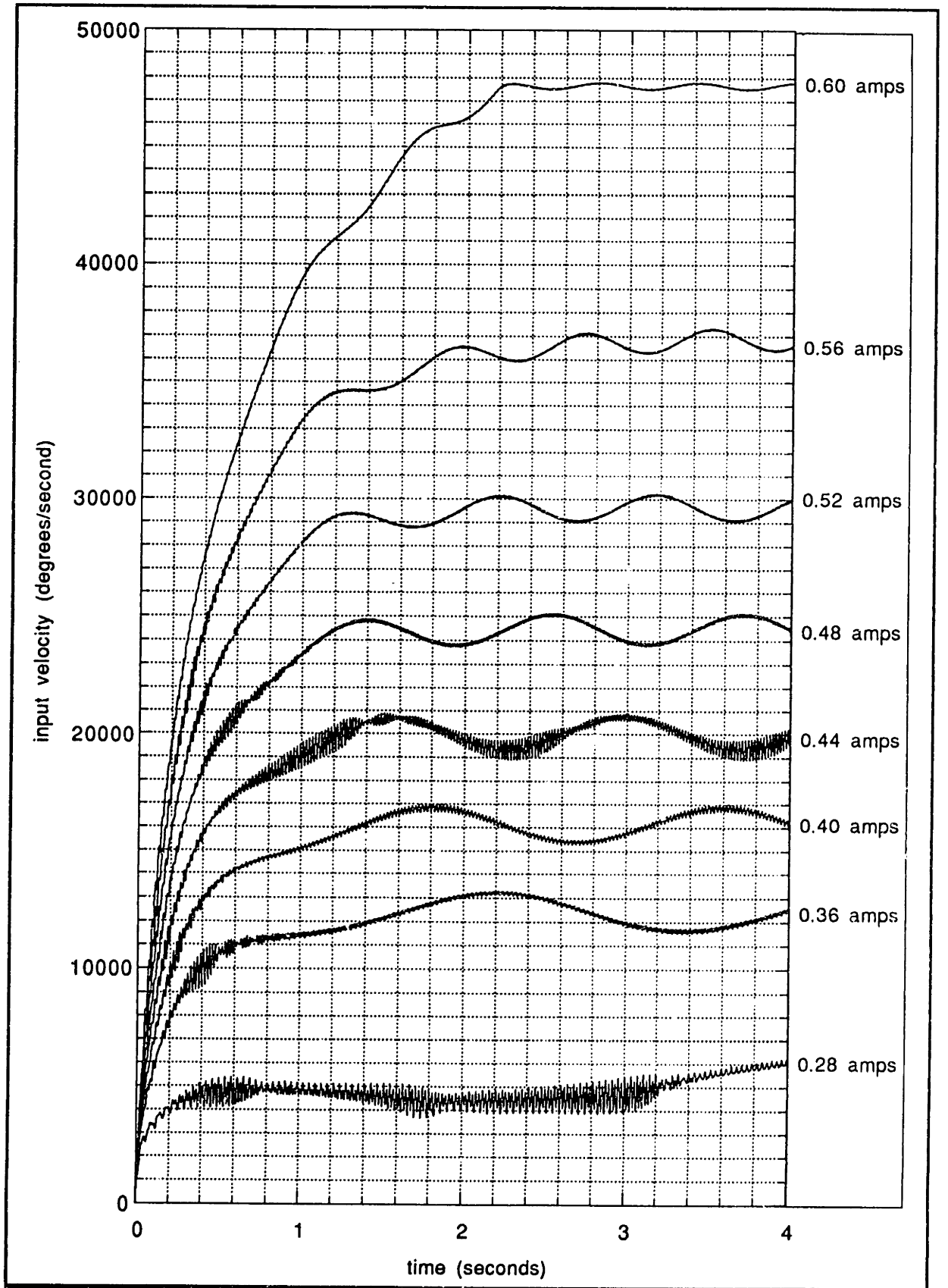

Figure E.3.2: Joint 3 input-velocity simulated step-responses

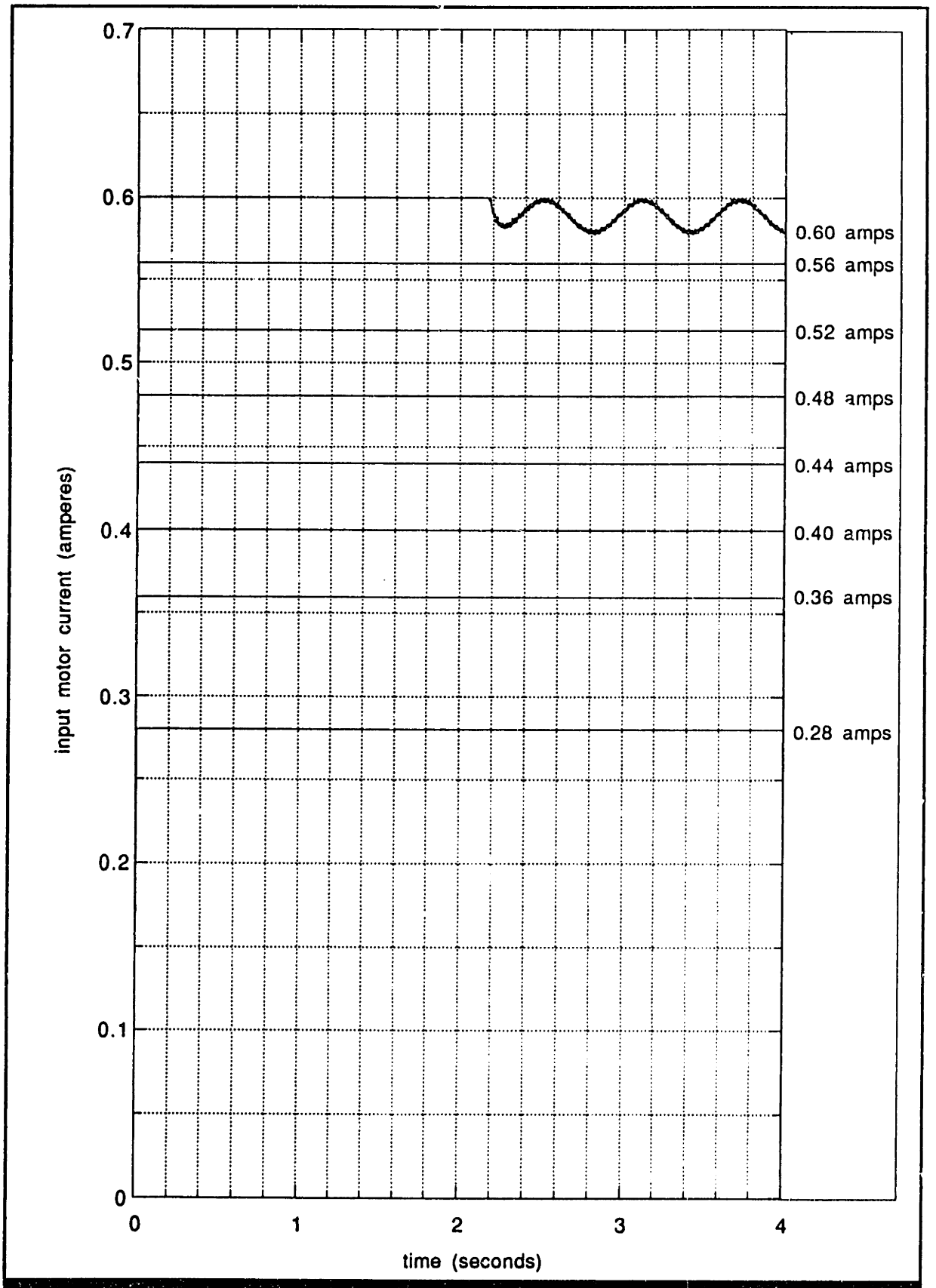

Figure E.3.3: Joint 3 input-current simulated step-responses

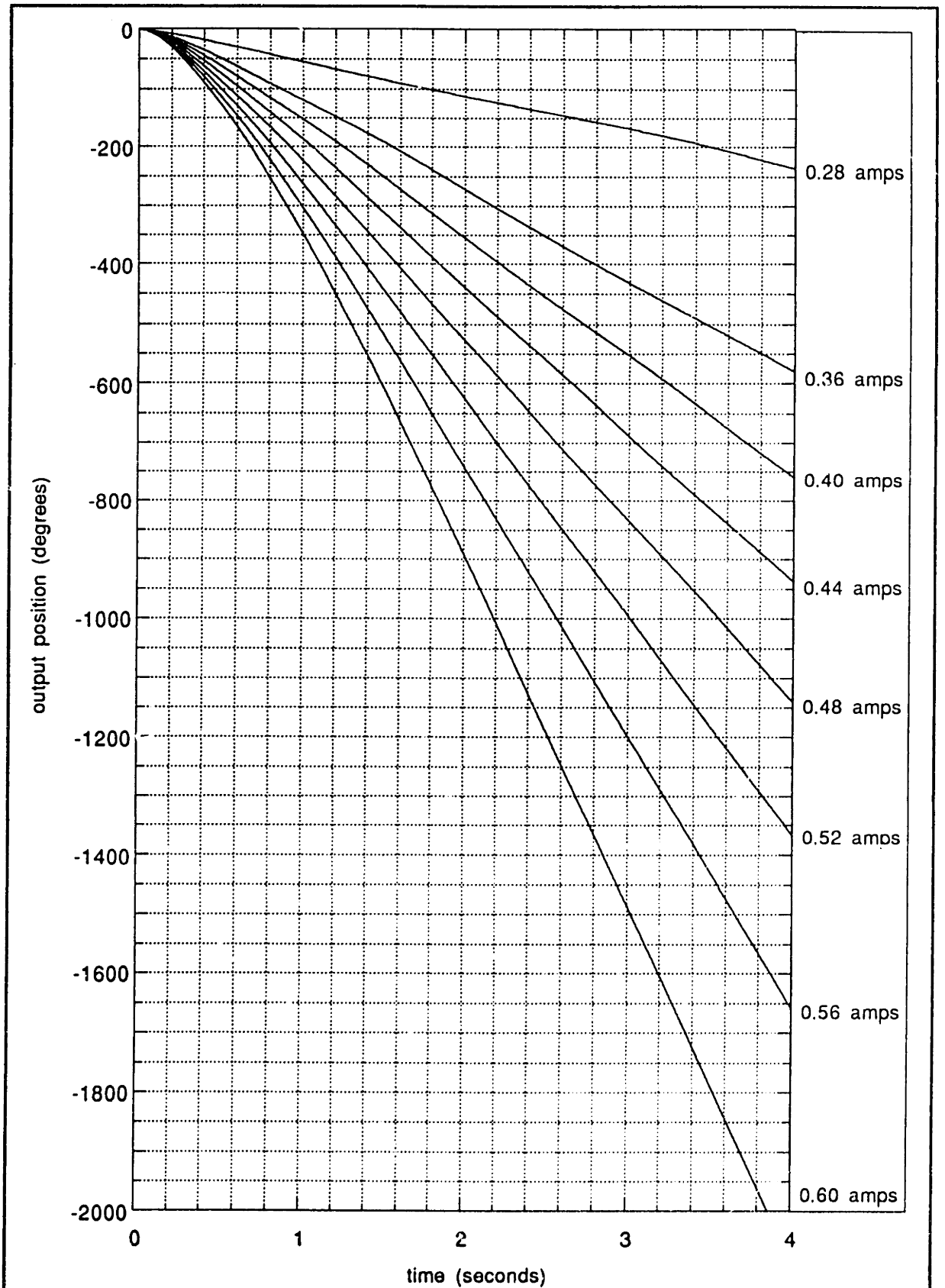

Figure E.3.4: Joint 3 output-position simulated step-responses

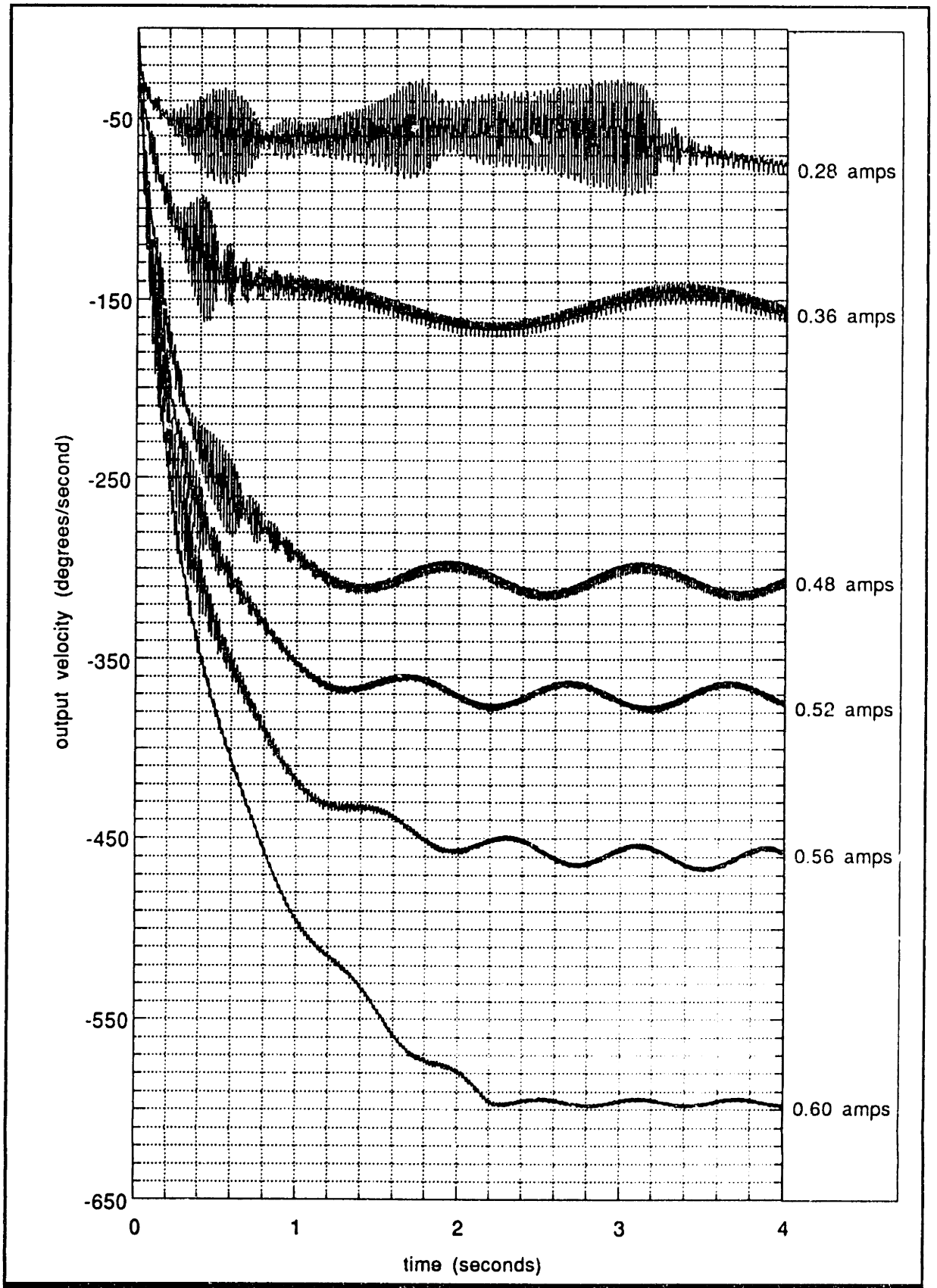

Figure E.3.5: Joint 3 output-velocity simulated step-responses

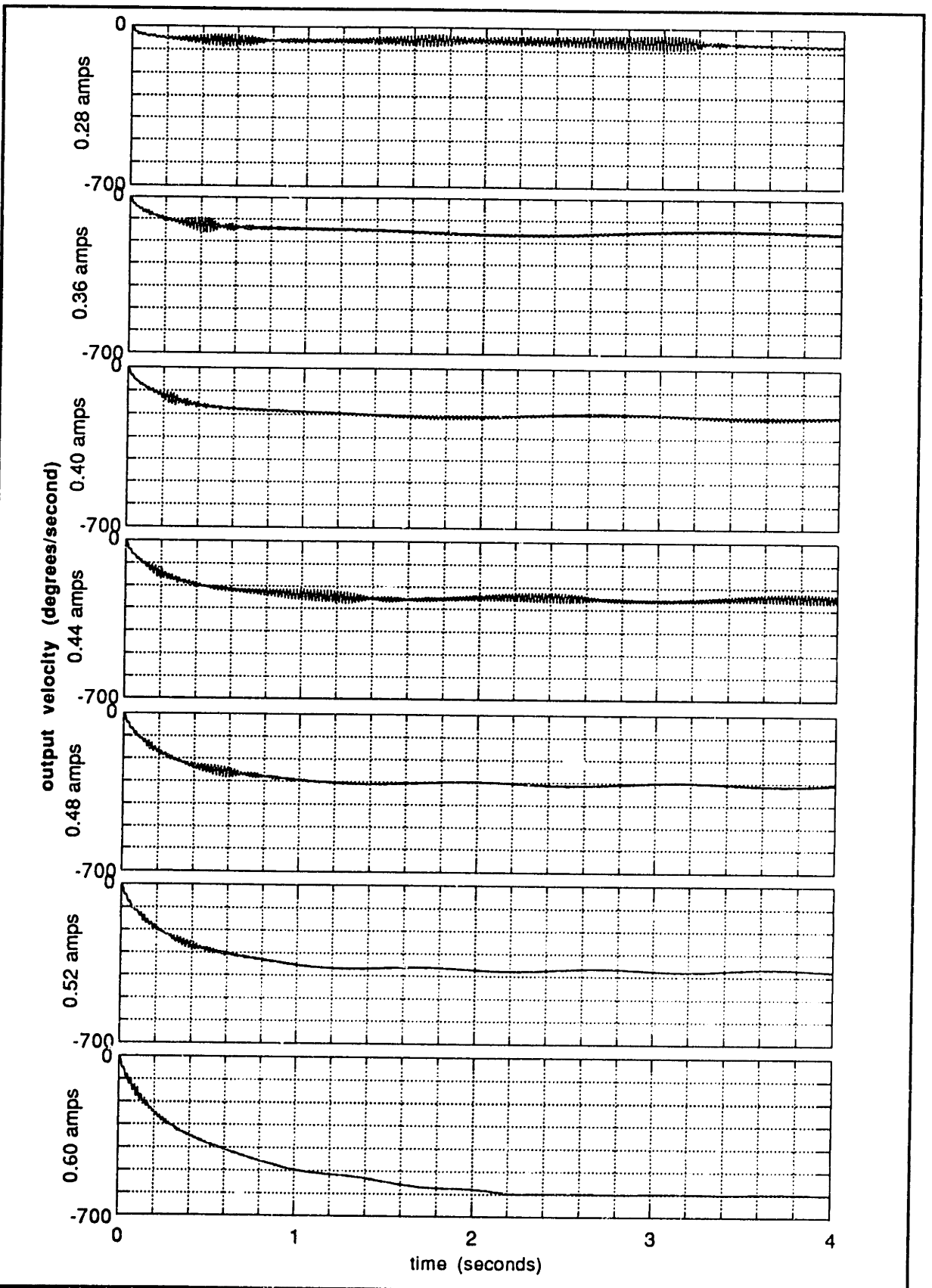

Figure E.3.6: Joint 3 output-velocity simulated step-responses

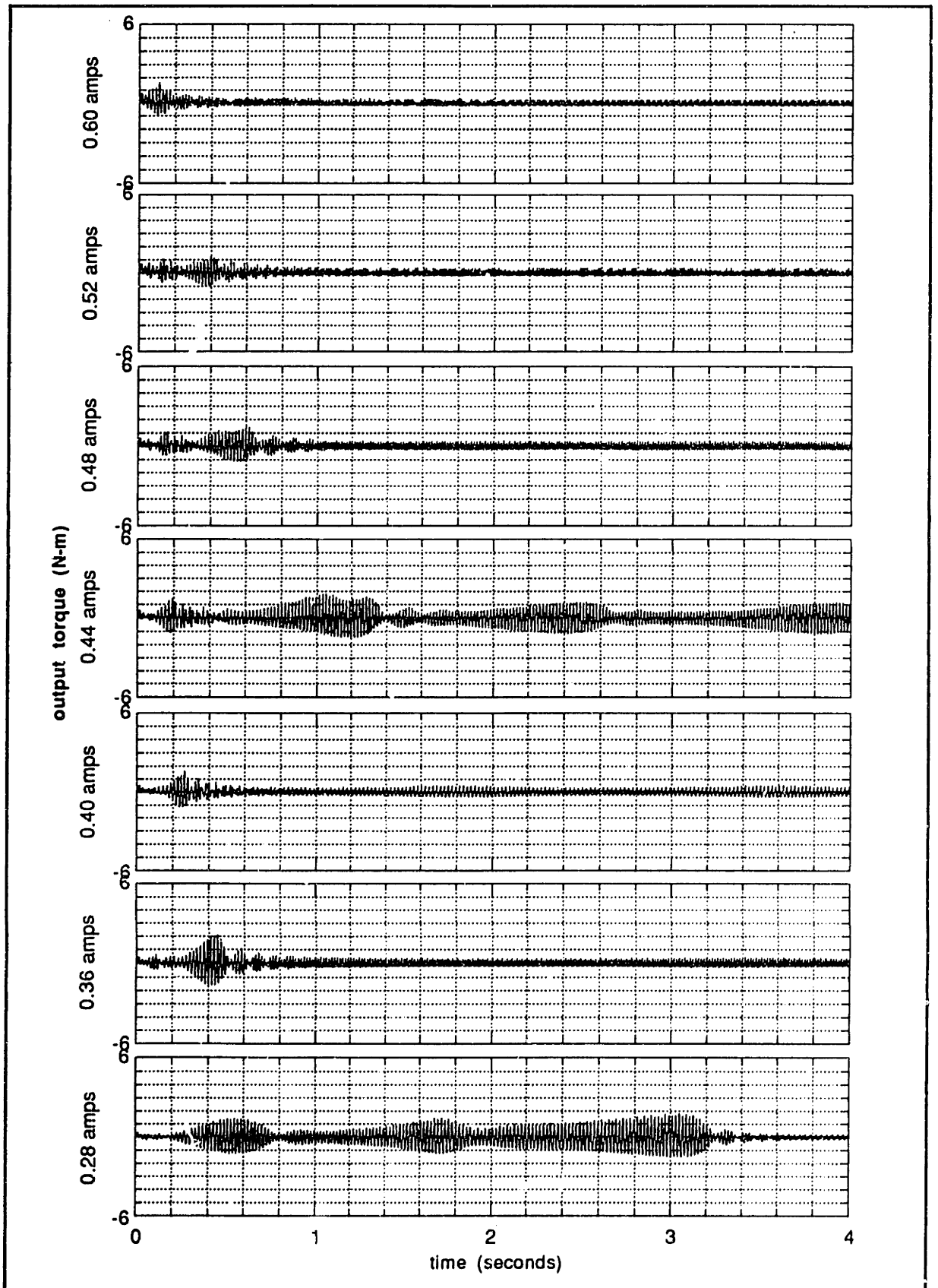

Figure E.3.7: Joint 3 output-torque simulated step-responses

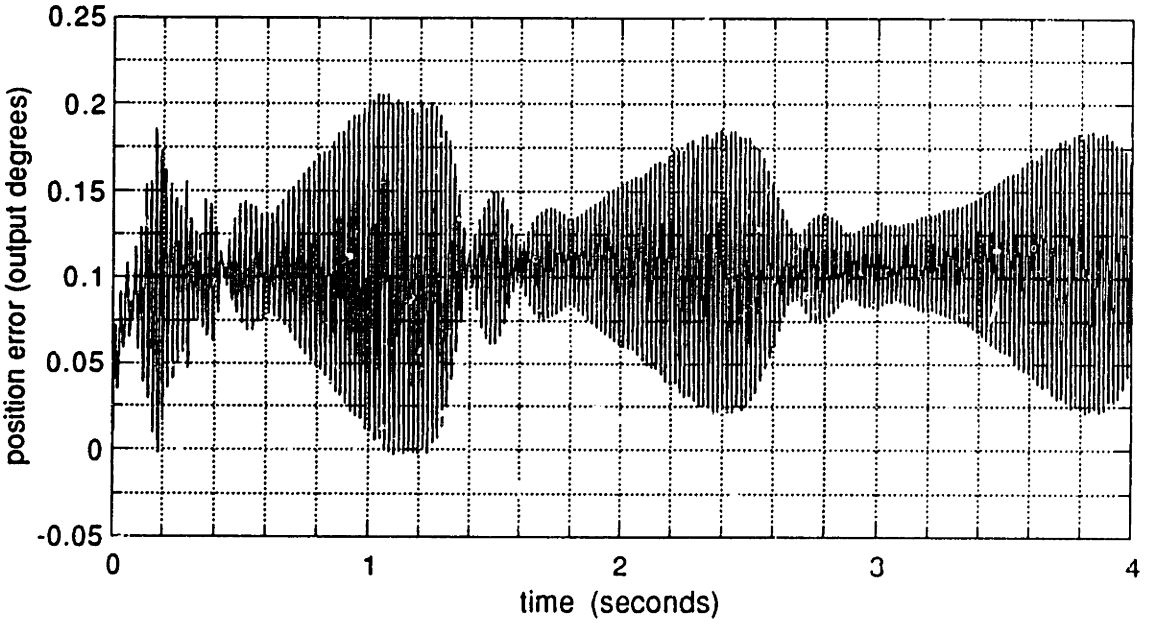

Figure E.3.8: Joint 3 simulated dynamic position error at 0.44 amps

Appendix F: Simulated Time-Response Plots for the Harmonic-Drive Model Including Gear-Tooth Geometry

This appendix contains a complete collection of all of the dynamic-response plots generated for each testing station using the harmonic-drive model including gear-tooth geometry. This model is derived and these results are discussed in section 3.7 of this document. The format of these illustrations is identical to the experimental time-response results presented in appendix D so that direct comparisons can be made easily. Using the numerical simulation described in section 3.1, values for the position, velocity, and torque in the model were calculated, and from the input and output position data, the dynamic position-error across the transmission was derived. A summary of all of the plots shown in this appendix and their corresponding plot numbers is given in table F.1. For each of the plots listed in this table except the dynamic position-error figure, time-response curves are plotted for several different motor-current step-commands. Depending on the visual appearance of the data, the different response curves on each of these plots are either plotted on a single axis or plotted on separate axes. For the sake of clarity, the output-velocity response data for each harmonic drive is plotted in both of these ways. In the case of the dynamic position-error plots, a single time-response curve is shown, rather than several, from which generalizations about the behavior of dynamic position-error in all operating ranges are made.

Table F.1: Summary of simulated time-response plot numbers			
	Joint 1	**Joint 2**	**Joint 3**
Input Position	F.1.1	F.2.1	F.3.1
Input Velocity	F.1.2	F.2.2	F.3.2
Input Current	F.1.3	F.2.3	F.3.3
Output Position	F.1.4	F.2.4	F.3.4
Output Velocity - view 1	F.1.5	F.2.5	F.3.5
Output Velocity - view 2	F.1.6	F.2.6	F.3.6
Output Torque	F.1.7	F.2.7	F.3.7
Dynamic Position Error	F.1.8	F.2.8	F.3.8

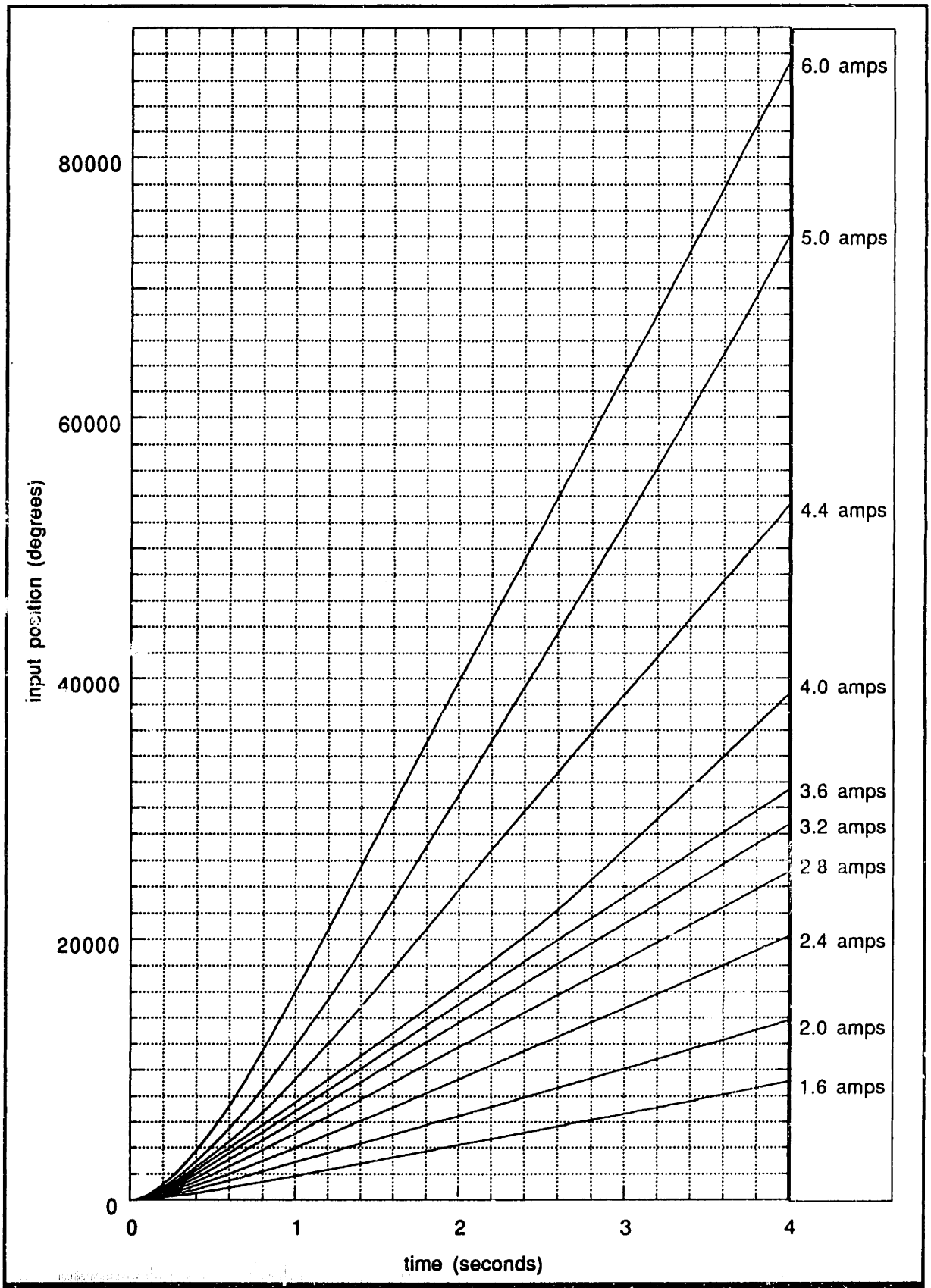

Figure F.1.1: Joint 1 input-position simulated step-responses

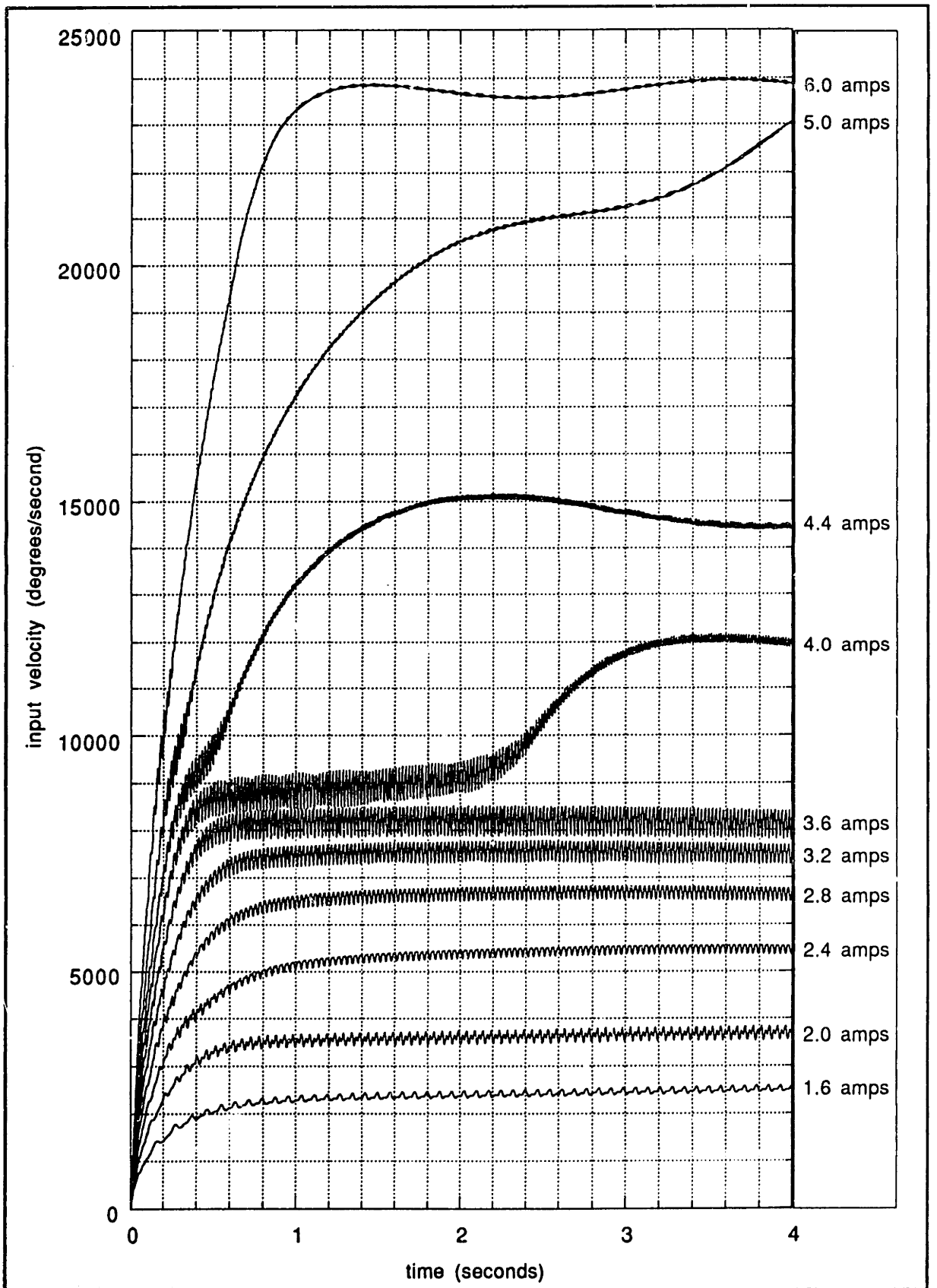

Figure F.1.2: Joint 1 input-velocity simulated step-responses

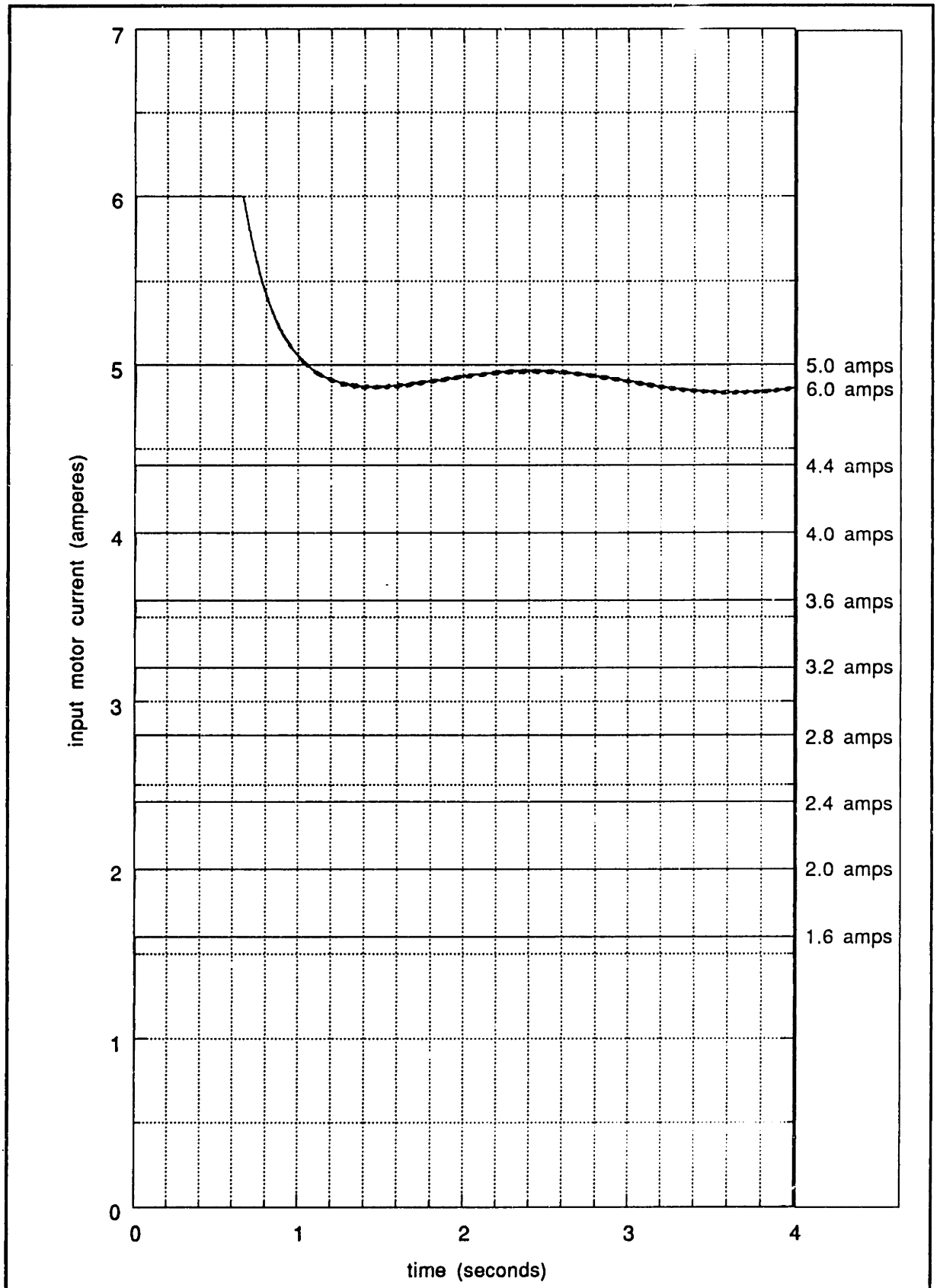

Figure F.1.3: Joint 1 input-current simulated step-responses

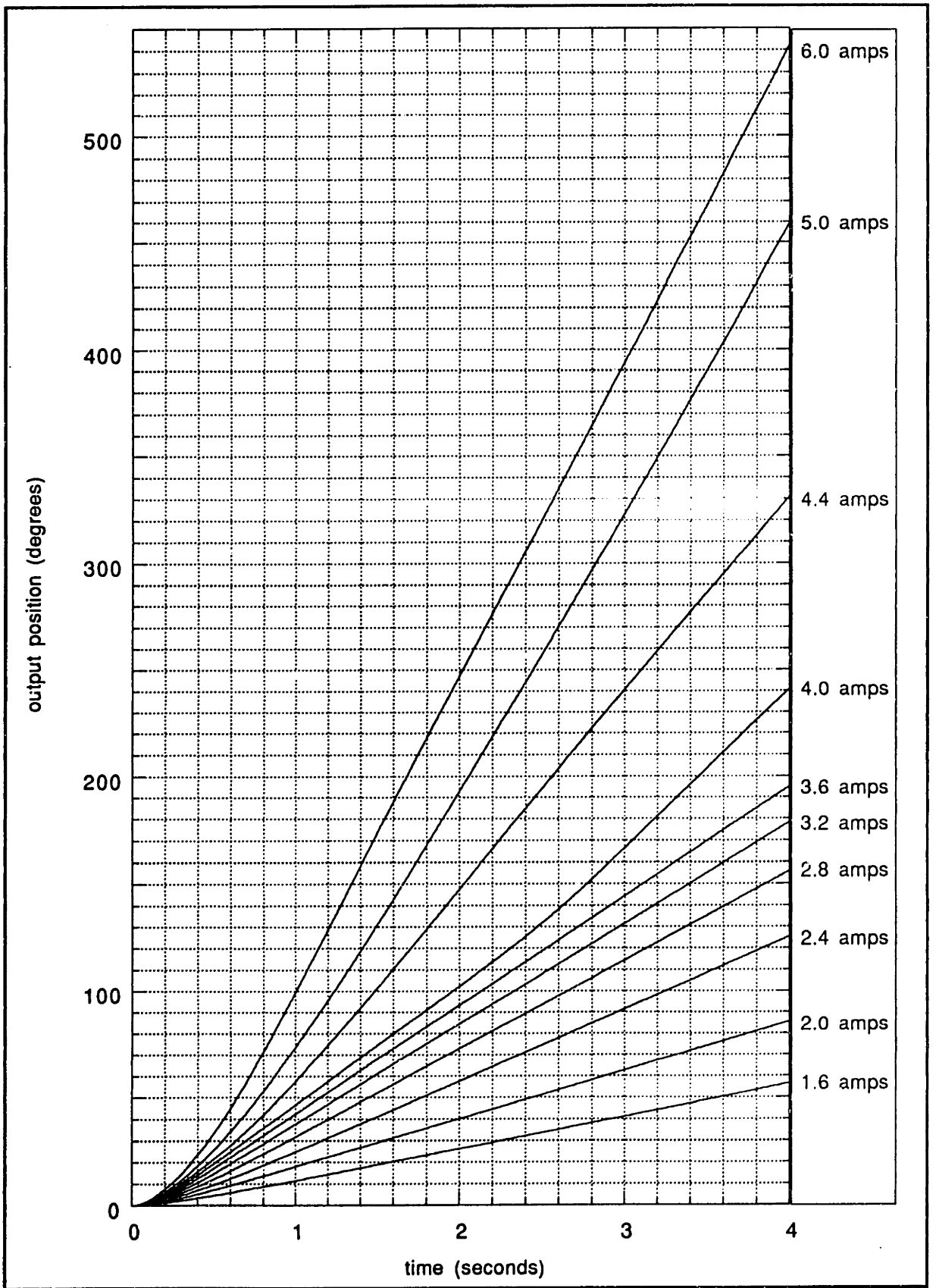

Figure F.1.4: Joint 1 output-position simulated step-responses

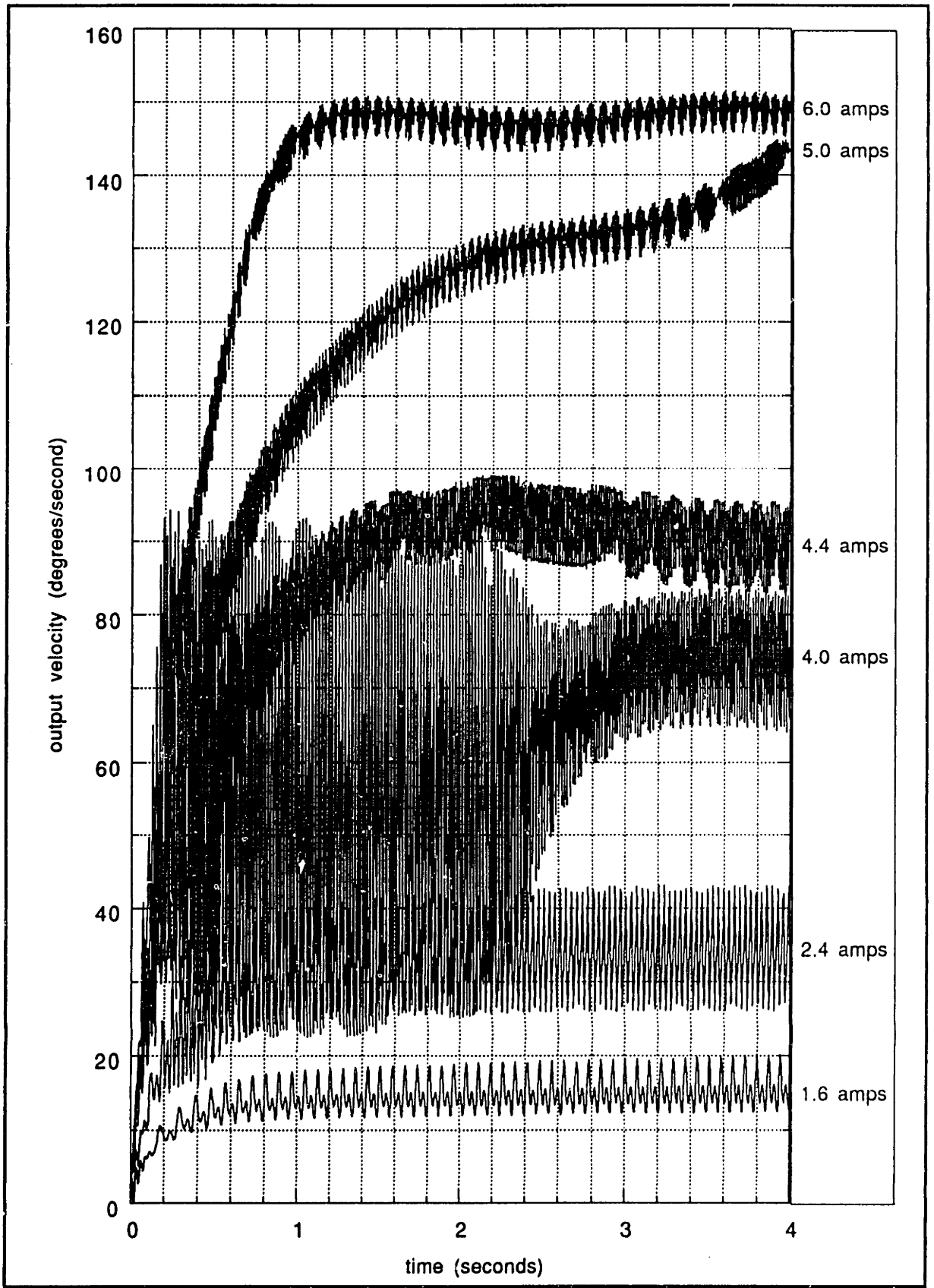

Figure F.1.5: Joint 1 output-velocity simulated step-responses

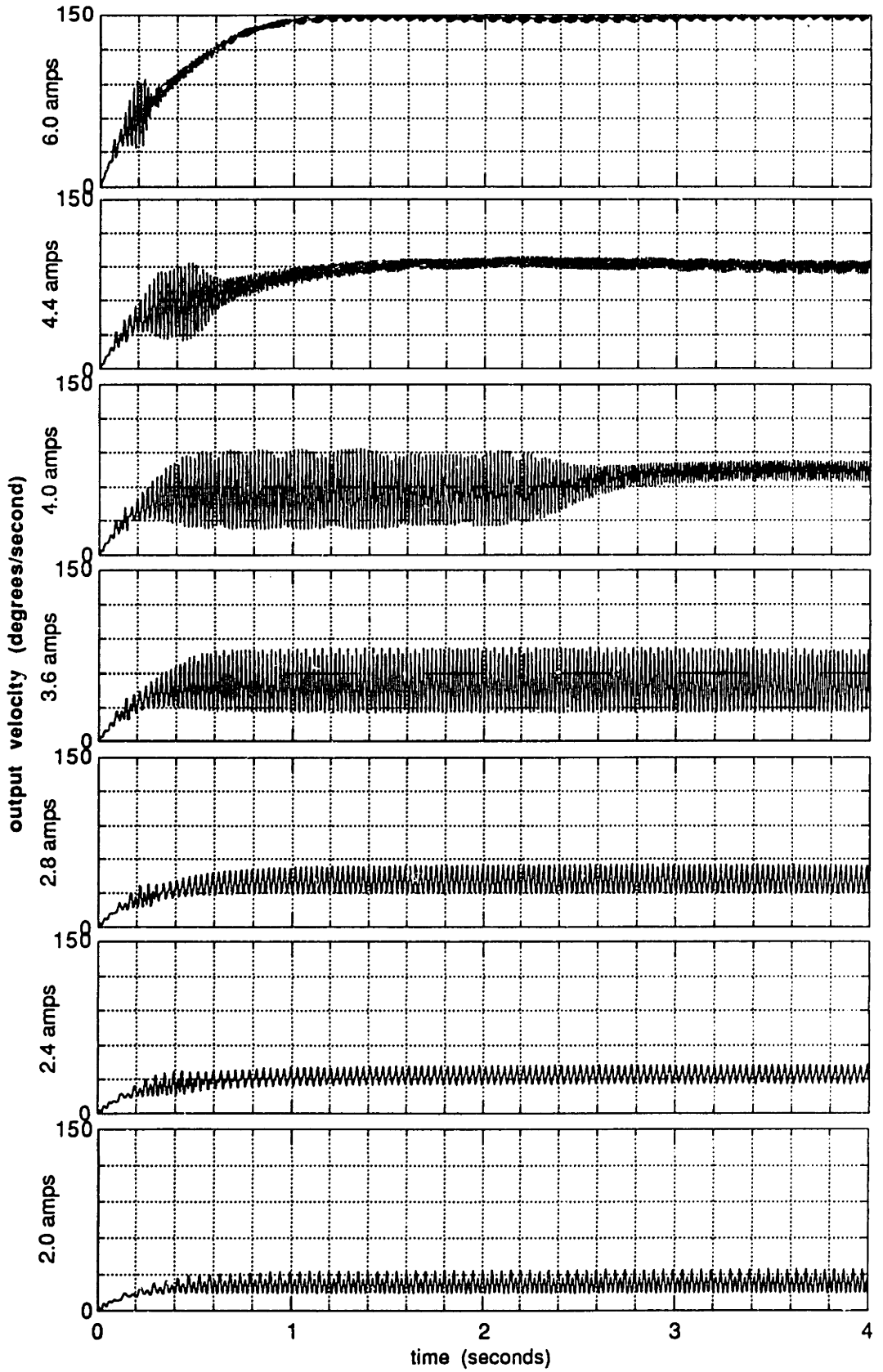

Figure F.1.6: Joint 1 output-velocity simulated step-responses

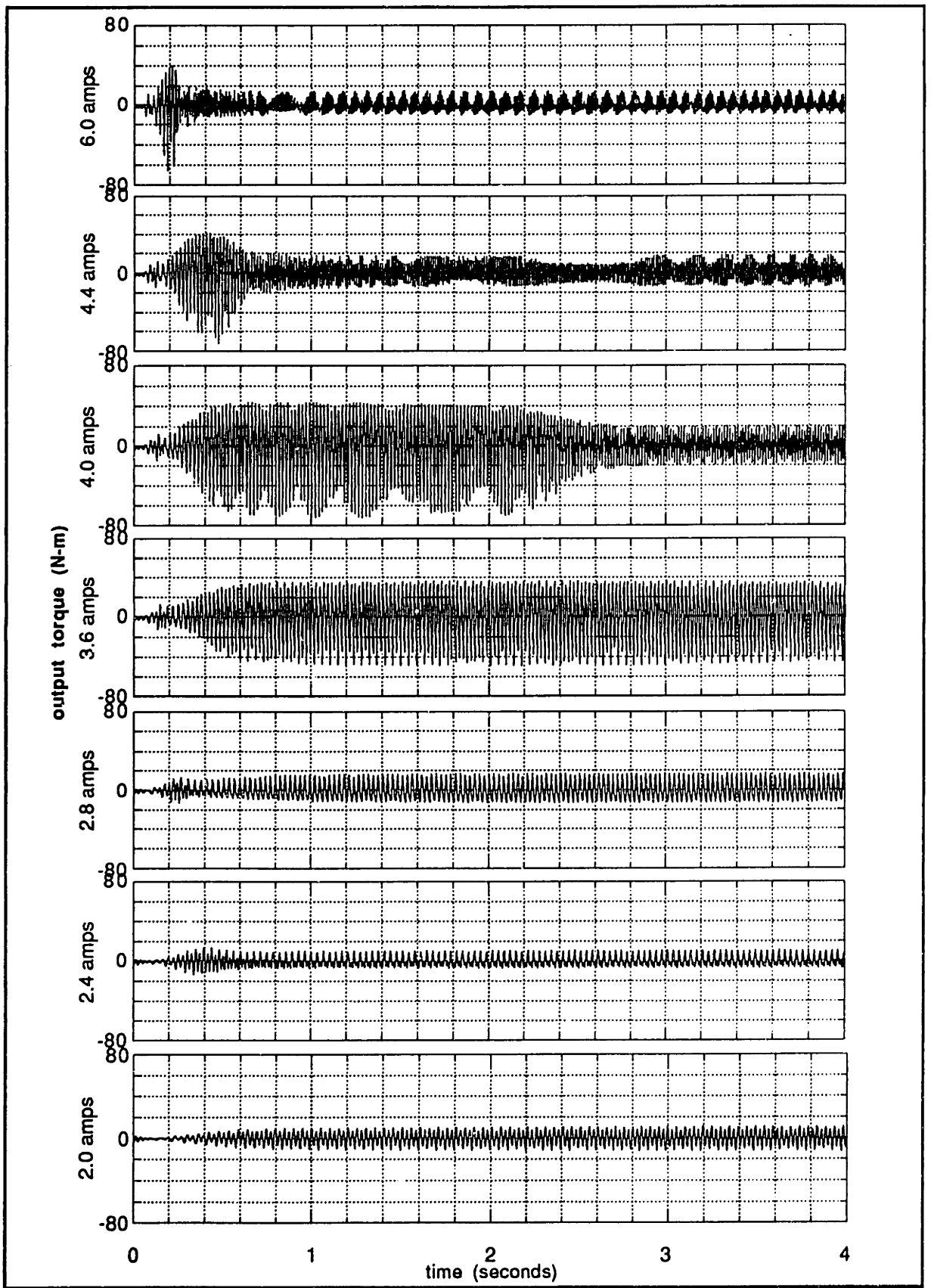

Figure F.1.7: Joint 1 output-torque simulated step-responses

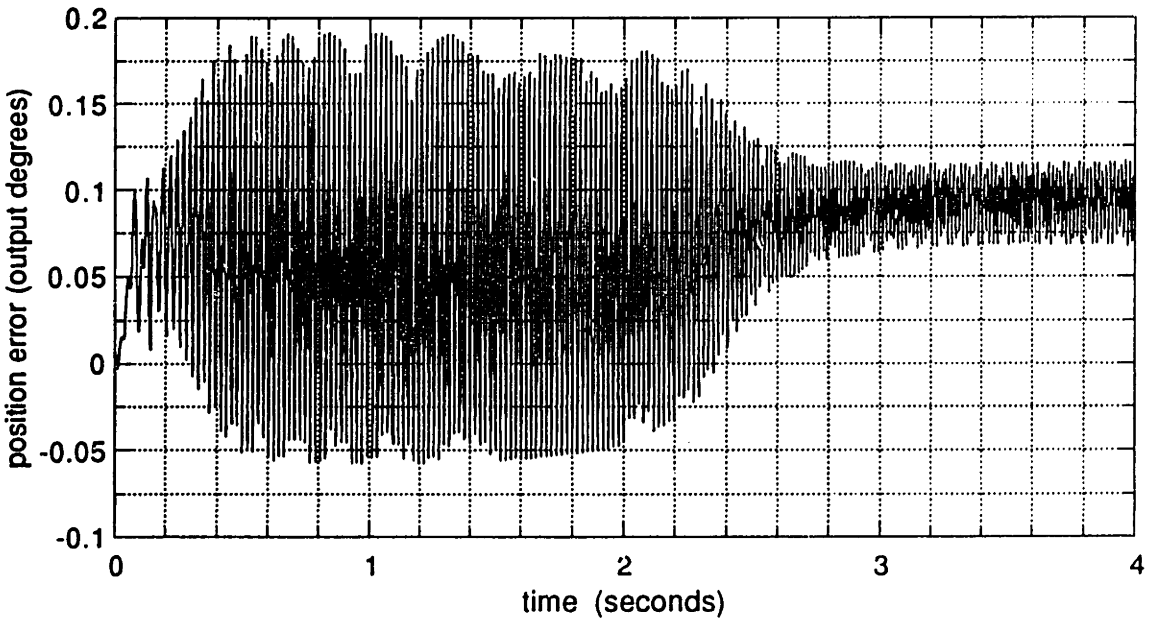

Figure F.1.8: Joint 1 simulated dynamic position error at 4.0 amps

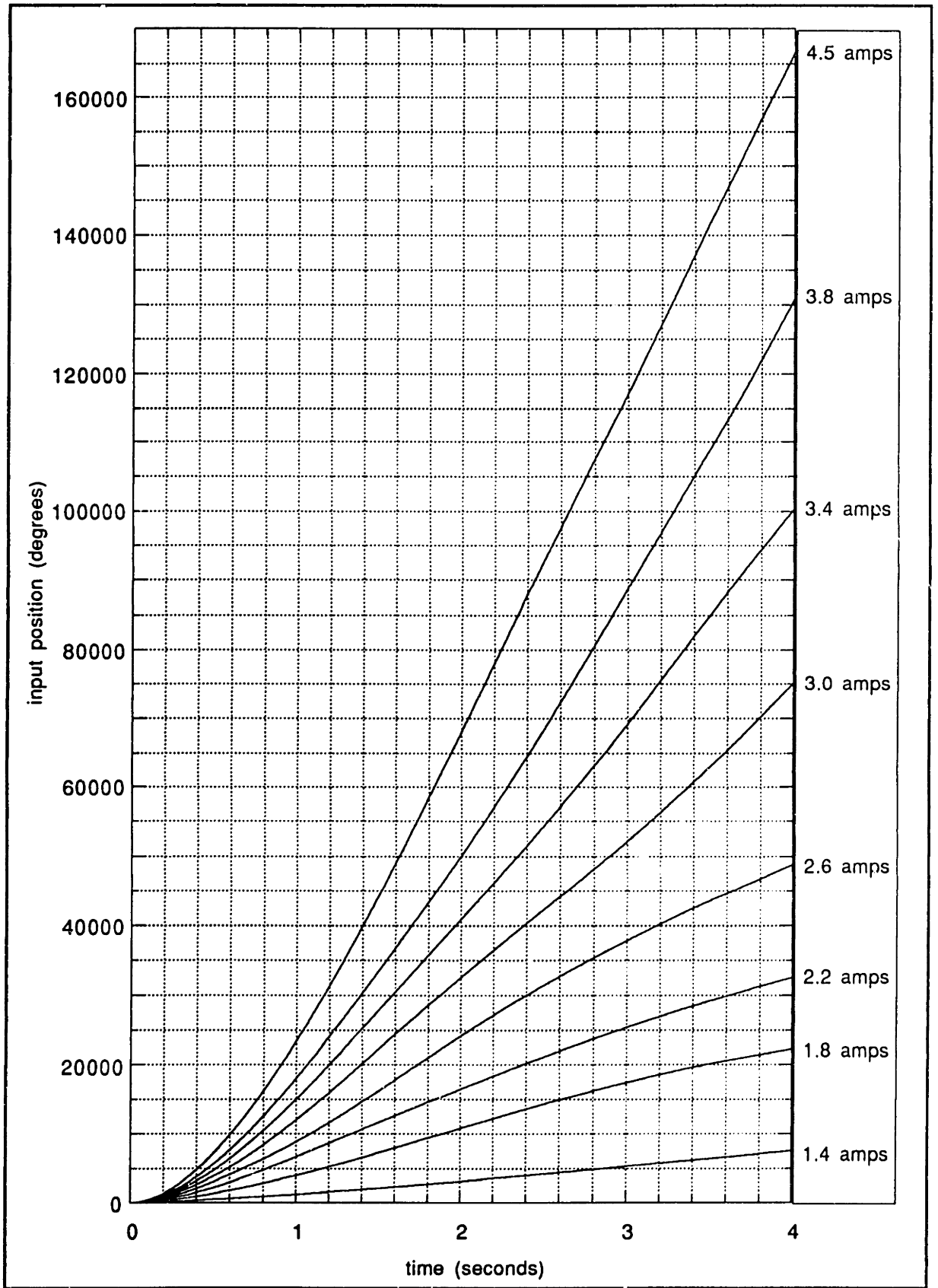

Figure F.2.1: Joint 2 input-position simulated step-responses

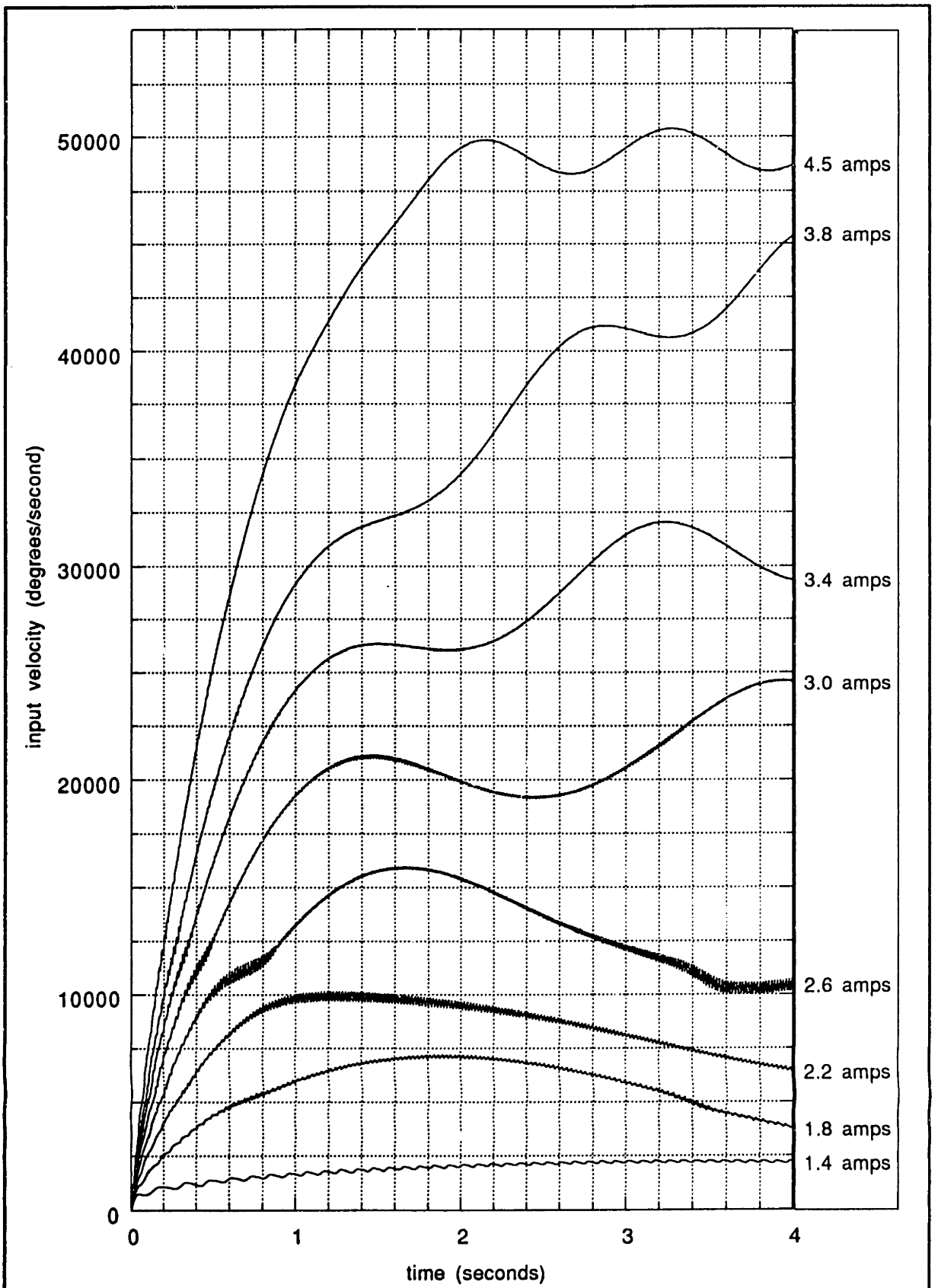

Figure F.2.2: Joint 2 input-velocity simulated step-responses

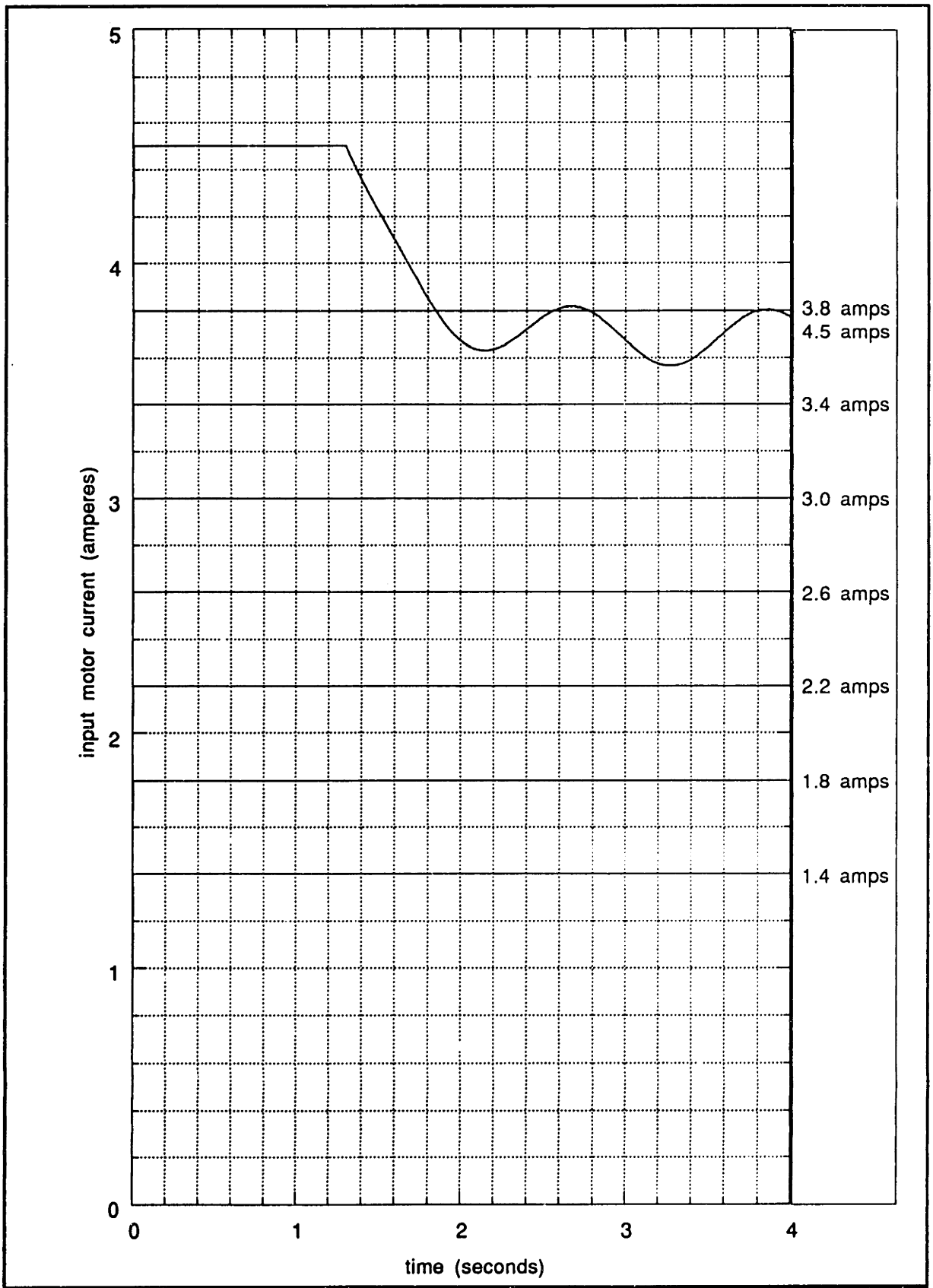

Figure F.2.3: Joint 2 input-current simulated step-responses

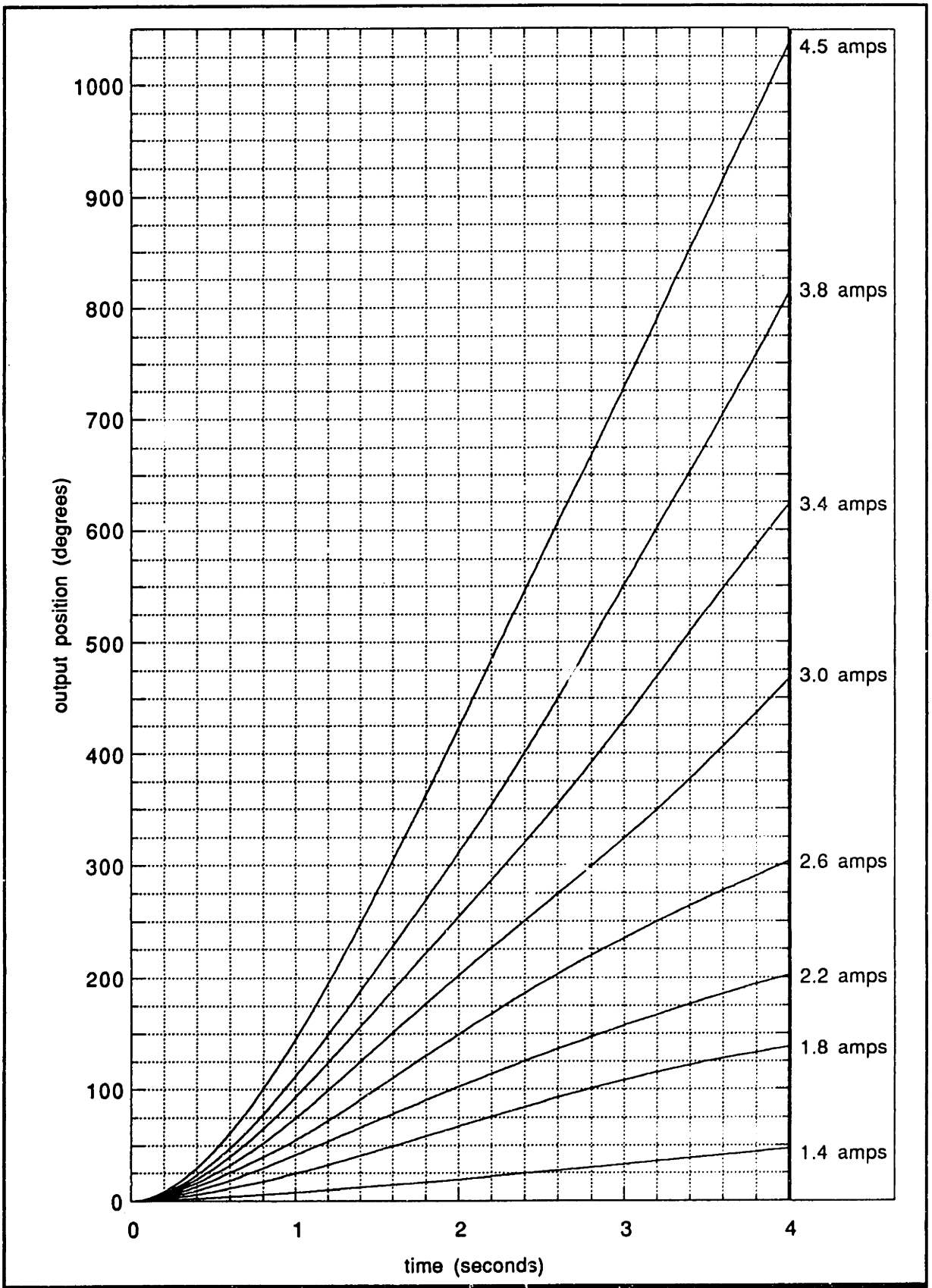

Figure F.2.4: Joint 2 output-position simulated step-responses

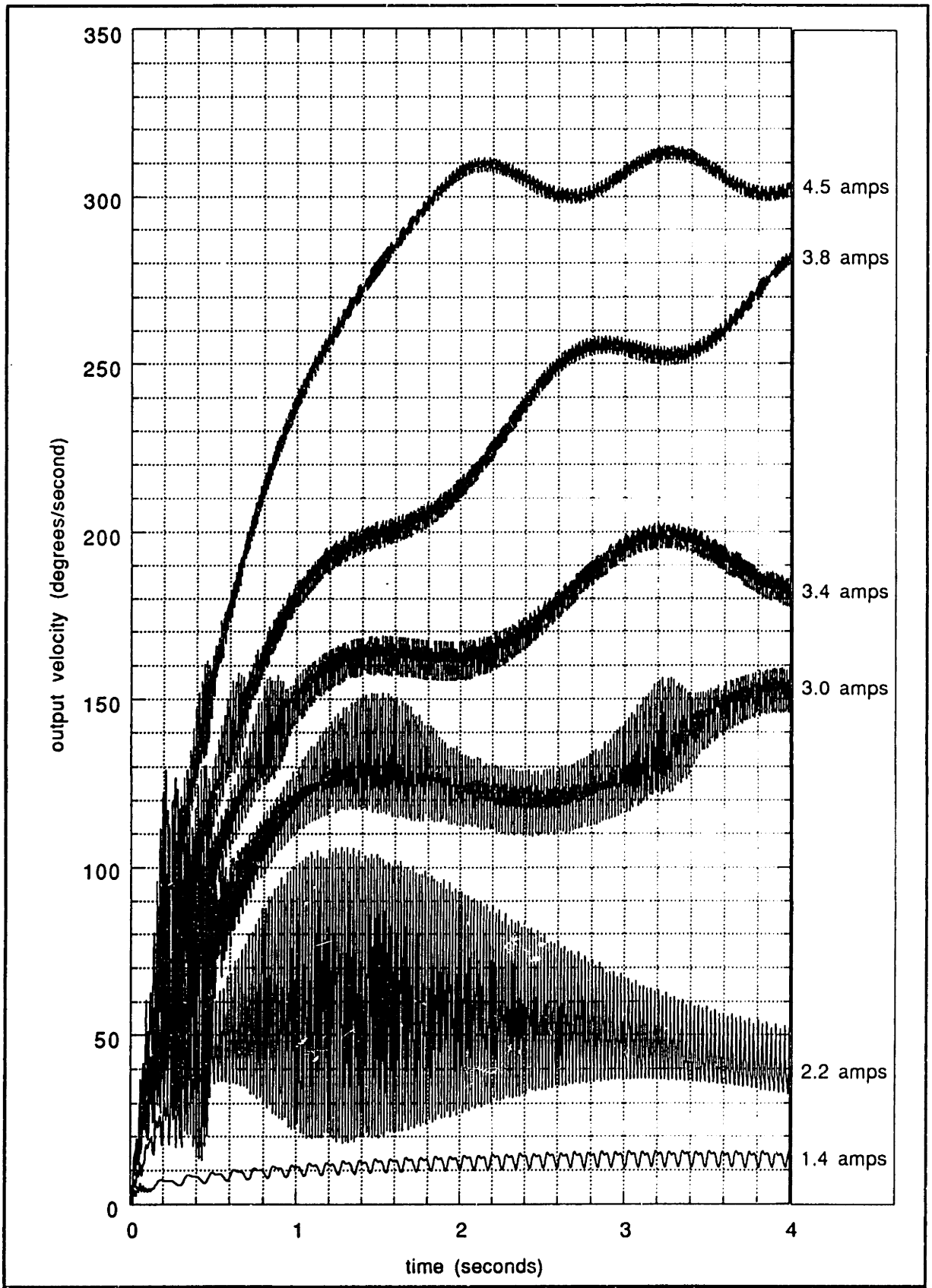

Figure F.2.5: Joint 2 output-velocity simulated step-responses

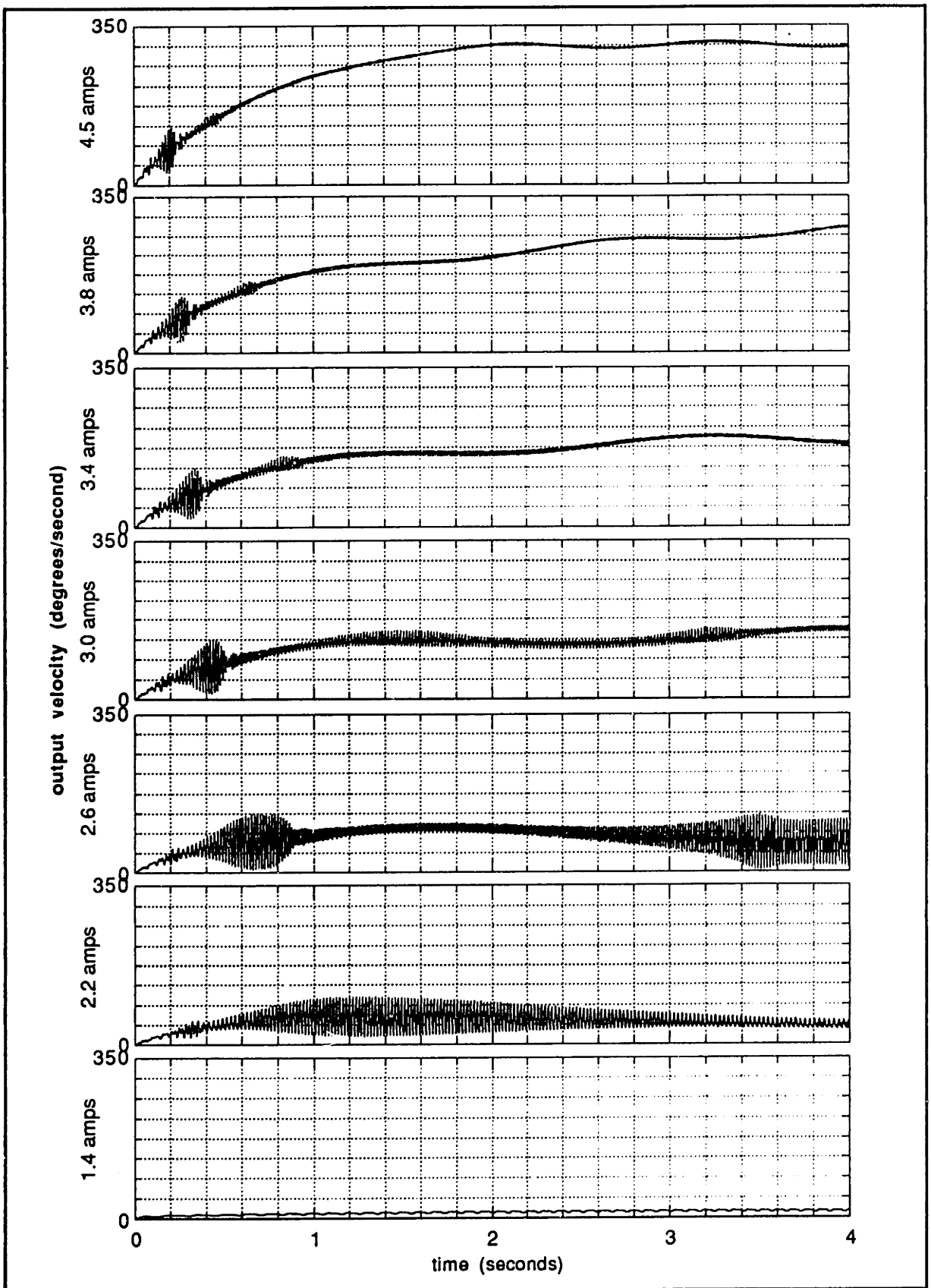

Figure F.2.6: Joint 2 output-velocity simulated step-responses

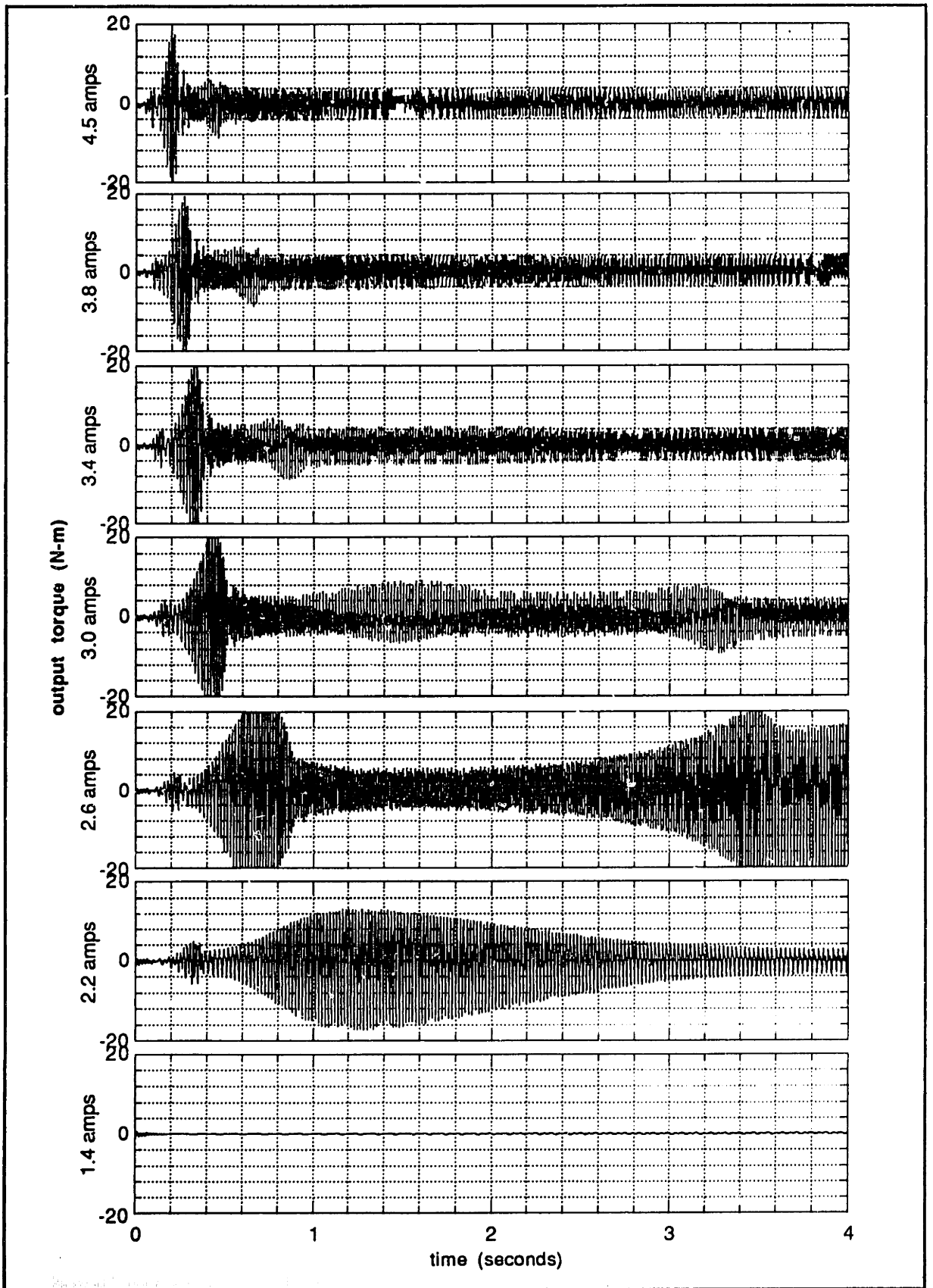

Figure F.2.7: Joint 2 output-torque simulated step-responses

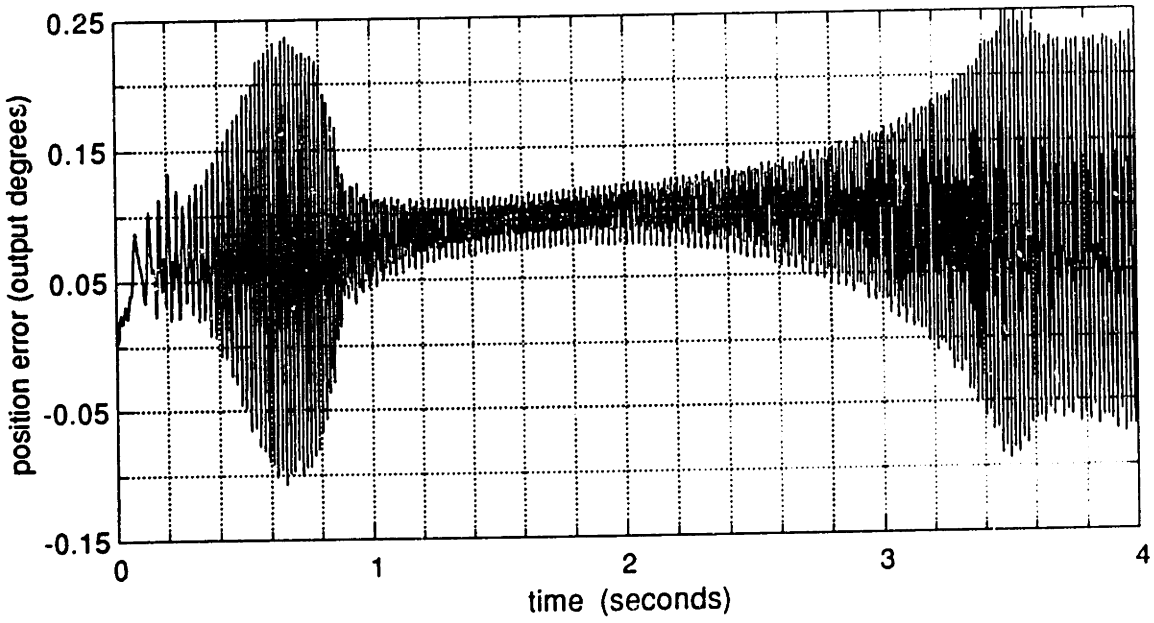

Figure F.2.8: Joint 2 simulated dynamic position-error at 2.6 amps

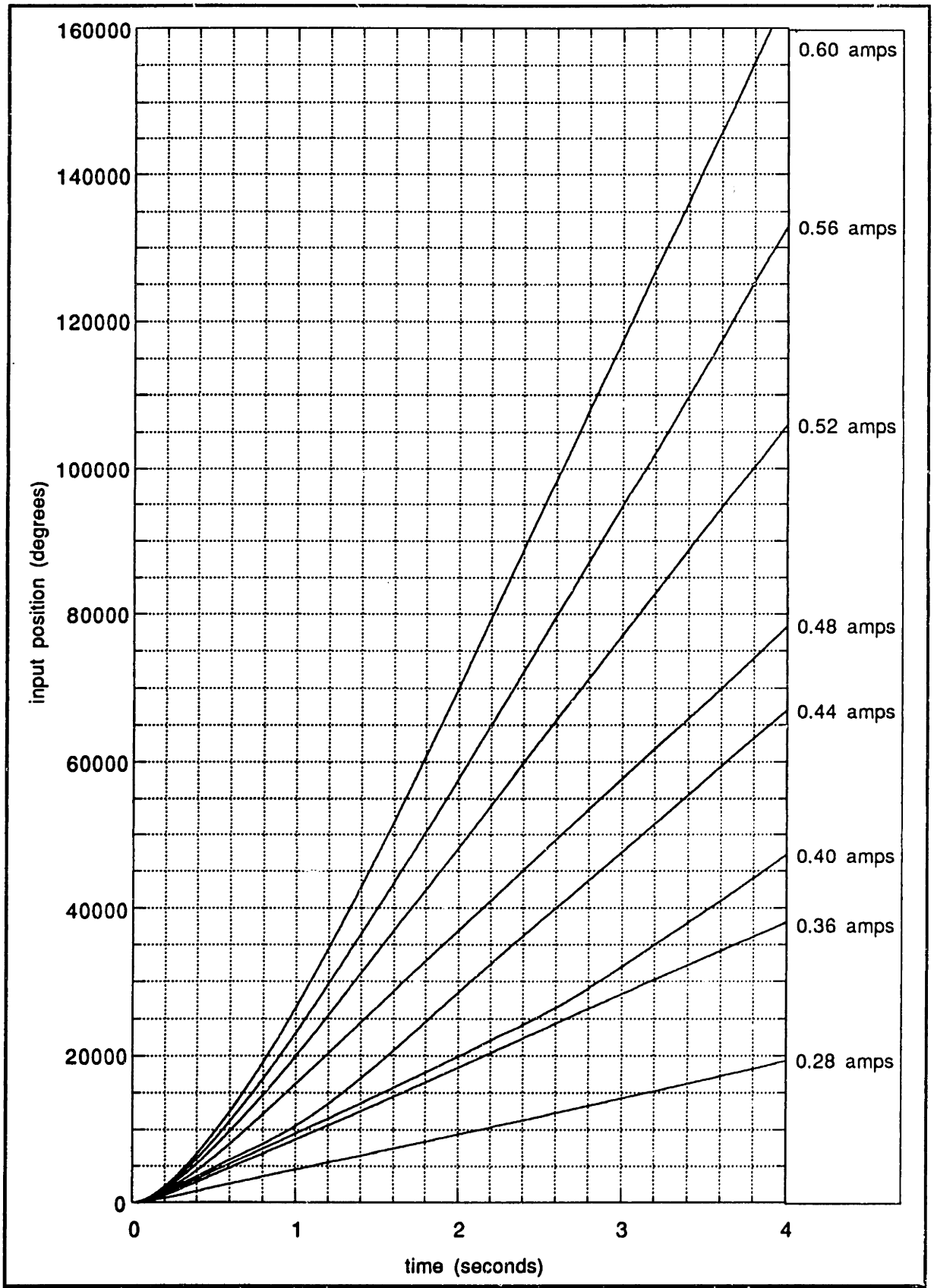

Figure F.3.1: Joint 3 input-position simulated step-responses

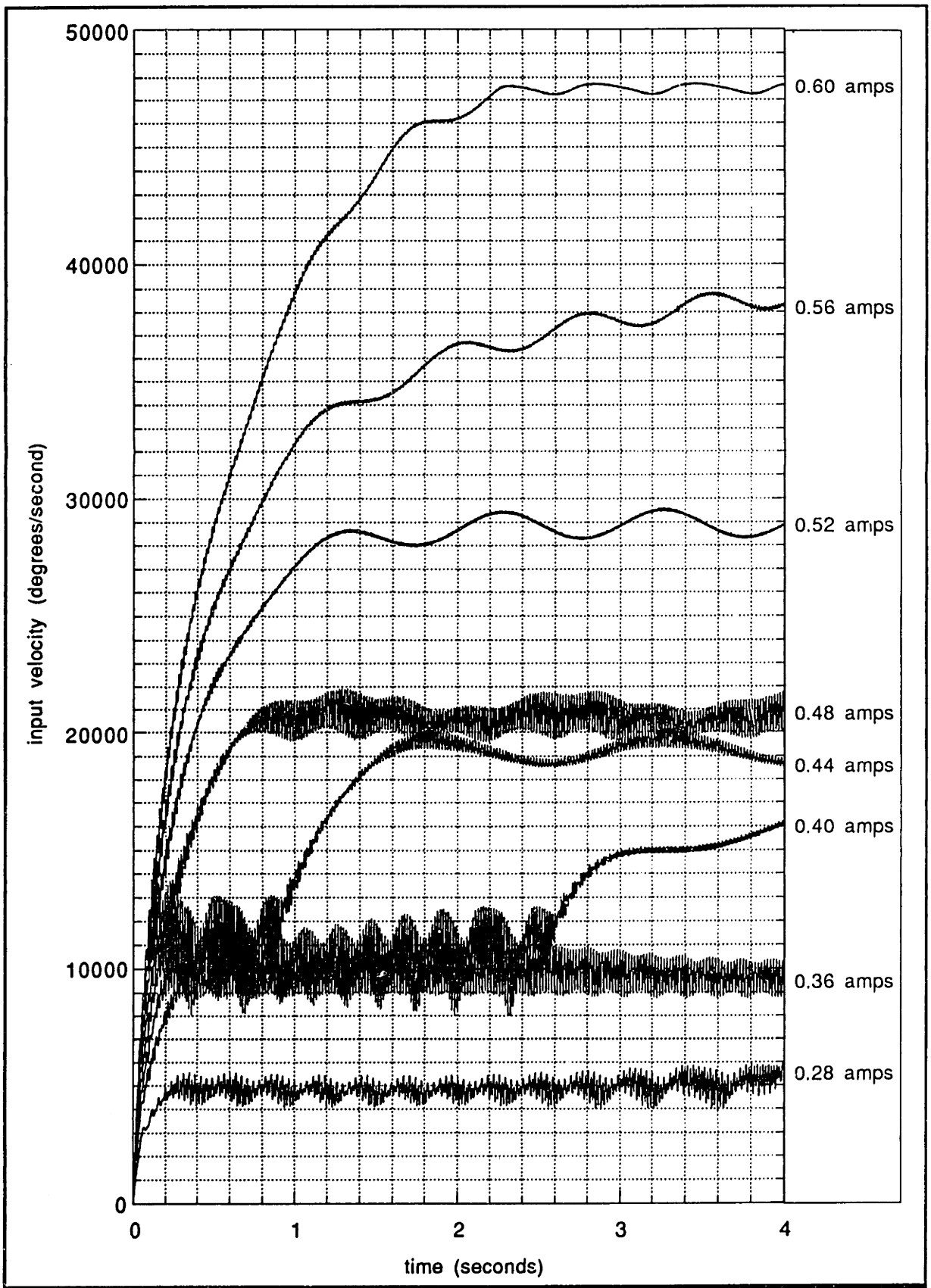

Figure F.3.2: Joint 3 input-velocity simulated step-responses

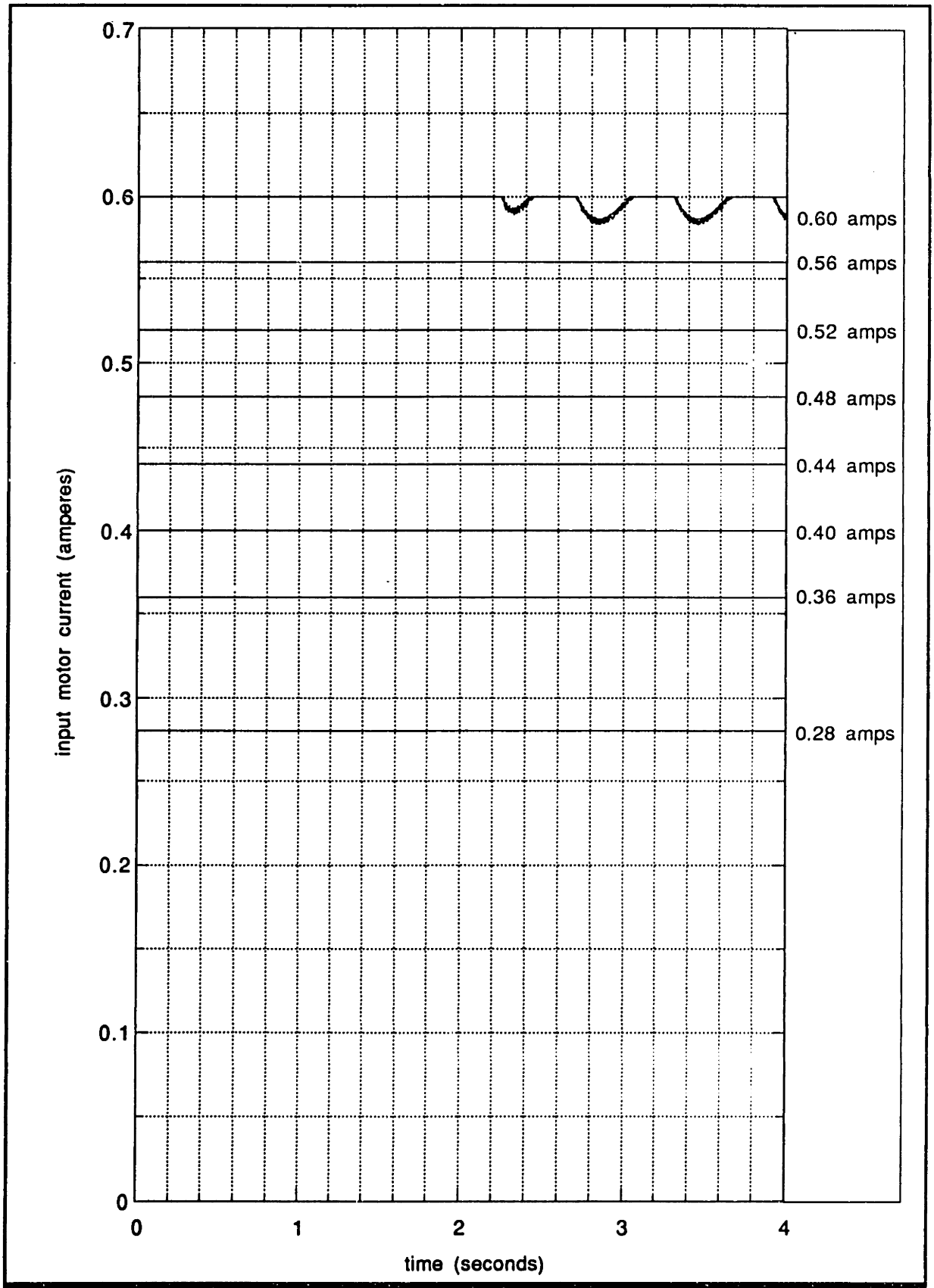

Figure F.3.3: Joint 3 input-current simulated step-responses

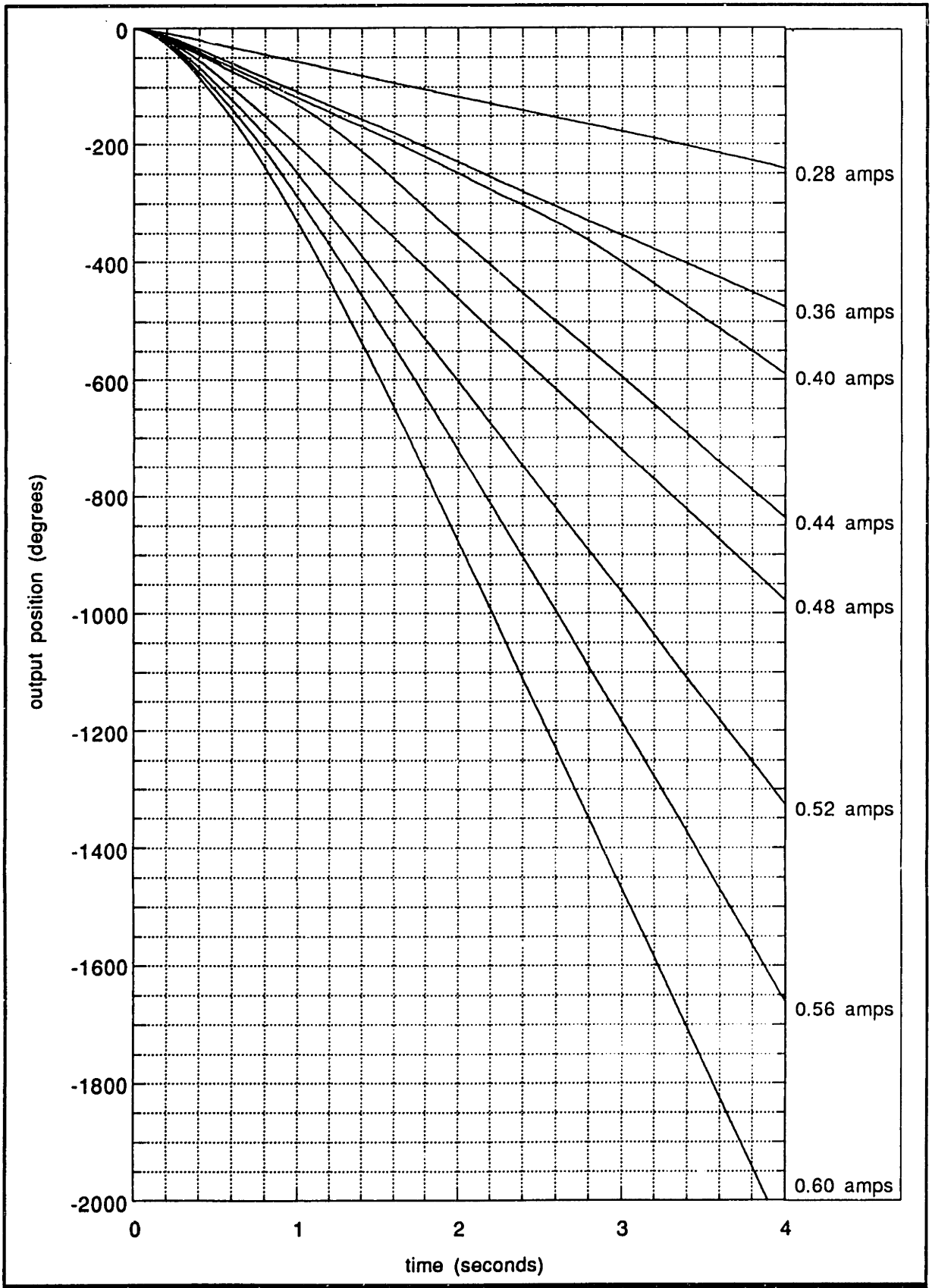

Figure F.3.4: Joint 3 output-position simulated step-responses.

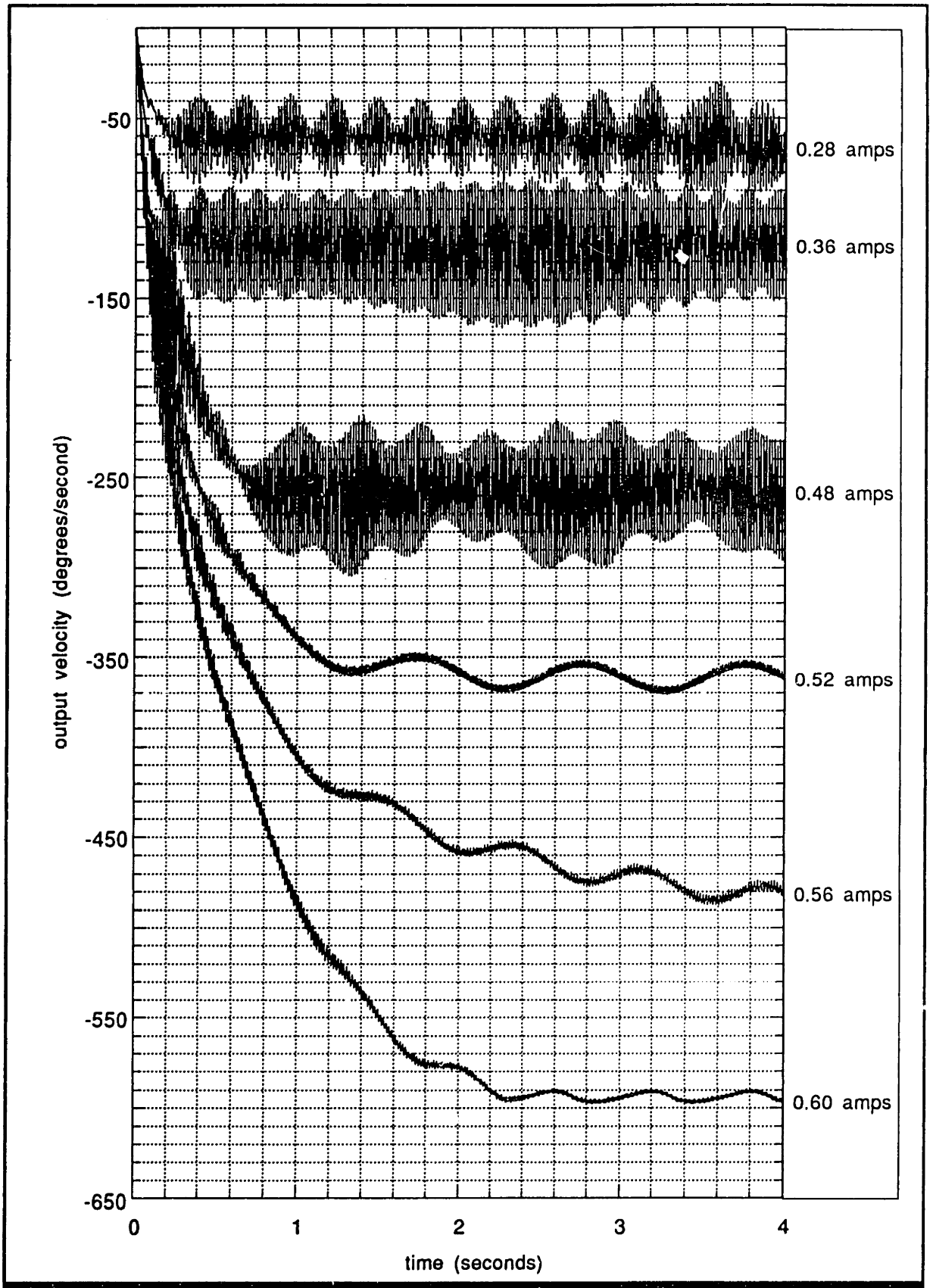

Figure F.3.5: Joint 3 output-velocity simulated step-responses

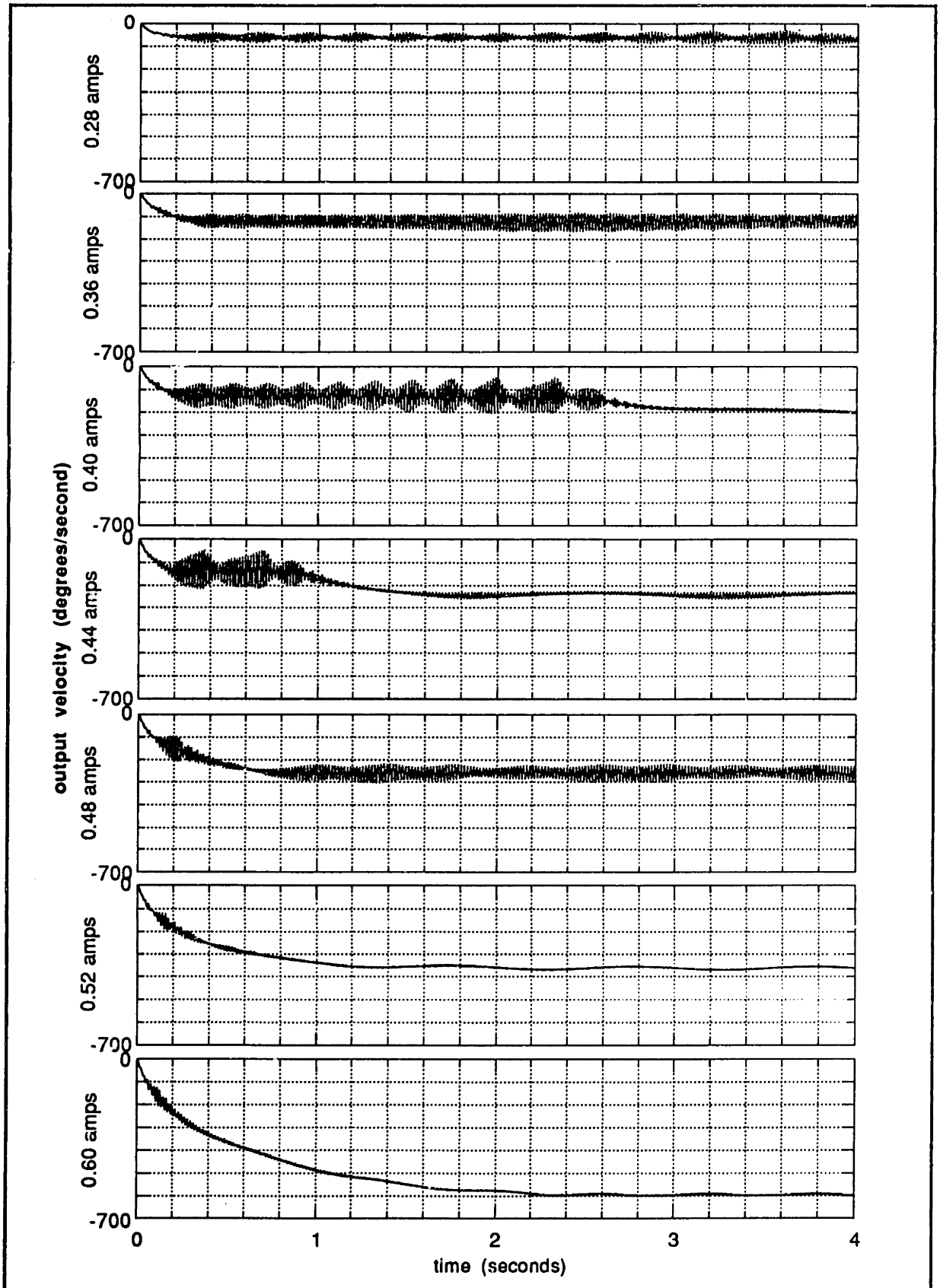

Figure F.3.6: Joint 3 output-velocity simulated step-responses

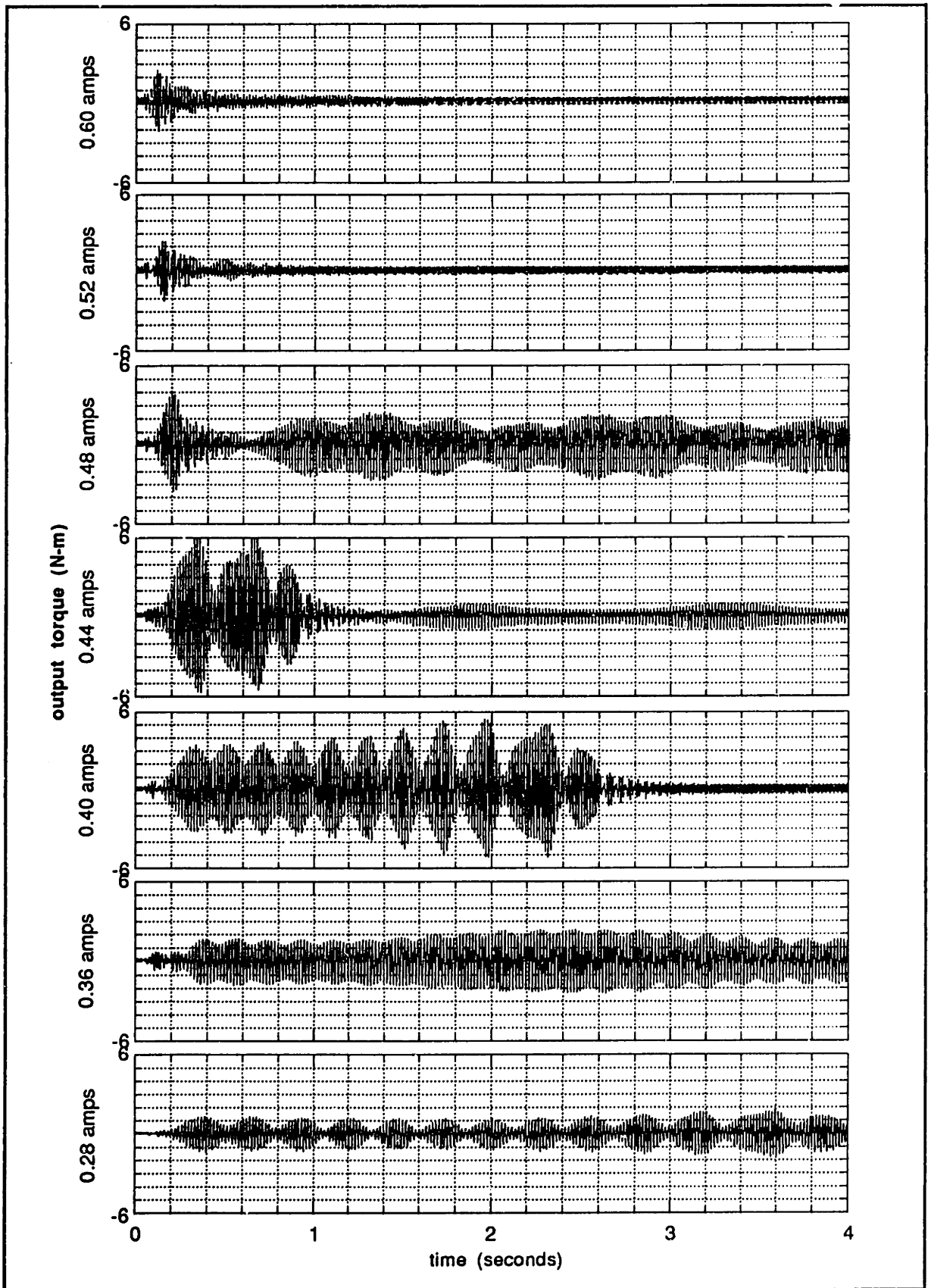

Figure F.3.7: Joint 3 output-torque simulated step-responses

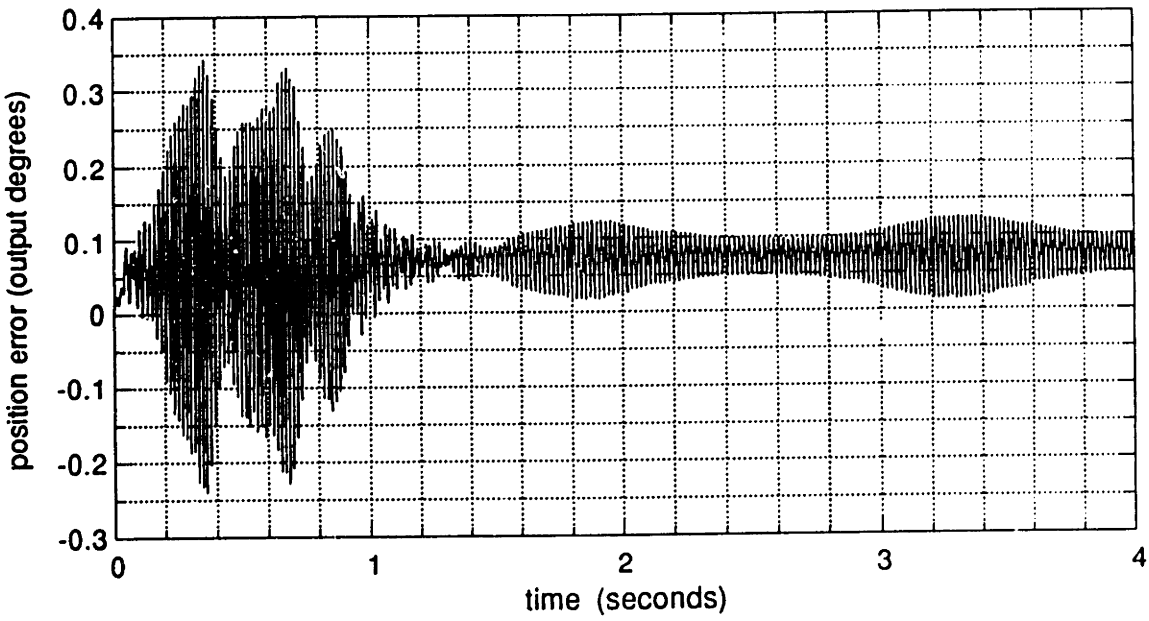

Figure F.3.8: Joint 3 simulated dynamic position error at 0.44 amps